

**SIMPLIFIED REMAINING SERVICE LIFE CALCULATION OF
ORTHOTROPIC STEEL DECKS AT ROAD BRIDGES AND
STRENGTHENING WITH CONCRETE**

**VEREINFACHTE RESTLEBENSDAUERBERECHNUNG VON
ORTHOTROPEN PLATTEN BEI STRASSENBRÜCKEN UND
VERSTÄRKUNG DURCH BETON**

Dissertation

Submitted at the
Faculty of Civil Engineering of the
Technical University Graz

from

Dipl.-Ing. Friedrich Novak

Primary Reviewer:

Univ.-Prof. Dipl.-Ing. Dr. techn. Harald UNTERWEGER

Secondary Reviewer:

Univ.-Prof. Dr.Ir. Johan Maljaars

TABLE OF CONTENTS

1. Introduction.....	1
1.1. Research activities in the past	1
1.1.1. <i>Simplified realistic fatigue load models on road bridges – historical development</i>	1
1.1.2. <i>Resistance models regarding to fatigue phenomena</i>	5
1.1.3. <i>Strengthening of existing road bridges with orthotropic steel decks</i>	7
1.2. Overview of this thesis	7
1.3. Objectives of this thesis.....	9
2. Orthotropic steel bridge decks – general and fatigue phenomena.....	10
2.1. General	10
2.2. Construction of orthotropic steel bridge decks.....	10
2.3. Historical development.....	13
2.3.1. <i>Orthotropic steel bridge deck with open longitudinal ribs</i>	13
2.3.2. <i>Orthotropic steel bridge deck with closed longitudinal ribs (trough ribs)</i>	15
2.3.3. <i>Representative orthotropic bridge decks</i>	18
2.4. Fatigue cracks within orthotropic steel bridge decks	19
2.4.1. <i>Overview of analysed notch details</i>	21
2.4.2. <i>Detail D1a: Welded connection of longitudinal rib to deck plate – Fatigue cracks in the deck plate</i>	22
2.4.3. <i>Detail D1b: Welded connection of longitudinal rib to deck plate – Fatigue cracks in the trough web</i>	26
2.4.4. <i>Detail D2: Welded connection of the longitudinal rib to the cross girder – Fatigue cracks in the longitudinal rib</i>	27
2.4.5. <i>Detail D3: Welded connection of the cross girder to the deck plate near a field connection – Fatigue cracks in the cross girder’s web</i>	29
2.5. Fatigue load models according to Eurocode 1	33
2.5.1. <i>Fatigue load model FLM 3 with one fictive vehicle and damage equivalent factors λ</i>	33
2.5.2. <i>Fatigue load models FLM 4, FLM 4* and FLM 2 with realistic vehicles</i>	35

2.6.	General approach of fatigue assessment according Eurocode.....	41
2.7.	S-N detail classification of the critical details	44
2.8.	Recommendations for fatigue assessment according to the IIW - documentation.....	46
2.9.	Constructional recommendations for orthotropic steel decks on road bridges according to the actual Eurocode	48
3.	Calculation of equivalent constant amplitude stress ranges $\Delta\sigma_e$ for orthotropic steel decks.....	50
3.1.	General concept of fatigue assessment at orthotropic steel decks	52
3.2.	Analysed representative steel decks	54
3.2.1.	<i>Model A: Orthotropic bridge deck with open longitudinal ribs.....</i>	<i>54</i>
3.2.2.	<i>Model B: Orthotropic bridge deck with trough longitudinal ribs and a cross girder spacing of 2m.....</i>	<i>60</i>
3.2.3.	<i>Model C: Orthotropic bridge deck with trough longitudinal ribs and cross girder spacing of 4m.....</i>	<i>67</i>
3.2.4.	<i>Model D: Orthotropic bridge deck with open longitudinal ribs – cross girder with bolted connections</i>	<i>74</i>
3.3.	Critical locations of the details with accurate load positions	79
3.3.1.	<i>Position of detail D1a and relevant lane position for maximum stresses.....</i>	<i>80</i>
3.3.2.	<i>Critical lane position for maximum stresses at detail D1b.....</i>	<i>84</i>
3.3.3.	<i>Position of detail D2 and relevant lane position for maximum stresses.....</i>	<i>84</i>
3.3.4.	<i>Lane and load/vehicle position for the maximum stresses at Detail D3.....</i>	<i>88</i>
3.4.	Simulation of heavy traffic crossings	100
3.4.1.	<i>Overview of the principal procedure</i>	<i>100</i>
3.4.2.	<i>Model A: Orthotropic bridge deck with open longitudinal ribs.....</i>	<i>102</i>
3.4.3.	<i>Model B: Orthotropic bridge deck with trough longitudinal ribs and cross girder spacing of 2m.....</i>	<i>114</i>
3.4.4.	<i>Model C: Orthotropic bridge deck with trough longitudinal ribs and cross girder spacing of 4m.....</i>	<i>122</i>

3.4.5.	<i>Model D: Orthotropic bridge deck with open longitudinal ribs – cross girder with field splices</i>	130
3.5.	Damage percentage of the individual vehicle types T1 to T5 for details D1 and D2.....	133
3.5.1.	<i>Detail D1a</i>	134
3.5.2.	<i>Detail D2</i>	138
3.5.3.	<i>Comparison of the damage percentages of the individual vehicle types</i>	142
4.	Influence of realistic axles geometries and lateral distribution of heavy vehicles	143
4.1.	Introduction	143
4.2.	Centric track configuration.....	144
4.3.	Realistic axle- and wheel geometries for lorry type T3.....	145
4.3.1.	<i>Axle/wheel type A</i>	147
4.3.2.	<i>Axle/wheel type B</i>	148
4.3.3.	<i>Axle/wheel type C</i>	149
4.3.4.	<i>Accurate realistic axle/wheel geometries based on Eurocode</i>	150
4.4.	Analysed frequency distributions for transverse lane position of the lorries	151
4.4.1.	<i>Frequency distribution LFT I - according to Eurocode</i>	151
4.4.2.	<i>Frequency distributions LFT II and LFT III - based on field measurements</i>	151
4.5.	Lateral influence lines	156
4.5.1.	<i>Model A</i>	156
4.5.2.	<i>Model B</i>	160
4.5.3.	<i>Model C</i>	165
4.6.	General Concept of considering realistic axle geometries and lateral distribution for Detail D1a and D2.....	170
4.7.	Modified general concept of considering realistic axle geometries and lateral distribution for Detail D1b	175
4.8.	Results of numerical calculations due to consideration of realistic axle geometries.....	182
4.8.1.	<i>Model A</i>	182

4.8.2.	<i>Model B</i>	187
4.8.3.	<i>Model C</i>	193
4.9.	Results of numerical calculations due to consideration of realistic axle geometries and lateral heavy traffic distribution	199
4.9.1.	<i>Model A</i>	199
4.9.2.	<i>Model B</i>	205
4.9.3.	<i>Model C</i>	217
4.10.	Comparison of the damage equivalent stress ranges $\Delta\sigma_e$	228
4.11.	Damage percentage of the individual vehicle types T1 to T5	231
4.11.1.	<i>Detail D1a</i>	232
4.11.2.	<i>Detail D2</i>	234
4.12.	Concluding Remarks for considering realistic axle geometries and lateral distribution of heavy vehicles	237
5.	Strengthening of orthotropic steel decks with a concrete plate	238
5.1.	Modified remaining service life calculation for strengthened structures	238
5.1.1.	<i>Project specific assumptions</i>	238
5.1.2.	<i>Remaining fatigue life for strengthened structures</i>	241
5.2.	Analysed FE-models for the strengthened orthotropic steel deck.....	243
5.2.1.	<i>Model E-1: Orthotropic bridge deck with open longitudinal ribs – including a concrete pavement (detailed mesh refinement in the steel structure)</i>	244
5.2.2.	<i>Model E-2: Orthotropic bridge deck with open longitudinal ribs – including a concrete pavement (detailed mesh refinement in the UHPFRC plate)</i>	247
5.2.3.	<i>Model F: Orthotropic bridge deck with open longitudinal ribs – cross girder with bolted connections – including a concrete pavement</i>	248
5.3.	Damage calculation before strengthening in detail D1a, D2, (D3)	249
5.3.1.	<i>General</i>	249
5.3.2.	<i>Detail D1a – Damage at the steel deck before strengthening</i>	249
5.3.3.	<i>Detail D2 – Damage at the steel deck before strengthening</i>	250
5.3.4.	<i>Detail D3 – Simplified damage at the steel deck before strengthening</i>	251

5.4.	Stress spectra and stress level after strengthening in detail D1a, D2, (D3).....	252
5.4.1.	<i>Detail D1a – stress level after strengthening.....</i>	<i>252</i>
5.4.2.	<i>Detail D2 – stress spectra and stress level after strengthening.....</i>	<i>254</i>
5.4.3.	<i>Stress reduction level of detail D3.....</i>	<i>261</i>
5.5.	Fatigue life predictions including strengthening.....	264
5.5.1.	<i>Detail D1a.....</i>	<i>264</i>
5.5.2.	<i>Detail D2.....</i>	<i>266</i>
5.5.3.	<i>Detail D3.....</i>	<i>268</i>
5.6.	Full scale tests.....	269
5.6.1.	<i>General.....</i>	<i>269</i>
5.6.2.	<i>Geometrical dimensions, production and position of the strain gauges.....</i>	<i>270</i>
5.6.3.	<i>Measuring instrumentation and testing load sequence.....</i>	<i>277</i>
5.6.4.	<i>Numerical stresses for steel deck with asphalt pavement – reference values (before strengthening).....</i>	<i>283</i>
5.6.5.	<i>Steel deck – results and evaluation of the measurements.....</i>	<i>285</i>
5.6.6.	<i>Concrete plate – results and evaluation of the measurements.....</i>	<i>304</i>
5.6.7.	<i>Effective Young’s Modulus of the concrete $E_{c,eff}$ based on steel deck measurements at the full scale tests.....</i>	<i>310</i>
5.6.8.	<i>Concluding Remarks regarding to the full scale tests.....</i>	<i>318</i>
6.	Conclusions and Outlook.....	319
	References.....	322
	Annex A – Simulation of heavy traffic crossings.....	A-1

ACKNOWLEDGEMENTS / DANKSAGUNG

Ein großes herzliches Dankeschön ergeht an meinen Betreuer Univ.-Prof. Dipl.-Ing. Dr. techn. Harald Unterweger für seine umfassende Unterstützung und konstruktive Kritik. Ich bedanke mich dafür, dass er an die Arbeit und an meine Fähigkeiten zur Umsetzung geglaubt hat und sehr viel seiner Zeit investiert hat.

Vielen Dank an Univ.-Prof. Dr.Ir. Johan Maljaars für die investierte Zeit zur Begutachtung meiner Arbeit und für die Korrekturen, welche zu einer Verbesserung beitrugen.

Thanks' to Univ.-Prof. Dr.Ir. Johan Maljaars for your invested time of reading, commenting and correcting my work which surely improved this thesis.

Vielen Dank an Univ.-Prof. Dr.-Ing. habil. Viet Tue Nguyen und Priv.-Doz. Dipl.-Ing. Dr.techn. Bernhard Freytag für die konstruktive Zusammenarbeit im gemeinsamen Forschungsprojekt. Weiters vielen Dank an Amtsdirektor Ing. Uwe Fülöp für die messtechnische Betreuung am Großversuch und danke an die Kollegen des LKI und IBB, welche ebenfalls mitgewirkt haben.

Vielen Dank an all meine Arbeitskollegen für die schöne Zeit am Institut. Insbesondere bedanke ich mich bei Sarah Loschan, Andreas Schörghofer, Alexander Ecker und Andreas Kampleitner für ihr ehrliches Feedback und die Anregungen, deren Hinweise die Arbeit erst auf den richtigen Kurs brachten.

Vielen Dank an meinen guten Freund Joshua Tapley für all die anregenden und konstruktiven Gespräche und vor Allem für die umfassenden grammatikalischen Korrekturen der Arbeit.

Vielen Dank an meine ganze Familie für all den Rückhalt und die Unterstützung. Danke liebe Mama, dass du immer an mich glaubst und immer für mich da bist. Besonders bedanke ich mich bei meiner Frau Jasmin und meinen beiden Kindern Peter und Marlene für all die seelische und mentale Unterstützung. Durch euch bekommt alles in meinem Leben sowie auch diese Arbeit eine besondere Bedeutung. Danke Jasmin, dass du immer ein offenes Ohr für mich hast, mir mit Rat zur Seite stehst und mich in Allem vorantreibst.

ABSTRACT / SUMMARY

Orthotropic steel bridge decks for slender and long spanned girder bridges were frequently built in the 60ties and 70ties in Europe, especially in Germany and Austria. In the design of such bridge decks, only the ultimate load carrying capacity was considered, without taking fatigue aspects into account. Due to the dramatic increase in heavy traffic on the European road network, often the calculated remaining fatigue life is exhausted, after only 50 years of service life.

Within this dissertation the critical details were analysed for four different models to include a wide range of bridge deck geometries from 1960 until now. A steel bridge deck with flat steel longitudinal ribs, two decks with longitudinal trough ribs and a local model of a cross girder with bolted joints of web and bottom flange were taken into account. In summary, three significant notch details were analysed. Detail D1 represents the welded connection of the longitudinal rib to the deck plate, detail D2 is the welded connection of the longitudinal rib to the cross girder and detail D3 is the welded connection of the cross girder's web to the deck plate near the bolted joint. Detail D1 was split into detail D1a, where the stresses at the bottom of the deck plate were considered and detail D1b, where the stresses at the outer surface of the trough web were taken into account.

First, a heavy traffic simulation was performed using finite element models of the steel decks and took the structural stress concept with its recommendations referring to the finite element mesh into account. The beneficial effect of an increased wheel contact area due to the asphalt layer was also taken into consideration. The current fatigue load model FLM 4 from the Eurocode [1] with its five lorry types and three different axle types was applied, and the gross weight of each lorry type was also adapted to "weigh-in-motion" measurements on an Austrian highway bridge. The wheel loads were in general applied directly above the studied details and were located centrally above the mid-axis of the longitudinal rib's web. A lateral shift of the individual lorries, in transverse bridge direction within the lane, was not considered in this first step, which can be seen as the reference with a central track configuration of all axle/wheel types. Additionally, the damage percentage of each lorry type from FLM 4 was calculated for the details and lorry type T3, the articulated lorry causes maximum damage in all details.

Geometric measurements for the lorry type T3 showed that the axle geometry of the driving axle does not correspond with the simplified model assumptions [48]. Therefore, in a second step, the axle geometry for this lorry type T3 was improved. Also, a central track configuration for all vehicles is not realistic. Therefore, in a third step, simulations under consideration of heavy vehicle

driving characteristics with realistic axle geometries were performed. The results, related to the damage equivalent constant amplitude stress ranges $\Delta\sigma_{e,i}$, showed a positive effect on the details D1a and D2, the welded connection between the deck plate and the longitudinal rib. For detail D1b, the consideration of these effects is essential to calculate appropriate results for fatigue assessment.

Furthermore, extensive numerical studies were performed for the strengthening solution of an orthotropic deck with flat longitudinal ribs with an Ultra High Performance Concrete (UHPC) layer, which replaced the asphalt. The challenge was to increase the service life of such orthotropic bridge decks to at least 50 years after strengthening. The research activities were based on a very slender orthotropic deck, with a deck plate slenderness of $e_{LR}/t_{DP} = 36$. Two significant details for fatigue of such a representative bridge deck with flat longitudinal ribs were analysed, detail D1a and D2. The finite element model was extended with the UHPC layer to determine the stress reduction factors in the details D1a and D2 after strengthening. The concrete cracking was firstly conservatively considered with an effective Young's Modulus $E_{c,eff} = E_c/4$. Based on the numerical simulations, at least 50 years service life can be estimated with an 80 mm thick UHPC-pavement for both details. Based on these studies full scale tests on an orthotropic deck specimen were done, including overload effects (increased axle loads) and severe temperature effects (simulation of a cold rain event on a hot summer day) to stimulate concrete cracking. The full scale tests together with the numerical studies showed excellent results for the remaining fatigue life of an orthotropic deck with flat longitudinal ribs.

Finally, numerical studies based on the full scale tests were carried out to derive an appropriate effective Young's Modulus for the concrete in order to determine an accurate stress level within the steel deck.

PRELIMINARY REMARKS

At the beginning this PhD thesis needs some comments and information about some simplified assumptions based on a practical engineering approach, which are perhaps not expected in a PhD work.

a.) Simplified load model and numerical model of the bridge deck

The basis of the calculation of the remaining service life is a simulation of the heavy traffic (crossing of the individual lorries), to get the stress spectra in the relevant details of the bridge deck and the corresponding fatigue damage. The aims in this work are simple models, which are easy to apply in design office. Therefore, fatigue load model FLM 4 of the Eurocode EN 1991-2 [1] was chosen as a basis and the numerical model of the bridge deck includes only the steel deck without asphalt layer, but with the application of modified, increased wheel patches. For the practical application also the assumption was made, that all individual lorries cross the bridge in a central position within each lane (no horizontal shift in transverse bridge direction).

b.) Consequences of these simplifications

It is clear that with the studied simplified models, also with some improvements (e. g. including the scatter of the lorry position in transverse bridge direction), no accurate assessment of the fatigue damage and the remaining service life of the orthotropic deck is possible. That means that for practical applications always strain measurements at the relevant details under service are necessary to verify or also to calibrate the numerical model for the simulation of the heavy vehicles (comparison of measured and calculated stress spectra). This procedure is necessary to consider also the effects of: i) dynamic increase of static axle loads, ii) other lorry types and overloads, iii) real effect of the asphalt layer to the stresses in the steel deck.

Therefore, also the presented reduced fatigue load model FLM 4*, that is based on recent weigh in motion measurements on highways in Austria, is only valid for the representation of the traffic in the past and for considering bridges directly on this route.

c.) Fatigue assessment of selected details – assumption of the fatigue strength

For the studied orthotropic bridge deck with open longitudinal ribs at all assessed details, a crack in front of the weld toe was assumed. For detail D2 (see Figure 9.a), this assumption was verified in fatigue tests [2]. Also for detail D3 (see Figure 20), this crack type was detected [3]. For detail D1, no cracks of this type were observed, but the danger of a not studied root failure seems not critical (see Figure 13).

For all three studied details the geometric stress approach (“hot spot stress”) was applied, with a fatigue strength based on the Eurocode EN 1993-1-9 [4].

For the studied orthotropic bridge decks with closed longitudinal ribs, also the geometrical stress approach was applied. This means that also only cracks at the weld toe were considered here. For detail D1a and D1b (see Figure 14 and Figure 15), cracks at the weld root are expected in practice, leading to a reduced fatigue strength. The overestimation of the fatigue strength of detail D1 for closed longitudinal stiffeners within this work is acceptable, because the strengthening of this bridge deck type was not analysed. The fatigue assessment was limited to the analyses of the damage parts of the individual lorry types and the change of the fatigue damage if the position of the lorries in transverse direction is not fixed to the centre of the lane. In both studies, the effect of a reduced fatigue strength and a different position (weld toe instead of weld root) seems very small.

d.) Effect of the strengthening of the orthotropic bridge deck with concrete

This study was limited to the orthotropic bridge deck with open longitudinal stiffeners, where the fatigue strength and the crack type were assumed in an appropriate way. To show the beneficial stress reduction at the strengthened bridge deck, the comparison with a bridge deck with asphalt layer was done (reference values). Here, the simplified model was used again, based on numerical calculations for the full scale test (see Section 5.6) with the steel deck only, but including the increased wheel patch area of the wheels (representing a hot summer day with limited beneficial effect of the asphalt layer).

e.) Assessment of fatigue damage for different details – assumptions for critical positions on the deck and specification of the lane position in transverse direction

e.1.) For detail D1 and D2 (see Figure 9) the stress influence lines in transverse direction of the bridge are very short (e. g. Figure 146, Figure 148 for the deck with open longitudinal ribs; Figure 151, Figure 152, Figure 154 for closed longitudinal ribs) and therefore only 1 lane must be considered.

For the bridge deck with open longitudinal ribs (see Figure 9.a), the critical points on the bridge deck for detail D1 and D2 were chosen for detailed analyses of the fatigue damage. The reference position of the lane, with central position of each lorry, was chosen as the worst condition, directly above the longitudinal rib axis (see Figure 68).

For the bridge deck with closed longitudinal ribs (see Figure 9.b), the assumptions were not modified (see Figure 68). Therefore, the reference lane position and the studied detail position on the deck is sometimes not the worst one. Nevertheless, the calculated effect of the variation of the lorry position in transverse bridge direction to the equivalent stress range and the analyses of the individual damage parts of each lorry type should be nearly the same.

e.2.) Only for detail D3 (see Figure 20), the lorry crossings on different lanes have an important influence to the fatigue damage. For the analyses, the lane positions of an existing bridge structure were selected

(see Figure 19). Only the two lanes within the two main girders were considered. No detailed interaction of both lanes was simulated, because the lorry crossings in only one lane showed insufficient remaining fatigue life. For this detail the strengthening effect due to the concrete layer (reduction of the stress cycles) was studied only in a preliminary numerical analysis, because no test data was available for this detail to calibrate the numerical model.

f.) Calculation of the fatigue damage and assumed fatigue limit $\Delta\sigma_L$

The calculation of the fatigue damage was done in a simplified manner, based on the Eurocode-rules of EN 1993-1-9, including the reduced damage of stress cycles below the fatigue limit $\Delta\sigma_D$ at the beginning of the service life (see Figure 31). If, at the time of strengthening of the orthotropic deck, the numerical analyses (after calibration based on measured stress spectra) shows no further remaining fatigue life, but no cracks can be found at the critical details, only a simplified approach based on EN 1993-1-9 was considered (see Concept 2 in Section 5.1.2.2, Figure 235). After strengthening, the maximum occurring stress cycles must be lower than the fatigue limit $\Delta\sigma_L$. This engineering assumption, based on design standards only, needs further scientific research in the future.

Within this work, no information for appropriate safety factors γ_M are suggested. This value should also be chosen based on the available traffic data of the past for the analysed bridge. Due to the fact that the suggested numerical simulation model always needs measurements of stress spectra for a calibration and validation, values of $\gamma_M = 1.0$ are also possible. For the verification of the strengthening, higher values for the factor γ_M are suggested due to the uncertainties of the heavy traffic developments in the future.

1. Introduction

1.1. Research activities in the past

1.1.1. Simplified realistic fatigue load models on road bridges – historical development

In the field of civil engineering, the critical load cases with its appropriate load levels are usually applied as static loads that causes maximum stresses. Within the fatigue assessment this basic concept delivers insufficient results and therefore a rated summation of the damages due to the loads during the whole life cycle is necessary. The demanded stresses in the very local notch details have to be determined as realistic linear elastic stresses and therefore the local plastifications cannot be assumed anymore.

For the fatigue assessment, a consideration of realistic single lorries with its axle distances and axle loads are important to calculate fatigue damages with sufficient accuracy. With regard to a practicable application of the individual lorries within numerical simulations, the availability of simplified fatigue load models is required with the possibility of adjustments, depending on the local traffic conditions. Therefore, the fatigue load models that are presented in the actual Eurocode form the basis in this thesis. A short historical development of several load models on road bridges is described below.

– Investigations in load models on road bridges in the past from *Sedlacek* and *Jacquemoud* [5]:
The final method presented in [5] is based on measurements and numerical simulations from [6]. The resulting fatigue load model can be seen as a further development and completion of the investigations in [6]. The fatigue load model consists of 3 representative vehicle categories (single lorry, lorry with trailer, articulated lorry). 4 parameters have been indicated for a complete description of the model vehicles (total weight, axle loads, axle distances, relative frequency of each lorry type). These parameters were based on in situ measurements which have been carried out in Germany, France and Switzerland and represent the average values of the most frequent lorry types.

In summary 14 lorry types represent 95% of the entire heavy traffic (see [5]) but its frequency of occurrence is strongly specific relating to the individual countries. Just 3 to 5 lorry types are decisive for every country. The measurements, related to the frequency of each lorry type, showed less difference for similar route classes (local versus international routes) within one country. A significant higher difference in the route types (long- or short-distance traffic) could be observed. These observations confirm the usefulness of a simplified load model with a restricted number of lorry types and the definition of reference values for the relative frequencies of these types.

The developed fatigue load model in [5] specifies equivalent total axle weights Q_e based on the measured results (Germany $Q_e = 232\text{kN}$, France $Q_e = 230\text{kN}$, Switzerland $Q_e = 182\text{kN}$). The values Q_e were determined under consideration of the Miner Rule which includes a linear damage accumulation and a linearity between the loads and its occurring stresses. These equivalent total weights Q_e have to be used for the calculation of the equivalent constant amplitude stress range $\Delta\sigma_e$ (simulation of a bridge crossing of the equivalent axle load Q_e) in combination with several correction parameters that are mentioned above and the appropriate detail's influence line. This simplified stress range calculation is basically developed for the fatigue assessment of main girders. The fatigue behaviour at orthotropic decks includes additionally very local notch details and for an adequate determination of the occurring stresses, several other factors like the FE-model of the exact structure and the wheel contact patches have to be considered, but are not available in [5].

Also investigations relating to the closed longitudinal ribs on orthotropic steel decks were done in [5]. The influence of the lane position referring to the heavy traffic loads in transverse bridge direction has to be considered with an optimised correction parameter. This parameter scales the value for Q_e (see [5]) and is based on numerical calculations under the consideration of a simplified static system where one longitudinal rib was modelled as continuous beam that is rigidly supported at the cross girders. The frequency distribution in transverse bridge direction was taken from the British Standard BS5400, Part 10 (1980) [7], which is described as a normal distribution. Later measurements showed that the heavy traffic has much more directional stability and a normal distribution delivers less sufficiency [8] [9] [10].

– Comparison of several fatigue load models in the past from *Schütz* [10]:

In the time from 1970 to 1980, many load models for road bridges relating to the ultimate limit state and the fatigue assessment have been developed. *Schütz* compared in summary 7 load models in [10], based on comparative calculations on an infinite, rigidly supported continuous beam including a variation of the span length. The following developed load models were considered: *Sedlacek/Jacquemoud* [5], *König/Puche/Gerhardt* [11] [12], *Nather* [13], *Klassen* [14], *Tschemmerneegg* [15] [16], SIA 160 [17], DIN 1072 [18]. The results from these load models were additionally compared to measurements that were performed on the Brohltal-bridge (Germany) by the Fraunhofer Institute for Structural Durability and System Reliability LBF [19] [20].

From the numerous comparative calculations in [10], it can be stated that load models, which consists only of a single vehicle, are generally unsuitable for a fatigue verification because of the large variations referring to the equivalent loads. It could also be confirmed that the individual axles of a vehicle are decisive for local details. Secondary load bearing elements (e. g. cross girders) are increasingly stressed

by the total weight of the vehicles when the area of influence increases. The influence of the vehicle's length also affects the number of stress cycles in secondary load bearing elements. In contrast, only the lorry's total weight is important for global structural elements, because the vehicles act approximately as single loads. The influence of the vehicle sequence generally may be neglected and therefore, the consideration of only independent vehicles is sufficient.

- Pre-normative background studies relating to the actual fatigue load models according to EN 1991-2:

The literature from *Sanpaolesi/Croce* [21] illustrates the relevant background information relating to the actual Eurocode EN 1991-2 [1]. Within this document also the basic assumptions and specifications for the development of the fatigue load models FLM 1 to FLM 5 are presented. The available registered European traffic comes from two large measurement campaigns (1977 to 1982 in France, Germany, Great Britain, Italy, Holland and 1984 to 1988 on several routes around Europe). The fatigue load models FLM 1 to FLM 5 are based on the traffic measurements which have been recorded in Auxerre (France) because its traffic conditions represent very well the main characteristics of the European's long distance routes. This decision of selecting the Auxerre traffic and its reliability was additionally checked by measurements that have been performed in other countries [21].

An important statement can be concluded based on the traffic measurements: The heavy vehicle's speed and its lengths are poorly correlated and these parameters are practically independent from the axle loads as well as the total vehicle weights.

The following trends of the European heavy traffic can be observed based on the recorded traffic data but should be confirmed by measurements in the future:

- Increase of the frequency of articulated lorries and simultaneously a reduction of the lorries with trailer
- Decrease of the frequency of the lorries with 3 axles
- Increase of the average total weight per lorry

The Eurocode gives the possibility of two different types of fatigue verifications:

- Boundless fatigue life assessment: $\Delta\sigma_{\max} < \Delta\sigma_D$
- Fatigue damage calculation, based on a simulation of the crossing vehicles, under consideration of a trilinear S-N curve – verification: $D_{\text{sum}} < 1.0$

For each kind of fatigue assessment two fatigue load models are intended. The first one is essential, conservative and easy to use where the second one has more refinement as well as a better accuracy but is more complex. Finally, 4 fatigue load models are indicated:

- FLM 1 and 2 for boundless fatigue life assessment
- FLM 3 and 4 for fatigue damage calculation

FLM 1 is directly derived from the load model for the ultimate limit state and consists generally of various predefined surface load pressures on each lane in combination with 2 concentrated axle loads per lane. FLM 3 comprises of a fictive symmetrical 4 axle vehicle (fatigue vehicle) with 120kN per axle. This load model gives accurate results relating to span lengths more than 10m and has to be used in combination with several damage equivalent factors λ . The most detailed load models are FLM 2 and 4 which represent load spectra that are constituted by 5 standardised heavy vehicles, which are representative for the common European heavy traffic. FLM 2 comprises of a set of lorries with frequent values of axle loads and FLM 4 comprises of a set of lorries with equivalent values of axle loads. (Note: this will be shown later in detail, see Section 2.5.2)

Additionally, fatigue load model FLM 5 is available which consists of the same lorry types as FLM 2 and FLM 4, but allows the possibility of several modifications (axle loads, total vehicle weight, lorry frequency) according to local traffic measurements. This fatigue load model leads to the most accurate fatigue verification of any individual construction.

Finally, the accuracy of the above mentioned fatigue load models has been verified in [21] by comparing the calculated bending moments due to each load model at 3 different continuous beam systems (single, double and triple span girders) including a bridge span variation between 3 to 100m. Resulting bending moments have been taken into account at predefined positions (midspan, internal supports). As reference, the resulting bending moments due to the real traffic that has been recorded in Auxerre were chosen. As predicted, the simple load model FLM 1 appears very safe sided, especially for short span length under 20m, while FLM 2 delivers more reliable results. Fatigue load model FLM 3 first looked unsafe for span length above 30m but with a little modification in terms of the application of a second vehicle driving 40m behind, this problem could be solved. Worth mentioning is the very good fitting of fatigue load model FLM 4 with the results due to the real traffic.

In conclusion it can be stated that FLM 4 gives accurate results relating to the stress calculation at main girders of bridges with continuous beam systems. These structural members are not affected by a lateral shift of the individual lorries within the traffic lane due to heavy traffic driving characteristics (central position of lorries within each lane is assumed). A simplified respectively coarse modelling of the static system in the global analysis is generally sufficient (no detailed modelling of the orthotropic deck). For

the application of this load models on orthotropic steel decks with its very local notch details which are strongly depending on the local load transmission, a verification of this load model seems necessary (part of this thesis).

1.1.2. Resistance models regarding to fatigue phenomena

According to the current state of the art, 2 different approaches can be recognised. First concept is sufficient for a verification of the service life referring to fatigue phenomena and can be applied at non-cracked structural elements. Therefore, the availability of normed “Wöhler”, respectively S-N curves is of crucial importance. The second available concept is much more complex by applying methodologies of fracture mechanics and this is necessary for already cracked elements at the observation time. Some basic characteristics of these two concepts are listed below:

- Simplified resistance models by using appropriate S-N curves

In summary 3 different concepts are available within the fatigue verification under consideration of S-N curves. The nominal stress concept, the structural stress concept (or hot spot stress concept) and the notch stress concept. The differentiation between these 3 methods can be generally recognised in the modelling technique and the accompanying stress calculation of the detail. The nominal stress concept is the easiest method and also very practicable in its application. The stress determination within this concept is restricted to normal stresses referring to bending moments and normal forces due to the global load carrying behaviour, such as bridge’s main girders (bending and membrane stresses determined with beam elements). The geometrical caused stress increase due to a detailed modelling of the structure, such as stiffeners, can be included within the structural stress or hot spot stress concept. Therefore, a modelling with beam elements is insufficient and a model design of at least using shell elements is necessary. The stress increase because of the very local notch effect should be excluded in the structural stress method (this effect is considered with a reduced fatigue strength) and therefore several linear extrapolation methods of the stress to the weld toe have been developed. The stress increase due to the very local notch effect of the welded connection is, in addition to the geometrical stress increase, included in the notch stress concept. This concept requires the most sophisticated modelling effort and needs sub modelling technique in most cases. The weld itself has to be modelled with very precise specifications regarding to the performance of the weld toe (notch effect modelled as fillet with $r = 1\text{mm}$), maximum applicable element size and element type. By considering the notch stress concept only one value $\Delta\sigma_R$ is specified as resistance which is independent from any detail category. As already mentioned, the availability of appropriate S-N curves relating to the analysed detail with its fatigue strength is crucial regarding to the nominal and the structural stress concept.

Detailed information regarding to each concept can be found in several literatures, for example in the books of *Haibach* [22] and *Radaj* [23] and a brief description is shown in Section 2.6 to 2.8.

- More sophisticated resistance models based on fracture mechanics

For already cracked members the fatigue concepts using S-N curves is not sufficient anymore and therefore more complex methods are necessary for a crack growth prediction. In order to be able to evaluate a defect or a crack with fracture mechanics, always the interaction of 3 essential parameters: i) material, ii) geometry (structural element and crack length) and, iii) stress level have to be taken into account. If 2 of the 3 parameters are known quantities, the third can be determined. For example, if the material properties and the stress level are known, the crack length can be calculated by using fracture mechanics. It should be noted that the boundary conditions or significant factors influencing the element's service life are changing over the time. For example, crack growth leads to a reduced element's cross section and an increase of the occurring stress. Also increased traffic on bridges leads to a faster crack growth in the element and a further assessment is required.

For the use of fracture mechanics, a crack modelling is necessary, whereby the once according to Griffith [24] is most known that can be used for linear elastic fracture mechanics. The most important parameter is therefore the stress intensity factor K , which describes the intensity of the singular stress field at the crack tip. This essential parameter is required because in the field of fracture mechanics, the stress alone is not enough for a crack evaluation.

Detailed information referring to methodology and application of fracture mechanics is well described in several literature, for example *Anderson* [24] and *Kuna* [25].

Fracture mechanics has also been applied at recent research studies relating to the fatigue assessment at orthotropic steel bridge decks with the aim of a fatigue life verification regarding to an crack initiation and propagation in the analysed details [26] [27].

With regard to the development of an optimised but even simplified fatigue load model for practical applications on orthotropic steel decks, only the consideration of also a simplified resistance model is appropriate within the studies in this thesis. Therefore, the performed fatigue assessment in this thesis of specific notch details has been carried out under consideration of the linear elastic damage accumulation by using the appropriate S-N curve for each analysed detail.

1.1.3. Strengthening of existing road bridges with orthotropic steel decks

With regard to existing steel road bridges in Europe, that were frequently built from 1960 to 1980, only the ultimate load carrying capacity of orthotropic decks was considered until about 1980. First damages due to fatigue phenomena were detected around the year 2000 [28] and extensive research and development was done since that time with the aim to develop an economic strengthening method that reduces dramatically the local stress ranges in the orthotropic deck because of the heavy traffic. Many methods have been developed which are not mentioned in this work, only the strengthening method with a concrete pavement instead of the asphalt layer is considered. An important requirement is that the dead load of the carriageway shouldn't be increased by the strengthening method, therefore thin concrete layers ($t_c \leq 80\text{mm}$) are necessary with nearly the same thickness as the actually asphalt pavement. So the standard concrete cannot comply with this essential condition and Ultra High Performance Concrete (UHPC) with fibre reinforcement is required (UHPRC). Research projects and applications from France and Japan of this type of strengthening can be found in [28], [29] and [30]. The most practical experience of strengthening the orthotropic steel deck with UHPC as pavement instead of the asphalt layer has been done in the Netherlands and meanwhile several bridges have been retrofitted [31] [32].

1.2. Overview of this thesis

This work in general deals with the consideration of realistic load effects at road bridges in Europe referring to fatigue phenomena and improvements to the actual fatigue load models from the Eurocode [1]. First, the realistic wheel and axle geometries of the appropriate heavy vehicle, that causes the maximum damage in all analysed details, have been taken into account. Second, the driving characteristics of the heavy vehicles within a lane (position of the wheels in transverse direction of the bridge deck) by using the appropriate lateral frequency distributions based on measurements [8] have been investigated.

At last, the essential results of a research project are presented that contains a strengthening method for orthotropic steel decks on road bridges, which is based on a solution developed in the Netherlands [28]. The strengthening method consists of a concrete layer instead of the asphalt. In addition to numerical investigations, full scale tests have been performed and within this Ph.D. thesis additional numerical calculations referring to an overall effective Young Modulus have been done.

For every further investigation it was essential to define representative steel bridge decks with accurate geometrical dimensions. A pool of data with many steel bridge decks beginning from 1950 was generated and out of these important information three different types of bridge decks could be taken out for modelling. The summary of the historical development of orthotropic steel bridge decks and the chosen representative decks are illustrated in Section 2.3.

The definition of the significant notch details referring to fatigue phenomena was based on the results of a project in Austria [33] and in summary three different details have been analysed that are presented in Section 2.4.

The actual recommended fatigue load models according to the Eurocode EN 1991-2 [1] are presented in Section 2.5. For the numerical simulations fatigue load model FLM 4 has been applied and an asphalt pavement was considered by an increased wheel contact area due to a load distribution through the thickness of the asphalt layer with an angle of 45° , based on detailed studies in [34].

The calculation of the remaining service life of existing orthotropic steel decks without taking into account any lateral wheel load shifts is presented in Section 3. For the performance of the numerical simulations, in summary four finite element models have been developed which are described in Section 3.2. A FEM-model for a deck with flat steel longitudinal rib and a very high deck plate slenderness was created. Another two FEM-models with trough longitudinal ribs and a cross girder interval of 2.0m and 4.0m were created. In addition, a local FEM-model of one cross girder with bolted connections was created. The results of the simulations due to the heavy traffic crossings with centric track configuration, at the longitudinal ribs in lateral direction, of all vehicles are presented in Section 3.4.

The investigations of considering realistic axle geometries, heavy traffic driving characteristics (vehicle position in transverse direction) and its influence in fatigue assessment of the analysed details is presented in Section 4. Within this Section the centric track configuration is described in detail (see Section 4.2), the measured axle/wheel geometries are illustrated (see Section 4.3) and the general concept for consideration of the lateral shifting effects of the wheel loads is described in detail (see Section 4.6 and 4.7). Also the calculated lateral influence lines for each detail are plotted for every model (see Section 4.5). In addition, the analysed frequency distributions for consideration of driving characteristics (see Section 4.4) are illustrated and finally the results for the effect of a lateral shifting of the wheel loads are shown (see Section 4.8 and 4.9).

Finally, the relevant results of a research project are presented in Section 5, with the challenging aim to increase the service life of such orthotropic bridge decks to at least 50 years after strengthening the steel bridge deck by using Ultra High Performance Concrete (UHPC) with fibre reinforcement. Extensive numerical studies were carried out and for validation and calibration of the numerical stress reduction factors, full scale tests have been performed. Additional numerical studies referring to the full scale test specimen with an UHPC layer have been done to verify a realistic overall effective Young Modulus of the concrete by taking the measured strains in the steel deck of the full scale tests into account.

1.3. Objectives of this thesis

This thesis can be seen as an effort to overcome the lack of information regarding to a realistic but simple load modelling referring to a fatigue assessment of existing orthotropic steel decks with linear elastic damage accumulation. Additionally, a strengthening with UHPFRC pavement of these older, fatigue affected steel decks should be evaluated by several numerical simulations based on the stress reduction factors relating to common and representative notch details. Based on performed full scale tests on an orthotropic bridge deck and the accompanying measurements, an effective overall Concrete's Young's Modulus $E_{c,eff}$, that includes the concrete cracking, should be derived for the implementation on further numerical simulations. Thereby the following points are noted as objectives of this thesis:

- Selection of 2 or 3 existing common and representative orthotropic steel decks on European road bridges for further investigations
- Definition of several common and very frequent notch details on the representative steel decks
- Specifications regarding to the location of the critical notch details and its individual decisive load position
- Calculation and presentation of equivalent constant amplitude stress ranges, based on traffic simulations, referring to the defined frequent notch details at the representative steel decks
- Filtering of the damage percentages of each lorry type based on the equivalent constant amplitude stress ranges for a detection of the most damaging vehicle within the chosen load model
- Specification of accurate axle- and wheel geometries based on simple but effective in situ measurements of actual common lorries
- Determination and evaluation of the consideration of a lateral shift of the lorries within a lane due to heavy traffic driving characteristics by using appropriate frequency distributions in transverse bridge direction based on measurements
- Evaluation of the influence and changes regarding to realistic heavy traffic driving characteristics on the lorry's damage percentage in relation to a fully centric traffic configuration
- Modifying an existing strengthening method that has been developed in the Netherlands regarding to several additional local requirements in Austria; a thin Ultra High Performance Fibre Reinforced Concrete (UHPFRC) instead of the common asphalt pavement
- Evaluation of the strengthening method by means of extensive numerical studies and determination of stress reduction factors referring to the defined critical notch details
- Verification of the numerical results regarding to the strengthened steel deck on the basis of measurements of full scale tests in the laboratory; the experiments should also include the effects of overloaded axles and an additional thermal constraining event that should simulate a sudden thundershower on a very hot summer day

- Specification of an overall effective concrete's Young's Modulus derived from the full scale tests, for accurate stress calculations in fatigue analysis

2. Orthotropic steel bridge decks – general and fatigue phenomena

2.1. General

Within this Section the common construction types and geometrical dimensions of orthotropic steel bridge decks on road bridges in Europe, with focus on Germany and Austria, are presented (see Section 2.2). These constructional and geometrical parameters also have changed over the years of realisation and this historical development is also illustrated in the following diagrams. The diagrams with construction type and dimensions are in relation to the year of manufacturing, deck plate slenderness and several other reference values so that a few decks could be picked out for analyses, which should represent a wide range of existing orthotropic bridge decks in Europe (see Section 2.3). At these orthotropic steel decks, 3 different construction details have been analysed, which occur very often and have high local stresses due to the wheel loads of the heavy vehicles. The notch details are described in detail in Section 2.4. The recommended fatigue load models from the Eurocode [1] are illustrated in Section 2.5. The general approach for fatigue assessment according to the Eurocode [4] is shown in Section 2.6 and the S-N curves, that are used in this thesis, referring to the analysed notch details are plotted in Section 2.7. For all details the structural stress method was used to generate appropriate results for these very local details. Therefore, the finite element mesh was adapted according to the recommendations for the use of the structural stress concept [35] (see Section 2.8).

2.2. Construction of orthotropic steel bridge decks

The orthotropic steel deck connects the main girders of a bridge structure in the transverse direction and distributes the local heavy traffic loads from the carriageway to the main girders of the bridge. Generally, the orthotropic steel deck comprises of the following components:

- the deck plate on the top,
- the longitudinal ribs in longitudinal bridge direction and
- the cross girders in transverse direction.

The components of the orthotropic steel deck are plotted in Figure 1. The steel deck has in longitudinal bridge direction a quite different stiffness as in transverse direction because of its individual stiffeners (cross girders and longitudinal ribs). Hence, the steel deck is not isotropic. Because of the usually orthogonal ordered stiffeners in longitudinal and transverse direction, the system is called orthogonal-anisotropic, or briefly, orthotropic. Basically, there are two different types of longitudinal ribs:

- open longitudinal ribs as shown in Figure 1.a

- closed longitudinal ribs as shown in Figure 1.b

Additionally, many types of open and closed longitudinal ribs have been developed over the years of manufacturing and the most commonly used are illustrated in Figure 1.

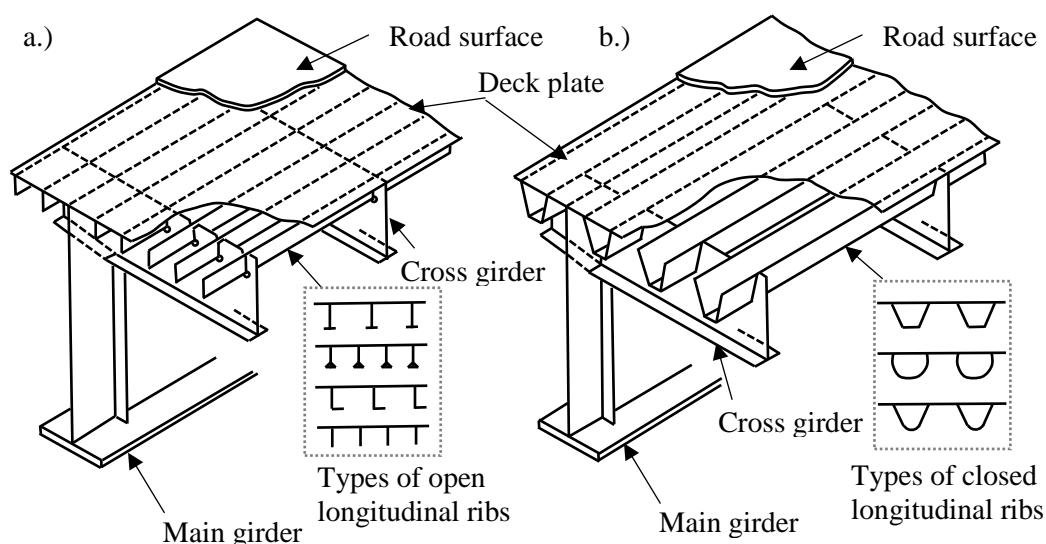


Figure 1: components of the orthotropic steel deck: a.) with open longitudinal ribs; b.) with closed longitudinal ribs [36]

For the development of appropriate calculation models regarding to fatigue assessment at orthotropic steel decks, a differentiation in two essential load carrying behaviours is useful:

- Global load carrying behaviour

With regard to the global bridge system in longitudinal direction which is schematically shown in Figure 2 (continuous beam as example), the orthotropic steel deck is acting as the upper flange of the main girder. The drawing shows an exemplary load case F_{vehicle} and the occurring bending moment M_i in section i . Therefore, membrane longitudinal normal stress $\sigma_{i,\text{top}} = \sigma_{i,\text{max}}$ (see Figure 2, Section A-A) occur in the steel deck due to the global bending of the main girder.

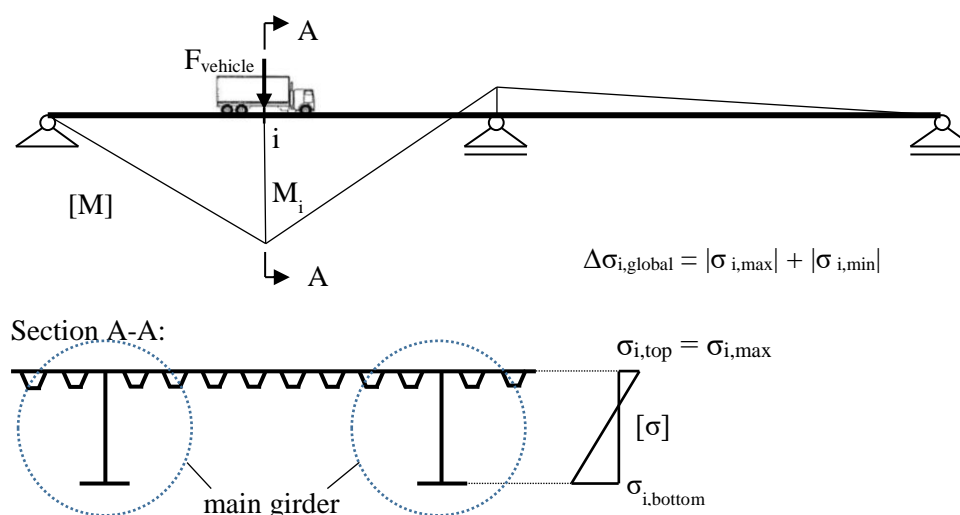


Figure 2: schematic drawing for the explanation of the global load carrying behaviour

Under consideration of the minimum occurring stress $\sigma_{i,\min}$ due to the appropriate load case, the stress range $\Delta\sigma_{i,\text{global}}$ can be calculated. This stress range at the steel deck is negligible small in relation to the occurring stress ranges due to the local load carrying behaviour, which is described below (nearly no fatigue damage occurs).

- Local load carrying behaviour

Under consideration of the bridge's cross section (see Figure 3), the wheel loads F_{wheel} of the heavy traffic vehicles have to be transferred from the carriageway to the main girders. This load distribution can be implemented with a longitudinal and transverse stiffened deck plate, the orthotropic deck. Figure 3 illustrates a schematical drawing of the transverse deformations referring to the bending of the orthotropic deck due to vertical traffic loads. The occurring stress ranges $\Delta\sigma_{\text{local}}$ in the very local notch details (shown later in detail) and its induced fatigue damages are important for the fatigue life of the orthotropic deck.

It should be noted that the effect of the deformations from the main girders to the local stresses in the steel deck in general are negligible and therefore the main girders need not be modelled and can be seen as fixed supports in vertical direction (example for local calculation model see Figure 4).

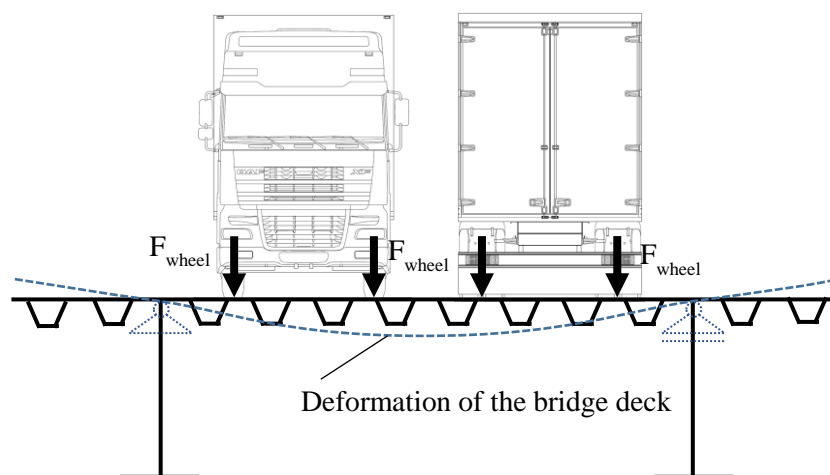


Figure 3: schematic drawing for the explanation of the local load carrying behaviour

Typically, the deck plate on road bridges is covered by a wearing surface like an asphalt pavement or a very thin epoxy layer at movable bridges. This wearing surface protects the steel construction against corrosion due to salt and leads to reduced stresses due to the heavy traffic wheels.

- Additional remark for cross girders: If the bridge deck consists of more than two main girders an interaction of the global and the local behaviour occurs. An ignoring of the global effect must be checked in detail (global bending in the cross girder if the vertical deformations at each main girder are not on a straight line in transverse bridge direction. For bridge decks with more than two main girders also the local model cannot be limited to the part between the two main girders. For bridge sections with only two main girders, a reduced local model (see Figure 3) in transverse direction is only possible if no traffic lanes are outside the main girders.

2.3. Historical development

In this Section the data of existing orthotropic steel decks at road bridges in Germany and Austria [37] is plotted in diagrams. This summary includes steel decks with open and closed longitudinal ribs with different executions of each rib type.

2.3.1. Orthotropic steel bridge deck with open longitudinal ribs

In the early years of manufacturing orthotropic steel decks in Europe (~1950 to 1975), open longitudinal ribs were frequently used. The different types of open longitudinal ribs are shown in Figure 1.a. Figure 4 illustrates a schematic local FE-model of the bridge deck between the main girders and includes 5 cross girders with its components and the geometrical notations that are necessary to understand the following diagrams. The data of the individual bridge decks with open longitudinal ribs is plotted in different diagrams in Figure 5 [37]. Figure 5.a shows the height of construction referring to the height

of the longitudinal rib h_{LR} as a function of the cross girder's interval e_{CG} . Figure 5.b shows the slenderness of the longitudinal rib e_{CG}/h_{LR} in relation to the cross girder's interval e_{CG} . Figure 5.c shows the deck plate slenderness e_{LR}/t_{DP} relating to the year of manufacture. Figure 5.d shows the bending stiffness of the longitudinal rib – including the deck plate – $J_{y,LR}$ as a function of the cross girder interval e_{CG} . For further investigations referring to bridge decks with open longitudinal ribs, a bridge with a very high deck plate slenderness of $e_{LR}/t_{DP} = 36$ of the steel deck was chosen.

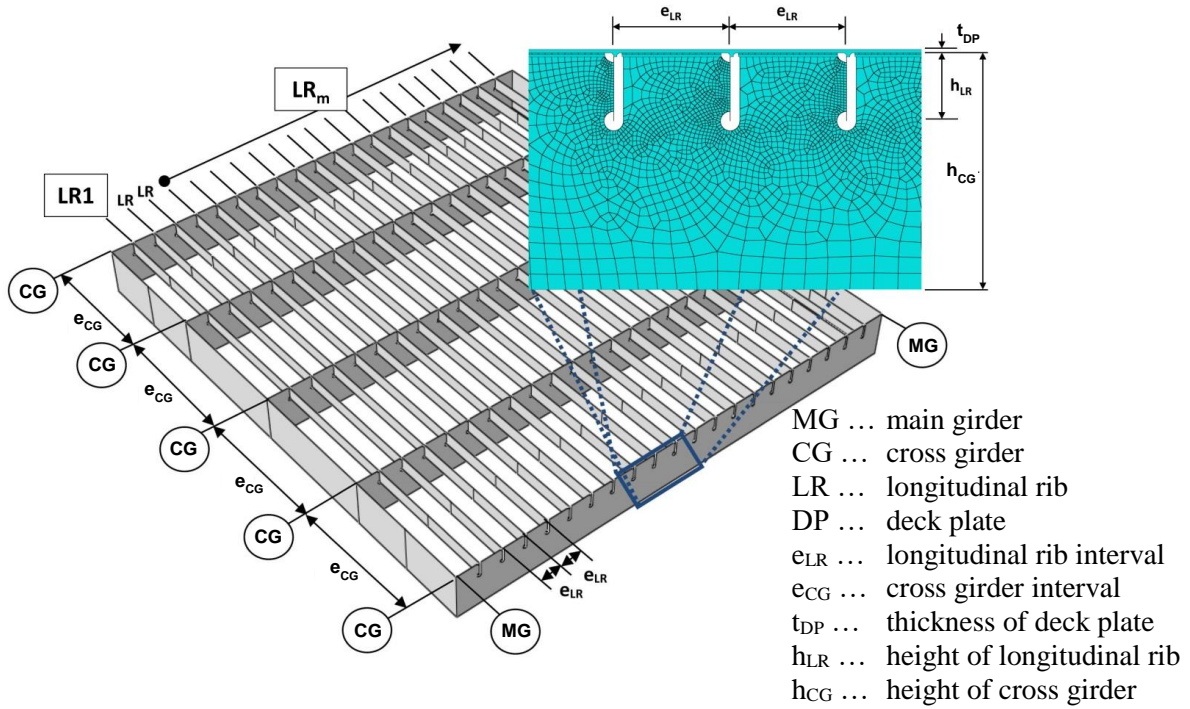


Figure 4: schematic local FE-model of an orthotropic steel bridge deck with open longitudinal ribs and notations for components and geometry

The Praterbridge in Austria, manufactured 1970, was selected for representing the decks with open longitudinal ribs. This bridge is marked in red in the diagrams of Figure 5.

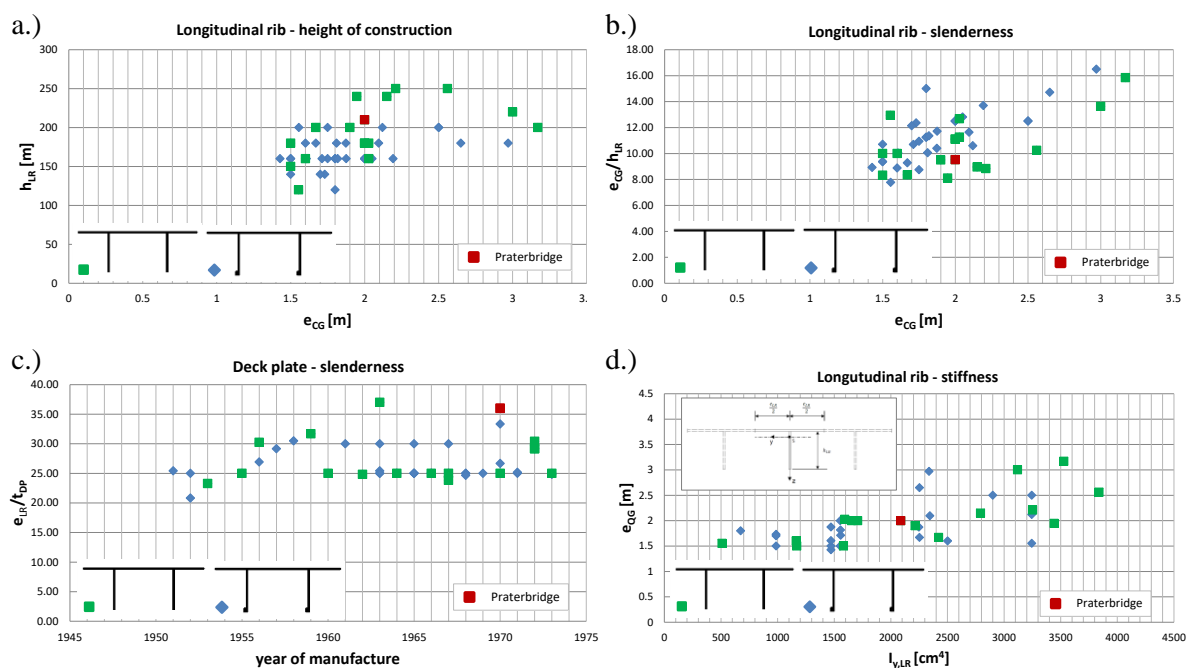


Figure 5: data diagrams of existing bridges with orthotropic steel deck plate and open longitudinal ribs [38]: a.) h_{LR} in relation to e_{CG} ; b.) e_{CG}/h_{LR} in relation to e_{CG} ; c.) e_{LR}/t_{DP} in relation to the year of construction; d.) e_{CG} in relation to $J_{y,LR}$;

2.3.2. Orthotropic steel bridge deck with closed longitudinal ribs (trough ribs)

Since about 1965 the orthotropic steel decks in Europe were more and more built with closed longitudinal ribs and nowadays road bridges with orthotropic decks are commonly constructed with this type of longitudinal ribs, respectively trough ribs [39]. Because of its higher bending stiffness in relation to open longitudinal ribs a bigger interval of the cross girders can be realised which leads to a higher efficiency. The different types of closed longitudinal ribs are shown in Figure 1.b. Figure 6 illustrates a schematic local FE-model of the bridge deck between the main girders and includes 5 cross girders with its components and the geometrical notations that are necessary to understand the following diagrams. The data of the bridge decks with closed longitudinal ribs is plotted in different diagrams in Figure 7. Figure 7.a shows the height of construction referring to the height of the longitudinal rib h_{LR} as a function of the cross girder's interval e_{CG} . Figure 7.b shows the slenderness of the longitudinal rib e_{CG}/h_{LR} in relation to the cross girder's interval e_{CG} . Figure 7.c shows the deck plate slenderness e_{LR}/t_{DP} relating to the year of construction. Figure 7.d shows the bending stiffness of the longitudinal rib – including the deck plate – $J_{y,LR}$ as a function of the cross girder interval e_{CG} . For further investigations referring to bridge decks with closed longitudinal ribs, two bridge decks with different cross girder intervals e_{CG} were chosen. Both bridge decks have trapezoidal longitudinal ribs with different geometry, but the deck plate slenderness has in both cases the same value of $e_{LR}/t_{DP} = 30$.

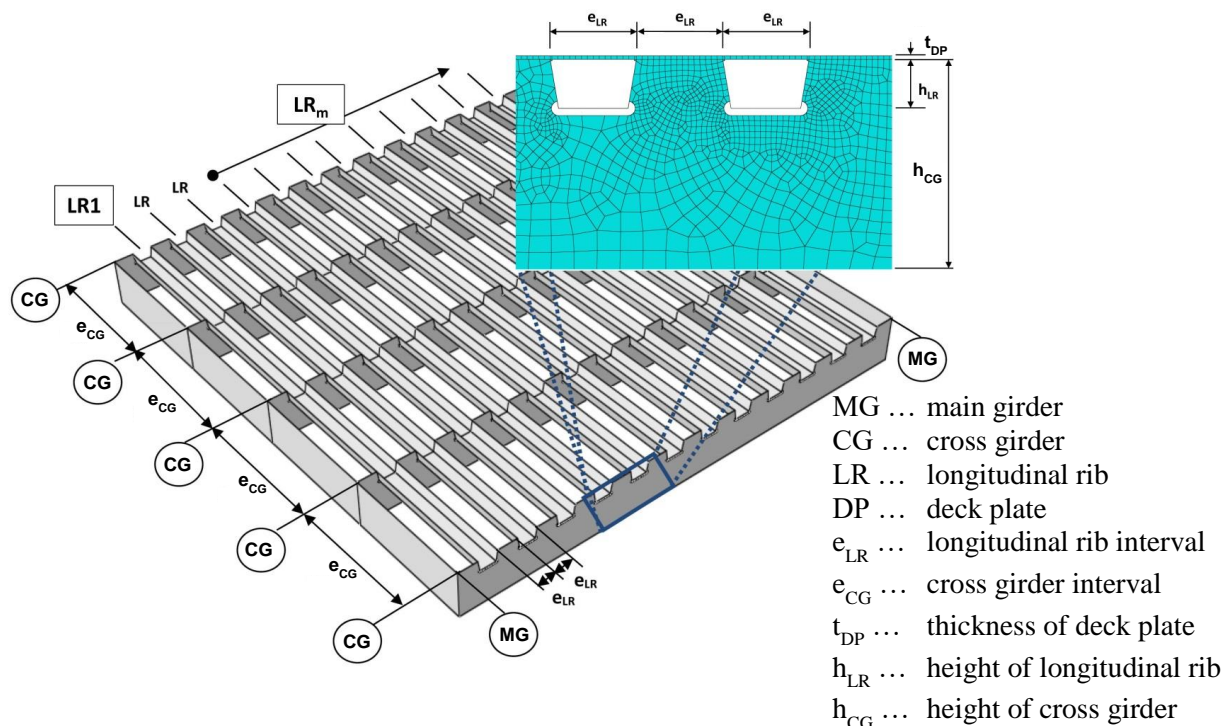


Figure 6: schematic local FE-model of an orthotropic steel bridge deck with closed longitudinal ribs and notations for components and geometry

The bridge “Stahlhochstraße Ludwigshafen”, manufactured 1969 in Germany and a bridge geometry from [40] were selected for representing the decks with closed longitudinal ribs which are marked in red and green in the diagrams of Figure 7.

The selection of these two bridges with its dimensions was based on:

- $e_{CG,1} = 2.0\text{m}$ represents the lower limit
- $e_{CG,1} = 4.0\text{m}$ should represent the upper limit of the main stream (fits good with the trendline in Figure 7.a)
- for $e_{CG,1} = 2.0\text{m}$, the deck was chosen with the highest longitudinal rib's slenderness (e_{CG} / h_{LR})

Figure 7.a shows additionally a trend line for the relationship of the height of the longitudinal rib h_{LR} and the cross girder interval e_{CG} . The height h_{LR} increases nearly linear with a higher value for e_{CG} . Therefore, the choice of a bridge deck with a cross girder interval of $e_{CG,1} = 2.0\text{m}$ and a bridge deck with $e_{CG,2} = 4.0\text{m}$ is reasonable to show the typical local behaviour of all of them. In Figure 7.b the same tendency can be realised for the longitudinal rib's slenderness e_{CG}/h_{LR} in relation to the cross girder interval e_{CG} . As it is shown in Figure 7.c, there is less variation in the deck plate slenderness referring to the closed longitudinal ribs and the most frequent value of $e_{LR}/t_{DP} = 25$ was chosen for further investigations. The actual Eurocode [41] gives recommendations for a minimum bending stiffness of

the longitudinal rib $J_{LR,y}$, which is additionally plotted in Figure 7.d. The value for $J_{LR,y}$ was calculated for 1 individual rib as shown in the sketch at Figure 7.d.

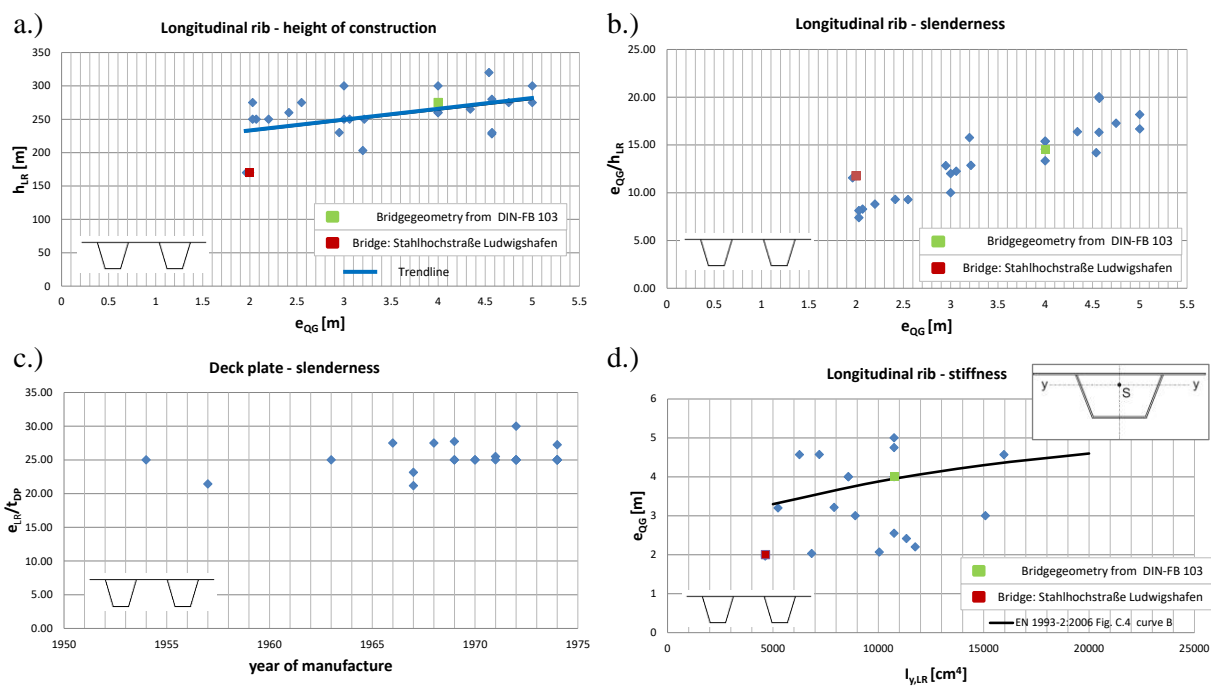
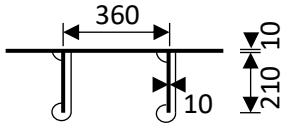
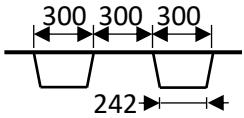
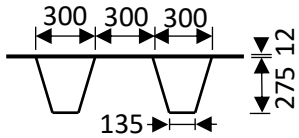


Figure 7: data diagrams of existing bridges with orthotropic steel deck plate and closed longitudinal ribs [38]: a.) h_{LR} in relation to e_{CG} ; b.) e_{CG}/h_{LR} in relation to e_{CG} ; c.) e_{LR}/t_{DP} in relation to the year of construction; d.) e_{CG} in relation to $J_{y,LR}$;

2.3.3. Representative orthotropic bridge decks

The three representative bridge decks are summed up in Table 1 with additional information of the geometrical dimensions, deck plate slenderness and bending stiffness of the cross girder in relation to the main girder interval. Model A and B represent bridge decks which are both built around the year 1970 and Model C is a practical example for modern orthotropic steel decks with a higher cross girder interval of $e_{CG} = 4.0\text{m}$ for more efficiency [40].

Table 1: representative orthotropic steel decks with open and closed longitudinal ribs of existing bridges, studied in this thesis (Model A, B and C)

FE-Model	Year of manufacture	Carriageway in cross section	h_{LR} [mm]	e_{CG} [mm]	e_{LR} [mm]	t_{DP} [mm]	e_{LR}/t_{DP} [-]	e_{MG} [mm]	h_{CG} [mm]	e_{MG}/h_{CG} [-]	$E \cdot J_{CG}/e_{MG}$ [kNcm]
Model A	1970		210	2000	360	10	36	7560	728	10,4	3.761.167
Model B	1969		170	2000	300	12	25	7500	728	10,3	3.939.027
Model C	-		275	4000	300	12	25	7500	728	10,3	4.168.701

h_{LR} height of the longitudinal rib

e_{CG} axial distance of the cross girders

e_{LR} axial distance of the webs from the longitudinal ribs

t_{DP} deck plate thickness

e_{MG} axial distance of the main girders

h_{CG} height of the cross girder

$E \cdot J_{CG}$ bending stiffness of the cross girder, including the deck plate (b_{eff} has been determined according to EN 1993-1-5, Section 3.2.1 [42])

The geometry of Model A, B and C was considered for modelling three finite element models which are presented in Section 3.2 in more detail. With these three models a wide range of existing orthotropic steel decks on road bridges in Europe can be taken into account.

2.4. Fatigue cracks within orthotropic steel bridge decks

As already mentioned only the ultimate load carrying capacity of orthotropic steel decks was considered in the design until about 1980 for applications in Germany and Austria. Due to the dramatic increase of the heavy traffic frequency and its axle loads, the local stresses in the critical details became higher and damages in relation to fatigue phenomena regarding to the dynamic effect of the vehicle crossings became more and more relevant.

Different types and locations of cracks observed in the orthotropic bridge deck in the Netherlands are given in [43]. Figure 8 shows an overview of these crack locations.

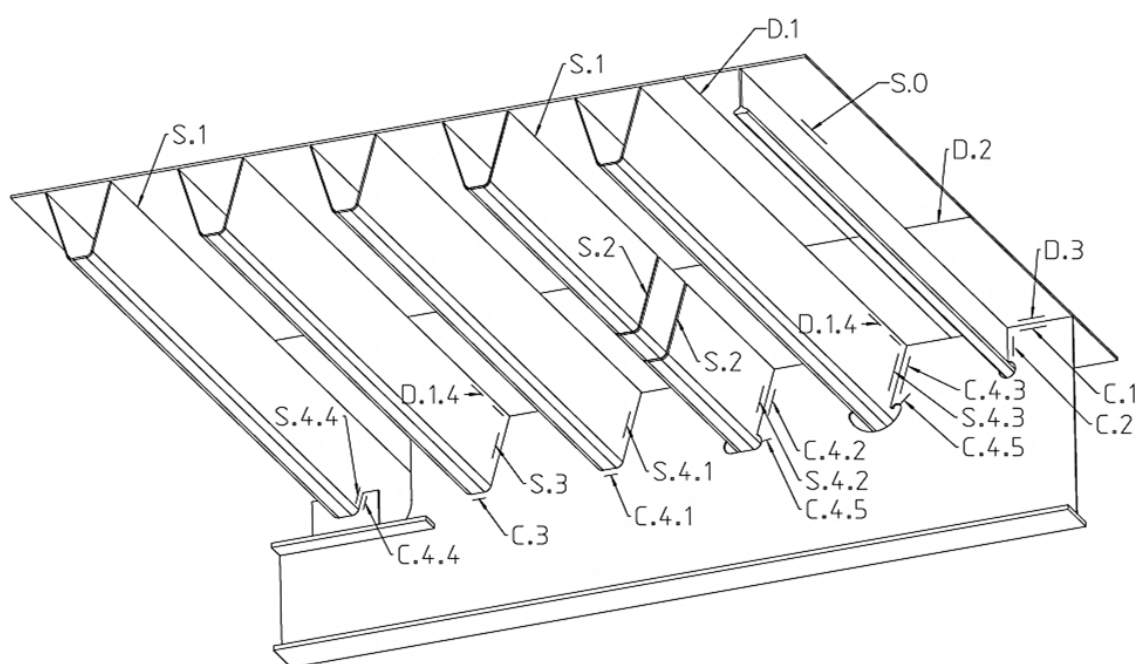


Figure 8: Susceptible locations for fatigue in orthotropic steel bridge decks [43]

Referring to Figure 8, the details and crack locations are explained in Table 2, where also the observations are indicated. The locations are restricted to the deck plate, the open and closed longitudinal ribs and the crossbeam. The crack initiation was usually observed at the weld toe but also a crack initiation at the weld root was observed sometimes [43]. The indication of (P) in Table 2 means a crack observation on a real bridge in the Netherlands. The indication of (T) stands for a crack observation in tests. At detail S.0 (open stiffener to deck plate weld) in Figure 8 and Table 2, no cracks were observed at existing bridges in the Netherlands until that time (about 2008). But actual analyses in Austria [44] showed a significant importance of taking this detail into consideration.

Table 2: Locations susceptible to fatigue, explanation to Figure 8 [43]

	Type	Observation	Location
Deck plate			
Longitudinal weld		No cracks	D.1
Transverse weld		No cracks	D.2
Deck plate to crossbeam		No cracks	D.3
Continuous closed stiffener to deck plate		Cracks, predominantly in bridges with a thin wearing course and in some heavily trafficked bridges with a thick wearing course (P),(T)	D.1.4
Open stiffener			
Stiffener to deck plate weld		No cracks	S.0
Closed stiffener			
Stiffener to deck plate weld		Numerous cracks in heavily trafficked bridges (P),(T)	S.1
Stiffener splice		Cracks in various bridges (P),(T)	S.2
Closed stiffener fitted between crossbeams	a	Cracks in various bridges (P),(T)	S.3
Continuous stiffener at crossbeam connection:			
1) Welded around	b1	Cracks in test specimens (T)	S.4.1
2) With oval cope hole	b2	Cracks in test specimens (T)	S.4.2
3) With Haibach cope hole	b3	Cracks in test specimens (T)	S.4.3
4) With plate support	b4	Cracks in test specimens (T)	S.4.4
On plate support			
Crossbeam			
Crossbeam web to deck plate weld		No cracks	C.1
Crossbeam to open stiffener		Cracks in crossbeam web near stiffener (P)	C.2
Crossbeam to closed stiffener between crossbeams	a	Cracks from stiffener and weld into crossbeam (P), (T)	C.3
Crossbeam to continuous closed stiffener:			
1) Welded around	b1		C.4.1
2) With cope hole	b2	Cracks in test specimens (T)	C.4.2
3) With Haibach cope hole	b3	Cracks in web near stiffener and at cope hole edge (P), (T)	C.4.3
4) With plate support	b4	Cracks in test specimens (T)	C.4.4
Crossbeam web, free edge of cope hole	b2,b3	No cracks	C.4.5
		Cracks in real crossbeams (P) and test specimens (T)	

(P) Practice

(T) Test

In this thesis the influence of considering realistic axle geometries and heavy traffic driving characteristics was carried out and therefore it was essential to define the significant details on common orthotropic steel bridge decks manufactured in Europe. In the following Sections these significant notch details are presented and described in detail after a short overview of fatigue cracks on the representative steel decks which were selected for further analyses (see Section 2.3.3, Table 1).

2.4.1. Overview of analysed notch details

Many cracks have been detected since the last centuries at orthotropic steel bridge decks and there are many notch details on such a construction. In this thesis just some of the most important and frequent notch details of the orthotropic deck have been taken into account, based on remaining fatigue life calculations on a bridge deck in Austria [44]. In summary 3 details were studied in detail, which occur very often and receive high stress ranges due to the heavy traffic crossings (note: see also preliminary remarks for chosen simplifications):

- **Detail D1:** the welded connection of the longitudinal rib to the deck plate with high bending stresses in the deck plate in transverse direction (see Figure 9);
Detail D1a: the bending stresses and their resulting stress ranges at the deck plate's bottom side are relevant at the weld toe ($\Delta\sigma_{DP}$);
Detail D1b: the bending stresses and their resulting stress ranges at the through web's outer side at the weld toe are relevant ($\Delta\sigma_{LR,D1}$); only relevant at bridge decks with closed longitudinal ribs;
- **Detail D2:** the welded connection of the longitudinal rib to the cross girder; the stresses and their resulting stress ranges at the bottom end of the weld of the longitudinal rib in longitudinal bridge direction are relevant ($\Delta\sigma_{LR}$, see Figure 9);
- **Detail D3:** the welded connection of the cross girder to deck plate, especially in the local area of the cross girder's field connection; the principal stresses in the cross girder's web at the weld toe are relevant (see Figure 21);

Figure 9 shows a schematic drawing of the analysed orthotropic steel bridge decks and the critical notch details D1 and D2. Figure 9.a illustrates the bridge deck with open longitudinal ribs and Figure 9.b shows the bridge deck with closed longitudinal ribs.

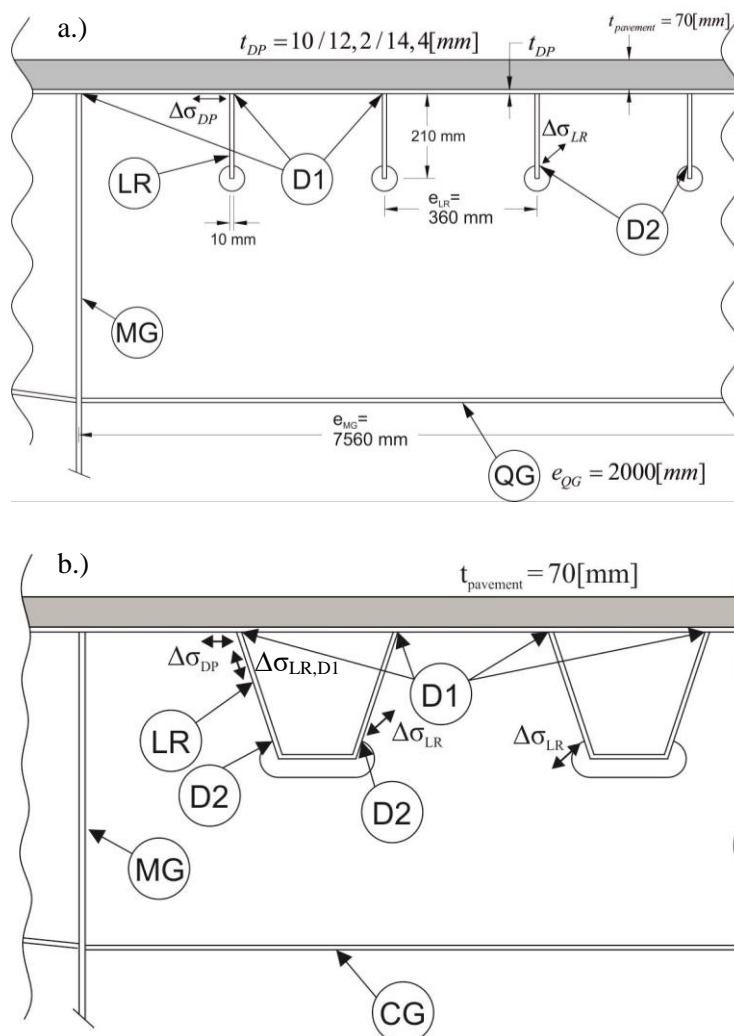


Figure 9: overview of the analysed critical notch details on an orthotropic steel deck; a.) with open longitudinal ribs; b.) with closed longitudinal ribs

All analysed notch details D1a, D1b, D2 and D3 are described in detail in the following Sections 2.4.2 to 2.4.5.

2.4.2. Detail D1a: Welded connection of longitudinal rib to deck plate – Fatigue cracks in the deck plate

Detail D1 represents the welded connection of the longitudinal rib to the deck plate. Within this thesis, the detail has been split into detail D1a and D1b. Both details represent the same welded connection but different points of interest have been taken into account for the numerical calculations of the stress ranges. At detail D1a, the stress ranges at the bottom side of the deck plate in transversal bridge direction, nearby the weld toe are relevant, where the crack initiation is expected. Figure 10 illustrates a crack in the deck plate along the trough rib's web with a length of approximately 650mm [28]. The crack initiation was on the deck plate's bottom side. Hence the crack has grown through the whole thickness

of the steel deck plate which leads to a critical lack of bending stiffness of the deck plate in that local area.

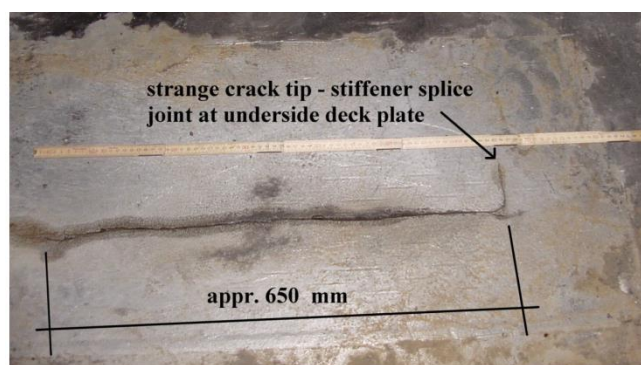


Figure 10: detail D1a - crack in the deck plate at orthotropic steel decks with trough ribs [28]

This specific notch detail has been analysed at orthotropic steel decks with open as well as closed longitudinal ribs. Section 2.4.2.1 gives a detailed description of the detail D1a at bridge decks with open longitudinal ribs and Section 2.4.2.2 describes detail D1a at bridge decks with closed longitudinal ribs.

At steel decks with trough ribs, the most frequent observed deck plate crack is located at the cross girder, respectively the crossbeam connection which is illustrated in Figure 11 [28]. This location of the deck plate crack is only present at steel decks with continuous trough longitudinal ribs passing through the cross girders with an additional cope hole. High stress peaks arise in the area of the cope holes due to the difference of the deck plate's bending stiffness. Directly above the cross girder's web, the deck plate is supported rigidly in vertical direction (see Figure 12, Section A-A). In the area of the cope hole (within the trough rib), the deck plate is deformable in vertical direction and is spanned between the trough rib webs. A detailed determination of the fatigue assessment referring to this notch detail under consideration of a simplified calculation model in combination with a modified fatigue load model and the application of fracture mechanics is given in [27].

An important part of this thesis is the determination and evaluation of the influence regarding to a lateral shift of the heavy vehicles and therefore a decisive location is necessary for detail D1a. Based on this both positions in longitudinal direction which are shown in Figure 11 have to be analysed. Position 1, at Section A-A, directly above the cross girder and Position 2, somewhere between the cross girders. Further investigations showed, that the location of detail D1a in a distance of e_{LR} away from the cross girder is decisive for Position 2 in the case of open stiffeners. For more detailed information see Section 3.3.1. This is in contrast to observations for orthotropic decks with closed longitudinal ribs, where Position 1 (see also Figure 12) is decisive (maximum stress cycles $\Delta\sigma$).

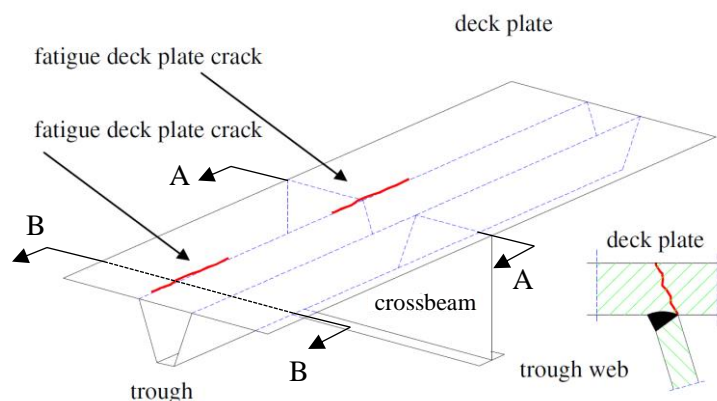


Figure 11: detail D1a - observed locations of crack in the deck plate at orthotropic steel decks with trough ribs [28]

With regard to a lateral load shifting at steel decks with trough ribs (different position of individual lorries in transverse direction, within the lane), the influence lines for the bending moment M_I at the trough web to deck plate connection have to be analysed. Figure 12 shows these transversal influence lines M_I for both positions in a schematically drawing for deck plate bending in transverse direction, ignoring the bending stiffness of the web of the longitudinal rib. The deck plate is simplified modelled as beam element. At Position 1, the deck plate is rigidly supported in vertical direction where the cross girder's web is located (see Figure 12). By comparing the influence lines in Figure 12, it can be recognised that the influence line referring to Position 2 has a much wider influence region than the one referring to Position 1. Therefore, this section was studied and not the relevant section directly at the cross beam (maximum stress cycles).

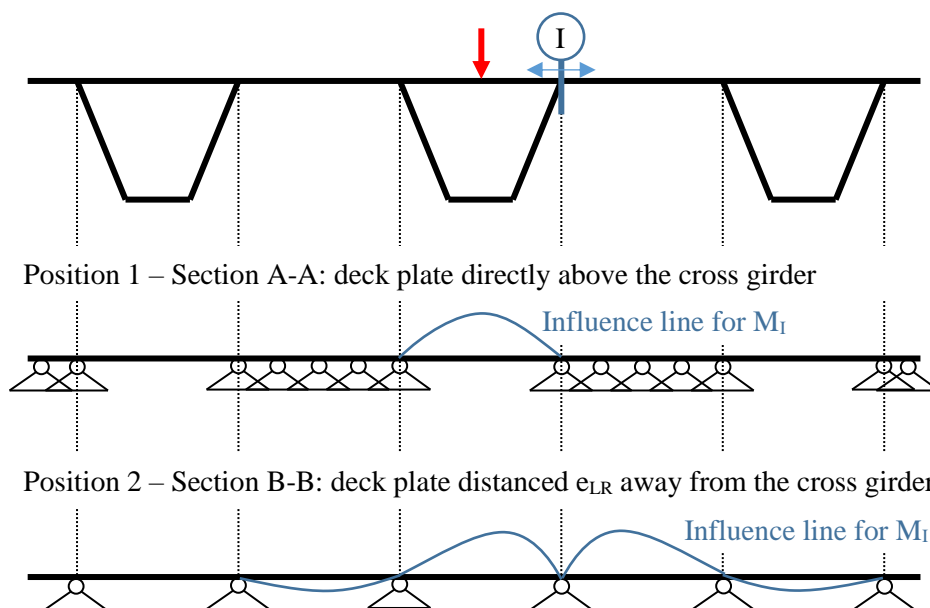


Figure 12: detail D1a - influence lines for the deck plate's support moment M_I in transverse direction relating to Section A-A (directly above cross girder) and Section B-B (distanced e_{LR} away from the cross girder)

For Position 1, the maximum bending moment in section I occurs due to a load position at midspan between the through webs. The curve is decreasing quickly and a load position out of this local region, above the considered cope hole, has nearly no influence to the bending moment M_I . For Position 2, the observed influence region referring to M_I is twice times wider than at Position 1. The influence line indicates maximum bending moment at the left and right sided field relating to the observed section I. Hence, Position 2 delivers worse stress spectra at detail D1a when the wheel load is shifting in transverse direction and is therefore decisive relating to further analyses regarding to the above mentioned effect.

2.4.2.1. Orthotropic deck with open longitudinal ribs (model A)

Detail D1a at orthotropic steel bridge decks with open longitudinal ribs is shown in Figure 13 with its flat steel longitudinal rib (LR) and the deck plate with its thickness t_{DP} . The welded connection of these two parts is conducted as double sided fillet weld and the relevant stress range $\Delta\sigma_{D1a}$, due to transverse bending of the deck plate, at the bottom side of the deck plate is marked in the drawing.

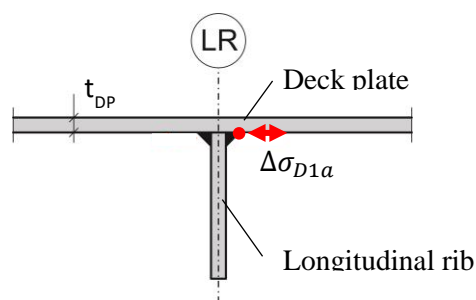


Figure 13: detail D1a at orthotropic steel decks with open longitudinal ribs

2.4.2.2. Orthotropic deck with closed longitudinal ribs (model B and C)

Detail D1a at orthotropic steel bridge decks with closed longitudinal ribs is shown in Figure 14 with its longitudinal trough rib and the deck plate with its thickness t_{DP} . The welded connection of the through web to the deck plate is conducted as full penetration weld with a $\approx t_{w,LR}$ and the relevant stress range $\Delta\sigma_{D1a}$ at the bottom side of the deck plate is marked in the drawing.

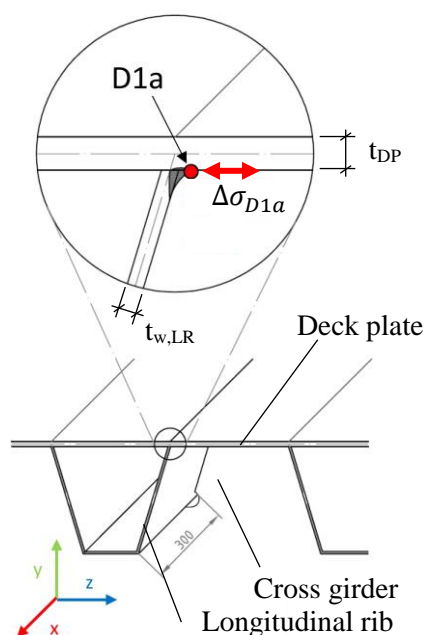


Figure 14: detail D1a at orthotropic steel decks with closed longitudinal ribs

2.4.3. Detail D1b: Welded connection of longitudinal rib to deck plate – Fatigue cracks in the trough web

Detail D1b at orthotropic steel bridge decks with closed longitudinal ribs is shown in Figure 15 with its longitudinal trough rib and the deck plate with its thickness t_{DP} . This detail D1b is only relevant at closed longitudinal ribs because of its torsional stiffness, which leads to vertical stresses in the longitudinal rib. The welded connection of the through web to the deck plate is conducted as full penetration weld with a $\approx t_{w,LR}$ and the relevant stress range $\Delta\sigma_{D1b}$ at the outer side of the through web is marked in the drawing.

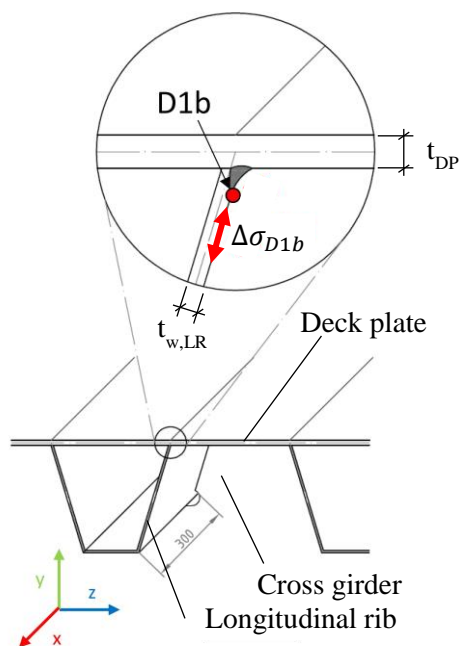


Figure 15: detail D1b at orthotropic steel decks with closed longitudinal ribs

2.4.4. Detail D2: Welded connection of the longitudinal rib to the cross girder – Fatigue cracks in the longitudinal rib

Detail D2 represents the welded connection of the longitudinal rib to the cross girder. Generally, the design of this connection can be split in two different types:

- a.) Continuous longitudinal ribs passing through the cross girders, with or without an additional cope hole in the cross girder's web (there is also a big variation in the geometry of the cope hole);
- b.) Discontinuous longitudinal ribs fitted into the crossbeam intervals;

Discontinuous longitudinal stiffeners are welded in between the crossbeams which leads to a reduced fatigue strength. In this thesis only the construction design with continuous longitudinal ribs passing through the cross girders with cope holes in the cross girder's webs is considered. Both types of longitudinal ribs (open and closed longitudinal ribs) have been taken into account. Figure 16 illustrates the different construction designs referring to the welded connection of the longitudinal rib to the cross girder [45].

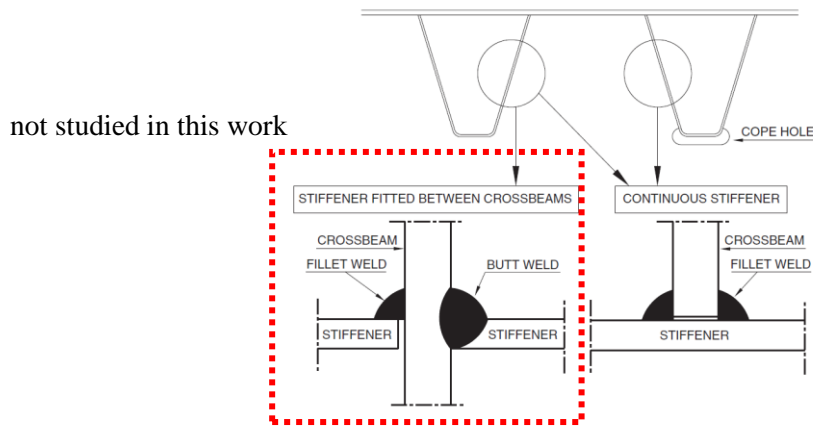


Figure 16: detail D2 – typical construction design of trough to cross girder connection [45]

2.4.4.1. Orthotropic deck with open longitudinal ribs (model A)

Detail D2 at orthotropic steel bridge decks with open longitudinal ribs is shown in Figure 17 with its flat steel longitudinal rib (LR) and the cross girder (CG). Only the case of a continuous longitudinal rib was studied. The welded connection of these two parts is conducted as double sided fillet weld and the relevant stress range $\Delta\sigma_{D2}$ (note: toe crack was studied, as it was observed in fatigue tests [52]) at the appropriate side of the longitudinal rib is marked in the drawing.

Note: More frequently, the longitudinal rib is welded to the web of the cross girder on both sides; this more beneficial solution (note: no eccentricity of the shear force leads to a reduced out of plane bending) is not studied in this thesis.

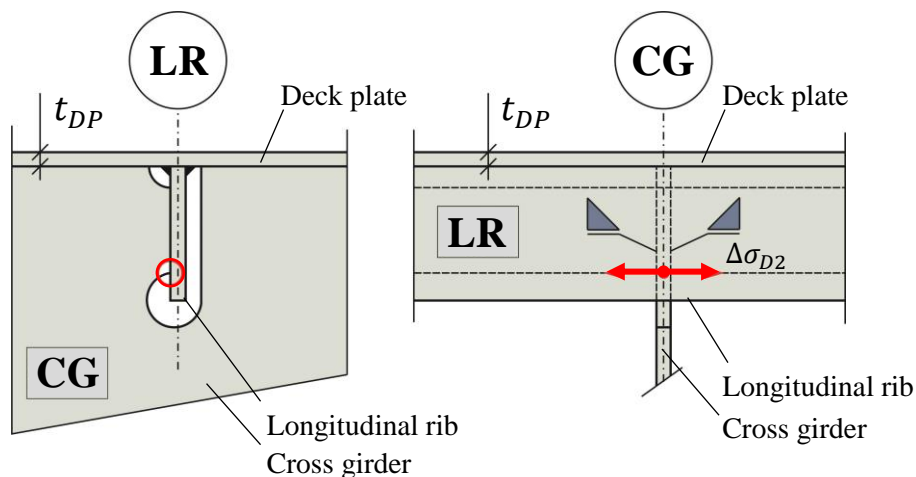


Figure 17: detail D2 at orthotropic steel decks with open longitudinal ribs

2.4.4.2. Orthotropic deck with closed longitudinal ribs (model B and C)

Detail D2 at orthotropic steel bridge decks with closed longitudinal ribs is shown in Figure 18 with its longitudinal trough rib and cross girder. The welded connection of the through web to the web of the cross girder is conducted as double sided fillet weld and the relevant stress range $\Delta\sigma_{D2}$ for a weld toe failure at the outer side of the trough web at the bottom of the weld is marked in the drawing.

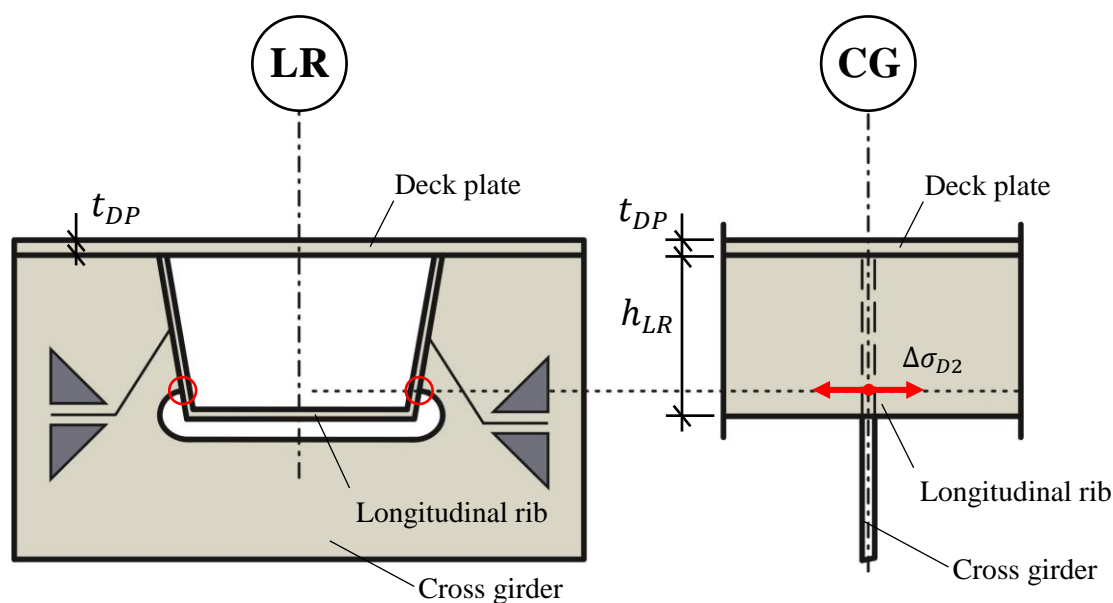


Figure 18: detail D2 at orthotropic steel decks with closed longitudinal ribs

2.4.5. Detail D3: Welded connection of the cross girder to the deck plate near a field connection – Fatigue cracks in the cross girder's web

Detail D3 represents the welded connection of the cross girder's web to the deck plate in the local area of the cross girder's field connection. Figure 19 shows a cross section of a highway bridge in Austria. In this picture the field connections of the cross girder between the main girders MG-A and MG-B are marked and noted from Joint I to Joint III. Joint I and III are located nearby the main girders and Joint II is located at midspan between the main girders. Because of the identical position, close to a main girder, Joint I and III are summarised for the analyses to Joint I/III.

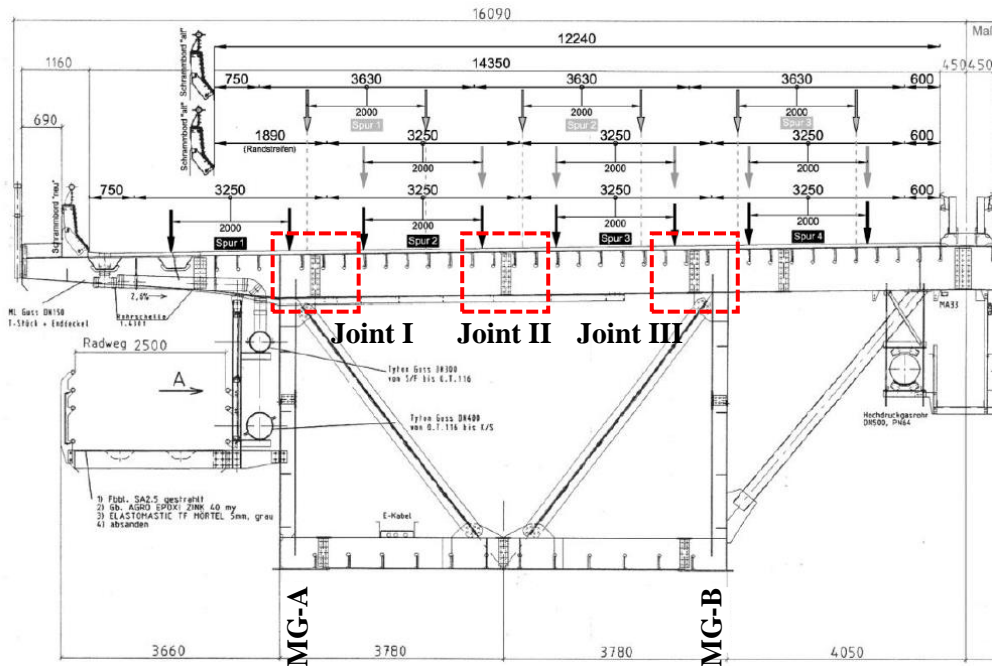


Figure 19: detail D3 – overview of field connections in cross girders at orthotropic steel decks with open longitudinal ribs (joint I, II and III)

Figure 20 illustrates the field connection Joint II on site where the cross girder, the flat steel longitudinal ribs and the deck plate can be seen in the local area of the bolted connection. The web of the cross girder is completely interrupted by the longitudinal ribs and their cope holes with the resulting region, named as “cross girder tooth”, which is additionally marked in Figure 20. As it can be seen in the picture, the welded connection of the cross girder’s web to the deck plate (detail D3) is also interrupted in this field because of the field connection and the deck plate connection has a butt weld with a permanent backing bar below.

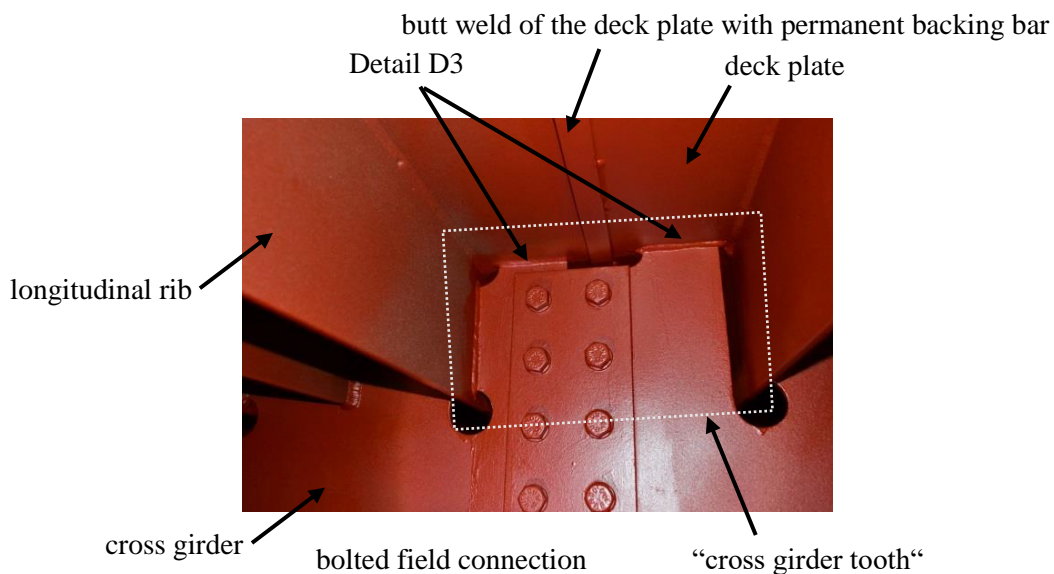


Figure 20: detail D3 – welded connection of cross girder to deck plate near field connection

Figure 21 illustrates the modelled connection of joint I/III near the main girders. A weld toe failure was analysed here, based on some observed cracks at the bridge deck. The welded connections of the cross girder tooth to the deck plate are usually executed as double sided fillet weld. The regions I to IV were studied in detail in the analyses and the maximum principal stresses due to the appropriate vehicle type according to fatigue load model FLM 4 occur at point A. The direction of the occurring principal stresses in point A is also plotted in Figure 21. Additionally, point B and C are marked and the occurring stresses there in relation to the maximum in point A is indicated. In point B, 45% and in point C, 75% of the stresses related to point A occur due to the decisive lorry type T2 (FLM 4 see Figure 24) on its critical load position (see Figure 81 and for more details see [3]).

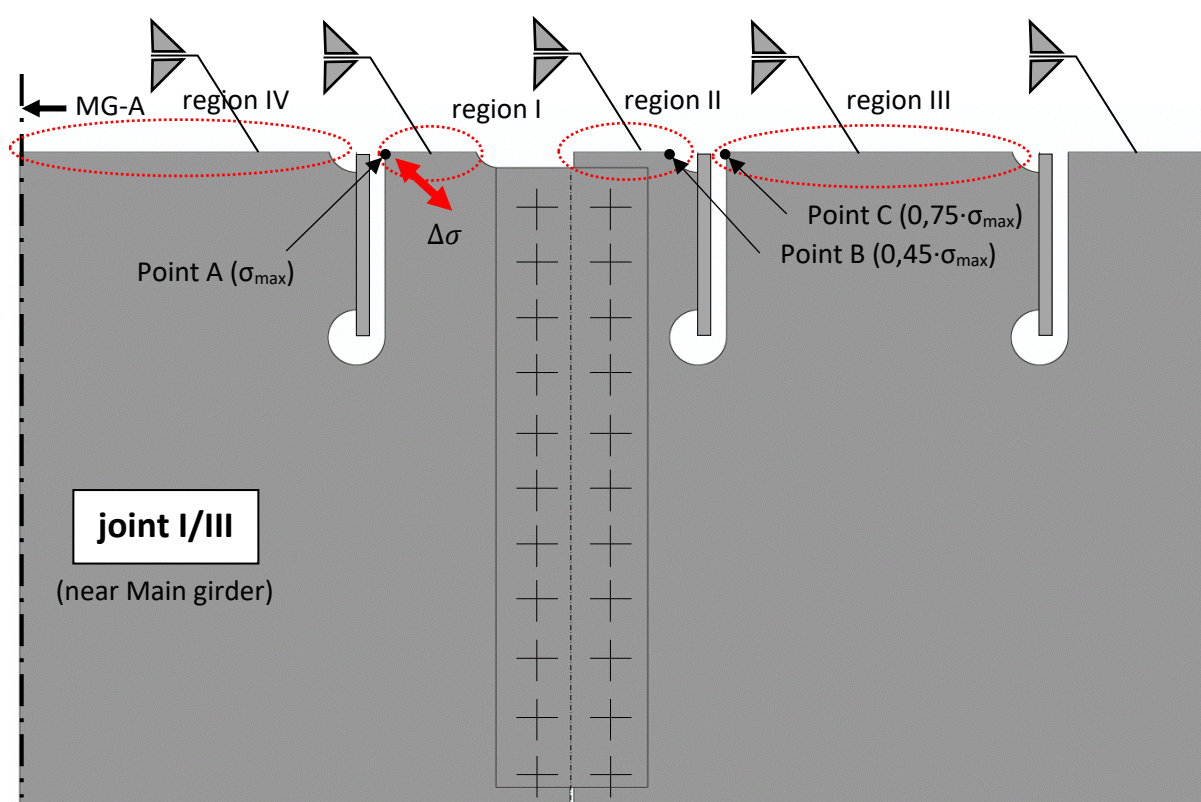


Figure 21: detail D3 – joint I respectively joint III, critical points and direction of max. Principal stresses $\Delta\sigma$

Figure 22 shows the modelled connection of joint II at midspan between the main girders. The welded connections of the cross girder tooth to the deck plate are also executed as double sided fillet weld, but the weld geometry itself was not implemented in the finite element model. The regions I to IV were studied in detail in the analyses. The maximum principal stresses referring to joint II due to the appropriate vehicle type according to fatigue load model FLM 4 occur at point D which are 70% related to point A of joint I/III. The direction of the occurring principal stresses in point D is also plotted in Figure 22. Additionally, point E and F are marked and the occurring stresses there in relation to the

maximum in point A (see joint I/III in Figure 21) is indicated. In point E, 50% and in point F, 40% of the stresses related to point A occur (for more details see [3]).

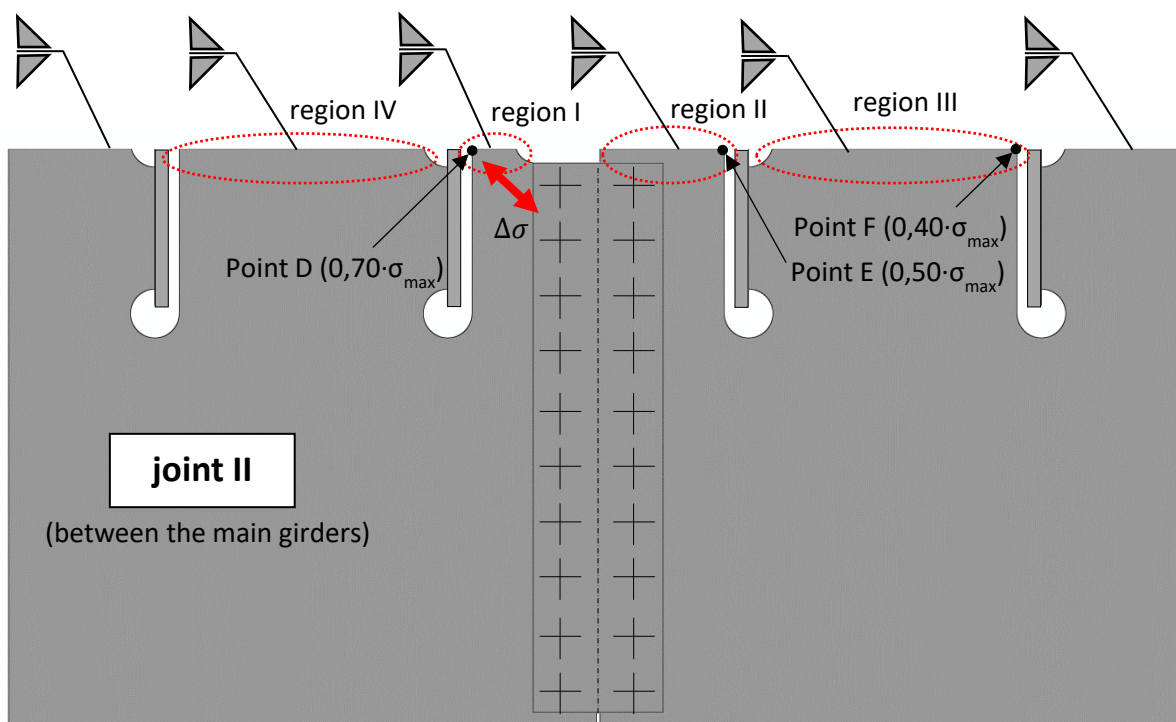


Figure 22: detail D3 – joint II, critical points and direction of max. Principal stresses $\Delta\sigma$; stress level based on Point A in joint I/III

2.5. Fatigue load models according to Eurocode 1

The actual fatigue load models for fatigue assessment of road- and highway bridges according to the Eurocode 1 [1] is presented in this Section. For the application of the nominal stress concept, fatigue load model FLM 3 with its fictive four-axle vehicle (see Figure 23) and the damage equivalent factors λ is usually used. This load model is commonly used for the fatigue assessment of the main girders of bridges because of its ease of use. But for the application of this load model the availability of the appropriate λ -factors is necessary. For the fatigue assessment at the very local details on an orthotropic steel bridge deck FLM 3 does not deliver appropriate results because of the fictive wheel patch areas for each axle (see also Figure 24 for FLM 4). The occurring stresses in the details are strongly dependent on the axle loads of the heavy vehicles as well as the wheel load geometries within an axle. Therefore, a more accurate load model with more realistic wheel geometries and axle loads is necessary. Fatigue load model FLM 4 includes 5 different lorry types and within a single vehicle 3 different axle types are indicated. This load model FLM 4 is much more detailed than FLM 3, so that it is appropriate for fatigue assessment of the very local details on an orthotropic bridge deck. Fatigue load model FLM 4 has also the possibility to adapt the axle loads and gross weights with weigh in motion measurements (called FLM 4* in this work). Fatigue load model FLM 2 is based on the same lorry and axle types as FLM 4, but higher axle loads and gross weights are indicated.

Fatigue load model FLM 3 is described in detail in Section 2.5.1 and the similar fatigue load models FLM 4, FLM 4* and FLM 2 are explained in Section 2.5.2.

2.5.1. Fatigue load model FLM 3 with one fictive vehicle and damage equivalent factors λ

The fictive vehicle of fatigue load model FLM 3 and its exemplary application on a girder bridge with 2 spans is illustrated in Figure 23.

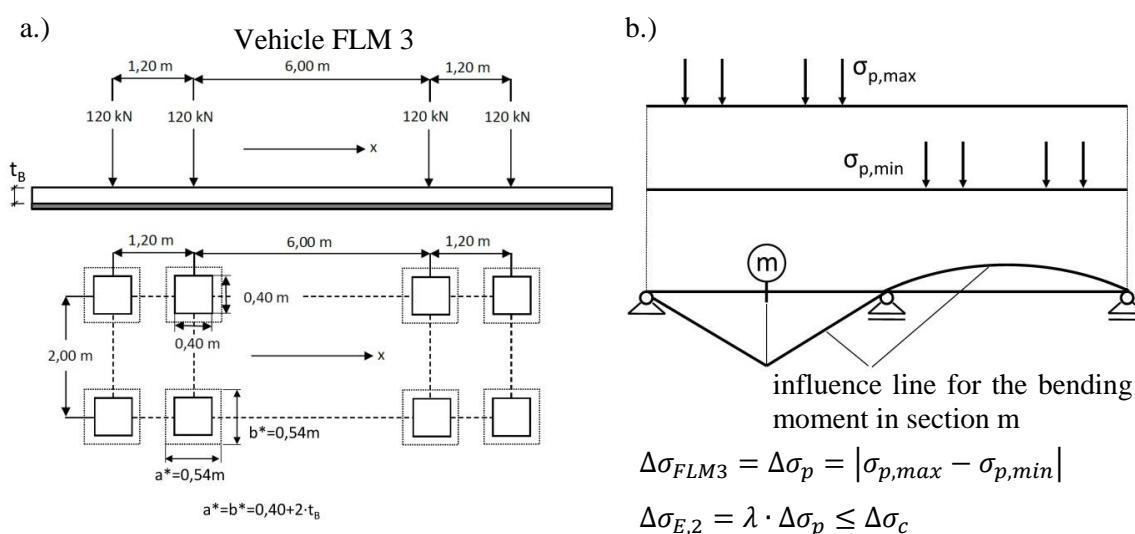


Figure 23: fatigue load model FLM 3: a.) fictive vehicle, geometry and axle loads; b.) exemplary schematic presentation of the application of FLM 3 for a girder bridge with 2 spans;

Figure 23.a shows the geometrical dimensions of the fictive vehicle with its 4 axles that have an interval of 1.20 and 6.0m, where every axle consists of 2 wheels with a wheel contact area of 40 x 40 cm. Every axle has a load of $F_A = 120$ kN. A simulation of the crossing of this vehicle over the bridge structure should be done in the most critical lane and the occurring maximum and minimum stresses ($\sigma_{p,max}$ and $\sigma_{p,min}$) in the analysed detail have to be determined. Alternatively, the vehicle has to be positioned on the appropriate locations for calculating the maximum and minimum stresses in the detail. As example Figure 23.b shows the application of FLM 3 on a girder bridge with 2 spans referring to detail m in the left span. The influence line for the bending moment is plotted as a sketch referring to section m. Under the approach of a constant section modulus W_y through the whole beam length the influence line for the bending moment $M_{y,i}$ is equivalent to the influence line for the longitudinal normal stresses ($\sigma_{x,i} = M_{y,i}/W_y$). The vehicle positions for the maximum occurring stress $\sigma_{p,max}$ and the minimum occurring stress $\sigma_{p,min}$ can be seen in Figure 23.b. The constant amplitude stress range $\Delta\sigma_{FLM3}$ relating to a crossing of the fictive vehicle from FLM 3 can be calculated (see Equation 1).

For fatigue assessment it is necessary to determine a damage equivalent constant amplitude stress range $\Delta\sigma_{E,2}$ relating to 2 Mio. number of cycles which is displayed in Equation 2. This determination of $\Delta\sigma_{E,2}$ needs the availability of a damage equivalent factor λ , that is shown in Equation 3. This factor λ consists of 4 different parameters λ_1 to λ_4 , which include several effects like span length of the girder, traffic volume and consideration of interaction between opposite lanes. A detailed explanation of all parameters for λ can be found underneath Equation 3. The verification relating to the fatigue assessment has to done according to Equation 4.

Fatigue assessment:

$$\Delta\sigma_{FLM3} = \Delta\sigma_p = |\sigma_{p,max} - \sigma_{p,min}| \quad \text{Equation 1}$$

$$\Delta\sigma_{E,2} = \lambda \cdot \Delta\sigma_p \leq \Delta\sigma_c \quad \text{Equation 2}$$

$$\lambda = \lambda_1 \cdot \lambda_2 \cdot \lambda_3 \cdot \lambda_4 \leq \lambda_{max} \quad \text{Equation 3}$$

- λ_1 factor for the damage effect of traffic which depends on the length of the critical influence line or area
- λ_2 factor for the traffic volume
- λ_3 factor for the design life of the bridge
- λ_4 factor for the traffic on other lanes
- λ_{max} is the maximum λ -value taking account of the fatigue limit $\Delta\sigma_D$

$$\gamma_{Ff} \cdot \Delta\sigma_{E,2} \leq \frac{\Delta\sigma_c}{\gamma_{Mf}} \quad \text{Equation 4}$$

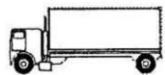
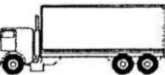
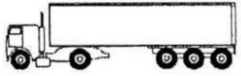
The recommendation according to the actual Eurocode [1] referring to the partial factor for the action effects specifies $\gamma_{FF} = 1.0$. The recommended values for the partial factor γ_{Mf} referring the fatigue strength according to the Eurocode [4] are plotted in Table 3.

Table 3: recommended values for partial factor γ_{Mf} according to EN 1993-1-9 [4] referring to fatigue strength

assessment method	consequence of failure	
	low consequence	high consequence
damage tolerant	1.00	1.15
safe life	1.15	1.35

2.5.2. Fatigue load models FLM 4, FLM 4* and FLM 2 with realistic vehicles

For fatigue assessment of such very local details like the ones on orthotropic steel bridge decks (detail D1, D2 and D3 described in Section 2.4.2 to 2.4.5), fatigue load model FLM 3 (see Section 2.5.1) does not deliver appropriate results because of its unrealistic, fictive vehicle [1]. Therefore, the Eurocode recommends fatigue load model FLM 4 which is presented in terms of a table in Figure 24.

type	lorry type	axle spacing [m]	wheel type resp. axle type	lorry percentage \bar{n}_i [%]	FLM 4*		FLM 4		FLM 2	
					A_i	G_{tot}	A_i	G_{tot}	A_i	G_{tot}
T1		4.50	A B	20	49,7 92,3	142 (71%)*	70 130	200	90 190	280
T2		4.20 1.30	A B B	5	61,6 105,7 105,7	273 (88%)*	70 120 120	310	80 140 140	360
T3		3.20 5.20 1.30 1.30	A B C C	50	51,4 110,2 66,1 66,1	360 (73%)*	70 150 90 90	490	90 180 120 120	630
T4		3.40 6.00 1.80	A B B B	15	52,1 104,1 66,9 66,9	290 (74%)*	70 140 90 90	390	90 190 140 140	560
T5		4.80 3.60 4.40 1.30	A B C C	10	49,9 92,7 64,2 57,1 57,1	321 (71%)*	70 130 90 80 80	450	90 180 120 110 110	610

* percentage of FLM 4

Figure 24: fatigue load models FLM 4, FLM 4* and FLM 2

As illustrated in Figure 24, there is a differentiation in 5 lorry types. There is also a variation of the axle geometry within a single vehicle where 3 different axle types are stated. These 3 axle types are shown in Figure 25 where axle type A and C are the single and axle type B is the double wheeled one. By taking a closer look at the table in Figure 24 it can be noted that axle type A is always the leading axle, axle type B with its twin tyres is the driving axle and axle type C is used for the axles of the trailers.

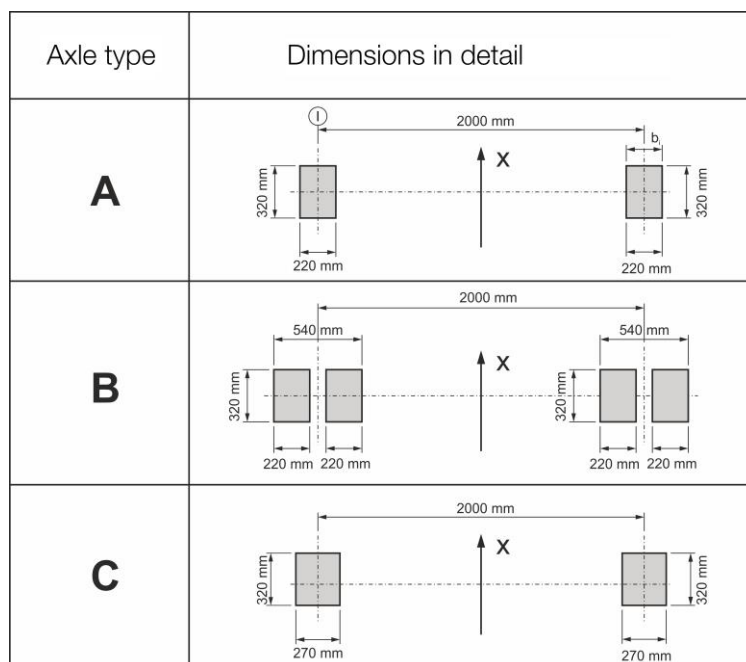


Figure 25: fatigue load models FLM 4, FLM 4* and FLM 2: 3 different axle types A, B and C

The fatigue load model FLM 4, presented in Figure 24 also includes specifications according to the frequency of occurrence and the plotted values are in relation to highway routes with long distances. Therefore, lorry type T3, the articulated lorry has the highest value of 50%. The axle loads of each lorry type as well as the gross weights are presented in Figure 24, where again lorry type T3 has the highest values. The axle load of the driving axle referring to lorry type T3 is $F_A = 150$ kN and the gross weight of T3 is $G_{ges} = 490$ kN.

The stated values in this table for the axle loads and gross weights are very high in relation to the actual highest permissible total weights and axle loads in Central Europe, but they also consider future traffic developments. In Austria, the actual highest permissible total weight of articulated lorries (lorry type T3) has a value of 380 kN and the highest permissible axle load is actually 115 kN for driving axles and 100 kN for all other axles [46]. The highest permissible total weight for vehicles with 5 or 6 axles has in Germany a value of 400 kN and the legal requirements according to the highest axle loads are equal to Austria [47].

Therefore, the fatigue load model FLM 4 according to Eurocode gives the opportunity to adapt the parameters for the axle loads and gross weights based on weigh in motion measurements. Figure 24 presents FLM 4*, where the indicated values have been adjusted based on weigh in motion

measurements on a very high frequented highway road in Austria, near Vienna [44]. This load model FLM 4* is also suitable for the determination of the fatigue damage of existing steel bridges if additional measurements for a verification of the stress spectra are done (proof of overloads, dynamic effects, etc.). Otherwise the calculations are too conservative.

The highest values for axle loads and gross weights are obtained by fatigue load model FLM 2, which is also illustrated in the table at Figure 24. This fatigue load model leads to a fatigue endurable design of the analysed notch detail on new bridge projects under consideration of an increasing development regarding to the heavy traffic loads. This load model is also reasonable for fatigue assessment of an existing bridge after strengthening, when any future damage is unacceptable.

In addition to the detailed specifications presented in Figure 24 relating to the fatigue load models FLM 4, FLM 4* and FLM 2, the consideration of a load distribution through the thickness of the asphalt pavement is available which could be confirmed by numerical studies [34]. Within this numerical studies a load distribution angle of 45° could be verified. More conservative recommendation for this load distribution is given by de Jong [28]. In his thesis a non-uniformly distributed trapezoidal shape of the contact pressure on the deck plate is indicated based on numerical simulations at a 2D finite element model which is illustrated in Figure 26.a. At the implemented FE-model, the bottom nodes were restrained in all directions and no flexibility due to the orthotropic steel deck was considered. The recommendation for the load distribution which is plotted in Figure 26.b, is based on the calculated vertical stresses at the bottom line of the model.

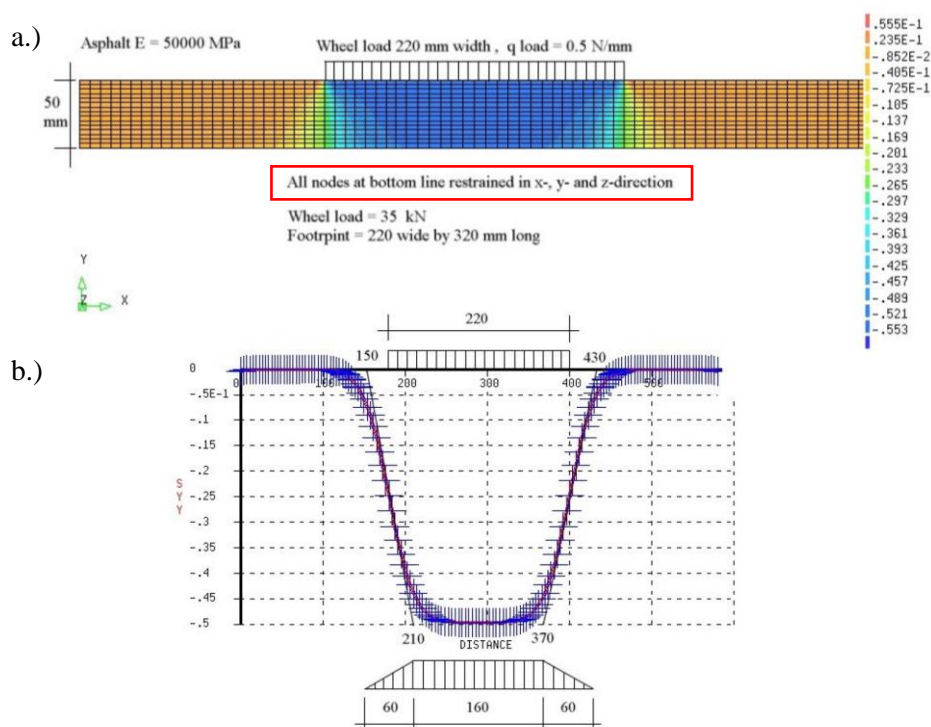


Figure 26: recommended load distribution according to de Jong [28] a.) local FE-model; b.) stresses in vertical direction at bottom line;

These assumptions seem to be very conservative for stress calculations, because of the assumed rigid support of the plate in the model of Figure 26, in the orthotropic deck and therefore numerical studies under consideration of the steel deck's flexibility and a variation of the asphalt stiffness have been done [34]. The evaluation of the load distribution has been done based on the occurring stresses in the analysed notch details (detail D1a and D2). An evaluation based on the vertical stresses seems to be not sufficient for this case. Figure 27 shows the 2 defined 3D FE-models regarding to the mentioned analyses with its geometrical dimensions, element types, interaction and boundary conditions. FE-model L2, which consists of the steel deck only and FE-model L2m, which includes also a pavement. At FE-model L2, the wheel load patch was applied directly on the steel deck. First, axle type B and C were applied with the dimensions according to the Eurocode [1] (see Figure 25). The result for detail D1a due to axle type B is exemplary shown in Figure 28 (model L2-b₀, maximum occurring stress $\sigma_{D1a} = -166 \text{ N/mm}^2$). In a second step, the wheel load patch was extended based on a load distribution through the thickness of the asphalt with an angle of 45° . The result for detail D1a due to the extended wheel load patch of axle type B is also shown in Figure 28 (model L2-b₀+ Δb , maximum occurring stress $\sigma_{D1a} = -95.9 \text{ N/mm}^2$). In a third step, an asphalt layer with a thickness of 7cm was applied (model L2m). Based on [40], 2 different asphalt Young's Modulus were taken into account as border line cases ($E_{\text{asphalt,summer}} = 600 \text{ N/mm}^2$ for $T = 40^\circ\text{C}$ and $E_{\text{asphalt,winter}} = 10,000 \text{ N/mm}^2$ for $T = 0^\circ\text{C}$). (note: only the results for the decisive "summer case" are shown, leading to the highest stress cycles $\Delta\sigma$) At model L2m, also a variation of the composite interaction between steel and pavement has been performed in the FE-model by border line case observation (with and without composite action). (note: the case with composite action means a rigid interface between steel deck and asphalt layer). For model L2m (both interface conditions), the wheel load geometry of axle type B and C according to the Eurocode [1] (see Figure 25) was applied. The maximum occurring stress in detail D1a due to axle type B is exemplary shown in Figure 28 for $E_{\text{asphalt,summer}} = 600 \text{ N/mm}^2$ (model L2m with composite action: $\sigma_{D1a} = -63.3 \text{ N/mm}^2$; model L2m without composite action: $\sigma_{D1a} = -94.4 \text{ N/mm}^2$).

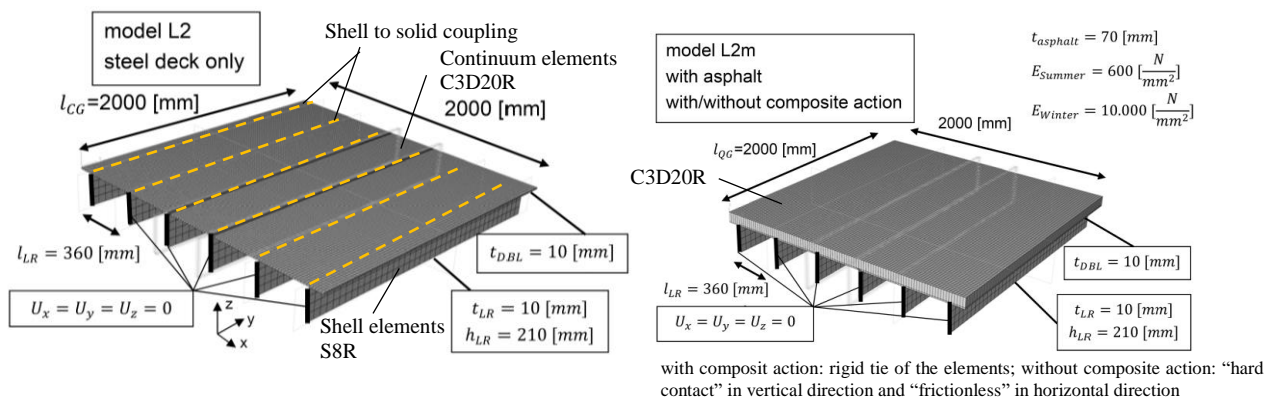


Figure 27: limited local FE-models for studying the effect of the asphalt layer [34]

The occurring stresses of the numerical calculations, referring to detail D1a due to axle type B with an axle load of $F_A = 100\text{kN}$ ($E_{\text{asphalt,summer}} = 600\text{ N/mm}^2$), are displayed in Figure 28.

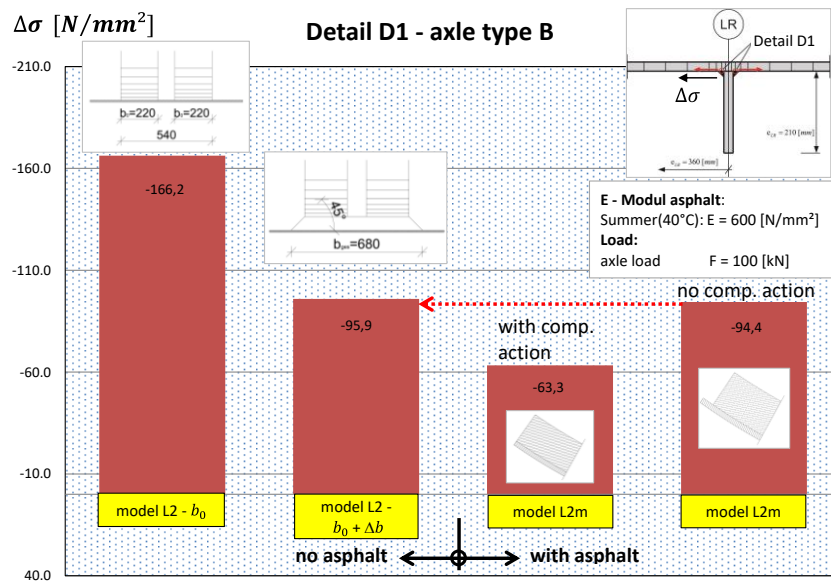


Figure 28: limited local FE-models for studying the effect of the asphalt layer [34]

By comparing the results in Figure 28, it can be recognised that the consideration of a load distribution angle of 45° through the asphalt thickness delivers at the steel deck model without pavement the same stresses in the notch detail as at the model with pavement (asphalt's E-Modulus for hot summer days and no composite action). For cold conditions of the asphalt layer, the stresses in the steel deck will therefore still be overestimated by this model (see Figure 29), leading to a conservative result.

This load distribution with an angle of 45° through the pavement's thickness leads to an extended wheel contact patch and respectively a reduced surface pressure on the steel deck. Figure 29 shows the consideration of this positive effect in a schematic drawing.

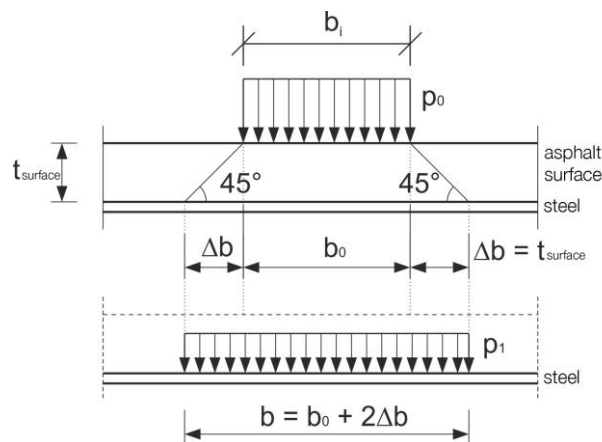


Figure 29: fatigue load models FLM 4, FLM 4* and FLM 2: extended wheel contact area under consideration of a load distribution through the thickness of the asphalt

Even when a fairly precise numerical study is carried out which may use realistic data of traffic loads (see FLM 4* in Figure 24), the real position of the individual lanes as well as the effect of the asphalt layer in summer by using an increased wheel contact area, a calculation of fatigue damage and remaining fatigue life always leads to a big scatter of possible service life predictions (uncertainties in dynamic effects, additional lorry types, different lane positions, etc.). Therefore, in practical cases, it is useful to make measurements for the stress spectra in service at representative details and to compare these measurements with the numerical predictions. It is also useful to make these measurements on hot summer days, as well as on colder conditions (e.g. at night), in order to show the effect of the asphalt layer at different temperatures. During the time of measurement of the stress spectra, it is also necessary to count the numbers of the different lorry types in the individual lanes. On this basis, it is possible to calculate numerical stress spectra, which are comparable with the measured ones referring to different details at the bridge deck. During the bridge assessment project in [44], measurements were done on 28 test points, including the deck plate (strain gauges at the bottom) and the longitudinal ribs. As an example, Figure 30 shows the results of the stress spectra at the bottom of a longitudinal rib at mid span between two cross girders. The shown numerical stress spectrum doesn't include any dynamic effects. Based on the analyses of all these measurements (calculation of equivalent stress spectra $\Delta\sigma_{e,numerical}$ and $\Delta\sigma_{e,measure}$ and comparison) , it was possible to show that - up to now - the numerical model gives sufficient conservative results for a realistic remaining fatigue life prediction.

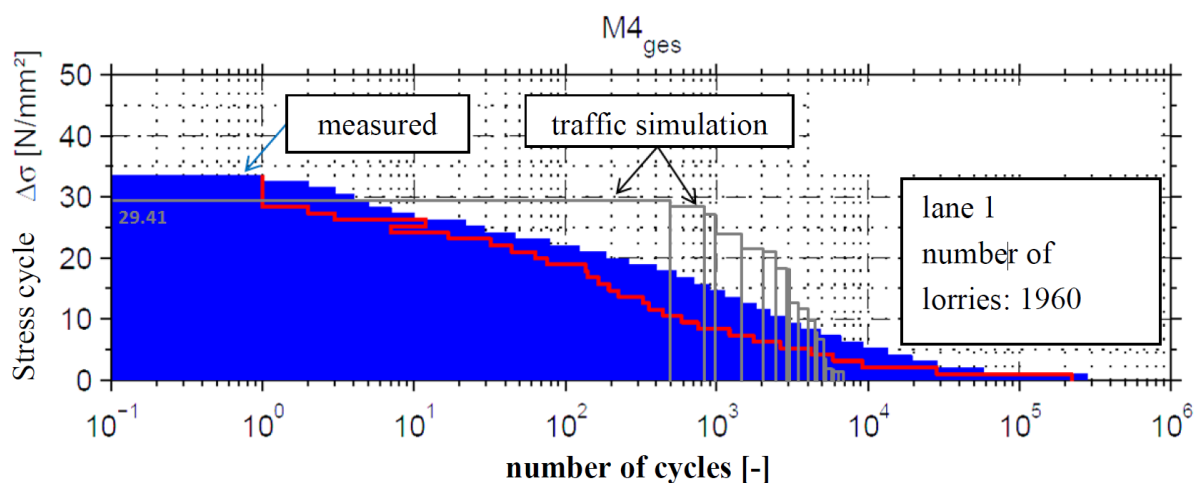


Figure 30: comparison of stress spectra at longitudinal rib's midspan (bottom) – measurements versus numerical model [44]

By taking a closer look at the stress spectra in Figure 30, it can be recognised that the numerically calculated maximum stress ranges match approximately with the measured ones. At 10^1 load cycles, the measured stress ranges are beginning to decrease which leads to a more saturated numerical stress range spectrum (reduced equivalent stress range $\Delta\sigma_e$). This observation can be declared by the lateral deviation

of the heavy vehicles from the ideal track position which leads to reduced stresses in the detail. Therefore, the lower measured stress ranges must not be seen as lower axle loads of the lorries.

Under consideration of these analyses and measurements (on 28 details), fatigue load model FLM 4* produces sufficient results referring to a verification of the fatigue damage on existing orthotropic steel decks. On this account, FLM 4* was considered in this thesis for the damage calculation in the past. The recommended fatigue load models according to the Eurocode [1], FLM 4 and FLM 2, include dynamic effects as well as future traffic development relating to the vehicle's axle loads. For this reason, these load models were considered for the calculation regarding to future damages at the steel deck. Furthermore, these load models also have benefits in its ease of use and can be modified very well based on weigh in motion measurements which make an application very adaptable and practicable. Also the effect of an increased wheel contact patch due to a load distribution through the asphalt layer of 45° is appropriate. Additionally, FLM 4 was considered in this thesis for investigations relating to the fatigue effect due to a lateral shifting of the lorries.

2.6. General approach of fatigue assessment according Eurocode

Figure 31 shows a schematic illustration of the fatigue assessment according to the Eurocode [4] using the appropriate S-N (stress range relating to number of cycles) curve. Equation 5 illustrates the function for the S-N curves. For example, 3 different stress ranges are plotted in the drawing and the damage D_i of each stress range can be calculated with the ratio of the number of cycles n_i in relation to the maximum allowable number of cycles N_i ($D_i = n_i/N_i$). The summed up damage in the notch detail can be determined based on a linear damage accumulation according to the modified Miner hypotheses with a gradient of $m = 3$ for $\Delta\sigma_i \geq \Delta\sigma_D$ and a gradient of $m = 5$ for $\Delta\sigma_D > \Delta\sigma_i > \Delta\sigma_L$. This damage accumulation is shown in Equation 6, as well as the assumption for the calculation of an damage equivalent constant amplitude stress range $\Delta\sigma_e$.

The third stress range in Figure 31 $\Delta\sigma_3$ has no fatigue damage because of its low value under the cut off limit $\Delta\sigma_L$. The first stress range $\Delta\sigma_1$ has a value above $\Delta\sigma_D$ and has to be considered as fully damaging, which means the usage of the S-N curve with a gradient of $m = 3$. The second stress range $\Delta\sigma_2$ has a lower value than $\Delta\sigma_D$ but this value is even higher than the cut off limit $\Delta\sigma_L$. So this stress range $\Delta\sigma_2$ has to be considered by using the S-N curve with a gradient of $m = 5$, which leads to less damage compared to the usage of the S-N curve with $m = 3$.

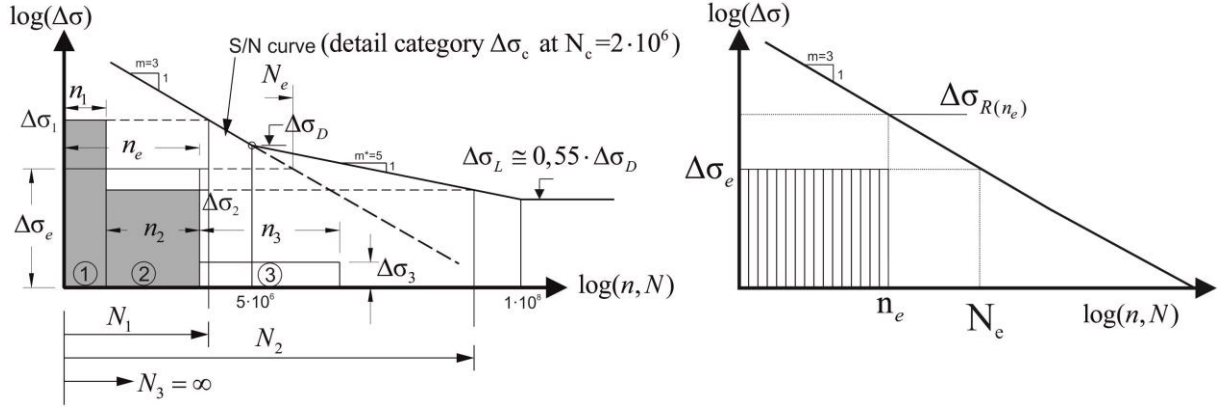


Figure 31: general approach of fatigue assessment according to Eurocode (S-N curve and stress range spectrum)

$$\Delta\sigma_i^m \cdot N_i = \Delta\sigma_D^m \cdot N_D \quad \text{Equation 5}$$

$$\text{For } \Delta\sigma_i \geq \Delta\sigma_D: \quad \Delta\sigma_i^3 \cdot N_i = \Delta\sigma_D^3 \cdot N_D$$

$$\text{For } \Delta\sigma_D > \Delta\sigma_i > \Delta\sigma_L: \quad \Delta\sigma_i^5 \cdot N_i = \Delta\sigma_D^5 \cdot N_D$$

With $N_D = 5 \cdot 10^6$

$$D_{\text{spectrum}} = \sum_{\Delta\sigma_i > \Delta\sigma_D} \frac{n_i}{N_i} + \sum_{\Delta\sigma_D > \Delta\sigma_j > \Delta\sigma_L} \frac{n_j}{N_j} = D_{e(\Delta\sigma_e)} = \frac{n_e}{N_e} \quad \text{Equation 6}$$

$$\text{For } \Delta\sigma_i \geq \Delta\sigma_D: \quad N_i = \left(\frac{\Delta\sigma_D}{\Delta\sigma_i}\right)^3 \cdot 5 \cdot 10^6$$

$$\text{For } \Delta\sigma_D > \Delta\sigma_j > \Delta\sigma_L: \quad N_j = \left(\frac{\Delta\sigma_D}{\Delta\sigma_j}\right)^5 \cdot 5 \cdot 10^6$$

$\Delta\sigma_c$... constant amplitude fatigue strength at $N_c = 2 \cdot 10^6$; equal to detail category

$\Delta\sigma_D$... Constant amplitude fatigue limit at $N_D = 5 \cdot 10^6$

$\Delta\sigma_L$... Cut-off limit at $N_L = 1 \cdot 10^8$

With the assumption from Equation 6 and a transformation, the damage equivalent constant amplitude stress range $\Delta\sigma_e$ can be calculated in relation to an individual number of cycles n_e (see Equation 7).

$$\Delta\sigma_e = \sqrt[3]{\left(\sum_{\Delta\sigma_i > \Delta\sigma_D} \Delta\sigma_i^3 \cdot n_i + \frac{1}{\Delta\sigma_D^2} \cdot \sum_{\Delta\sigma_D > \Delta\sigma_j > \Delta\sigma_L} \Delta\sigma_j^5 \cdot n_j \right) \cdot \frac{1}{n_e}} \quad \text{Equation 7}$$

The constant amplitude stress range $\Delta\sigma_e$ is relating to a constant linear SN curve with $m = 3$ that has no cut off limit (see right picture in Figure 31), because these effects (partial damage with $m = 5$, cut off limit) are already included within Equation 7. Therefore, it is also applicable if $\Delta\sigma_e > \Delta\sigma_D$. For the shown spectrum in Figure 31:

$$\Delta\sigma_e = \sqrt[3]{\left(\Delta\sigma_1^3 \cdot n_1 + \frac{1}{\Delta\sigma_D^2} \cdot \Delta\sigma_2^5 \cdot n_2\right) \cdot \frac{1}{n_e}}$$

The fatigue assessment based on the fatigue strength $\Delta\sigma_c$ relating to $N_c = 2 \cdot 10^6$ load cycles is shown in Equation 4 (see Section 2.5.1). Therefore, the damage equivalent constant amplitude stress range $\Delta\sigma_e$ has to be calculated according to Equation 7 for $n_e = 2 \cdot 10^6$ number of load cycles. This leads to:

$$\Delta\sigma_{E,2} = \Delta\sigma_e \cdot \sqrt[3]{\frac{n_e}{2 \cdot 10^6}}$$

Alternatively, the fatigue assessment can also be done based on the damage accumulation, according to Equation 6. The summed up damage D must not exceed the value 1.0 ($D_{\text{spectrum}} \leq 1.0$).

The calculation of the damage according to the modified Miner hypotheses with the stress ranges in Figure 31 is exemplary presented below:

$$D = \frac{n_1}{N_1} + \frac{n_2}{N_2} + \frac{n_3}{N_3}$$

$$\Delta\sigma_1 > \Delta\sigma_D: \quad \Delta\sigma_1^3 \cdot N_1 = \Delta\sigma_D^3 \cdot 5 \cdot 10^6 \quad \longrightarrow \quad N_1 = \left(\frac{\Delta\sigma_D}{\Delta\sigma_1}\right)^3 \cdot 5 \cdot 10^6$$

$$\Delta\sigma_D > \Delta\sigma_2 > \Delta\sigma_L: \quad \Delta\sigma_2^5 \cdot N_2 = \Delta\sigma_D^5 \cdot 5 \cdot 10^6 \quad \longrightarrow \quad N_2 = \left(\frac{\Delta\sigma_D}{\Delta\sigma_2}\right)^5 \cdot 5 \cdot 10^6$$

$$\Delta\sigma_3 < \Delta\sigma_L: \quad D_3 = 0 \quad \longrightarrow \quad N_3 = \infty$$

The fatigue assessment referring to any detail can be done according to the following steps:

1. Determination of the occurring stresses in the detail via heavy traffic simulation by using an appropriate fatigue load model (FLM 4, FLM 4* or FLM 2, see Figure 24), respectively determination of stress histories for every lorry crossing;
2. Determination of stress ranges for each lorry type based on the stress histories by using an appropriate cycle counting method like Rain flow- or Reservoir method;
3. Creation of a stress range spectrum for the analysed detail via size dependent arrangement of the counted stress ranges under consideration of the frequency percentage of each lorry type according to the chosen fatigue load model (recommendation of Eurocode [1], see Figure 24 or measured traffic data); the stress range spectrum can first be related to any desired number of lorries (for example $n_{\text{lorries}} = 100$);
4. Fatigue classification of the analysed detail and selection of the appropriate S-N-curves which is defined by $\Delta\sigma_c$, the constant amplitude fatigue strength at $N_c = 2 \cdot 10^6$;

5. Calculation of a damage equivalent constant amplitude stress range $\Delta\sigma_e$ under consideration of Equation 7 relating to n_e load cycles (for example $n_e = n_{\text{lorries}} = 100$) referring to the appropriate detail category with its fatigue strength $\Delta\sigma_c$ at $N_c = 2 \cdot 10^6$ (respectively $\Delta\sigma_D$ at $N_D = 5 \cdot 10^6$);
6. Scaling respectively stretching of the equivalent constant amplitude stress range $\Delta\sigma_e$ under consideration of the total number of lorries in the main lane referring to the observed time period; (Note: assumption that stress cycles of other lanes can be ignored) Figure 32 exemplary shows the total number of lorries referring to time period 1970 to 2020, based on measurements [44] (as example according to Figure 32: $n_{e,\text{total}} = n_{\text{lorries},\text{total}} = 49.2 \cdot 10^6$);

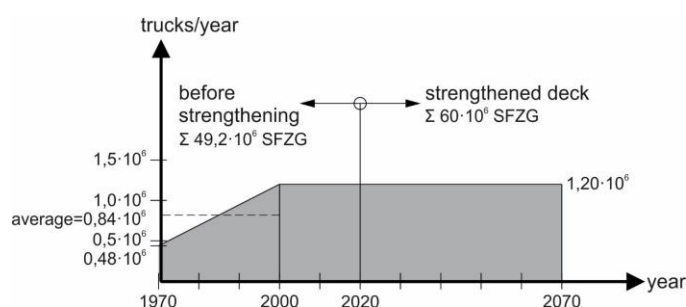


Figure 32: defined assumption referring to the number of lorries per year from 1970 to 2020 in the main lane (“SFZG” \triangleq lorry)

7. Determination of the maximum allowable load cycles $N_{R,e}$ relating to the equivalent constant amplitude stress range $\Delta\sigma_e$ by using Equation 5 with the fatigue strength $\Delta\sigma_c$ referring to the appropriate detail category at $N_c = 2 \cdot 10^6$ load cycles and $m = 3$ ($N_{R,e} = (\Delta\sigma_c/\Delta\sigma_e)^3 \cdot 2 \cdot 10^6$);
8. Calculation of the damage $D_{e,(\Delta\sigma_e)}$ for the detail on the basis of Equation 6 and by considering the total number of lorries in the observed time period $n_{e,\text{total}} = n_{\text{lorries},\text{total}}$ and fatigue verification:

$$D_{e,(\Delta\sigma_e)} = n_{e,\text{total}} / N_{R,e} \leq 1.0$$

2.7. S-N detail classification of the critical details

For fatigue assessment of any notch detail, a classification referring to the appropriate detail category is necessary. Recommendations for improved detail categories on orthotropic decks are shown in [45]. For the statistical analyses in [45] a wide range of data from the past was taken into consideration which were based on tests. Improved detail categories are given for the following details: i.) through to deck plate joint; ii.) through splice joint; iii.) trough to crossbeam joint; iv.) trough to deck plate and crossbeam joint; v.) crossbeam or longitudinal web to deck plate joint; vi.) butt joints in the deck plate. Exemplary for the detail through to deck plate joint, a fatigue strength of $\Delta\sigma_c = 125 \text{ N/mm}^2$ is proposed for a cracking in the deck plate relating to two million load cycles and based on nominal stresses [45]. For the detail trough to crossbeam joint (continuous trough to crossbeam joint with cope holes), a fatigue

strength of $\Delta\sigma_c = 125 \text{ N/mm}^2$ (failure of the trough web at the lower end of the weld) is proposed relating to two million load cycles and based on geometrical stresses (extrapolated to the weld toe in the web of the trough) [45]. Additionally, for the detail trough to deck plate and crossbeam joint (see Figure 11, cross section A-A – not considered in this work), a fatigue strength of $\Delta\sigma_c = 125 \text{ N/mm}^2$ is proposed relating to two million load cycles based on the geometric stress range $\Delta\sigma$ at the weld root in the deck plate [45]. Within all studies and analyses of the chosen details D1 to D3, presented in Section 2.4, the structural stress method (hot spot stress method) was applied. This stress method considers increased stresses at the notch details due to the local geometric conditions. Nonlinearities due to the notch effect of the welded connection must not be taken into account at the stress analysis of the structural stress method. Recommendations according to the relevant detail category are given in the actual Eurocode [4] which are illustrated in Figure 33. The analysed details D1, D2 and D3 are classified in a simplified form with the requirements of detail category 100, which is marked in Figure 33. All analyses have been carried out under consideration of the S-N curve with a fatigue strength of $\Delta\sigma_c = 100 \text{ N/mm}^2$.

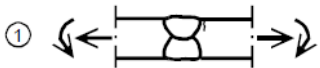
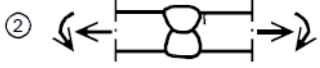
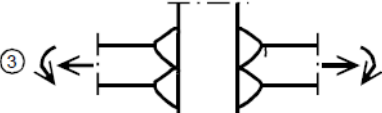
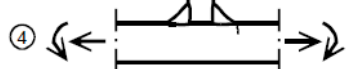
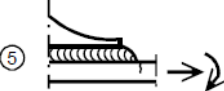
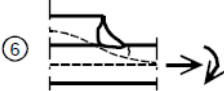
Detail category	Constructional detail	Description	Requirements
112		1) Full penetration butt joint.	1) - All welds ground flush to plate surface parallel to direction of the arrow. - Weld run-on and run-off pieces to be used and subsequently removed, plate edges to be ground flush in direction of stress. - Welded from both sides, checked by NDT. - For misalignment see NOTE 1.
100		2) Full penetration butt joint.	2) - Weld not ground flush - Weld run-on and run-off pieces to be used and subsequently removed, plate edges to be ground flush in direction of stress. - Welded from both sides. - For misalignment see NOTE 1.
100		3) Cruciform joint with full penetration K-butt welds.	3) - Weld toe angle $\leq 60^\circ$. - For misalignment see NOTE 1.
100		4) Non load-carrying fillet welds.	4) - Weld toe angle $\leq 60^\circ$. - See also NOTE 2.
100		5) Bracket ends, ends of longitudinal stiffeners.	5) - Weld toe angle $\leq 60^\circ$. - See also NOTE 2.
100		6) Cover plate ends and similar joints.	6) - Weld toe angle $\leq 60^\circ$. - See also NOTE 2.
90		7) Cruciform joints with load-carrying fillet welds.	7) - Weld toe angle $\leq 60^\circ$. - For misalignment see NOTE 1. - See also NOTE 2.

Figure 33: detail categories for use of the geometric (hot spot) stress method according to [4]

2.8. Recommendations for fatigue assessment according to the IIW - documentation

The actual Eurocode [4] proposes 3 different concepts for fatigue assessment:

- Nominal stress concept
- Structural stress or hot spot stress concept
- Notch stress concept

Within these 3 concepts there is a differentiation in the calculation of the stresses in the detail and the Eurocode recommends different detail categories depending on the chosen concept. Figure 34 shows a schematic illustration of the 3 different concepts for a T-joint.

The nominal stress concept includes membrane and bending stresses in the member. The very local effects like changes of the member's geometry or nonlinearities due to the notch effect of the weld are neglected in the stress calculation. The structural stress concept includes the local geometric effects of the member and the calculated stresses are higher than the nominal stresses (see Figure 34). For this reason, the structure has to be modelled much more in detail by using an appropriate finite element method model. Specific indications regarding to the finite element mesh and its element types are given by the International Institute of Welding (IIW) in [48]. The structural stress concept ignores the nonlinear effects due to the notch effect of the weld. The notch stress concept includes the local geometrical effects of the structure as well as the notch effect due to the welded connection. Therefore, a very detailed finite element model is necessary to get accurate results, which contain much higher values than the results of the other concepts (cf. Figure 34). The higher stresses in the notch stress concept are verified with significant higher fatigue resistances (e.g. $\Delta\sigma_c = 225 \text{ N/mm}^2$, based on IIW [48]).

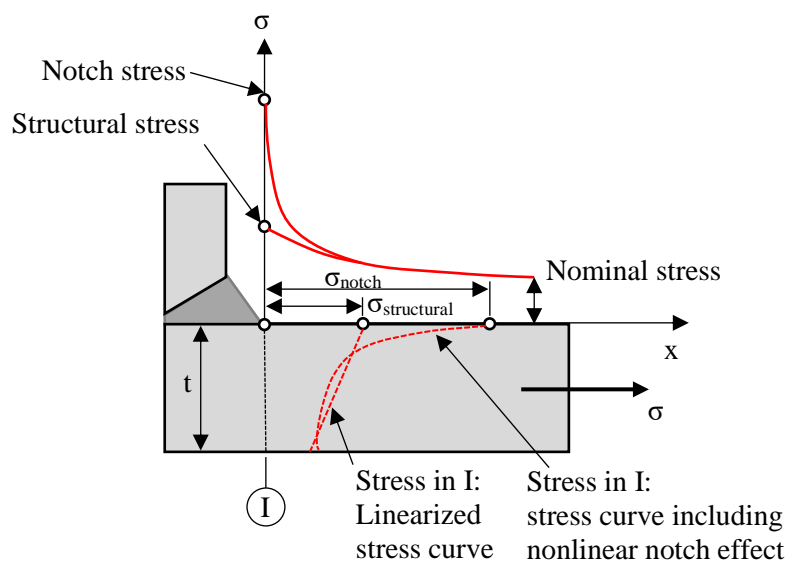


Figure 34: schematic illustration of the 3 different stress calculation concepts according to IIW (nominal stress method, structural stress method and notch stress method)

In this thesis only the structural stress or hot spot stress concept was used for the stress calculation in the appropriate details and therefore, the other two concepts are not described in detail. The specific rules of the structural stress concept relating to the finite element model according to the recommendations from the IIW are described in this Section (adequate rules in Eurocode are missing). As shown in Figure 34, the stresses in section I, in front of the weld, should only include the geometrical effects of the structure and a linearized stress curve through the thickness of the steel plate should be reproduced to eliminate nonlinear effects. The IIW recommends a linear extrapolation of the stresses from two reference points at the appropriate surface to the analysed weld toe on the basis of [35]. Figure 35 illustrates these linear extrapolations as examples for different types of fatigue-critical welds and different finite element meshes (fine or coarse mesh).

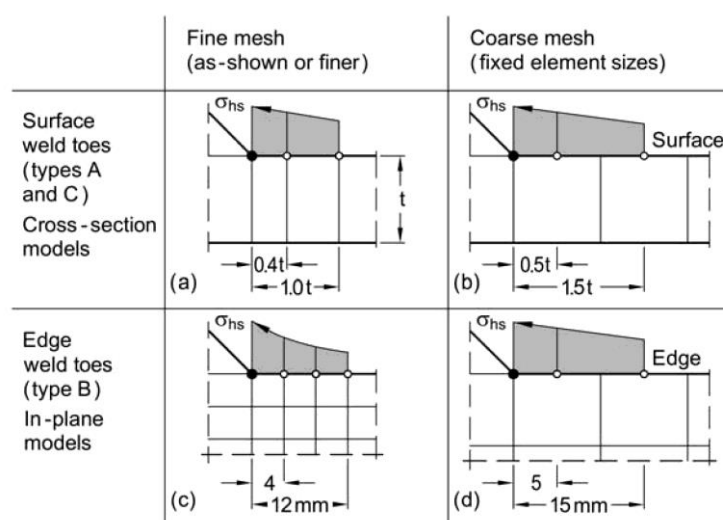


Figure 35: recommended extrapolation of surface or edge stresses to the hot spot in fine or coarse finite element meshes [35]: a.) surface weld toes with fine mesh; b.) surface weld toes with coarse mesh; c.) edge weld toes with fine mesh; d.) edge weld toes with coarse mesh;

The three different types of weld toes A, B and C are shown in Figure 36 [35]:

- the weld toes on the plate surface at the ends of attachments (type A)
- the weld toes on the plate edge at the ends of attachments (type B)
- the weld toes on the plate surfaces amid the weld along an attachment (type C)

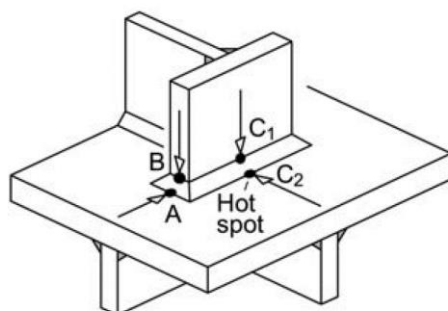


Figure 36: 3 types of fatigue-critical weld toes (type A, B and C) in plate-type reference structure proposed by Fricke [35]

The stresses at the analysed critical details, described in Section 2.4 have been calculated with the structural stress concept by using the linear extrapolation under consideration of the geometrical proposals for the reference points according to Figure 35.a (type C relating to Figure 36). The first reference point is located at a distance of $1.0 \cdot t$ relating to the weld toe and the second one is placed at a distance of $0.4 \cdot t$ relating to the weld toe, where t is the thickness of the analysed steel plate.

For the stress linearization through the thickness of the steel plate a quadratic element type was chosen with reduced integration. More information about the finite element modelling can be found in Section 3.2, where the analysed representative steel decks are described in detail.

2.9. Constructional recommendations for orthotropic steel decks on road bridges according to the actual Eurocode

The actual Eurocode [41] includes recommendations for light weight carriageways, such as orthotropic steel decks referring to the deck plate slenderness and a minimum bending stiffness of the longitudinal ribs.

– Deck plate slenderness

The thickness t_{DP} of the deck plate is generally depending on the heavy traffic classification, respectively on the axle and gross weights of the heavy vehicles that frequently drive on the observed route. The national annex is allowed to define regulations of the deck plate thickness. The following list shows the general recommendations referring to road bridges:

a.) Deck plate thickness in the area of the roadway

$t_{DP} \geq 14$ mm relating to a pavement with a thickness of $t_p \geq 70$ mm

$t_{DP} \geq 16$ mm relating to a pavement with a thickness of $t_p \geq 40$ mm

b.) Interval referring to the webs of the longitudinal ribs

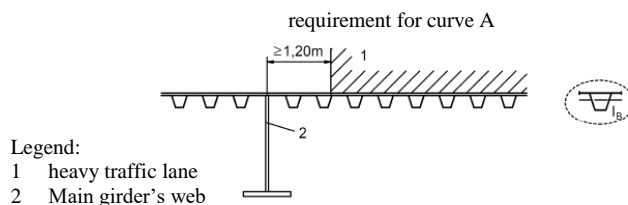
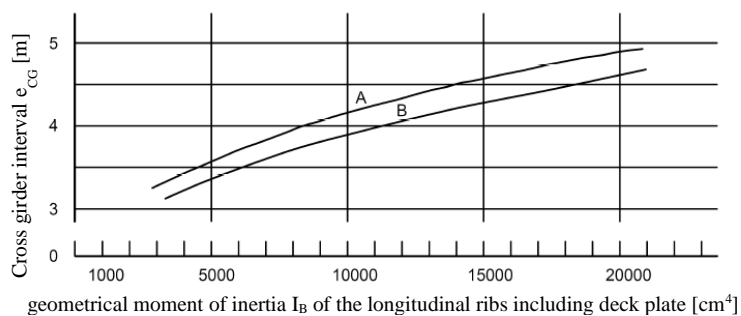
$e_{LR}/t_{DP} \leq 25$ and recommended interval $e_{LR} \leq 300$ mm

a local increase of e_{LR} is allowed up to 5%; for example, adjustment to the horizontal curve of the bridge

– Minimum bending stiffness of the longitudinal ribs

Figure 37 illustrates the recommended minimum bending stiffness of longitudinal ribs on orthotropic steel bridge decks according to the actual Eurocode [41]. The minimum moment of inertia I_B can be selected in the diagram depending on the cross girder interval e_{CG} . This parameter I_B relates to 1 longitudinal rib including its contributing deck plate parts (see sketch in Figure 37). 2 curves (A and B) are plotted in Figure 37, where curve B is the one that applies to longitudinal

ribs in the area of the heavy traffic lane. A description of the indications for the graphs A and B can be found in the notes on the bottom side of the picture. The sketches in Figure 37 shows trough longitudinal ribs but the diagram is applicable for every longitudinal rib type.



Note:

- a) Curve A applies to longitudinal ribs which are not included in b)
- b) Curve B applies to longitudinal ribs in the area of the heavy traffic lane in a distance of $L < 1.20\text{m}$ away from the main girder's web
- c) The picture applies to every type of longitudinal ribs

Figure 37: recommendations for minimum stiffness of longitudinal ribs on orthotropic steel road bridges according to the actual Eurocode [41]

3. Calculation of equivalent constant amplitude stress ranges $\Delta\sigma_e$ for orthotropic steel decks

This chapter generally includes the heavy traffic simulations of the 5 lorry types from fatigue load model FLM 4 and FLM 4* for 3 representative orthotropic steel bridge decks according to the recommendations of the Eurocode [1], [4], [41]. The chosen 3 orthotropic steel decks are shown in Section 2.3.3 and represent a wide range of common European light weight carriageways on existing bridges that were built in the 1960's and 1970's. The analyses have been determined for 3 notch details D1, D2 and D3 (see Section 2.4). The presented results in this Section have been carried out with the assumption of a centric track configuration in transverse direction of all heavy vehicles from the appropriate fatigue load model (FLM 4, FLM 4* or FLM 2) at the critical lane position. The centric track configuration is described in Section 4.2 in detail. The results in terms of stress range spectra are the basis for further analyses regarding to the influence of considering adapted, realistic axle geometries and a lateral distribution of the lorries in transverse direction. These analyses relating to eccentric wheel and lorry positions in transverse direction are presented in Section 4.

Section 3.1 gives an short overview of the procedure relating to the performance of a heavy traffic simulation with the appropriate fatigue load model.

The finite element models that should represent the 3 chosen orthotropic steel decks from Section 2.3.3 are illustrated and explained in Section 3.2. In summary 4 finite element models were necessary for the analyses on the selected details presented in Section 2.4:

- Model A: orthotropic bridge deck with open longitudinal ribs
- Model B: orthotropic bridge deck with trough longitudinal ribs and cross girder spacing of 2m
- Model C: Orthotropic bridge deck with trough longitudinal ribs and cross girder spacing of 4m
- Model D: Orthotropic bridge deck with open longitudinal ribs – cross girder with field splices

An overview of these 4 finite element models is given in Figure 38.

For the heavy traffic simulations, the knowledge of the appropriate critical load/lane position of the vehicles in transverse direction is necessary. Therefore, analyses have been carried out relating to the selected details D1, D2 and D3 which are presented and described in Section 3.3.

The representative results referring to the simulation of the heavy traffic crossings over the modelled carriageways are finally illustrated in Section 3.4 (Model A, B, C and D) where every lorry from the fatigue load model was considered separately. Influence lines for every axle type (axle type A, B and C, see Figure 25) according to fatigue load model FLM 4 (see Section 2.5.2) and relating to the analysed details (see Section 2.4) are plotted first. The calculated stresses in the detail points have been

determined under consideration of a load distribution of 45° through the thickness of an asphalt pavement with a thickness of $t_{\text{asphalt}} = 7\text{cm}$ (see Figure 29). With these influence lines and under consideration of the axle distances as well as the axle loads of the vehicle types (vehicle type T1 to T5, see Figure 24), the stress history curves have been calculated for every crossing of each vehicle type. With reservoir or rain-flow method the stress ranges could be counted isolated for every lorry type. The influence area for the fatigue-critical notch details is very local and there is no interaction between two sequent vehicles regarding to the occurring stress ranges. With these stress ranges, referring to each vehicle type, a stress range spectrum could be produced for every detail point and a damage equivalent constant amplitude stress range $\Delta\sigma_e$ in relation to $n_e = 100$ cycles was determined (note: n_e was selected equal to the number of lorries; the simulations in general were done with 100 vehicles $\rightarrow n_e = 100$). By scaling the number of load cycles with measured data at an existing bridge (number of lorries), a verification with regard to fatigue phenomena can be done.

The damage percentages of the individual vehicle types T1 to T5 from fatigue load model FLM 4 are shown in Section 3.5 for detail D1 and D2.

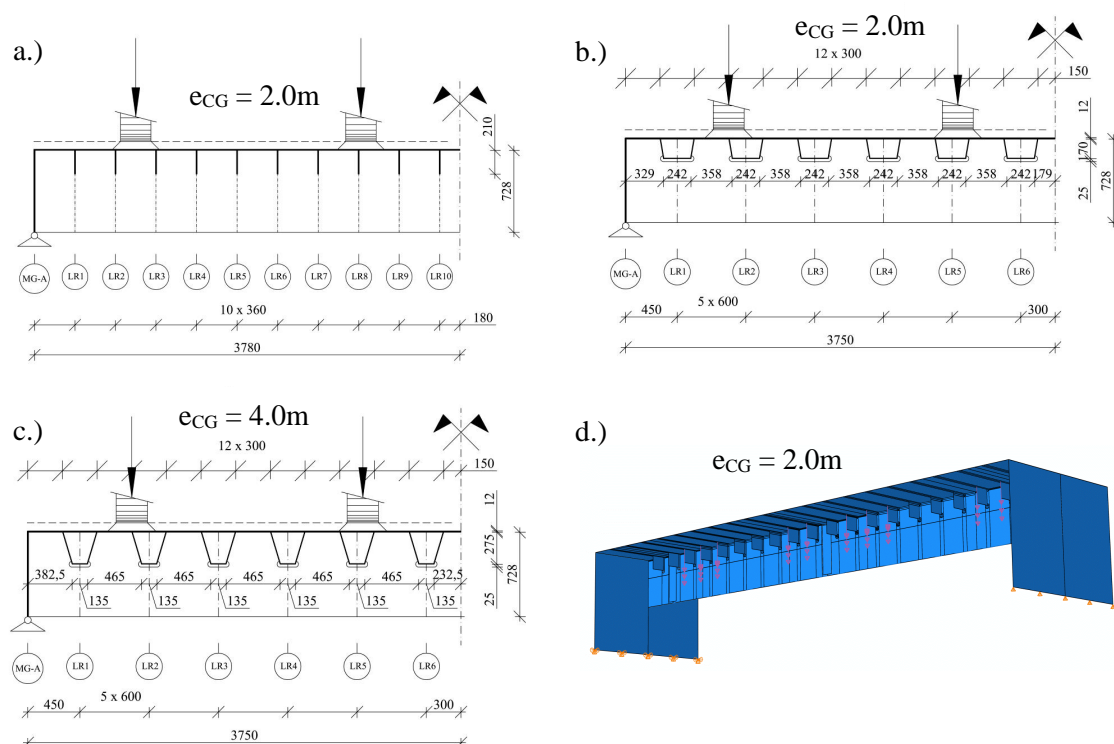


Figure 38: overview of the 4 finite element models: a.) Model A - open longitudinal ribs and $e_{CG} = 2.0\text{m}$; b.) Model B - closed longitudinal ribs and $e_{CG} = 2.0\text{m}$; c.) Model C - closed longitudinal ribs and $e_{CG} = 4.0\text{m}$; d.) Model D – open longitudinal ribs and cross girder with field splices (detail D3);

3.1. General concept of fatigue assessment at orthotropic steel decks

The procedure for the fatigue assessment of orthotropic steel decks is schematically illustrated in Figure 39, based on FLM 4. First a crossing of the 5 lorry types with its axle distances and axle loads has to be simulated based on a FE-model of the bridge deck which is shown in Figure 39.a. The appropriate stresses have to be determined at the chosen notch detail. For the calculation of accurate results in the detail by using the structural stress method (see Section 2.7 and 2.8), the finite element model has to fulfil the requirements relating to the mesh geometry and its element type (see Section 2.8) with regard to the linear stress extrapolation to the weld toe.

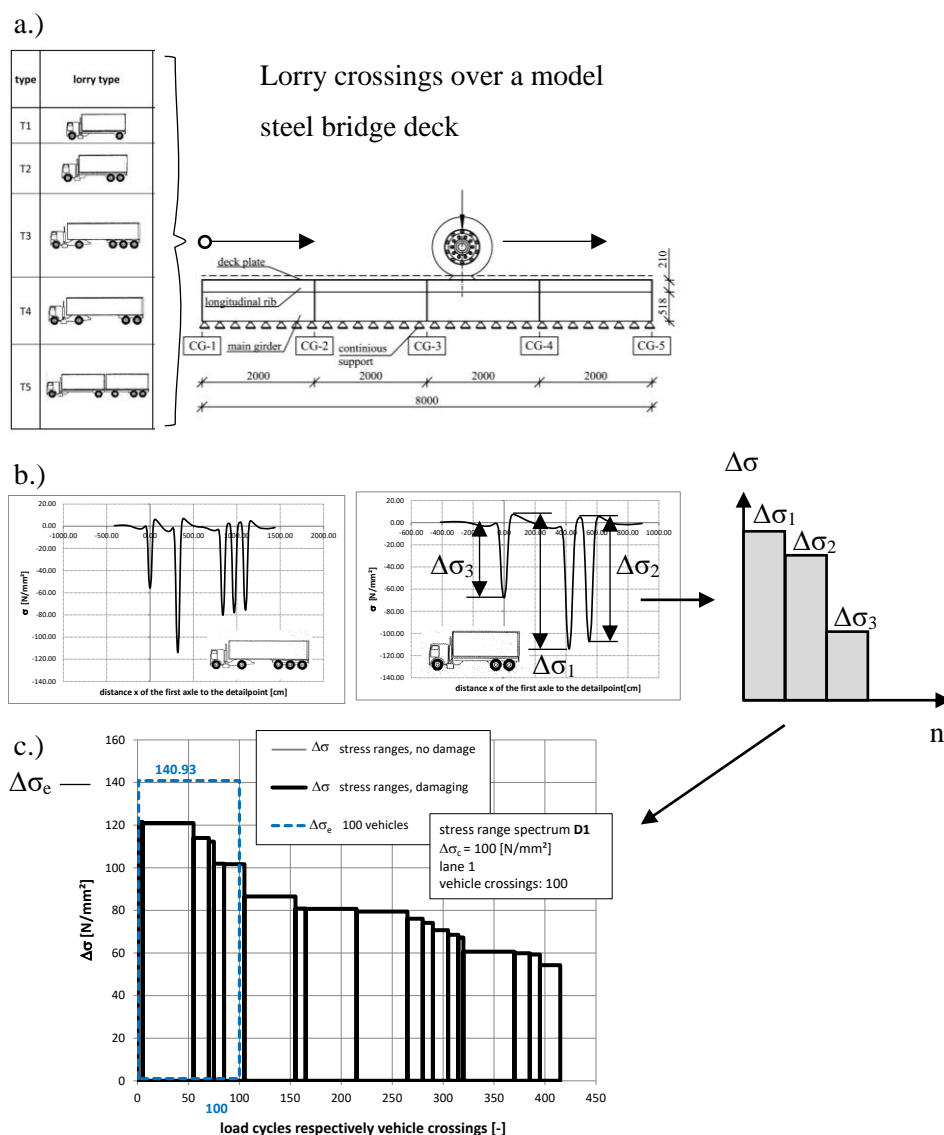


Figure 39: general concept of fatigue assessment at orthotropic steel bridge decks within a simplified schematic illustration: a.) simulation of lorry crossings; b.) stress-history for each lorry crossing; c.) stress range spectrum with $\Delta\sigma_e$

For the very local notch details of an orthotropic steel deck plate, that are explained in Section 2.4, the modelling of only the carriageway between the two main girders including 5 cross girders delivers sufficient results for the studied bridge deck with only two main girders and ignoring the effect of a lorry interaction on different lanes. The effects of the global load carrying behaviour of the bridge deck relating to the notch details of the orthotropic deck are negligibly small (orthotropic deck is part of the main girder's upper flange).

After the simulation of the heavy traffic crossings over the bridge deck, a stress history can be determined for every lorry type crossing referring to the analysed detail. For example Figure 39.b shows two stress history curves for detail D1a (welded connection of the longitudinal rib to the deck plate). With rain flow or reservoir method as cycle counting method and under consideration of the lorry percentages according to the fatigue load model, a stress range spectrum can be produced referring to a chosen number of stress cycles. Figure 39.c illustrates a stress range spectrum referring to detail D1a for crossing of altogether 100 lorries. In addition a damage equivalent constant amplitude stress range $\Delta\sigma_e$ can be determined which is also plotted in Figure 39.c relating to $n_e = 100$ load cycles (that means 1 stress cycle $\Delta\sigma_e$ due to 1 lorry crossing). The total number of cycles $n_{e,total}$ has to be adapted based on measurements on site for the studied bridge and then a value for the damage D_e can be calculated by using Equation 5 and Equation 6 (see Section 2.6).

As already shown in Section 2.6 – Figure 32, measured traffic data referring to the total number of lorries $n_{e,total}$ within the observed time period is necessary for the determination of a remaining fatigue life. Under consideration of the appropriate detail category referring to the detail, the maximum allowable load cycles relating to $\Delta\sigma_e$ can be determined ($N_{R,e} = (\Delta\sigma_c/\Delta\sigma_e)^3 \cdot 2 \cdot 10^6$). With this information the damage D_e of the analysed detail can be determined: $D_e = n_{e,total} / N_{R,e} \leq 1.0$. If this value exceeds 1.0, no further computational fatigue life is available. A crack inspection on site and, if necessary, a repair is required. If D_e is lower than 1.0, additional computational fatigue life is available. Therefore, the damage due to the future equivalent constant amplitude stress range $\Delta\sigma_{e,future}$ has to be lower than the difference between 1 and D_e ($D_{e,future} \leq 1.0 - D_e$).

This general concept for fatigue assessment with the procedure described above has been performed for the selected fatigue-critical notch details described in Section 2.4. The heavy traffic simulations have been carried out on 3 different representative orthotropic steel bridge decks which are explained in Section 2.3.3. In the following Section 3.2, the finite element models for these 3 representative bridge decks are shown, where altogether 4 FEM models were necessary to evaluate all notch details. Additionally, analyses referring to the critical load (lane) positions in transverse direction relating to the individual notch details have been done which are described in Section 3.3. The heavy traffic simulations itself are illustrated in Section 3.4, where selected results are presented.

3.2. Analysed representative steel decks

In summary 4 different finite element models have been carried out:

- Model A: orthotropic bridge deck with open longitudinal ribs (see Section 3.2.1)
- Model B: orthotropic bridge deck with trough longitudinal ribs and cross girder spacing of 2m (see Section 3.2.2)
- Model C: orthotropic bridge deck with trough longitudinal ribs and cross girder spacing of 4m (see Section 3.2.3)
- Model D: orthotropic bridge deck with open longitudinal ribs – cross girder with field splices (see Section 3.2.4)

All numerical studies have been performed with the software ABAQUS [49].

3.2.1. Model A: Orthotropic bridge deck with open longitudinal ribs

The finite element model – Model A, described below, consists of 2 main girders (only part of the web), a very slender deck plate, 20 open longitudinal ribs and 5 cross girders.

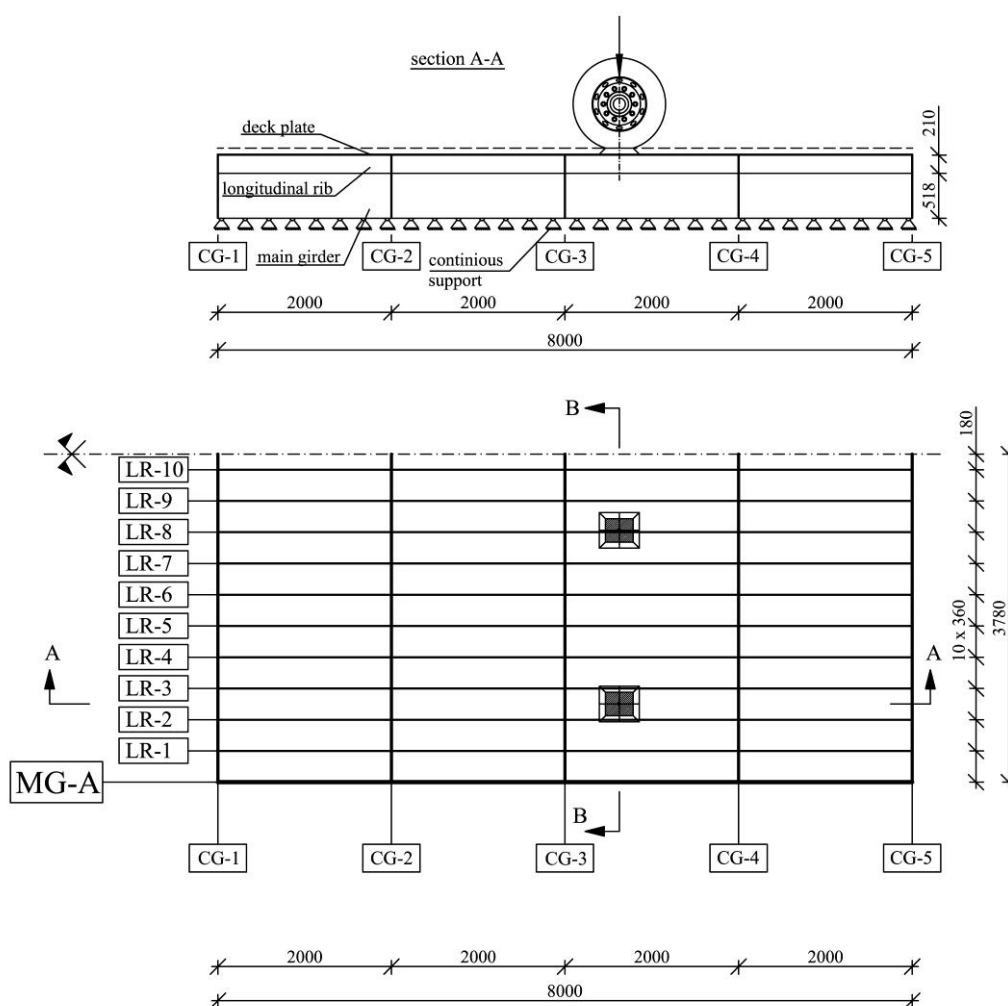


Figure 40: Model A – orthotropic steel deck with open longitudinal ribs (plan view and longitudinal section)

The overall dimensions of Model A are 8.0m in longitudinal and 7.56m in transverse direction. Figure 40 shows a plan view of the model and a longitudinal section in axial bridge direction (section A-A). Also the boundary conditions are illustrated schematically in the sketch. The model is supported on the lower edges of both main girders, because only the local bending behaviour of the steel deck is analysed.

The orthotropic deck was modelled between 2 main girders (MG-A to MG-B) and the plan view in Figure 40 illustrates the region from main girder MG-A to the mid axis of the bridge deck, so that 10 longitudinal ribs (LR-1 to LR-10) are plotted in this picture. The illustration also shows the geometrical dimension of all parts. The distance between the 2 main girders MG-A and MG-B has a value of $e_{MG} = 2 \cdot 3.78 = 7.56\text{m}$. The interval of the cross girders e_{CG} is 2.0m and the interval of the open longitudinal ribs is $e_{LR} = 0.36\text{m}$. The deck plate has a thickness of $t_{DP} = 10\text{mm}$ which leads to a deck plate slenderness of $e_{LR} / t_{DP} = 360 / 10 = 36$. This deck plate slenderness is higher than the recommended value in the actual Eurocode [41] which is $e_{LR} / t_{DP} \leq 25$. The longitudinal ribs were modelled with a thickness of $t_{LR} = 10\text{mm}$ and a height of $h_{LR} = 210\text{mm}$. These flat steel stiffeners have no flange on their bottom side and are conducted as continuous longitudinal ribs passing through the cross girders with an additional cope hole in the cross girder's web. The longitudinal ribs have a one sided (eccentric) fillet weld connection to the cross girder's web (see Figure 17) and a detailed illustration of the cope hole's model in the cross girders is shown in Figure 45.

As it can be seen in Figure 41, section B-B in transverse direction, the height of the main girders $h_{MG} = h_{CG} = 0.728\text{m}$ is modelled just to the bottom side of the cross girder's web and the main girders are supported along these bottom edges. A detailed description and illustration of the boundary conditions is following.

In Figure 41, the load distribution with an angle of 45° through the thickness of the pavement (dashed line) can be seen under the tyres. The pavement itself was not modelled. This beneficial load distribution was considered within an increased wheel contact patch of the axles according to the Eurocode (see Figure 25 and Figure 29).

The whole finite element model for Model A is illustrated in Figure 42. Also the global coordinate system is plotted in this picture and the x-axis indicates the longitudinal direction of the bridge. The orthotropic steel deck was modelled between the 2 main girders (MG-A and MG-B).

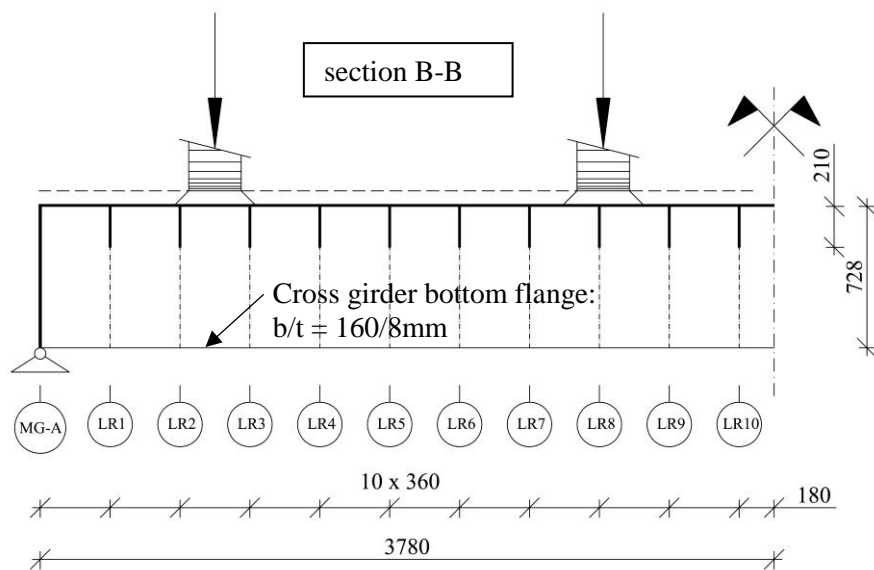


Figure 41: Modell A – orthotropic steel deck with open longitudinal ribs (section B-B)

The overhanging parts of the deck outside the main girders have nearly the same load bearing behaviour as the ones between the main girders and therefore these outer parts haven't been modelled. As already mentioned, just the steel structure without any pavement was modelled and the whole assembly consists of steel material with linear elastic material behaviour. The Young Modulus of the steel is $E_s = 210.000$ N/mm² and the Poisson Ratio has a value of $\nu = 0.3$.

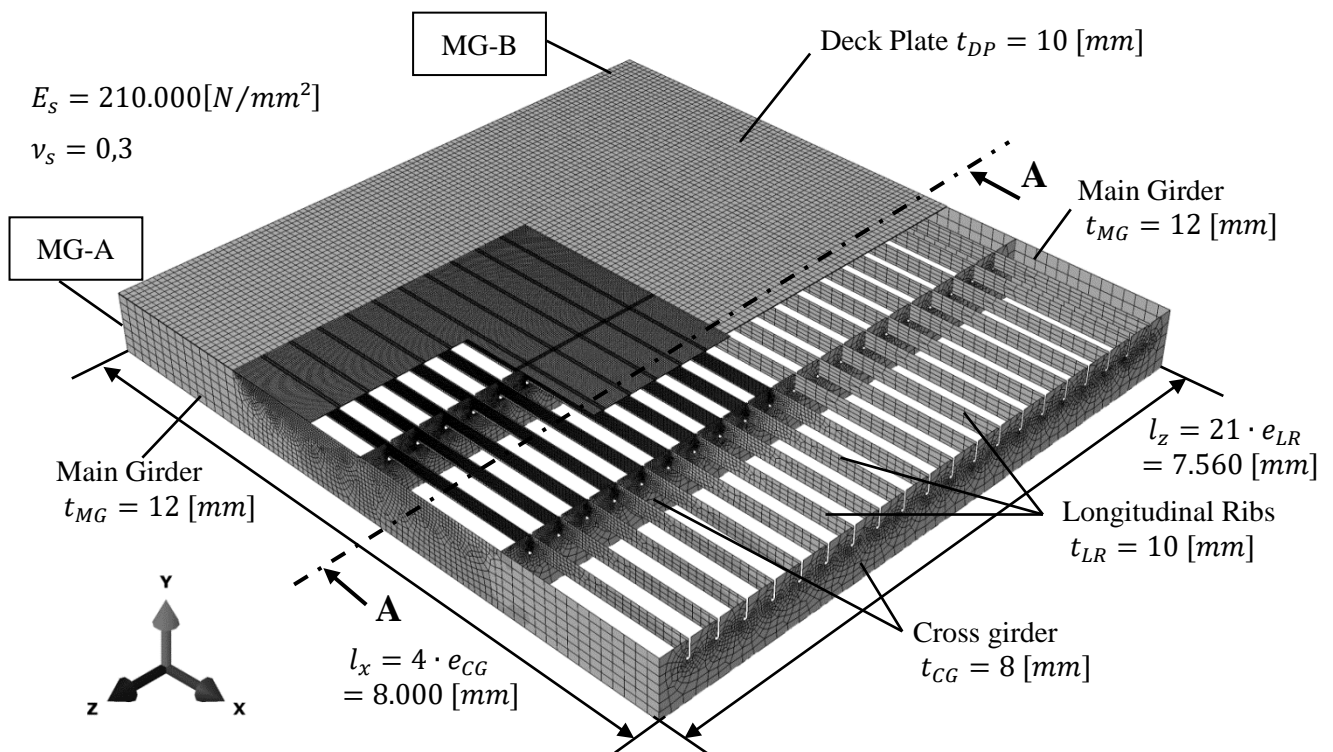


Figure 42: FEM-Modell A – orthotropic steel deck with open longitudinal ribs (overview)

In summary the finite element model that is shown in Figure 42 consists of the following parts:

- Web of the Main Girder (MG):
 - Thickness of the web $t_{MG} = 12\text{mm}$
 - Reduced height of the main girder $h_{MG} = 728\text{mm}$
 - Interval between the main girders $e_{MG} = 7.56\text{m}$
 - Modelled with quadratic shell elements with reduced integration (type S8R in ABAQUS)
 - Element size is varying from $26 \times 26\text{mm}$ to approximately $150 \times 100\text{mm}$
 - Supported in vertical direction on the bottom edge line of the main girder's web
- Cross Girder (CG):
 - Thickness of the web $t_{CG} = 8\text{mm}$
 - Height of the cross girder $h_{CG} = 728\text{mm}$
 - Dimensions of the bottom flange of the cross girder $160 \times 8\text{mm}$
 - Interval between the cross girders $e_{CG} = 2.0\text{m}$
 - Cross girder's web modelled with quadratic shell elements with reduced integration, element type S8R
 - Element size of the shell elements at the cross girder's web is varying from $10 \times 10\text{mm}$ to approximately $150 \times 200\text{mm}$
 - Bottom flange ($b/t = 160/8\text{mm}$) of the cross girder is modelled with linear beam elements, element type B31
 - Element size of the beam elements at the bottom flange is 50mm
 - The cross girder is rigid tied to the main girders
- Longitudinal Rib (LR):
 - Flat steel plates with a plate thickness of $t_{LR} = 10\text{mm}$
 - Height of the longitudinal ribs $h_{LR} = 210\text{mm}$
 - Interval between the longitudinal ribs $e_{LR} = 360\text{mm}$
 - Modelled with quadratic shell elements with reduced integration, element type S8R
 - Element size is varying from $20 \times 10\text{mm}$ to approximately $150 \times 80\text{mm}$
 - Flat steel plates are connected one sided to the cross girder (eccentric) with cope holes in the cross girders web and are fixed together with rigid transition conditions
- Deck Plate (DP):
 - Thickness of the deck plate $t_{DP} = 10\text{mm}$
 - Deck plate slenderness $e_{LR}/t_{DP} = 360/10 = 36$
 - Modelled with quadratic continuum elements with reduced integration, element type C3D20R
 - Element size is varying from $20 \times 20 \times 10\text{mm}$ to approximately $80 \times 72 \times 10\text{mm}$
 - Deck plate has a rigid tie connection to the longitudinal ribs, the cross girders and the main girders

Figure 43 shows a cross section (section A-A) of the finite element model that is displayed in Figure 42. The defined boundary conditions at the bottom edges of the main girders are shown in detail. At the bottom edge of the left main girder MG-A, the displacements in all directions U_x , U_y and U_z are fixed as well as the rotation around the z-axis ($U_x = U_y = U_z = Rot_z = 0$). At the bottom edge of the right main girder MG-B, the displacements in the x and y direction as well as the rotation around the z-axis are fixed ($U_x = U_y = Rot_z = 0$). An additionally enlargement of the welded connection between longitudinal rib and cross girder shows the cope holes with their geometrical dimensions in detail. The height of the longitudinal ribs h_{LR} and its interval among each other e_{LR} is also shown in Figure 43 as well as the main girder's interval e_{MG} .

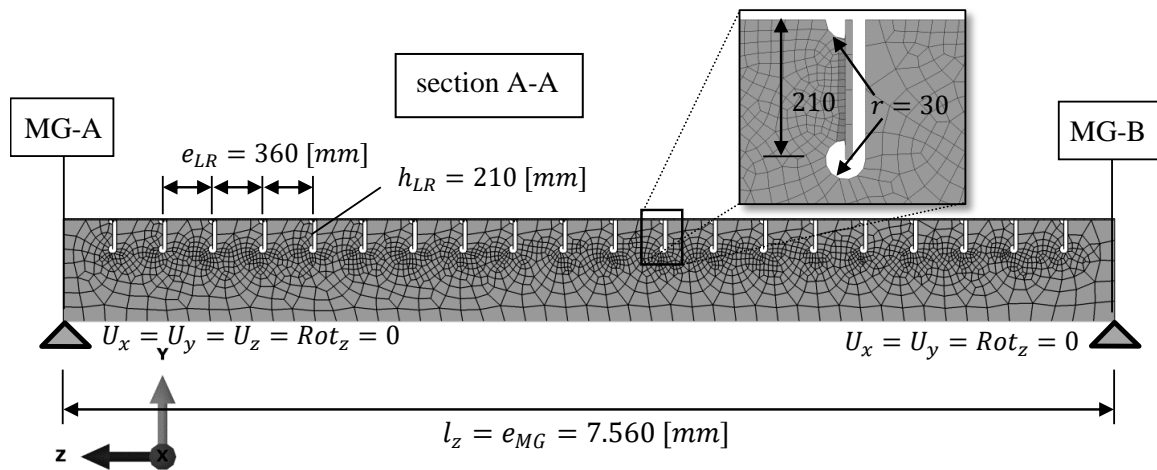


Figure 43: FEM-Modell A – orthotropic steel deck with open longitudinal ribs (section A-A)

Figure 44 illustrates the modelling of the deck plate by partitioning into 2 regions, Region A and Region B. As it can be seen in the picture, there is a differentiation in the element size to reduce significantly the degrees of freedom that causes less calculation time. Both regions of the deck plate include quadratic continuum elements with reduced integration, element type C3D20R. Region A of the deck plate contains a finer mesh with an element size of 20x20x10mm and Region B of the deck plate contains a coarse mesh with an element size of 80x72x10mm (see Figure 44).

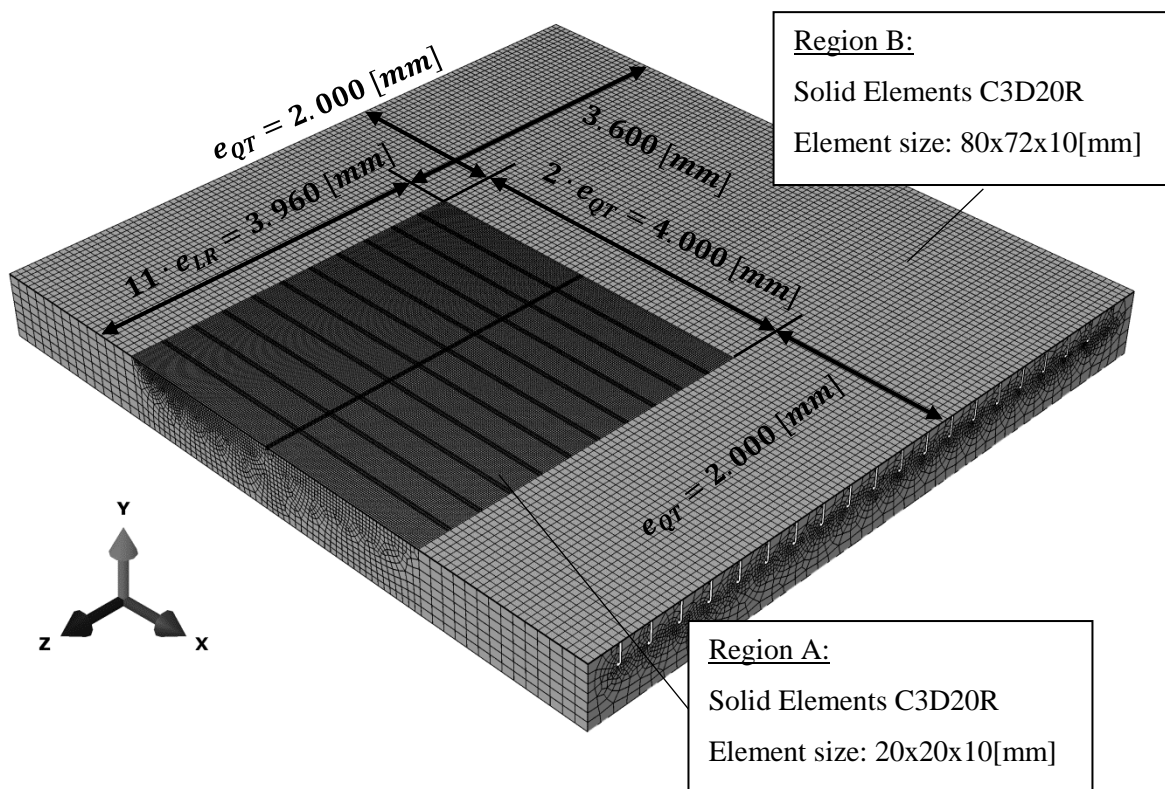


Figure 44: FEM-Modell A – Mesh of the deck plate

In addition to the mesh refinement in Region A, the welds referring to the connection of the deck plate to the longitudinal ribs and the deck plate to the cross girders have also been modelled by using quadratic continuum elements with reduced integration (C3D20R). In the model – as a simplification – full penetration welds are assumed (ignoring the gap between deck plate and longitudinal rib), which leads to nearly the same bending stresses in the deck plate. These local modifications which are necessary for the hot spot stress calculation are illustrated in Figure 45. According to the recommendations referring to the linear extrapolation of the stresses to the weld toe, another mesh refinement in the deck plate (Region A) has been applied in the local areas of the longitudinal rib to the deck plate connections (see Figure 35.a). With this local mesh refinements nodes have been created that are needed as reference points for the linear stress extrapolation. These reference points need to be located in a distance of $0.4 \cdot t_{DP}$ and $1.0 \cdot t_{DP}$ away from the weld toe. The constraints of the shell elements (longitudinal rib and cross girder) to the continuum elements (welds as solid) were defined as shell to solid coupling. With this specification, the displacements in all directions as well as the rotations could be transferred in a correct way.

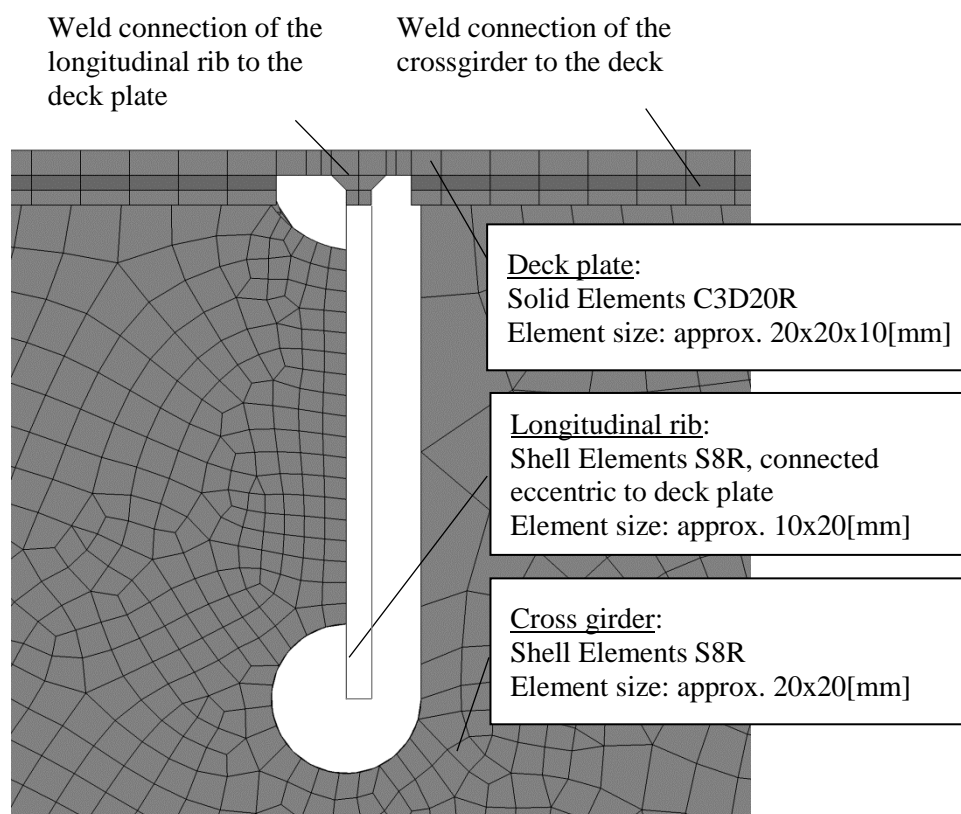


Figure 45: FEM-Modell A – Modelling of the welded connections, longitudinal rib and cross girder to deck plate

3.2.2. Model B: Orthotropic bridge deck with trough longitudinal ribs and a cross girder spacing of 2m

The finite element model for Model B, described below, consists of 2 main girders, a slender deck plate, 12 closed longitudinal ribs (trough ribs) and 5 cross girders. Model B's overall dimensions are 8.0m in longitudinal and 7.50m in transverse direction. A plan view of the model is shown in Figure 46 as well as a longitudinal section in axial bridge direction (section A-A). Additionally, the illustration shows schematically the boundary conditions where the model's support is located on the lower edges of both main girders.

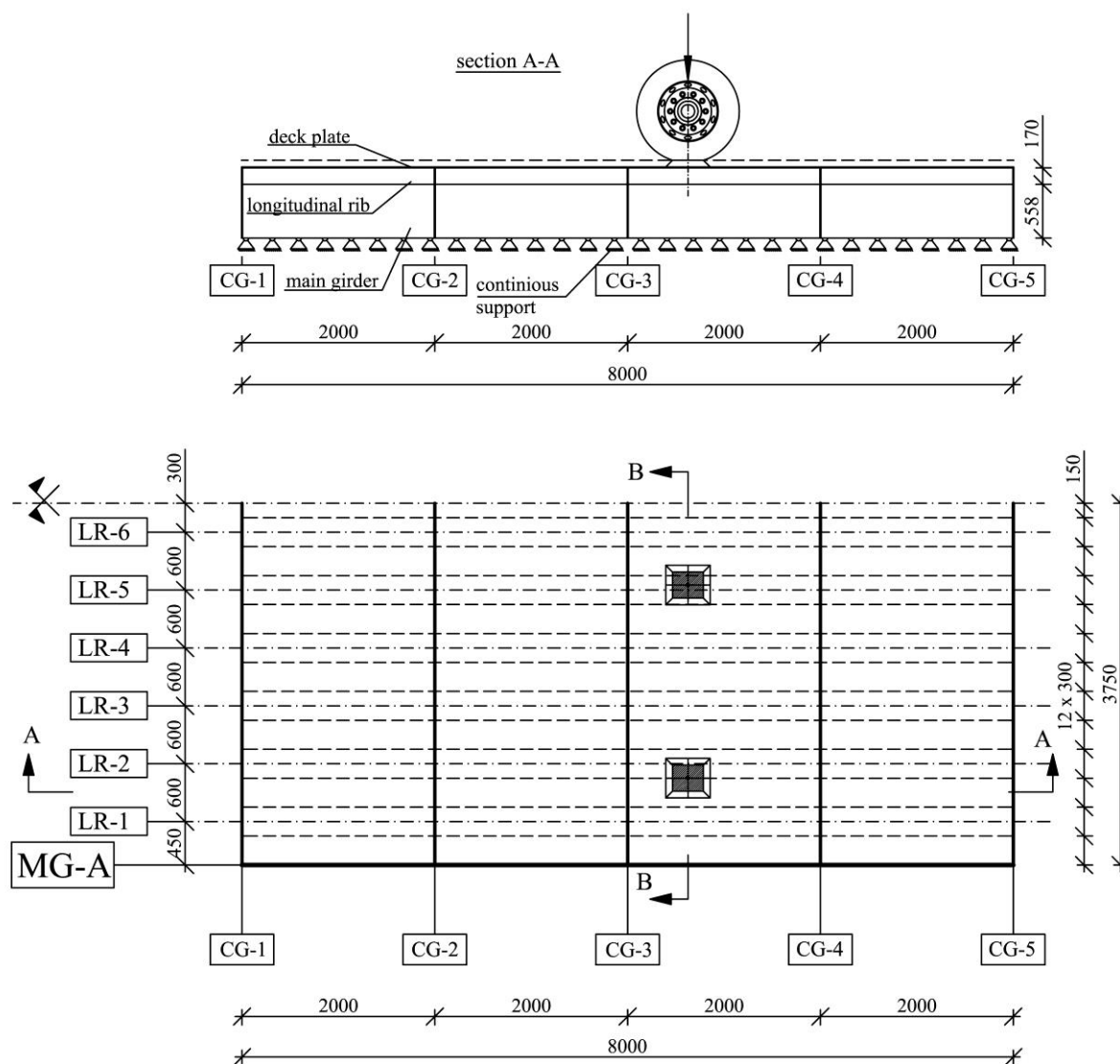


Figure 46: Modell B – orthotropic steel deck with trough longitudinal ribs and cross girder spacing of 2m (plan view and longitudinal section)

Between the 2 main girders (MG-A to MG-B) the orthotropic deck was modelled, which is illustrated in the plan view of Figure 46 where the region from main girder MG-A to the mid axis of the bridge deck can be seen. In this picture 6 longitudinal ribs (LR-1 to LR-6) are plotted. Additionally, the geometrical dimension of all parts are shown. The main girder's distance to each other (MG-A to MG-B) has a value of $e_{MG} = 2 \cdot 3.75 = 7.50\text{m}$. The cross girder's interval e_{CG} is 2.0m and the trough rib web's interval is $e_{LR} = 0.30\text{m}$. The deck plate's thickness is $t_{DP} = 12\text{mm}$ which leads to a deck plate slenderness of $e_{LR} / t_{DP} = 300 / 12 = 25$. This deck plate slenderness has the same value than the recommended limit of the actual Eurocode [41] which is $e_{LR} / t_{DP} \leq 25$. The trough rib's plate thickness was modelled with $t_{LR} = 6\text{mm}$ and the trough rib's height is $h_{LR} = 170\text{mm}$. These trough longitudinal stiffeners are conducted as continuous longitudinal ribs passing through the cross girders with an

additional cope hole in the cross girder's web. The trough ribs have on both outer web sides a welded connection to the cross girder's web (see Figure 18) and a detailed illustration of the cope holes model in the cross girders is shown in Figure 51.

As shown in Figure 47, section B-B in transverse direction, the main girder's height is modelled just to the bottom side of the cross girder's web with $h_{MG} = h_{CG} = 0.728\text{m}$. The main girders are supported along its bottom edges. In the following, a detailed description and visualisation of the boundary conditions is given. When taking a closer look at Figure 47, the load distribution with an angle of 45° through the thickness of the pavement (dashed line) can be detected underneath the tyres. The pavement itself was not modelled. An increased wheel contact patch of the axles according to the Eurocode (see Figure 25 and Figure 29) considered the beneficial load distribution of the pavement.

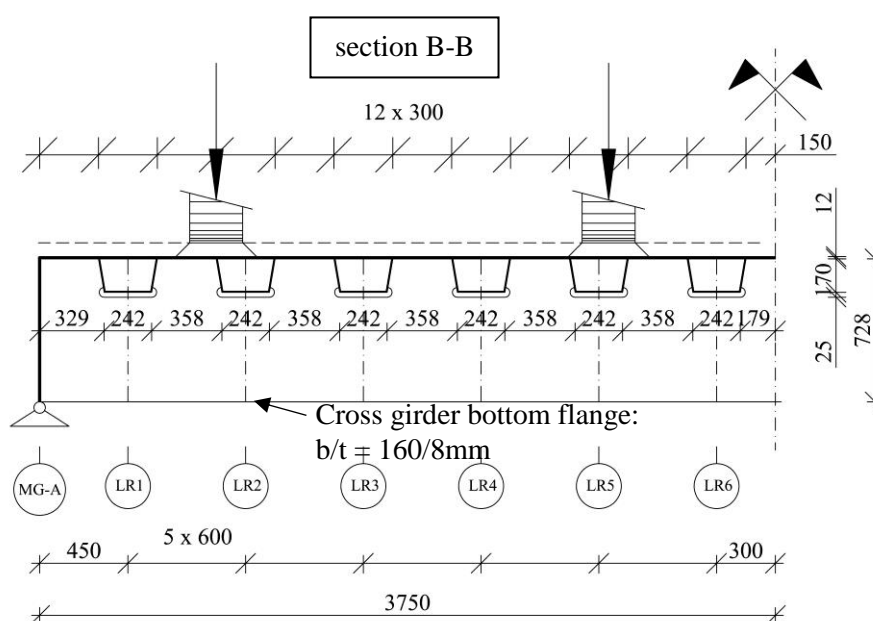


Figure 47: Modell B – orthotropic steel deck with trough longitudinal ribs (section B-B)

Figure 48 illustrates the entire finite element model for Model B. The illustration also shows the global coordinate system where the x-axis indicates the longitudinal bridge direction. The load bearing behaviour of the overhanging parts outside the main girders is equal to the steel deck's behaviour between MG-A and MG-B. Therefore, these outer parts haven't been modelled. The pavement was not modelled, just the steel structure, where a linear elastic material behaviour was implemented. The Young Modulus of the steel is $E_S = 210.000\text{ N/mm}^2$ and the Poisson Ratio has a value of $\nu = 0.3$.

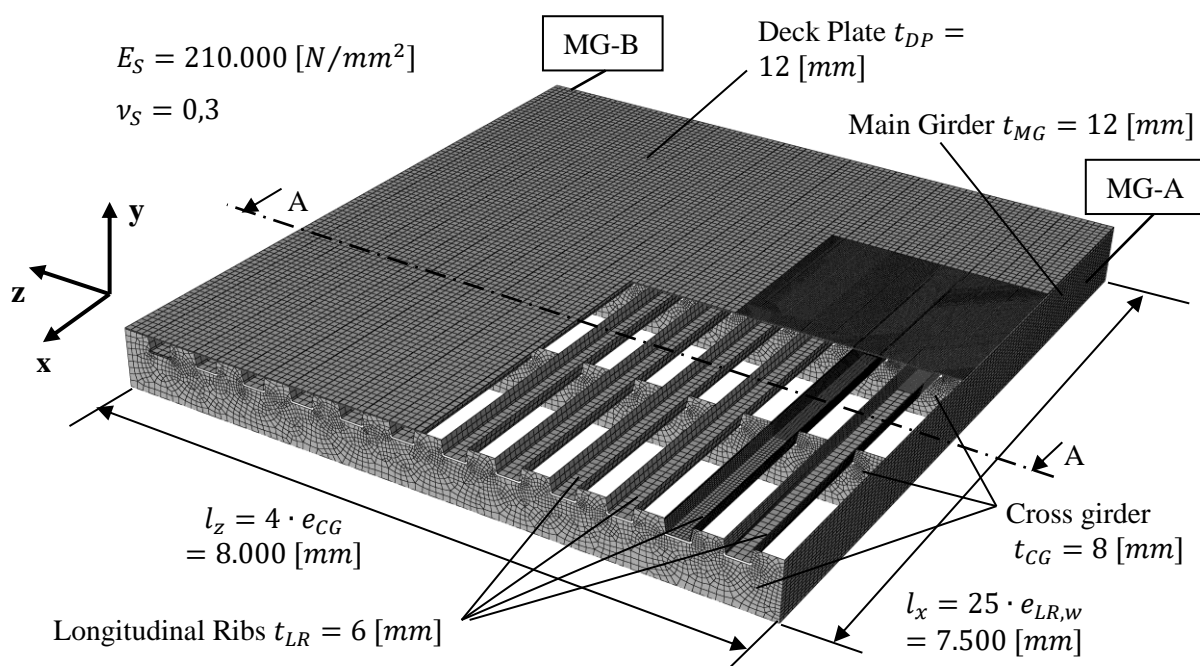


Figure 48: FEM-Modell B – orthotropic steel deck with trough longitudinal ribs (overview)

In summary the finite element model that is shown in Figure 48 consists of the following parts:

- Part of the Main Girder (MG):
 - Thickness of the web $t_{MG} = 12\text{mm}$
 - Reduced height of the main girder $h_{MG} = 728\text{mm}$
 - Interval between the main girders $e_{MG} = 7.50\text{m}$
 - Modelled with quadratic shell elements with reduced integration, element type S8R
 - Element size is $40 \times 80\text{mm}$
 - Supported on the bottom edge line of the main girder's web

- Cross Girder (CG):
 - Thickness of the web $t_{CG} = 8\text{mm}$
 - Height of the cross girder $h_{CG} = 728\text{mm}$
 - Dimensions of the bottom flange of the cross girder $160 \times 8\text{mm}$
 - Interval between the cross girders $e_{CG} = 2.0\text{m}$
 - Cross girder's web modelled with quadratic shell elements with reduced integration, element type S8R
 - Element size of the shell elements at the cross girder's web is varying from $20 \times 20\text{mm}$ to approximately $80 \times 60\text{mm}$
 - Bottom flange of the cross girder ($b/t = 160/8\text{mm}$) is modelled with linear beam elements, element type B31

- Element size of the beam elements at the bottom flange is 50mm
- The cross girder is rigid tied to the main girders
- Longitudinal Rib (LR):
 - Trough ribs with a plate thickness of $t_{LR} = 6\text{mm}$
 - Height of the longitudinal ribs $h_{LR} = 170\text{mm}$
 - Interval between the trough webs of the longitudinal ribs $e_{LR} = 300\text{mm}$
 - Modelled with quadratic shell elements with reduced integration, element type S8R
 - Element size is varying from 20x20mm to 20x80mm
 - Trough webs are connected on the outer sides to the cross girder with cope holes in the cross girders web and are fixed together with rigid transition conditions
- Deck Plate (DP):
 - Thickness of the deck plate $t_{DP} = 12\text{mm}$
 - Deck plate slenderness $e_{LR}/t_{DP} = 300/12 = 25$
 - Modelled with quadratic continuum elements with reduced integration, element type C3D20R
 - Element size is varying from 20x20x12mm to approximately 80x75x12mm
 - Deck plate has a rigid tie connection to the longitudinal ribs, the cross girders and the main girders

A cross section (section A-A) of the finite element model that is displayed in Figure 48 is shown in Figure 49. The picture shows the defined boundary conditions at the main girder's bottom edges in detail. At the bottom edge of the left main girder MG-A, the displacements in all directions U_x , U_y and U_z are fixed as well as the rotation around the z-axis ($U_x = U_y = U_z = \text{Rot}_z = 0$). At the bottom edge of the right main girder MG-B, the displacements in the x and y direction as well as the rotation around the z-axis are fixed ($U_x = U_y = \text{Rot}_z = 0$). The cope holes in the cross girder's web are shown in an additionally enlargement of the welded connection between longitudinal rib and cross girder with its geometrical dimensions. Figure 49 also shows the height of the longitudinal ribs h_{LR} and the interval of the through webs among each other as well as the main girder's interval e_{MG} .

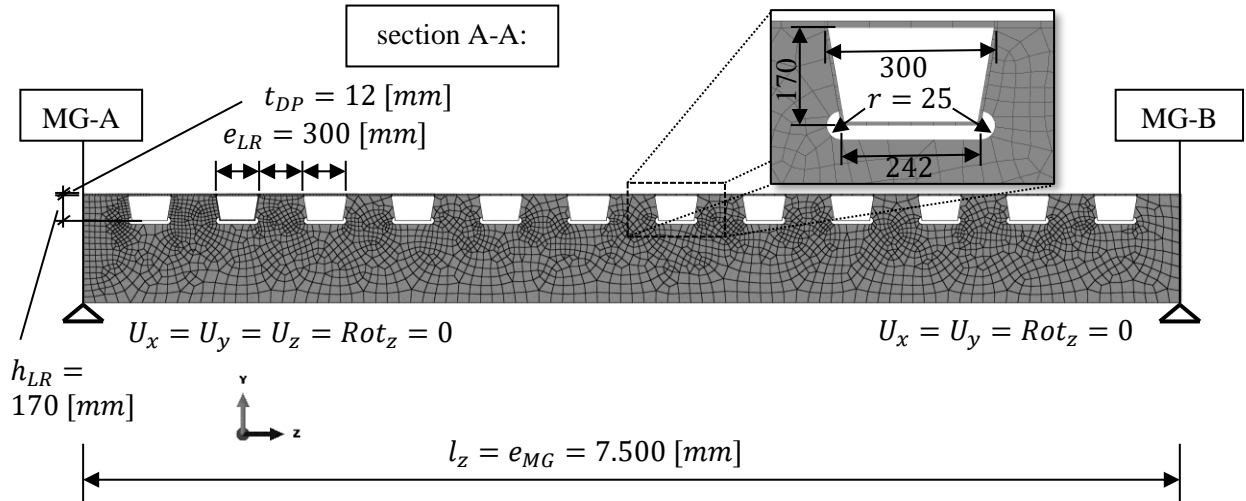


Figure 49: FEM-Modell B – orthotropic steel deck with through longitudinal ribs (section A-A)

The deck plate was modelled with a partition into 2 regions which are illustrated in Figure 50 (Region A and Region B). The element size between these 2 regions is different as it can be seen in the picture. This process has been done to reduce significantly the degrees of freedom which causes less calculation time. For both regions of the deck plate quadratic continuum elements with reduced integration were used (element type C3D20R). The deck plate's Region A contains a finer mesh with an element size of 20x20x12mm. Region B contains a coarse mesh with an element size of 80x75x12mm (see Figure 50).

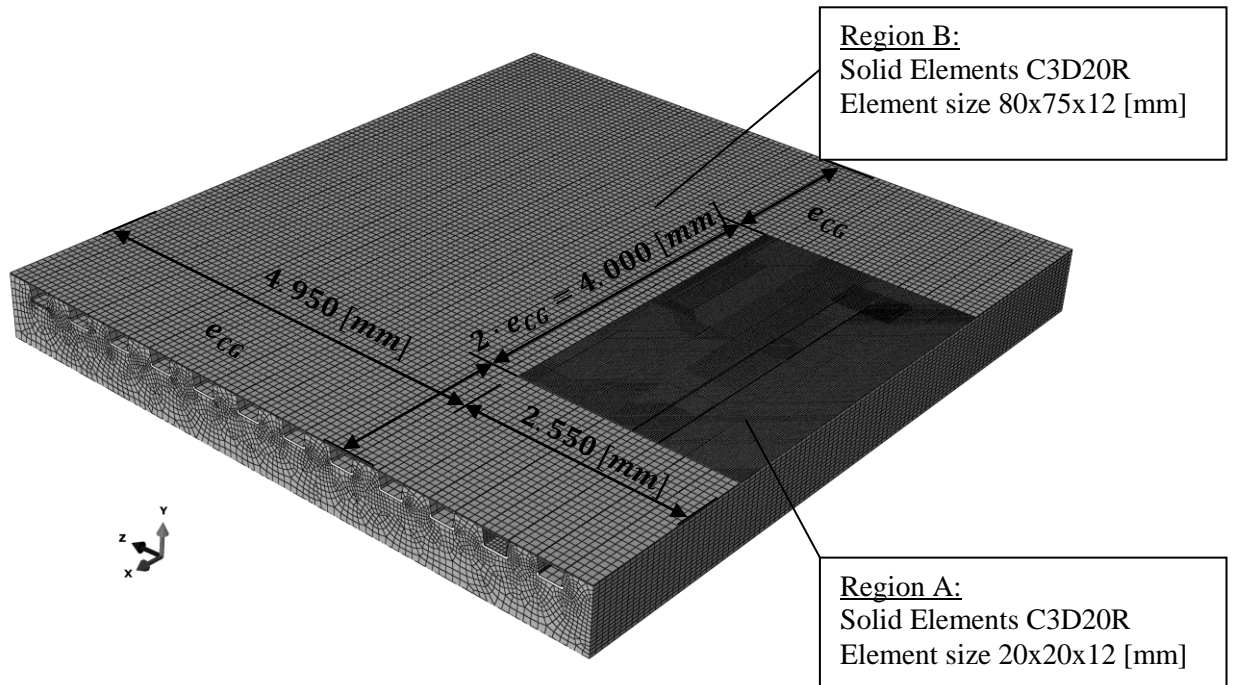


Figure 50: FEM-Modell B – Mesh of the deck plate

Further investigations relating to the critical location of the notch details showed that the welds at the longitudinal rib close to the main girder (LR-1 or LR-12) are decisive. These analyses are presented later on in Section 3.3. The load application of the increased wheel contact patch due to axle type B (see Figure 25 and Figure 29) was not possible at LR-1 because there was not enough space between LR-1 and the main girder MG-A. Therefore, the second longitudinal rib LR-2 was chosen for the analyses at Model B (note: the results of longitudinal rib LR-2 are similar to LR-1). For the calculation of accurate results referring to notch detail D1b (see Section 2.4.3) the modelling of the relevant trough rib LR-2 by using quadratic continuum elements with reduced integration (C3D20R) was necessary (see Figure 51). All other longitudinal ribs (LR-1 and LR-3 to LR-12) have been modelled by using shell elements (see Figure 52).

– Additional modifications at longitudinal rib LR-2:

According to the recommendations referring to the linear extrapolation of the stresses to the weld toe, another mesh refinement in the deck plate (Region A) has been applied in the local areas of the longitudinal rib to deck plate connections (see Figure 35.a). With this local mesh refinements, which were necessary for the hot spot stress calculation, nodes have been created that are needed as reference points for the linear stress extrapolation. These reference points need to be located in a distance of $0.4 \cdot t_{DP}$ and $1.0 \cdot t_{DP}$ away from the weld toe and are illustrated in Figure 51.

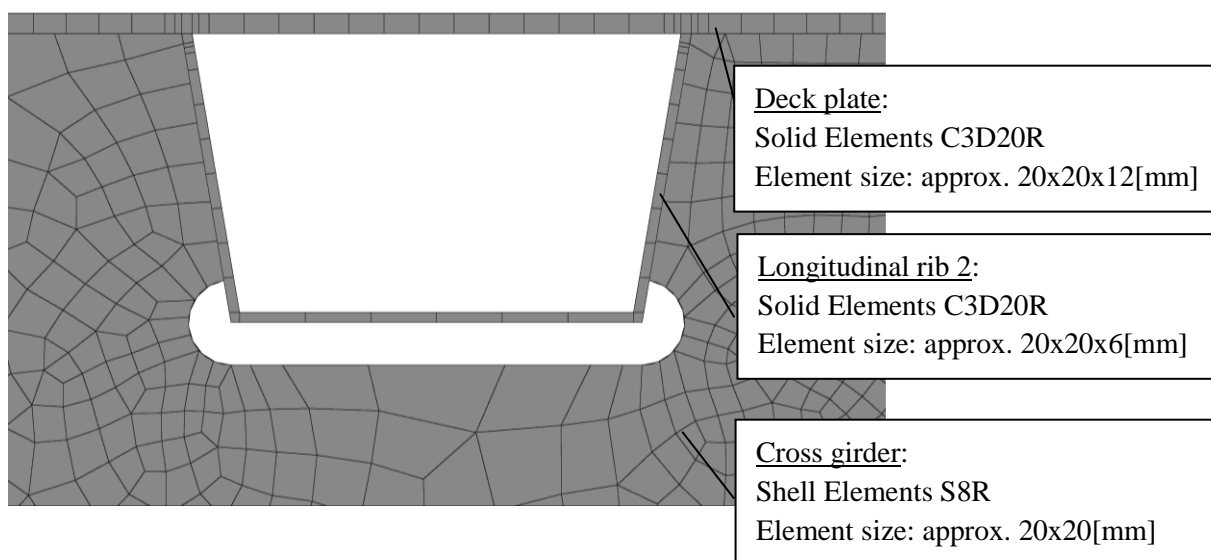


Figure 51: FEM-Modell B – Modelling of the through rib LR-2 with continuum elements including the weld connections to deck plate

- Additional modifications at longitudinal ribs LR-1 and LR-3 to LR-12:

The welds referring to the connection of the deck plate to the longitudinal ribs (LR-1 and LR-3 to LR-12) also have been modelled by using quadratic continuum elements with reduced integration (C3D20R). These local modifications which are necessary for accurate transition conditions between the solid deck plate and the shell trough ribs are illustrated in Figure 52. The constraint of the shell elements (longitudinal rib) to the continuum elements (welds as solid) was defined as shell to solid coupling. With this specification, the displacements in all directions as well as the rotations could be transferred in a correct way.

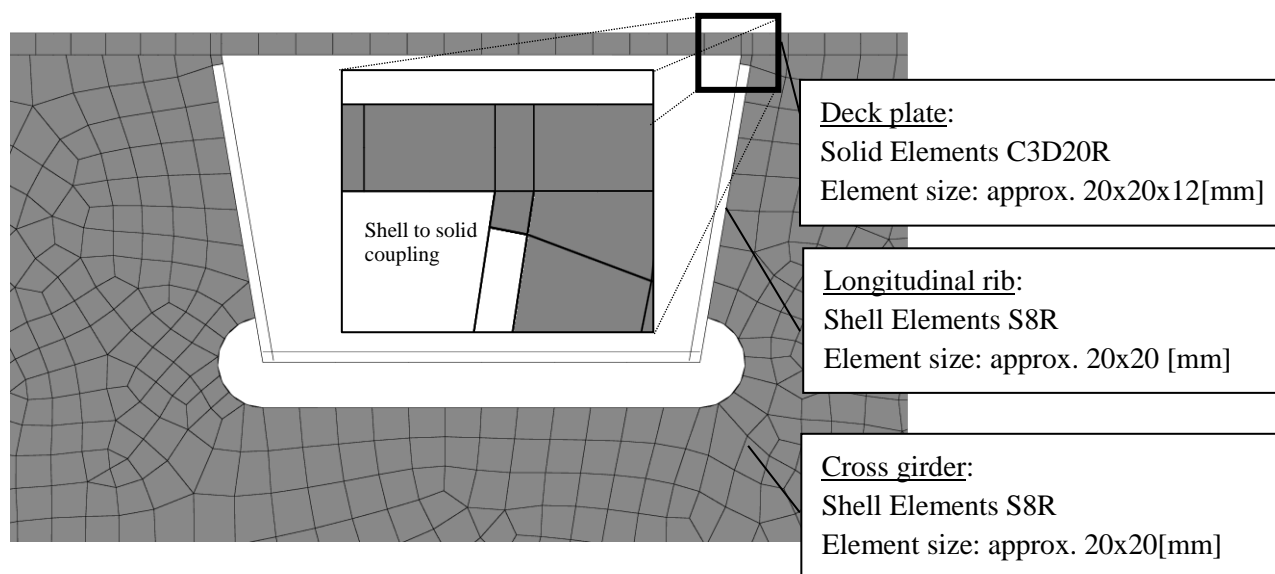


Figure 52: FEM-Modell B – Modelling of the through rib LR-1 and LR-3 to LR-12 with shell elements and the weld connections to deck plate with continuum elements

3.2.3. Model C: Orthotropic bridge deck with trough longitudinal ribs and cross girder spacing of 4m

The finite element model for Model C is described below and consists of 2 main girders, a slender deck plate, 12 closed longitudinal ribs (trough ribs) and 5 cross girders. Model C's overall dimensions are 16.0m in longitudinal and 7.50m in transverse direction. A model's plan view and a longitudinal section in axial bridge direction (section A-A) is shown in Figure 53. The boundary conditions are additionally illustrated in the sketch. The main girder web's lower edges are supported.

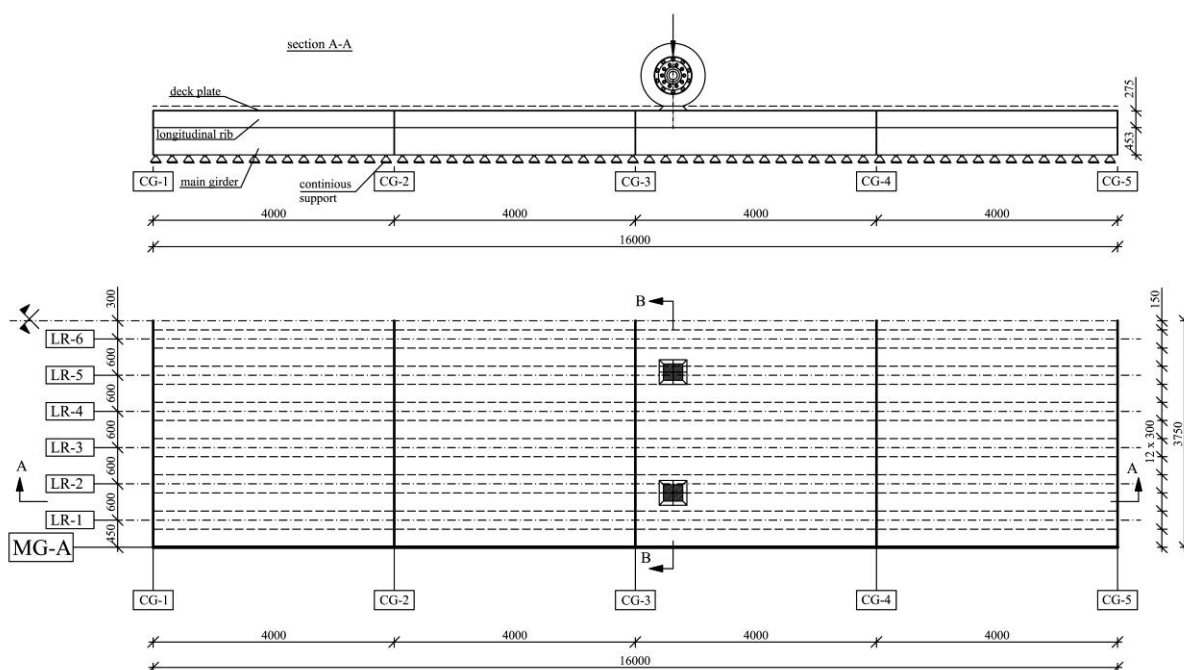


Figure 53: Modell C – orthotropic steel deck with trough longitudinal ribs and cross girder spacing of 4m (plan view and longitudinal section)

Between the 2 main girders (MG-A to MG-B) the orthotropic deck was modelled. A part of this region, from main girder MG-A to the mid axis of the bridge deck, is shown in the plan view of Figure 53. Therefore, 6 longitudinal ribs (LR-1 to LR-6) are plotted in this picture. Also the geometrical dimensions of each part is illustrated. The main girder's distance between MG-A and MG-B has a value of $e_{MG} = 2 \cdot 3.75 = 7.50\text{m}$. The cross girder's interval is $e_{CG} = 4.0\text{m}$ and the trough rib web's interval is $e_{LR} = 0.30\text{m}$. The deck plate has a thickness of $t_{DP} = 12\text{mm}$ which leads to a deck plate slenderness of $e_{LR} / t_{DP} = 300 / 12 = 25$. The recommended deck plate slenderness limit of the actual Eurocode [41] is $e_{LR} / t_{DP} \leq 25$ which is equal to the slenderness of model C. The trough ribs were modelled with a plate thickness of $t_{LR} = 6\text{mm}$ and a height of $h_{LR} = 275\text{mm}$. The trough ribs are modelled as continuous longitudinal ribs passing through the cross girders. An additional cope hole in the cross girder's web has also been modelled. On both outer web sides, there is a welded connection of the trough ribs to the cross girder's web. A detailed illustration of the cope holes in the cross girders is shown in Figure 58.

In Figure 54, section B-B, the height of the main girders with a value of $h_{MG} = h_{CG} = 0.728\text{m}$ can be seen. The main girders are modelled just to the bottom side of the cross girder's web and the main girders are supported along these bottom edges.

The whole finite element model for Model B is illustrated in Figure 55 and exhibits maximum dimensions of $l_x = 16.0\text{m}$ to $l_z = 7.50\text{m}$.

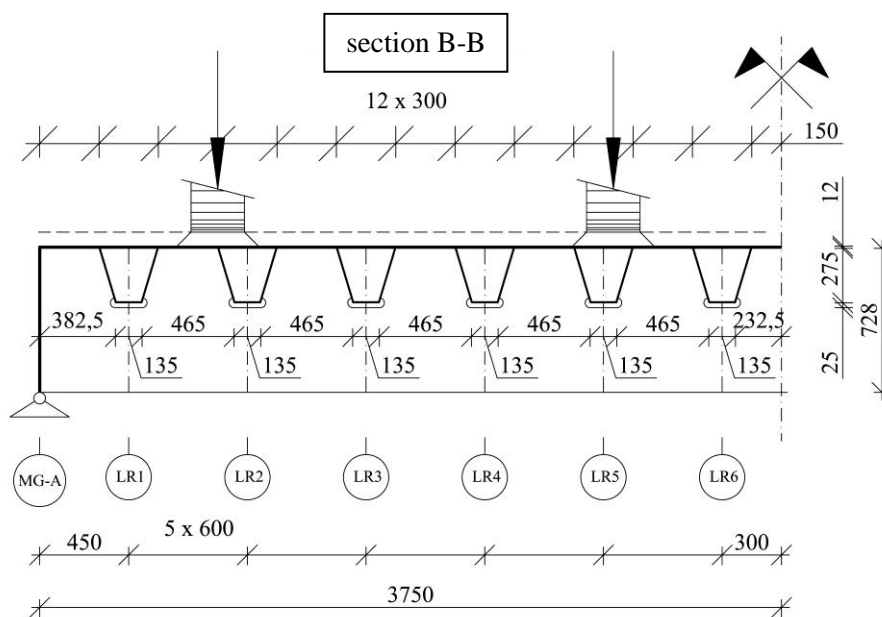


Figure 54: Modell C – orthotropic steel deck with trough longitudinal ribs (section B-B)

Also, the global coordinate system is plotted in this picture and the x-axis indicates the longitudinal direction of the bridge.

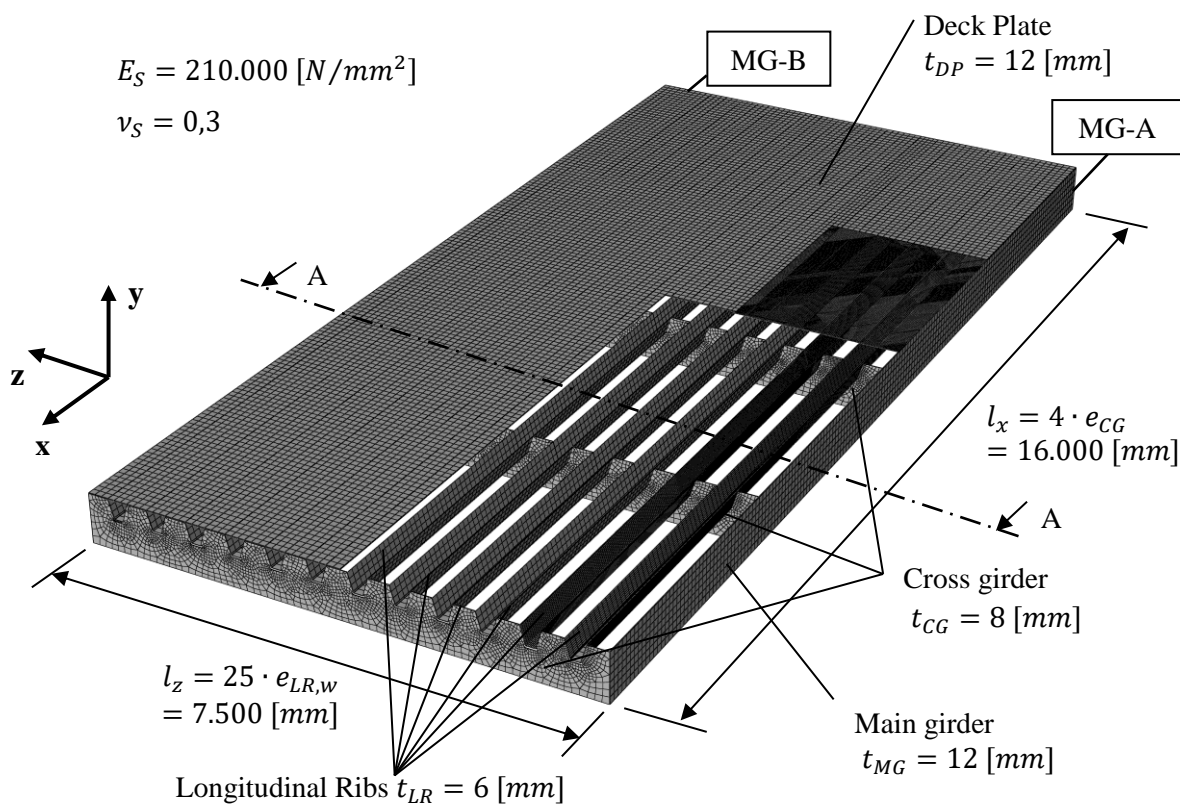


Figure 55: FEM-Modell C – orthotropic steel deck with trough longitudinal ribs (overview)

In summary the finite element model that is shown in Figure 55 consists of the following parts:

- Part of the Main Girder (MG):
 - Thickness of the web $t_{MG} = 12\text{mm}$
 - Reduced height of the main girder $h_{MG} = 728\text{mm}$
 - Interval between the main girders $e_{MG} = 7.50\text{m}$
 - Modelled with quadratic shell elements with reduced integration, element type S8R
 - Element size is $100 \times 100\text{mm}$
 - Supported on the bottom edge line of the main girder's web

- Cross Girder (CG):
 - Thickness of the web $t_{CG} = 8\text{mm}$
 - Height of the cross girder $h_{CG} = 728\text{mm}$
 - Dimensions of the bottom flange of the cross girder $160 \times 8\text{mm}$
 - Interval between the cross girders $e_{CG} = 4.0\text{m}$
 - Cross girder's web modelled with quadratic shell elements with reduced integration, element type S8R
 - Element size of the shell elements at the cross girder's web is varying from $15 \times 15\text{mm}$ to approximately $100 \times 100\text{mm}$
 - Bottom flange of the cross girder ($b/t = 160/8$) is modelled with linear beam elements, element type B31
 - Element size of the beam elements at the bottom flange is 50mm
 - The cross girder is rigid tied to the main girders

- Longitudinal Rib (LR):
 - Trough ribs with a plate thickness of $t_{LR} = 6\text{mm}$
 - Height of the longitudinal ribs $h_{LR} = 275\text{mm}$
 - Interval between the trough webs of the longitudinal ribs $e_{LR} = 300\text{mm}$
 - Modelled with quadratic shell elements with reduced integration, element type S8R
 - Element size is varying from $20 \times 20\text{mm}$ to $100 \times 80\text{mm}$
 - Trough webs are connected on the outer sides to the cross girder with cope holes in the cross girders web and are fixed together with rigid transition conditions

- Deck Plate (DP):
 - Thickness of the deck plate $t_{DP} = 12\text{mm}$
 - Deck plate slenderness $e_{LR}/t_{DP} = 300/12 = 25$
 - Modelled with quadratic continuum elements with reduced integration, element type C3D20R
 - Element size is varying from $20 \times 20 \times 12\text{mm}$ to approximately $100 \times 100 \times 12\text{mm}$

- Deck plate has a rigid tie connection to the longitudinal ribs, the cross girders and the main girders

A cross section (section A-A) of the finite element model, which is presented in Figure 55, is shown in Figure 56. A detailed description of the boundary conditions at the main girder's bottom edges can also be found in the picture. At the bottom edge of the left main girder MG-A, the displacements in all directions U_x , U_y and U_z are fixed as well as the rotation around the z-axis ($U_x = U_y = U_z = Rot_z = 0$). At the bottom edge of the right main girder MG-B, the displacements in the x and y direction as well as the rotation around the z-axis are fixed ($U_x = U_y = Rot_z = 0$). An enlargement of the welded connection between longitudinal rib and cross girder shows additionally the geometrical dimensions of the cope holes in the cross girder's web. The height of the longitudinal ribs h_{LR} and the interval of the through webs among each other e_{LR} is also shown in Figure 56 as well as the main girder's interval e_{MG} .

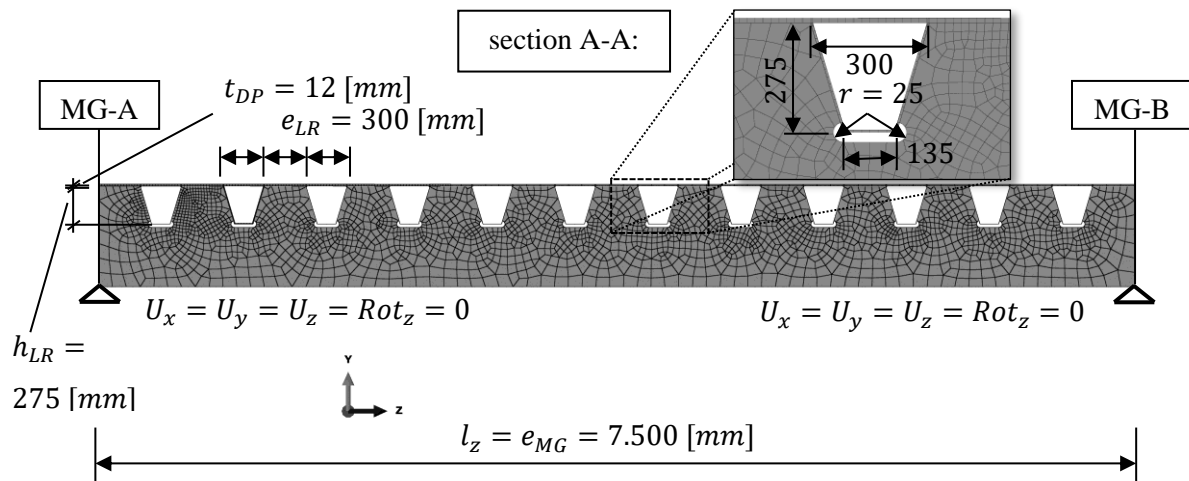


Figure 56: FEM-Modell C – orthotropic steel deck with through longitudinal ribs (section A-A)

The deck plate has been partitioned into 2 Regions Region A and Region B (see Figure 57). This partition has been done to reduce significantly the degrees of freedom because there is a big difference in the element sizes of the regions. For both regions quadratic continuum elements with reduced integration have been used (element type C3D20R). Region A of the deck plate contains a finer mesh with an element size of 20x20x12mm and Region B of the deck plate contains a coarse mesh with an element size of 100x100x12mm (see Figure 57).

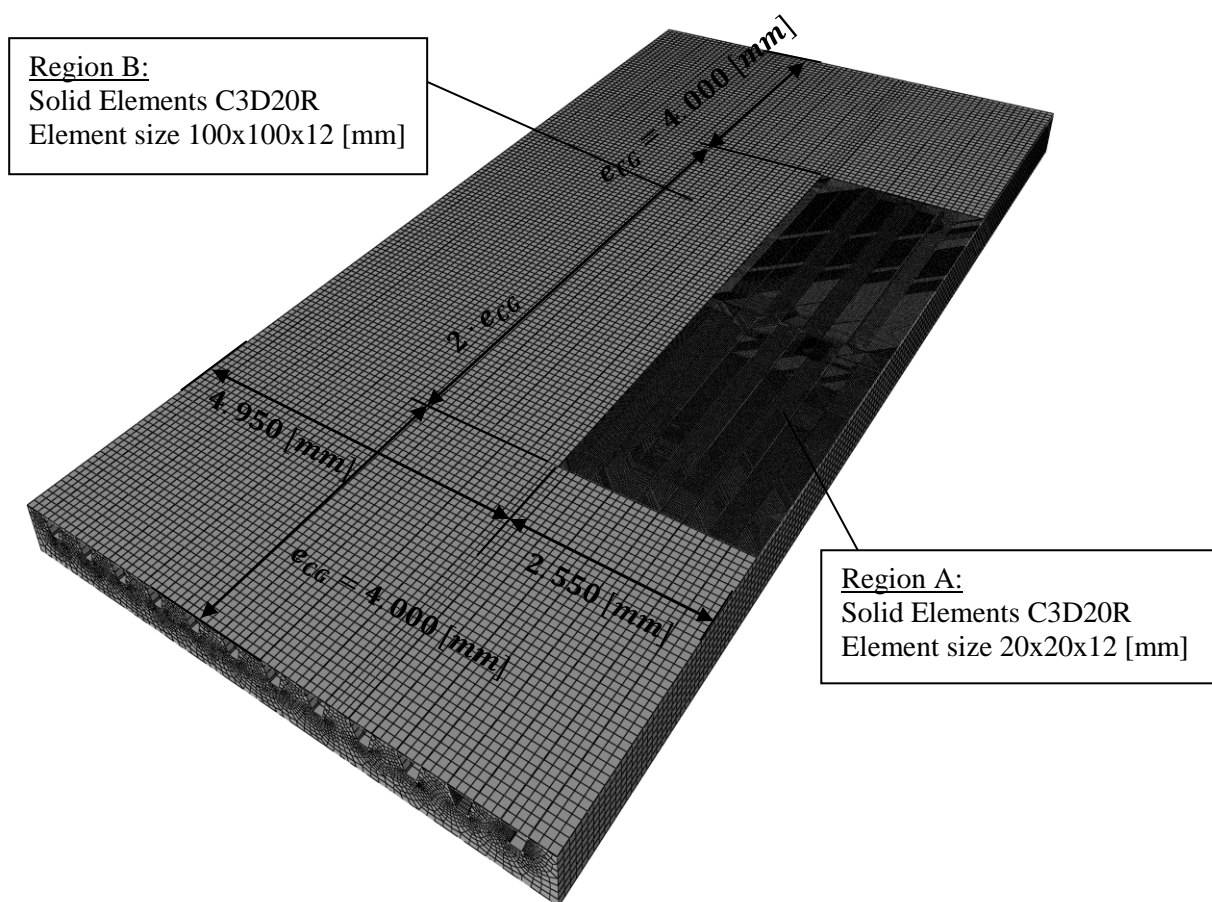


Figure 57: FEM-Modell C – Mesh of the deck plate

The longitudinal ribs close to the main girder (LR-1 or LR-12) are decisive for the analysed details which could be confirmed by further investigations relating to the critical location of the notch details. These analyses are presented later on in Section 3.3. Because of a lack of space between LR-1 and the main girder MG-A, a load application of the increased wheel contact patch of axle type B (see Figure 25 and Figure 29) was not possible at LR-1. On this account the second longitudinal rib LR-2 was chosen for the analyses at Model C. As already described at model B in Section 3.2.2, it was necessary to model the relevant trough rib LR-2 also with quadratic continuum elements (element type C3D20R, see Figure 58). All other longitudinal ribs (LR-1 and LR-3 to LR-12) have been modelled by using shell elements (see Figure 59).

– Additional modifications at longitudinal rib LR-2:

Another mesh refinement in the deck plate (Region A) has been applied in the local areas of the longitudinal rib to deck plate connections. This mesh refinement has been done according to the recommendations referring to the linear extrapolation of the stresses to the weld toe (see Figure 35.a). Within these local mesh refinements, reference points have been created for the use of the hot spot stress method.

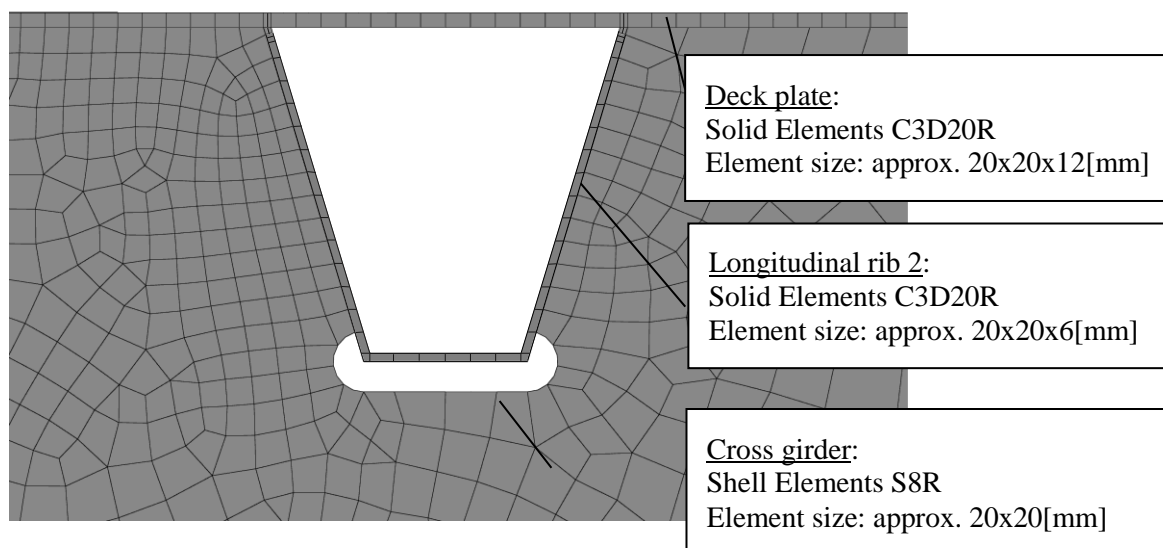


Figure 58: FEM-Modell C – Modelling of the through rib LR-2 with continuum elements including the welded connections to deck plate

– Additional modifications at longitudinal ribs LR-1 and LR-3 to LR-12:

The welds of LR-1 and LR-3 to LR-12 to the deck plate have also been modelled with solid elements (element type C3D20R), although the longitudinal ribs are modelled with shell elements. This procedure was necessary to create accurate transition conditions between the solid deck plate and the shell trough ribs which are illustrated in Figure 59. The constraint of the shell elements (longitudinal rib) to the continuum elements (welds as solid) was defined as shell to solid coupling. With this specification, the displacements in all directions as well as the rotations could be transferred in a correct way.

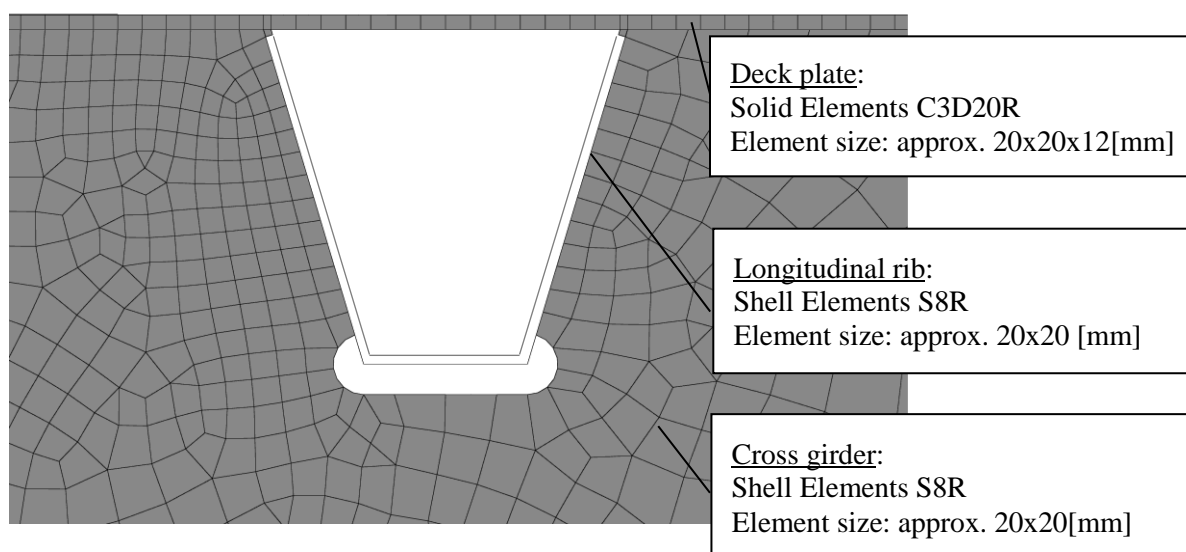


Figure 59: FEM-Modell C – Modelling of the through rib LR-1 and LR-3 to LR-12 with shell elements and the welded connections to deck plate with continuum elements

3.2.4. Model D: Orthotropic bridge deck with open longitudinal ribs – cross girder with bolted connections

The finite element model for Model D is described below and consists of 1 cross girder between 2 main girders, including a very slender deck plate and 20 open longitudinal ribs (flat steel ribs). The overall dimensions of Model D are 2.0m in longitudinal bridge direction (identical to the distance between the cross girders e_{CG}) and 7.56m in transverse bridge direction. The length of the longitudinal ribs is only 400mm in the model (see Figure 61). The geometrical dimensions of all parts (main girder, cross girder, longitudinal rib and deck plate) are completely the same as for Model A, which are presented in Section 3.2.1. Because of the very local notch detail (detail D3, see Section 2.4.5) that has been analysed with this – more or less 2D – finite element model, a consideration of only one cross girder was chosen. To get the correct loading due to the heavy traffic for this 2D-model, additional analyses on Model A were done (see Section 3.3.4). Figure 60 shows an isometric view of the model, where the bolted field splices of the cross girder has been modelled with its connection plates at joint I, II and III. Preloaded bolts are used and therefore a slip can be ignored for the fatigue verification. Also the boundary conditions are illustrated schematically in the sketch as well as the global coordinate system where the x-axis indicates the longitudinal direction of the bridge. The model is supported on the lower edges of both main girders. Just the steel structure without any pavement was modelled and the whole assembly consists of steel material with linear elastic material behaviour. The Young Modulus of the steel is $E_S = 210.000 \text{ N/mm}^2$ and the Poisson Ratio has a value of $\nu = 0.3$.

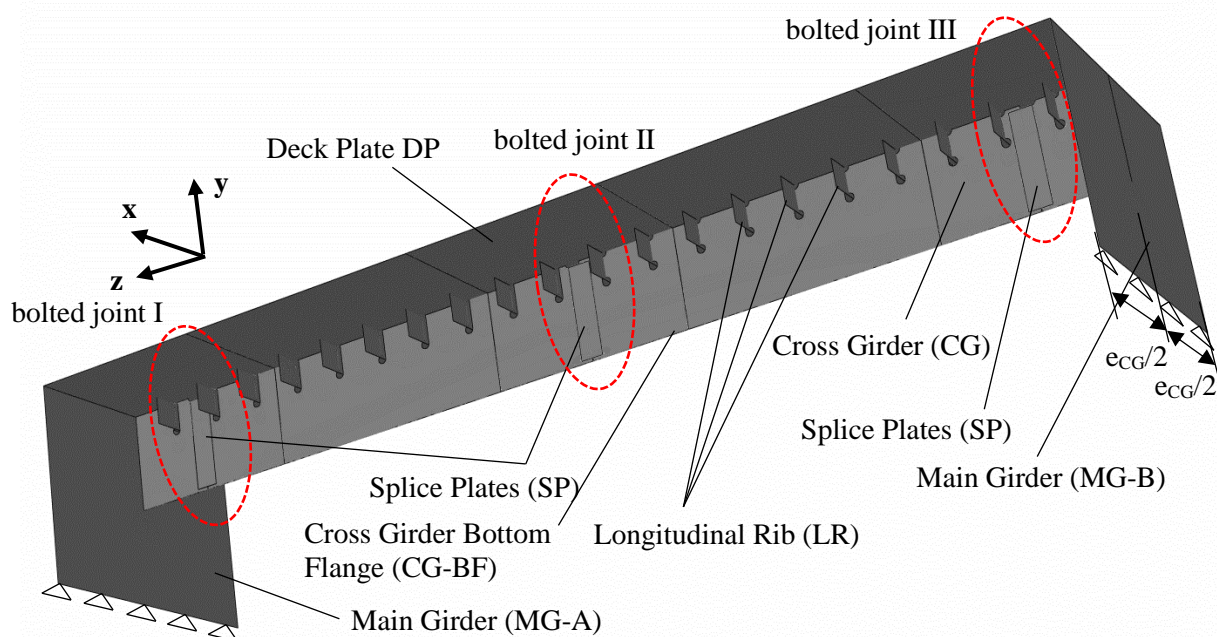


Figure 60: Modell D – orthotropic steel deck with open longitudinal ribs – cross girder with bolted connections (isometric drawing)

In summary the finite element model that is shown in Figure 60 consists of the following parts:

- Part of the Main Girder (MG):
 - Thickness of the web $t_{MG} = 12\text{mm}$
 - Height of the main girder (only part of the web) $h_{MG} = 1440\text{mm}$
 - Interval between the main girders $e_{MG} = 7.56\text{m}$
 - Modelled with quadratic shell elements with reduced integration, element type S8R
 - Element size is $50 \times 50\text{mm}$
 - Supported on the bottom edge line of the main girder's web
- Cross Girder (CG):
 - Thickness of the web $t_{CG} = 8\text{mm}$
 - Height of the cross girder $h_{CG} = 728\text{mm}$
 - Dimensions of the bottom flange of the cross girder: $160 \times 8\text{mm}$
 - Cross girder's web modelled with quadratic shell elements with reduced integration, element type S8R
 - Element size of the shell elements at the cross girder's web is varying from $2 \times 2\text{mm}$ to $30 \times 30\text{mm}$
 - Bottom flange of the cross girder (CG-BF) is modelled with linear beam elements, element type B31
 - Element size of the beam elements at the bottom flange is 100mm
 - The cross girder is rigid tied to the main girders
- Longitudinal Rib (LR):

- Flat steel plates with a plate thickness of $t_{LR} = 10\text{mm}$
- Height of the longitudinal ribs $h_{LR} = 210\text{mm}$
- Reduced length of the ribs in the model: 400mm
- Interval between the longitudinal ribs $e_{LR} = 360\text{mm}$
- Modelled with quadratic shell elements with reduced integration, element type S8R
- Element size is varying from 8x8mm to approximately 28x28mm
- Flat steel plates are connected one sided to the cross girder (eccentric) with cope holes in the cross girders web and are fixed together with rigid transition conditions
- Deck Plate (DP):
 - Thickness of the deck plate $t_{DP} = 10\text{mm}$
 - Deck plate slenderness $e_{LR}/t_{DP} = 360/10 = 36$
 - Modelled with quadratic shell elements with reduced integration, element type S8R
 - Element size is varying from 2x8mm to approximately 30x30mm
 - Deck plate has a rigid tie connection to the longitudinal ribs, the cross girders and the main girders
- Splice Plates (SP):
 - On both sides of the cross girder's web
 - Thickness of the splice plates $t_{SP} = 6\text{mm}$
 - Height and width of the splice plate $h_{SP} \times b_{SP} = 675 \times 160\text{mm}$
 - Modelled with quadratic shell elements with reduced integration, element type S8R
 - Element size is 6x6mm
 - Splice plates are rigid connected to the cross girder's web, because a slip can be ignored due to the preloaded bolts for the fatigue load level

A top view of the finite element model can be seen in Figure 61, where most of the parts are shown. The distance between the 2 main girders MG-A and MG-B has a value of $e_{MG} = 7.56\text{m}$. The interval of the cross girders e_{CG} is 2.0m according to Model A and the interval of the longitudinal ribs is $e_{LR} = 0.36\text{m}$. The deck plate has a thickness of $t_{DP} = 10\text{mm}$ which leads to a deck plate slenderness of $e_{LR}/t_{DP} = 360/10 = 36$. The flat steel longitudinal ribs were modelled with a plate thickness of $t_{LR} = 10\text{mm}$ and a height of $h_{LR} = 210\text{mm}$. These longitudinal stiffeners are conducted as continuous longitudinal ribs passing through the cross girders with an additional cope hole in the cross girder's web, but with limited length of 400mm (200mm in each direction perpendicular to the web of the cross girder). The longitudinal ribs have a one-sided (eccentric) fillet weld connection to the cross girder's web and a detailed illustration of the cope holes in the cross girders is shown in Figure 62. It was not necessary to model the longitudinal ribs along the whole length of the deck plate, because they have no influence to the load carrying behaviour of the studied details of the cross girder. The longitudinal ribs have been

modelled with a length of 200mm on both sides of the cross girder which was necessary for the load application on their ends (see Figure 61). The loads due to the decisive vehicles according to fatigue load model FLM 4 (see Section 2.5.2) on each lane were applied as line edge loads (in global y-direction) on the individual longitudinal ribs (LR-3 to LR-5, LR-9 and LR-10, LR-11 to LR-13, LR-18 and LR-19, see Figure 61), based on the results of the 3D-model A of the orthotropic deck (Model A). The determination of the loads in the longitudinal ribs is presented in Section 3.3.4.

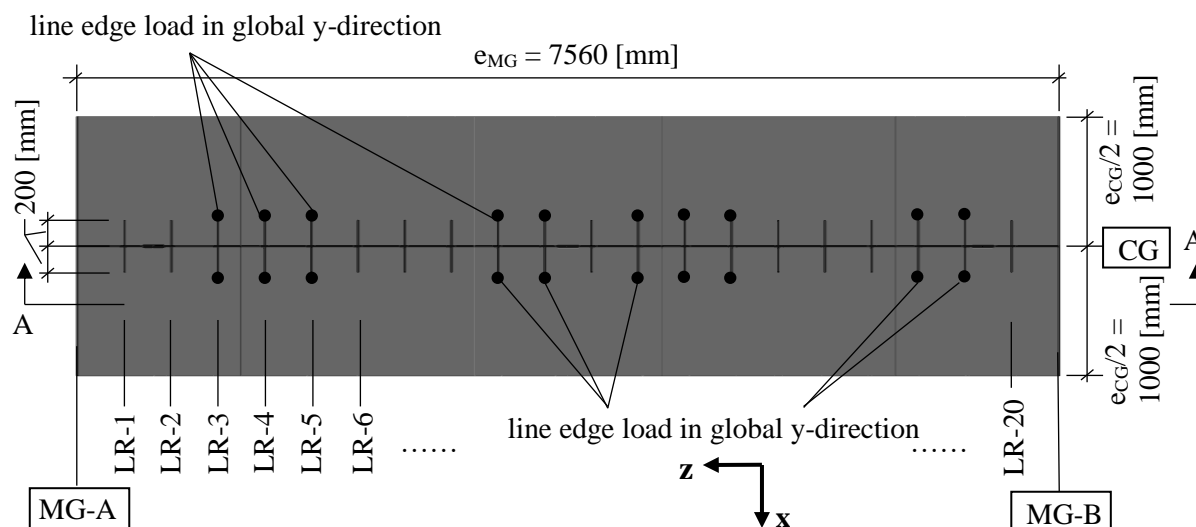


Figure 61: Modell D – orthotropic steel deck with open longitudinal ribs – cross girder with bolted connections (top view)

As it can be seen in Figure 62, section A-A, the reduced height of the main girders in the model is $h_{MG} = 1140\text{mm}$ and the height of the cross girder is $h_{CG} = 0.728\text{m}$. The defined boundary conditions at the bottom edges of the main girders are shown in detail. At the bottom edge of the left main girder MG-A, the displacements in all directions U_x , U_y and U_z are fixed. At the bottom edge of the right main girder MG-B, the displacements in the y direction is fixed ($U_y = 0$). An additional enlargement of the plate connection between longitudinal rib and cross girder shows the cope holes with its geometrical dimensions in detail. The height of the longitudinal ribs h_{LR} and its interval among each other e_{LR} is also shown in Figure 62 as well as the main girder's interval e_{MG} . Another enlargement shows the connection of the field splice plates in detail with a cope hole in the cross girder's web.

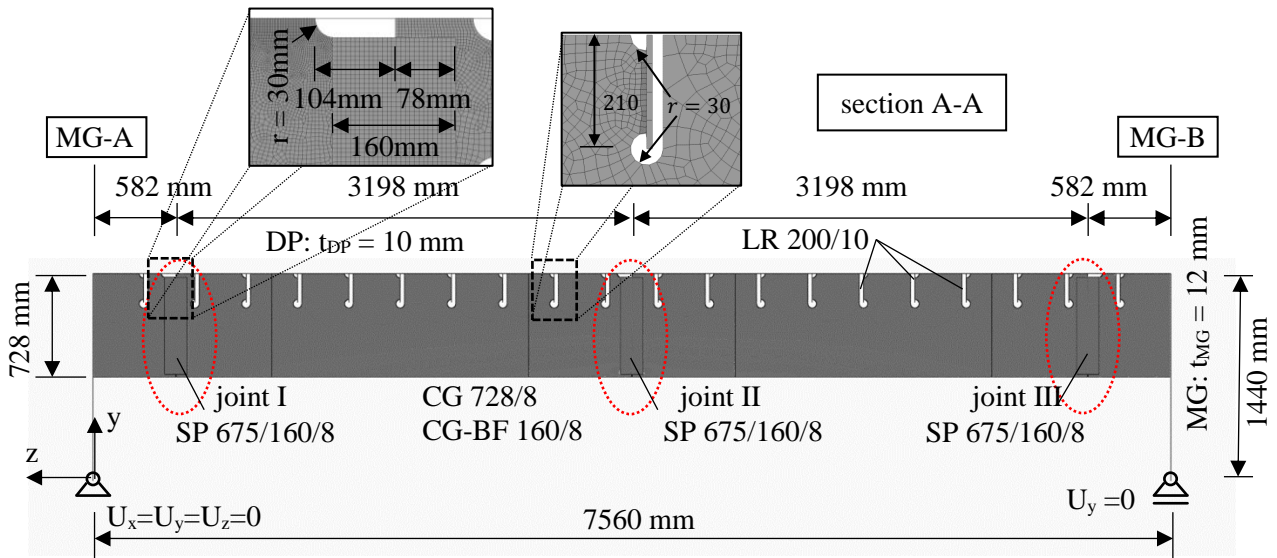


Figure 62: Modell D – orthotropic steel deck with trough longitudinal ribs (section A-A)

The pre-stressed friction type connection bolts haven't been modelled. With the assumption of a fully pre-stressed connection condition without slip, the splice plates were modelled with a rigid transition condition between the plate surfaces.

Figure 63 illustrates the load application due to the individual vehicles of load model FLM 4 and FLM 4* with edge line loads on the individual ends of the longitudinal ribs in an isometric view. The determination of the accurate line loads due to the relevant vehicle type from fatigue load model FLM 4 is shown in Section 3.3.4. As shown in the drawing in Figure 61, the line loads have been applied symmetrical around the cross girder's axis, where Figure 63 only shows the loads on the front side of the model.

load application along the surface edges of the longitudinal ribs on both sides of the cross girder

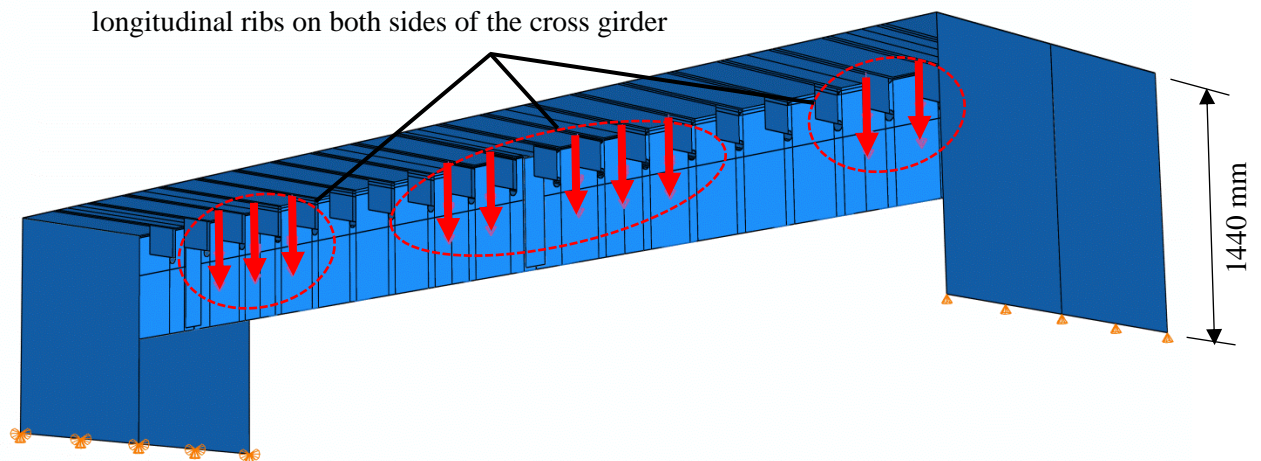


Figure 63: Modell D – orthotropic steel deck with open longitudinal ribs, load application (isometric view) due to heavy traffic loads

Figure 64 illustrates the modelling of the cross girder's web by partitioning into 2 regions, Region A and Region B. As it can be seen in the picture, there is a differentiation in the element size to reduce significantly the degrees of freedom that causes less calculation time. Both regions of the deck plate include quadratic shell elements with reduced integration, element type S8R. Region A contains a finer mesh with an element size of approximately 8x8mm and Region B contains a coarse mesh with an element size of about 30x30mm. Additional local mesh refinements have been created in the very local areas of the bolted field splices near the web to deck plate welded connections. These local areas are marked in Figure 64 and an additional enlargement shows the finite element mesh in detail where element sizes of about 2x2mm are obtained.

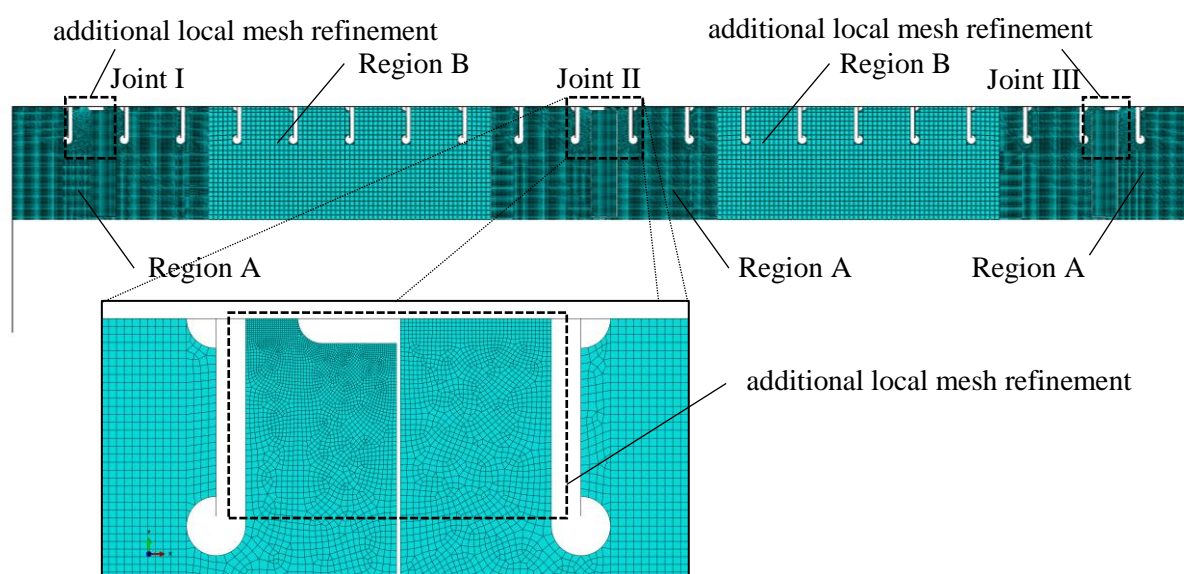


Figure 64: Modell D – orthotropic steel deck with open longitudinal ribs, mesh refinements (front view)

3.3. Critical locations of the details with accurate load positions

For the studied details D1 and D2 it was necessary to find the most critical location on the orthotropic deck with the highest stress ranges $\Delta\sigma$ due to traffic load model FLM 4 and FLM 4*. Additionally, it was necessary to find out the relevant lane position in transverse direction for each studied detail (D1, D2, D3). The following analyses have been carried out at the representative orthotropic steel deck with open longitudinal ribs (Model A and D, see Section 3.2.1 and Section 3.2.4) and the results referring to the critical load positions are similar for the other models with closed longitudinal ribs.

This Section is partitioned into the following parts:

- Section 3.3.1: Calculation of the critical load/lane position in transverse direction in relation to notch detail D1a (welded connection of the longitudinal rib to the deck plate, where the stress ranges in the deck plate are relevant) and most critical location of detail D1
- Section 3.3.2: Explanation referring to the behaviour of the load/lane position in transverse direction in relation to notch detail D1b (welded connection of the longitudinal rib to the deck plate, where the stress ranges in the longitudinal rib are relevant)
- Section 3.3.3: Calculation of the critical load/lane position in transverse direction in relation to notch detail D2 (welded connection of the longitudinal rib to the cross girder, where the stress ranges in the longitudinal rib are relevant)
- Section 3.3.4: Calculation of the critical load/lane position in transverse direction in relation to notch detail D3 (welded connection of the cross girder's web to the deck plate in the very local area of a bolted field splice of the cross girder where the stress ranges in the web of the cross girder are relevant)

3.3.1. Position of detail D1a and relevant lane position for maximum stresses

For the simulation of the heavy traffic crossings over the modelled orthotropic steel bridge deck, there exists nearly no interaction of the individual axles within a vehicle. Hence an isolated consideration of every axle is possible. The dimensions of the wheel contact patches are impacting the occurring stresses in the detail strongly and therefore a differentiation in the axles is necessary. As presented in Section 2.5.2, fatigue load model FLM 4, FLM 4* and FLM 2 include 3 different axle types A, B and C. Under consideration of a beneficial load distribution of 45° through the thickness of the asphalt pavement, increased wheel contact patches can be used that are illustrated in Figure 65. A thickness of $t_p = 70\text{mm}$ was taken into account for the calculation of these contact patches.

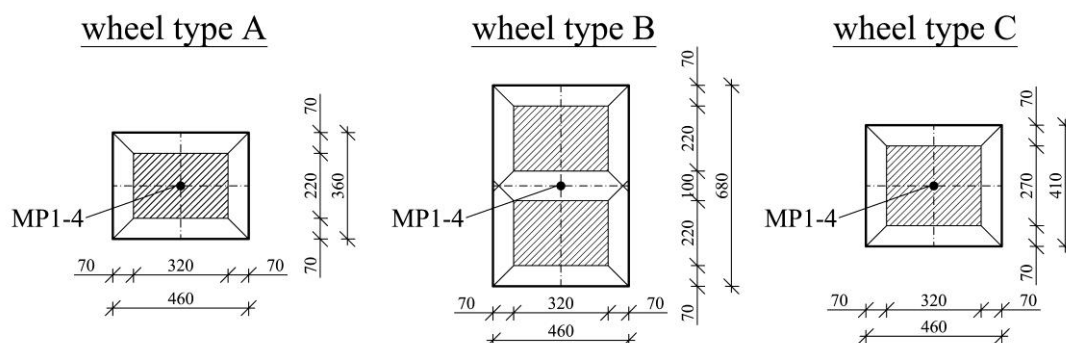


Figure 65: increased wheel contact patches of axle type A,B and C due to a load distribution of the pavement relating to a pavement thickness of $t_p = 70\text{mm}$

When comparing axle type A and C in Figure 65, it can be stated that there is very less difference in its dimensions and therefore only axle type C was chosen to represent all single wheeled axles of type A and C. Axle type B and C (note: wheel loads type C are heavier than those of type A) have been located at many different positions on the finite element model with open longitudinal ribs and Figure 66 shows an overview of the analysed measuring points MP1 to MP4 to find out the most critical location of detail D1a. As it can be seen in Figure 65 and also in Figure 66, the centre of the wheel contact patch was always positioned directly on the analysed detail D1a.

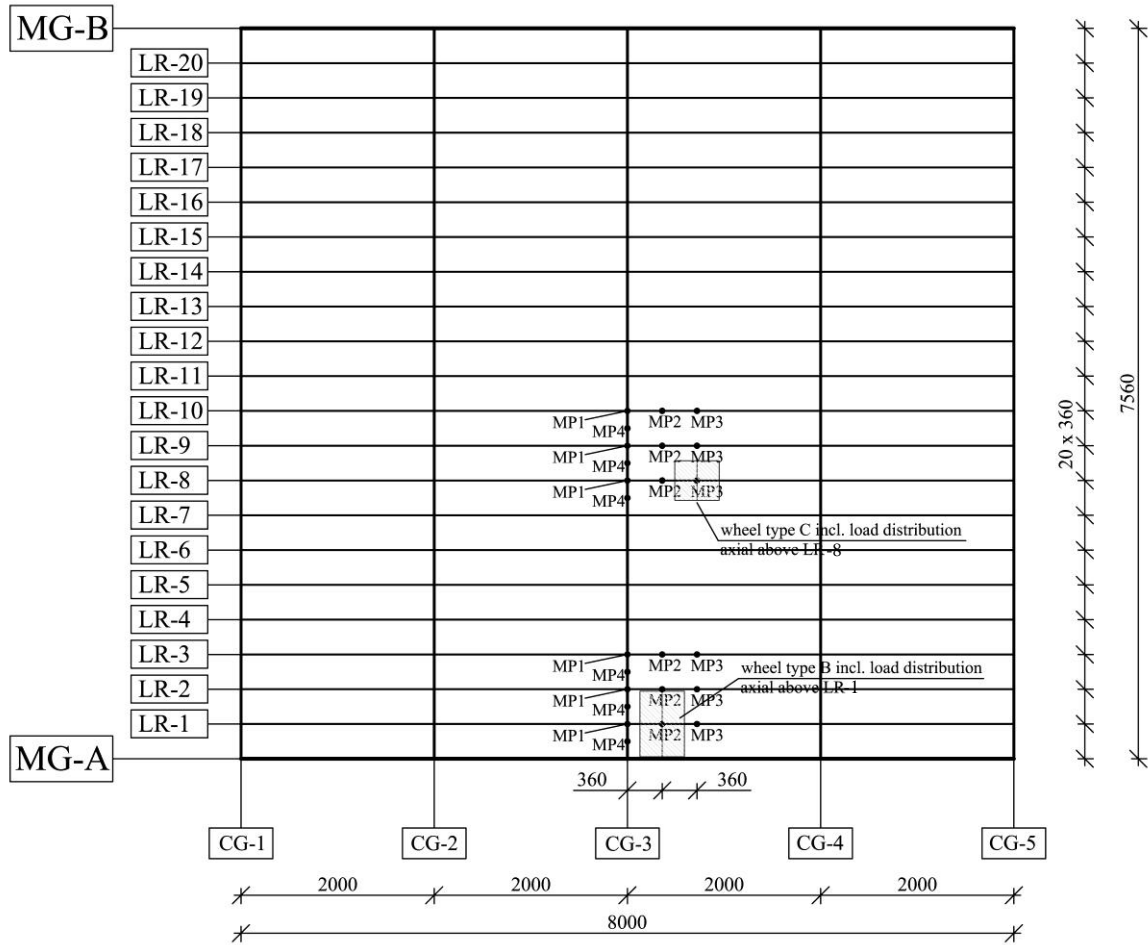


Figure 66: Detail D1a – overview (plan view) of the analysed measuring points MP1 to MP4

Figure 67 compares the results in terms of stresses for the analysed measuring points MP1 to MP4 at the bottom surface of the deck plate due to axle/wheel type B and an axle load of $F_a = 100\text{kN}$. Measuring point MP2 shows the highest occurring stresses in detail D1a at longitudinal rib LR-1. This longitudinal rib LR-1 is located next to the main girder MG-A and the distance of MP2 to the cross girder is equal to the longitudinal rib's interval of $e_{LR} = 360\text{mm}$. (note: for all analysed locations of D1, it was observed that the stresses due to loading $\sigma_{x,MP,DP}$ are nearly equal to $\Delta\sigma_{x,MP,DP}$ due to wheel crossing)

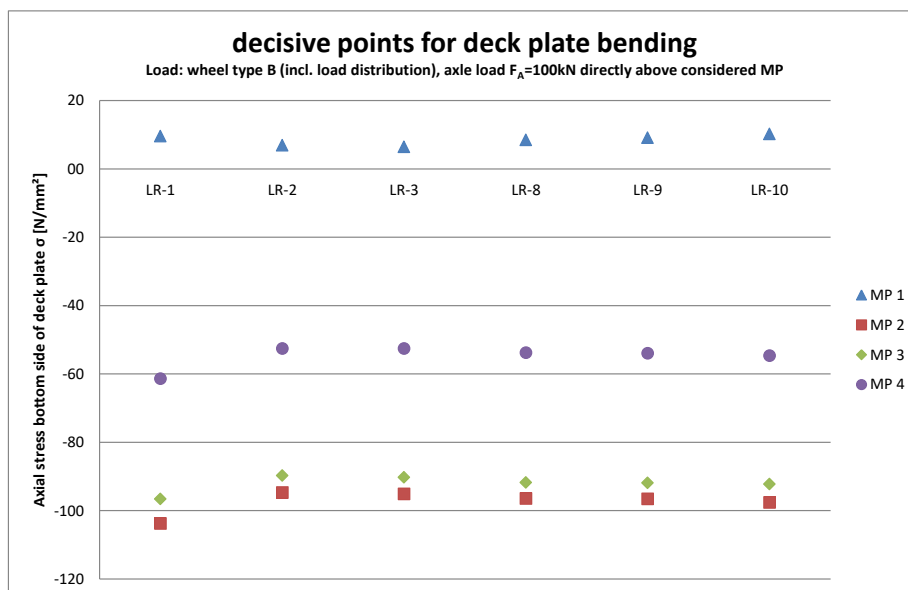


Figure 67: Detail D1a – stresses at the bottom deck plate surface due to axle/wheel type B and an axle load of $F_A = 100\text{kN}$ for the analysed measuring points MP1 to MP4

Table 4 additionally illustrates the calculated values in more detail which are plotted in the diagram of Figure 67. All stresses have been determined under an application of the wheel load directly above the longitudinal rib's web axis (see Figure 68). A transvers location between the ribs causes less stresses for detail D1, D2 (see Table 5).

Table 4: Detail D1a – Stresses $\sigma_{x,MP,DP}$ in the measuring points MP1 to MP4 due to axle/wheel type B and a axle load of $F_a = 100\text{kN}$

$\sigma_{x,MP,DP}$ [N/mm ²]	MP 1	MP 2	MP 3	MP 4
LR-1	9.6	-103.8	-96.6	-61.4
LR-2	6.9	-94.7	-89.7	-52.6
LR-3	6.5	-95.1	-90.3	-52.6
LR-8	8.5	-96.5	-91.8	-53.8
LR-9	9.1	-96.6	-91.9	-54.0
LR-10	10.2	-97.6	-92.3	-54.7

With these results it generally can be stated that the nearest longitudinal rib to the main girder is decisive referring to notch detail D1a and the occurring stress have the highest value in a distance of e_{LR} away from the cross girder (point MP 2 in Figure 66). Additional analyses regarding to the appropriate – most critical – wheel position in transverse direction (mid position between 2 longitudinal ribs or central above the longitudinal rib) have been carried out. Both axle types, single and double wheeled, have been taken into account and the occurring stresses in notch detail D1a are plotted in Table 5 for point MP 2. It can be stated that the central position of the tyre is decisive for both axle types.

Table 5: decisive load/lane position in transverse direction referring to detail D1a in MP 2 (axle load $F_a = 100kN$)

decisive lane position in transverse direction of the bridge		
	$\sigma_{x,MP2,DP}$ [N/mm ²]	
	central above LR-1	between LR-1 and LR-2
Wheel type B	-103.8	-71.11
Wheel type C	-115.7	-82.25

In summary, the maximum stresses referring to detail D1a occur at the longitudinal rib (LR-1) next to the main girder (MG-A). The decisive position for detail D1 in longitudinal bridge direction is distanced e_{LR} relating to the cross girder (CG-3). The centre of the wheel contact patch has to be positioned directly above detail D1 to get the highest stresses.

The critical lane position described above is illustrated in Figure 68. Figure 68.a shows Model A with its open longitudinal ribs and the decisive position of the single and double wheeled axles. Because of further analyses regarding to an influence of a lateral shift of the vehicles due to heavy traffic driving characteristics, the second or third longitudinal rib (LR-2, LR-3) has to be taken into account (similar results expected) due to a lack of space at LR-1 (end of the model at the main girder). Therefore Figure 68.b shows exemplary the appropriate studied lane position for single and double wheeled axles at Model B with closed longitudinal ribs. For Model A (see Figure 68.a), the loading above LR-3 was studied in detail (see Section 3.4.2).

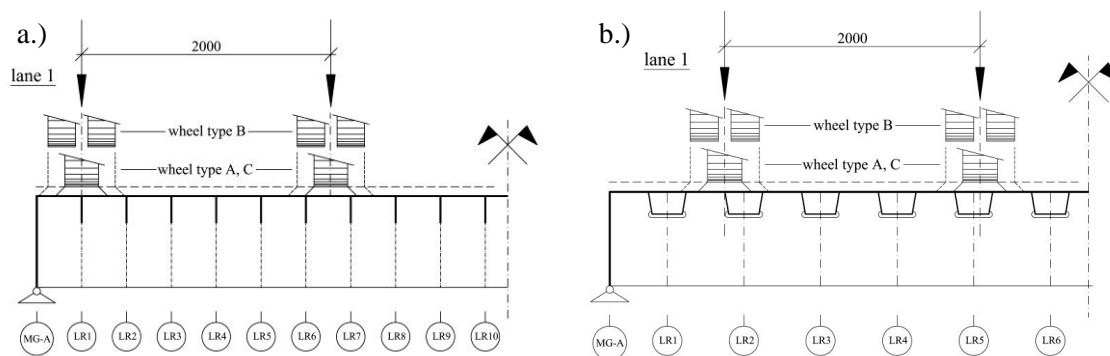


Figure 68: Detail D1a – critical lane position for a.) Model A and b.) Model B

3.3.2. Critical lane position for maximum stresses at detail D1b

For Detail D1b the same welded connection as for detail D1a has to be considered. At D1b the stress ranges in the longitudinal rib's web are relevant. Relevant stresses in detail D1b only occur for closed longitudinal ribs. A detailed description of notch detail D1b can be found in Section 2.4.3. At detail D1b the same point of interest as at detail D1a has to be considered which is presented in Section 3.3.1. The maximum stresses referring to detail D1b also occur at the longitudinal rib (LR-1) next to the main girder (MG-A). The decisive position in longitudinal bridge direction is distanced e_{LR} relating to the cross girder (CG-3).

In comparison of detail D1b to D1a, there is a quite important difference regarding to the heavy traffic simulation over the carriageway. At detail D1a there exists no interaction of the different sequential vehicles and even no interaction of the axles within a single vehicle. At detail D1b the bending stresses in the through webs are relevant and the bending moment's algebraic sign depends on the lateral position of the wheel. Hence an isolated consideration of every axle is not possible at detail D1b. A random sequence of the vehicle types from the appropriate fatigue load model has to be created including a lateral shift of the vehicles within the lane due to heavy traffic driving characteristics. With this random vehicle sequence the heavy traffic simulation over the bridge deck has to be done to determine sufficient results for the applying stress cycles. A detailed description of these lateral effects as well as further analyses to that behaviour are presented in Section 4.

In summary, the maximum stresses referring to detail D1b occur at the longitudinal rib (LR-1) next to the main girder (MG-A). The decisive position in longitudinal bridge direction is distanced e_{LR} relating to the cross girder (CG-3). Because of the dependency of the lateral wheel position on the bending moment's algebraic sign, it is not possible to define a general, decisive lane position in cross bridge direction of the vehicles. A heavy traffic simulation with a random sequence of the vehicles including a lateral shifting of the lorries is essential for the calculation of sufficient results at detail D1b.

3.3.3. Position of detail D2 and relevant lane position for maximum stresses

Detail D2 represents the welded connection of the longitudinal rib to the cross girder where the stress ranges in the longitudinal rib's web in longitudinal bridge direction are relevant. A detailed description of notch detail D2 can be found in Section 2.4.4. The following analyses are relevant for continuous longitudinal ribs passing through the cross girders, with an additional cope hole in the cross girder's web. The results referring to the critical load positions have been determined at a representative orthotropic steel deck with open longitudinal ribs (Model A, see Section 3.2.1) and are similar for decks with closed longitudinal ribs.

The connection to the cross girder is generally equal for all longitudinal ribs at the orthotropic steel bridge deck. But there is a differentiation in the load carrying behaviour of the longitudinal ribs due to different vertical stiffness at the supporting cross girders, depending on the location in transverse direction. Near the main girder, the cross girder acts as rigid vertical support. The support of longitudinal ribs in the middle between two main girders has significant more flexibility than the ones near the main girders. Because of this differentiation in the supporting effect, there is a lack of clarity referring to the decisive longitudinal rib regarding to the maximum occurring stress ranges $\Delta\sigma$ at notch detail D2. Therefore, crossings of axle type B with an axle load of $F_A = 100\text{kN}$ have been simulated. Axle type B indicates the highest axle loads within fatigue load model FLM 4, FLM 4* and FLM 2 (see Section 2.5.2). The first crossing was considered at the longitudinal rib next to the main girder (LR-1). The second crossing was progressed at the longitudinal rib in the middle between two main girders (LR-9). At both simulations the centre of the wheel contact patch B was positioned directly above the longitudinal rib's mid axis.

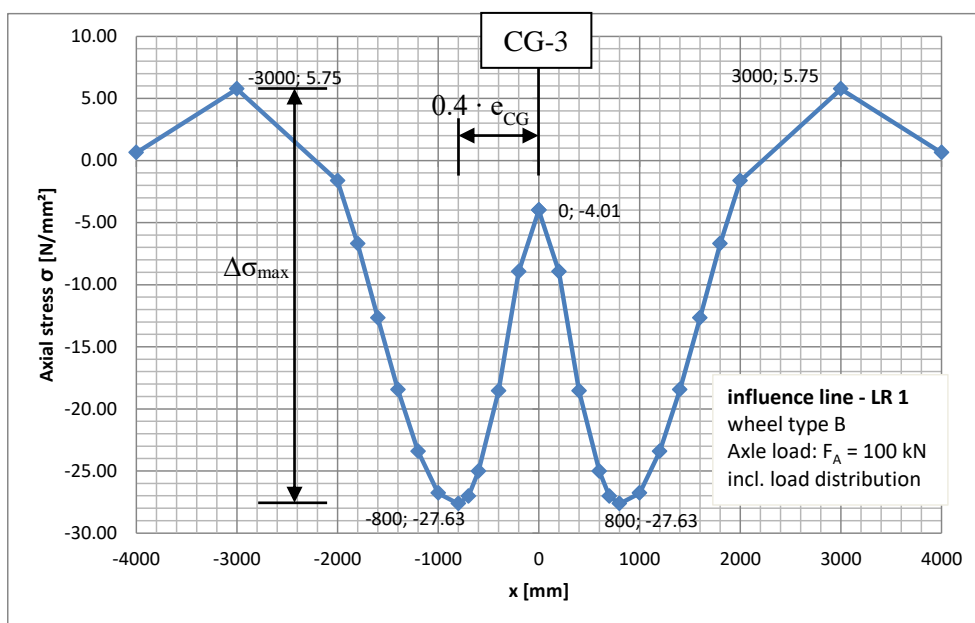


Figure 69: influence line referring to detail D2 at longitudinal rib LR-1 due to wheel type B under an axle load of $F_A = 100\text{kN}$

The occurring stresses in detail D2 due to a crossing of axle type B with an axle load of $F_A = 100\text{kN}$ at the longitudinal rib LR-1 are plotted in Figure 69. The values x on the horizontal axis in the diagram specify the distance of the load in relation to the analysed detail D2 at the central cross girder CG-3 in model A (see Figure 66 in Section 3.3.1). This stress-history curve is equivalent to the stress-history curve due to a crossing of axle type B. The stress-history curve referring to a crossing of axle type B at longitudinal rib LR-9 with an axle load of $F_A = 100\text{kN}$ is illustrated in Figure 70.

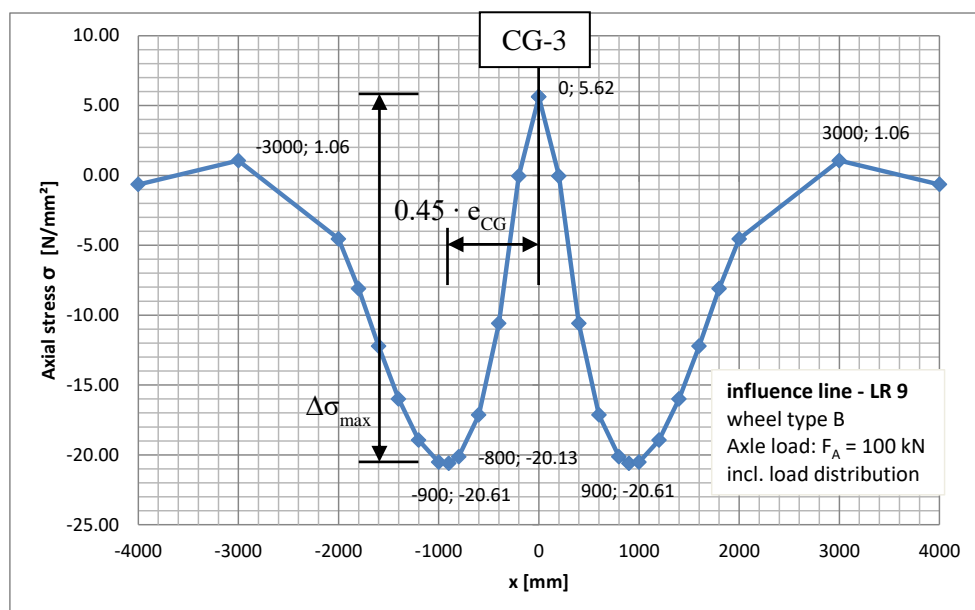


Figure 70: influence line referring to detail D2 at longitudinal rib LR-9 due to wheel type B under an axle load of $F_A = 100\text{kN}$

Based on the stress-history curves in Figure 69 and Figure 70, the maximum stress ranges $\Delta\sigma$ can be determined due to a crossing of axle B with an axle load of $F_A = 100\text{kN}$. The results for the stress ranges $\Delta\sigma$ are plotted in Table 6 relating to LR-1 to LR-3 and LR-7 to LR-9.

By comparing the values for $\Delta\sigma$ in Table 6 it can be stated that the highest values occur at the longitudinal rib next to the main girder (LR-1). This is also true for a crossing of a vehicle of FLM 4 and FLM 4*.

Table 6: decisive position in transverse direction of detail D2 (occurring stresses and stress ranges due to a crossing of axle type B with an axle load of $F_A = 100kN$)

	x [mm]	σ [N/mm ²]	$\Delta\sigma$ [N/mm ²]
LR-1	800	-27.63	33.4
	3000	5.75	
LR-2	800	-26.24	31.0
	3000	4.79	
LR-3	800	-25.16	29.1
	3000	3.94	
LR-7	900	-21.71	25.7
	0	3.98	
LR-8	900	-21.10	26.0
	0	4.90	
LR-9	900	-20.61	26.2
	0	5.62	

In summary, the maximum stresses referring to detail D2 occur at the longitudinal rib (LR-1) next to the main girder (MG-A). The decisive position in longitudinal bridge direction to get the highest stress is distanced $0.4 \cdot e_{CG}$ relating to the cross girder (CG-3, see Figure 69). The centre of the wheel contact patch has to be positioned directly above the appropriate longitudinal rib's mid axis – for all details D2. The critical lane position, referring to detail D2, described above is the same as for detail D1a (see Section 3.3.1) and is again illustrated in Figure 71. Figure 71.a shows Model A with its open longitudinal ribs and the decisive position of the single and double wheeled axles. Because of further analyses regarding to an influence of a lateral shift of the vehicles due to heavy traffic driving characteristics, the second longitudinal rib LR-2 has to be taken into account due to a lack of space at LR-1 (end of the FE-model). Therefore, Figure 71.b shows exemplary the appropriate studied lane position for single and double wheeled axles at Model B with closed longitudinal ribs.

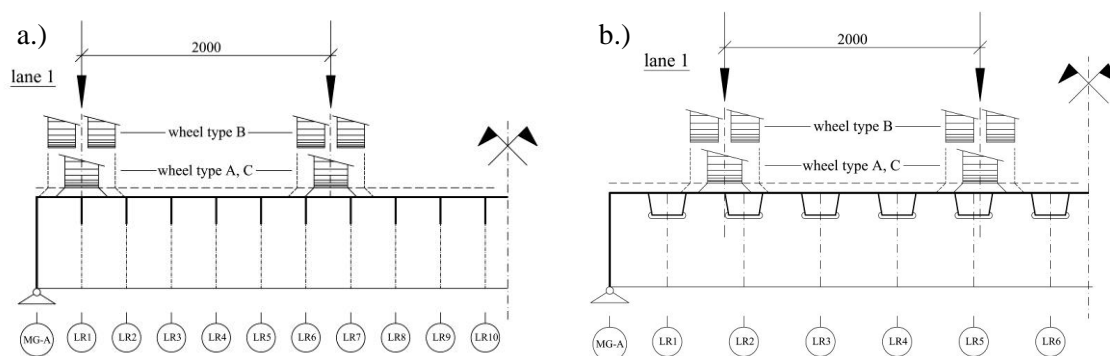


Figure 71: Detail D2 – critical lane position for a.) Model A and b.) Model B

3.3.4. Lane and load/vehicle position for the maximum stresses at Detail D3

Detail D3 represents the welded connection of the cross girder to the deck plate in the very local area of the bolted field splices within a cross girder. The stress ranges in the cross girder's web due to the heavy traffic crossings are relevant. A detailed description of notch detail D3 can be found in Section 2.4.5. The results referring to the critical load position have been determined at a representative orthotropic steel deck with open longitudinal ribs (Model A, see Section 3.2.1). Further detailed analyses referring to detail D3 have been done by using Model D (see Section 3.2.4), which is a detailed cut out of Model A for the cross girder and includes the bolted field splices at the analysed cross girder. Because of the high influence of the lane position on the carriageway in transverse direction to the occurring stresses in the local notch detail, it was necessary to consider the real lane positions of Model A. The position of these real lanes in transverse direction are illustrated in Figure 72 and were selected based on a studied highway bridge. In summary 4 lanes (Lane 1 to Lane 4) are illustrated in the bridge's cross section and also the bolted field splices are shown in this picture. Only the carriageway between the 2 main girders MG-A and MG-B was modelled and therefore the regions out of these limits were neglected. Lane 2 and Lane 3 were taken into account for the analyses referring to detail D3 at Model A. By comparing these two lanes, 2 significant wheel/load positions in transverse direction can be identified. Wheel or load position L1, where the wheel load is located close to the bolted field splice near the main girder and load position L2, where the wheel load is located close to the bolted field splice in the middle between the main girders.

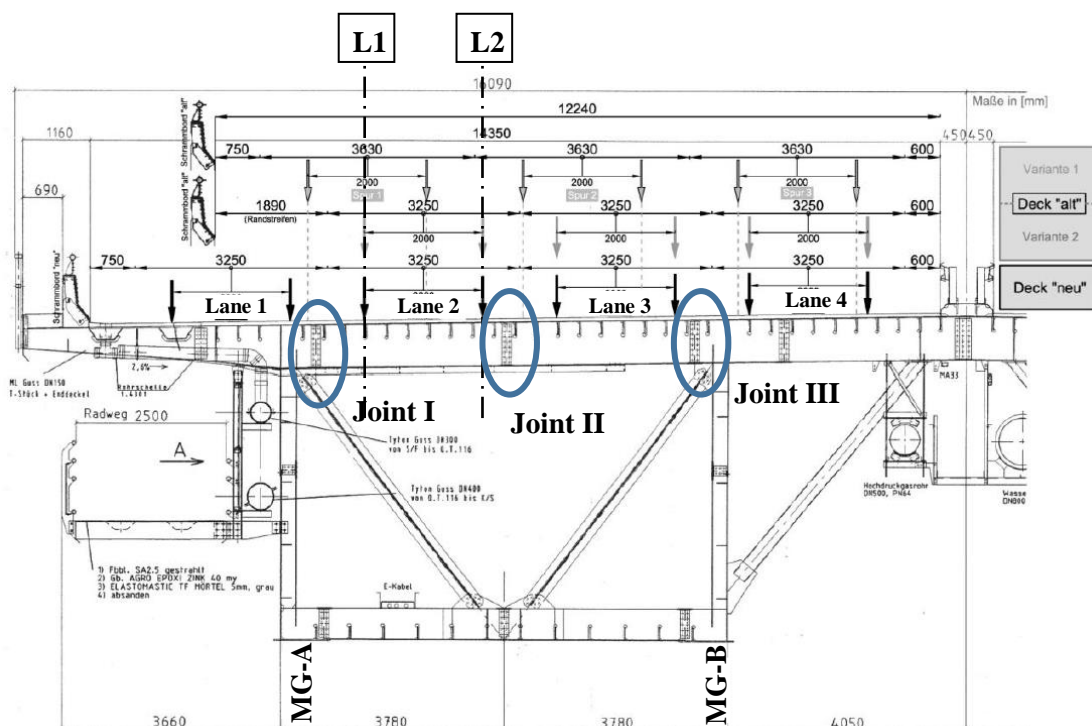


Figure 72: real lane positions in transverse direction of Model A and critical wheel positions at section L1 and L2

Lane 3 exhibits similar wheel/load positions in transverse bridge direction and therefore only lane 2 was considered for the calculation of the critical load or lane position referring to detail D3. Nevertheless, also the effect of a parallel vehicle crossing on lane 2 and 3 could be analysed based on a summary of the individual load cases.

In addition to the load position in transverse bridge direction, the occurring stresses in detail D3 are also depending on the location of the load (respectively the whole vehicle) in longitudinal bridge direction. Therefore, a determination of an influence line in longitudinal bridge direction relating to the reaction force $V_{\text{sum,CG-1}}$ (also more detailed for each longitudinal rib to get the correct loading in Model D) at the analysed cross girder was necessary for the mid cross girder which is subsequently indicated as CG-1. This longitudinal influence line has been calculated under consideration of axle type C including an increased wheel contact patch (see Figure 25 and Figure 29) with a wheel load of $F_w = 100\text{kN}$. The resulting influence lines due to axle type C have been assumed also for axle type B and A.

In summary 2 load positions in transverse (L1, L2) and 3 in longitudinal bridge direction have been taken into account for the determination of 2 influence lines in longitudinal bridge direction. One influence line at position L1 and one influence line at position L2 (see Figure 72). At position L1, the centre of the wheel contact patch is located directly above the longitudinal rib's mid axis of LR-4. At position L2, the centre of the wheel contact patch is located in the middle between LR-9 and LR-10. At longitudinal load position A, the wheel load is located directly above the analysed cross girder CG-1 (see Figure 73). At longitudinal load position B, the wheel load is located directly above a cross girder next to the analysed cross girder (at CG-0, see Figure 74). At longitudinal load position C, the wheel load is located in a distance of 1.30m away from the analysed cross girder ($x=1.30$, see Figure 75).

The occurring shear forces in the appropriate longitudinal ribs have been measured from the finite element model A due to every load case. These shear forces in the longitudinal ribs have been selected in a distance of 200mm away from the analysed cross girder (loads in model D, see Figure 63) and are shown in detail in the following pictures.

Figure 73 illustrates 2 load cases at longitudinal load position A, where the wheel load is positioned directly above CG-1. This picture also shows the definition of the load cases, L1_CG-1 (Figure 73.a) and L2_CG-1 (Figure 73.b). For this load case the shear forces have been selected at the connection of the longitudinal rib to CG-0 with an offset of 200mm towards CG-1. Due to load case L1_CG-1 the shear forces at the appropriate longitudinal ribs LR-1 to LR-10 have been measured which are marked in Figure 73.a: $V_{\text{LR-1,CG-0}}$, $V_{\text{LR-2,CG-0}}$, $V_{\text{LR-3,CG-0}}$, $V_{\text{LR-4,CG-0}}$, $V_{\text{LR-5,CG-0}}$, $V_{\text{LR-6,CG-0}}$, $V_{\text{LR-7,CG-0}}$, $V_{\text{LR-8,CG-0}}$, $V_{\text{LR-9,CG-0}}$, $V_{\text{LR-10,CG-0}}$

The reaction force $V_{\text{sum,L1_CG-1}}$ at cross girder CG-1 is calculated by the direct load F_w and the individual values $V_{\text{LR-1,CG-0}}$:

$$V_{\text{sum,L1_CG-1}} = F_w - 2 \cdot \Sigma(V_{\text{LR-1,CG-0}} + V_{\text{LR-2,CG-0}} + \dots + V_{\text{LR-10,CG-0}});$$

Due to load case L2_CG-1 the shear forces at the appropriate longitudinal ribs LR-5 to LR-14 have been measured which are marked in Figure 73.b: $V_{\text{LR-5,CG-0}}$, $V_{\text{LR-6,CG-0}}$, $V_{\text{LR-7,CG-0}}$, $V_{\text{LR-8,CG-0}}$, $V_{\text{LR-9,CG-0}}$, $V_{\text{LR-10,CG-0}}$, $V_{\text{LR-11,CG-0}}$, $V_{\text{LR-12,CG-0}}$, $V_{\text{LR-13,CG-0}}$, $V_{\text{LR-14,CG-0}}$

The reaction force $V_{\text{sum,L2_CG-1}}$ at cross girder CG-1 is calculated by the direct load F_w and the individual values $V_{\text{LR-2,CG-0}}$:

$$V_{\text{sum,L2_CG-1}} = F_w - 2 \cdot \Sigma(V_{\text{LR-5,CG-0}} + V_{\text{LR-6,CG-0}} + \dots + V_{\text{LR-14,CG-0}});$$

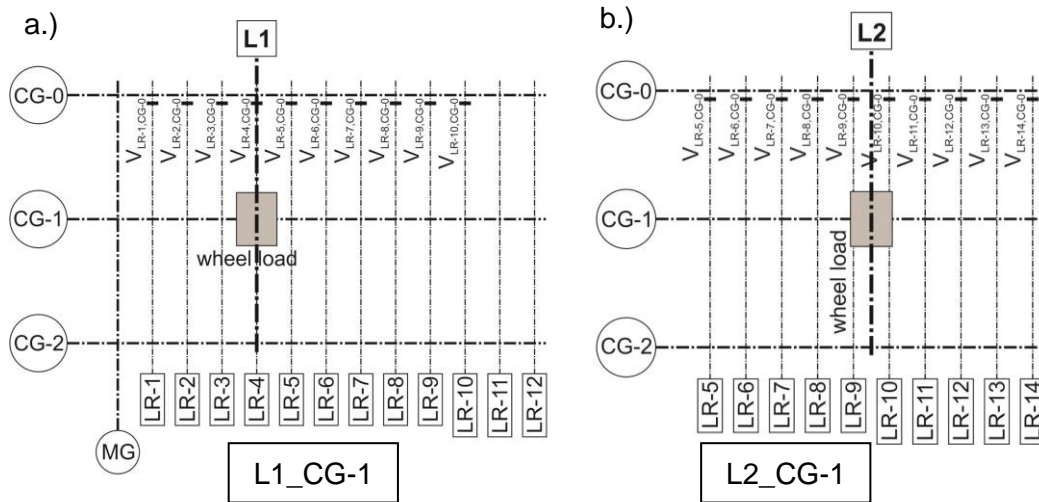


Figure 73: illustration of 2 load cases with longitudinal load position A at cross girder CG-1: a.) wheel load directly above LR-4 (L1_CG-1); b.) wheel load in the middle between LR-9 and LR-10 (L2_CG-1)

Figure 74 illustrates 2 load cases at longitudinal load position B, where the wheel load is positioned directly above CG-0. This picture also shows the definition of the load cases, L1_CG-0 (Figure 74.a) and L2_CG-0 (Figure 74.b). For this load case the shear forces have been selected at the connections of the longitudinal rib to CG-1 with an offset of 200mm towards CG-0. Due to load case L1_CG-0 the shear forces at the appropriate longitudinal ribs LR-1 to LR-10 have been measured which are marked in Figure 74.a:

$$V_{\text{LR-1,CG-1}}, V_{\text{LR-2,CG-1}}, V_{\text{LR-3,CG-1}}, V_{\text{LR-4,CG-1}}, V_{\text{LR-5,CG-1}}, V_{\text{LR-6,CG-1}}, V_{\text{LR-7,CG-1}}, V_{\text{LR-8,CG-1}}, \\ V_{\text{LR-9,CG-1}}, V_{\text{LR-10,CG-1}};$$

The reaction force $V_{\text{sum,L1_CG-0}}$ for cross girder CG-1 is now based on:

$$V_{\text{sum,L1_CG-0}} = \Sigma(V_{\text{LR-1,CG-1}} + V_{\text{LR-2,CG-1}} + \dots + V_{\text{LR-10,CG-1}});$$

Due to load case L2_CG-0 the shear forces at the appropriate longitudinal ribs LR-5 to LR-14 have been measured which are marked in Figure 74.b: $V_{\text{LR-5,CG-1}}$, $V_{\text{LR-6,CG-1}}$, $V_{\text{LR-7,CG-1}}$, $V_{\text{LR-8,CG-1}}$, $V_{\text{LR-9,CG-1}}$, $V_{\text{LR-10,CG-1}}$, $V_{\text{LR-11,CG-1}}$, $V_{\text{LR-12,CG-1}}$, $V_{\text{LR-13,CG-1}}$, $V_{\text{LR-14,CG-1}}$; $V_{\text{sum,CG-1}} = \Sigma(V_{\text{LR-1,CG-1}} + V_{\text{LR-2,CG-1}} + \dots + V_{\text{LR-10,CG-1}})$);

The reaction force $V_{\text{sum,L2_CG-0}}$ for cross girder CG-1 leads do:

$$V_{\text{sum,L2_CG-0}} = \Sigma(V_{\text{LR-5,CG-1}} + V_{\text{LR-6,CG-1}} + \dots + V_{\text{LR-14,CG-1}});$$

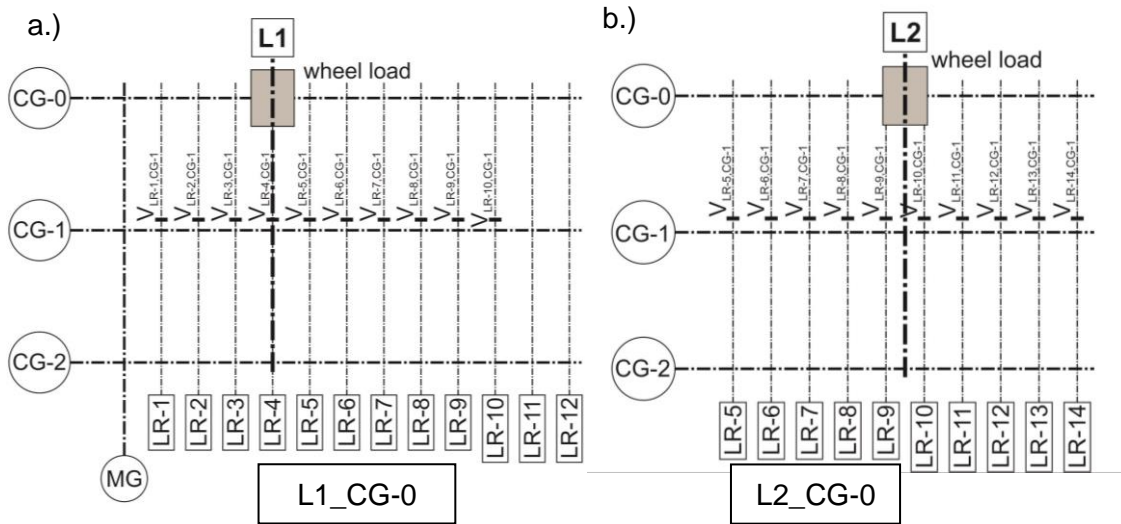


Figure 74: illustration of 2 load cases with longitudinal load position B at cross girder CG-0: a.) wheel load directly above LR-4 (L1_CG-0); b.) wheel load in the middle between LR-9 and LR-10 (L2_CG-0)

Figure 75 illustrates 2 load cases at longitudinal load position C, where the wheel load is positioned between CG-0 and CG-1 in a distance of $x = 1.30\text{m}$ away from CG-1. This picture also shows the definition of the load cases, L1_x=1.30 (Figure 75.a) and L2_x=1.30 (Figure 75.b). At this load case the shear forces have been selected at the connection of the longitudinal rib to CG-1 with an offset of 200mm towards CG-0. Due to load case L1_x=1.30 the shear forces at the appropriate longitudinal ribs LR-1 to LR-10 have been measured which are marked in Figure 75.a: $V_{\text{LR-1,CG-1}}$, $V_{\text{LR-2,CG-1}}$, $V_{\text{LR-3,CG-1}}$, $V_{\text{LR-4,CG-1}}$, $V_{\text{LR-5,CG-1}}$, $V_{\text{LR-6,CG-1}}$, $V_{\text{LR-7,CG-1}}$, $V_{\text{LR-8,CG-1}}$, $V_{\text{LR-9,CG-1}}$, $V_{\text{LR-10,CG-1}}$

The reaction force $V_{\text{sum,L1_x=1.30}}$ for cross girder CG-1 leads to:

$$V_{\text{sum,L1_x=1.30}} = \Sigma(V_{\text{LR-1,CG-1}} + V_{\text{LR-2,CG-1}} + \dots + V_{\text{LR-10,CG-1}});$$

Due to load case $L2_{x=1.30}$ the shear forces at the appropriate longitudinal ribs LR-5 to LR-14 have been measured which are marked in Figure 75.b: $V_{LR-5,CG-1}$, $V_{LR-6,CG-1}$, $V_{LR-7,CG-1}$, $V_{LR-8,CG-1}$, $V_{LR-9,CG-1}$, $V_{LR-10,CG-1}$, $V_{LR-11,CG-1}$, $V_{LR-12,CG-1}$, $V_{LR-13,CG-1}$, $V_{LR-14,CG-1}$

The reaction force $V_{sum,L2_{x=1.30}}$ for cross girder CG-1 leads to:

$$V_{sum,L2_{x=1.30}} = \Sigma(V_{LR-5,CG-1} + V_{LR-6,CG-1} + \dots + V_{LR-14,CG-1});$$

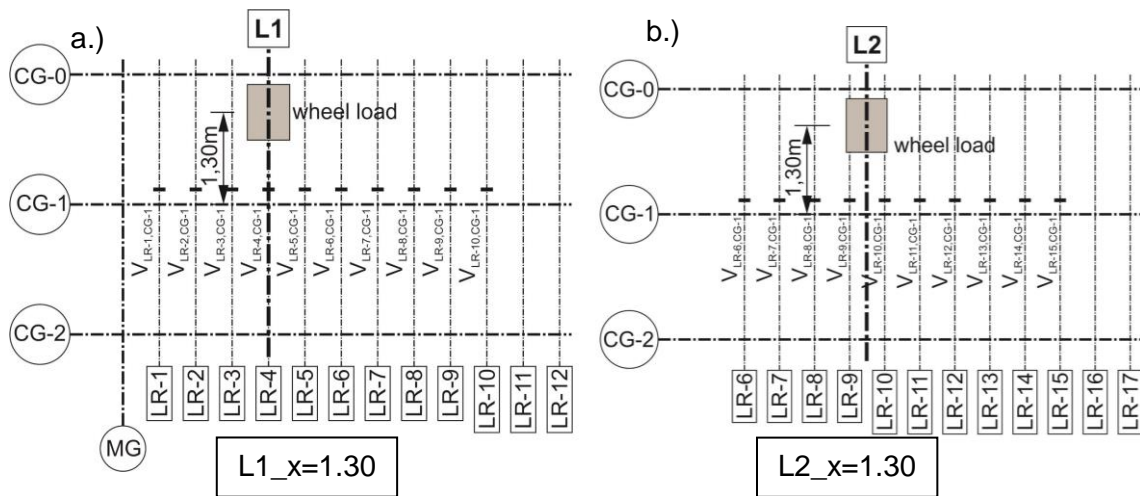


Figure 75: illustration of 2 load cases with longitudinal load position C between cross girder CG-0 and CG-1: a.) wheel load directly above LR-4 ($L1_{x=1.30}$); b.) wheel load in the middle between LR-9 and LR-10 ($L2_{x=1.30}$)

In summary, all analysed load cases that are displayed in Figure 73 to Figure 75 are summed up in Table 7 with its wheel load position in longitudinal and transverse direction. The resulting reaction force $V_{sum,CG-1}$ at cross girder CG-1 for each load case due to axle type C with a wheel load of $F_w = 100\text{kN}$ (note: only for detail D3 the wheel load $F_w = 100\text{kN}$ was used as reference load instead of the axle load) are plotted which are necessary for the determination of the influence lines referring to cross girder CG-1 in longitudinal bridge direction.

Table 7: analysed load cases with differentiation in longitudinal and cross bridge direction referring to detail D3 (with reaction forces $V_{sum,CG-1}$ at cross girder CG-1, axle type C with an wheel load of $F_w = 100kN$)

cross direction	wheel load position Longitudinal direction	indication of load case	$V_{sum,CG-1}$ [kN]
L1	at CG-1	L1_CG-1	80.25
	at CG-0	L1_CG-0	9.19
	x = 1.30 m	L1_x=1.30	34.45
L2	at QT-1	L2_CG-1	64.74
	at QT-0	L2_CG-0	16.29
	x = 1.30 m	L2_x=1.30	33.79

With the results of $V_{sum,CG-1}$ at cross girder CG-1 that are shown in Table 7 the determination of 2 influence lines in longitudinal bridge direction referring to section L1 and L2 was possible. For example, load case L1_CG-1, $V_{sum,CG-1} = 80.25$ kN $\rightarrow \eta_{L1} = V_{sum} / F_w = 80.25 / 100 \approx 0.80$;

Figure 76 shows the 2 calculated influence lines in longitudinal bridge direction at section L1 and L2 (see Figure 72) relating to the reaction force $V_{sum,CG-1}$ at cross girder CG-1 due to wheel load $F_w = 100kN$. Also the determined values η_{L1} and η_{L2} referring to the load cases described above are plotted.

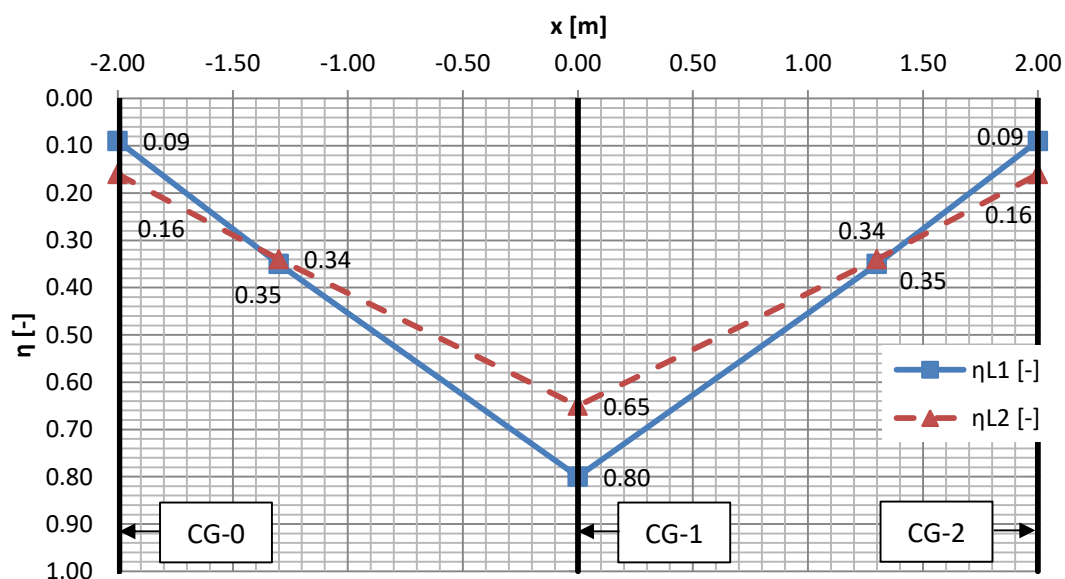


Figure 76: illustration of the calculated influence lines for the wheel loads in longitudinal bridge direction at lateral position L1 (η_{L1}) and L2 (η_{L2})

Additionally to the plotted graphs in Figure 76 the values are listed in Table 8.

As it can be seen in Figure 76, there is more load concentration at cross girder CG-1 when the loading is at section L1 near the main girder because of the higher bridge deck stiffness in this region. The

influence line for loading in section L2 shows better load distribution of the wheel load to the other cross girders because of more flexibility in the mid region between the main girders. When the wheel load is located directly above the analysed cross girder CG-1, at position L1 80% and at position L2 65% of the whole wheel load is transferred directly by cross girder CG-1 to the main girders. When the wheel load is located directly above cross girder CG-0, at position L1 9% and at position L2 16 % of the whole wheel load is transferred to cross girder CG-1.

Table 8: values η_{L1} and η_{L2} for the calculated influence lines in longitudinal bridge direction (see Figure 76)

x [m]	η_{L1} [-]	η_{L2} [-]
-2.00	0.09	0.16
-1.30	0.35	0.34
0.00	0.80	0.65
1.30	0.35	0.34
2.00	0.09	0.16

- Evaluation of the cross girder influence lines for single vehicles from FLM 4 and FLM 4*

With the influence lines presented in Figure 76 relating to cross girder CG-1 for loading in section L1 and L2 and under consideration of the vehicles according to FLM 4 (see Section 2.5.2) the critical vehicle type and its location in longitudinal bridge direction could be verified. Every lorry type was positioned most unfavourable under consideration of the axle distances and axle loads of every vehicle from FLM 4 and FLM 4*. This procedure is illustrated in Figure 77 where the critical location of each lorry type can be seen with its axle loads depending on the chosen fatigue load model.

(note: only axle loads within $-2.0 < x < 2.0\text{m}$ are shown)

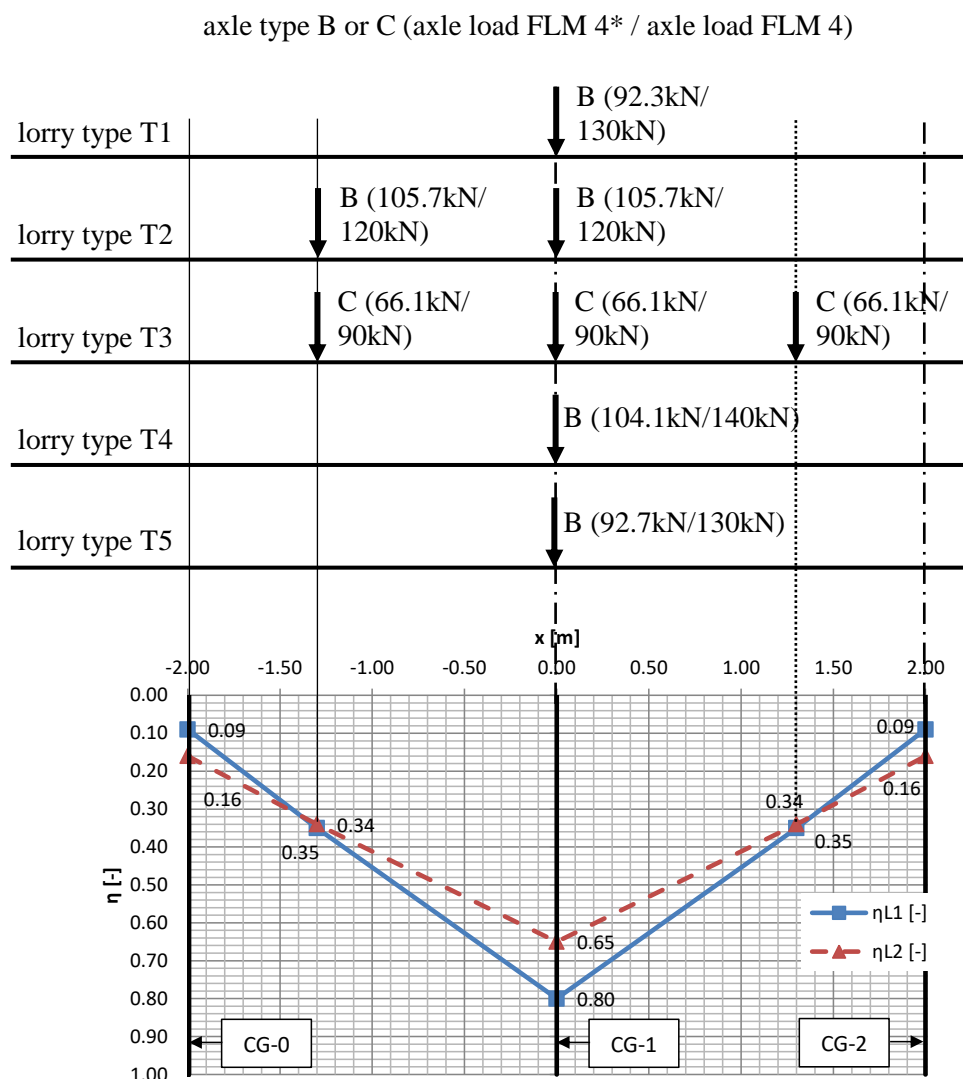


Figure 77: evaluation of the cross girder influence lines for wheel loads at section L1 and L2 for single vehicles from fatigue load model FLM 4 and FLM 4*

Under consideration of the axle loads and the appropriate η values from the influence lines, the maximum reaction force F_{CG} referring to cross girder CG-1 could be verified relating to loadings in section L1 and L2.

The results referring to the evaluation of the cross girder influence lines at section L1 and L2 are plotted in Table 9 under consideration of fatigue load model FLM 4 and FLM 4* (see Section 2.5.2, Figure 24).

Table 9: results for reaction forces F_{CG} [kN] in cross girder CG-1 referring to the evaluation of the cross girder influence lines for wheel loads in section L1 and L2 for every lorry type from fatigue load model FLM 4 and FLM 4*

F_{CG} [kN] lorry type	wheel loads in section L1		wheel loads in section L2	
	FLM 4	FLM 4*	FLM 4	FLM 4*
T1	104.0	73.8	84.5	60.0
T2	138.0	121.6	118.8	104.6
T3	135.0	99.2	119.7	87.9
T4	112.0	83.3	91.0	67.7
T5	104.0	74.2	84.5	60.3

As shown in Table 9, lorry type T2 with its position in longitudinal bridge direction as illustrated in Figure 77 leads to the maximum reaction force relating to cross girder CG-1.

– Distribution of the individual wheel loads to the individual longitudinal ribs

Because of the modelling technique of Model D, which is presented in Section 3.2.4 with a 2D model of the cross girder, it was necessary to define a distribution function for the transferred load to the cross girder in each longitudinal rib, relating to each wheel load position. The longitudinal ribs have been modelled with a length of only 200mm both sided of the analysed cross girder. Along the outer edges of the appropriate longitudinal ribs the loads were applied by using shell edge line loads which are illustrated in Figure 61 and Figure 63. It was necessary to consider different load distributions for the wheel loads to the individual longitudinal ribs depending on the location of the wheel load in longitudinal and transverse bridge direction.

– Wheel loads at Section L1:

Figure 78 shows the load distribution of the wheel load to the individual longitudinal ribs for two different load cases. The wheel load distribution due to load case L1_1.30 is plotted in Figure 78.a. 67% of the overall load F_{CG} is transferred via the longitudinal rib LR-4 to cross girder CG-1 and 15% of the load is transferred via LR-3 and LR-5. The wheel load distribution due to load case L1_CG-1 is plotted in Figure 78.b. At this load case the wheel load is located directly above the analysed cross girder and a simplified safe sided model, that is shown in Figure 78.b, for the load distribution was sufficient. 72% of the overall load F_{CG} is transferred via the longitudinal rib LR-4 to cross girder CG-1 and 14% of the load is transferred via LR-3 and LR-5.

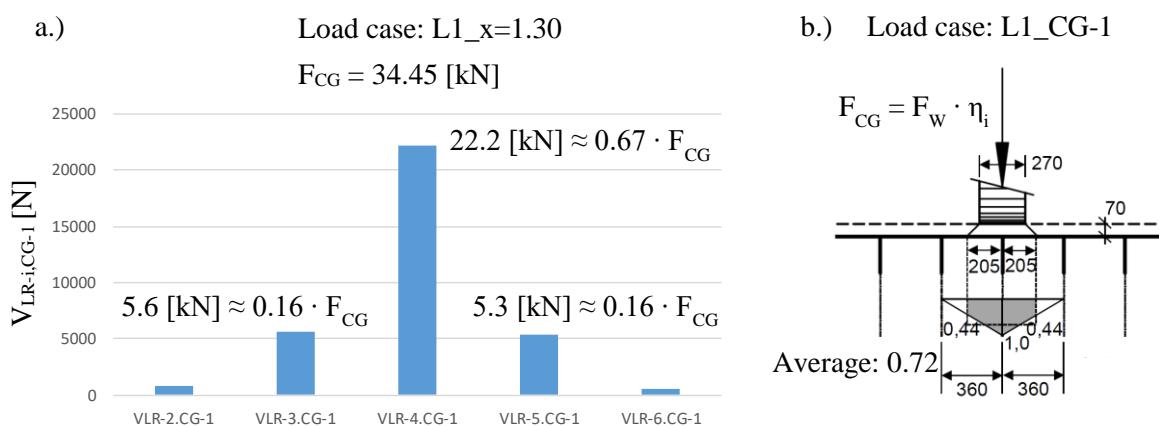


Figure 78: load distribution of the wheel load to the longitudinal ribs for different loading of cross girder CG-1: a.) load case L1_x=1.30; b.) load case L1_CG-1;

Because of the small difference between the load distribution due to the load cases L1_x=1.30 and L1_CG-1 (see Figure 78.a and Figure 78.b), a general load distribution rule relating to wheel loads at section L1 delivers sufficient results that has no dependency on the load position in longitudinal bridge direction. Therefore, the averages of the results in Figure 78 for the relevant longitudinal ribs LR-4 and LR-3/LR-5 have been calculated, which are plotted in Table 10. In summary, at section L1 70% of the wheel load is transferred via LR-4 and 15% is transferred via LR-3 and LR-5.

Table 10: percentages referring to the load distribution of the wheel load to the longitudinal ribs for the load cases L1_CG-1, L1_x=1.30 and their averages

	L1_x=1.30	L1_CG-1	average
LR-4	67.0%	72.0%	70.0%
LR-3 + LR-5	16.5%	14.0%	15.0%

– Wheel loads at Section L2:

Figure 79 shows the load distribution of the wheel load to the relevant longitudinal ribs for load case L2_x=1.30. 50% of the overall load F_{CG} is transferred via the longitudinal rib LR-9 to cross girder CG-1 and also 50% of the load is transferred via LR-10.

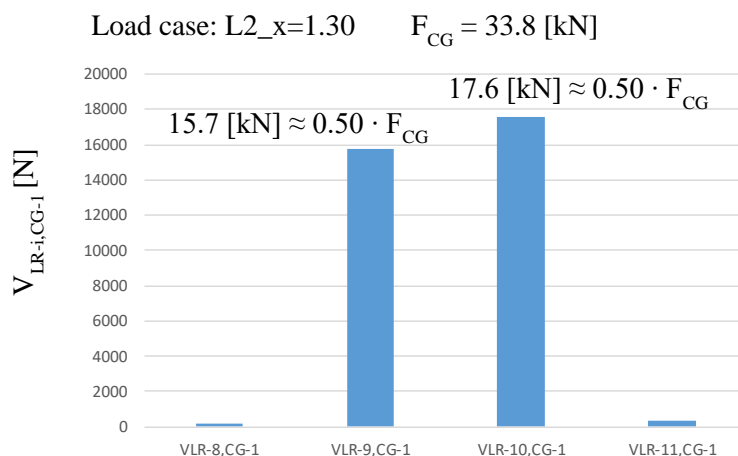


Figure 79: load distribution of the wheel load to the longitudinal ribs for different loading of cross girder CG-1 relating to load case L2_x=1.30

- Summary of loading at the individual longitudinal ribs in Model D referring to the wheel loads at section L1 and L2

The summary of the analyses relating to the wheel load distribution at section L1 and L2 to the individual longitudinal ribs is shown in Figure 80. Under consideration of these distribution rules the resulting load due to the critical vehicle type on its critical position in longitudinal bridge direction (F_{CG} , see Table 9) was applied at finite element model D (see Figure 61 and Figure 63).

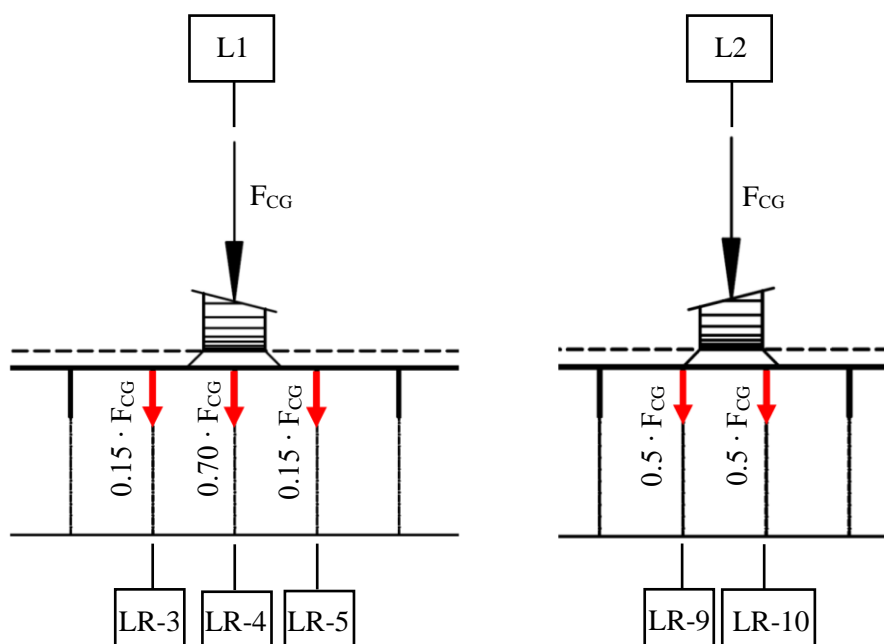


Figure 80: loading in Model: transferred wheel load parts at the longitudinal ribs to the cross girder referring to the wheel load to the appropriate longitudinal ribs at section L1 and L2

- Application of the relevant lorry type T2 (FLM 4) for the critical load position and determination of the shell edge loads for the finite element model D

Figure 81 displays the critical position of the relevant vehicle T2 for detail D3 that has been determined. It includes the calculation of the loads P [kN] which were then applied at the finite element model D. The axle load of lorry type T2 in FLM 4* has a value of $F_A = 105.7$ kN (see Figure 77) and every wheel has a load of $P_w = 105.7/2 = 52.9$ kN. The appropriate η -values from the cross girder influence line are illustrated in Figure 77. The load distribution to the individual longitudinal ribs can be seen in Figure 80.

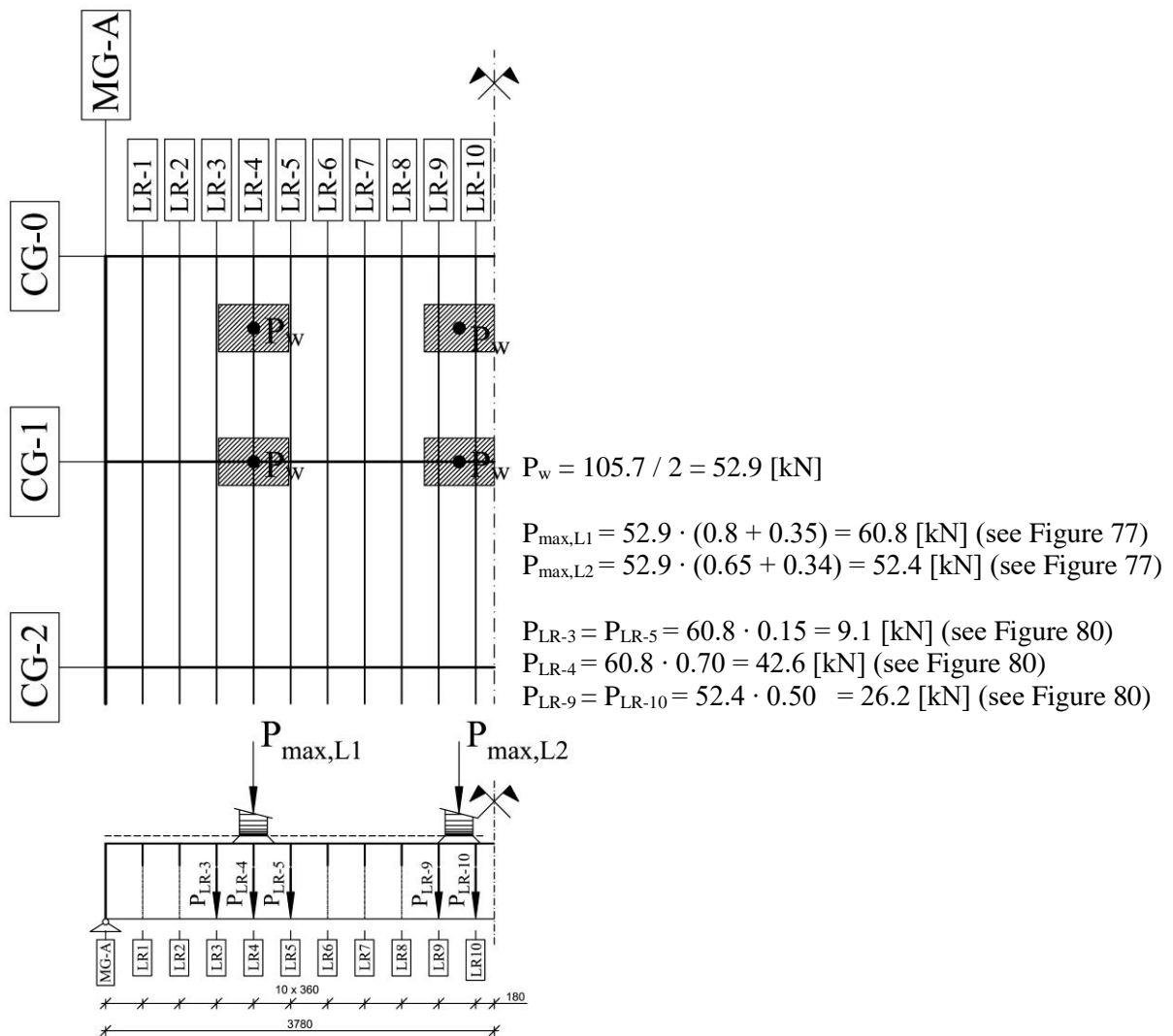


Figure 81: relevant lorry type T2 (FLM 4*) with its critical load position and determination of the shell edge loads for the finite element model D

3.4. Simulation of heavy traffic crossings

3.4.1. Overview of the principal procedure

In this Section the procedure and the results of the heavy traffic simulations for the finite element models A, B, C and D are shown. A detailed description of the finite element models can be found in Section 3.2. The stresses have been determined on an orthotropic steel bridge deck for the analysed notch details (D1, D2, D3) which are illustrated and explained in Section 2.4. For the simulations of the heavy traffic crossings over the analysed bridge decks fatigue load model FLM 4 and FLM 4* have been taken into account which are described in Section 2.5.2. Increased wheel contact patches were considered that are illustrated in Figure 65.

The analysed details D1a, D1b and D2 show a very local influence area and therefore no interaction of the wheel loads within a single axle appears. Therefore, also beside lanes can be ignored. All simulations have been carried out by just modelling one single or double wheeled contact patch load, which gives accurate results. For detail D3 the position of the lanes (lane 2, 3) was based on the studied bridge deck (see Figure 72).

The stresses in the notch details have been calculated under consideration of a centric configuration of the wheels in transverse direction. No lateral shift of the wheels and vehicles respectively in transverse direction was taken into account.

The following list gives an overview of the results shown in this Section 3.4 according to the calculations referring to the heavy traffic simulations of the vehicles from the chosen fatigue load model at orthotropic steel bridge decks:

- Model A: orthotropic bridge deck with open longitudinal ribs and cross girder interval $e_{QT} = 2.0\text{m}$
Results for detail D1a in Section 3.4.2.1 and results for detail D2 in Section 3.4.2.2
- Model B: orthotropic bridge deck with trough ribs and cross girder interval $e_{QT} = 2.0\text{m}$
Results for detail D1a in Section 3.4.3.1, detail D1b in Section 3.4.3.2 and detail D2 in Section 3.4.3.3
- Model C: orthotropic bridge deck with trough ribs and cross girder interval $e_{QT} = 4.0\text{m}$
Results for detail D1a in Section 3.4.4.1, detail D1b in Section 3.4.4.2 and detail D2 in Section 3.4.4.3
- Model D: orthotropic bridge deck with open longitudinal ribs – cross girder with field splices
Results for detail D3, joint I and III (near main girder) and joint II (between the main girders) in Section 3.4.5

In summary 3 individual steps had been done for the heavy traffic simulation, which are listed first in a very short form and then are explained in detail:

- Step 1: Determination of influence lines for the 3 wheel types A, B and C at every detail in longitudinal bridge direction.
- Step 2: Calculation of stress-history curves in every detail for every vehicle type under consideration of the axle distances and the axle loads depending on the lorries from the fatigue load model (see Figure 24 in Section 2.5.2).
- Step 3: Stress cycle counting with Rain flow- or Reservoir method and generation of a stress range spectrum due to a centric track configuration.
- Additional explanations:

For a realistic reproduction of the occurring stress ranges $\Delta\sigma_i$ due to the crossing of the vehicles from fatigue load model FLM 4 and FLM 4* the modelling of the wheel contact patches of every single axle including a load distribution through the asphalt pavement is an essential part. This beneficial load distribution is schematically shown in Figure 83 under every tyre. To get a better overview of the results of each axle type, the crossing of every axle A, B and C was done with a standardised axle load of $F_A = 100\text{kN}$. The single axle was adapted at many load positions in longitudinal bridge direction and the linear numerical simulations were carried out under consideration of a static behaviour only. Any dynamic effect was not considered in the numerical calculations. With the results of the individual load cases for each axle type, influence lines in longitudinal bridge direction could be determined, relating to an axle load of $F_A = 100\text{kN}$.

Figure 82 shows a schematic representation of the simulation of the heavy traffic crossings with centric track configuration. After creating the influence lines in longitudinal bridge direction for all three wheel types (A, B and C) in each analysed detail point, stress histories relating to the axle configuration of each lorry type (T1 to T5, see Figure 24) could be determined (see Figure 82.a). With Reservoir method the stress ranges $\Delta\sigma_i$ have been counted for every lorry type. The stress ranges were then summed up in a stress range spectrum for each analysed detail based on altogether 100 vehicle crossings and under consideration of the frequency of occurrence for long distance roads (see Figure 82.b). Finally, a damage equivalent constant amplitude stress range $\Delta\sigma_e$ could be verified relating to 100 load cycles. All analyses have been carried out under consideration of the S-N curve with a fatigue strength of $\Delta\sigma_c = 100\text{ N/mm}^2$ (see Section 2.7).

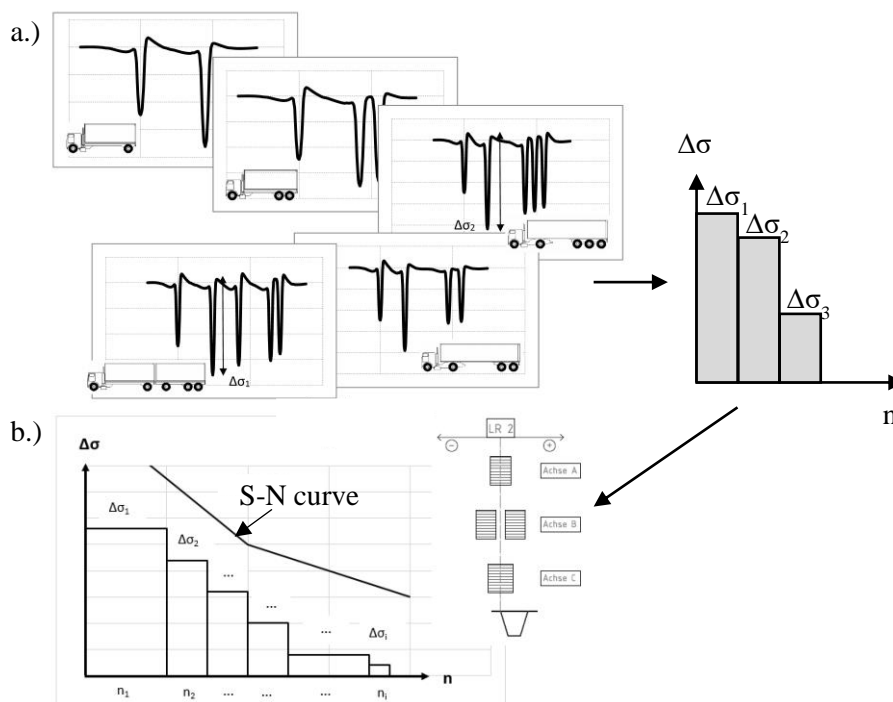


Figure 82: a.) schematic representation of stress-history curves for the 5 vehicle types from FLM-4; b.) determination of stress spectra by cycle counting of stress ranges $\Delta\sigma$ for each lorry type and integration of traffic configuration;

The whole simulation of the heavy traffic crossings with centric track configuration for all models and details can be found in Annex A and the essential results were presented in the following Sections.

3.4.2. Model A: Orthotropic bridge deck with open longitudinal ribs

This Section presents the results of the heavy traffic simulations under consideration of fatigue load model FLM 4 and also FLM 4* at FEM-model A, restricted to two lane positions in transverse direction. A detailed description of FEM-model A can be found in Section 3.2.1 and the applied fatigue load models are presented in Section 2.5.2. The stresses in the critical notch details D1a, D1b and D2 have been calculated and a detailed description of these points is shown in Section 2.4. The determination of the critical lane position referring to the details D1 and D2 is shown in Section 3.3 and is additionally illustrated below in Figure 83. Due to a lack of space at LR-1, lane 1 (end of the model at the main girder), the consideration of LR-3, lane 2, was necessary for further analyses regarding to a lateral wheel shifting. A calculation of a remaining service life after 50 years was performed at LR-1 (lane 1) and therefore, FLM 4* was used. At LR-3 (lane 2), no fatigue assessment has been done and therefore only FLM 4 was taken into account.

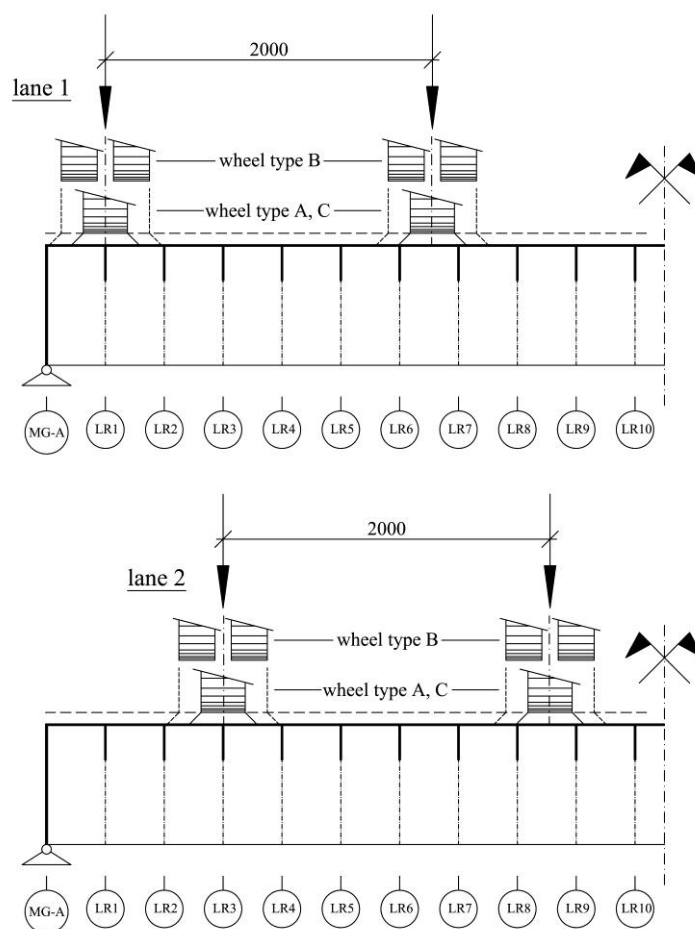


Figure 83: analysed lane positions lane 1 and lane 2 in transverse direction at Model A

3.4.2.1. Detail D1a

The analysed detail point D1a at lane 1 is located at longitudinal rib LR-1, measuring point MP-2 (see Figure 66 in Section 3.3.1). At lane 2, detail D1a is located at longitudinal rib LR-3. At both lanes D1a is in a distance of $e_{LR} = 360\text{mm}$ away from the mid cross girder. Figure 84 illustrates the calculated influence lines in longitudinal bridge direction due to axle/wheel type B and C with an increased wheel contact patch and an axle load of $F_A = 100\text{kN}$. In Figure 84.a the occurring stresses in the analysed detail D1a are plotted due to axle type B at LR-1 (lane 1) depending on the position of the axle in longitudinal bridge direction. Figure 84.b shows the occurring stresses in detail D1a due to axle type B at LR-3 (lane 2). As already shown in Table 4 (see Section 3.3.1), the maximum stress occurs at LR-1 (lane 1), where a stress of $\sigma_{D1a,LR-1,B} = -103.78\text{ N/mm}^2$ can be observed due to axle type B (see Figure 84.a). The presented influence line at LR-3 (see Figure 84.b) with a maximum stress of $\sigma_{D1a,LR-3,B} = -94.48\text{ N/mm}^2$ shows less difference compared to the one at LR-1. The influence lines referring to the single wheeled axles C are shown in Figure 84.c (LR-1, lane 1) and Figure 84.d (LR-2, lane 2), where also less difference can be observed. The maximum occurring stress at longitudinal rib LR-1 due to axle type C

has a value of $\sigma_{D1a,LR-1,C} = -115.70 \text{ N/mm}^2$ (see Figure 84.c). The wheel contact patches of axle type B (680x460mm) and C (410x460mm) are quite different in its width (see Figure 65 in Section 3.3.1). Therefore, the width of the twin tyres are about 1.7 times larger than the single wheeled ones, leading to reduced surface pressure, when both axles have the same axle load. But with regards to the resulting stresses, presented in Figure 84.a and c., there is not that much differentiation ($\sigma_{D1a,LR-1,C} / \sigma_{D1a,LR-1,B} = 1.1$). Hence, there is less difference between the results due to the axle types, because the extended wheel contact patches' geometry is large in relation to the longitudinal rib's interval. Therefore, a difference of only 10% could be observed between axle type B and C.

The calculation of influence lines in longitudinal bridge direction at lane 1 and 2 has also been carried out for axle/wheel type A which are not plotted in this Section.

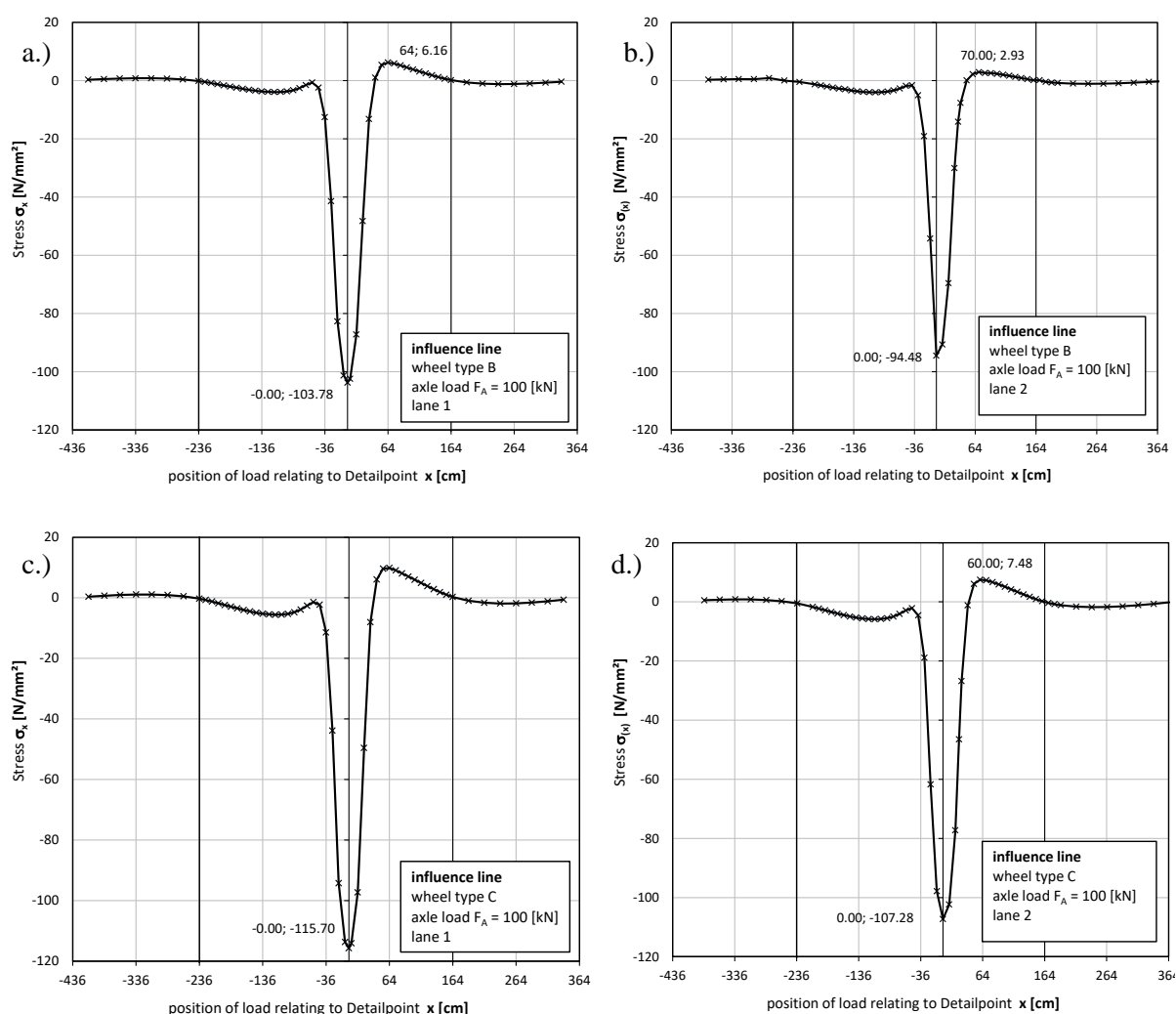


Figure 84: Model A – Detail D1a – influence lines in longitudinal bridge direction due to axle/wheel type B and C and axle load $F_A = 100 \text{ kN}$: a.) axle type B at LR-1 (lane 1); b.) axle type B at LR-3 (lane 2); c.) axle type C at LR-1 (lane 1); d.) axle type C at LR-3 (lane 2);

Figure 85 illustrates the stress history for detail D1a at LR-3 (lane 2) in centric position due to a crossing of lorry type T3 according to fatigue load model FLM 4 (see Section 2.5.2). The occurring stress ranges $\Delta\sigma_i$ have been counted with Rain flow-method and are also shown in the visualisation. The marked stress ranges $\Delta\sigma_i$ in the stress history curve show very good, that every axle from the vehicle produces a separate stress range.

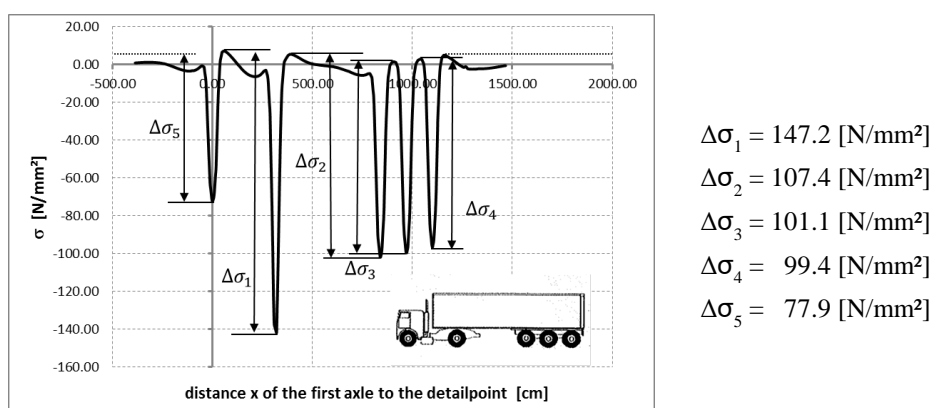


Figure 85: Model A – Detail D1a at LR-3 – stress history relating to a crossing of lorry type T3 according to FLM 4 at lane 2

As illustrated in Figure 85, the highest stress range $\Delta\sigma_1$ is caused by the heaviest axle of the lorry which in that case, is the driving axle of the articulated lorry. Therefore, it can be noticed that at every lorry, the highest axle load F_A of the vehicle produces at detail D1a the highest stress range within a single lorry.

The calculation of stress history curves at lane 1 and 2 have also been carried out for all other lorry types from fatigue load model FLM 4, respectively FLM 4*, which are not plotted in this Section.

– Stress range spectra due to FLM 4 and FLM 4* referring to LR-1 (lane 1)

Figure 86 shows the resulting stress range spectrum for detail D1a at LR-1 (MP2, see Figure 66) due to the weigh in motion modified fatigue load model FLM 4* at lane 1 relating to in summary 100 lorries. The frequency of occurrence was chosen for long distance routes (see Figure 24 in Section 2.5.2) and therefore the following number of lorries is presented: lorry type T1 – $n_1 = 20$, lorry type T2 – $n_2 = 5$, lorry type T3 – $n_3 = 50$, lorry type T4 – $n_4 = 10$, lorry type T5 – $n_5 = 10$;

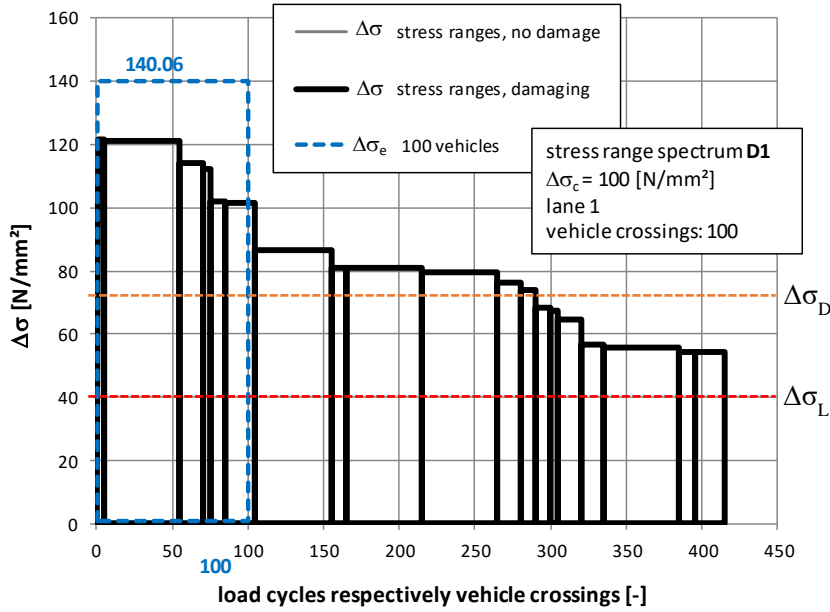


Figure 86: Model A – Detail D1a at LR-1 – stress range spectrum relating to a crossing of in summary 100 lorries according to FLM 4* and centric track configuration

Additionally, Figure 87 shows the resulting stress range spectrum for detail D1a at LR-1 (MP2, see Figure 66) due to the unmodified fatigue load model FLM 4 at lane 1, also relating to in summary 100 lorries. The frequency of the individual lorry types is the same as for FLM 4*.

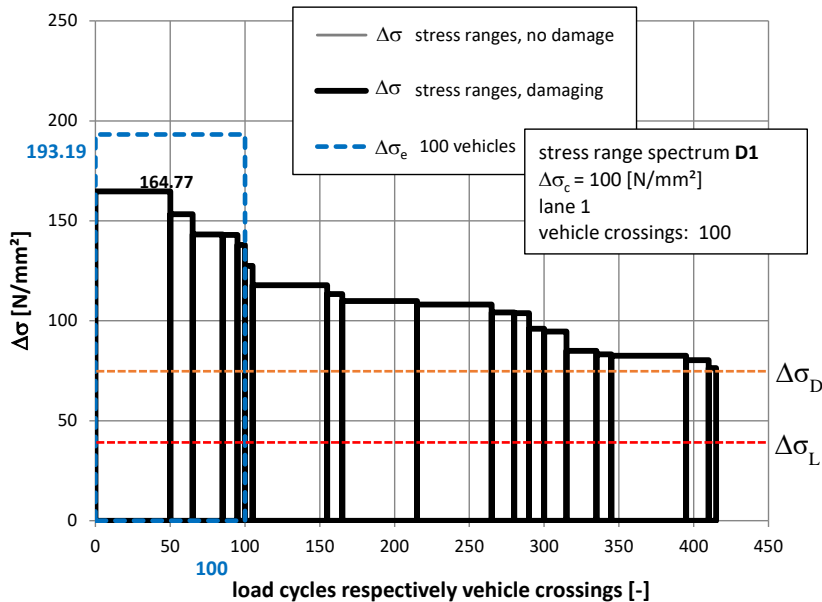


Figure 87: Model A – Detail D1a at LR-1 – stress range spectrum relating to a crossing of in summary 100 lorries according to FLM 4 and centric track configuration

Both pictures (Figure 86 and Figure 87) also show a damage equivalent constant amplitude stress range $\Delta\sigma_e$ relating to $n_e = 100$ number of load cycles. This values have been determined by using Equation 6

and Equation 7 (see Section 2.6) and under consideration of the appropriate S-N curve with a fatigue strength of $\Delta\sigma_c = 100 \text{ N/mm}^2$. Stress ranges which are lower than the cut off limit for fatigue $\Delta\sigma_L$ do not have any damaging effect. This cut off limit $\Delta\sigma_L$ is also shown in the figures as well as the constant amplitude fatigue limit $\Delta\sigma_D$ at $N_D = 5 \cdot 10^6$, where stress ranges which are lower than $\Delta\sigma_D$ have less damaging effect ($m = 5$) than stress ranges above $\Delta\sigma_D$ ($m = 3$).

By comparing the two stress range spectra from Figure 86 and Figure 87 it can be stated, that the higher stress ranges in Figure 87 are caused by the higher axle loads due to the chosen fatigue load model ($F_{A,i,FLM4} > F_{A,i,FLM4^*}$). The equivalent constant amplitude stress range for FLM 4 relating to FLM 4* is: $\Delta\sigma_{e,D1a,FLM4} / \Delta\sigma_{e,D1a,FLM4^*} = 193.19/140.06 = 1.38 \rightarrow \Delta\sigma_{e,D1a,FLM4} = 1.38 \cdot \Delta\sigma_{e,D1a,FLM4^*}$.

Regarding to the indications in Figure 24 in Section 2.5.2, the weighted average gross weight of the lorries of FLM 4* is:

$$G_{\text{tot,av,FLM4}^*} = (0.2 \cdot 142 + 0.05 \cdot 273 + 0.5 \cdot 360 + 0.15 \cdot 290 + 0.1 \cdot 321)/1 = 297.65 \text{ kN}$$

The gross weight's weighted average due to FLM 4 is:

$$G_{\text{tot,av,FLM4}} = (0.2 \cdot 200 + 0.05 \cdot 310 + 0.5 \cdot 490 + 0.15 \cdot 390 + 0.1 \cdot 450)/1 = 404 \text{ kN}$$

The load increase referring to the gross weights of FLM 4 in relation to FLM 4* is:

$$G_{\text{tot,av,FLM4}} / G_{\text{tot,av,FLM4}^*} = 404 / 297.65 = 1.36 \rightarrow G_{\text{tot,av,FLM4}} = 1.36 \cdot G_{\text{tot,av,FLM4}^*}$$

The distribution of the lorry's gross weights (T1 to T5) to the individual axles is equal for both load models FLM 4 and FLM 4*. Hence, there is quite a linear relationship between the loads and the occurring equivalent stress ranges in this case, because of the very high stress ranges. In both spectra, there is no stress range below the cut off limit for fatigue $\Delta\sigma_L$. Because of the higher load levels in FLM 4, every stress range in Figure 87 is higher than $\Delta\sigma_D$ and the damages were therefore calculated with a S-N-curve's slope of $m = 3$. Regarding to the stress ranges due to FLM 4* in Figure 86, a few of them were considered with a flatter slope of the S-N-curve ($m = 5$), which causes less damaging effect. The relationship of the resulting damages due to FLM 4 and FLM 4* is shown below:

- FLM 4: $N_{e,D1a,FLM4} = (\Delta\sigma_c / \Delta\sigma_{e,D1a,FLM4})^3 \cdot 2 \cdot 10^6 = (100 / 193.19)^3 \cdot 2 \cdot 10^6 = 0.2774 \cdot 10^6$;
 $D_{e,D1a,FLM4} = n_e / N_{e,D1a,FLM4} = 100 / (0.2774 \cdot 10^6) = 0.36 \cdot 10^{(-3)}$
- FLM 4*: $N_{e,D1a,FLM4^*} = (\Delta\sigma_c / \Delta\sigma_{e,D1a,FLM4^*})^3 \cdot 2 \cdot 10^6 = (100 / 140.06)^3 \cdot 2 \cdot 10^6 = 0.7279 \cdot 10^6$;
 $D_{e,D1a,FLM4^*} = n_e / N_{e,D1a,FLM4^*} = 100 / (0.7279 \cdot 10^6) = 0.14 \cdot 10^{(-3)}$

$$\rightarrow D_{e,D1a,FLM4} / D_{e,D1a,FLM4^*} = (n_e / N_{e,D1a,FLM4}) / (n_e / N_{e,D1a,FLM4^*}) = N_{e,D1a,FLM4^*} / N_{e,D1a,FLM4} = 2.6$$

An increase of the loads of 36% causes in this case an equivalent stress range increase of 38%. Regarding to the damage in the analysed detail D1a, the stress cycles due to FLM 4 cause in this case a 2.6 times higher damage in the detail than due to FLM 4*.

- Stress range spectrum due to FLM 4 referring to lane 2

Figure 88 shows the resulting stress range spectrum for detail D1a due to the unmodified fatigue load model FLM 4 at lane 2 relating to in summary 100 lorries.

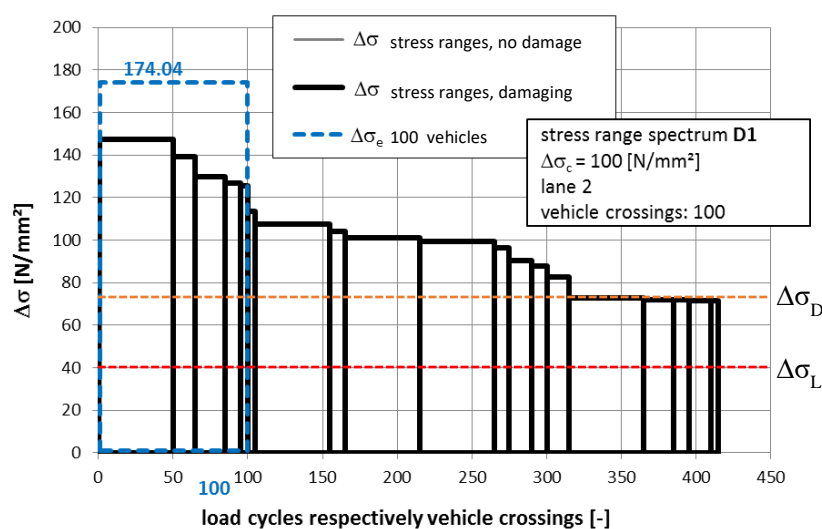


Figure 88: Model A – Detail D1a at LR-3 – stress range spectrum relating to a crossing of in summary 100 lorries according to FLM 4 and centric track configuration

Figure 88 also shows a damage equivalent constant amplitude stress range $\Delta\sigma_e$ relating to $n_e = 100$ number of load cycles. This values have been determined by using Equation 6 and Equation 7 (see Section 2.6) and under consideration of the appropriate S-N curve with a fatigue strength of $\Delta\sigma_c = 100$ N/mm². This stress range spectrum at LR-3 (lane 2) is the basis for further investigations referring to detail D1a and a lateral shift of the vehicles due to driving characteristics which are presented in Section 4.

The stress range spectra in Figure 87 and Figure 88 are relating to the same load level FLM 4 and therefore a comparison is possible. As already shown in Section 3.3.1, a location of detail D1a at LR-1 (lane 1), near the main girder delivers maximum stresses. This recognition is confirmed by the lower equivalent constant amplitude stress range at LR-3 (lane 2) relating to the one at LR-1. At the spectrum at LR-1, all stress ranges are higher than $\Delta\sigma_D$, whereas at LR-3 the last 5 stress ranges are lower than $\Delta\sigma_D$ and therefore were considered with a flatter S-N-curve's slope of $m = 5$. At LR-1, the equivalent constant amplitude stress range $\Delta\sigma_{e,D1a,LR-1} = 193.19$ N/mm² has a 11% higher value than at LR-3, where

a value of $\Delta\sigma_{e,D1a,LR-3} = 174.04 \text{ N/mm}^2$ was calculated. The maximum stress range at the spectrum for LR-1 is $\Delta\sigma_{\max,D1a,LR-1} = 164.8 \text{ N/mm}^2$ and for LR-3, $\Delta\sigma_{\max,D1a,LR-3} = 147.2 \text{ N/mm}^2$. Therefore, the maximum occurring stress range for LR-1 is also about 12% higher than for LR-3. By considering the resulting damages for the stress range spectra in Figure 87 and Figure 88, a difference which is shown below can be recognised:

- LR-1: $N_{e,D1a,LR-1} = (\Delta\sigma_c / \Delta\sigma_{e,D1a,LR-1})^3 \cdot 2 \cdot 10^6 = (100 / 193.19)^3 \cdot 2 \cdot 10^6 = 0.2774 \cdot 10^6$;
 $D_{e,D1a,LR-1} = n_e / N_{e,D1a,LR-1} = 100 / (0.2774 \cdot 10^6) = 0.36 \cdot 10^{(-3)}$
- LR-3: $N_{e,D1a,LR-3} = (\Delta\sigma_c / \Delta\sigma_{e,D1a,LR-3})^3 \cdot 2 \cdot 10^6 = (100 / 174.04)^3 \cdot 2 \cdot 10^6 = 0.3794 \cdot 10^6$;
 $D_{e,D1a,LR-3} = n_e / N_{e,D1a,LR-3} = 100 / (0.3794 \cdot 10^6) = 0.26 \cdot 10^{(-3)}$

$$\rightarrow D_{e,D1a,LR-1} / D_{e,D1a,LR-3} = (n_e / N_{e,D1a,LR-1}) / (n_e / N_{e,D1a,LR-3}) = N_{e,D1a,LR-3} / N_{e,D1a,LR-1} = 1.37$$

The occurring equivalent stress range $\Delta\sigma_e$, determined due to the same load level FLM 4, is for LR-1 (lane 1) 11% higher than for LR-3 (lane 2), but the consequential damage is for LR-1 37% higher than for LR-3.

3.4.2.2. Detail D2

The analysed detail point D2 at lane 1 is located at longitudinal rib LR-1, on the bottom side of the welded connection of the longitudinal rib to the cross girder (see Section 3.3.3). At lane 2, detail D2 is located at longitudinal rib LR-3. The calculated influence lines in longitudinal bridge direction due to axle/wheel type B and C with an increased wheel contact patch and an axle load of $F_A = 100\text{kN}$ are illustrated in Figure 89. Figure 89.a shows the occurring stresses in the analysed detail D2 due to axle type B at LR-1 (lane 1) depending on the position of the axle in longitudinal bridge direction. Figure 89.b shows the occurring stresses in detail D2 due to axle type B at LR-3 (lane 2). The influence lines due to the single wheeled axle type C are shown Figure 89.c (at LR-1, lane 1) and Figure 89.d (at LR-3, lane 2).

The calculation of influence lines in longitudinal bridge direction at lane 1 and 2 has also been carried out for axle/wheel type A which are not plotted in this Section.

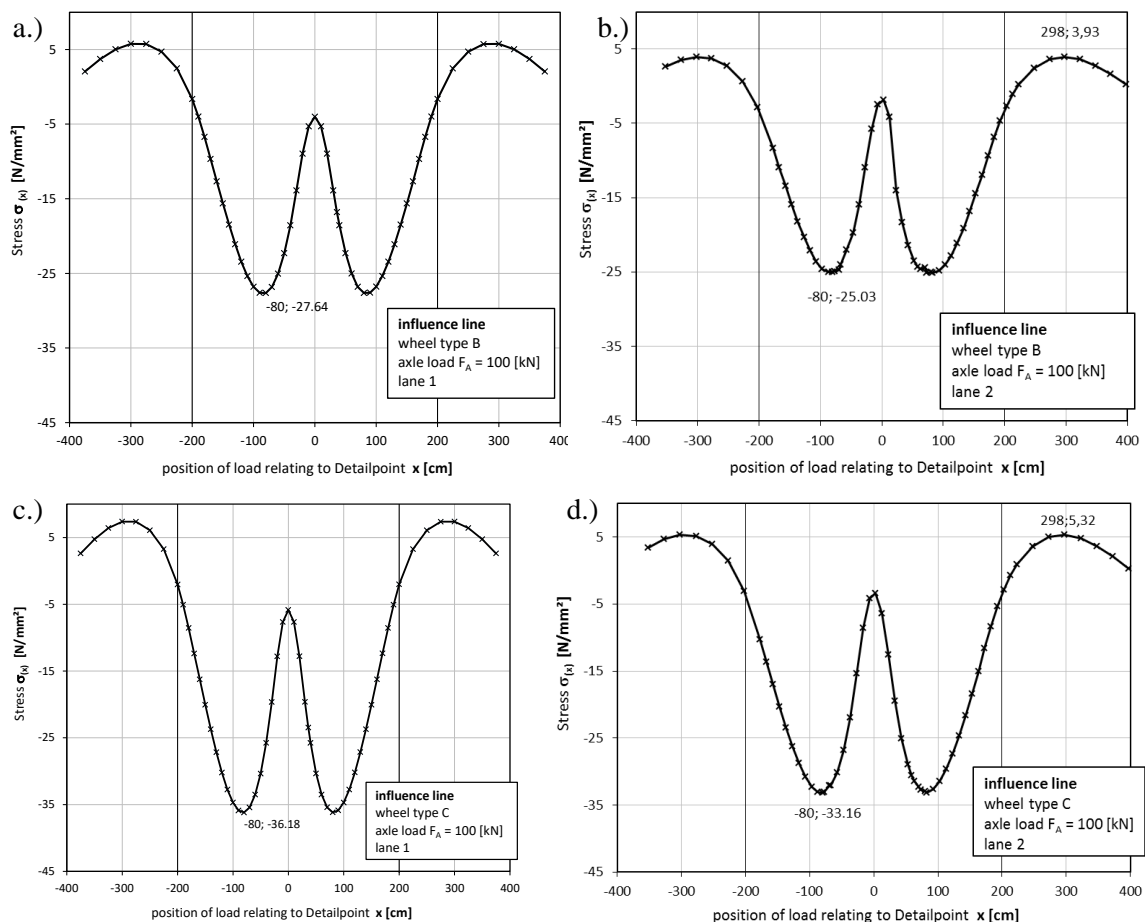


Figure 89: Model A – Detail D2 – influence lines in longitudinal bridge direction due to axle/wheel type B and C and axle load $F_A = 100\text{kN}$: a.) axle type B at LR-1 (lane 1); b.) axle type B at LR-3 (lane 2); c.) axle type C at LR-1 (lane 1); d.) axle type C at LR-3 (lane 2);

By comparing the influence lines for axle type B with twin tyres in Figure 89.a (at LR-1, lane 1) and Figure 89.b (LR-3, lane 2), less difference can be observed. The maximum occurring stress in detail D2 differs about 10% but the load location in longitudinal direction referring to the maximum stress is the same ($e = 80\text{cm}$ away from the cross girder). Same observations can be done for the influence lines relating to the single wheeled axle type C in Figure 89.c and Figure 89.d. More significant difference can be recognised when comparing the maxima of the influence lines for single and double wheeled axles (Figure 89.a and Figure 89.c). Due to the single wheeled axle type C, a higher stress level occurs in D2 than for axle type B when the same axle load is applied. The occurring stress due to axle type C is 31% higher than due to axle type B (36.18 N/mm^2 instead of 27.64 N/mm^2). This higher stress level for axle type C is caused by a smaller width of the wheel contact patch relating to axle type B. Due to the wider axle type B, the load can be distributed much better to the nearby longitudinal ribs which reduces the stresses in the directly loaded longitudinal rib.

Figure 90 illustrates the stress history for detail D2 at LR-3 due to a crossing of lorry type T3 according to fatigue load model FLM 4 (see Section 2.5.2) at lane 2 (see Figure 83). The occurring stress ranges

$\Delta\sigma_i$ have been counted with Rain flow-method and are also shown in the visualisation. The plotted graph in the diagram shows very good the superposing stresses due to the last 3 axles from the trailer that causes the maximum stress range $\Delta\sigma_1$.

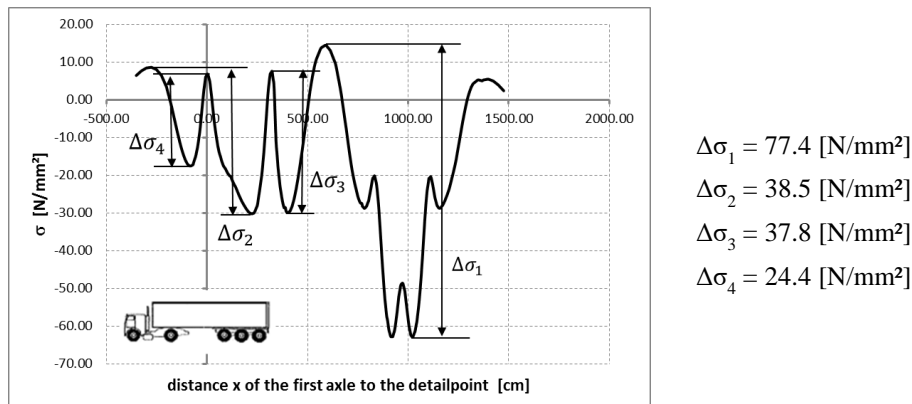


Figure 90: Model A – Detail D2 at LR-3 – stress history curve relating to a crossing of lorry type T3 according to FLM 4 at lane 2

The calculation of stress history curves at lane 1 and 2 have also been carried out for all other lorry types from fatigue load model FLM 4, respectively FLM 4*, which are not plotted in this Section.

- Stress range spectra due to FLM 4 and FLM 4* at LR-1 referring to lane 1

The resulting stress range spectrum for detail D2 due to the weigh in motion modified fatigue load model FLM 4* at LR-1 (lane 1) is shown in Figure 91 relating to in summary 100 lorries.

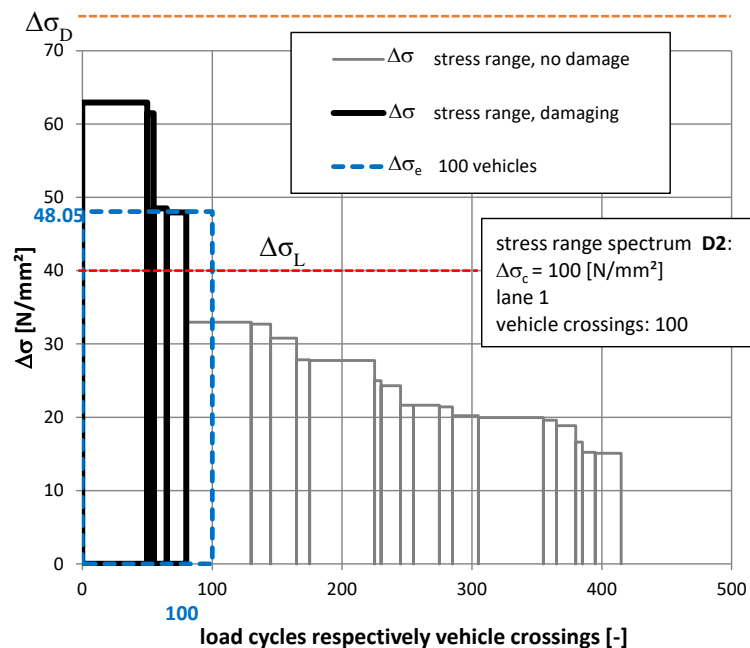


Figure 91: Model A – Detail D2 at LR-1 – stress range spectrum relating to a crossing of in summary 100 lorries according to FLM 4* at lane 1 and centric track configuration

Additionally, Figure 92 shows the resulting stress range spectrum for detail D2 due to the unmodified fatigue load model FLM 4 at lane 1 relating to in summary 100 lorries.

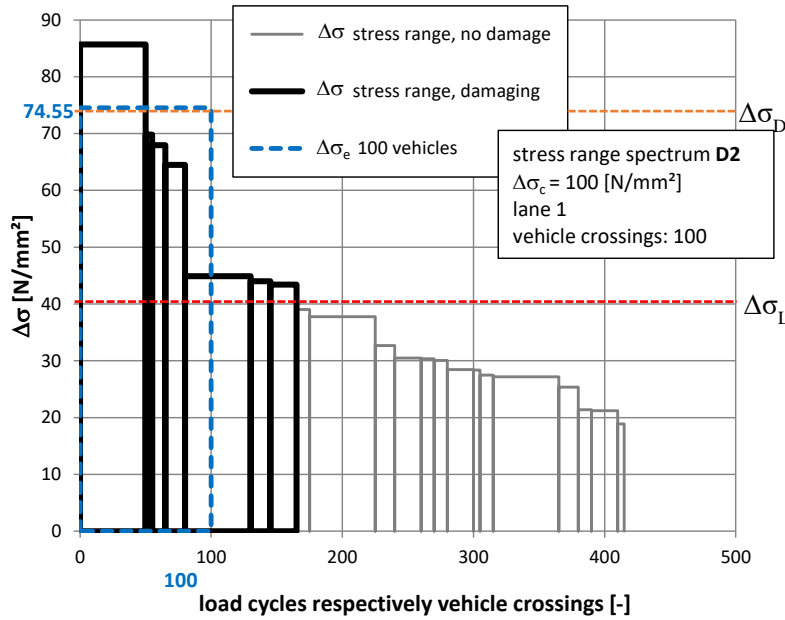


Figure 92: Model A – Detail D2 at LR-1 – stress range spectrum relating to a crossing of in summary 100 lorries according to FLM 4 at lane 1 and centric track configuration

Both pictures (Figure 91 and Figure 92) also show a damage equivalent constant amplitude stress range $\Delta\sigma_e$ relating to $n_e = 100$ number of load cycles. This values have been determined by using Equation 6 and Equation 7 (see Section 2.6) and under consideration of the appropriate S-N curve with a fatigue strength of $\Delta\sigma_c = 100$ N/mm². Additionally, the constant amplitude fatigue limit $\Delta\sigma_D$ at $N_D = 5 \cdot 10^6$ is shown in the pictures as well as the cut off limit for fatigue $\Delta\sigma_L$.

The stress range spectrum due to FLM 4 (Figure 92) has a higher equivalent constant amplitude stress range $\Delta\sigma_e$ as due to FLM 4* (Figure 91) because of the higher load levels. In the spectrum due to FLM 4*, only 4 stress ranges have a damaging effect at detail D2 and even the maximum stress range is under the fatigue limit $\Delta\sigma_D$. In that case, a theoretical boundless life time would be available which was ignored regarding to the conducted analyses. Hence, these 4 stress ranges were considered with a S-N-curve's slope of $m = 5$ in the damage calculation. The equivalent constant amplitude stress range for FLM 4 relating to FLM 4* is: $\Delta\sigma_{e,D2,FLM4} / \Delta\sigma_{e,D2,FLM4*} = 74.55/48.05 = 1.55 \rightarrow \Delta\sigma_{e,D2,FLM4} = 1.55 \cdot \Delta\sigma_{e,D2,FLM4*}$. Regarding to the vehicle's gross weights, the weighted average of FLM 4 relating to FLM 4* is $404/297.65 = 1.36$. Hence, there is no linear increase relating to the loads and the stress range $\Delta\sigma_e$, because of the consideration of the fatigue's cut off limit. The relation of the damages due to FLM 4

and FLM 4* is $D_{e,D2,FLM4} / D_{e,D2,FLM4*} = 3.73$. Hence, a load increase of 36% causes in this case an equivalent stress range increase of 55% and finally a damage increase of 273%.

- Stress range spectrum due to FLM 4 at LR-3 referring to lane 2

Figure 93 shows the resulting stress range spectrum for detail D2 at LR-3 due to the unmodified fatigue load model FLM 4 at lane 2 relating to in summary 100 lorries.

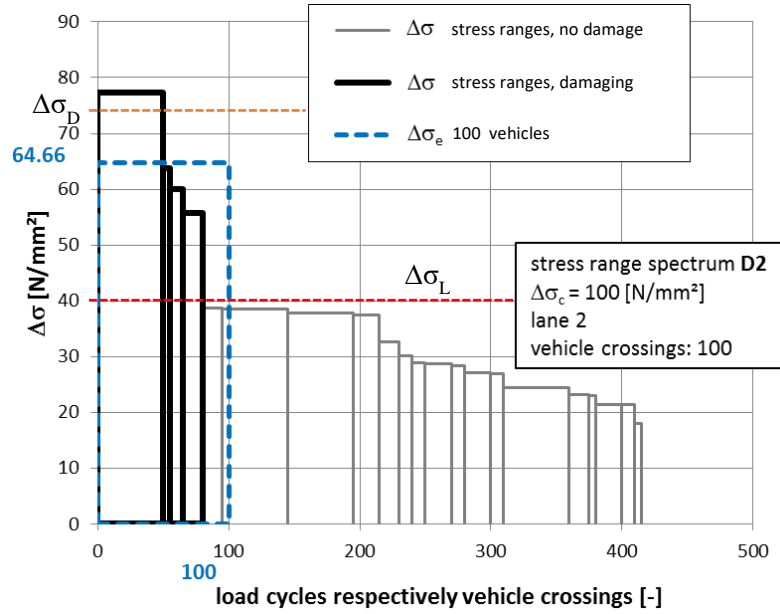


Figure 93: Model A – Detail D2 at LR-3 – stress range spectrum relating to a crossing of in summary 100 lorries according to FLM 4 at lane 2 and centric track configuration

Figure 93 also shows a damage equivalent constant amplitude stress range $\Delta\sigma_e$ relating to $n_e = 100$ number of load cycles. This values have been determined by using Equation 6 and Equation 7 (see Section 2.6) and under consideration of the appropriate S-N curve with a fatigue strength of $\Delta\sigma_c = 100$ N/mm². This stress range spectrum at lane 2 is the basis for further investigations referring to detail D2 and a lateral shift of the vehicles due to driving characteristics which are presented in Section 4.

The stress range spectra in Figure 92 and Figure 93 are caused by the same load level FLM 4, but have different detail locations. The equivalent stress range due to FLM 4 is for LR-1 $\Delta\sigma_{e,D2,LR-1} = 74.55$ N/mm² and for LR-3 $\Delta\sigma_{e,D2,LR-3} = 64.66$ N/mm². The relation between these two equivalent stress ranges is:

$$\Delta\sigma_{e,D2,LR-1} / \Delta\sigma_{e,D2,LR-3} = 1.15 \rightarrow \Delta\sigma_{e,D2,LR-1} = 1.15 \cdot \Delta\sigma_{e,D2,LR-3}.$$

The following difference regarding to the calculated damages at LR-1 and LR-3 can be observed:

$$- \text{LR-1: } N_{e,D2,LR-1} = (\Delta\sigma_c / \Delta\sigma_{e,D2,LR-1})^3 \cdot 2 \cdot 10^6 = (100 / 74.55)^3 \cdot 2 \cdot 10^6 = 4.8271 \cdot 10^6;$$

$$- \text{LR-3: } N_{e,D2,LR-3} = (\Delta\sigma_c / \Delta\sigma_{e,D2,LR-3})^3 \cdot 2 \cdot 10^6 = (100 / 64.66)^3 \cdot 2 \cdot 10^6 = 7.3981 \cdot 10^6;$$

$$\rightarrow D_{e,D2,LR-1} / D_{e,D2,LR-3} = (n_e / N_{e,D2,LR-1}) / (n_e / N_{e,D2,LR-3}) = N_{e,D2,LR-3} / N_{e,D2,LR-1} = 1.53$$

Under consideration of the same load level, in this case, an equivalent stress range increase of 15% can be recognised for a detail location at LR-1 relating to LR-3. Finally, the in this case calculated damage is for LR-1 53% higher than for LR-3.

3.4.3. Model B: Orthotropic bridge deck with trough longitudinal ribs and cross girder spacing of 2m

This Section presents the results of the heavy traffic simulations under consideration of fatigue load model FLM 4 at FEM-model B. A detailed description of FEM-model B can be found in Section 3.2.2 and the applied fatigue load models are presented in Section 2.5.2. The stresses in the critical notch details D1a, D1b and D2 have been calculated and a detailed description of these points is shown in Section 2.4. In the following, the results are presented for the so called “lane 1” – position of the traffic loads, illustrated below in Figure 94.

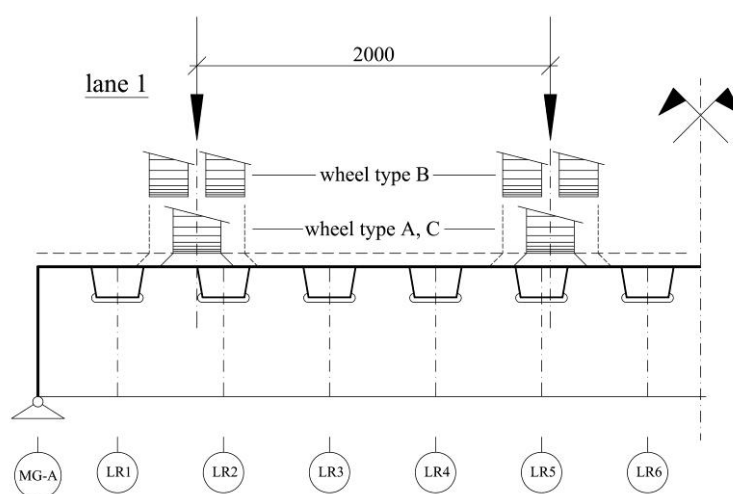


Figure 94: analysed lane position lane 1 in cross bridge direction at Model B

3.4.3.1. Detail D1a

The analysed detail point D1a for lane 1 loading is located at longitudinal rib LR-2, at the left through web. Notch detail D1a is in longitudinal a distance of $e_{LR} = 300\text{mm}$ away from the mid cross girder. Figure 95 illustrates the calculated influence line in longitudinal bridge direction due to axle/wheel type B and C with an increased wheel contact patch and an axle load of $F_A = 100\text{kN}$.

The calculation of influence lines in longitudinal bridge direction at lane 1 has also been carried out for axle/wheel type A which are not plotted in this Section.

Figure 95.a shows the influence line due to axle type B with twin tyres and Figure 95.b shows the influence line due to axle type C with a single wheel. Both curves show a very local influence area directly in the detail's region, which is similar to the influence lines at the deck with open longitudinal ribs (see Figure 84 in Section 3.4.2.1). In contrast to the stresses in Figure 84.a (axle type B) and Figure 84.c (axles type C) at a bridge deck with flat steel ribs, where 10% difference could be observed, there

is more difference between single and double wheeled axles regarding to decks with closed longitudinal ribs. The critical load case referring to D1a delivers for axle type B a maximum stress of $\sigma_{D1a,B} = -55.61$ N/mm² and for axle type C a maximum stress of $\sigma_{D1a,C} = -71.21$ N/mm² ($\sigma_{D1a,C}/\sigma_{D1a,B} = 1.28$). Therefore, a differentiation of 28% could be recognised between axle type B and C for detail D1a at steel decks with trough longitudinal ribs.

Additionally, the stress level in Figure 95 (model B with trough ribs) is generally lower than in Figure 84 (model A with flat steel ribs). The deck plate slenderness is a very important parameter that strongly influences the stresses in detail D1a and these slenderness is quite different for model A and B. A higher deck plate slenderness causes higher stresses in the detail. Model A has a deck plate slenderness of $e_{LR}/t_{DP} = 36$ and model B has a slenderness of $e_{LR}/t_{DP} = 25$. A maximum stress due to axle type C of $\sigma_{A,D1a,C} = -107.28$ N/mm² (see Figure 84.d) can be recognised at model A, LR-3 and $\sigma_{B,D1a,C} = -71.21$ N/mm² (see Figure 95.b) at model B ($\sigma_{A,D1a,C} / \sigma_{B,D1a,C} = 1.51$). Due to axle type B, the maximum stresses in D1a at LR-3 are $\sigma_{A,D1a,B} = -94.48$ N/mm² (see Figure 84.b) for model A and $\sigma_{B,D1a,B} = -55.61$ N/mm² (see Figure 95.a) for model B ($\sigma_{A,D1a,B} / \sigma_{B,D1a,B} = 1.7$). Because of the higher deck plate slenderness of model A, the occurring stresses in D1a are 51% (axle type C) and 70% (axle type B) higher than at model B.

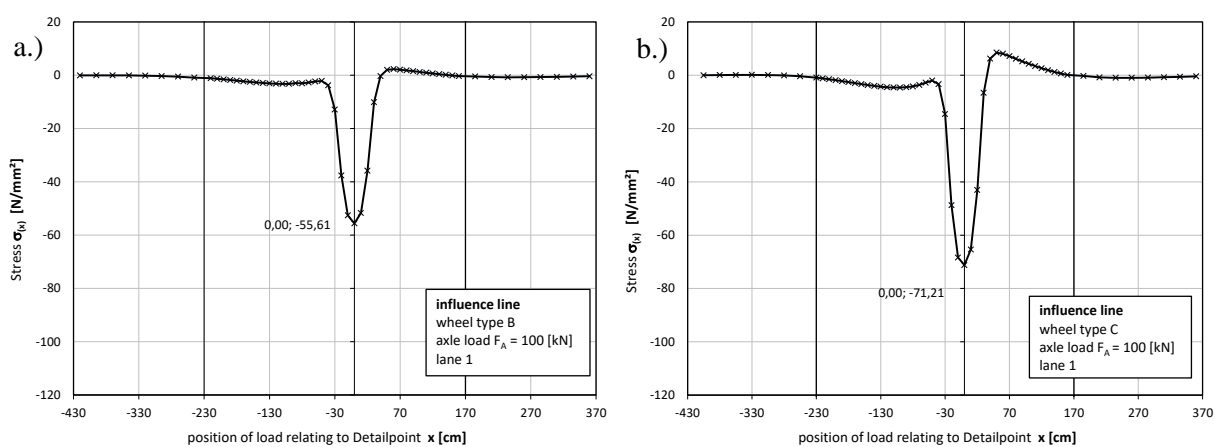


Figure 95: Model B – Detail D1a – influence lines in longitudinal bridge direction due to an axle load of $F_A = 100$ kN and: a.) axle type B; b.) axle type C

Figure 96 illustrates the stress history for detail D1a due to a crossing of lorry type T3 according to fatigue load model FLM 4 (see Section 2.5.2) at lane 1 (see Figure 94). The occurring stress ranges $\Delta\sigma_i$ have been counted with Rain flow-method and are also shown in the figure. The plotted graph in the diagram shows very good, that every axle from the vehicle produces a separate stress range.

The maximum stress range in Figure 96 (model B) has a value of $\Delta\sigma_{B,T3,max} = \Delta\sigma_{B,T3,1} = 89.9$ N/mm² and is caused by the driving axle of the articulated lorry (lorry type T3) which consists of axle type B. The

maximum stress range in Figure 85 in Section 3.4.2.1 (model A) is $\Delta\sigma_{A,T3,max} = \Delta\sigma_{A,T3,1} = 147.2 \text{ N/mm}^2$, which is also caused by the driving axle of T3. The relation between these two stress ranges is $\Delta\sigma_{A,T3,1} / \Delta\sigma_{B,T3,1} = 1.64$ which is almost similar to the observed stress increase referring to the influence lines shown above. The stress range $\Delta\sigma_{B,T3,2} = 71.9 \text{ N/mm}^2$ at model B (see Figure 96) and $\Delta\sigma_{A,T3,2} = 107.4 \text{ N/mm}^2$ at model A are both caused by axle type C ($\Delta\sigma_{A,T3,2} / \Delta\sigma_{B,T3,2} = 1.49$). Therefore, this relation is quite similar to the one observed at the axle type C's influence line.

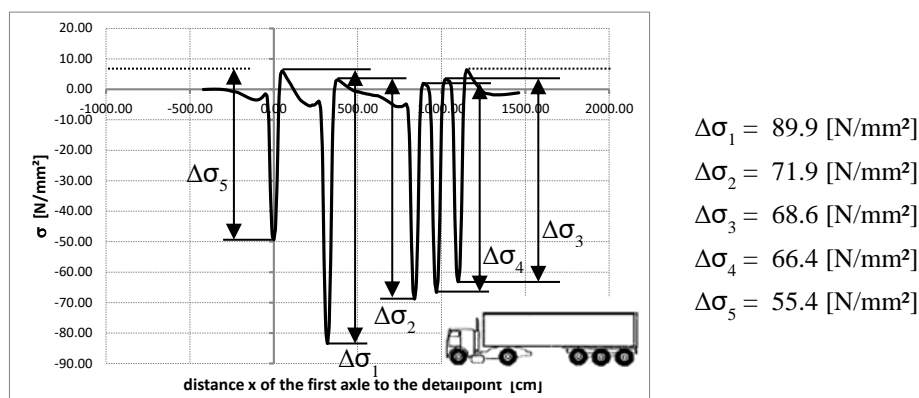


Figure 96: Model B – Detail D1a – stress history curve relating to a crossing of lorry type T3 according to FLM 4 at lane 1

The calculation of stress history curves at lane 1 has also been carried out for all other lorry types from fatigue load model FLM 4 which are not plotted in this Section.

- Stress range spectra due to FLM 4 referring to lane 1

Figure 97 shows the resulting stress range spectrum for detail D1a due to fatigue load model FLM 4 at lane 1 relating to in summary 100 lorries.

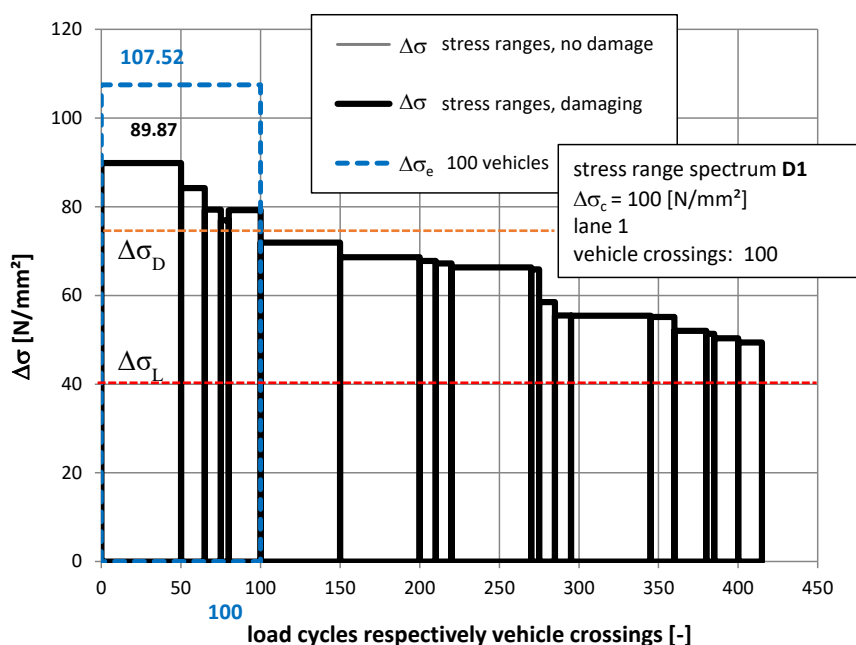


Figure 97: Model B – Detail D1a – stress range spectrum relating to a crossing of in summary 100 lorries according to FLM 4 at lane 1 and centric track configuration

Figure 97 also shows a damage equivalent constant amplitude stress range $\Delta\sigma_e$ relating to $n_e = 100$ number of load cycles. This values have been determined by using Equation 6 and Equation 7 (see Section 2.6) and under consideration of the appropriate S-N curve with a fatigue strength of $\Delta\sigma_c = 100$ N/mm². This stress range spectrum at lane 1 is the basis for further investigations referring to detail D1a and a lateral shift of the vehicles due to driving characteristics which are presented in Section 4.

The stress range spectrum in Figure 97 relating to model B (deck with trough ribs) can be compared to the stress range spectrum in Figure 88 in Section 3.4.2.1 which relates to model A (deck with flat steel ribs). Both spectra have been determined under consideration of FLM 4. The equivalent constant amplitude stress range $\Delta\sigma_{e,A,D1a} = 174.04$ for model A at LR-3 (see Figure 88) and $\Delta\sigma_{e,B,D1a} = 107.52$ for model B (see Figure 97) can now be compared. The relation between these two values is $\Delta\sigma_{e,A,D1a} / \Delta\sigma_{e,B,D1a} = 1.62$. The relation between the equivalent stress ranges $\Delta\sigma_e$ for model A and B is practically the same as the relation between the occurring stress ranges $\Delta\sigma_{max}$ due to the lorry crossing of type T3 (axle type B $\rightarrow \Delta\sigma_{A,T3,1} / \Delta\sigma_{B,T3,1} = 1.64$). As already mentioned, this higher stress level at model A is caused by the higher slenderness of the deck plate. At the stress range spectrum for model A (see Figure 88 in Section 3.4.2.1) almost every stress range is considered fully damaging with a S-N-curve's slope

of $m = 3$ ($\Delta\sigma_i > \Delta\sigma_D$). Most stress ranges in the spectrum for model B (see Figure 97) are below the fatigue limit $\Delta\sigma_D$ and are therefore considered with a S-N-curve's slope of $m = 5$. Only 5 stress ranges are above $\Delta\sigma_D$ and considered with $m = 3$.

3.4.3.2. Detail D1b

The analysed detail point D1b for lane 1 loading is located at longitudinal rib LR-2, at the left through web. Notch detail D1b is in a longitudinal distance of $e_{LR} = 300\text{mm}$ away from the mid cross girder. Figure 98 illustrates the calculated influence line in longitudinal bridge direction due to axle/wheel type B and C with an increased wheel contact patch and an axle load of $F_A = 100\text{kN}$. The occurring stresses in the analysed detail D1b are plotted due to axle type B at lane 1 (LR-2) depending on the position of the axle in longitudinal bridge direction.

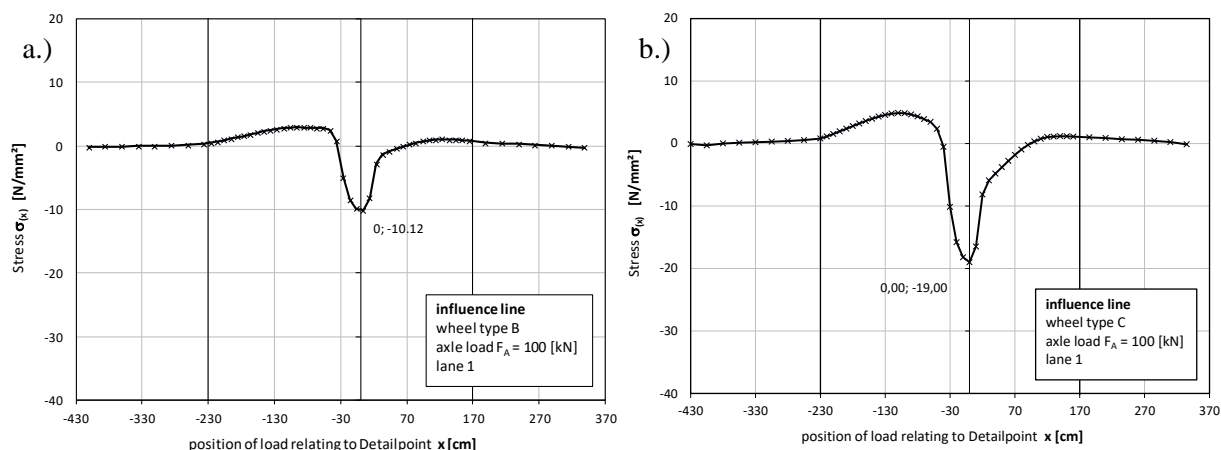


Figure 98: Model B – Detail D1b – influence lines in longitudinal bridge direction due an axle load of $F_A = 100\text{kN}$ and: a.) axle type B; b.) axle type C;

As it can be observed in Figure 98, the occurring stresses in the troughs' web (D1b) are very small compared to the stresses in the deck plate (D1a, see Figure 95). Figure 98.a shows the stresses due to axle type B and a maximum value of $\sigma_{D1b,B} = -10.12\text{ N/mm}^2$ can be seen, whereas the maximum stress of $\sigma_{D1a,B} = -55.61\text{ N/mm}^2$ in D1a occurs (see Figure 95.a). In relation of $\sigma_{D1a,B} / \sigma_{D1b,B}$, the stresses due to axle type B are in D1a 5.5 times higher than in D1b. The same observation can be done for axle type C. Figure 98.b shows a maximum stress of $\sigma_{D1b,C} = -19.0\text{ N/mm}^2$ for D1b and Figure 95.b shows a value of $\sigma_{D1a,C} = -71.21\text{ N/mm}^2$ for D1a due to axle type C. In relation to each other ($\sigma_{D1a,C} / \sigma_{D1b,C}$), the stresses due to axle type C, are in D1a 3.7 times higher than in D1b.

Figure 99 illustrates the stress history for detail D1b due to a crossing of lorry type T3 according to fatigue load model FLM 4 (see Section 2.5.2) at lane 1 (see Figure 94). The occurring stress ranges $\Delta\sigma_i$

have been counted with Rain flow-method and are also shown in the visualisation. Every axle from the vehicle produces a separate stress range and the stress level is small.

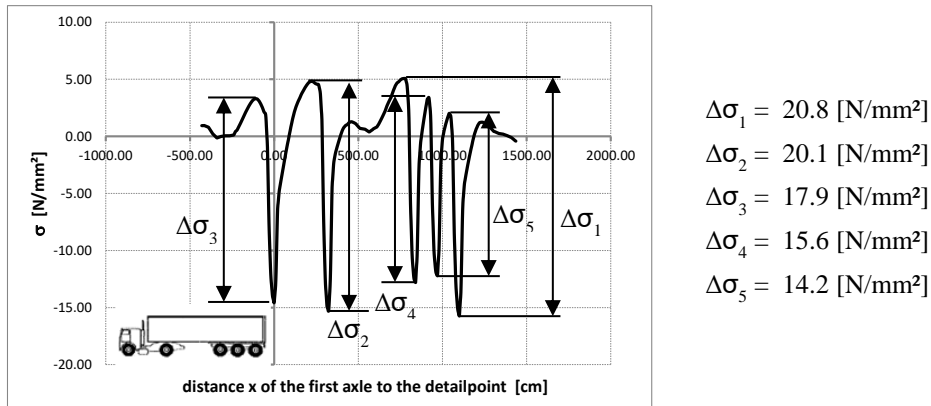


Figure 99: Model B – Detail D1b – stress history curve relating to a crossing of lorry type T3 according to FLM 4 at lane 1

– Stress range spectra due to FLM 4 referring to lane 1

Figure 100 shows the resulting stress range spectrum for detail D1b due to fatigue load model FLM 4 at lane 1 relating to in summary 100 lorries.

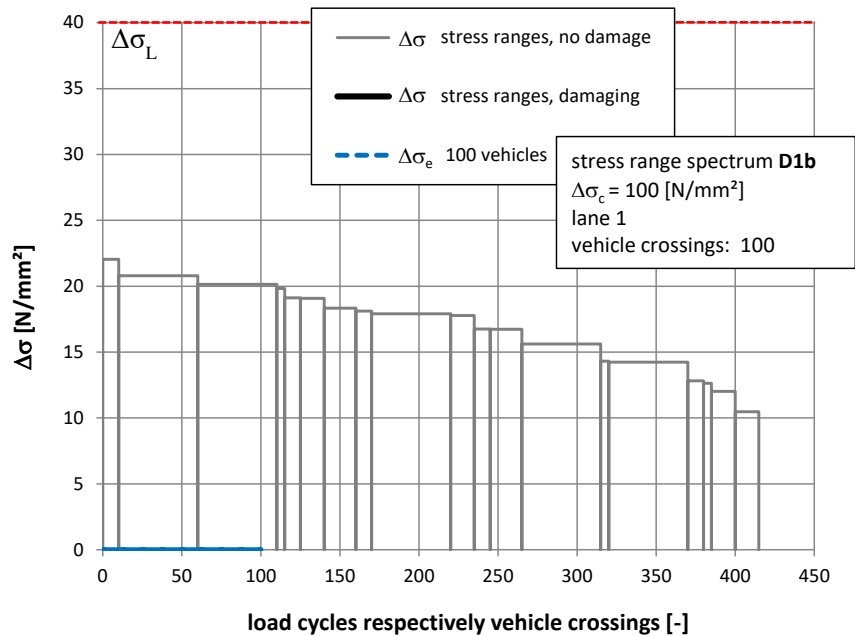


Figure 100: Model B – Detail D1b – stress range spectrum relating to a crossing of in summary 100 lorries according to FLM 4 at lane 1 and centric track configuration

As illustrated in Figure 100, the occurring stresses and their resulting stress ranges are smaller than the cut off limit with $\Delta\sigma_L = 40$ N/mm² (for S-N curve with a fatigue strength of $\Delta\sigma_c = 100$ N/mm²). Hence,

no damage occurs at this detail due to all centric lorry crossings (all wheels and vehicles have a centric lateral position when crossing the bridge deck). Later analyses will show a significant higher damaging effect when considering a lateral distribution of the heavy vehicles due to heavy traffic driving characteristics. The stress ranges from the spectrum presented in Figure 100 at lane 1 are the basis for further investigations referring to detail D1b and a lateral shift of the vehicles which are presented in Section 4.

3.4.3.3. Detail D2

The analysed detail point D2 at lane 1 is located at longitudinal rib LR-2, on the bottom side of the welded connection of the longitudinal rib to the cross girder (see Section 3.3.3). Figure 101 illustrates the calculated influence line in longitudinal bridge direction due to axle/wheel type B and C with an increased wheel contact patch and an axle load of $F_A = 100\text{kN}$.

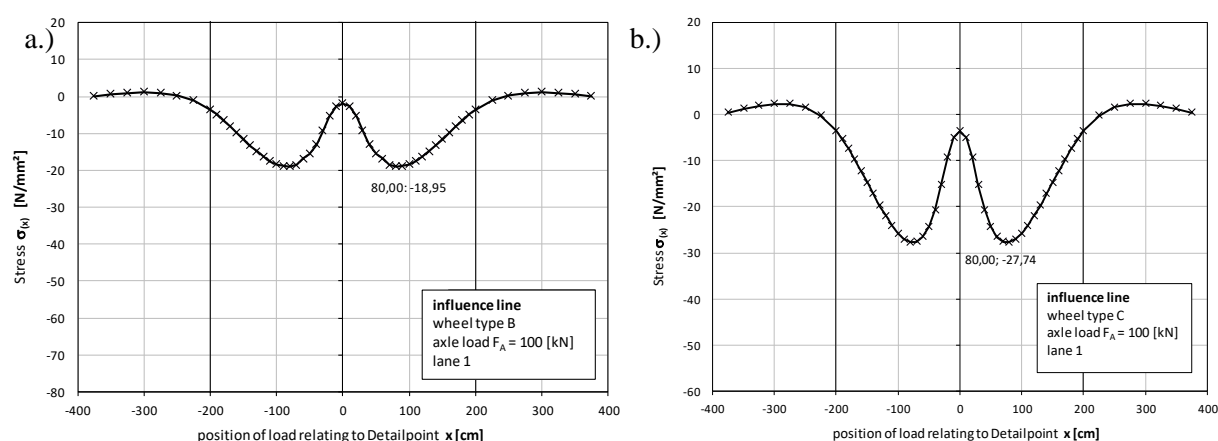


Figure 101: Model B – Detail D2 – influence line in longitudinal bridge direction due to axle/wheel type B and axle load $F_A = 100\text{kN}$ at lane 1

The occurring stresses in detail D2 are shown in Figure 101.a due to axle type B and Figure 101.b due to axle type C. In both diagrams, the stress level is lower than at model A, the deck with flat steel longitudinal ribs (see Figure 89.b and d.). The stresses in D2 due to axle type B are at model B $\sigma_{B,D2,B} = -18.95\text{ N/mm}^2$, and at LR-3 of model A $\sigma_{A,D2,B} = -25.03\text{ N/mm}^2$. In relation, the stresses in D2 due to axle type B are at model A 1.3 times higher than at model B. The detail D2's stresses due to axle type C are at model B $\sigma_{B,D2,C} = -27.74\text{ N/mm}^2$, and at LR-3 of model A $\sigma_{A,D2,C} = -33.16\text{ N/mm}^2$. The stresses at model A are in D2 due to axle type C, 1.2 times higher than at model B.

The stress history for detail D2 due to a crossing of lorry type T3 according to fatigue load model FLM 4 (see Section 2.5.2) at lane 1 (see Figure 94) is illustrated in Figure 102. The occurring stress ranges $\Delta\sigma_i$ have been counted with Rain flow-method and are also shown in the graphic. The plotted graph in

the diagram shows very good the superposing stresses of the last 3 axles from the trailer that causes the maximum stress range $\Delta\sigma_1$.

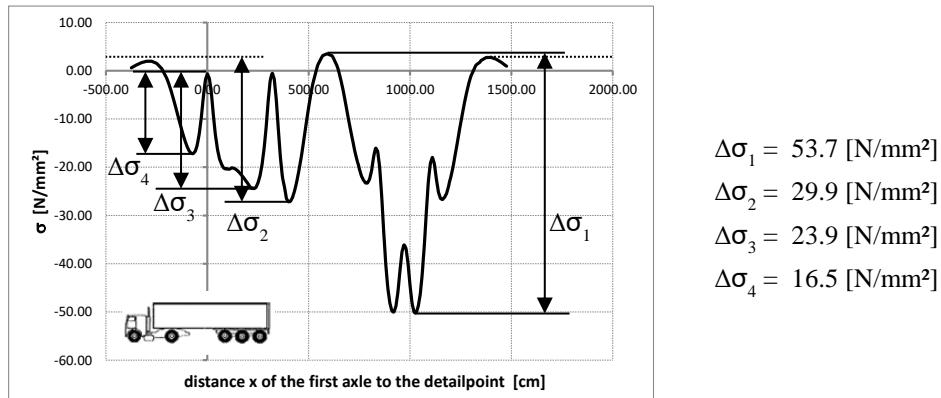


Figure 102: Model B – Detail D2 – stress history curve relating to a crossing of lorry type T3 according to FLM 4 at lane 1

In comparison to the stress history curve for model A, which is presented in Figure 90 (see Section 3.4.2.2), less difference can be observed except the stress level. The maximum stress range due to a crossing of lorry type T3 causes at model A a maximum stress range of $\Delta\sigma_{A,T3,max} = \Delta\sigma_{A,T3,1} = 77.4$ N/mm² and at model B a maximum stress range of $\Delta\sigma_{B,T3,max} = \Delta\sigma_{B,T3,1} = 53.7$ N/mm². Both stress ranges are caused by axle type C and in relation, the max. stress range is at model A 1.44 times higher than at model B.

– Stress range spectra due to FLM 4 referring to lane 1

Figure 103 shows the resulting stress range spectrum for detail D2 due to fatigue load model FLM 4 at lane 1 relating to in summary 100 lorries.

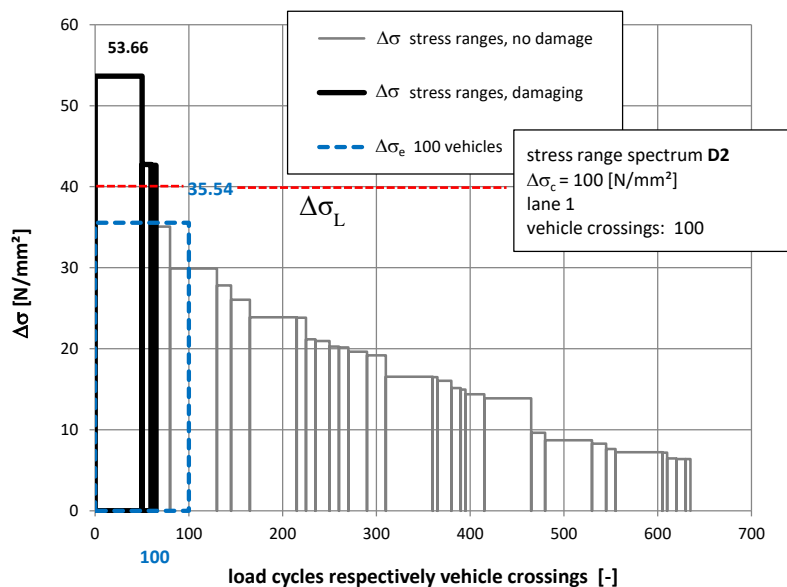


Figure 103: Model B – Detail D2 – stress range spectrum relating to a crossing of in summary 100 lorries according to FLM 4 at lane 1 and centric track configuration

Figure 103 also shows a damage equivalent constant amplitude stress range $\Delta\sigma_e$ relating to $n_e = 100$ number of load cycles. Equation 6 and Equation 7 (see Section 2.6) were used for the calculation of $\Delta\sigma_e$ where the appropriate S-N curve with a fatigue strength of $\Delta\sigma_e = 100 \text{ N/mm}^2$ was considered.

By comparing the stress range spectra referring to detail D2 for model A and B, which are illustrated in Figure 93 (model A, see Section 3.4.2.2) and Figure 103 (model B), the following observations can be done. The equivalent constant amplitude stress range at LR-3 of model A has a value of $\Delta\sigma_{e,D2,A} = 64.66 \text{ N/mm}^2$ and at model B $\Delta\sigma_{e,D2,B} = 35.54 \text{ N/mm}^2$. In relation ($\Delta\sigma_{e,D2,A} / \Delta\sigma_{e,D2,B} = 1.82$), the equivalent stress range at model A is 82% higher than the one at model B due to the same load level FLM 4.

At the stress range spectrum for model A, the highest stress range $\Delta\sigma_{\max,D2,A} = 77.37 \text{ N/mm}^2$ can be seen. For model B, a maximum stress range of $\Delta\sigma_{\max,D2,B} = 53.66 \text{ N/mm}^2$ can be recognised which is below the fatigue limit $\Delta\sigma_D$ at $N_D = 5 \cdot 10^6$. In relation ($\Delta\sigma_{\max,D2,A} / \Delta\sigma_{\max,D2,B} = 1.44$), model A's maximum stress range is 44% higher than the one for model B. In both cases this maximum stress range is caused by the last three axles of lorry type T3.

3.4.4. Model C: Orthotropic bridge deck with trough longitudinal ribs and cross girder spacing of 4m

This Section presents the results of the heavy traffic simulations under consideration of fatigue load model FLM 4 at FEM-model C. A detailed description of FEM-model C can be found in Section 3.2.3 and the applied fatigue load models are presented in Section 2.5.2. The stresses in the critical notch details D1a, D1b and D2 have been calculated and a detailed description of these points is shown in Section 2.4. In the following, the results are presented for the so called “lane 1”-position of the traffic loads, illustrated below in Figure 104.

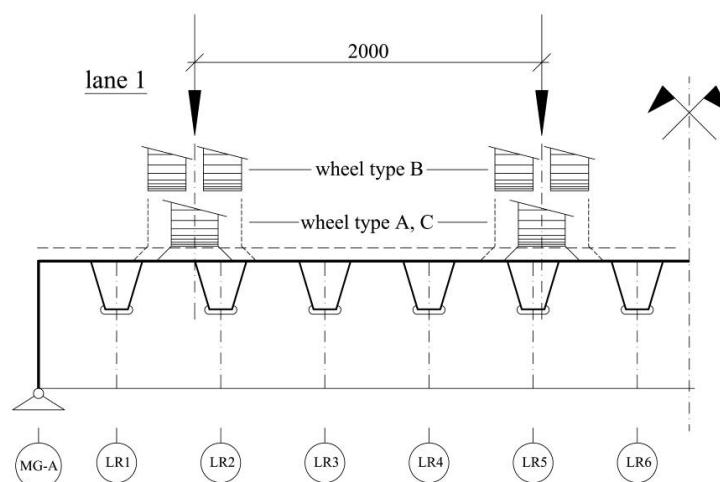


Figure 104: analysed lane position lane 1 in cross bridge direction at Model C

3.4.4.1. Detail D1a

Detail point D1a's location for lane 1 loading is situated at the left through web of longitudinal rib LR-2. This detail point is positioned in a longitudinal distance of $e_{LR} = 300\text{mm}$ away from the mid cross girder. The calculated influence lines in longitudinal bridge direction due to axle/wheel type B and C are illustrated in Figure 105. These influence lines have been calculated by considering an increased wheel contact patch and an axle load of $F_A = 100\text{kN}$.

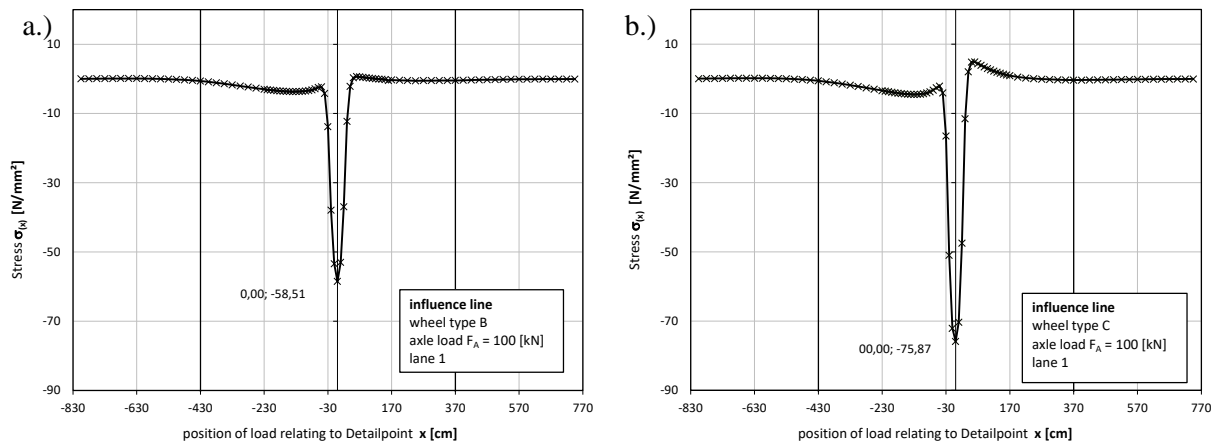


Figure 105: Model C – Detail D1a – influence lines in longitudinal bridge direction due to an axle load $F_A = 100\text{kN}$ and: a.) axle type B; b.) axle type C

When comparing the influence lines for model B (see Figure 95 in Section 3.4.3.1) and C (see Figure 105), very less difference can be observed because of the equal deck plate slenderness. Due to axle type B, the maximum stress in D1a is in model C 5% higher than in model B. Due to axle type C, the maximum stress is in model C 6% higher than in model B.

Figure 106 illustrates the stress history for detail D1a due to a crossing of lorry type T3 according to fatigue load model FLM 4 (see Section 2.5.2) at lane 1 (see Figure 104). Additionally, the graphic shows the occurring stress ranges $\Delta\sigma_i$ that have been counted with Rain flow-method.

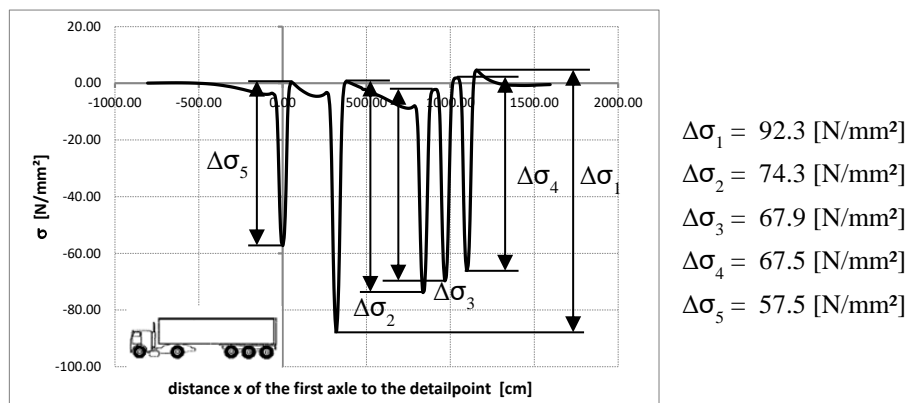


Figure 106: Model C – Detail D1a – stress to history curve relating to a crossing of lorry type T3 according to FLM 4 at lane 1

The stress history due to type T3 shows for model C in Figure 106 less difference in comparison to the one determined at model B which can be found in Figure 96 (see Section 3.4.3.1). The stress ranges differ about 1 to 3%.

- Stress range spectra due to FLM 4 referring to lane 1

Figure 107 shows the resulting stress range spectrum for detail D1a due to fatigue load model FLM 4 at lane 1 relating to in summary 100 lorries.

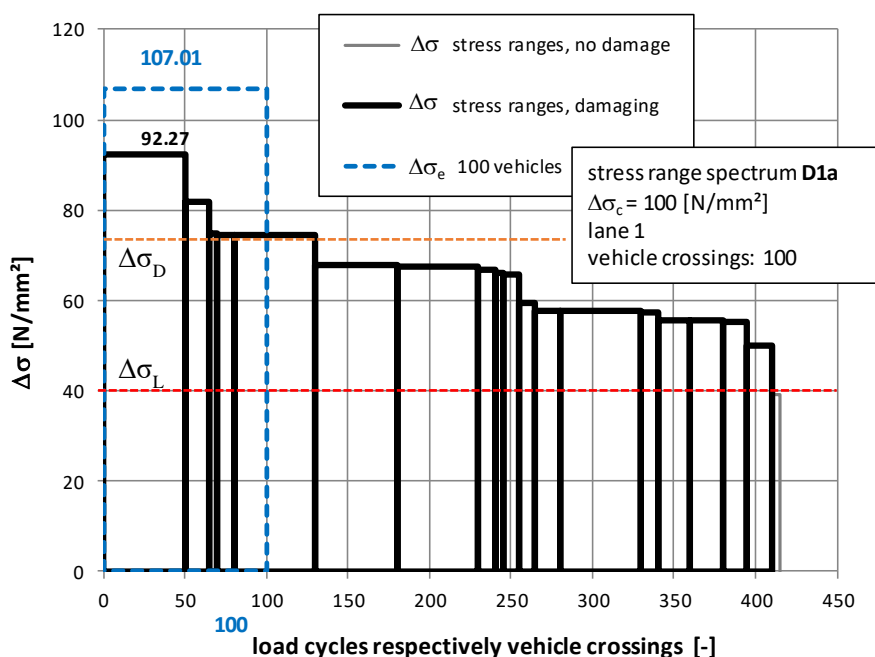


Figure 107: Model C – Detail D1a – stress range spectrum relating to a crossing of in summary 100 lorries according to FLM 4 at lane 1 and centric track configuration

Figure 107 also shows a damage equivalent constant amplitude stress range $\Delta\sigma_e$ relating to $n_e = 100$ number of load cycles. $\Delta\sigma_e$ was determined with Equation 6 and Equation 7 (see Section 2.6). Therefore, the appropriate S-N curve with a fatigue strength of $\Delta\sigma_c = 100 \text{ N/mm}^2$ was considered. With regards to further further investigations referring to a lateral shift of the vehicles due to driving characteristics (see Section 4) at detail D1a, this stress range spectrum at lane 1 is the basis.

The stress range spectrum in Figure 107 for model C is practically identical to the one for model B, which is presented in Figure 97 in Section 3.4.3.1. The equivalent constant amplitude stress range for model C is $\Delta\sigma_{e,D1a,C} = 107.01 \text{ N/mm}^2$ and the one for model B is $\Delta\sigma_{e,D1a,B} = 107.52 \text{ N/mm}^2$. Model B and C both have a deck plate slenderness of $e_{LR} / t_{DP} = 25$. The equivalent constant amplitude stress range for model A is $\Delta\sigma_{e,D1a,A} = 174.04 \text{ N/mm}^2$ (see Figure 88 in Section 3.4.2.1), where a deck plate slenderness of $e_{LR} / t_{DP} = 36$ can be recognised. Hence, due to the increase of the deck plate slenderness

of model A, the equivalent stress range is 62% higher than for model B and C. The calculated damage relating to $\Delta\sigma_{e,B} \approx \Delta\sigma_{e,C} = 107.5 \text{ N/mm}^2$ ($n_e = 100$) for model B and C is $D_{D1a,B} = D_{D1a,C} = 6.2115 \cdot 10^{-5}$ and the damage for model A is $D_{D1a,A} = 2.6358 \cdot 10^{-4}$ relating to $\Delta\sigma_{e,A} = 174.04 \text{ N/mm}^2$ ($n_e = 100$). Therefore, the damage at detail D1a is for model A 4.2x higher than for model B and C.

3.4.4.2. Detail D1b

The location of detail point D1b is for lane 1 loading at longitudinal rib LR-2's left through web. The notch detail D1b is situated in a longitudinal distance of $e_{LR} = 300\text{mm}$ away from the mid cross girder. The calculated influence line in longitudinal bridge direction due to axle/wheel type B is illustrated in Figure 108. This lines were determined with an increased wheel contact patch and an axle load of $F_A = 100\text{kN}$.

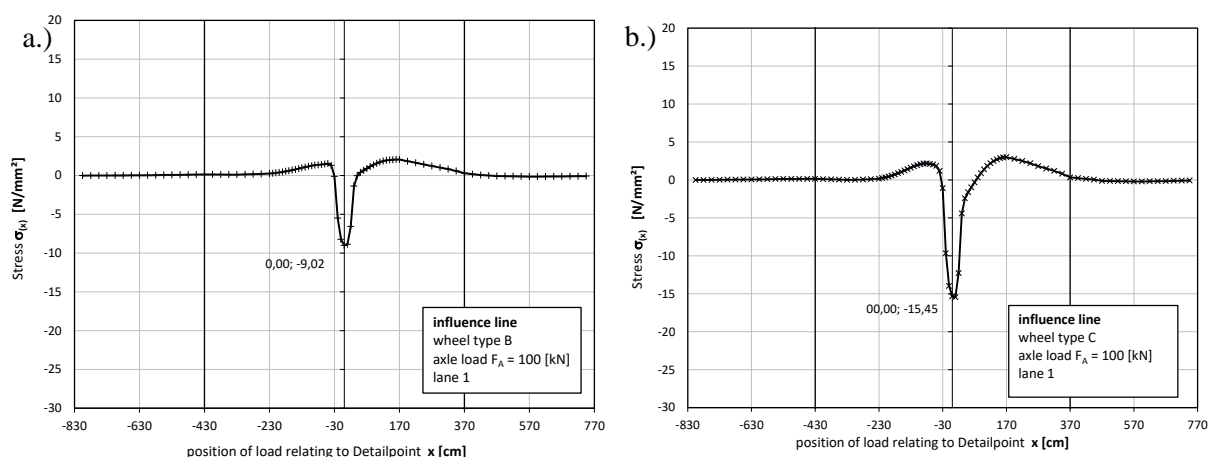


Figure 108: Model C – Detail D1b – influence lines in longitudinal bridge direction due to axle/wheel type B and axle load $F_A = 100\text{kN}$ at lane 1

Due to a uniform axle load, the determined stresses for D1b at model C in Figure 108 are similar to the stresses at model B (see Figure 98 in Section 3.4.3.2). Referring to axle type B, the maximum stress for model C is $\sigma_{\max,D1b,B,C} = -9.02 \text{ N/mm}^2$ (see Figure 108.a) and for model B, $\sigma_{\max,D1b,B,B} = -10.12 \text{ N/mm}^2$ (see Figure 98.a). Due to axle type C, maximum stress for model C is $\sigma_{\max,D1b,C,C} = -15.45 \text{ N/mm}^2$ (see Figure 108.b) and for model B, $\sigma_{\max,D1b,C,B} = -19.0 \text{ N/mm}^2$ (see Figure 98.b). Hence, due to axle type B, a difference of 12% and due to axle type C a difference of 23% can be stated.

Figure 109 illustrates the stress history for detail D1b due to a crossing of lorry type T3 according to fatigue load model FLM 4 (see Section 2.5.2) at lane 1 (see Figure 104). The occurring stress ranges $\Delta\sigma_i$ have been counted with Rain flow-method and are also shown in the graph.

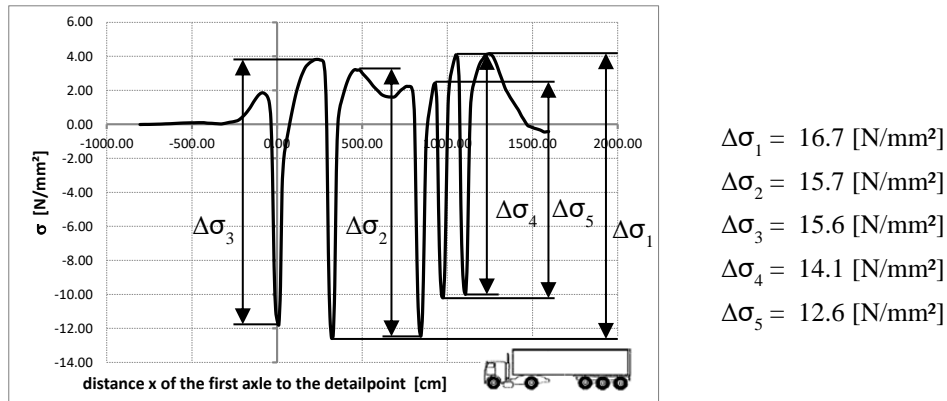


Figure 109: Model C – Detail D1b – stress history curve relating to a crossing of lorry type T3 according to FLM 4 at lane 1

Same as at model B (see Figure 99 in Section 3.4.3.2), small stress ranges also occur at model C in D1b due to a crossing of lorry type T3 which are shown in Figure 109. The maximum stress range due to lorry type T3 is $\Delta\sigma_1 = 16.7$ N/mm² which is below the cut of limit for fatigue ($\Delta\sigma_L = 40.2$ N/mm²).

– Stress range spectra due to FLM 4 referring to lane 1

Figure 110 shows the resulting stress range spectrum for detail D1b due to fatigue load model FLM 4 at lane 1 relating to in summary 100 lorries.

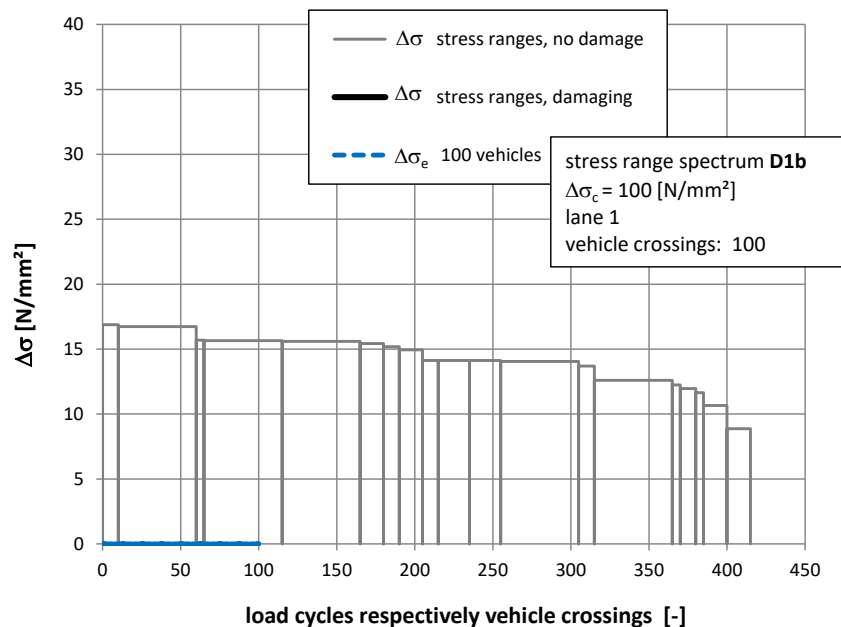


Figure 110: Model C – Detail D1b – stress range spectrum relating to a crossing of in summary 100 lorries according to FLM 4 at lane 1 and centric track configuration

In Figure 110 are the occurring stress ranges shown which are below the cut off limit $\Delta\sigma_L = 40$ N/mm² (for S-N curve with a fatigue strength of $\Delta\sigma_c = 100$ N/mm²). In this case, no fatigue damaging effect

occurs at this detail because of an all centric vehicle crossing where all wheels and vehicles have a centric lateral position. The consideration of a heavy vehicles' lateral distribution due to heavy traffic driving characteristics gives a significant damaging effect which will be shown later on. The spectrum's stress ranges in Figure 110 are the basis for further investigations referring to detail D1b and a lateral shift of the vehicles. These analyses are presented in Section 4.

3.4.4.3. Detail D2

For lane 1 loading, the analysed detail point D2 is located at the bottom side of the longitudinal rib LR-2 's welded connection to the cross girder (Section 3.3.3). Figure 111 illustrates the calculated influence line in longitudinal bridge direction due to axle/wheel type B. An increased wheel contact patch and an axle load of $F_A = 100\text{kN}$ was considered.

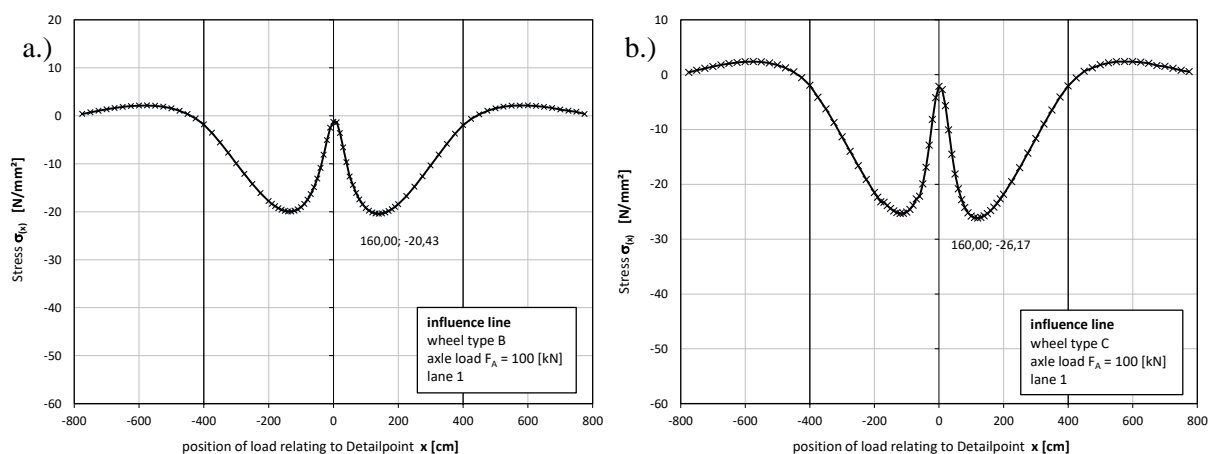


Figure 111: Model C – Detail D2 – influence line in longitudinal bridge direction due to an axle load of $F_A = 100\text{kN}$ and: a.) axle type B; b.) axle type C;

In comparison of the influence lines in Figure 111 (model C with $e_{CG} = 4\text{m}$) to the curves in Figure 101 (see Section 3.4.3.3, model B with $e_{CG} = 2\text{m}$), less difference can be observed regarding to the maximum occurring stresses due to an uniform axle load although the cross girder interval is quite different. Due to axle type B, a difference of $(20.43/18.95=1.08)$ 8% and due to axle type C a difference of $(27.74/26.17=1.06)$ 6% can be recognised.

Additionally, the maximum stresses at the welded connection of the longitudinal rib's web to the deck plate in the middle between 2 cross girders (detail D2*) have been determined due to axle type B and C. Therefore, the wheel loads were also located at midspan between the cross girders, centric above the left web of LR-2 (Figure 104). The maximum stresses σ_x in longitudinal bridge direction due to an axle load of $F_A = 100\text{kN}$ are $\sigma_{x,D2^*,B} = -9.1\text{ N/mm}^2$ for axle type B and $\sigma_{x,D2^*,C} = -12.8\text{ N/mm}^2$ for axle type

C. In comparison to the maximum occurring stresses in detail D2 (see Figure 111), it can be stated that the occurring stresses in D2* are significantly lower ($\sigma_{x,D2^*,B} / \sigma_{x,D2,B} = -9.1 / -20.43 = 0.45$; $\sigma_{x,D2^*,C} / \sigma_{x,D2,C} = -12.8 / -26.17 = 0.49$). According to the Eurocode [4], for detail D2* also a fatigue strength of $\Delta\sigma_c = 100 \text{ N/mm}^2$ (manual or automatic butt welds carried out from one side only, particularly for box girders) can be selected. Because of the significantly lower stresses for detail D2* at midspan relating to detail D2 at the cross girder connection ($\sigma_{x,D2^*,C} = 0.49 \cdot \sigma_{x,D2,C}$), much more fatigue damage occurs in detail D2. Therefore, detail D2* was not considered in this work.

Figure 112 illustrates the stress history for detail D2 due to a crossing of lorry type T3 according to fatigue load model FLM 4 (see Section 2.5.2) at lane 1 (see Figure 104). The occurring stress ranges $\Delta\sigma_i$ have been counted with Rain flow-method and are also shown in the visualisation.

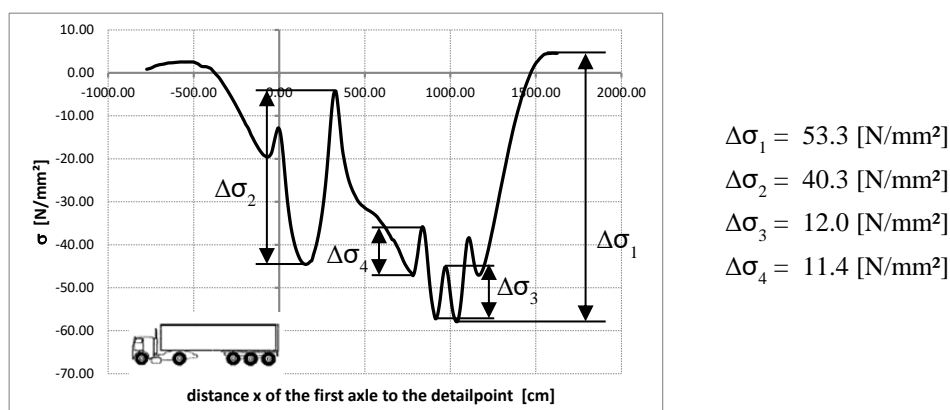


Figure 112: Model C – Detail D2 – stress history curve relating to a crossing of lorry type T3 according to FLM 4 at lane 1

- Stress range spectra due to FLM 4 referring to lane 1

Figure 113 shows the resulting stress range spectrum for detail D2 due to fatigue load model FLM 4 at lane 1 relating to in summary 100 lorries.

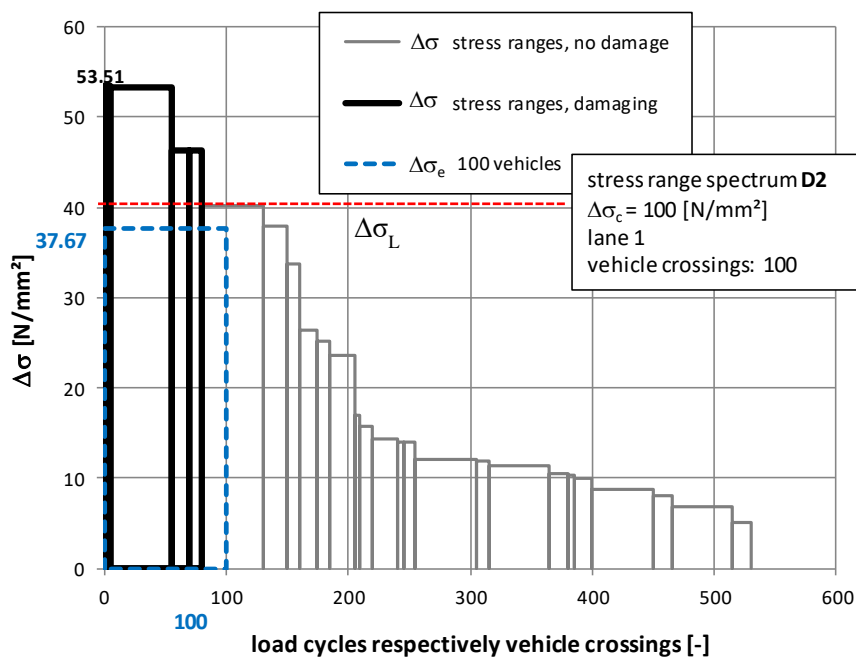


Figure 113: Model C – Detail D2 – stress range spectrum relating to a crossing of in summary 100 lorries according to FLM 4 at lane 1 and centric track configuration

Figure 113 also shows a damage equivalent constant amplitude stress range $\Delta\sigma_e$ relating to $n_e = 100$ number of load cycles. For this value $\Delta\sigma_e$ Equation 6 and Equation 7 was used (see Section 2.6). The appropriate S-N curve with a fatigue strength of $\Delta\sigma_c = 100 \text{ N/mm}^2$ have been taken into account. By comparing the detail D2's stress range spectra for model B (see Figure 103 in Section 3.4.3.3) and model C (see Figure 113), less difference be seen. The constant amplitude stress range for model B is $\Delta\sigma_{e,D2,B} = 35.54 \text{ N/mm}^2$ and for model C $\Delta\sigma_{e,D2,C} = 37.67 \text{ N/mm}^2$. In relation ($\Delta\sigma_{e,D2,C} / \Delta\sigma_{e,D2,B} = 1.06$), the equivalent stress range for model C is 6% higher than for model B. The maximum occurring stress range is practically identical for both models ($\sigma_{\max,D2,B} = 53.66 \approx \sigma_{\max,D2,C} = 53.51 \text{ N/mm}^2$). In comparison to the detail D2's stress range spectrum for model A with open longitudinal ribs (see Figure 93 in Section 3.4.2.2), a significant higher difference can be stated. The equivalent constant amplitude stress range for model A is $\Delta\sigma_{e,D2,A} = 64.66 \text{ N/mm}^2$, which is 72% higher than the one of model C. The detail D2's damage at model C relating to $\Delta\sigma_{e,D2,C}$ and $n_e = 100$ is $D_{D2,C} = 2.673 \cdot 10^{-6}$ and the damage at model A for $\Delta\sigma_{e,D2,A}$ and $n_e = 100$ is $D_{D2,A} = 13.52 \cdot 10^{-6}$. In this case a 5x higher fatigue damaging effect at detail D2 for model A can be stated relating to model C. It is additionally worth mentioning that the maximum stress range which also causes the most damaging effect in D2 is at every model caused by the last 3 axles of lorry type T3.

3.4.5. Model D: Orthotropic bridge deck with open longitudinal ribs – cross girder with field splices

In this Section the relevant results of the simulations relating to the fatigue critical stresses in the local area of the bolted field splices of the cross girder are presented. These results have been calculated under consideration of fatigue load model FLM 4* at FEM-model D. Section 3.2.4 gives a detailed description of FEM-model D and the appropriate applied fatigue critical load model is presented in Section 2.5.2. The stresses in the critical notch details D3 have been calculated and a detailed description of this point is shown in Section 2.4.5. The determination of the relevant vehicle type – type T2 – and its critical position in longitudinal direction referring to detail D3 is shown in Section 3.3.4.

Figure 114 shows an overview of the occurring stresses according to von Mises due to lorry type T2 (FLM 4*) and its critical position relating to D3 (see Figure 81 in Section 3.3.4) on lane 2 (see Figure 72 in Section 3.3.4).

The resulting stresses due to the critical load position of the relevant vehicle type T2 according to FLM 4* (see Figure 81 in Section 3.3.4) can be stated as maximum fatigue critical stresses σ_{\max} because of a heavy traffic simulation (maximum principal stresses must be used). The minimum stresses in the detail can be simplified assumed as $\sigma_{\min} = 0$ due to an unloaded condition of the bridge deck. The resulting value of the stress range $\Delta\sigma_{\max}$ has then the same value as σ_{\max} ($\Delta\sigma_{\max} = |\sigma_{\min}| + |\sigma_{\max}| = 0 + |\sigma_{\max}| = |\sigma_{\max}|$).

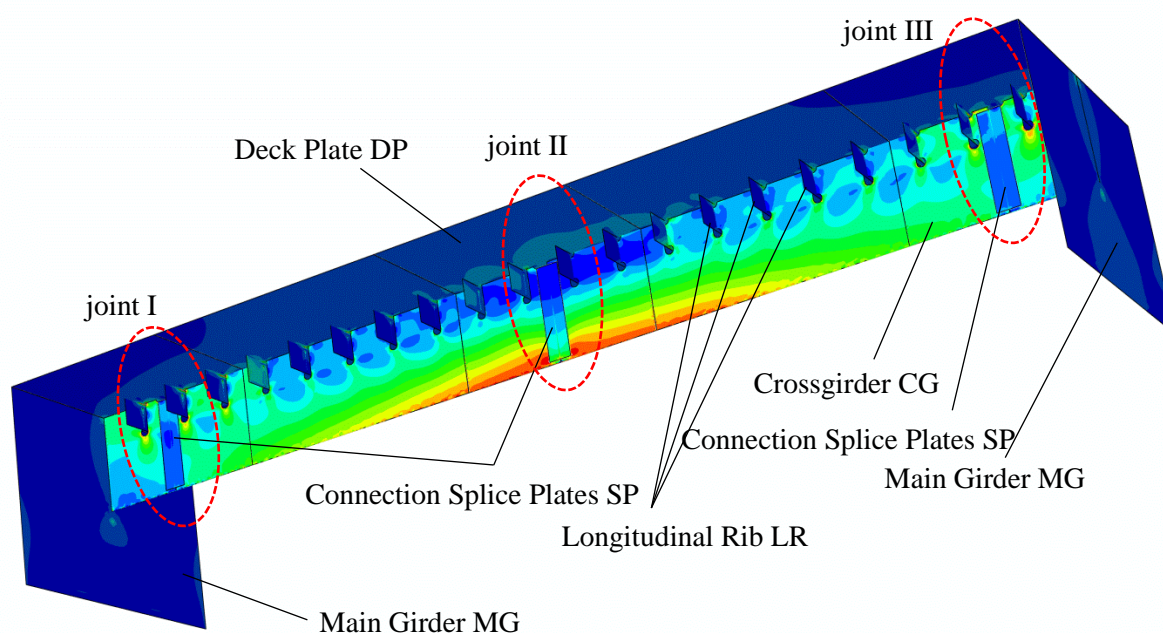


Figure 114: Model D – Detail D3 – overview of the occurring stresses according to von Mises due to lorry type T2 (FLM 4*) on lane 2 (see Figure 72)

A detailed documentation of the numerically calculated stresses in the local area of the web tooth near the bolted field splices can be found in Annex A.

The upper edge of the cross girder's web in the following graphics is corresponding to the weld toe of the welded connection between cross girder and deck plate. Hence, the determined stresses can be simplified assumed as structural stresses (hot spot stresses) and therefore, the structural stress concept has to be used. The S-N classification according to the Eurocode [4] indicates for this notch detail D3 a fatigue strength of $\Delta\sigma_c = 100 \text{ N/mm}^2$ (see Section 2.7).

Figure 115 and Figure 116 illustrate the maximum occurring principal stresses in the local areas of joint I/III and joint II (see Figure 114). The upper edge of the cross girder's web is partitioned into 4 regions (region I to region IV) and the points with the maximum principal stresses in this area are indicated (Point A to Point F).

Additionally, a relative comparison relating to point A, that has the maximum principal stresses σ_{\max} , is given in Figure 115 and Figure 116. The maximum principal stress in point A has a value of $\sigma_{\max} = 120 \text{ N/mm}^2$. These very high stresses are located along a length of about 6mm and are decreasing very rapidly.

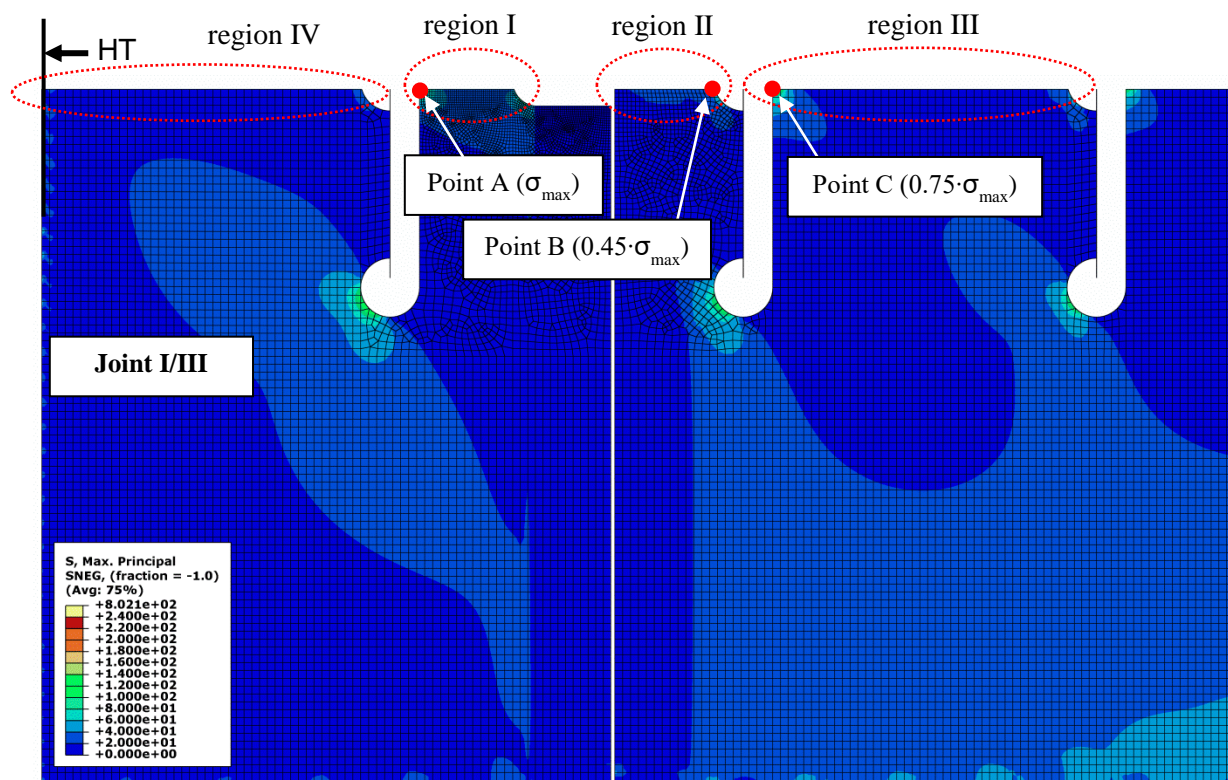


Figure 115: Model D – Detail D3 – maximal principal stresses in joint I and III due to lorry type T2 (FLM 4*) at lane 2

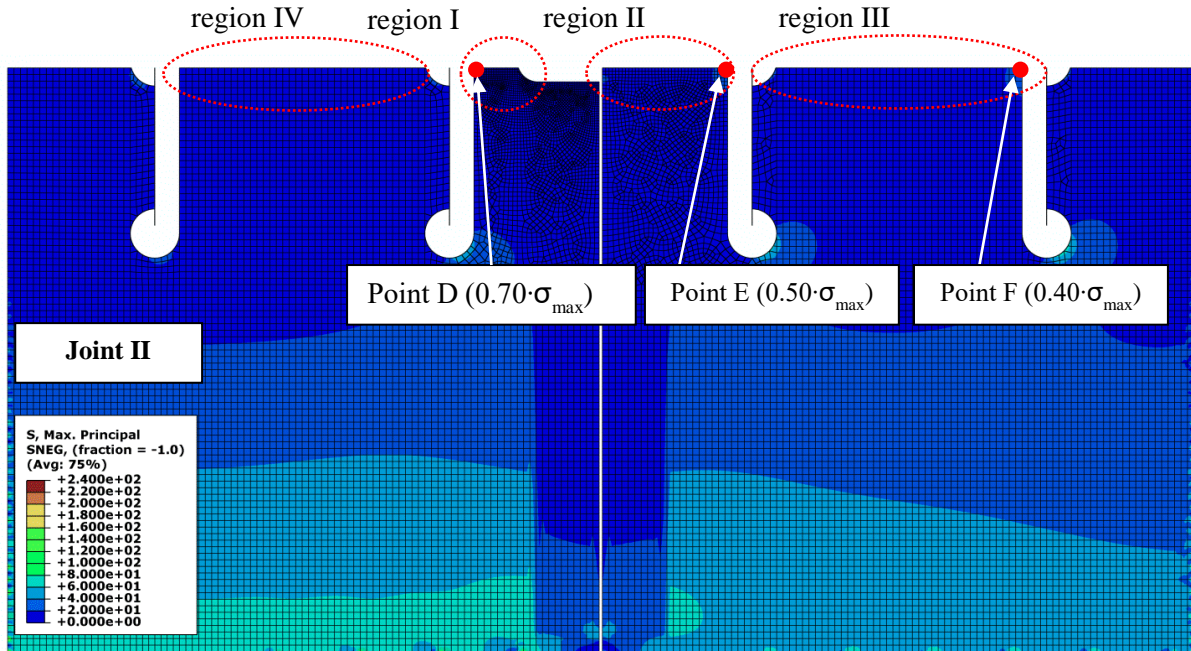


Figure 116: Model D – Detail D3 – maximal principal stresses in joint II due to lorry type T2 (FLM 4*) at lane 2

The maximum principal stresses at joint II (Figure 116) are a little bit smaller than the ones at joint I/III (Figure 115) due to the analysed loading situation. Point D in joint II has a stress value of $0.70 \cdot \sigma_{\max} = 0.70 \cdot 120 = 84 \text{ N/mm}^2$.

With regard to a verification of a life cycle time of the local detail point D3, a simplified evaluation for the applied lorry type T2 is possible based on the calculated stresses in Figure 115 and Figure 116. Therefore, the following assumptions have to be taken into account:

- Frequency of occurrence for lorry type T2 on transit routes: 5% (see Figure 24 in Section 2.5.2)
- Number of lorries per year in the main lane: $1 \cdot 10^6$ (based on measurements in [44])

Under consideration of point A at joint I/III in Figure 115, with the maximum stresses of 120 N/mm^2 , a computational life cycle time t_{lc} can be calculated based on Equation 6 (see Section 2.6):

Maximum stress range spectrum due to lorry type T2: $\Delta\sigma_{D3,T2} = |\sigma_{\max} - \sigma_{\min}| = |120 - 0| = 120 \text{ N/mm}^2$

Maximum available number of cycles for lorry type T2: $N_{\Delta\sigma T2} = (\Delta\sigma_c / \Delta\sigma_{D3,T2})^3 \cdot 2 \cdot 10^6 = (100 / 120)^3 \cdot 2 \cdot 10^6 = 1.1574 \cdot 10^6$

Number of lorry type T2 in the total life cycle time: $n_{T2,tot} = (\text{T2 lorries per year}) \cdot (\text{life cycle time}) = n_{T2,year} \cdot t_{lc} = (1 \cdot 10^6 \cdot 0.05) \cdot t_{lc}$

Maximum damage of lorry type T2 in the main lane: $D_{D3,T2} = n_{T2,tot} / N_{\Delta\sigma T2} \leq 1.0 \rightarrow (n_{T2,year} \cdot t_{lc}) / N_{\Delta\sigma T2} \leq 1.0 \rightarrow t_{lc} \leq (1.0 \cdot N_{\Delta\sigma T2}) / n_{T2,year} = (1.0 \cdot 1.1574 \cdot 10^6) / (1 \cdot 10^6 \cdot 0.05) \rightarrow t_{lc} \leq 23.1 \text{ years}$

With the mentioned assumptions above regarding to the traffic data, a consideration of only lorry type T2 leads at detail D3 to a computational life cycle time under 23 years which is far below the desired life time of 100 years for a bridge construction. A consideration of all lorry types would therefore lead to much less available life time.

Under consideration of the same assumptions, the computational life cycle time t_{lc} for point D at joint II in Figure 116 can be calculated with $0.7 \cdot \sigma_{max} = 0.7 \cdot 120 = 84 \text{ N/mm}^2$. With the same procedure as at point A, the computational life time of 67.5 years could be determined by considering only lorry type T2, which is also below the desired 100 years.

In conclusion it can be stated, that the numerically calculated stresses in detail D3 are very high and there is a high risk of crack initiation in both analysed joints (I/III and II). Further analyses relating to a lateral shift of the vehicle and its wheels haven't been done because there are also relatively high stresses in the points of the nearby regions of point A and D. For example point C in region III (see Figure 115) has an occurring stress of $0.75 \cdot \sigma_{max} = 0.75 \cdot 120 = 90 \text{ N/mm}^2$. By considering lateral shifting vehicles the damaging effect in the analysed point A would decrease but significantly increase in the nearby regions where also a very high risk of crack initiation is expected. Therefore, detail D3 is not considered in Section 4. This detail point was considered only for the evaluation of the steel deck strengthening with an UHPFRC pavement which is presented in Section 5.

3.5. Damage percentage of the individual vehicle types T1 to T5 for details D1 and D2

In this section the damage percentages of the individual lorry types T1 to T5 from fatigue load model FLM 4 and FLM 4* (see Section 2.5.2) are presented referring to the details D1a and D2 at the FEM-Models A, B and C. A detailed explanation can be found in Section 2.4.2 for detail D1a and in Section 2.4.4 for detail D2. A description and presentation of the analysed FEM-models is given in Section 3.2.

The numerical results in terms of constant amplitude stress ranges $\Delta\sigma_e$ for FLM 4 are represented in Section 3.4 due to a centric wheel and vehicle position. A description of the centric track configuration (centric wheels and vehicles) can be found in Section 3.4.

The following list gives an overview of the results according to the calculations referring to the heavy traffic simulations with centric track configuration and its damage parts for the 5 lorry types from fatigue load model FLM 4:

- Detail D1a: welded connection of the longitudinal rib to the deck plate
Damage parts for Model A in Section 3.5.1.1, for Model B in Section 3.5.1.2 and for Model C in Section 3.5.1.3
- Detail D2: welded connection of the longitudinal rib to the cross girder

Damage parts for Model A in Section 3.5.2.1, for Model B in Section 3.5.2.2 and for Model C in Section 3.5.2.3

For the following illustrations a colour assignment was chosen to clearly see the stress spectrum parts for the 5 lorry types of fatigue load model FLM 4 which is shown in Figure 117.

type	lorry type
T1	
T2	
T3	
T4	
T5	

Figure 117: FLM 4 – colour assignment for the damage of the individual lorry types (T1 to T5)

3.5.1. Detail D1a

In this section the damage percentage of the individual lorry types T1 to T5 is presented referring to detail D1a, the welded connection of the longitudinal rib to the deck plate.

3.5.1.1. Model A

The stress range spectrum referring to detail D1a due to FLM 4* at LR-1 is shown for a summary of 100 vehicles in Figure 118. The shown stress range spectrum is similar to one in Figure 86 in Section 3.4.2.1. The individual stress ranges of the different lorry types are coloured based on the colour code presented in Figure 117. Additionally, every stress range is indicated in terms of its belonging axle within the vehicle and its axle/wheel type. A definition of the notations in the picture regarding to the axle number within a vehicle and its axle/wheel type is given for every stress range.

axle number 2 (starting at the leading axle)

For example, the notation of the first, highest stress range $\Delta\sigma_1$: T2 - 2 - B — Axle/wheel type B

lorry type T2

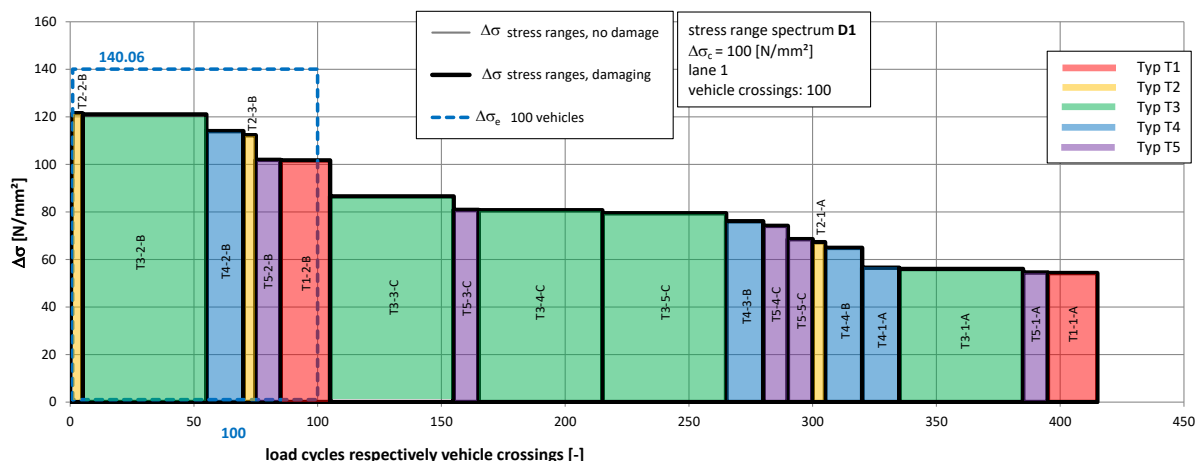
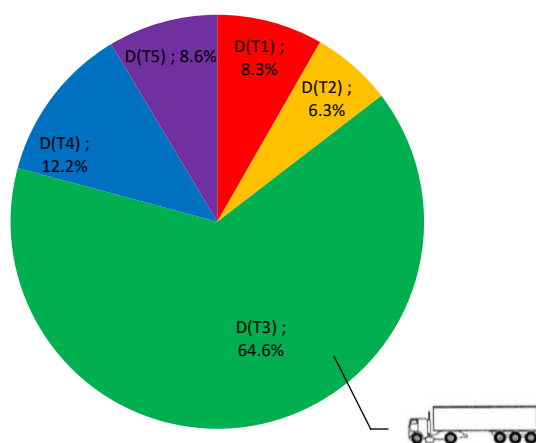


Figure 118: Model A, LR-1 – detail D1a: stress range spectrum for a centric track configuration due to FLM 4*

Figure 119 shows the individual damage parts for each lorry type according to detail D1a at Model A with open longitudinal ribs and a cross girder interval of $e_{CG} = 2.0\text{m}$.

It can be stated, that lorry type T3, the articulated lorry, causes the maximum damage at the analysed detail with 65%. A consideration of higher load levels delivers similar damages of the individual lorries. The damage percentage of detail D1a at LR-3 due to FLM 4 is shown in Figure 228 in Section 4.11.1.1, where lorry type T3 also causes 65% of the whole damage in the detail.



FLM 4*: centric wheels + centric vehicles

Figure 119: Detail D1a – Model A, percentage of damage of the individual lorry types T1 to T5 with centric wheels and vehicles according to FLM 4*

3.5.1.2. Model B

Figure 120 illustrates detail D1a's stress range spectrum due to FLM 4 at LR-1 under consideration of 100 vehicles in total. This stress range spectrum is equal to the one which is presented in Figure 97 of Section 3.4.3.1. A coloration of the individual stress ranges due to the different lorry types is shown in the picture based on the colour code presented in Figure 117. Every stress range has an additional indication relating to its belonging axle within the vehicle and its axle/wheel type.

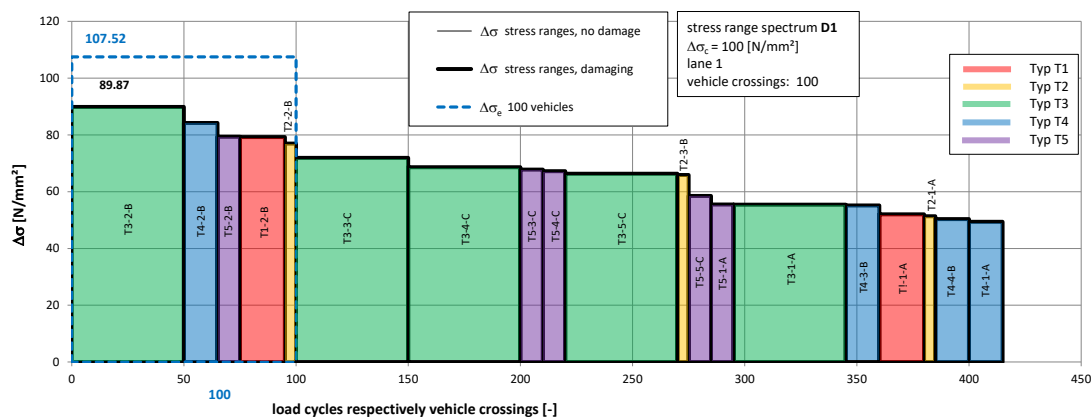
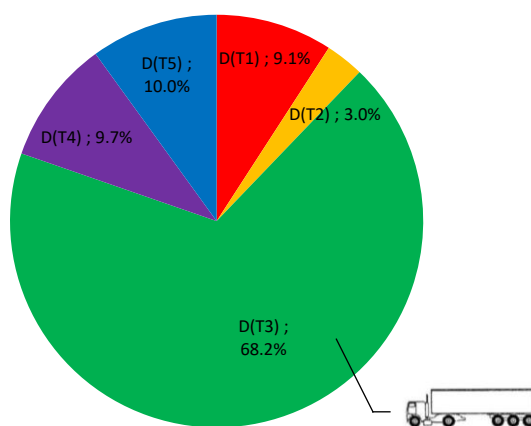


Figure 120: Model B, LR-1 – detail D1a: stress range spectrum for a centric track configuration due to FLM 4

Figure 121 shows the damage parts of each lorry type according to detail D1a at Model B with through longitudinal ribs and a cross girder interval of $e_{CG} = 2.0$ m.



FLM 4: centric wheels + centric vehicles

Figure 121: Detail D1a – Model B, percentage of damage of the individual lorry types T1 to T5 with centric wheels and vehicles according to FLM 4

Lorry type T3, the articulated lorry, causes the maximum damage at the analysed detail with 68%. Additionally, it can be noted, that there is less difference to the damage parts of the lorries determined at model A, where type T3 causes 65% (see Figure 119 and Figure 228).

3.5.1.3. Model C

Detail D1a's stress range spectrum due to FLM 4 at LR-1 is presented in Figure 122 for a summary of 100 vehicles. The shown stress range spectrum is similar to the one in Figure 107 in Section 3.4.4.1. The different lorry type's individual stress ranges are coloured based on the colour code which is shown in Figure 117. An additional indication of the stress ranges is given regarding to its belonging axle within the vehicle and its axle/wheel type.

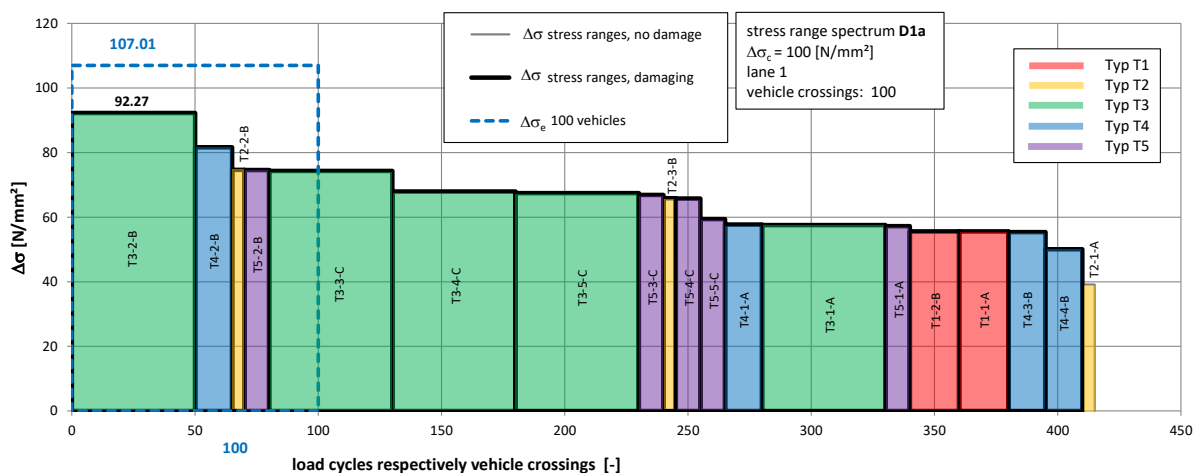
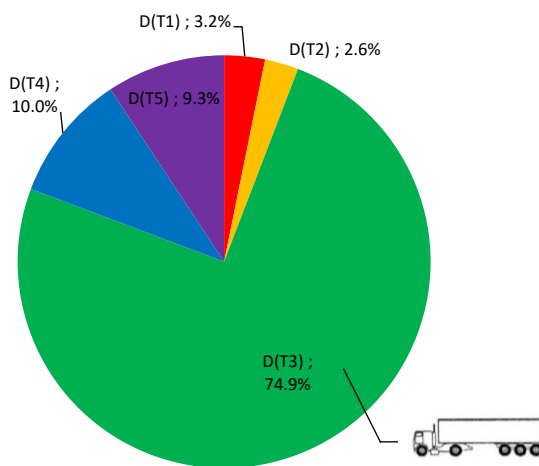


Figure 122: Model C, LR-1 – detail D1a: stress range spectrum for a centric track configuration due to FLM 4

Figure 123 shows the damage parts of each lorry type according to detail D1a at Model C with through longitudinal ribs and a cross girder interval of $e_{CG} = 4.0m$.



FLM 4: centric wheels + centric vehicles

Figure 123: Detail D1a – Model C, percentage of damage of the individual lorry types T1 to T5 with centric wheels and vehicles according to FLM 4

It can be noted, that lorry type T3, the articulated lorry, causes with 75% the maximum damage part at the analysed detail. At model A lorry type T3's damage part is 65% and at model B, T3's damage part is 68%. In every analysed model, lorry type T3 has the most dominating damage at detail D1a from 65 to 75%.

3.5.2. Detail D2

In this section the damage percentage of the individual lorry types T1 to T5 is presented referring to detail D2, the welded connection of the longitudinal rib to the cross girder.

3.5.2.1. Model A

The stress range spectrum referring to detail D2 for LR-1, due to FLM 4* is shown for a summary of 100 vehicles in Figure 124. The stress range spectrum is similar to the one in Figure 91 in Section 3.4.2.2. The colours in the figure show the individual stress ranges whereby the colour code can be found in Figure 117. In addition, there is an indication of every stress range of the different lorry types which belongs on the axles within the vehicle and its axle/wheel type.

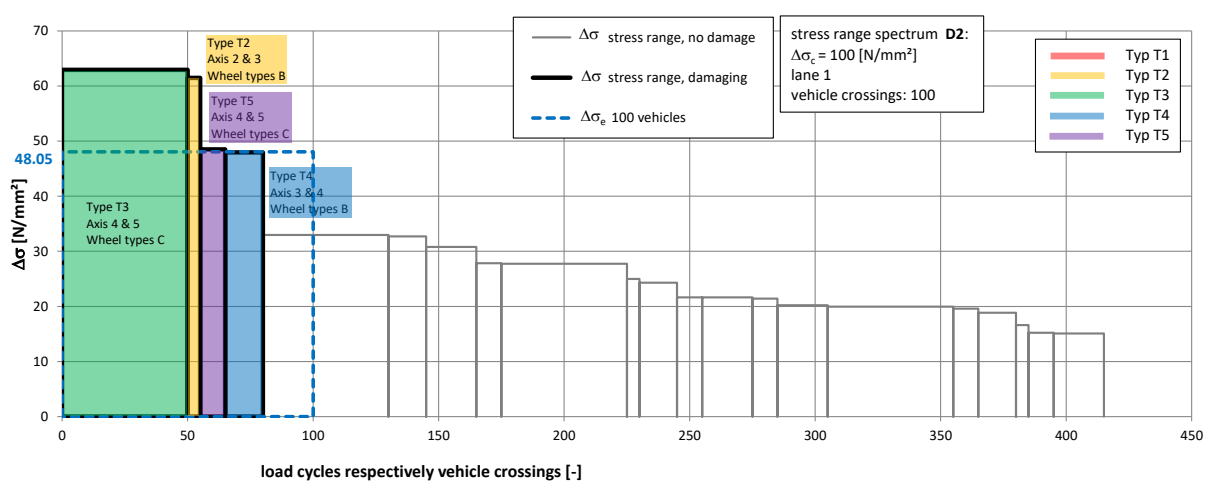
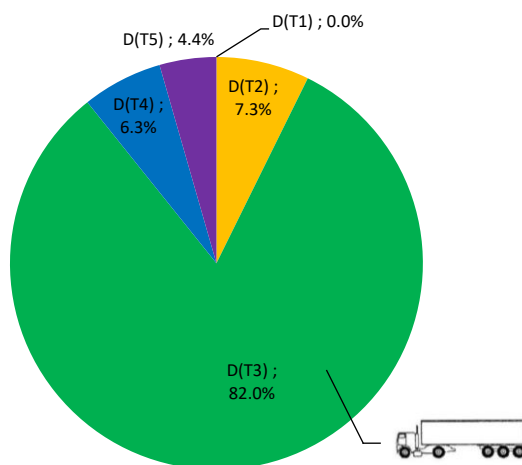


Figure 124: Model A, LR-1 – detail D2: stress range spectrum for a centric track configuration due to FLM 4*

The damage parts of each lorry type are shown in Figure 125 according to detail D2 at Model A with open longitudinal ribs and a cross girder interval of $e_{CG} = 2.0\text{m}$.



FLM 4*: centric wheels + centric vehicles

Figure 125: Detail D2 at LR-1 – Model A, percentage of damage of the individual lorry types T1 to T5 with centric wheels and vehicles according to FLM 4*

It is worth mentioning, that the maximum damage of 82% at the analysed detail D2 is caused by lorry type T3 which represents the articulated lorry. The diagram shows the damage parts of 4 different lorry types, but FLM 4* includes 5 types. Hence, lorry type T1 doesn't causes any damage at the detail because of its axle geometry which consists only of 2 axles, where no superposing effect occurs.

The graphic in Figure 231 in Section 4.11.2.1 shows a damage part of 86% of lorry type T3 due to FLM 4, but at LR-3.

3.5.2.2. Model B

The stress range spectrum referring to detail D2 due to FLM 4 at LR-2 (left web) is shown for a summary of 100 vehicles in Figure 126. The stress range spectrum is similar to the one in Figure 103 in Section 3.4.3.3. The different lorry types' individual stress ranges are coloured in the diagram based on the colour code presented in Figure 117. Every stress range is additionally indicated in terms of its belonging axle within the vehicle and its axle/wheel type.

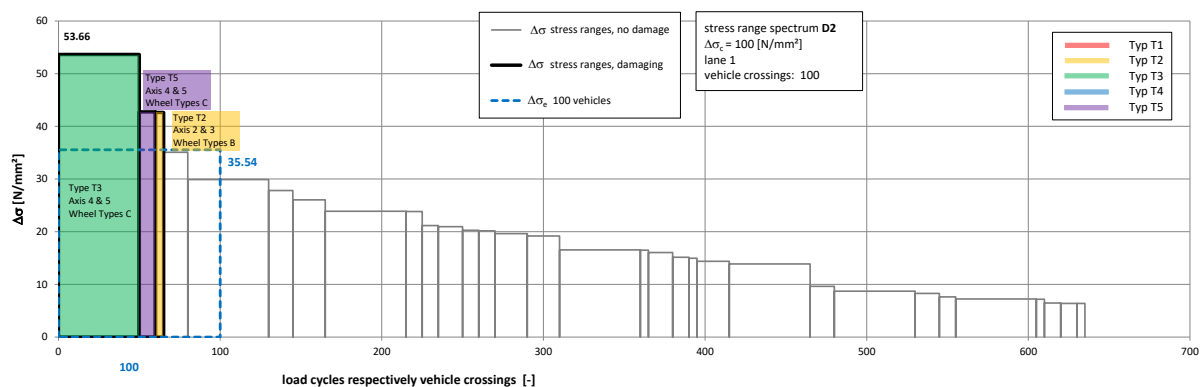
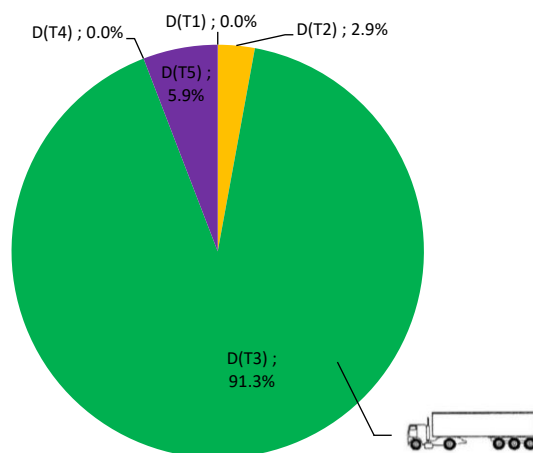


Figure 126: Model B, LR-1 – detail D2: stress range spectrum for a centric track configuration due to FLM 4

An illustration of the damage parts of each lorry type can be found in Figure 127 according to detail D2 at Model B with trough longitudinal ribs and a cross girder interval of $e_{QT} = 2.0\text{m}$.



FLM 4: centric wheels + centric vehicles

Figure 127: Detail D2 at LR-2, left web – Model B, percentage of damage of the individual lorry types T1 to T5 with centric wheels and vehicles according to FLM 4

It can be stated, that lorry type T3, the articulated lorry, causes the maximum damage at the analysed detail D2 with 91%. At model A, LR-3, also a damage part of 91% could be detected for T3 in detail D2 due to FLM 4 which is shown in Figure 231 in Section 4.11.2.1.

In addition, Figure 127 shows the damage parts of 3 different lorry types. Lorry type T1 and T4 doesn't cause any damage in detail D2 at model B.

3.5.2.3. Model C

The stress range spectrum referring to detail D2 due to FLM 4 at LR-2 (left web) is shown for a summary of 100 vehicles in Figure 128. The stress range spectrum is similar to the one in Figure 113 in Section

3.4.4.3. The individual stress ranges of the different lorry types are coloured based on the colour code presented in Figure 117. Additionally, every stress range is indicated in terms of its belonging axle within the vehicle and its axle/wheel type.

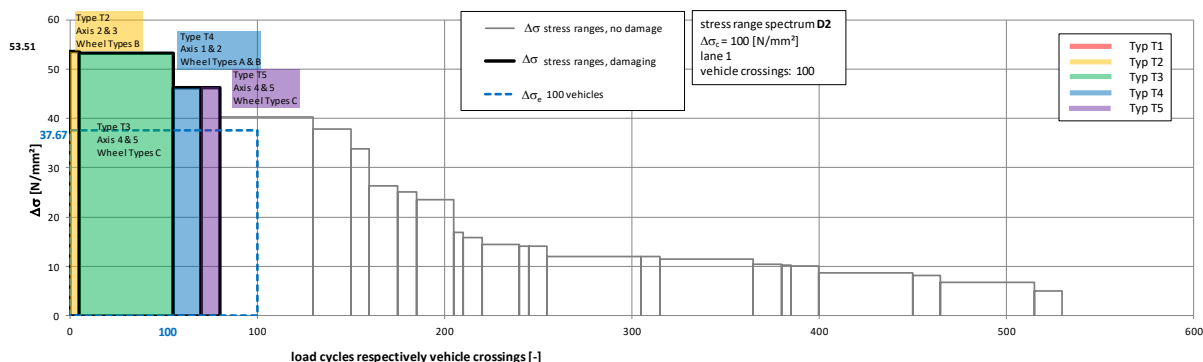
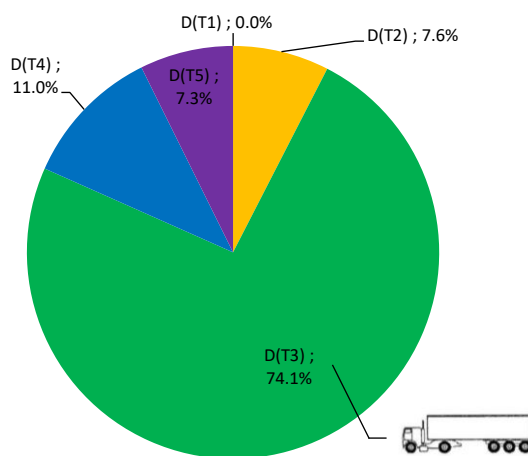


Figure 128: Model C, LR-2, left web – detail D2: stress range spectrum for a centric track configuration due to FLM 4

Figure 129 shows the damage parts of each lorry type according to detail D2 at Model C with trough longitudinal ribs and a cross girder interval of $e_{CG} = 4.0m$.



FLM 4: centric wheels + centric vehicles

Figure 129: Detail D2, LR-2, left web – Model C, percentage of damage of the individual lorry types T1 to T5 with centric wheels and vehicles according to FLM 4

The articulated lorry, lorry type T3, causes the maximum damage at the analysed detail with 74%. At model B ($e_{CG} = 2m$), T3 dominates the damage splitting with 91% (see Figure 127) due to the same load level as at model C ($e_{CG} = 4m$). Therefore, it can be observed, that the axle geometry of lorry type T3 is worse on decks with an cross girder's interval of 2m. Figure 129 additionally shows no fatigue damage due to lorry type T1.

3.5.3. Comparison of the damage percentages of the individual vehicle types

A comparison of the results regarding to the percentages of each individual lorry type from FLM 4 and FLM 4* at the analysed details D1a and D2 is presented in Table 11.

Table 11: comparison of the damage percentages of the individual lorry types

detail	Model	detail location, load level	T1 [%]	T2 [%]	T3 [%]	T4 [%]	T5 [%]
D1a	Model A	LR-1, FLM 4*	8.3	6.3	64.6	12.2	8.6
		LR-3, FLM 4	9.6	3.6	65.0	12.3	9.6
	Model B	LR-2 (left web), FLM 4	9.1	3.0	68.2	9.7	10.0
	Model C	LR-2 (left web), FLM 4	3.2	2.6	74.9	10.0	9.3
D2	Model A	LR-1, FLM 4*	0	7.3	82.0	6.3	4.4
		LR-3, FLM 4	0	3.6	85.6	5.5	5.3
	Model B	LR-2 (left web), FLM 4	0	2.9	91.3	0	5.9
	Model C	LR-2 (left web), FLM 4	0	7.6	74.1	11.0	7.3

It is worth mentioning, that in every analysed case, lorry type T3 causes the maximum damage which is because of the chosen frequency of occurrence of 50% for long distance routes. Nevertheless, very high stress ranges occur in every analysed detail due to vehicle type T3. For detail D1a, the observed damage part of T3 goes from 65 to 75%. For detail D2, the observed damage part of T3 goes from 74 to 91%. Also a very interesting observation is, that lorry type T1 never causes any damage at D2 for every analysed model. Lorry type T2 also has less damaging effect for both analysed details. The damage part of lorry type T2 for detail D1a goes from 2.6 to 6.3% and for D2 from 3.6 to 7.6%. In conclusion it can be noted, that particular attention should be given to the articulated lorry type T3.

4. Influence of realistic axles geometries and lateral distribution of heavy vehicles

4.1. Introduction

The results of the heavy traffic simulations, that are presented in Section 3.4, are based on the assumption of a centric lane position of all vehicles in transverse bridge direction as well as a centric position of every wheel directly above the web axis of the analysed longitudinal rib. These assumption lead to a conservative fatigue assessment of the steel bridge deck for nearly all details (not for D1b). When taking a closer look at the recommended fatigue load model according to the actual Eurocode, it can be noted that the geometry of the axle and wheel types does not represent the realistic dimensions of the actual heavy vehicles. The simulation of the heavy traffic crossings in Section 3.4 and the analyses according to the damage percentages of the individual vehicle types (see Section 3.5) showed that lorry type T3, the articulated lorry causes the highest amount of damage in all analysed details. Therefore, it is reasonable to make more precise investigations in realistic axle geometries of lorry type T3. A consideration of a frequency distribution in transverse bridge direction, to represent the driving characteristics of heavy traffic vehicles within a lane, can also affect the results of fatigue assessment dramatically. This consideration has been done in terms of a lateral shift of the individual wheels. The numerical calculations showed that these consideration is essential, especially for detail D1b. Without taking these effects into account, no fatigue damage occurs (see Section 3.4.3.2 and 3.4.4.2). Further investigations, which are illustrated in this chapter showed, that fatigue damage occurs by shifting the wheels in transverse bridge direction. For detail D1a and D2 always a decreasing effect could be determined by considering heavy vehicles driving characteristics (variation of lorry positions in transverse direction). In Section 4.2 the centric track configuration is again specified which is the reference and the thereby resulting stress range spectra with their damage equivalent constant amplitude stress ranges $\Delta\sigma_{e,i}$ are the basis. Measurements on the axle and wheel geometry of lorry type T3 have been carried out and are illustrated in Section 4.3, as well as a proposal for considering these realistic axle/wheel geometries within fatigue load model FLM 4. Section 4.6 and 4.7 include a detailed explanation of considering realistic axle geometries in addition to a lateral frequency distribution for the wheel positions in transverse direction referring to the analysed details D1a, D1b and D2. The determined influence lines in transverse bridge direction according to a lateral shift of the single and double wheeled axles are plotted in Section 4.5. In summary 3 different frequency distributions in transverse bridge direction, for considering heavy traffic driving characteristics, have been taken into account which are displayed in Section 4.4. In Section 4.8 the results of the numerical calculations at the FEM-Models A, B and C due to a consideration of only realistic axle geometries are illustrated. Section 4.9 shows the results of the numerical calculations at the same FEM-Models due to a consideration of realistic axle geometries and a lateral heavy traffic frequency distribution for the lane position in transverse direction. A comparison of all results within a table in terms of damage equivalent

constant amplitude stress ranges $\Delta\sigma_{e,i}$ is presented in Section 4.10. The damage percentages of the individual vehicles referring to FLM 4 are shown in Section 4.11. Section 4.12 gives a briefly conclusion of the most important results.

4.2. Centric track configuration

The position of the wheel's axles directly above the axis of the longitudinal rib is defined as centric track configuration for the open longitudinal ribs, shown again in Figure 130. At Model A longitudinal rib LR-3 was chosen for the detailed study with load position lane 2.

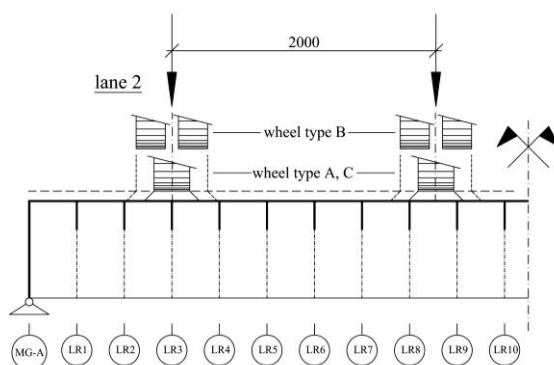


Figure 130: centric track configuration for Model A at lane 2

Figure 131 shows again the definition of the centric track configuration for the two models with trapezoidal longitudinal ribs Model B ($e_{CG} = 2$ [m]) and Model C ($e_{CG} = 4$ [m]). The axles of all wheel types are located directly above the left web of longitudinal rib LR-2.

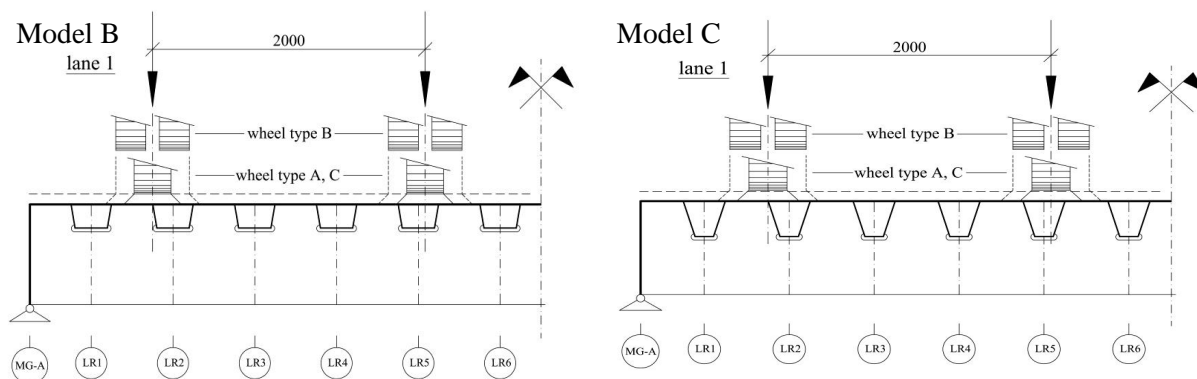


Figure 131: centric track configuration for Model B and Model C

4.3. Realistic axle- and wheel geometries for lorry type T3

For calculating the remaining service life of existing bridge decks or for fatigue assessment of future bridge projects a load model as close to reality as possible is necessary for the very local notch details of an orthotropic bridge deck. Therefore, the fatigue load model FLM 4 according to the Eurocode EN 1991-2 [1] with its 5 lorry types is a good approach but there is a lack of accuracy in the stated axle geometries for the 3 different axle types A, B and C.

Figure 132 illustrates the actually stated axle geometry from the Eurocode in comparison to the axle geometry of a common semi-trailer tractor. A significant difference can be recognized. At the axle geometries of the Eurocode all wheel contact patches from the 3 different axle types (A, B and C) have the same mid axis and the distance between all these mid axes is the same ($e_A = e_B = e_C = 2000\text{mm}$, see Figure 132.a). Figure 132.b shows the axle geometries of axle type A and B within a common semi-trailer tractor and different distances between the mid axes of the wheel contact patches can be realised ($e_A \neq e_B \neq e_C$, see Figure 132.b).

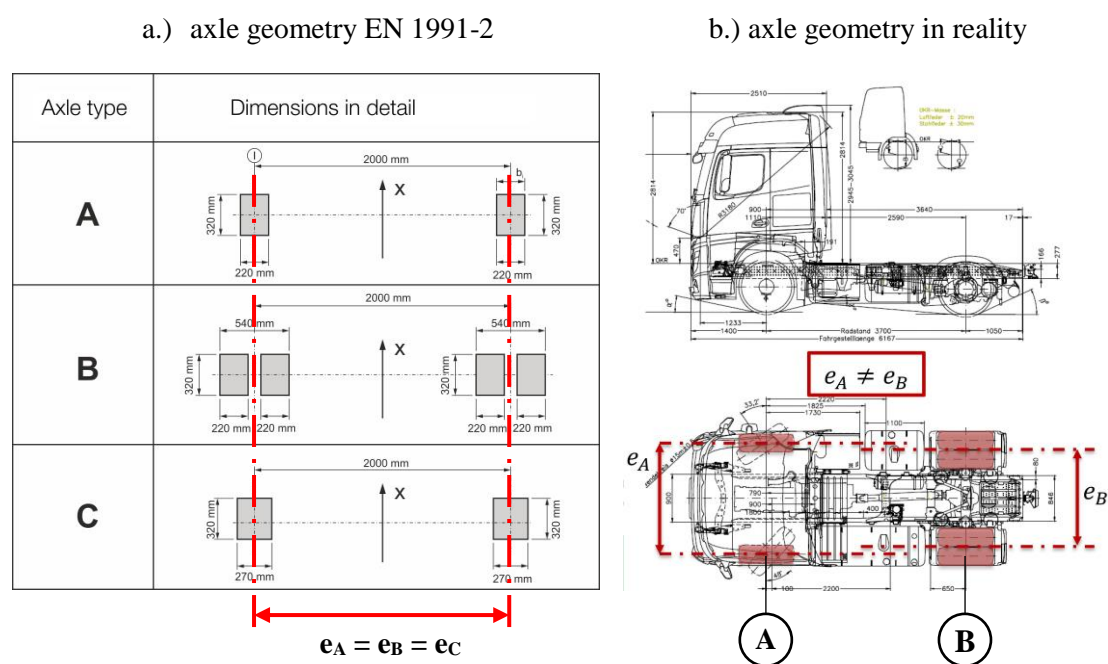


Figure 132: axle geometry according to EN 1991-2 in comparison to the axle geometry of a common semi-trailer tractor

To verify the realistic axle geometries of actual heavy vehicles measurements referring to the 3 wheel types have been carried out for lorry type T3, the articulated lorry. This lorry type needs particular attention because this vehicle causes the maximum damage (65% to 91%) at the analysed details, as the heavy traffic simulations with centric track configuration has indicated (see Section 3.5). These simulations have been done with the lorry percentage of 50% for long distance routes (e.g. highways) according to the Eurocode. Other lorry percentage distributions with $h_{T3} < 50\%$ would deliver less

damage ratio of lorry type T3, but orthotropic steel decks are frequently built at long spanned highway bridges and the maximum stress ranges are caused by lorry type T3 anyway.

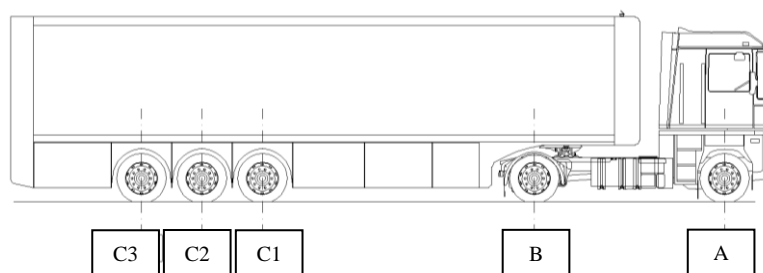
In summary measurements on 3 articulated lorries of different manufacturers have been carried out. At all vehicles the wheel contact patches have been measured with a very simple method, where just 2 sheets of paper and a measuring tape were needed. The two sheets were inserted between the wheel and the asphalt pavement as far as possible and the distance between these two sheets was taken from the measuring tape with an accuracy to 0.5 [cm]. Figure 133 demonstrates this very simple measurement procedure at a wheel.



Figure 133: simple measuring method for getting the accurate wheel contact patch geometry

The wheel dimensions at every axle of the heavy vehicle were registered and are summed up in Table 12. Vehicle 1 and 2 from the table used standard wheel dimensions which are used mostly at articulated lorries. Vehicle 3 had wide-base tyres at the axles of the semi-trailer that are more unusual.

Table 12: registered wheel dimensions of the measured articulated lorries – type T3



	wheel dimensions		
	vehicle 1	vehicle 2	vehicle 3
leading axle A	315/70 R22.5	385/65 R22.5	315/60 R22.5
driving axle B	315/70 R22.5	315/70 R22.5	295/70 R22.5
semi-trailer axle C1 to C3	385/65 R22.5	385/65 R22.5	455/40 R22.5

After consulting a few forwarding agents, it could be concluded that, there are 2 wheel dimensions that are commonly used for that lorry type (315/70 R22.5 and 385/65 R22.5). For the driving axle wheel dimension 315/70 R22.5 is commonly used. For the leading axle wheel dimensions 315/70 R22.5 and 385/65 R22.5 are used very often and for the axles of the semi-trailer wheel dimension 385/65 R22.5 is preferred. This means that the geometries of the wheel contact patches do not have a high spreading width and an adjustment of the distances e_A , e_B and e_C between these wheel contact patches from the Eurocode (see Figure 132.a) would deliver more sufficient results for analyses in relation to fatigue phenomena. In Section 4.3.1, 4.3.2 and 4.3.3 the results of the measurements referring to the axle geometries of axle/wheel type A, B and C are displayed in detail as well as additional notations and information are given about wheel dimension, axle load and tyre pressure as it was available.

4.3.1. Axle/wheel type A

The results of the measurements in relation to axle/wheel type A, the leading axle, are illustrated in Figure 134. Vehicle 3 has been measured 2 times, at first without and then with loading.

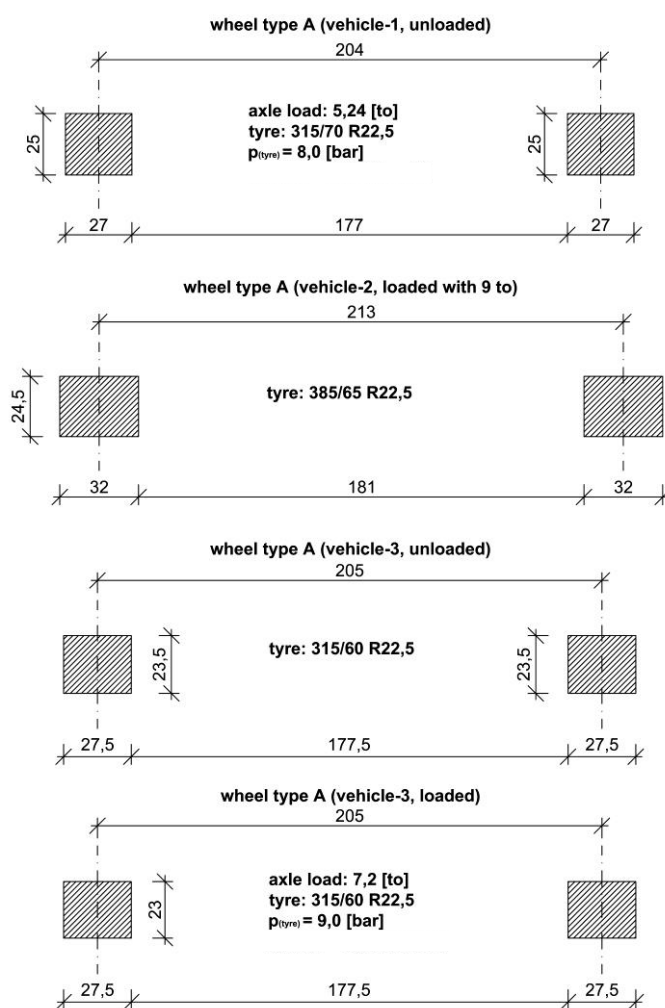


Figure 134: measured axle geometries referring to wheel type A at the leading axle (dimensions in cm)

In summary it could be summed up that the measured values in relation to the geometry of the wheel contact patches and the axles for axle type A have small deviations. Only vehicle 2 has a higher width because of the bigger wheel dimensions. The distance between the mid axes of the wheel contact patches is uniform and has a value of $e_A = 2.05$ [m].

4.3.2. Axle/wheel type B

The results of the measurements in relation to axle/wheel type B, the driving axle, are illustrated in Figure 135. Vehicle 3 has been measured 2 times, at first without and then with loading.

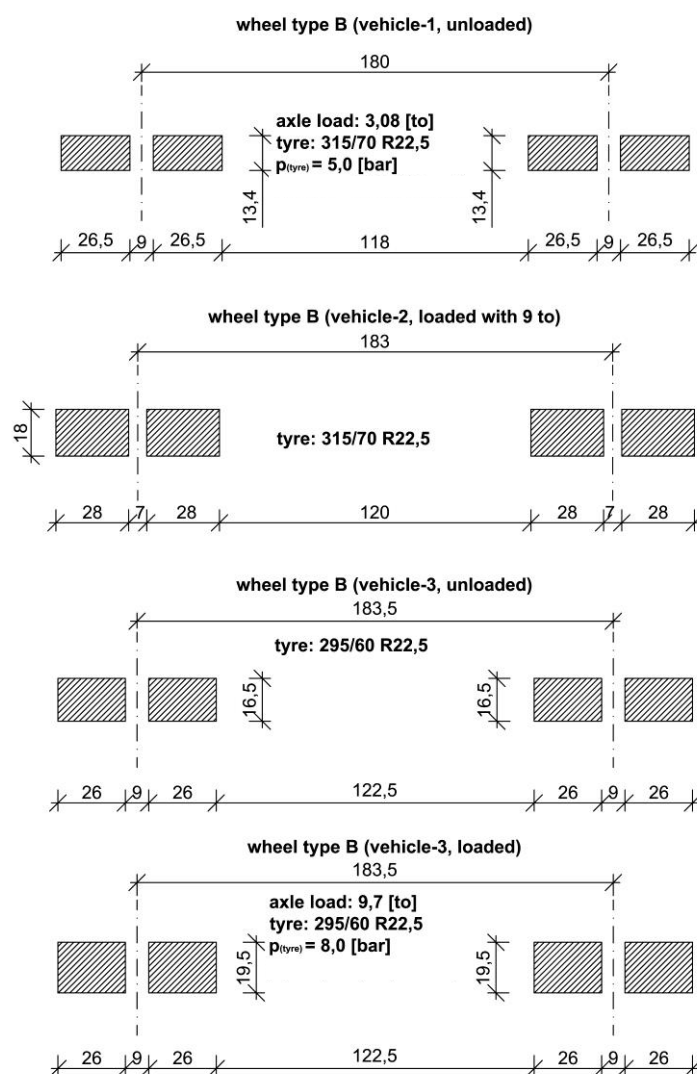


Figure 135: measured axle geometries referring to wheel type B at the driving axle (dimensions in cm)

Also for axle/wheel type B, small deviations relating to the width of the wheel contact patches could be verified. The length of the wheel contact patch varies from 13.4 to 19.5 [cm]. The distance between the mid axes of the wheel contact patches is uniform and has a value of about $e_B = 1.80$ to 1.83 [m].

4.3.3. Axle/wheel type C

The results of the measurements in relation to axle/wheel type C, the semi-trailer axle, are illustrated in Figure 136. Vehicle 3 has been measured 2 times, at first without and then with loading.

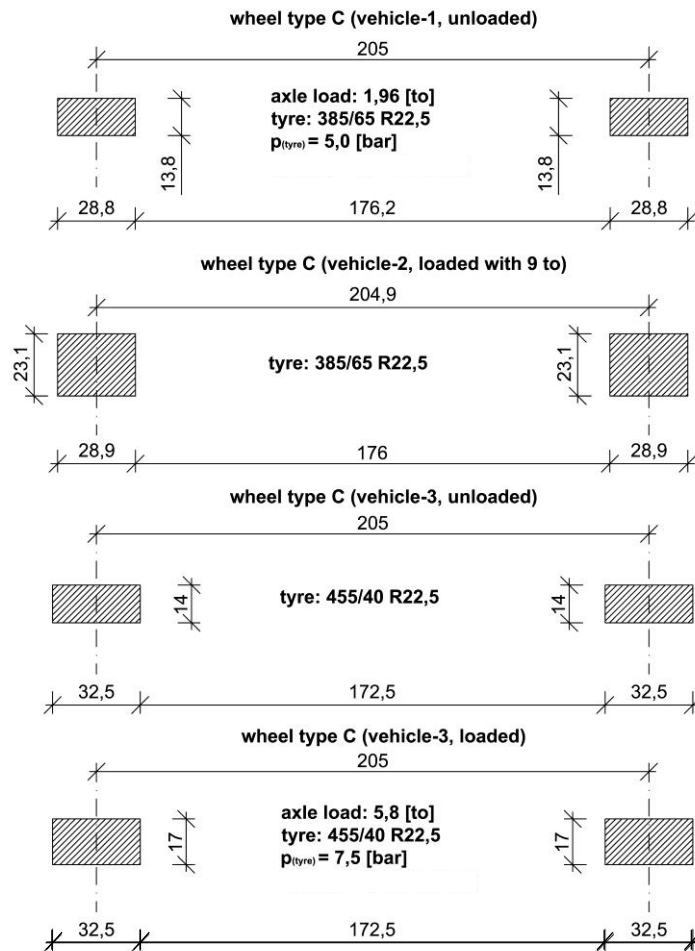


Figure 136: measured axle geometries referring to wheel type C at the semi-trailer axle

The measured values of the geometries from axle A3 to A5 (see Table 12), the semi-trailer axles, had very small deviations and based on this observation they have been averaged for every vehicle. Vehicle 1 and 2 have the same averaged widths of the wheel contact patches for axle/wheel type C ($b_{C,1} = 29$ cm). Vehicle 3 had wide-base tyres at the axles of the semi-trailer and therefore a larger width of the wheel contact patches ($b_{C,2} = 32.5$ cm) was measured. As it is shown in Figure 136, the loading has an influence at the length of the wheel contact patch, because the measured value of the loaded vehicle 2 is larger than the unloaded vehicle. The length varies from $l_C = 14.0$ to 23.0 cm. A measurement of the axle loads of vehicle 2 and the unloaded vehicle 3 was not possible and therefore no further declaration can be done. The axle loads of the semi-trailer A3 to A5 have a large variance anyway, because it strongly depends on many varying factors as the kind of the loading or the spreading of the loading within the trailer. The distance between the mid axes of the wheel contact patches is uniform and has a

value of $e_C = 2.05$ m for trailers with standard wheel dimensions and also for trailers with wide base tyres.

4.3.4. Accurate realistic axle/wheel geometries based on Eurocode

The measurements indicated that the actual geometry of the axles according to Eurocode (see Figure 132.a) is not completely conforming to the axle and wheel geometries of heavy vehicles in reality. The measurements from Section 4.3.1 to 4.3.3 were limited to vehicle type T3, the articulated lorry (see Section 2.5.2) but little adjustment of the Eurocode's axle geometry would deliver more accurate results for every vehicle type. An adjustment of the wheel contact patches seems not necessary because there are too much unknown factors that influences the load contact surface, like axle load, tyre pressure and wheel manufacturer. Furthermore, these 3 axle types with its wheel geometry should represent the wheel contact patches of all 5 lorry types in a sufficient manner for a simple load model for practical application. The common lane width of slow lanes on highways in Austria and Germany varies between 3.5m and 3.75m [50].

The measured mid axes distances of the wheel contact patches referring to the single wheeled axles (axle/wheel type A and C) fit very well to the Eurocode. The measurements at lorry type T3 showed values of $e_A = e_C = 2.05$ m, compared to 2.0m in the Eurocode. For consideration of all 5 lorry types the actual value of $e_A = e_C = 2.00$ m as stated in the Eurocode is appropriate. The measured mid axes distances of the wheel contact patches referring to the double wheeled axles (axle/wheel type B) does not fit to the Eurocode. The measurements at lorry type T3 shows a reduced value of $e_B = 1.80$ m compared to the Eurocode (see Figure 132.a, $e_B = 2.0$ m). As proposal for a simplified load model that considers all 5 lorry types from the Eurocode, the wheel contact patches of axle/wheel type B have to be shifted inwards ($\Delta e_B = 100$ mm per side). Figure 137 illustrates this proposal – used in this work – and shows the geometrical dimensions of all 3 axle/wheel types in detail.

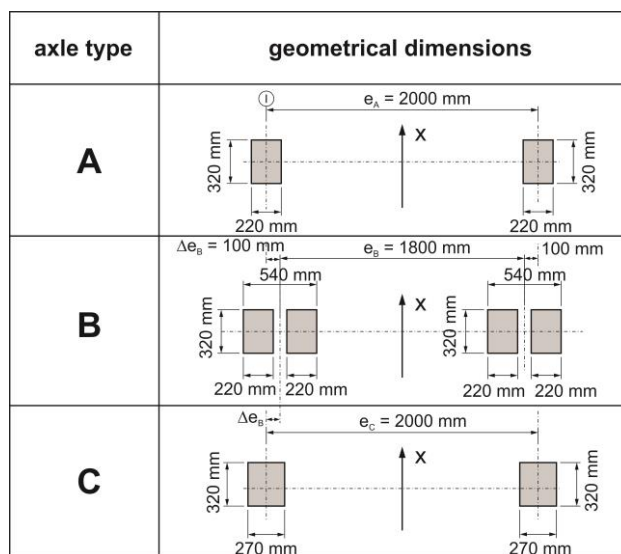


Figure 137: FLM 4-mod: proposal for considering realistic axle geometry

With this simple adjustment of shifting both wheels of axle type B inwards the mid axis distances of the wheel contact patches $e_B = 1.80$ m fits very well to the measurements at lorry type T3 and is appropriate for all 5 lorry types.

4.4. Analysed frequency distributions for transverse lane position of the lorries

In this Section the frequency distributions that have been used for considering the driving characteristics of the heavy vehicles in transverse direction within a lane are presented. In summary 3 different frequency distributions were taken into account. Frequency distribution I (LFT I) is described in Section 4.4.1 and is based on the recommendation of the actual Eurocode EN 1991-2 [1]. Frequency distribution LFT II and LFT III are based on measurements that have been carried out within the dissertation of Ronald Blab [8] on Austrian highways in 1995. Section 4.4.2 gives a detailed description of these frequency distributions. Several factors affect the frequency distribution based on [8] and for the calculations relating to a consideration of the heavy traffic driving characteristics only the lane width was varied. Frequency distribution II (LFT II) is in relation to a lane width of $b_1 = 3.50$ m and frequency distribution III (LFT III) is in relation to a lane width of $b_1 = 4.00$ m.

4.4.1. Frequency distribution LFT I - according to Eurocode

Figure 138 shows the frequency distribution according to EN 1991-2 [1]. 50 % of the heavy traffic crosses the bridge in a centric lane position $x = 0$ (± 5 cm), 18 % are driving left- or rightwards in a distance of ± 10 cm away from the center and 7 % are driving left- or rightwards in a distance of ± 20 cm away from the centre of the lane ($x = 0$).

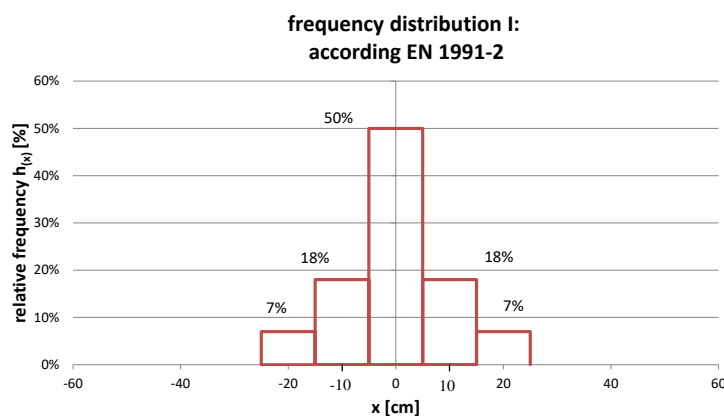


Figure 138: frequency distribution LFT I according to Eurocode [1]

4.4.2. Frequency distributions LFT II and LFT III - based on field measurements

In this Section the frequency distribution LFT II and LFT III are described in detail. These frequency distributions are based on measurements that have been carried out in [8] on the Austrian road network in 1995. Figure 139 shows a simplified illustration of the measuring method referring to the heavy traffic

driving characteristics. The heavy vehicle drove over a measuring mat that was composed of a fine matrix of pressure sensors that delivered the signal through a registration unit into a computer.

In summary 27 measuring profiles on different routes have been taken into account for the measurements that have a very high heavy traffic volume and different lane width as well as different rut depths.

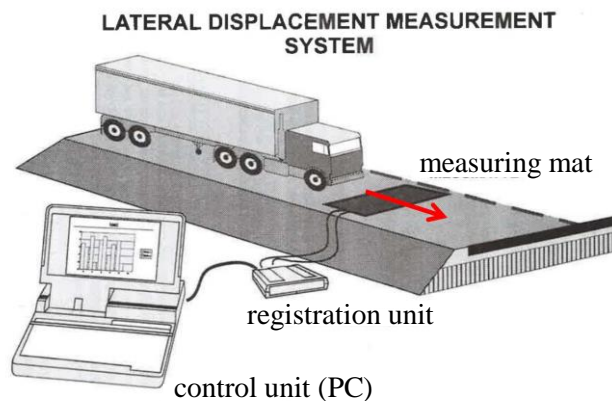


Figure 139: schematic illustration of the measuring method referring to heavy traffic driving characteristics [8]

With a programmed software a differentiation in passenger cars, lightweight and heavyweight vehicles was possible and only the results for heavy vehicles have been taken into account for frequency distribution LFT II and LFT III. Based on the measuring results a differentiation in 4 essential parameters was necessary that have a significant influence to the standard deviation of the appropriate distribution function. The following 4 parameters characterise the lateral displacement of heavy vehicles inside the lane:

- Lane width
- Vehicle width
- Rut depth
- Vehicle velocity

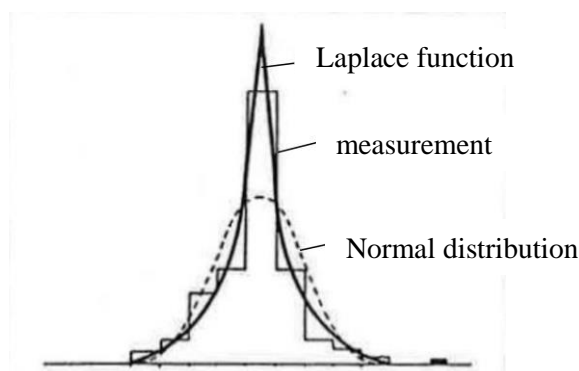


Figure 140: schematic comparison of the measurements referring to Normal and Laplace distribution function [8]

Figure 140 illustrates a comparison of the measurements to Normal and Laplace distribution function. At this picture it can be seen very well that the Laplace distribution function approximates the measured results much better than a Normal distribution function and therefore the Laplace distribution function is proposed in [8]. The general Laplace probability density function is shown in Equation 8 and Equation 9 with the parameter λ , that is affected by the standard deviation σ .

$$f(x) = \frac{1}{2 \cdot \lambda} \cdot e^{\left(\frac{-|x-\mu|}{\lambda}\right)} \tag{Equation 8}$$

$$\lambda = \sigma / \sqrt{2} \tag{Equation 9}$$

For the standard deviation σ , diagrams are plotted in [8] with a differentiation of single and double wheeled axles as well as different rut depths (note: rut depths is the same as depth of lane grooves). For the analyses referring to the influence of the heavy traffic driving characteristics on the fatigue assessment of orthotropic steel decks, only rut depths less than 10 mm have been considered. Figure 141 shows two diagrams where the standard deviation σ can be picked out as a function of the lane width and the vehicle velocity for roads with rut depths < 10 mm.

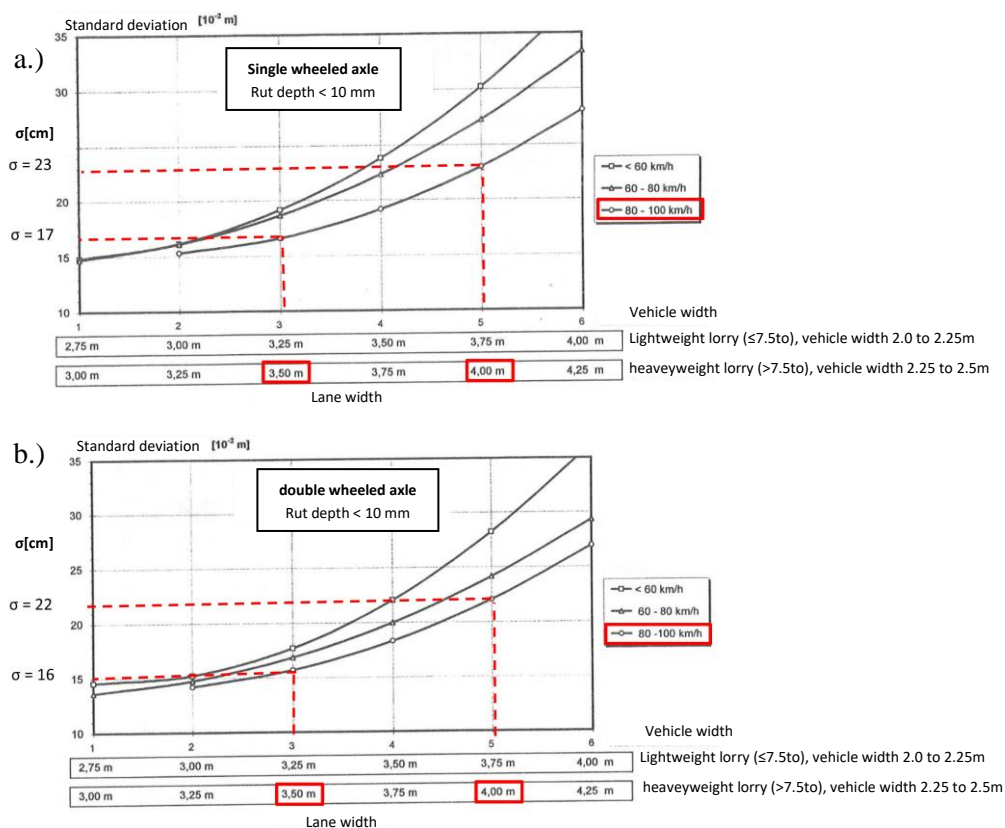


Figure 141: standard deviation σ as a function of lane width and vehicle velocity for rut depths < 10mm [8]; a.) σ due to single wheeled axles; b.) σ due to double wheeled axles

In Figure 141.a the functions for σ due to single wheeled axles and in Figure 141.b the functions for σ due to double wheeled axles are plotted. There is a separation into two vehicle classes (horizontal axis: light- and heavyweight vehicle) depending on the relation of the vehicle width to the lane width. In [8], it could be observed, that vehicles with a higher vehicle width to lane width relation are more driving in the centre of the lane. Because orthotropic steel decks are mainly built at bridges with a large span length on long distance routes, only the σ function for vehicle velocity from 80 to 100 km/h is considered (also the speed of each vehicle was measured in [8]). The standard deviations σ were taken for lane width $b_1 = 3.50$ m and $b_1 = 4.00$ m (see Figure 141). With these standard deviations and the Laplace density function (Equation 8), the relative frequencies were calculated with an increment size of $\Delta x = 10$ cm. The relative frequencies in transverse bridge direction for single and double wheeled axles and lane width of 3.50m as well as 4.00m are plotted in Figure 142:

- Figure 142.a: relative frequency distribution for single wheeled axles and lane width of 3.50m
- Figure 142.b: relative frequency distribution for double wheeled axles and lane width of 3.50m
- Figure 142.c: relative frequency distribution for single wheeled axles and lane width of 4.00m
- Figure 142.d: relative frequency distribution for double wheeled axles and lane width of 4.00m

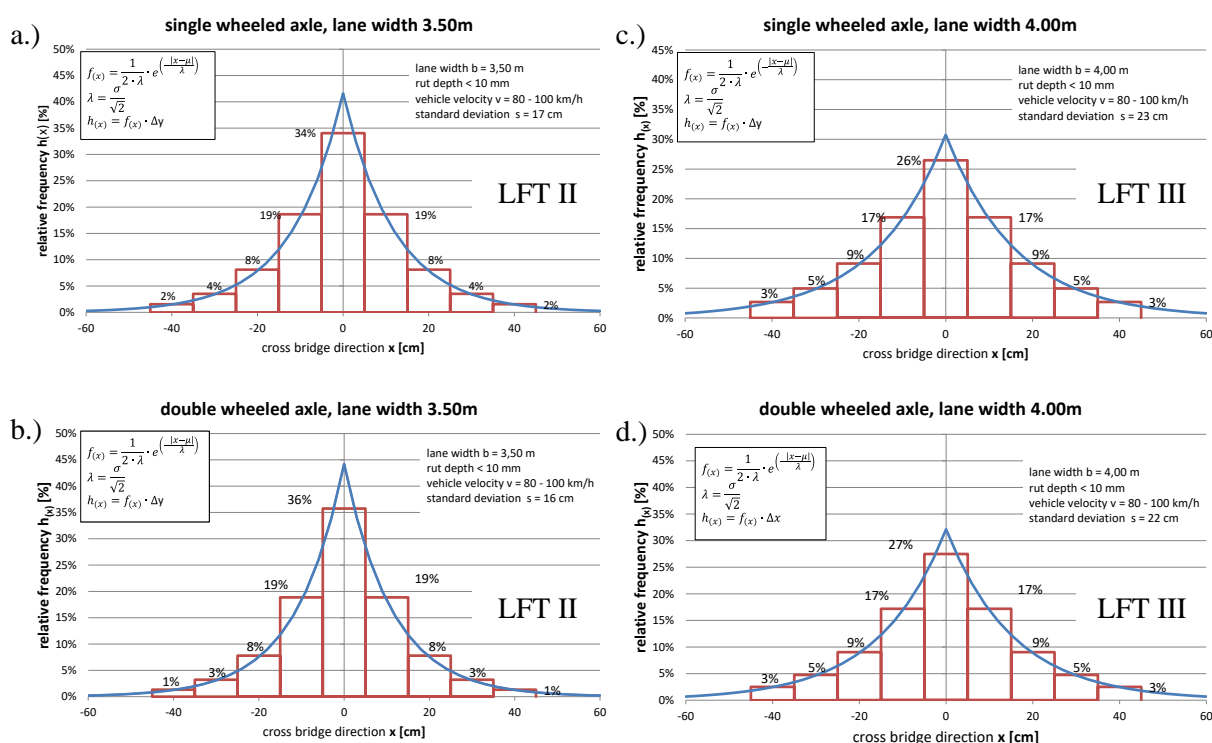


Figure 142: density functions and relative frequency: a.) single wheeled axles and lane width of 3.50m; b.) double wheeled axles and lane width of 3.50m (both LFT II); c.) single wheeled axles and lane width of 4.00m; d.) double wheeled axles and lane width of 4.00m (both LFT III)

By comparing the diagrams in Figure 142.a and Figure 142.b it can be realised that there is a negligible difference between the relative frequency distributions of single and double wheeled axles for lane width

of 3.50m. Therefore the relative frequency distribution due to double wheeled axles (Figure 142.b) was chosen for further investigations referring to a lane width of 3.50m and is declared as frequency distribution LFT II (Lane Frequency Type II) which is illustrated in Figure 143.a.

The diagram of the relative frequency distribution for single wheeled axles in Figure 142.c also has a negligible difference in comparison to the distribution in Figure 142.d for double wheeled axles where both distributions are related to a lane width of 4.00m. Therefore, the relative frequency distribution due to single wheeled axles (Figure 142.c) was chosen for continued analysis referring to a lane width of 4.00m and is appointed as frequency distribution LFT III (Lane Frequency Type II) which is presented in Figure 143.b.

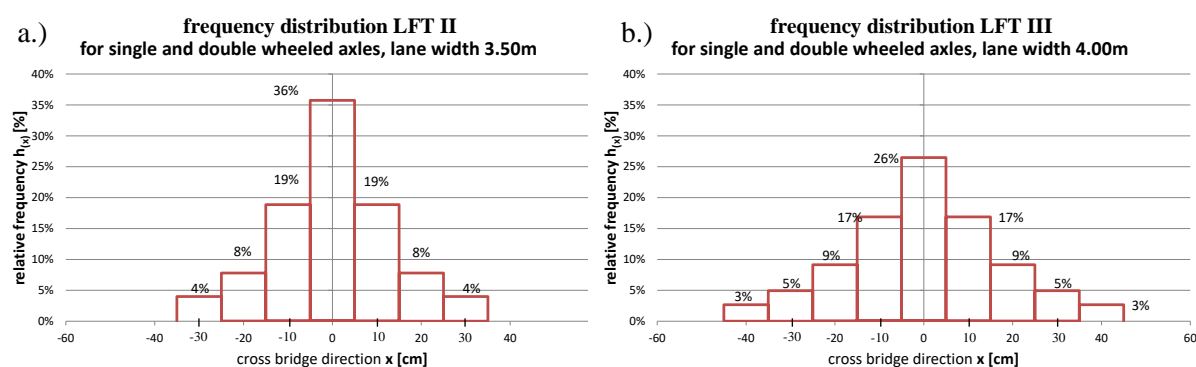


Figure 143: relative frequency distributions in transverse bridge direction for single and double wheeled axles: a.) frequency distribution LFT II for lane width of 3.50m; b.) frequency distribution LFT III for lane width of 4.00m;

According to the lateral influence lines for detail D1a and D2 (for example Figure 151 and Figure 154) the maximum stress occurs due to a centric wheel load position directly above the axis of the longitudinal rib's web. A lateral shift of the wheel load causes therefore a reduction of the fatigue damage at the detail points D1a and D2. Therefore, a concentrated frequency distribution with a small standard deviation σ is required. For the analysis of the details D1a and D2 (see Section 2.4.2 and 2.4.4) referring to the heavy vehicle's driving characteristics in transverse bridge direction the appropriate frequency distribution LFT II according to a lane width of 3.50m from Figure 143.a was chosen.

According to the lateral influence lines for detail D1b (for example Figure 152) the maximum stress is occurring due to a lateral shifted wheel load position of $\pm(20$ to $30\text{cm})$ in relation to the axis of the analysed through rib's web. A lateral shift of the wheel load causes therefore an increased fatigue damage for the detail point D1b and a spread frequency distribution with a larger standard deviation σ is required. Further calculations of detail D1b (see Section 2.4.3) referring to the heavy vehicle's driving characteristics in transverse bridge direction have been carried out by considering the appropriate frequency distribution LFT III according to a lane width of 4.00m from Figure 143.b.

4.5. Lateral influence lines

For simulations under consideration of realistic axle geometries and a lateral shift of the axles due to the driving characteristics of the heavy traffic, influence lines in transverse bridge direction were necessary for every detail (D1a, D1b and D2) at every analysed model (Model A, B and C). These lateral influence lines were determined at the appropriate positions in longitudinal bridge direction for every detail (based on the results for centric position, in lane position $x = 0$). This appropriate position is the wheel load location in longitudinal bridge direction, where the maximum stress according to amount in the analysed detail occurs.

4.5.1. Model A

In this Section the lateral influence lines for the analysed details D1a and D2 referring to Model A are illustrated. A detailed description of Modell A is located in Section 3.2.1. The influence lines were determined for single and double wheeled axles. Axle/wheel type A and C, the single wheeled axles have nearly the same geometry and therefore an influence line in transverse bridge direction for axle/wheel type A has been determined and was also used for analysis due to axle/wheel type C. All influence lines in transverse bridge direction for Model A are related to lane 2, which is shown again in Figure 144. The maximum occurring stress in the detail due to a centric wheel position (see Figure 144) indicates $\eta = (-1.0)$. The standardisation to (-1.0) was chosen to illustrate the occurring tensile and compressive stresses at the detail. Negative values for η imply compressive stresses and positive values for η imply tensile stresses.

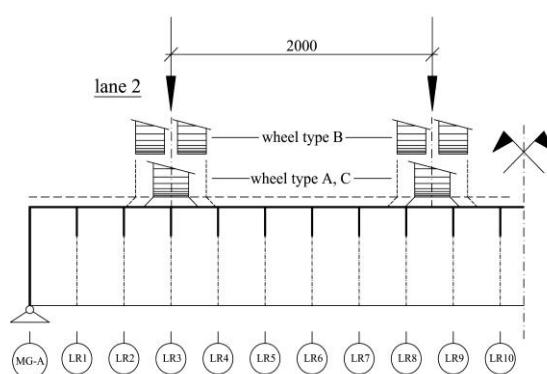


Figure 144: Model A – lane 2

As mentioned before, the analysed details D1a and D2 (see Section 2.4) restrict a very local influence area in transverse bridge direction and therefore no interaction of the wheel loads within a single axle appears. All influence lines have been calculated by just modelling one single or double wheeled contact patch load.

4.5.1.1. Detail D1a

Figure 145.a shows again the influence line in longitudinal bridge direction for Model A relating to detail D1a and a reference axle load of $F_A = 100$ kN for centric position (lane 2). The highest stress occurs when the wheel load is positioned directly above the detail D1a. As shown in the picture, primarily compressive stresses are occurring at this detail and the influence area is very small. The stresses in the detail are rapidly decaying when the wheel load is leaving the considered detail point. Figure 145.b shows the appropriate position for the determination of the influence lines in transverse bridge direction in a plan view. The wheel load was shifted in both cross directions (plus/minus according to Figure 145.b) with an interval of $\Delta x = 100$ mm. The stresses were calculated for every load position and finally the results have been summed up in diagrams.

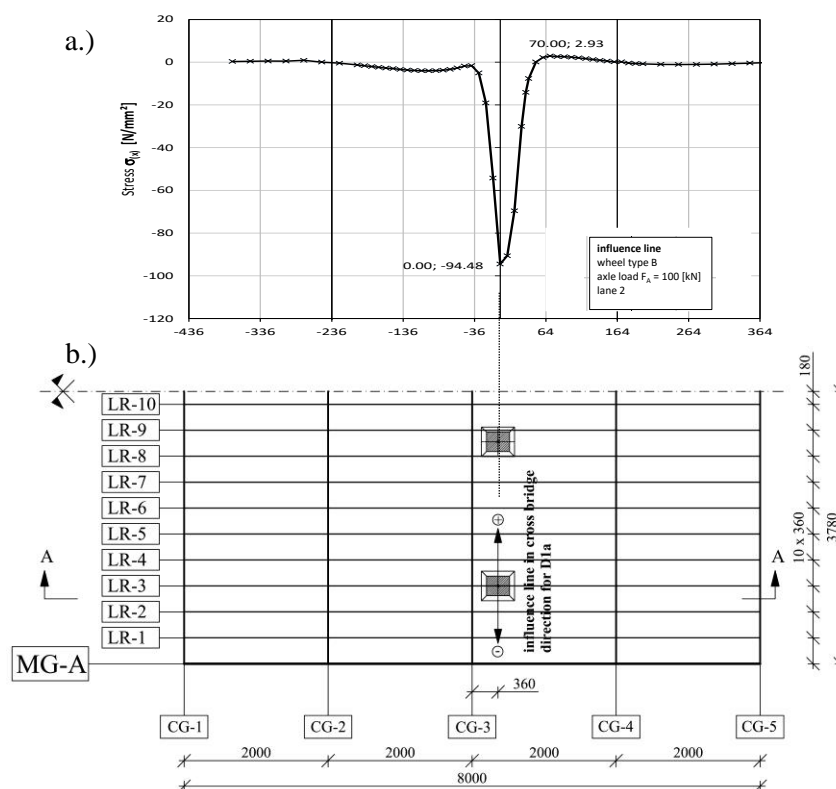


Figure 145: Model A – detail D1a: appropriate position for influence line in transverse bridge direction; a.) influence line in longitudinal bridge direction referring to detail D1a and centric position; b.) plan-view of the appropriate wheel load position

The influence lines in transverse bridge direction for detail D1a are plotted in Figure 146. Figure 146.a illustrates the transverse influence line for single wheeled axle types due to axle type A. Figure 146.b shows the transverse influence line for double wheeled axles due to axle type B. Both transverse influence lines are not completely symmetric relating to the vertical axis at $x = 0$, because of the finite element model geometry (see Figure 145, no geometrical symmetry relating to LR-3). In both diagrams of Figure 146 an additional curve is drawn, which is fully symmetric referring to the vertical axis at $x =$

0. Further numerical calculations regarding consideration of realistic axle geometry and driving characteristics have been done by using the conservatively simplified, symmetric influence line in transverse bridge direction.

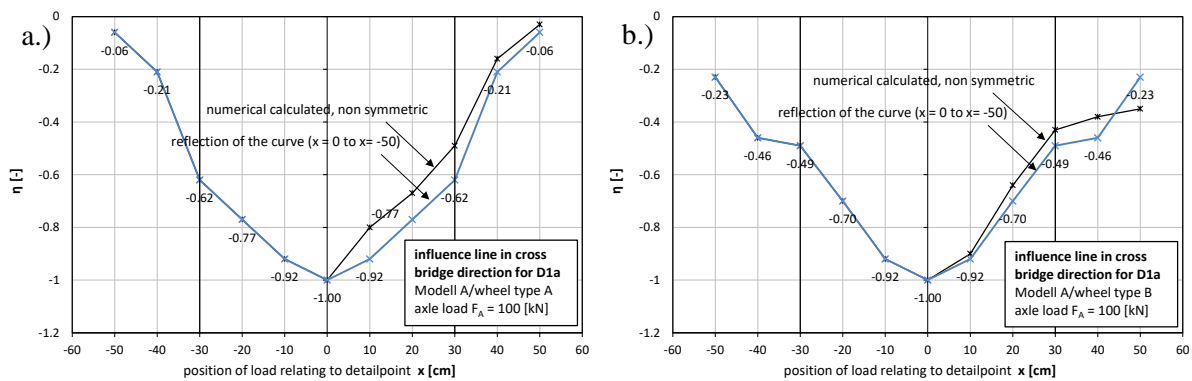


Figure 146: Model A – detail D1a influence lines in transverse bridge direction; a.) for single wheeled axles (axle type A and C); b.) for double wheeled axles (axle type B)

4.5.1.2. Detail D2

Figure 147.a shows again the influence line in longitudinal bridge direction for Model A relating to detail D2 and a reference axle load of $F_A = 100$ kN for centric position (lane 2). The highest stress is occurring when the wheel load is positioned in a distance of $e = 800$ mm apart from detail D2 the mid cross girder CG-3. As shown in the picture, primarily compressive stresses are occurring at this detail and symmetry of the curve relating to the vertical axis at $x = 0$ can be detected. Figure 147.b shows a plan view with the appropriate position for the influence line determination in transverse bridge direction. The wheel load was shifted in both transverse directions (plus/minus according to Figure 20.b) with an interval of $\Delta x = 100$ mm. The stress calculation was performed for every load position and finally the results have been summed up in diagrams.

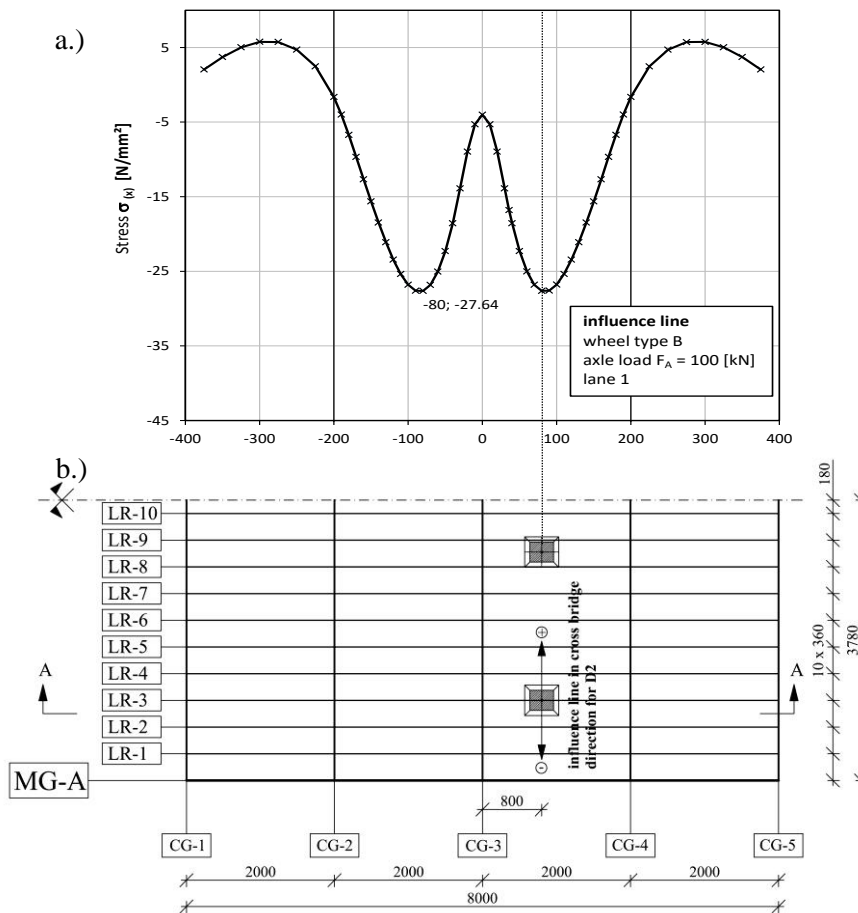


Figure 147: Model A – detail D2: appropriate position for influence line in transverse bridge direction; a.) influence line in longitudinal bridge direction referring to detail D2 and centric position; b.) plan-view of the appropriate wheel load position

Figure 148 shows the influence lines in transverse bridge direction for detail D2. Figure 148.a illustrates the transverse influence line for single wheeled axle types due to axle type A. Figure 148.b shows the transverse influence line for double wheeled axles due to axle type B. Both transverse influence lines are not completely symmetric relating to the vertical axis at $x = 0$, because of the single-sided connection of the longitudinal rib to the cross girder. A detailed description of detail D2 can be found in Section 2.4.4.

The maximum occurring stress in detail D2 due to a centric wheel position (see Figure 144) is indicated as $\eta = (-1.0)$. The determined stresses for the individual transverse positions are relating to this centric wheel's stress value. Therefore, negative values for η imply compressive stresses and positive values for η imply tensile stresses. As it can be seen in Figure 148.a, an increase of the stresses in D2 due to the shifting of the wheel load from the centric position can be detected for detail D2. The maximum stress occurs due to a wheel load location of $x = -100$ mm (see Figure 148.a). This effect can be declared by the single-sided support of the longitudinal rib and the increasing transverse bending due to the wheel load shift.

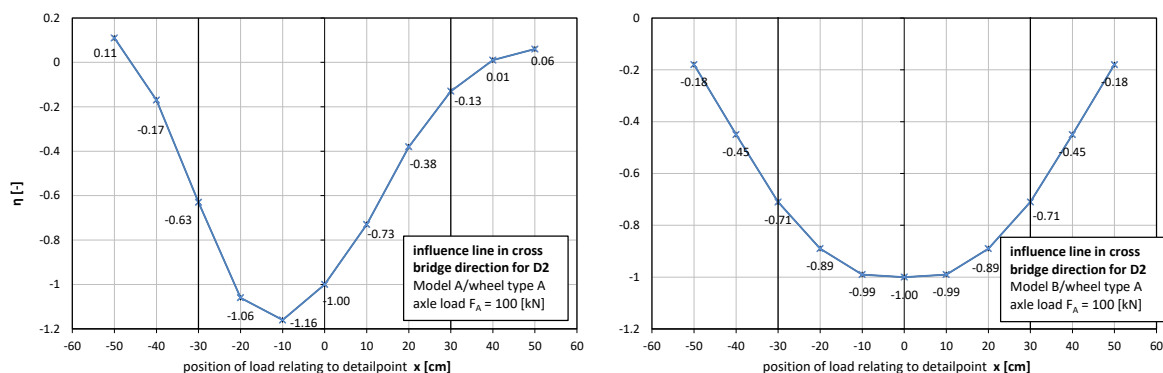


Figure 148: Model A – detail D2 influence lines in transverse bridge direction; a.) for single wheeled axles (axle type A and C); b.) for double wheeled axles (axle type B)

4.5.2. Model B

The lateral influence lines for the analysed details D1a, D1b and D2 referring to Model B are illustrated in this Section. A detailed description of Model B is located in Section 3.2.2. The influence lines were again determined for single and double wheeled axles. All influence lines in transverse bridge direction for Model B are related to lane 1, which is shown again in Figure 149.

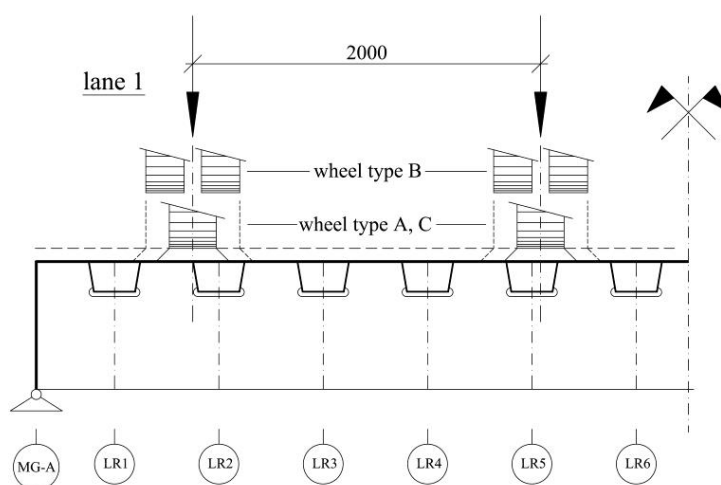


Figure 149: Model B – lane 1

4.5.2.1. Detail D1a

Figure 150.a shows the influence line in longitudinal bridge direction for Model B relating to detail D1a and a reference axle load of $F_A = 100$ kN for centric position (lane 1). The highest stress is occurring when the wheel load is positioned directly above the detail D1a, which is located in a distance of $e_{LR} = 300$ mm apart from the mid cross girder CG-3. Figure 150.a shows very well that primarily compressive stresses occur in this detail and the influence area is very small. The same observations at detail D1a for

model B can be done as for model A. When the wheel load is leaving the considered detail point the stress is decaying rapidly. Figure 150.b shows the appropriate position for the determination of the influence lines in transverse bridge direction in a plan view. A wheel load shifting was done in both transverse directions (plus/minus according to Figure 150.b) with an interval of $\Delta x = 100$ mm. The stresses were calculated for every load position and finally the results have been summed up in diagrams.

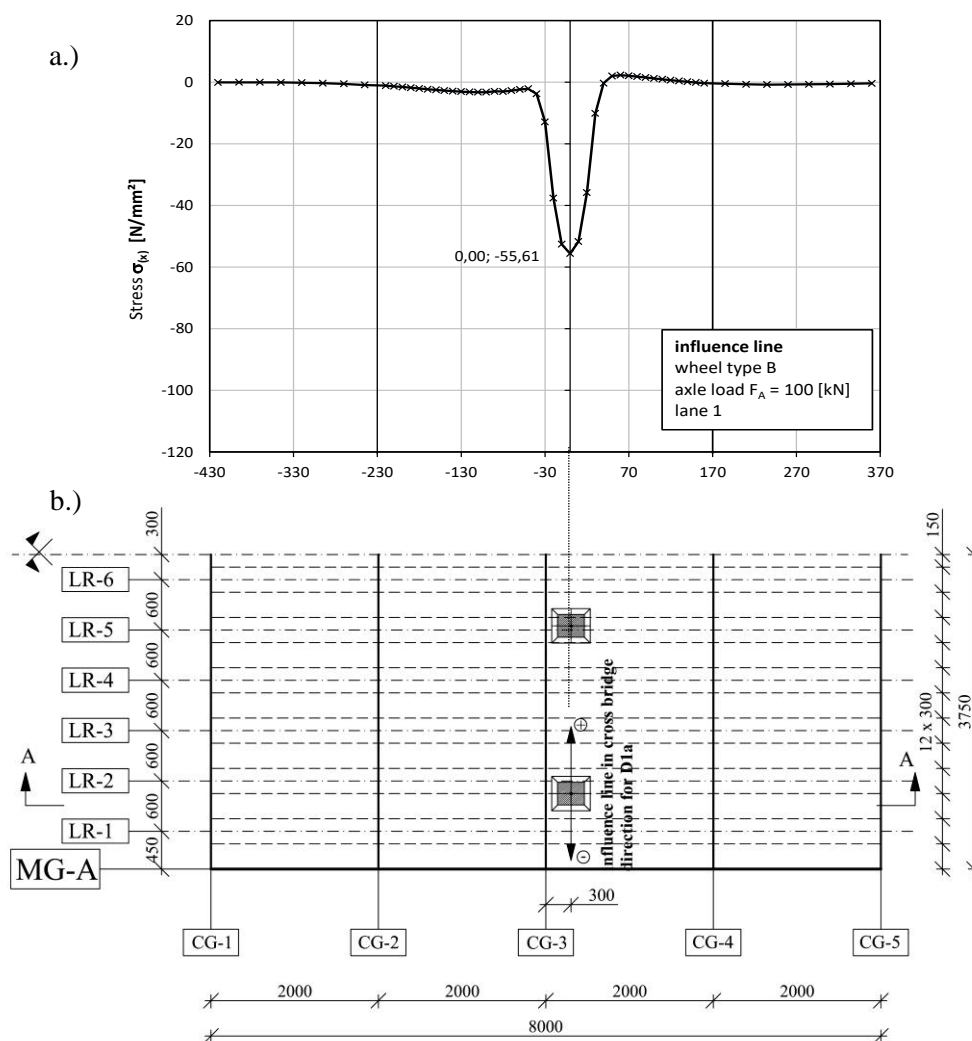


Figure 150: Model B – detail D1a: appropriate position for influence line in transverse bridge direction; a.) influence line in longitudinal bridge direction referring to detail D1a and centric position; b.) plan-view of the appropriate wheel load position

The influence lines in transverse bridge direction for detail D1a are plotted in Figure 151. Figure 151.a illustrates the transverse influence line for single wheeled axle types due to axle type A. Figure 151.b shows the transverse influence line for double wheeled axles due to axle type B. Again, both transverse influence lines are not completely symmetric relating to the vertical axis at $x = 0$, because of the finite element model geometry (see Figure 150, no geometrical symmetry relating to the considered web of

LR-2). In both diagrams of Figure 151, an additional curve is drawn that is fully symmetric referring to the vertical axis at $x = 0$, which is the basis for further analyses.

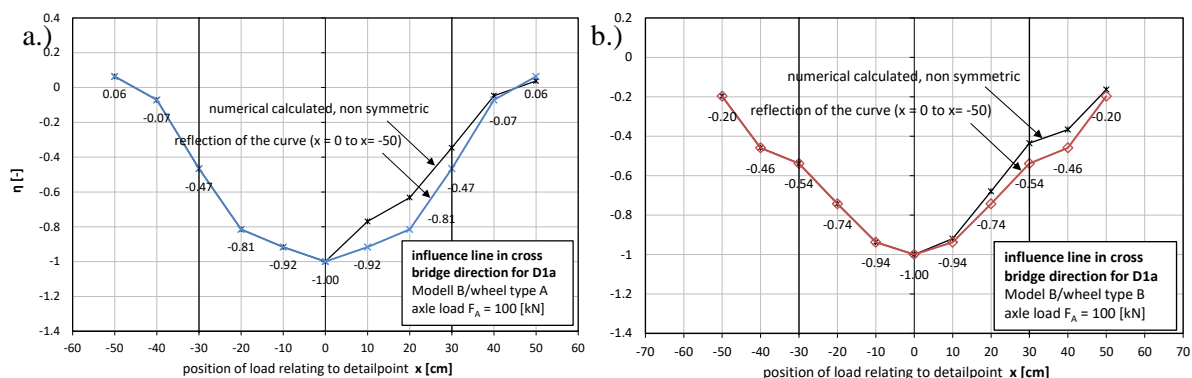


Figure 151: Model B – detail D1a influence lines in transverse bridge direction; a.) for single wheeled axles (axle type A and C); b.) for double wheeled axles (axle type B)

4.5.2.2. Detail D1b

The same wheel load position in longitudinal bridge direction as for detail D1a is appropriate for detail D1b, which is shown in Figure 150. The highest stress occurs due to a wheel load position directly above the detail D1b. This location is in a distance of $e_{LR} = 300$ mm apart from the mid cross girder CG-3. The plan view in Figure 150.b shows the appropriate position for the determination of the influence lines in transverse bridge direction. The wheel load was shifted in both transverse directions (plus/minus according to Figure 150.b) with an interval of $\Delta x = 100$ mm. The stresses were calculated for every load position and finally the results have been summed up in diagrams.

The influence lines in transverse bridge direction for detail D1b are plotted in Figure 152. Figure 152.a illustrates the transverse influence line for single wheeled axle types due to axle type A. Figure 152.b shows the transverse influence line for double wheeled axles due to axle type B.

The occurring stress in Figure 152 for detail D1b due to a centric wheel position at $x = 0$ (see Figure 149) indicates $\eta = \sigma_{D1b,x=i} / \sigma_{D1b,x=0} = (-1.0)$. Negative values for η imply compressive stresses and positive values for η imply tensile stresses. As it can be seen in Figure 152, by shifting the wheel load leftwards ($x < 0$), compressive stress in the detail D1b occurs and by shifting the wheel load rightwards ($x > 0$), tensile stress in the detail D1b occurs. Therefore, the algebraic sign of the occurring stress in detail D1b depends on the position of the wheel load in transverse bridge direction and the highest stress is arising when the wheel load is located at $x = -20$ cm due to single wheeled axles and $x = -30$ cm relating to double wheeled axles. Therefore, a calculation of the remaining service life under consideration of a lateral shift of the heavy vehicles and its wheel loads is required at this detail D1b with such special characteristics.

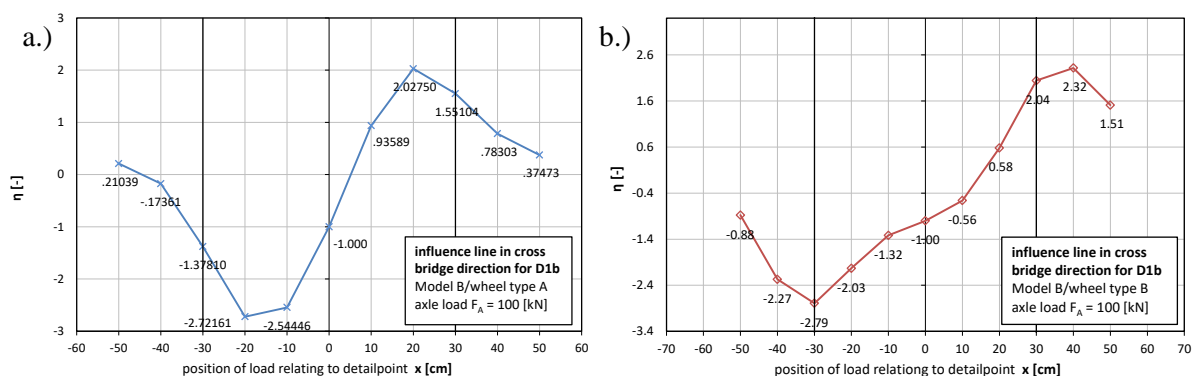


Figure 152: Model B – detail D1b influence lines in transverse bridge direction; a.) for single wheeled axles (axle type A and C); b.) for double wheeled axles (axle type B)

4.5.2.3. Detail D2

The influence line in longitudinal bridge direction for Model B relating to detail D2 and a reference axle load of $F_A = 100$ kN is shown Figure 153.a for centric position (lane 1). By positioning the wheel load in a distance of $e = 800$ mm apart from detail D2 (at the mid cross girder CG-3) the highest stress is occurring. As shown in the picture, primarily compressive stresses are occurring at this detail and symmetry of the curve relating to the vertical axis at $x = 0$ can be detected. The appropriate position for the influence line determination in transverse bridge direction is shown in the plan view of Figure 153.b. The wheel load was shifted in both cross directions (plus/minus according to Figure 153.b) with an interval of $\Delta x = 100$ mm. The stress calculation was done for every load position and finally diagrams sum up the results.

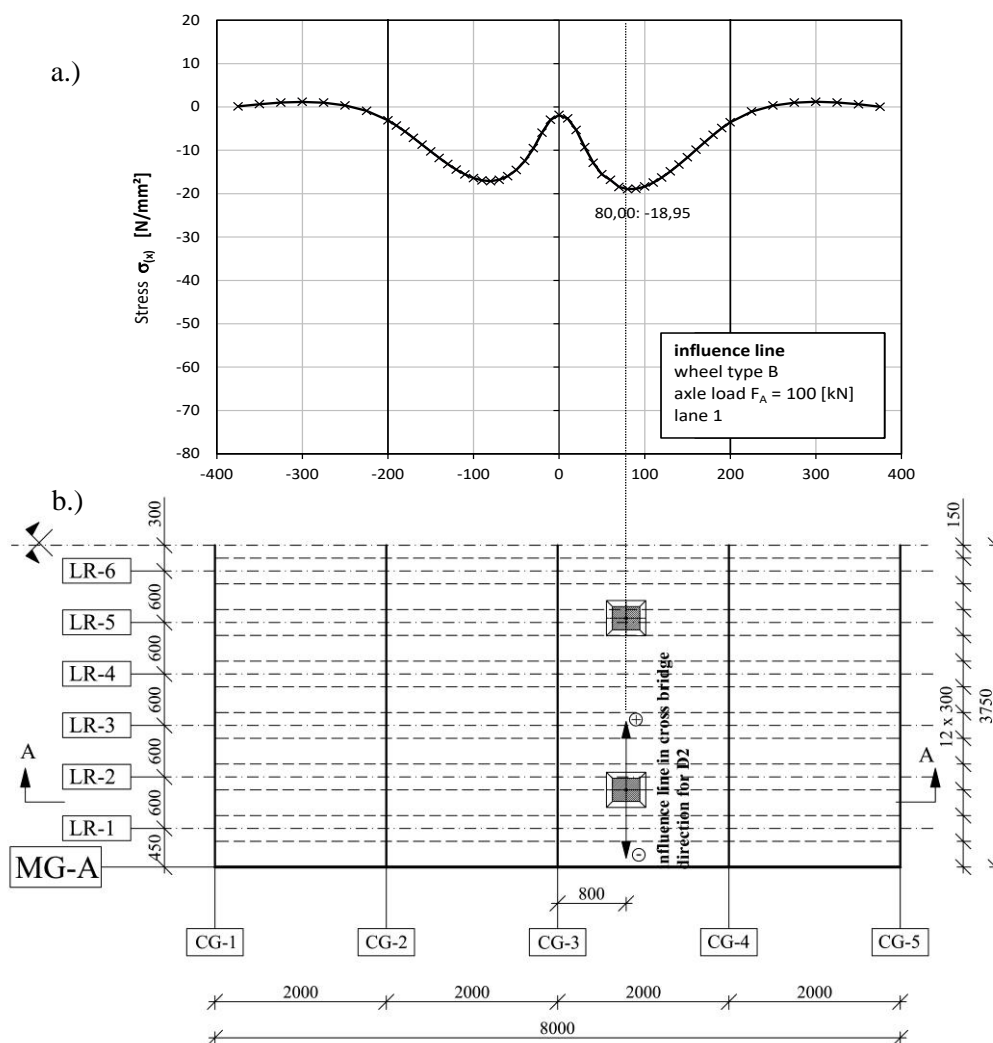


Figure 153: Model B – detail D2: appropriate position for influence line in transverse bridge direction; a.) influence line in longitudinal bridge direction referring to detail D2 and centric position; b.) plan-view of the appropriate wheel load position

The influence lines in transverse bridge direction for detail D2 are plotted in Figure 154. Figure 154.a illustrates the transverse influence line for single wheeled axle types due to axle type A. Figure 154.b shows the transverse influence line for double wheeled axles due to axle type B. Both transverse influence lines are not completely symmetric relating to the vertical axis at $x = 0$. A detailed description of detail D2 can be found in Section 2.4.4.

The occurring stress in Figure 154 due to a centric wheel load position $x = 0$, directly above the mid axis of the analysed longitudinal rib's web (see Figure 149) indicates $\eta = (-1.0)$. Therefore, negative values for η imply compressive stresses and positive values for η imply tensile stresses.

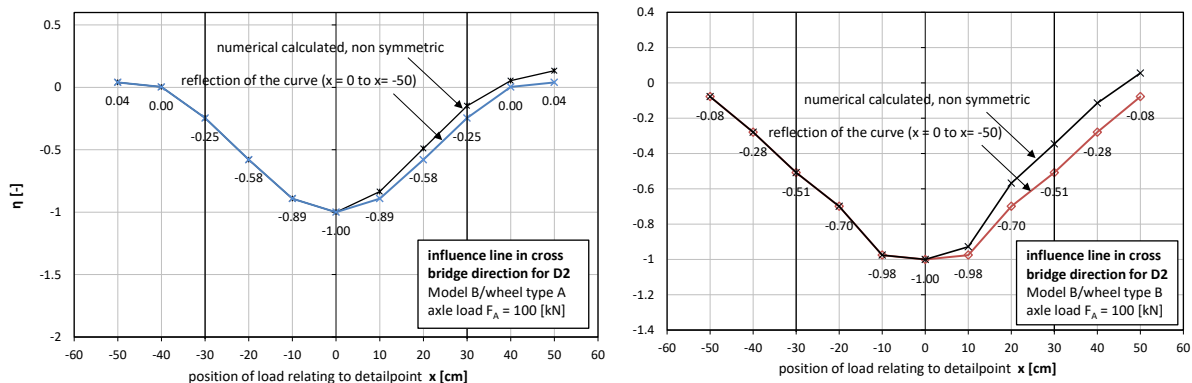


Figure 154: Model B – detail D2 influence lines in transverse bridge direction; a.) for single wheeled axles (axle type A and C); b.) for double wheeled axles (axle type B)

4.5.3. Model C

The lateral influence lines for the analysed details D1a, D1b and D2 referring to Model C are illustrated in this Section. A detailed description of Model C is located in Section 3.2.3. The influence lines were determined for single and double wheeled axles. All influence lines in transverse bridge direction for Model C are related to lane 1, which is shown in Figure 155.

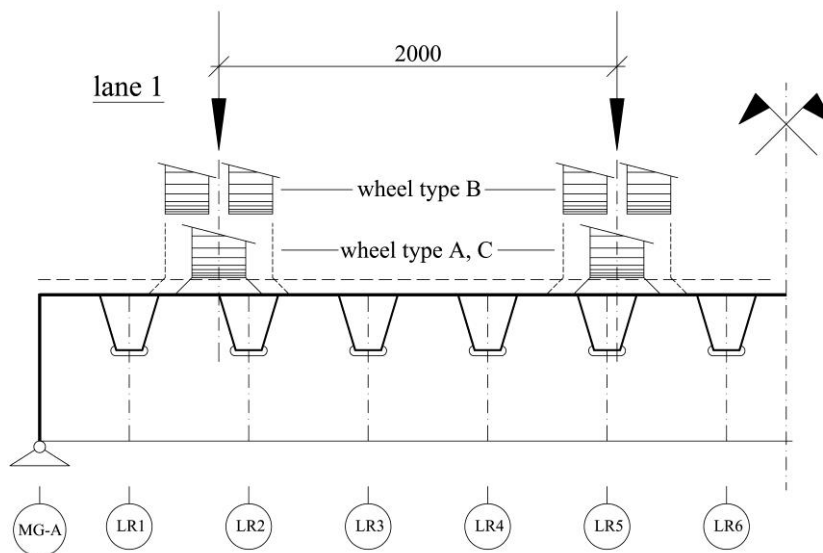


Figure 155: Model C – lane 1

4.5.3.1. Detail D1a

Figure 156.a shows the influence line in longitudinal bridge direction for Model C relating to detail D1a and a reference axle load of $F_A = 100$ kN for centric position (lane 1). A wheel load position directly above the detail D1a causes the highest stress. This location is in a distance of $e_{LR} = 300$ mm apart from the mid cross girder CG-3. Figure 156.a primarily shows compressive stresses at this detail as well as a very small influence area. Because of this small influence area, the stresses in the detail are decaying rapidly when the wheel load is leaving the considered detail point. Figure 156.b shows a plan view with the appropriate position for the determination of the influence lines in transverse bridge direction in. The wheel load was shifted in both cross directions (plus/minus according to Figure 156.b) with an interval of $\Delta x = 100$ mm. The stresses were calculated for every load position and finally the results have been summed up in diagrams.

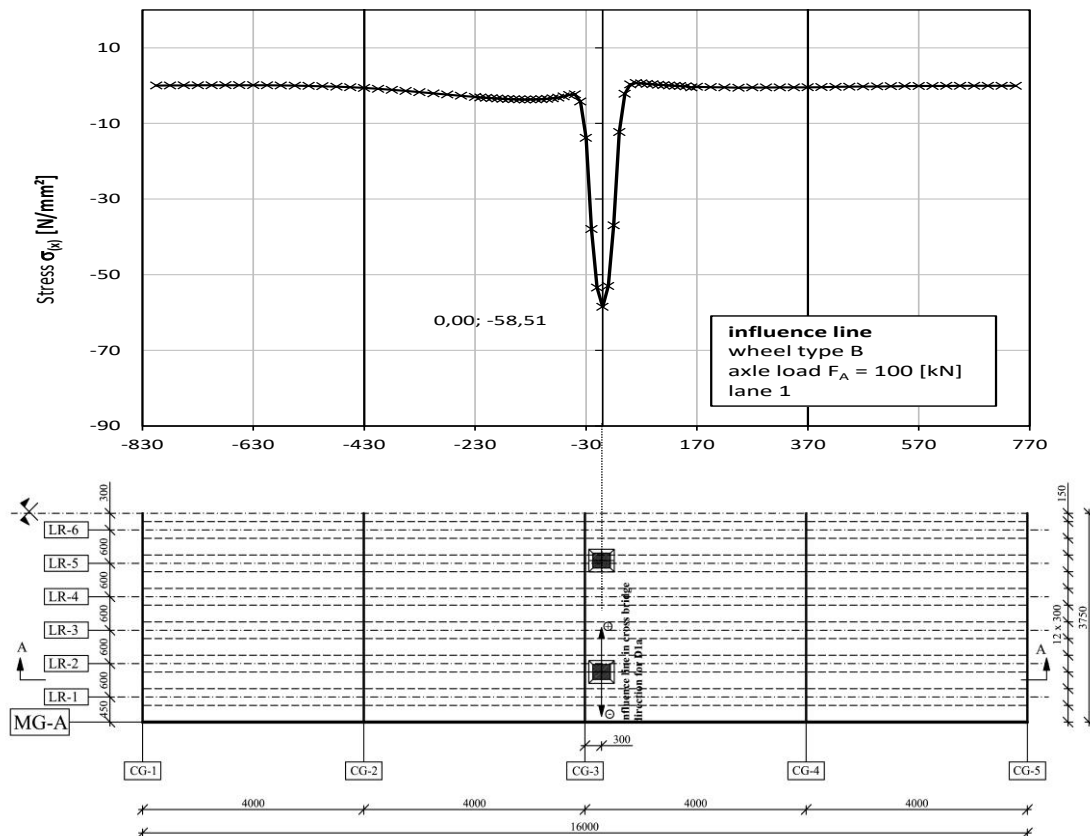


Figure 156: Model C – detail D1a: appropriate position for influence line in cross bridge direction; a.) influence line in longitudinal bridge direction referring to detail D1a and centric position; b.) plan-view of the appropriate wheel load position

The influence lines in transverse bridge direction for detail D1a are plotted in Figure 157. Figure 157.a illustrates the transverse influence line for single wheeled axle types due to axle type A. Figure 157.b shows the transverse influence line for double wheeled axles due to axle type B.

As already mentioned before, the occurring stress in the detail due to centric wheel position (see Figure 155) at $x = 0$ indicates $\eta = (-1)$. The stresses due to all other transverse wheel positions are related to the centric one ($x = 0$). Negative values for η imply compressive stresses and positive values for η imply tensile stresses.

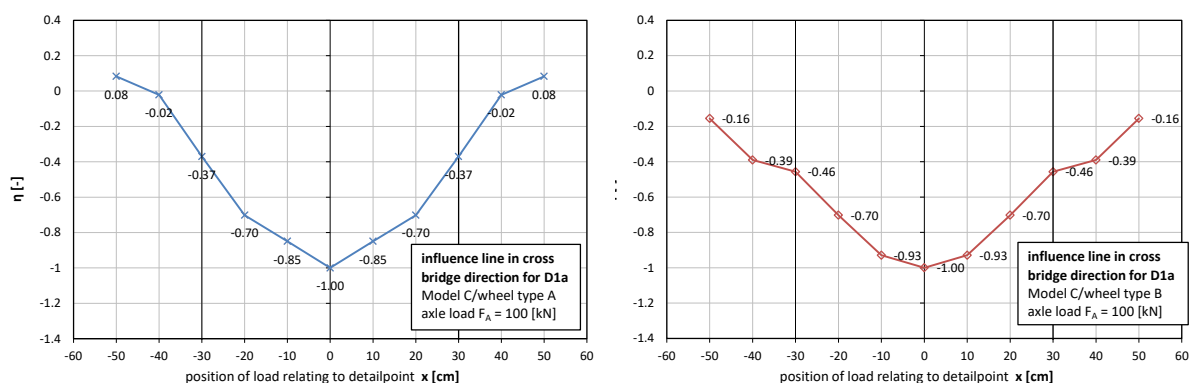


Figure 157: Model C – detail D1a influence lines in transverse bridge direction; a.) for single wheeled axles (axle type A and C); b.) for double wheeled axles (axle type B)

4.5.3.2. Detail D1b

For detail D1b, the same wheel load position in longitudinal bridge direction as for detail D1a is appropriate, which is shown in Figure 156. The highest stress is occurring when the wheel load is positioned directly above the detail D1b, which is located in a distance of $e_{LR} = 300$ mm apart from the mid cross girder CG-3. Also at detail D1b primarily compressive stresses are occurring at this detail when the wheel load crosses the bridge deck centric above the longitudinal rib's web and the wheel load does not shift in transverse bridge direction. The influence area is very small and stresses in the detail are rapidly decaying when the wheel load is leaving the considered detail point. Figure 156.b shows the appropriate position for the determination of the influence lines in transverse bridge direction in a plan view. The wheel load was shifted in both cross directions (plus/minus according to Figure 156.b) with an interval of $\Delta x = 100$ mm. The stresses were calculated for every load position and finally the results have been summed up in diagrams.

Figure 158 illustrates the influence lines in transverse bridge direction for detail D1b. Figure 158.a shows the transverse influence line for single wheeled axle types due to axle type A. The transverse influence line for double wheeled axles due to axle type B is plotted in Figure 158.b.

The following observations can be done according to Figure 158: a wheel load shifting leftwards ($x < 0$), causes compressive stresses in the detail D1b and a wheel load shifting rightwards ($x > 0$), causes tensile stresses in the detail D1b. Therefore, the occurring stresses algebraic sign in detail D1b depends on the wheel load's position in transverse bridge direction. The highest stress in D1b because of single

wheeled axles arises due to wheel load location $x = -20\text{cm}$ and for double wheeled axles $x = -30\text{cm}$ causes the highest stress. A calculation of the remaining service life under consideration of a lateral shift of the heavy vehicles and its wheel loads is required at this detail D1b with such special characteristics.

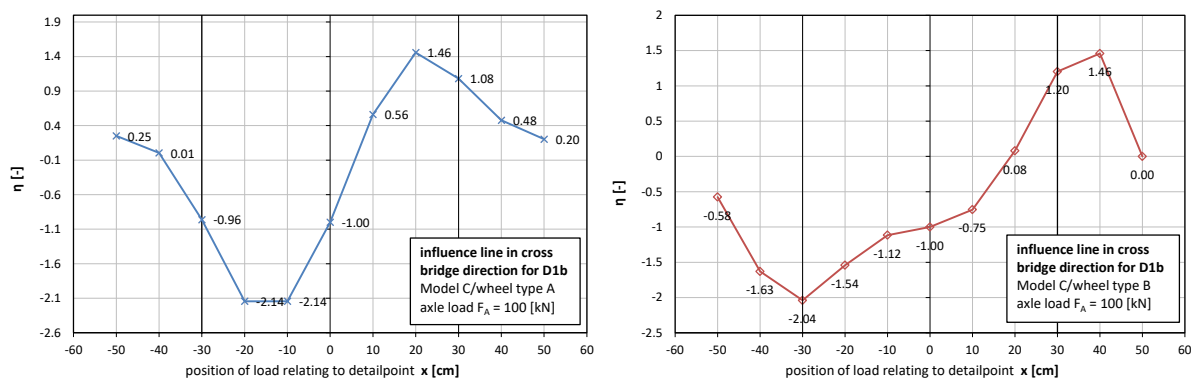


Figure 158: Model C – detail D1b influence lines in transverse bridge direction; a.) for single wheeled axles (axle type A and C); b.) for double wheeled axles (axle type B)

4.5.3.3. Detail D2

The influence line in longitudinal bridge direction for Model C relating to detail D2 and a reference axle load of $F_A = 100\text{ kN}$ for centric position is illustrated in Figure 159.a. The wheel load position, in a distance of $e = 1600\text{ mm}$ apart from detail D2 at the mid cross girder CG-3, causes the highest stress. The picture primarily shows compressive stresses at this detail and a symmetry of the curve relating to the vertical axis at $x = 0$ can be observed. Figure 159.b shows the appropriate position for the determination of the influence lines in transverse bridge direction in a plan view. A wheel load shift in both transverse directions (plus/minus according to Figure 159.b) with an interval of $\Delta x = 100\text{ mm}$ had been done. The stresses were calculated for every load position and finally the results have been summed up in diagrams.

The transverse influence lines for detail D2 are plotted in Figure 160. Figure 160.a illustrates the transverse influence line for single wheeled axle types due to axle type A. Figure 160.b shows the transverse influence line for double wheeled axles due to axle type B. Both transverse influence lines are not completely symmetric relating to the vertical axis at $x = 0$.

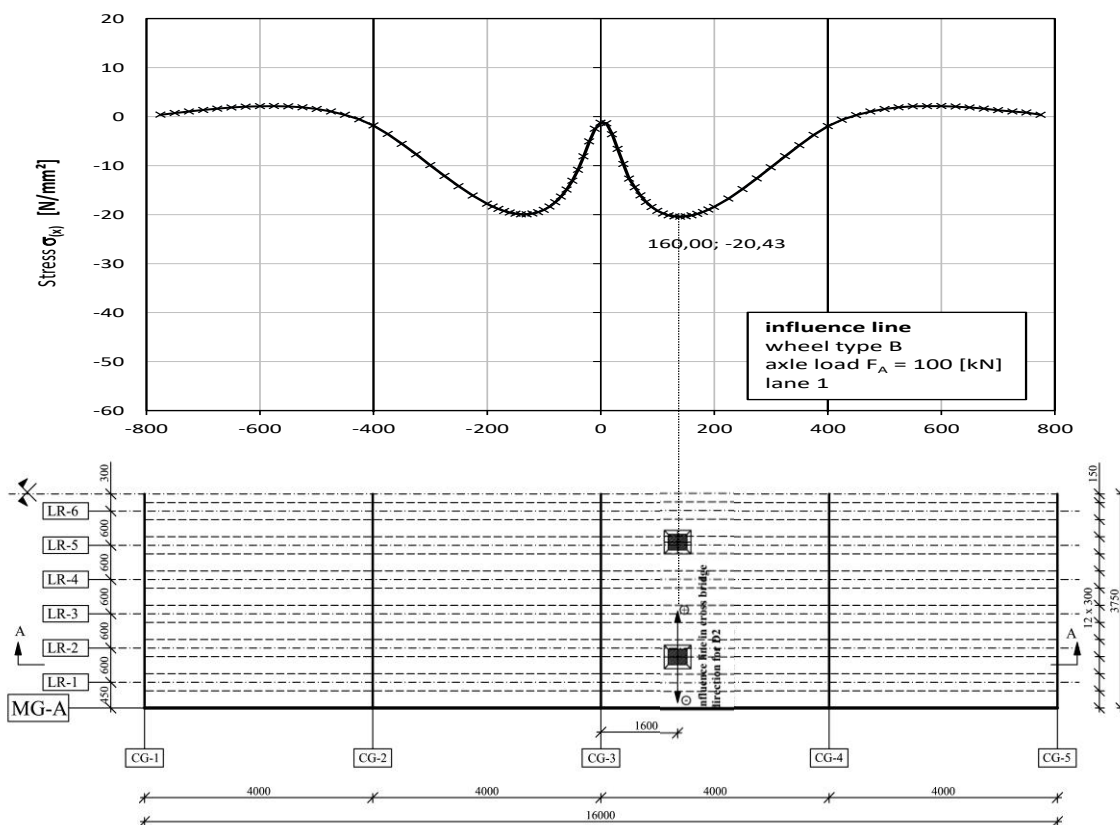


Figure 159: Model C – detail D2: appropriate position for influence line in transverse bridge direction; a.) influence line in longitudinal bridge direction referring to detail D2 and centric position; b.) plan-view of the appropriate wheel load position

The maximum occurring stress in Figure 160, due to centric wheel position $x = 0$, is indicated as $\eta = (-1.0)$. This stress level is the basis and the occurring stresses due to all other transversal positions are in relation to the one with centric wheel position. Again, negative values for η imply compressive stresses and positive values for η imply tensile stresses.

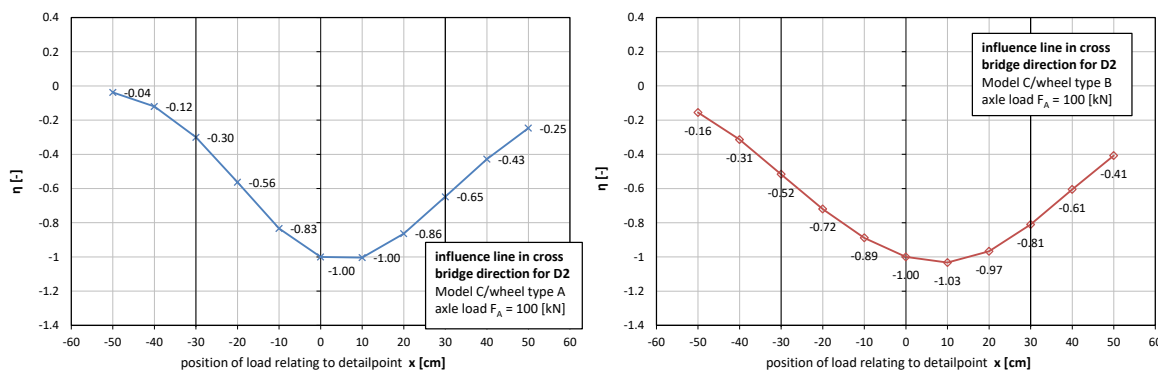


Figure 160: Model C – detail D2 influence lines in transverse bridge direction; a.) for single wheeled axles (axle type A and C); b.) for double wheeled axles (axle type B)

4.6. General Concept of considering realistic axle geometries and lateral distribution for Detail D1a and D2

In this chapter, the steps of considering realistic axle geometries and a lateral distribution for the positions of the individual lorries in a lane are explained. In summary 8 steps had been done, which are listed first in a very short form and then are explained in more detail.

Procedure I: Simulation of the heavy traffic crossings for centric track configuration

The individual steps 1 to 3, presented in Section 3.4, are summed up again.

- Step 1: Determination of influence lines for the 3 wheel types A, B and C at every detail in longitudinal bridge direction.
- Step 2: Calculation of stress-history curves in every detail for every vehicle type under consideration of the axle distances and the axle loads depending on the lorries from the fatigue load model (see Figure 24 in Section 2.5.2).
- Step 3: Stress cycle counting with Rain flow- or Reservoir method for each vehicle type crossing and generation of a stress range spectrum due to a centric track configuration.

Calculation of equivalent stress range $\Delta\sigma_{e,I}$

Procedure II: Consideration of realistic axle geometries

- Step 4: Calculation of influence lines in transverse bridge direction for every detail due to single and double wheeled axle types and shift of axle B with Δe_B (see Figure 137 in Section 4.3.4).

For a consideration of realistic axle geometries with different positions in transverse direction to each detail, it was necessary to determine influence lines in transverse bridge direction for single and double wheeled axle types at the critical load positions in longitudinal direction. These critical load positions are located where the maximum stresses in the detail occur and could be verified, taking the influence lines in longitudinal bridge direction due to centric wheel position into account. Figure 161 illustrates the influence lines in transverse bridge direction for single and double wheeled axles referring to detail D1a, the welded connection of the longitudinal rib to the deck plate.

Realistic axle geometries could be taken into account with a lateral shift Δe_B of the appropriate axle or wheel types so that the outer faces of the wheels nearly match together as it is shown in Figure 161, based on Figure 137 in Section 4.3.4 (Note: wheel type C defines Δe_B , because for wheel type A the results of wheel type C are chosen). In the picture the single wheeled axles (A and C) are placed with a distance of Δe_B away from the through web's axis to the left. In the calculations this displacement was considered by offsetting the transversal influence line with

Δe_B to the right. The appropriate stress ranges due to axle type A and C could then be modified with the value η_A (at position 0), which is shown in Figure 161.

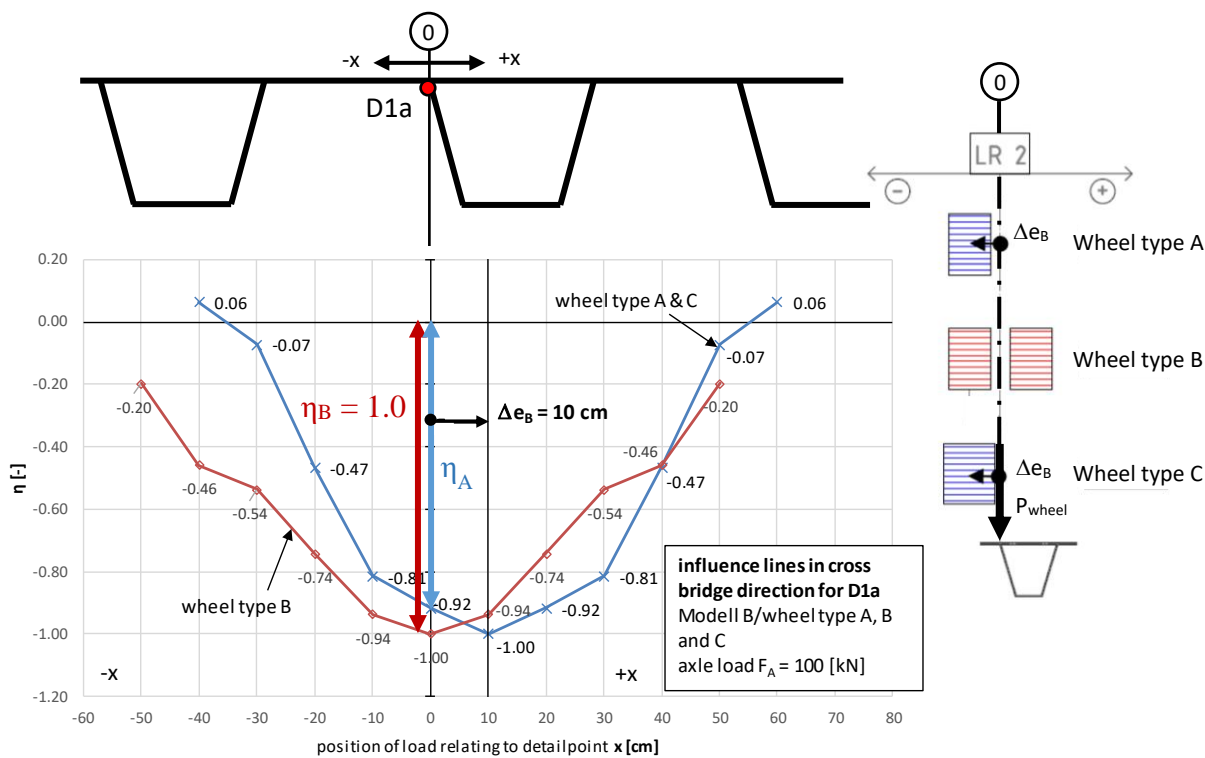


Figure 161: schematic representation of the influence lines in transverse bridge direction for single and double wheeled axles and lateral shift of the single wheeled axle for considering realistic axle geometries

- Step 5: Determination of a stress range spectrum taking realistic axle geometries into account. Scaling of the relevant stress ranges using the appropriate scale factors from the influence line in transverse bridge direction (Step 4).

The modifying of the stress range spectrum, based on centric track configuration for all lorries and all wheels (see Section 3.4) is shown in Figure 162. Here as example the stress ranges as a result of the single wheeled axles (A and C) are modified with the parameter η_A from the transverse influence line ($\Delta\sigma_I \cdot \eta_A$, see Figure 162). This parameter η_A as well as the appropriate transverse influence line for wheel type A and C are shown in Figure 161. The stress ranges due to the double wheeled axle B are unchanged. Figure 161 shows a value of $\eta_B = 1.0$. In summery a new modified stress spectrum and a damage equivalent constant amplitude stress range $\Delta\sigma_{e,II}$ could be calculated. This value was compared to the value for a centric track configuration $\Delta\sigma_{e,I}$. Note: Also the centric position of wheel types A and C with a shift of wheel type B was checked, which gives more beneficial results (smaller fatigue damage)

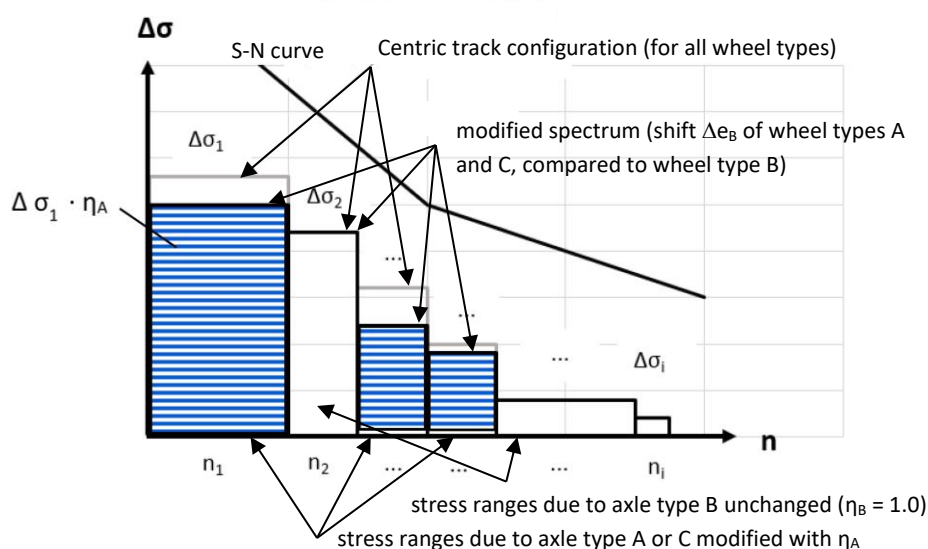


Figure 162: schematic representation of modifying the appropriate stress ranges due to centric wheel position to consider realistic axle geometries, but centric lorry position

Procedure III: Consideration of realistic axle geometries and a lateral distribution of the heavy traffic vehicles

- Step 6: Choosing an applicable frequency distribution in transverse bridge direction from measurements or based on Eurocode [41] – see Section 4.4.

Figure 163.a shows for example the transverse frequency distribution LFT I from [41] for considering driving characteristics of the heavy traffic. In this distribution 5 positions in transverse bridge direction are included. The probability is given in percent and 50 % of all vehicles are driving in a centric lane position.

- Step 7: Locating the appropriate transverse influence lines (based on the position of each detail) with a transverse shift of $e_{A,C} = \Delta e_B = 100\text{mm}$ for wheel type B; calculation of the modifying load parameters η at the transverse positions relating to the frequency distribution.

Figure 163.b shows the transversal influence lines for axle type B and A/C. As shown in Figure 163 (right side), axle type A and C are positioned left to detail point D1a in a distance of $e_{A,C}$ away from the detail point if wheel type B is centric, according to Figure 137 in Section 4.3.4. Therefore, the transverse influence line for axle type A and C is shifted to the right side with $e_{A,C}$ (see Figure 163.b). The individual parameters η_A and η_B referring to the transverse positions -20cm (A1), -10cm (A2), 0 (A3), +10cm (A4), +20cm (A5) can be read out from Figure 163.b. The belonging frequency for each transverse position A1 to A5 can be taken from Figure 163.a.

In Figure 163.b, the parameters $\eta_{A,i}$ for axle type A are coloured based on its transverse position. Green for transverse position -20cm (A1) and +20cm (A2). Purple for transverse position -10cm (A2) and +10cm (A4). Orange for transverse position 0 (A3).

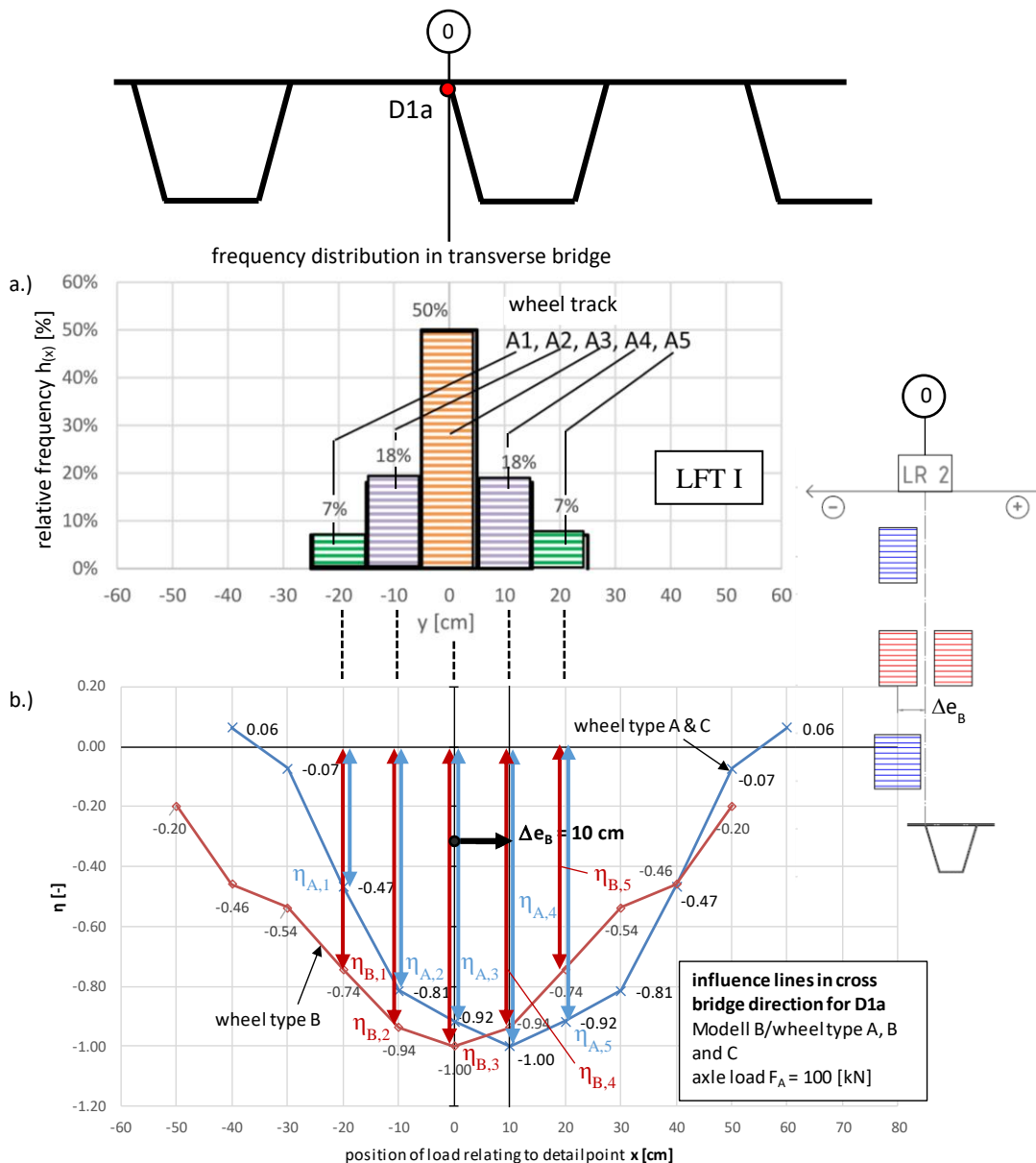


Figure 163: a.) frequency distribution in transverse bridge direction b.) influence lines in transverse bridge direction for single and double wheeled axles and lateral shift of the single wheeled axles;

- Step 8: Modifying the stress ranges from the spectrum with centric track configuration (results of Step 1 to 3) in terms of stress range value and number of cycles
 - Splitting the number of cycles belonging to the stress range by using the lateral frequency distribution
 - Scaling the stress range value by using the modifying load parameters η dependent on the transverse position and the wheel type

With the values for the frequency in transverse direction (see Figure 163.a), every stress range from the spectrum with centric wheel position could be partitioned in its number of cycles for wheel positions -20, -10, 0, +10, +20 (see Figure 163.a). Figure 164 shows exemplary the partition of the highest stress range $\Delta\sigma_1$. This partition has been done for the transverse positions A1 to A5, which are shown in Figure 163 and corresponds with the chosen colour code. The number of cycles n_1 for $\Delta\sigma_1$ has to be split into 5 new number of cycles (position A1: $n_1 \cdot 9\%$, position A2: $n_1 \cdot 18\%$, position A3: $n_1 \cdot 50\%$, position A4: $n_1 \cdot 18\%$, position A5: $n_1 \cdot 9\%$). Afterwards, these 5 new stress ranges have to be modified with its appropriate load parameters $\eta_{A,i}$ which are shown in Figure 163.b based on its transverse position ($\Delta\sigma_{1,A1} = \Delta\sigma_1 \cdot \eta_{A1}$; $\Delta\sigma_{1,A2} = \Delta\sigma_1 \cdot \eta_{A2}$; $\Delta\sigma_{1,A3} = \Delta\sigma_1 \cdot \eta_{A3}$; $\Delta\sigma_{1,A4} = \Delta\sigma_1 \cdot \eta_{A4}$; $\Delta\sigma_{1,A5} = \Delta\sigma_1 \cdot \eta_{A5}$). This procedure has to be done for every stress range of the spectrum to get a new modified stress range spectrum. Finally, damage equivalent constant amplitude stress ranges $\Delta\sigma_{e,III}$ were calculated for procedure III relating to 100 lorry crossings. These $\Delta\sigma_{e,III}$ have been compared with the reference case $\Delta\sigma_{e,I}$ to illustrate the effects of heavy traffic driving characteristics.

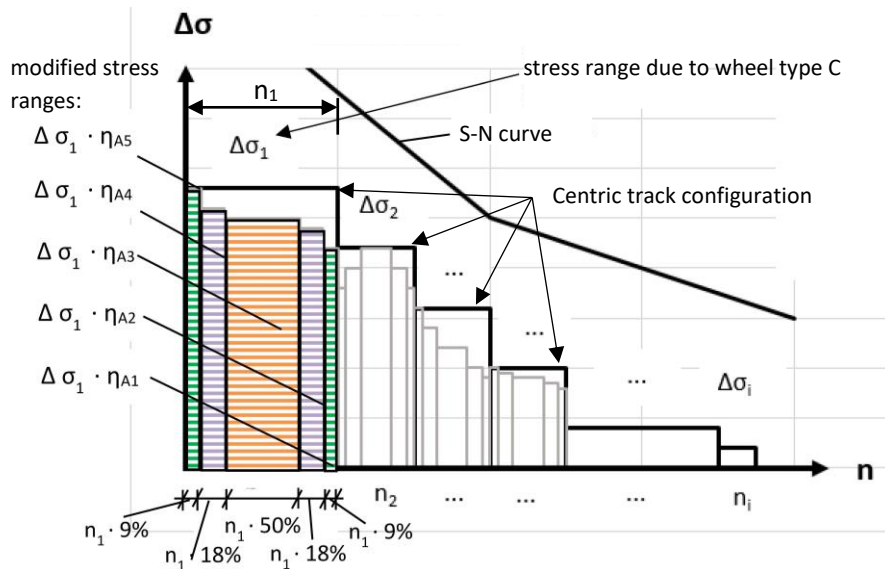


Figure 164: schematic representation of modifying the appropriate stress ranges due to considering realistic axle geometries and driving characteristics of heavy traffic

4.7. Modified general concept of considering realistic axle geometries and lateral distribution for Detail D1b

Detail D1b is the same welded connection as detail D1a, the weld that connects the longitudinal rib's web to the deck plate. At detail D1b, the normal stresses at the outer side of the through web have to be taken into account. At the bottom side of the deck plate (detail D1a) always compression stresses occur due to every location of the wheel load in transverse bridge direction. Figure 165 shows the deformations of the finite element model due to a single wheeled load at different positions in transverse direction. At Figure 165.a the single wheel load is located left sided to the analysed trough web's axis. Due to load position A and thereby arising rotation of the deck plate ($+\varphi$), in D1a compressive stresses and in D1b tensile stresses occur. At Figure 165.b the single wheel load is located right sided to the analysed trough web's axis. Due to load position B and thereby arising rotation of the deck plate in opposite direction ($-\varphi$), in D1a again compressive stresses occur but in D1b now also compressive stresses occur.

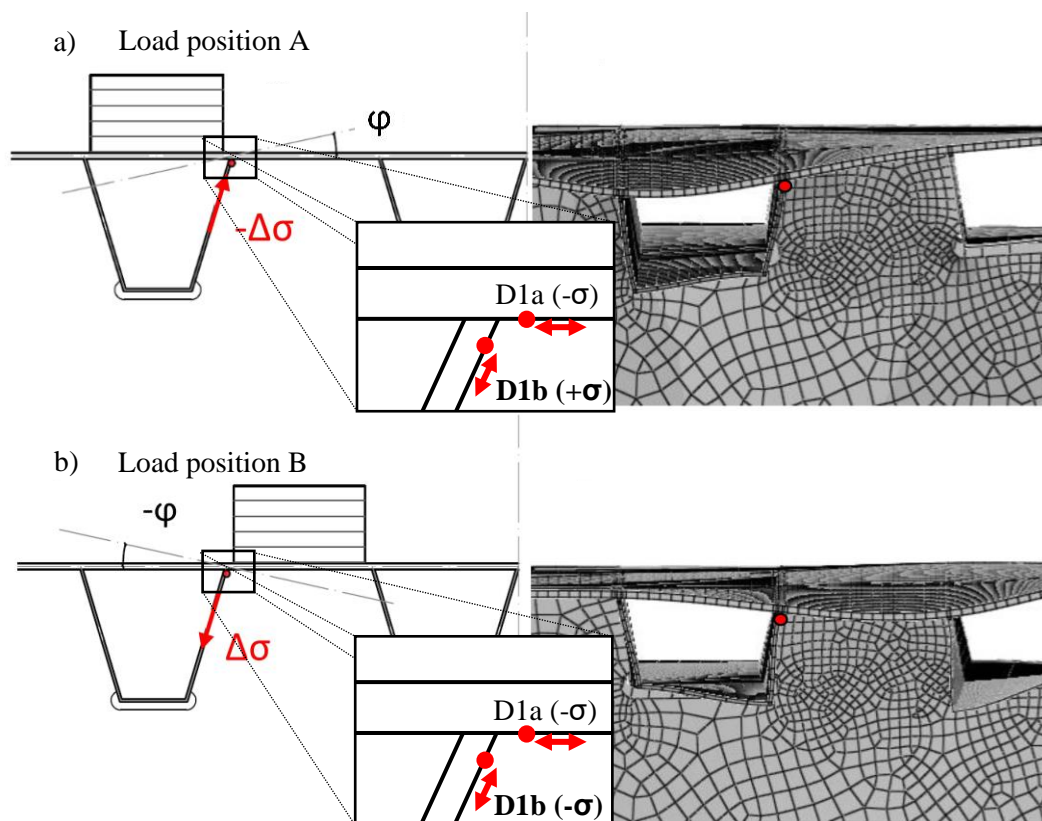


Figure 165: deformations of the FEM-model with trough ribs due to a single wheel; a.) single wheel load located left sided to the trough web's axis b.) single wheel load located right sided to the trough web's axis

So the plus/minus sign of the stress in D1b changes by moving the wheel load in transverse direction relating to the trough web's axis and thereby the highest stress ranges $\Delta\sigma$ in D1b are coming from different vehicles on different transverse positions. The stress ranges $\Delta\sigma_i$ are dependent on the position

of the wheel load in transverse bridge direction as well as the sequence and individual transverse position of the vehicle type crossings (T1 to T5) over the bridge deck. Figure 166.b shows as example the influence lines in transverse bridge direction for single and double wheeled axles referring to detail D1b, where the influence line for double wheeled axles is again shifted by Δe_B to consider realistic axle geometries. Negative values for η represent compressive stresses in D1b and positive values for η represent tensile stresses in D1b. With this picture the effect of the trough web bending depending on the load position in transverse direction is illustrated. The curves are standardised and especially for single wheeled axles a lateral shift of the wheel delivers a dramatically increase of the stress ranges in D1b. A heavy traffic simulation with centric track configuration (see Section 4.2) of all axle types would result in too low stress ranges and a consideration of a lateral shift of the wheels due to the driving characteristics is essential. Note: for detail D1b the centric position of wheel types A and C gives the highest fatigue damage.

Figure 166.a shows for example a frequency distribution based on measurements for considering driving characteristics of heavy traffic (see Section 4.4.2). With this frequency distribution and the influence lines in transverse bridge direction a simulation of the crossings of lorry types T1 to T5 has to be done. Note: the frequency distribution LFT I, based on the Eurocode (see Figure 163.a), gives a smaller fatigue damage.

For every position in transverse direction (lane axis -4 to +4; -40cm to +40cm, with $\Delta = 10$ cm in Figure 166.a) an influence line in longitudinal bridge direction for single and double wheeled axles was calculated. Figure 167 exemplary illustrates the influence lines in longitudinal bridge direction related to wheel type A for 3 different wheel positions in transverse directions ($x=0$ cm, $x=-20$ cm, $x=+20$ cm). The influence line for $x=0$ cm in transverse direction is the basis influence line (see Figure 167). The influence lines in longitudinal bridge directions for the positions $x=-20$ cm and $x=+20$ cm have been determined in a simplified manner by scaling the basis influence line ($x=0$ cm) with the appropriate factor η_A from Figure 166.b ($\eta_{A,-20} = -2.72$ and $\eta_{A,+20} = 2.03$). The curves in Figure 166.b are modified in such a way that negative η -values represent compressive stresses in the detail D1b.

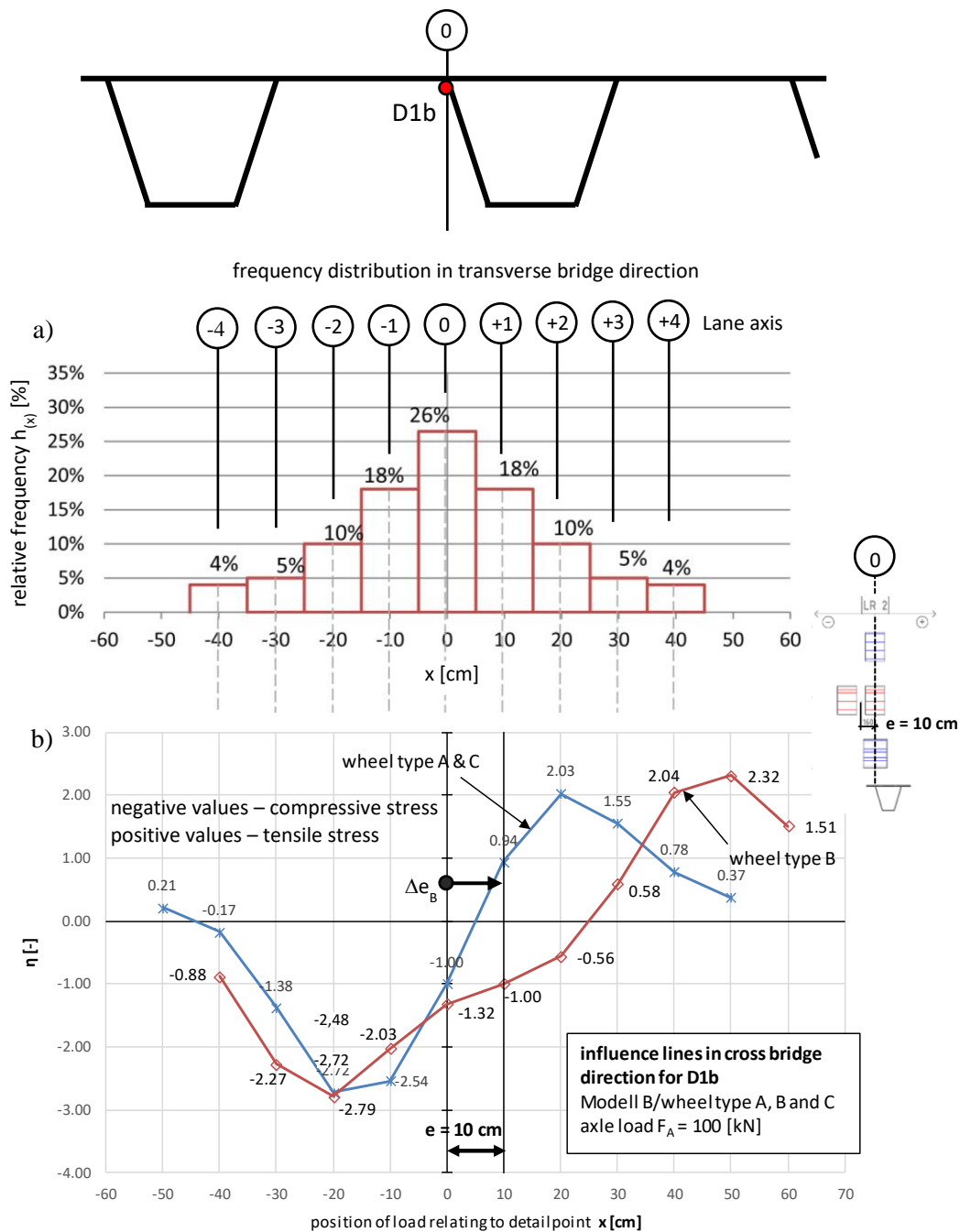


Figure 166: a.) frequency distribution in transverse bridge direction; b.) influence lines referring to detail D1b (Model B) in transverse bridge direction for single and double wheeled axles;

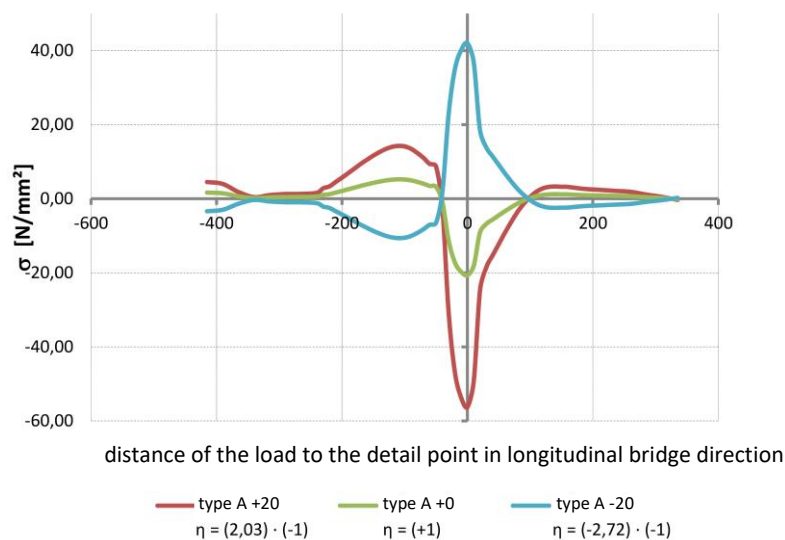


Figure 167: influence lines in longitudinal bridge direction for detail D1b (Model B), different positions in transverse bridge direction ($x=0\text{cm}$, $x=+20\text{cm}$, $x=-20\text{cm}$) related to wheel type A

This scaling procedure was done for wheel type A, B and C and per wheel type 9 influence lines in longitudinal bridge direction have been determined (lane axis -4 to +4, see Figure 166). As it is shown in Figure 166.b, realistic axle geometries already have been taken into account by shifting the appropriate transverse influence line (for wheel type B) with the value of $\Delta e_B = 10\text{cm}$ to the right. Next the individual stress history curves due to the lorry crossings (T1 to T5) in each lane axis (-4 to +4) were determined by considering the lorry's axle distances and its axle loads from fatigue load model FLM-4. Figure 168 exemplary shows the stress history curves due to vehicle type T1 for 3 different positions in transverse bridge direction ($x=0\text{cm}$, $x=-20\text{cm}$ and $x=+20\text{cm}$). One lorry type has got 9 stress history curves and fatigue load model FLM-4 includes 5 lorry types, so in summary 45 stress history curves have been calculated to include every possible transverse position a vehicle can have in the studied lane at driving across the bridge deck.

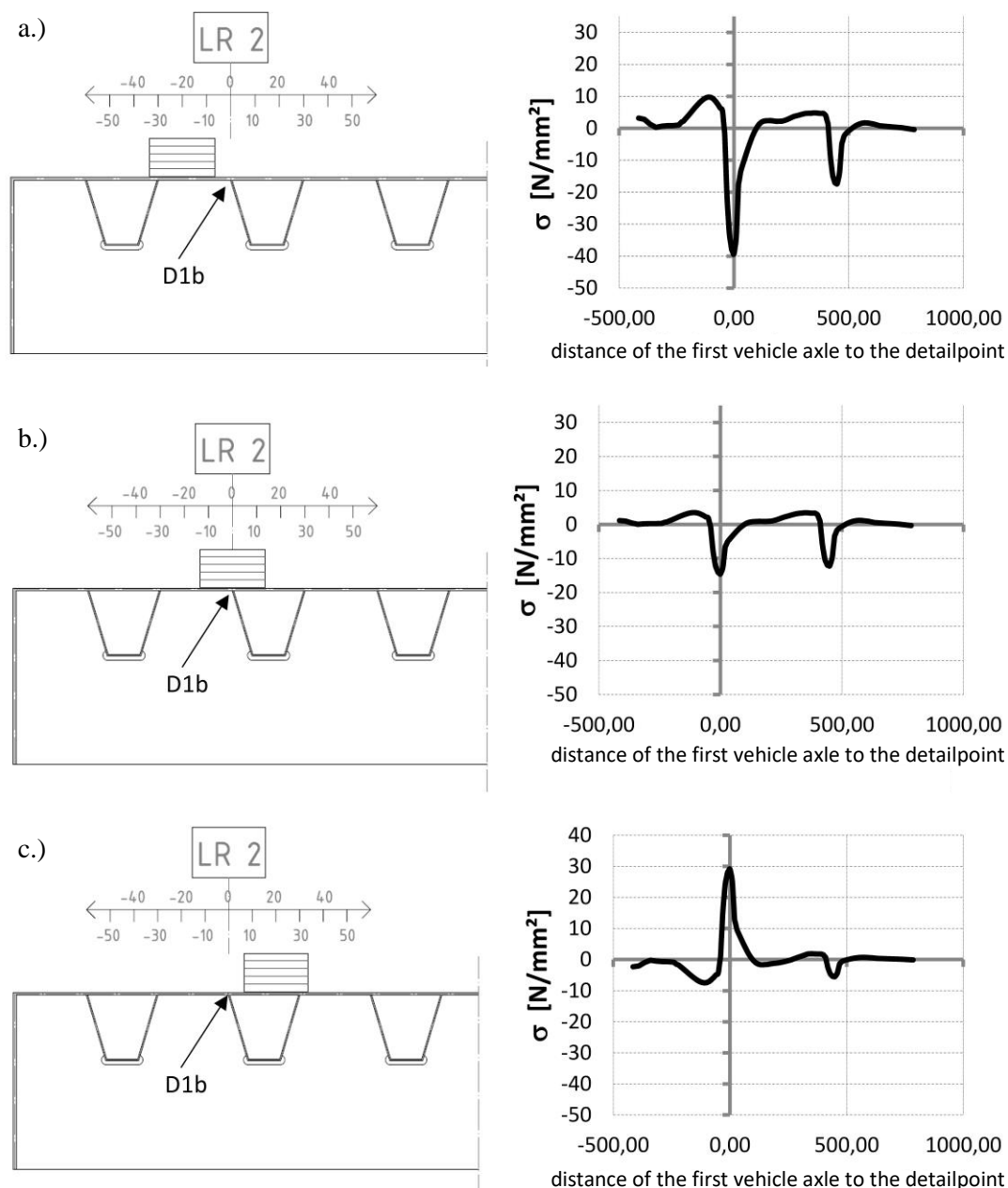
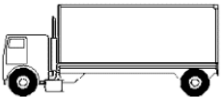
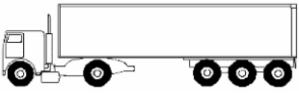
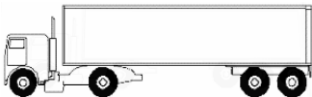


Figure 168: stress history curves for vehicle type T1 for transverse position a.) $x = -20\text{cm}$, b.) $x = 0\text{cm}$ and c.) $x = +20\text{cm}$ referring to detail D1b, Model B

The 45 stress history curves have to be strung together under consideration of the lorry percentage according to fatigue load model FLM-4 (see Figure 24 in Section 2.5.2). Table 13 summarises these 45 transverse positions of the 5 lorry types with their number of crossings (n_i) relating to a defined frequency distribution (h_i see Figure 166.a) and under consideration of the lorry percentage of FLM-4 (n_{Ti}) for long distance routes (see Figure 24), such as highways. In the table below, the data are plotted for altogether 100,000 lorries.

Table 13: summary of vehicle positions in transverse bridge direction for FLM 4 and lane frequency distribution LFT III (100,000 lorries in total)

vehicle type	Vehicle Position x_i [cm]	n_i	h_i	n_i
T1 	-40	(20 %) 20000	0.04	800
	-30		0.05	1000
	-20		0.1	2000
	-10		0.18	3600
	0		0.26	5200
	10		0.18	3600
	20		0.1	2000
	30		0.05	1000
	40		0.04	800
T2 	-40	(5%) 5000	0.04	200
	-30		0.05	250
	-20		0.1	500
	-10		0.18	900
	0		0.26	1300
	10		0.18	900
	20		0.1	500
	30		0.05	250
	40		0.04	200
T3 	-40	(50%) 50000	0.04	2000
	-30		0.05	2500
	-20		0.1	5000
	-10		0.18	9000
	0		0.26	13000
	10		0.18	9000
	20		0.1	5000
	30		0.05	2500
	40		0.04	2000
T4 	-40	(15%) 15000	0.04	600
	-30		0.05	750
	-20		0.1	1500
	-10		0.18	2700
	0		0.26	3900
	10		0.18	2700
	20		0.1	1500
	30		0.05	750
	40		0.04	600
T5 	-40	(10%) 10000	0.04	400
	-30		0.05	500
	-20		0.1	1000
	-10		0.18	1800
	0		0.26	2600
	10		0.18	1800
	20		0.1	1000
	30		0.05	500
	40		0.04	400

With Rain flow method as cycle counting concept the stress ranges and their occurring number of cycles are dependent on the chronology of the stress history curves from the individual lorry types and their different transverse positions. Therefore, a simulation of the vehicle crossings with a random chronology and a high number of total vehicles was necessary. As Table 13 already showed, an overall vehicle's number of 100,000 was chosen for the simulations and it could be confirmed that this number is enough to get sufficient results by using a random sequence for the 45 stress history curves.

Figure 169 illustrates for example a cut out of the total stress history assembly of the 100,000 crossings with 5 lorry types and their different positions in transverse bridge direction. In this short sequence first vehicle type T3 crosses the bridge deck at transverse position $x=+20\text{cm}$ and is followed by vehicle type T1 at $x=-10\text{cm}$ and vehicle type T5 at $x=+20\text{cm}$. The maximum occurring stress range in this cut out, when ignoring all other stresses except the plotted ones in the picture, is made up of $\sigma_{T1,-1}$ due to lorry type T1 at $x=-10\text{cm}$ (σ_{\min} , lane axis -1) and $\sigma_{T5,+2}$ due to lorry type T5 at $x=+20\text{cm}$ (σ_{\max} , lane axis +2).

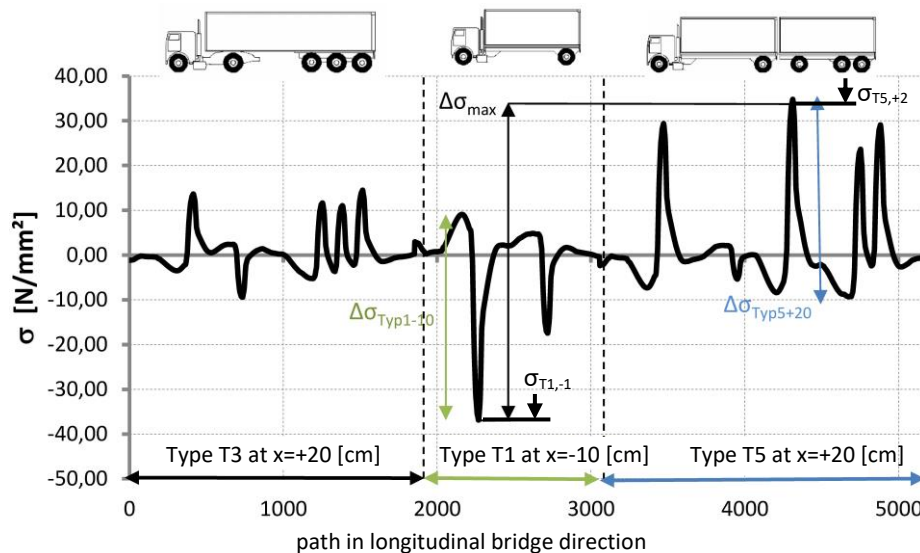


Figure 169: cut out of assembled stress history curve for 100,000 lorry crossings (FLM 4)

The same procedure of cycle counting with Rain flow method was done for the whole stress history curve referring to altogether 100,000 lorries and a damage equivalent constant amplitude stress range $\Delta\sigma_{e,III}$ has been determined. Again, $\Delta\sigma_{e,III}$ is based on $n_e = 100,000$ stress cycles. The results of this heavy traffic simulation referring to detail D1b under consideration of driving characteristics and realistic axle geometries are presented in Section 4.9 for the analysed models B and C with trough ribs.

4.8. Results of numerical calculations due to consideration of realistic axle geometries

The results of the numerical simulations of the heavy vehicle traffic at the FEM-models A, B and C (see Section 3.2) referring to the analysed details D1a, D1b and D2 (see Section 2.4) under consideration of realistic axle geometries are presented in this Section. The basis is always the stress range spectrum of the analysed detail with centric track configuration and axle geometries based on Eurocode (FLM 4, FLM 4*, see Section 3.4). The relevant stress ranges have been scaled by using the appropriate influence line in transverse bridge direction (see Section 4.5). The realistic axle geometries are illustrated in Figure 137 in Section 4.3.4.

The following list gives an overview of the results according to the calculations referring to the consideration of realistic axle geometries and its influence in fatigue assessment at orthotropic steel decks:

- Model A: orthotropic bridge deck with open longitudinal ribs and cross girder interval $e_{QT} = 2.0\text{m}$
Results for detail D1a in Section 4.8.1.1 and results for detail D2 in Section 4.8.1.2
- Model B: orthotropic bridge deck with trough ribs and cross girder interval $e_{QT} = 2.0\text{m}$
Results for detail D1a in Section 4.8.2.1, detail D1b in Section 4.8.2.2 and detail D2 in Section 4.8.2.3
- Model C: orthotropic bridge deck with trough ribs and cross girder interval $e_{QT} = 4.0\text{m}$
Results for detail D1a in Section 4.8.3.1, detail D1b in Section 4.8.3.2 and detail D2 in Section 4.8.3.3

4.8.1. Model A

This Section presents the results of considering realistic axle geometries of heavy vehicles at FEM-model A. A detailed description of FEM-model A can be found in Section 3.2.1.

4.8.1.1. Detail D1a

a.) Reference case: fatigue load model FLM 4 and centric wheel position

A detailed explanation of detail D1a can be found in Section 2.4.2. The calculated stress range spectrum is presented in Section 3.4.2.1, Figure 88. This reference stress range spectrum is determined due to fatigue load model FLM 4 (see Section 2.5.2, Figure 24) and is related to a centric track configuration of all wheel loads at LR-3 (see Figure 107 in Section 3.4.4). Figure 170 shows again this reference stress range spectrum. In addition, the stress ranges are coloured according to the individual lorry types from fatigue load model FLM 4 as it is shown in the legend on the right side of the picture. The following notation additionally defines the axle number within a vehicle and its axle/wheel type for every stress range.

axle number 2 (starting at the leading axle)
 For example, the notation of the first, highest stress range $\Delta\sigma_1$: T3-2-B
 lorry type T3 Axle/wheel type B

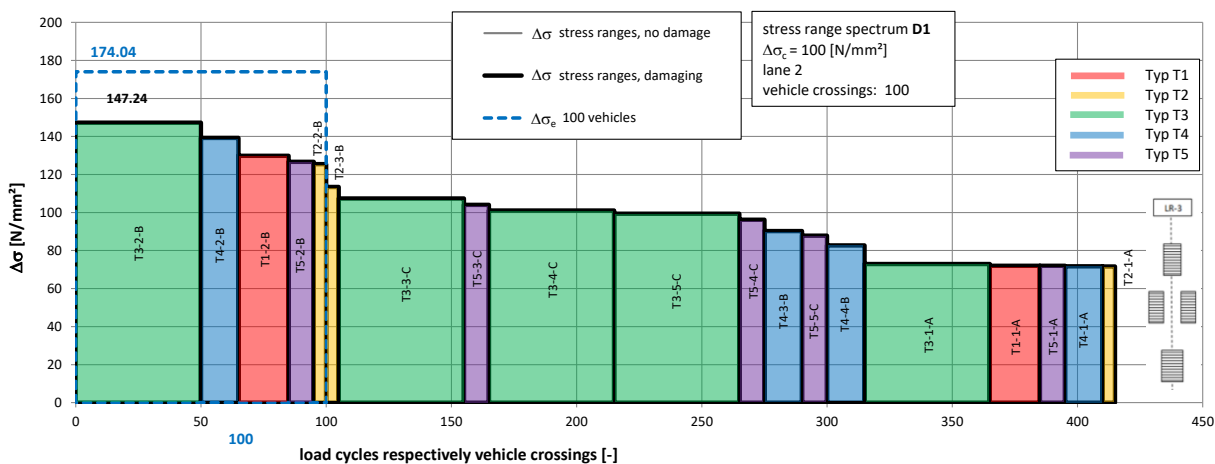


Figure 170: Model A, detail D1a at LR-3 with centric wheel position: stress range spectrum for a centric track configuration due to FLM 4

b.) Centric lorry crossings with eccentric wheel position (FLM 4-mod)

For consideration of the realistic axle geometries, based on Figure 137 in Section 4.3.4, the appropriate stress ranges from Figure 170 were scaled with the corresponding parameter η due to a lateral shift of the single wheeled axles. Additional calculations showed that a lateral shift of the single wheeled axle types A and C gives the most conservative result for detail D1a at Model A. That means that the axis of wheel type B of each lorry is equal to the axis of LR-3. According to the measured wheel geometries (see Section 4.3) a lateral shift of the wheel types A and C with $e = 10\text{cm}$ is necessary. Therefore the parameter η was selected at $x = -10\text{cm}$ from the lateral influence line for the single wheeled axles that is plotted in Figure 171 ($\eta = (-0.92) \cdot (-1) = 0.92$).

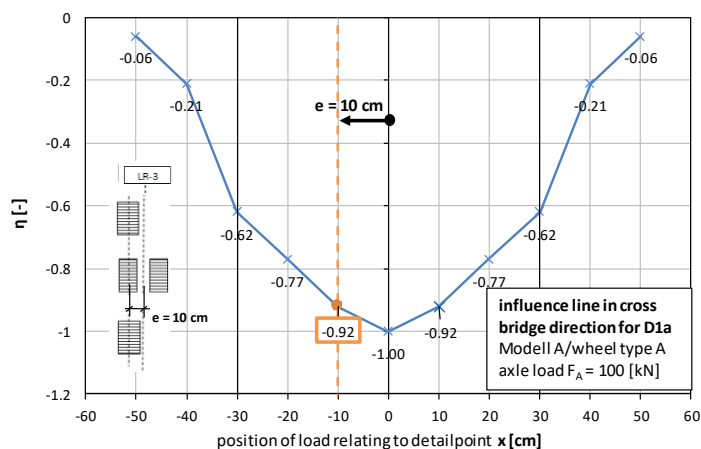


Figure 171: Model A – detail D1a at LR-3: influence line in transverse bridge direction for single wheeled axles (axle type A and C), symmetrical to the vertical axis at $x = 0$

The resulting stress range spectrum for detail D1a at Model A is presented in Figure 172.

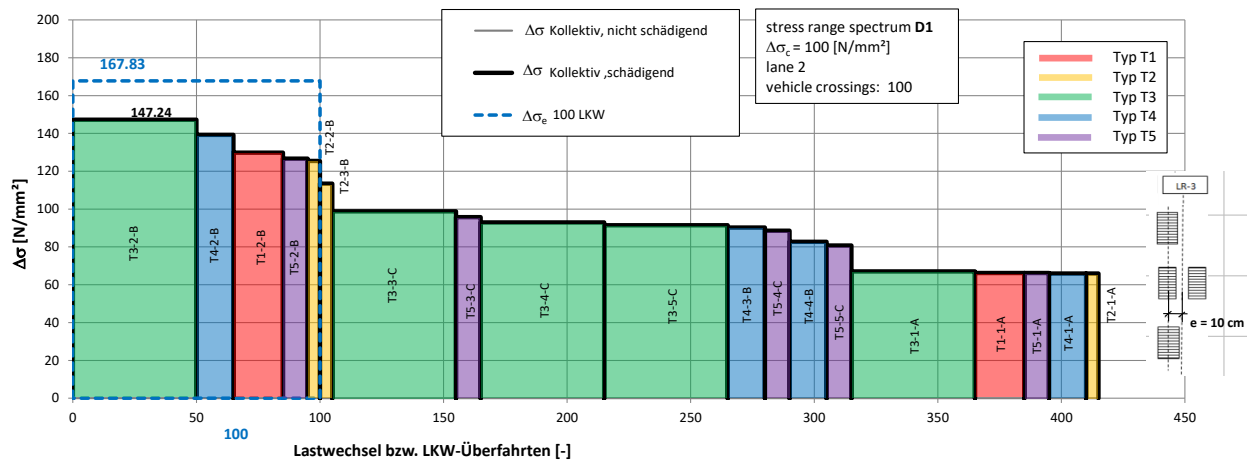


Figure 172: Model A, detail D1a at LR-3: stress range spectrum under consideration of realistic axle geometries due to FLM 4-mod

A comparison of the calculated damage equivalent stress ranges $\Delta\sigma_e$ is shown in Table 14:

Table 14: Model A – detail D1a at LR-3: comparison of $\Delta\sigma_e$ for $n_e = 100$ lorry crossings due to centric lorry position

	centric wheel position, FLM 4	eccentric wheel position, FLM 4-mod
	$\Delta\sigma_{e,I}$	$\Delta\sigma_{e,II}$
$\Delta\sigma_e$ [N/mm ²]	174.04 (1.0)	167.83 (0.96)

As it can be seen in Table 14 the consideration of realistic axle geometries causes at detail D1a a reduction of the damage equivalent stress range $\Delta\sigma_e$ of 4% referring to Model A.

The damage parts of the individual lorry types are equal for both stress range spectra in Figure 170 and Figure 172. This damage parts are shown in Figure 228 in Section 4.11.1.1, where lorry type T3 causes the maximum damage in the analysed detail with 65%.

4.8.1.2. Detail D2

a.) Reference case: fatigue load model FLM 4 and centric wheel position

Section 2.4.4 gives a detailed explanation of detail D2. The reference stress range spectrum is presented in Section 3.4.2.2, Figure 93. This reference stress range spectrum is determined due to fatigue load model FLM 4 (see Section 2.5.2, Figure 24) and is related to a centric track configuration of all wheel loads at LR-3 (see Figure 83). This reference stress range spectrum is again shown in Figure 173. In addition, the stress ranges are coloured according to the individual lorry types from fatigue load model FLM 4 as it is shown in the legend on the right side of the picture.

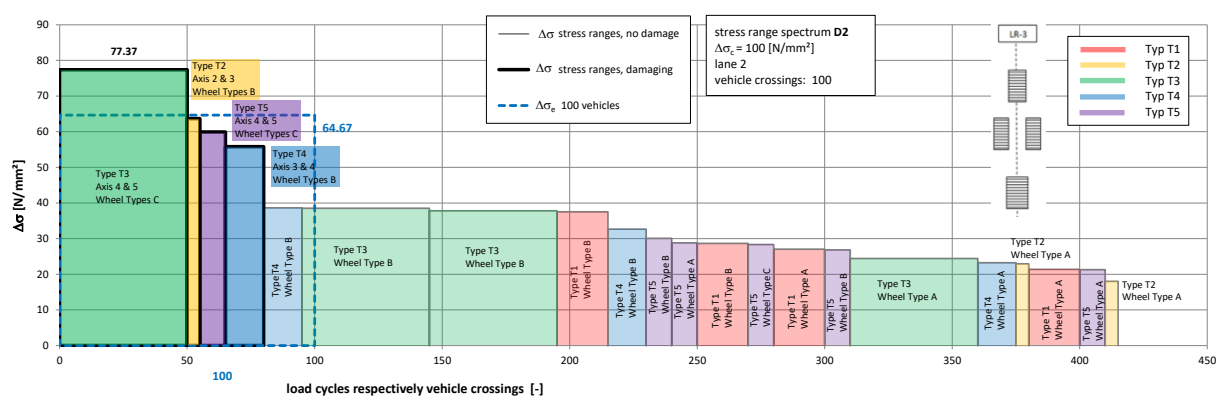


Figure 173: Model A, detail D2 at LR-3 with centric wheel position: stress range spectrum for a centric track configuration due to FLM 4

b.) Centric lorry crossing with eccentric wheel position (FLM 4-mod)

For considering realistic axle geometries, based on Figure 137, the appropriate stress ranges from Figure 173 were scaled with the corresponding parameter η due to a lateral shift of the single wheeled axles. A lateral shift of the single wheeled axle types A and C gives the most conservative result for detail D2 at Model A, which was confirmed by additional calculations. According to the measured wheel geometries (see Section 4.3) a lateral shift of the wheel types A and C with $e = 10\text{cm}$ is necessary. The accurate value is plotted in Figure 174 ($\eta = (-1.16) \cdot (-1) = 1.16$).

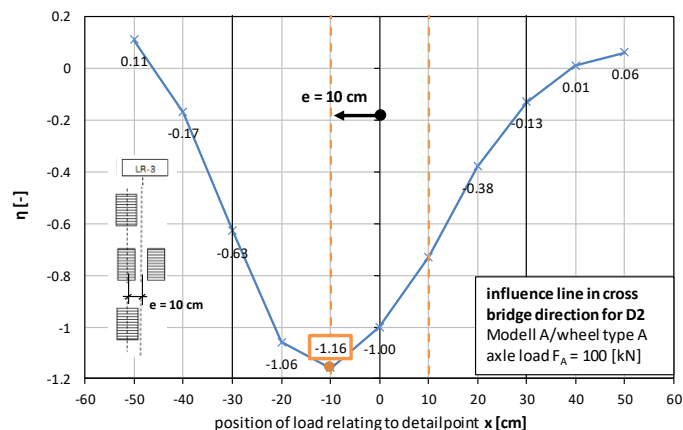


Figure 174: Model A – detail D2 at LR-3: influence line in transverse bridge direction for single wheeled axles

The resulting stress range spectrum for detail D2 at Model A is presented in Figure 175.

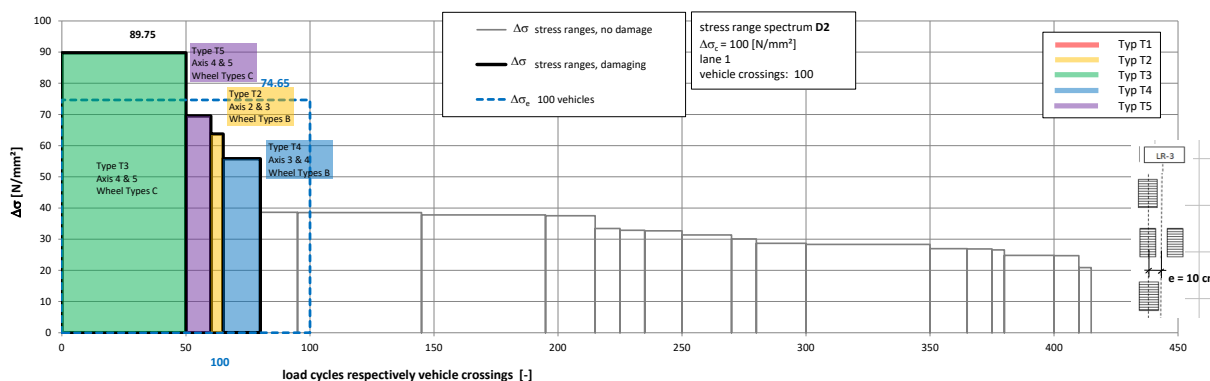


Figure 175: Model A – detail D2 at LR-3: stress range spectrum under consideration of realistic axle geometries due to FLM 4-mod

A comparison of the damage equivalent stress ranges $\Delta\sigma_e$ is shown in Table 15:

Table 15: Model A – detail D2 at LR-3: comparison of $\Delta\sigma_e$ for $n_e = 100$ lorry crossings due to centric lorry position

	centric wheel position – FLM 4	eccentric wheel position – FLM 4-mod
	$\Delta\sigma_{e,I}$	$\Delta\sigma_{e,II}$
$\Delta\sigma_e$ [N/mm ²]	64.67 (1.0)	74.65 (1.15)

By comparing the results in Table 15 it can be seen that the consideration of realistic axle geometries causes at detail D2 an increase of the damage equivalent stress range $\Delta\sigma_e$ of 15% referring to Model A. There is no significant difference regarding to the damage parts of the individual lorry types by comparing the stress range spectra in Figure 173 and Figure 175. In both cases, lorry type T3 causes the maximum damage with 85.6% (referring to Figure 173) and 86.6% (referring to Figure 175).

4.8.2. Model B

This Section presents the results of considering realistic axle geometries of heavy vehicles at FEM-model B. A detailed description of FEM-model B can be found in Section 3.2.2

4.8.2.1. Detail D1a

a.) Reference case: fatigue load model FLM 4 and centric wheel position

Section 2.4.2 shows a detailed explanation of detail D1a. The reference stress range spectrum is presented in Section 3.4.3.1, Figure 97. This reference stress range spectrum is calculated due to fatigue load model FLM 4 (see Section 2.5.2, Figure 24) and is related to a centric track configuration of all wheel loads at the web of LR-2 (see Figure 94 in Section 3.4.3) This reference stress range spectrum is again shown in Figure 176. Additionally, the stress ranges are coloured according to the lorry types from fatigue load model FLM 4 as it is shown in the legend on the right side of the picture.

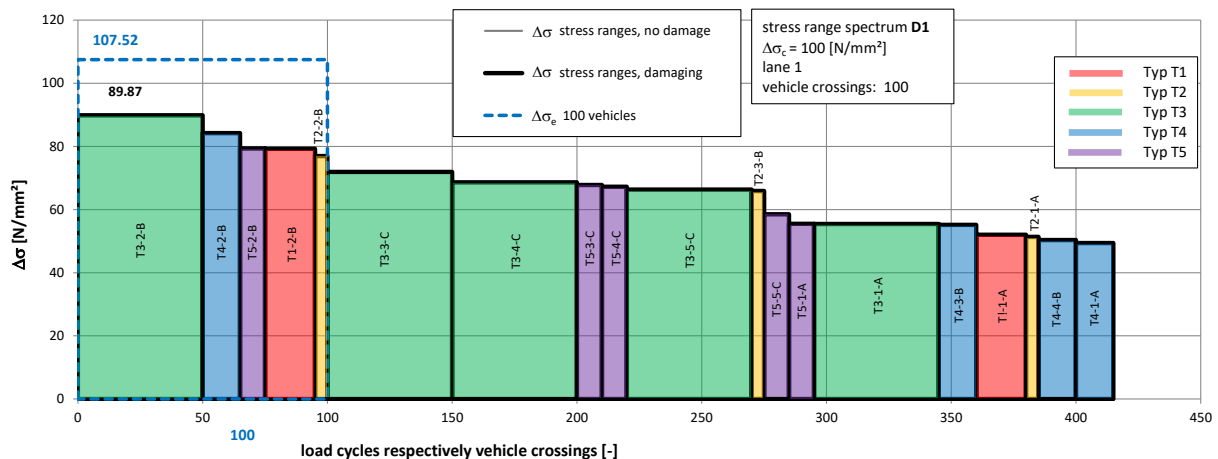


Figure 176: Model B – detail D1a at LR-2 with centric wheel position: stress range spectrum for a centric track configuration due to FLM 4

b.) Centric lorry crossing with eccentric wheel position (FLM 4-mod)

For consideration of realistic axle geometries, based on Figure 137, the appropriate stress ranges from Figure 176 were scaled with the corresponding parameter η due to a lateral shift of the single wheeled axles. Additional calculations showed that a lateral shift of the single wheeled axle types A and C gives the most conservative result for detail D1a at Model B. According to the measured wheel geometries (see Section 4.3) a lateral shift of the wheel types A and C with $e = 10\text{cm}$ is necessary. Therefore the parameter η was selected at $x = -10\text{cm}$ from the lateral influence line for single wheeled axles that is plotted in Figure 171 ($\eta = (-0.92) \cdot (-1) = 0.92$).

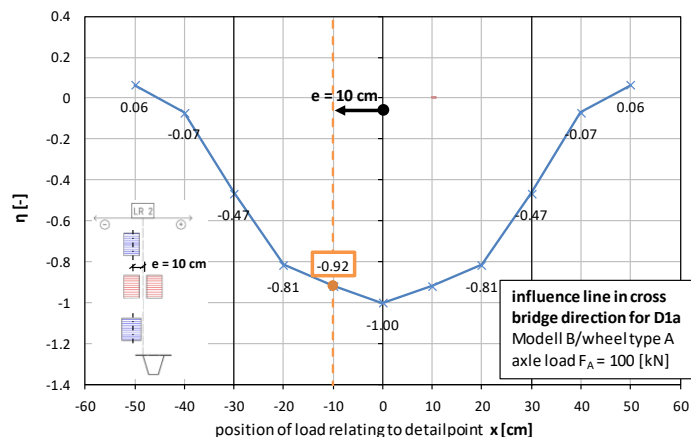


Figure 177: Model B – D1a influence line in cross bridge direction for single wheeled axles

The resulting stress range spectrum for detail D1a at Model B is presented in Figure 178.

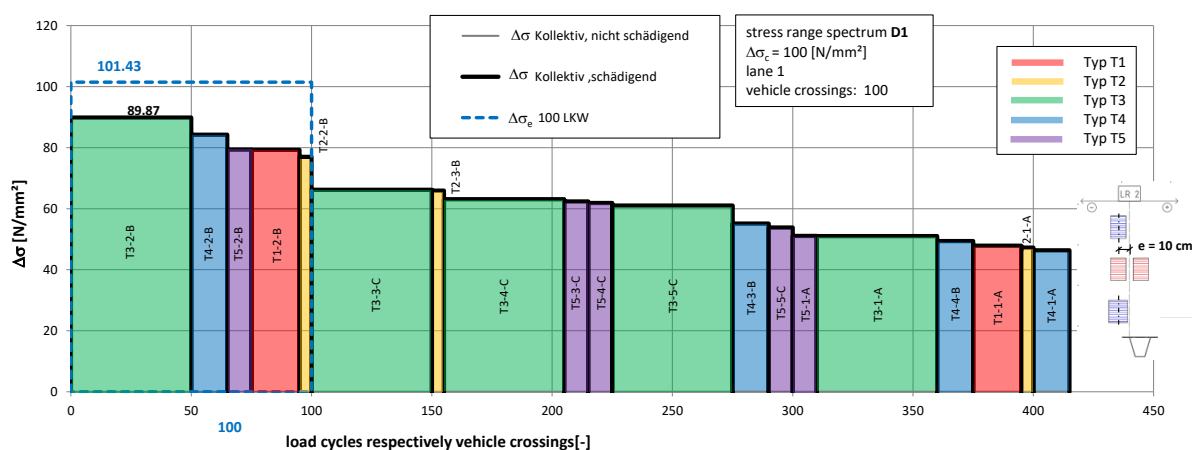


Figure 178: Model B – detail D1a at LR-2: stress range spectrum under consideration of realistic axle geometries due to FLM 4

A comparison of the damage equivalent stress ranges $\Delta\sigma_e$ is shown in Table 16:

Table 16: Model B – detail D1a at LR-2: comparison of $\Delta\sigma_e$ for $n_e = 100$ lorry crossings due to centric lorry position

	centric wheel position – FLM 4 $\Delta\sigma_{e,I}$	eccentric wheel position – FLM 4-mod $\Delta\sigma_{e,II}$
$\Delta\sigma_e$ [N/mm ²]	107.52 (1.0)	101.43 (0.94)

As shown in Table 16 the consideration of realistic axle geometries causes at detail D1a a reduction of the damage equivalent stress range $\Delta\sigma_e$ of 6% referring to Model B. The damage parts of the individual

lorry types under consideration of realistic axle geometries are nearly identical to the one with centric track configuration. Lorry type T3 causes the maximum damage in the detail in both cases. Referring to the stress range spectrum in Figure 176, lorry type T3 causes 68.2% (see Figure 229 in Section 4.11.1.2) of the whole damage. Referring to the spectrum in Figure 178, lorry type T3 causes 65.4% of the whole damage. The damage distribution of the lorry types T1, T2, T4 and T5 doesn't differ significantly.

4.8.2.2. Detail D1b

a.) Reference case: fatigue load model FLM 4 and centric wheel position

A detailed explanation of detail D1b can be found in Section 2.4.3. Section 3.4.3.2, Figure 100 presents the calculated reference stress range spectrum which has been determined due to fatigue load model FLM 4 (see Section 2.5.2, Figure 24) and under consideration of a centric track configuration of all wheel loads at the web of LR-2 (see Figure 94 in Section 3.4.3). This reference stress range spectrum is again shown in Figure 179. As it can be seen in the picture, no fatigue damage is occurring due to a centric wheel position of all axle/wheel types under consideration of the cut of limit $\Delta\sigma_L$ according to the appropriate S-N curve ($\Delta\sigma_c = 100 \text{ N/mm}^2$; $\Delta\sigma_L \approx 40 \text{ N/mm}^2$).

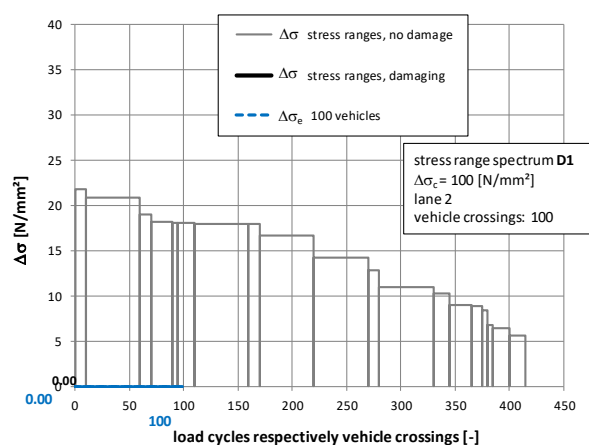


Figure 179: Model B – detail D1b at the web of LR-2: stress range spectrum for a centric track configuration due to FLM 4

b.) Centric lorry crossing with eccentric wheel position (FLM 4-mod)

Realistic axle geometries were considered based on Figure 137 in Section 4.3.4. A lateral shift of the double wheeled axles was considered and the appropriate stress ranges from Figure 179 were scaled with the corresponding parameter η . The most conservative result for detail D1b at Model B are given due to a lateral shift of the double wheeled axle type B which could be confirmed by additional calculations. According to the measured wheel geometries (see Section 4.3) a lateral shift of the wheel type B with $e = 10\text{cm}$ is necessary. Therefore, the parameter η was selected at $x = -10\text{cm}$ from the lateral influence line for double wheeled axles that is plotted in Figure 180 ($\eta = (-1.32) \cdot (-1) = 1.32$).

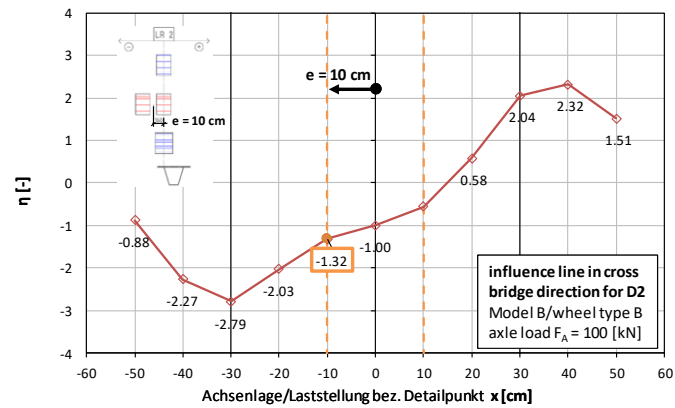


Figure 180: Model B – detail D1b at LR-2: influence line in transverse bridge direction for double wheeled axles

The resulting stress range spectrum for detail D1b at Model B is represented in Figure 181.

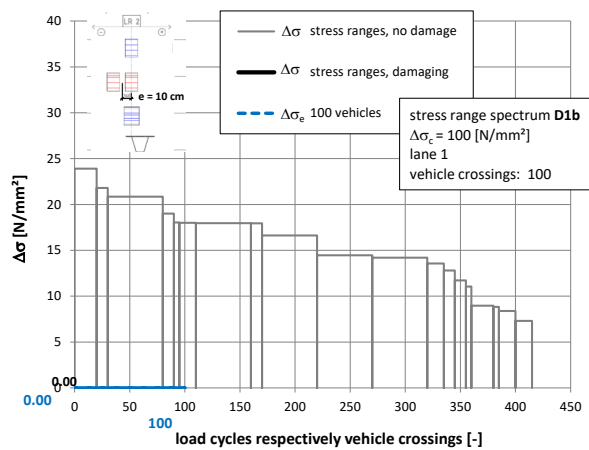


Figure 181: Model B – detail D1b at LR-2: stress range spectrum under consideration of realistic axle geometries due to FLM 4-mod

Also a consideration of realistic axle geometries gives no damage at detail D1b as it is shown in Figure 181 and a calculation of $\Delta\sigma_e$ is not necessary.

4.8.2.3. Detail D2

a.) Reference case: fatigue load model FLM 4 and centric wheel position

A detailed explanation of detail D2 can be found in Section 2.4.4. The reference stress range spectrum is presented in Section 3.4.3.3, Figure 103. Fatigue load model FLM 4 (see Section 2.5.2, Figure 24) has been considered for the determination of this reference stress range spectrum which relates to a centric track configuration of all wheel loads at LR-2 (see Figure 94 in Section 3.4.3). Figure 182 shows again this reference stress range spectrum. In addition, the stress ranges are coloured according to the lorry types from fatigue load model FLM 4 as it is shown in the legend on the right side of the picture.

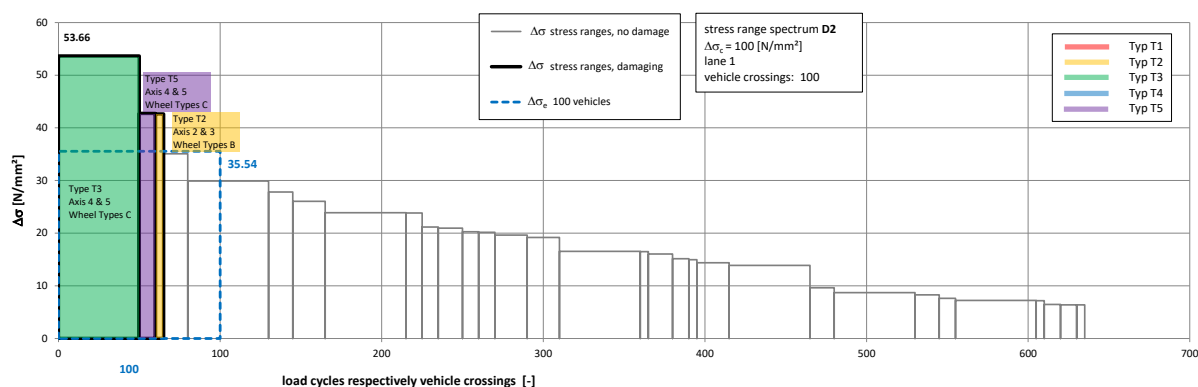


Figure 182: Model B – detail D2 at LR-2: stress range spectrum for a centric track configuration due to FLM 4

b.) Centric lorry crossing with eccentric wheel position (FLM 4-mod)

The realistic axle geometries are based on Figure 137 in Section 4.3.4. Due to a lateral shift of the double wheeled axle, the appropriate stress ranges from Figure 182 were scaled with the corresponding parameter η . Additional calculations showed the most conservative result with a lateral shift of the double wheeled axle type B for detail D2 at Model B. According to the measured wheel geometries (see Section 4.3) a lateral shift of the wheel type B with $e = 10\text{cm}$ is necessary. Therefore the parameter η , plotted in Figure 183, leads to: $(\eta = (-0.98) \cdot (-1) = 0.98)$.

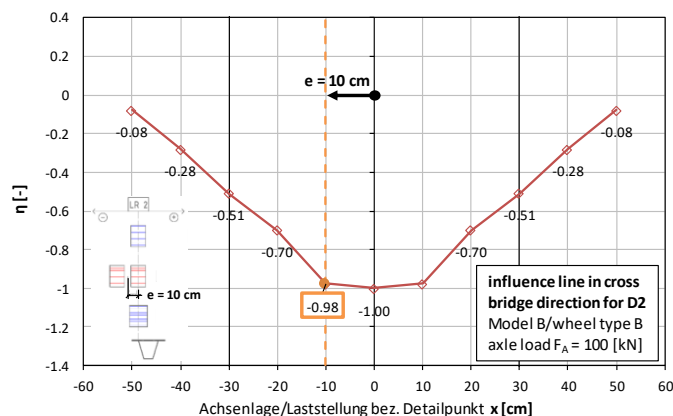


Figure 183: Model B – detail D2 at LR-2 influence line in transverse bridge direction for double wheeled axle

The resulting stress range spectrum for detail D2 at Model B is presented in Figure 184.

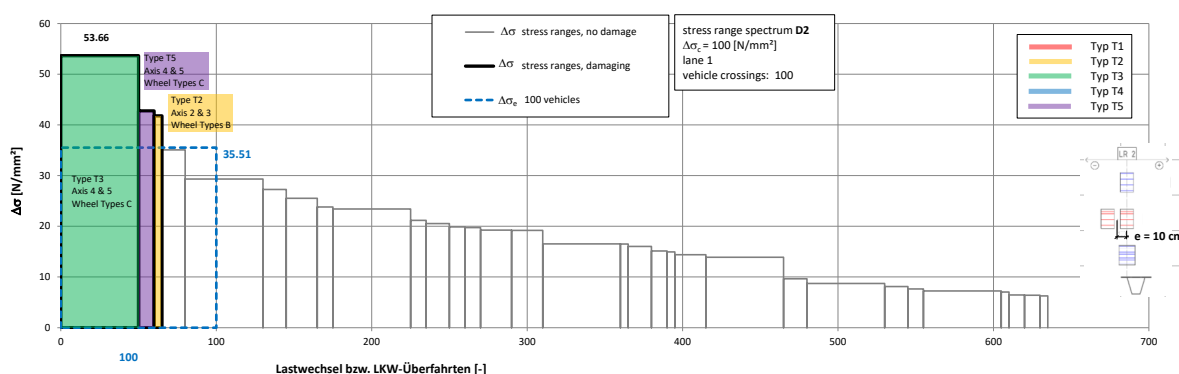


Figure 184: Model B – detail D2 at LR-2: stress range spectrum under consideration of realistic axle geometries due to FLM 4-mod

A comparison of the damage equivalent stress ranges $\Delta\sigma_e$ is shown in Table 17:

Table 17: Model B – detail D2 at LR-2: comparison of $\Delta\sigma_e$ for $n_e = 100$ lorry crossings due to centric lorry position

	centric wheel position – FLM 4 $\Delta\sigma_{e,I}$	eccentric wheel position – FLM 4-mod $\Delta\sigma_{e,II}$
$\Delta\sigma_e$ [N/mm ²]	35.54 (1.0)	35.51 (1.0)

As it can be seen in Table 17 the consideration of realistic axle geometries causes at detail D2 nearly no effect to the damage equivalent stress range $\Delta\sigma_e$ referring to Model B. The damage parts of the individual lorry types are practically equal and are shown in Figure 232 in Section 4.11.2.2. The maximum damage is caused by lorry type T3 with 91%.

4.8.3. Model C

This Section presents the results of considering realistic axle geometries of heavy vehicles at FEM-model C. A detailed description of FEM-model C can be found in Section 3.2.3.

4.8.3.1. Detail D1a

a.) Reference case: fatigue load model FLM 4 and centric wheel position

Section 2.4.2 gives a detailed explanation of detail D1a. Figure 107 in Section 3.4.4.1 shows the reference stress range spectrum. For the calculation of this reference stress range spectrum fatigue load model FLM 4 (see Section 2.5.2, Figure 24) was considered which was related to a centric track configuration of all wheel loads at the web of LR-2 (see Figure 104 in Section 3.4.4). This reference stress range spectrum is again shown in Figure 185. In addition, the colours of the individual stress ranges indicate the lorry types from fatigue load model FLM 4 as it is shown in the legend on the right side of the picture (for a detailed notation see Section 4.8.1.1).

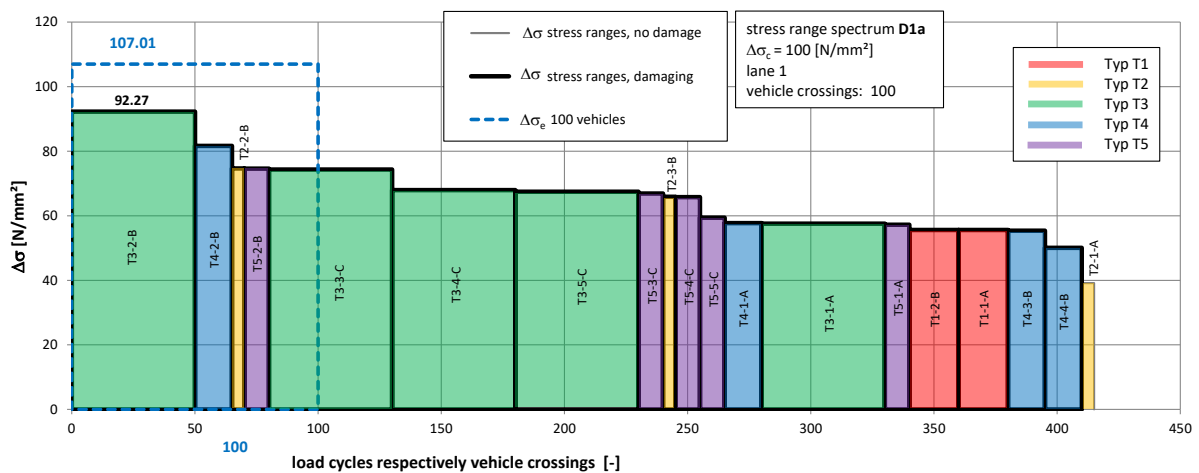


Figure 185: Model C – detail D1a at LR-2 with centric wheel position: stress range spectrum for a centric track configuration due to FLM 4

b.) Centric lorry crossing with eccentric wheel position (FLM 4-mod)

Based on Figure 137 in Section 4.3.4, the realistic axle geometries were considered. The appropriate stress ranges from Figure 185 were scaled with the corresponding parameter η due to a lateral shift of the single wheeled axles. Via additional calculations, a lateral shift of the single wheeled axle types A and C could be confirmed as the most conservative result for detail D1a at Model C. A lateral shift of the wheel types A and C with $e = 10\text{cm}$ is necessary according to the measured wheel geometries (see Section 4.3). Therefore the parameter η was selected at $x = -10\text{cm}$ from the lateral influence line for single wheeled axles that is plotted in Figure 186 ($\eta = (-0.85) \cdot (-1) = 0.85$).

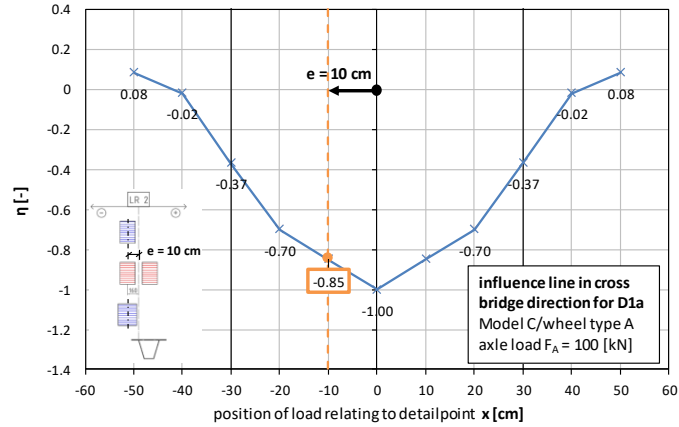


Figure 186: Model C – detail D1a at LR-2 influence line in transverse bridge direction for single wheeled axles

The resulting stress range spectrum for detail D1a at Model C is presented in Figure 187.

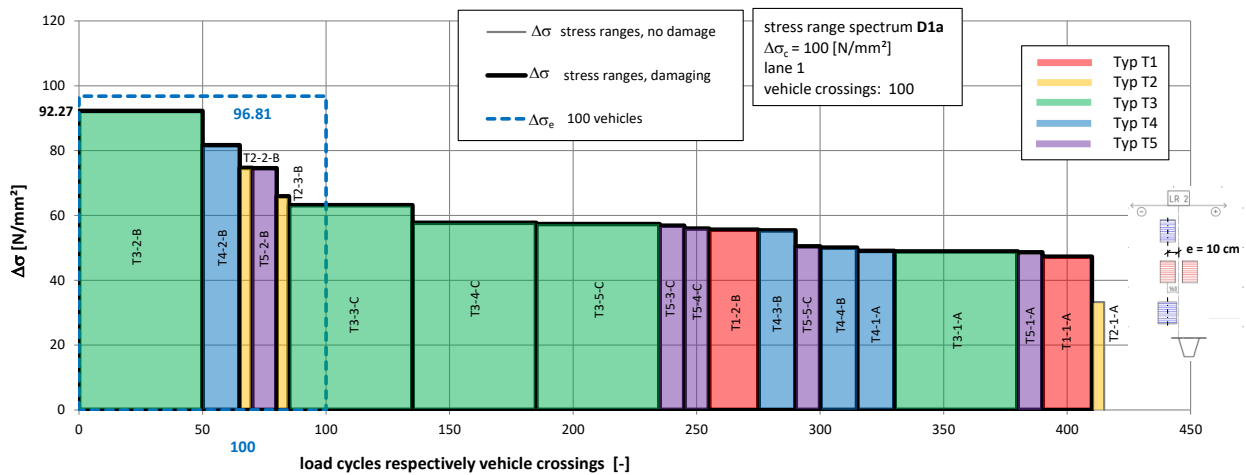


Figure 187: Model C – detail D1a at LR-2: stress range spectrum under consideration of realistic axle geometries due to FLM 4-mod

A comparison of the damage equivalent stress ranges $\Delta\sigma_e$ is shown in Table 18:

Table 18: Model C – detail D1a at LR-2: comparison of $\Delta\sigma_e$ for $n_e = 100$ lorry crossings due to centric lorry position

	centric wheel position – FLM 4 $\Delta\sigma_{e,I}$	eccentric wheel position – FLM 4-mod $\Delta\sigma_{e,II}$
$\Delta\sigma_e$ [N/mm ²]	107.01 (1.0)	96.81 (0.90)

As it can be seen in Table 18 the consideration of realistic axle geometries causes at detail D1a a reduction of the damage equivalent stress range $\Delta\sigma_e$ of 10% referring to Model C.

There is less difference at the damage parts of the individual lorry types referring to the spectra with and without realistic axle geometries. In both cases the maximum damage in the detail is caused by lorry type T3 (see Figure 230 in Section 4.11.1.3). Referring to the stress spectrum in Figure 185, lorry type T3 causes 74.9% of the whole damage and referring to the spectrum in Figure 187, lorry type T3 causes 72.8% of the whole damage.

4.8.3.2. Detail D1b

a.) Reference case: fatigue load model FLM 4 and centric wheel position

A detailed explanation of detail D1b can be found in Section 2.4.3. The reference stress range spectrum is presented in Section 3.4.4.2, Figure 110. This reference stress range spectrum is determined due to fatigue load model FLM 4 (see Section 2.5.2, Figure 24) and is related to a centric track configuration of all wheel loads at the web of LR-2 (see Figure 104 in Section 3.4.4). Figure 188 shows again this reference stress range spectrum. As it can be seen in the picture, no fatigue damage is occurring due to a centric wheel position of all axle/wheel types under consideration of the cut of limit $\Delta\sigma_L$ according to the appropriate S-N curve ($\Delta\sigma_c = 100 \text{ N/mm}^2$; $\Delta\sigma_L \approx 40 \text{ N/mm}^2$).

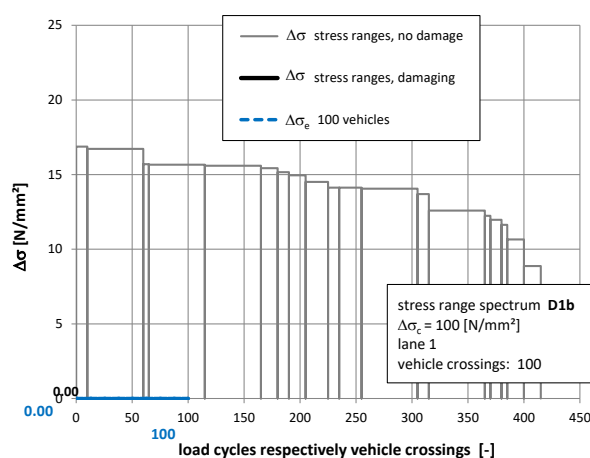


Figure 188: Model C – detail D1b at LR-2: stress range spectrum for a centric track configuration due to FLM 4

b.) Centric lorry crossing with eccentric wheel position (FLM 4-mod)

Realistic axle geometries were considered based on Figure 137 in Section 4.3.4. A scaling of the appropriate stress ranges from Figure 188 with the corresponding parameter η has been done. A lateral shift of the double wheeled axles was considered where additional calculations showed the most conservative result for detail D1b at Model C with a lateral shift of the double wheeled axle type B. Therefore, a lateral shift of the wheel type B with $e = 10\text{cm}$ according to the measured wheel geometries (see Section 4.3) was necessary. The parameter η was selected at $x = -10\text{cm}$ from the lateral influence line for double wheeled axles that is plotted in Figure 189 ($\eta = (-1.12) \cdot (-1) = 1.12$).

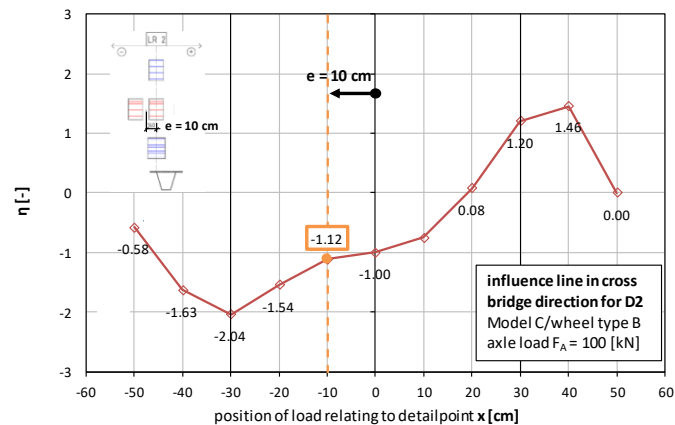


Figure 189: Model C – detail D1b at LR-2: influence line in transverse bridge direction for double wheeled axles

The resulting stress range spectrum for detail D1b at Model C is presented in Figure 190.

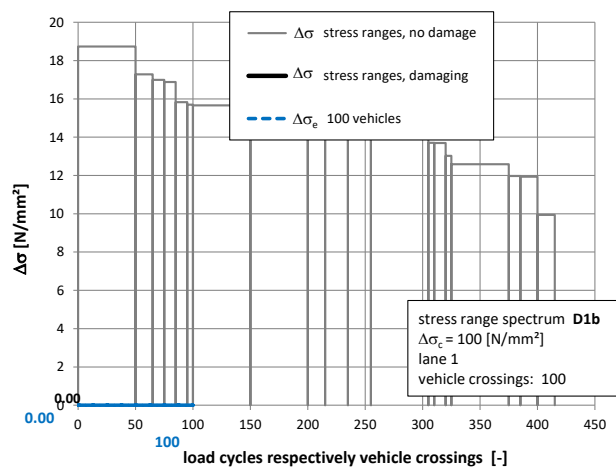


Figure 190: Model C – detail D1b at LR-2: stress range spectrum under consideration of realistic axle geometries due to FLM 4-mod

Also a consideration of realistic axle geometries gives no damage at detail D1b as it is shown in Figure 190 and a calculation of $\Delta\sigma_e$ is not necessary.

4.8.3.3. Detail D2

a.) Reference case: fatigue load model FLM 4 and centric wheel position

Section 2.4.4 gives a detailed explanation of detail D2. Figure 113 in Section 3.4.4.3 presents the reference stress range spectrum which has been calculated due to fatigue load model FLM 4 (see Section 2.5.2, Figure 24). This reference stress range spectrum is related to a centric track configuration of all wheel loads at the web of LR-2 (see Figure 104 in Section 3.4.4). Figure 191 shows again this reference stress range spectrum. In addition, the stress ranges are coloured according to the lorry types from fatigue load model FLM 4 as it is shown in the legend on the right side of the picture.

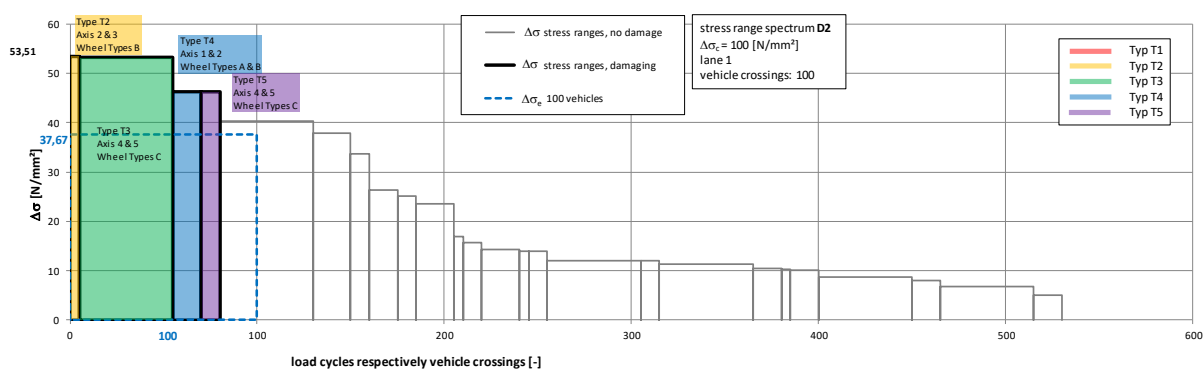


Figure 191: Model C – detail D2 at LR-2: stress range spectrum for a centric track configuration due to FLM 4

b.) Centric lorry crossing with eccentric wheel position (FLM 4-mod)

For consideration of realistic axle geometries, based on Figure 137 in Section 4.3.4, the appropriate stress ranges from Figure 191 were scaled with the corresponding parameter η due to a lateral shift of the double wheeled axle. Additional calculations showed that a lateral shift of the double wheeled axle type B gives the most conservative result for detail D2 at Model C. According to the measured wheel geometries (see Section 4.3) a lateral shift of the wheel type B with $e = 10\text{cm}$ is necessary. Therefore the parameter η was selected at $x = +10\text{cm}$ from the lateral influence line for single wheeled axles that is plotted in Figure 192 ($\eta = (-1.08) \cdot (-1) = 1.08$).

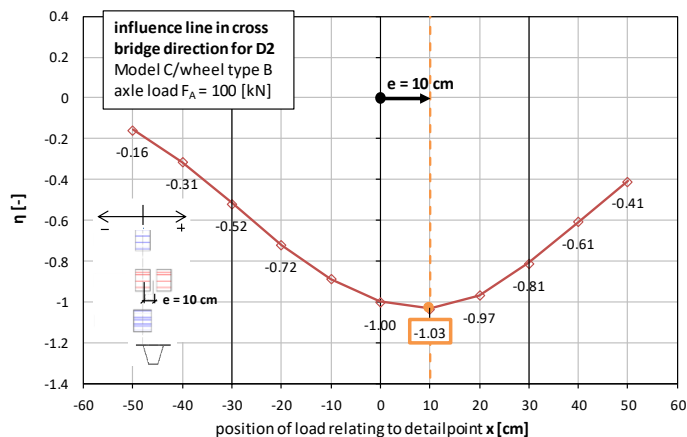


Figure 192: Model C – detail D2 at LR-2: influence line in transverse bridge direction for double wheeled axle

The resulting stress range spectrum for detail D2 at Model C is presented in Figure 193.

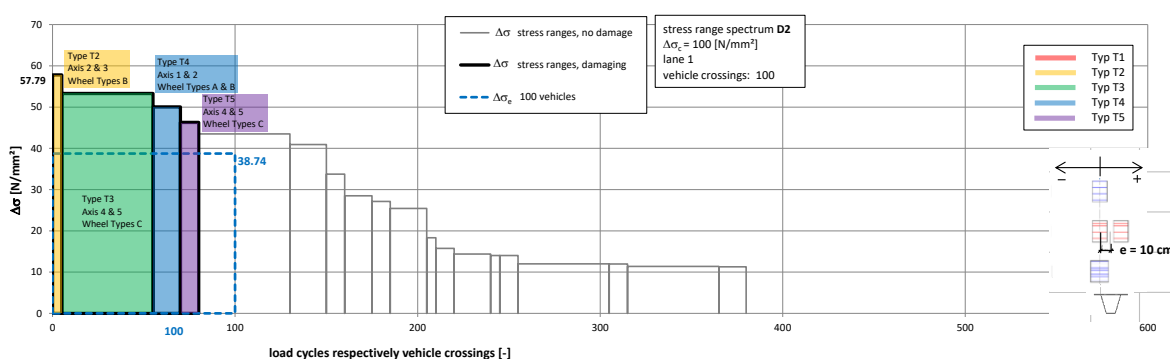


Figure 193: Model C – detail D2 at LR-2: stress range spectrum under consideration of realistic axle geometries due to FLM 4-mod

A comparison of the damage equivalent stress ranges $\Delta\sigma_e$ is shown in Table 19:

Table 19: Model C – detail D2 at LR-2: comparison of $\Delta\sigma_e$ for $n_e = 100$ lorry crossings due to centric lorry position

	centric wheel position – FLM 4	eccentric wheel position – FLM 4-mod
	$\Delta\sigma_{e,I}$	$\Delta\sigma_{e,II}$
$\Delta\sigma_e$ [N/mm ²]	37.67 (1.0)	38.74 (1.03)

As it can be seen in Table 19 the consideration of realistic axle geometries causes at detail D2 an increase of the damage equivalent stress range $\Delta\sigma_e$ of 3% referring to Model C. The damage parts of the individual lorry types relating to the stress range spectra in Figure 191 and Figure 193 show less difference. For both stress range spectra that are shown in these pictures, lorry type T3 causes the

maximum damage and lorry type T1 has no damaging effect. The damage parts are: lorry type T1 – 0% / 0% ($D_{T1,FLM 4} / D_{T1,FLM 4-mod}$); lorry type T2 – 7.6% / 10.2% ($D_{T2,FLM 4} / D_{T2,FLM 4-mod}$); lorry type T3 – 74.1% / 68.2% ($D_{T3,FLM 4} / D_{T3,FLM 4-mod}$); lorry type T4 – 11% / 14.9% ($D_{T4,FLM 4} / D_{T4,FLM 4-mod}$); lorry type T5 – 7.3% / 6.7% ($D_{T5,FLM 4} / D_{T5,FLM 4-mod}$);

4.9. Results of numerical calculations due to consideration of realistic axle geometries and lateral heavy traffic distribution

The results of the numerical simulations at the FEM-models A, B and C (see Section 3.2) referring to the appropriate details D1a, D1b and D2 (see Section 2.4) under consideration of realistic axle geometries and accurate driving characteristics are presented in this Section. The reference is always the stress range spectrum of the analysed detail with centric track configuration (see Section 3.4) and the relevant stress ranges have been scaled by using the appropriate influence line in transverse bridge direction (see Section 4.5). The number of cycles of each stress range has been split according to the appropriate frequency distribution in transverse bridge direction (see Section 4.4). The realistic axle geometries are illustrated at Figure 137 in Section 4.3.4. A detailed description of the procedure referring to the consideration of driving characteristics can be found in Section 4.6 (details D1a and D2) and 4.7 (detail D1b).

The following list gives an overview of the results according to the calculations referring to consideration of heavy traffic driving characteristics with realistic axle geometries and its influence in fatigue assessment at orthotropic steel decks:

- Model A: orthotropic bridge deck with open longitudinal ribs and cross girder interval $e_{QT} = 2.0m$
Results for detail D1a in Section 4.9.1.1 and results for detail D2 in Section 4.9.1.2
- Model B: orthotropic bridge deck with trough ribs and cross girder interval $e_{QT} = 2.0m$
Results for detail D1a in Section 4.9.2.1, detail D1b in Section 4.9.2.2 and detail D2 in Section 4.9.2.3
- Model C: orthotropic bridge deck with trough ribs and cross girder interval $e_{QT} = 4.0m$
Results for detail D1a in Section 4.9.3.1, detail D1b in Section 4.9.3.2 and detail D2 in Section 4.9.3.3

4.9.1. Model A

This Section presents the results of considering heavy traffic driving characteristics with realistic axle geometries at FEM-model A. A detailed description of FEM-model A can be found in Section 3.2.1.

4.9.1.1. Detail D1a

a.) Reference case: fatigue load model FLM 4 and centric wheel position

A detailed explanation of detail D1a can be found in Section 2.4.2. The reference stress range spectrum is presented in Section 3.4.2.1, Figure 88. This reference stress range spectrum is determined due to fatigue load model FLM 4 (see Section 2.5.2, Figure 24) and is related to a centric track configuration of all wheel loads at LR-3 (see Figure 83 in Section 3.4.2). Figure 194 shows again this reference stress range spectrum (identical to Figure 170 in Section 4.8.1.1).

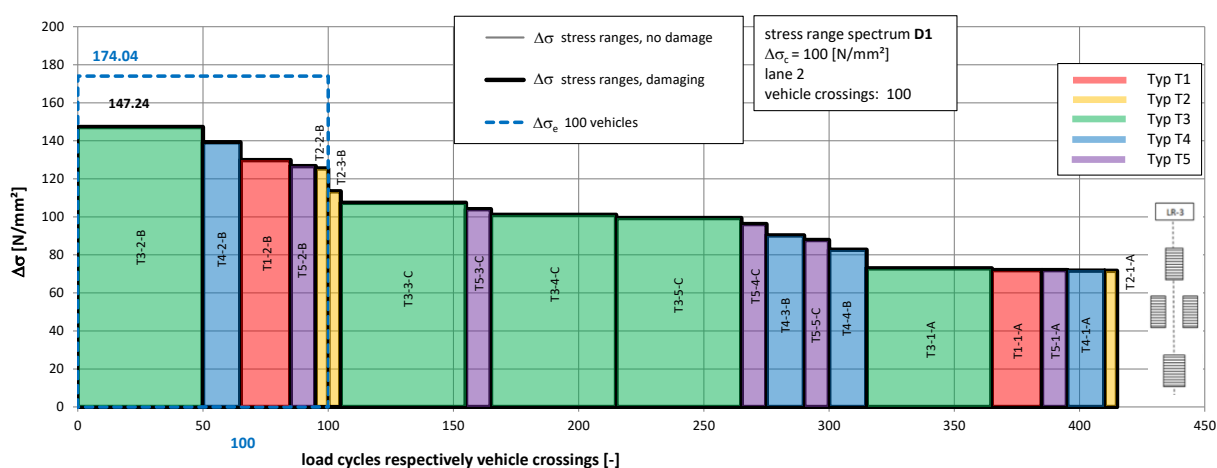


Figure 194: Model A – detail D1a at LR-3: stress range spectrum for a centric track configuration due to FLM 4

b.) Eccentric wheel and vehicle position

For consideration of heavy traffic driving characteristics with realistic axle geometries the appropriate stress ranges from Figure 194 were scaled with the corresponding parameter η as it is shown in Figure 195. Realistic axle geometries were considered by shifting the transverse influence line for single wheeled axles (axle type A and C) as shown in Figure 195.b. Additional calculations showed that a lateral shift of the single wheeled axle types A and C gives the most conservative result for detail D1a at Model A. According to the measured wheel geometries (see Figure 137 in Section 4.3) a lateral shift of the wheel types A and C with $e = 10\text{cm}$ is necessary. The parameters η were selected at $x = -30\text{cm}$ to $x = +30\text{cm}$ with an interval of $\Delta x = 10\text{cm}$, from the transverse influence lines for single and double wheeled axles, that are plotted in Figure 195.b. The sign of the curves in Figure 195.b is chosen, so that negative values represent compressive stress and positive values tensile stress. Figure 195.a illustrates the appropriate frequency distribution LFT II (identical to Figure 143.a in Section 4.4) in transverse bridge direction. The number of cycles of each stress range from Figure 194 has been portioned by taking this frequency distribution II (Figure 195.a) into account.

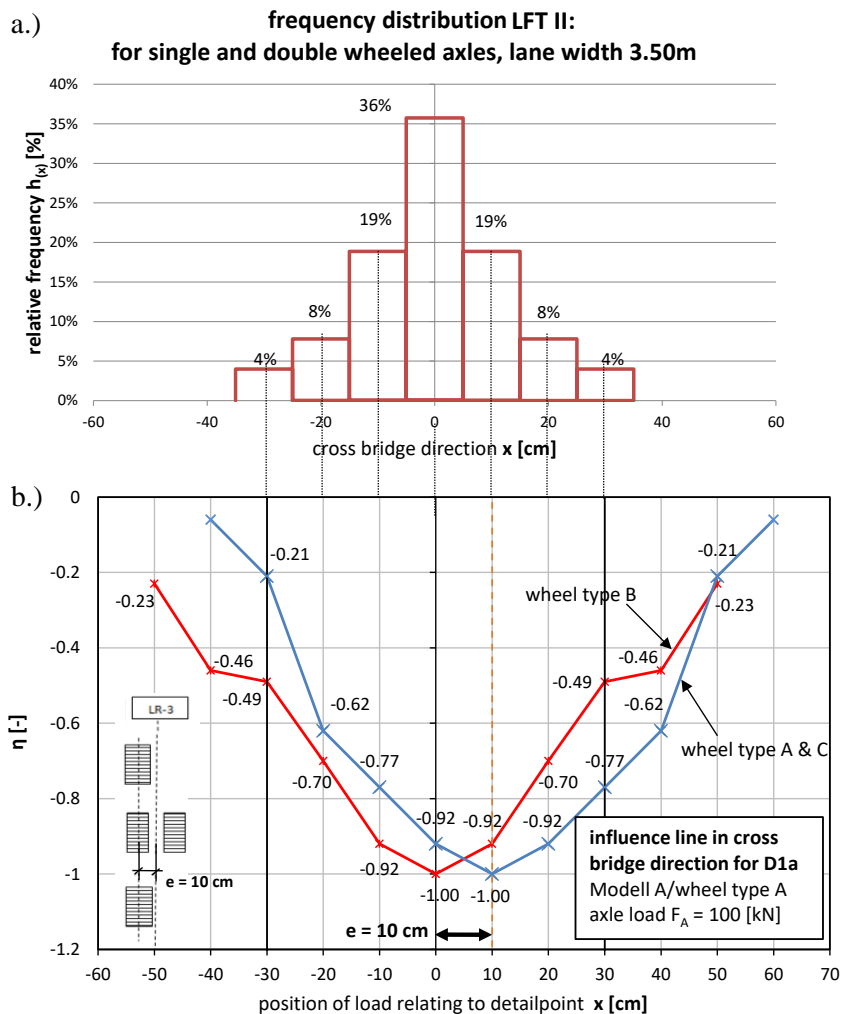


Figure 195: Model A – detail D1a at LR-3: a.) frequency distribution LFT II for a lane width of 3.50m; b.) influence line in transverse bridge direction for single and double wheeled axles (axle type A, B and C);

The resulting stress range spectrum under consideration of heavy vehicle driving characteristics (eccentric vehicle position) with realistic axle geometries (eccentric wheel position, based on Figure 137) is presented in Figure 196 for detail D1a at LR-3 of Model A.

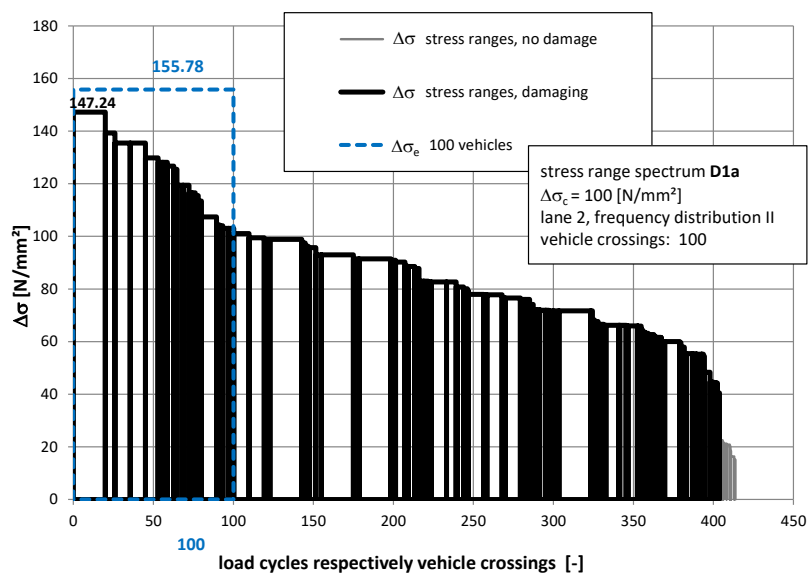


Figure 196: Model A – detail D1a at LR-3: stress range spectrum under consideration of heavy vehicle driving characteristics with realistic axle geometries due to FLM 4-mod

A comparison of the damage equivalent stress ranges $\Delta\sigma_e$ is shown in Table 20:

Table 20: Model A – detail D1a at LR-3: comparison of $\Delta\sigma_e$ for $n_e = 100$ lorry crossings due to eccentric vehicle and wheel position

	centric wheel position – FLM 4 $\Delta\sigma_{e,I}$	eccentric vehicle and wheel position – FLM 4-mod $\Delta\sigma_{e,III}$
$\Delta\sigma_e$ [N/mm ²]	174.04 (1.0)	155.78 (0.90)

As it can be seen in Table 20 the consideration of heavy vehicle driving characteristics with realistic axle geometries causes at detail D1a a reduction of the damage equivalent stress range $\Delta\sigma_e$ of 10% referring to Model A, with open longitudinal ribs.

4.9.1.2. Detail D2

a.) Reference case: fatigue load model FLM 4 and centric wheel position

A detailed explanation of detail D2 can be found in Section 2.4.4. Figure 93 in Section 3.4.2.2 presents the reference stress range spectrum. Fatigue load model FLM 4 (see Section 2.5.2, Figure 24) was considered for the calculation of this reference stress range spectrum which is related to a centric track configuration of all wheel loads at LR-3 (see Figure 83 in Section 3.4.2). Figure 197 shows again this reference stress range spectrum (identical to Figure 173 in Section 4.8.1.2).

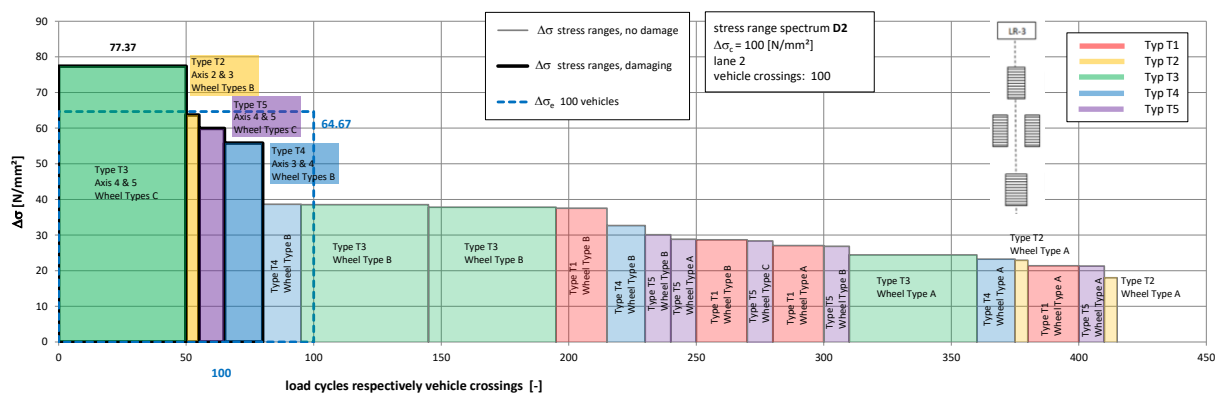


Figure 197: Model A – detail D2 at LR-3: stress range spectrum for a centric track configuration due to FLM 4

b.) Eccentric wheel and vehicle position

For consideration of heavy traffic driving characteristics with realistic axle geometries the same procedure has been done as already described in Section 4.9.1.1.b. The appropriate stress ranges from Figure 197 were scaled with the corresponding parameter η . Figure 198 shows therefore the values for the parameter η . A shifting of the transverse influence line for single wheeled axles (axle type A and C) considers realistic axle geometries (see Figure 198.b) which gives the most conservative result for detail D2 at LR-3 of Model A. A lateral shift of the wheel types A and C with $e = 10\text{cm}$ is necessary (see Figure 137 in Section 4.3). Figure 198.a illustrates the appropriate frequency distribution LFT II (identical to Figure 143.a in Section 4.4) in transverse bridge direction.

The resulting stress range spectrum under consideration of heavy vehicle driving characteristics (eccentric vehicle position) with realistic axle geometries (eccentric wheel position) is presented in Figure 199 for detail D2 at LR-3 of Model A.

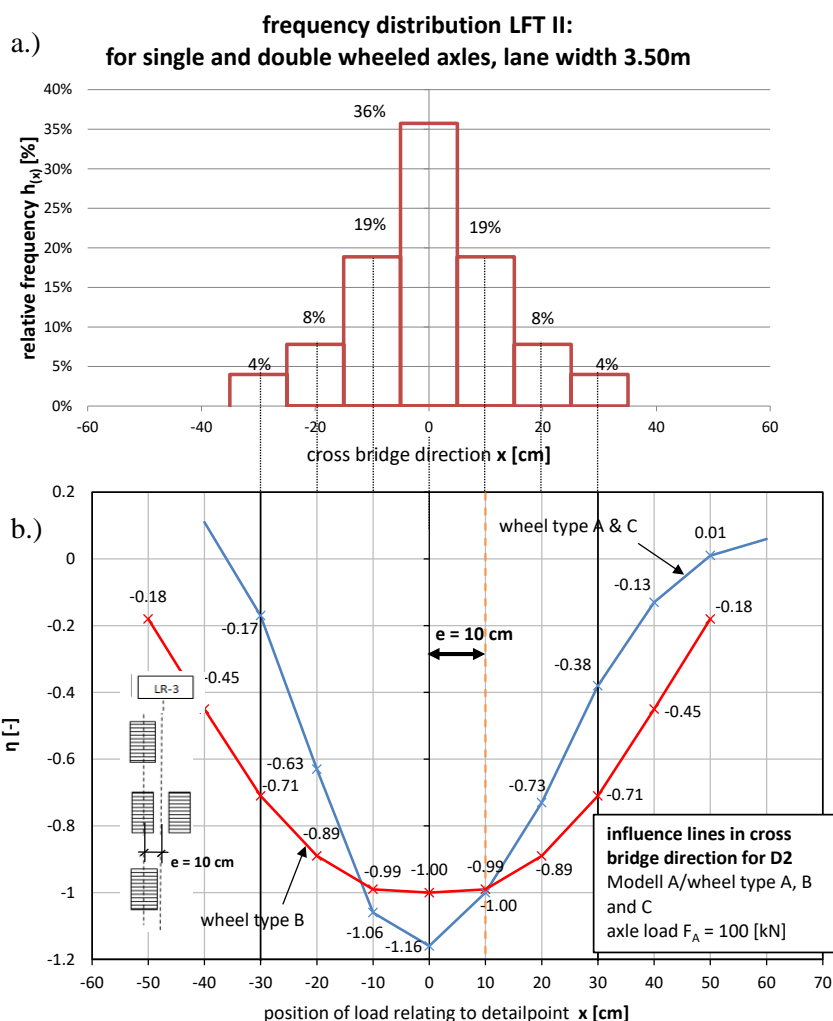


Figure 198: Model A – detail D2 at LR-3: a.) frequency distribution LFT II for a lane width of 3.50m; b.) influence line in transverse bridge direction for single and double wheeled axles (axle type A to C);

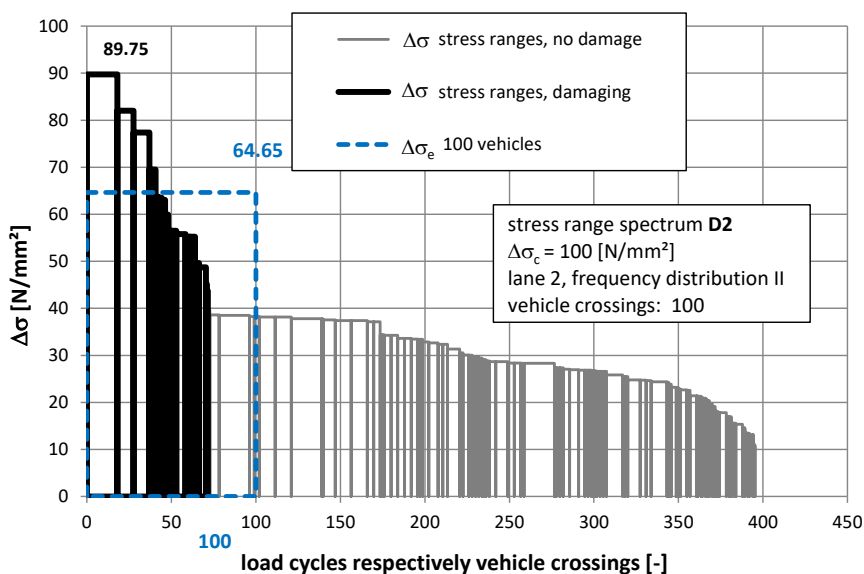


Figure 199: Model A – detail D2 at LR-3: stress range spectrum under consideration of heavy vehicle driving characteristics with realistic axle geometries due to FLM 4-mod

A comparison of the damage equivalent stress ranges $\Delta\sigma_e$ is shown in Table 21:

Table 21: Model A – detail D2 at LR-3: comparison of $\Delta\sigma_e$ for $n_e = 100$ lorry crossings due to eccentric vehicle and wheel position

	centric wheel position – FLM 4 $\Delta\sigma_{e,I}$	eccentric vehicle and wheel position – FLM 4-mod $\Delta\sigma_{e,III}$
$\Delta\sigma_e$ [N/mm ²]	64.67 (1.0)	64.65 (1.0)

By comparing the values in Table 21 it can be stated that the consideration of heavy vehicle driving characteristics with realistic axle geometries has no effect referring to the damage equivalent stress range $\Delta\sigma_e$ in detail D2 for Model A with open longitudinal ribs. It is worth mentioning that the maximum stress range in the spectrum of Figure 199 has a higher value than the ones in the spectrum of Figure 197 ($\Delta\sigma_{\max,I} = 77.4\text{N/mm}^2$ and $\Delta\sigma_{\max,III} = 89.8\text{N/mm}^2$). Because of the η -values ($\eta_{\max} = 1.16$) from the transverse influence line for single wheeled axles (see Figure 198.b), the maximum stress range increases ($\Delta\sigma_{\max,III} / \Delta\sigma_{\max,I} = 1.16$).

4.9.2. Model B

This Section presents the results of considering heavy traffic driving characteristics with realistic axle geometries at FEM-model B. A detailed description of FEM-model B can be found in Section 3.2.2.

4.9.2.1. Detail D1a

a.) Reference case: fatigue load model FLM 4 and centric wheel position

A detailed explanation of detail D1a can be found in Section 2.4.2. The reference stress range spectrum is presented in Section 3.4.3.1, Figure 97. This reference stress range spectrum is determined due to fatigue load model FLM 4 (see Section 2.5.2, Figure 24) and is related to a centric track configuration of all wheel loads at the web of LR-2 (see Figure 94 in Section 3.4.3). Figure 200 shows again this reference stress range spectrum (identical to Figure 176 in Section 4.8.2.1).

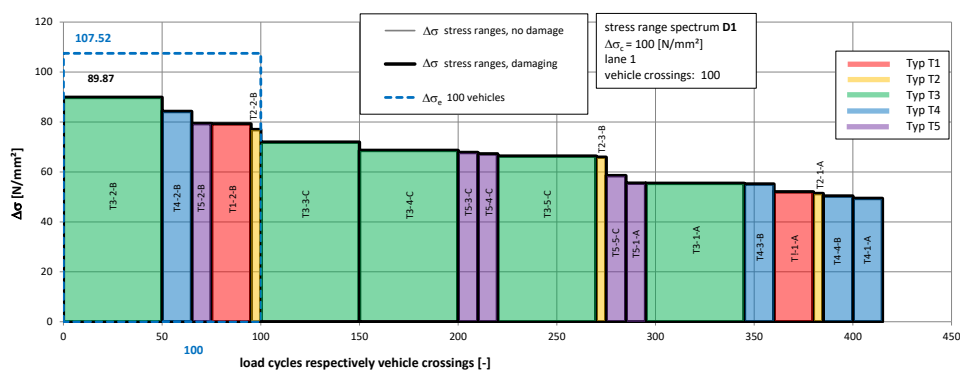


Figure 200: Model B – detail D1a at LR-2: stress range spectrum for a centric track configuration due to FLM 4

b.) Eccentric wheel and vehicle position

For consideration of heavy traffic driving characteristics with realistic axle geometries the same procedure has been done as already described in Section 4.9.1.1.b. Figure 201 shows the parameters η for the scaling procedure. A shifting of the transverse influence line for single wheeled axles (axle type A and C) includes realistic axle geometries (see Figure 201.b, $e = 10\text{cm}$). Figure 201.a illustrates the appropriate frequency distribution LFT II (identical to Figure 143.a in Section 4.4) in transverse bridge direction.

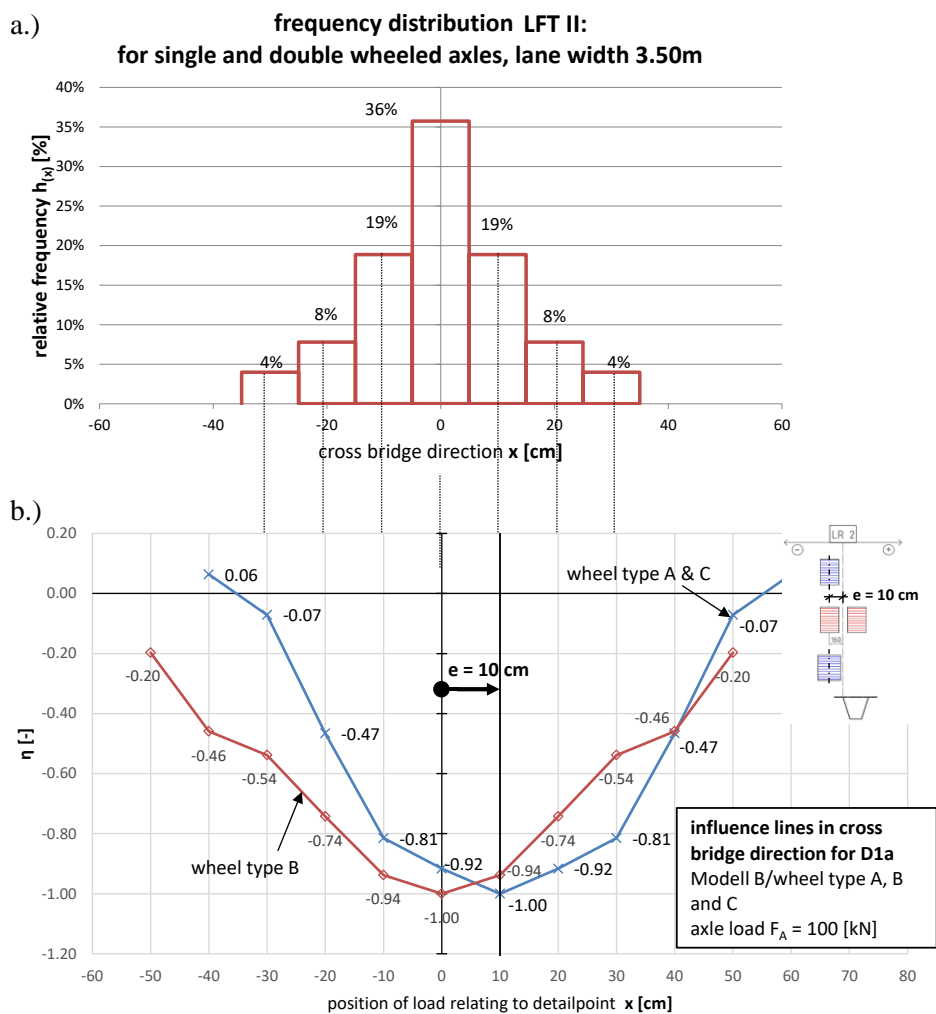


Figure 201: Model B – detail D1a at LR-2: a.) frequency distribution LFT II for a lane width of 3.50m; b.) influence line in transverse bridge direction for single and double wheeled axles (axle type A, B and C);

The resulting stress range spectrum under consideration of heavy vehicle driving characteristics (eccentric vehicle position) with realistic axle geometries (eccentric wheel position) is presented in Figure 202 for detail D1a at LR-2 of Model B.

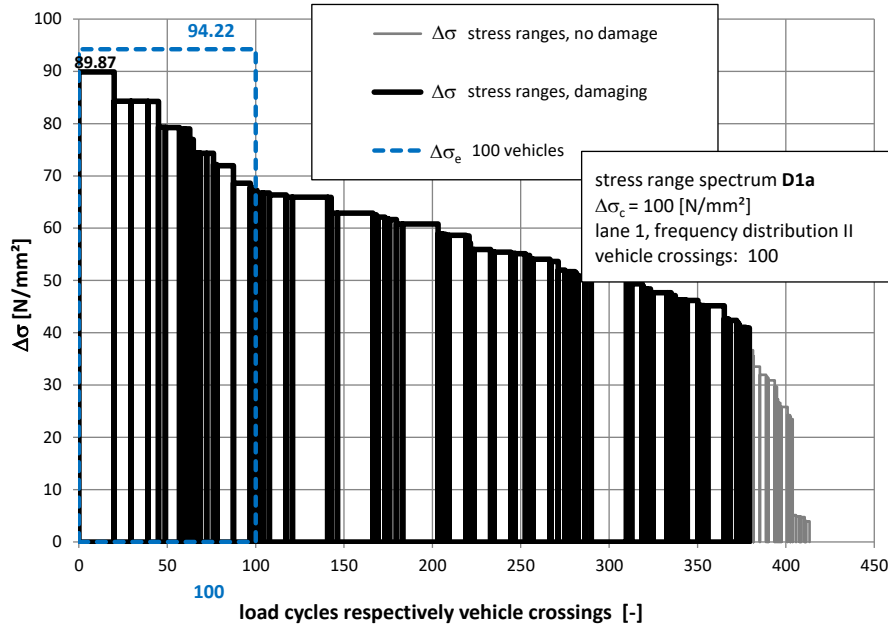


Figure 202: Model B – detail D1a at LR-2: stress range spectrum under consideration of heavy vehicle driving characteristics with realistic axle geometries due to FLM 4-mod

A comparison of the damage equivalent stress ranges $\Delta\sigma_e$ is shown in Table 22:

Table 22: Model B – detail D1a at LR-2: comparison of $\Delta\sigma_e$ for $n_e = 100$ lorry crossings due to eccentric vehicle and wheel position

	centric wheel position – FLM 4 $\Delta\sigma_{e,I}$	eccentric vehicle and wheel position FLM 4-mod $\Delta\sigma_{e,III}$
$\Delta\sigma_e$ [N/mm ²]	107.52 (1.0)	94.22 (0.88)

As it can be seen in Table 22 the consideration of heavy vehicle driving characteristics with realistic axle geometries causes at detail D1a a reduction of the damage equivalent stress range $\Delta\sigma_e$ of 12% referring to Model B.

In addition, Figure 203 shows the stress range spectrum under consideration of eccentric wheels and vehicles by using frequency distribution LFT I (see Figure 138 in Section 4.4.1). By comparing the stress range spectra in Figure 202 (LFT II) and Figure 203 (LFT I), practically no difference can be detected in its shape. At LFT I, 50% and at LFT II, 40% of the vehicles are crossing the bridge on the critical transverse position. Therefore, the damage equivalent stress range $\Delta\sigma_{e,D1a,LFT-I}$ under consideration of LFT I is slightly higher than $\Delta\sigma_{e,D1a,LFT-II}$ under consideration of LFT II ($\Delta\sigma_{e,D1a,LFT-I} / \Delta\sigma_{e,D1a,LFT-II} = 96.90 / 94.22 = 1.03$).

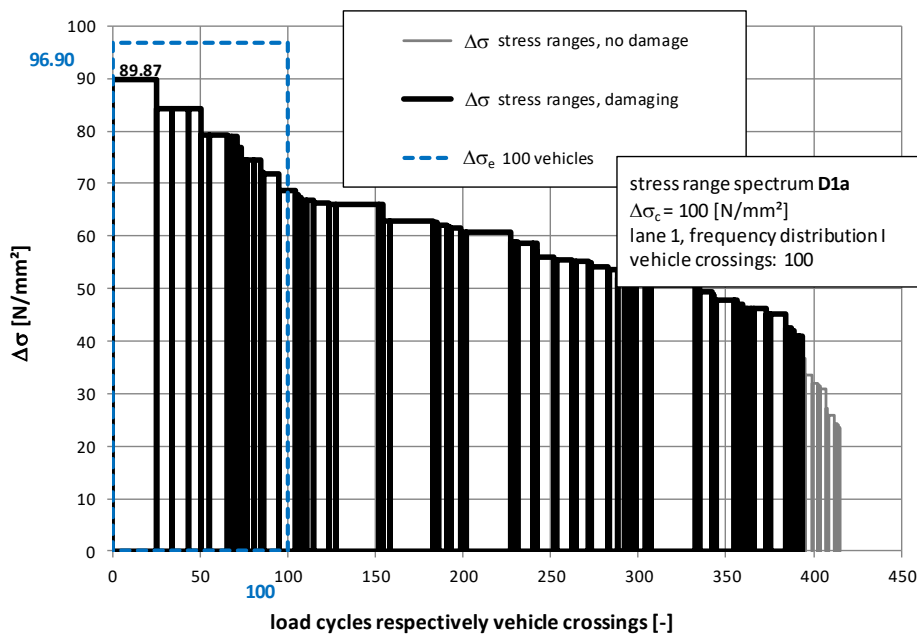


Figure 203: Model B – detail D1a at LR-2: stress range spectrum under consideration of heavy vehicle driving characteristics (LFT I) with realistic axle geometries due to FLM 4-mod

4.9.2.2. Detail D1b

a.) Reference case: fatigue load model FLM 4 and centric wheel position

A detailed explanation of detail D1b can be found in Section 2.4.3. Figure 100 in Section 3.4.3.2 presents the reference stress range spectrum, which has been determined due to fatigue load model FLM 4 (see Section 2.5.2, Figure 24) and is related to a centric track configuration of all wheel loads at the web of LR-2 (see Figure 94 in Section 3.4.3). Figure 204 shows again this reference stress range spectrum (identical to Figure 179 in Section 4.8.2.2). As it can be seen in the picture, no fatigue damage is occurring due to a centric wheel position of all axle/wheel types under consideration of the cut of limit $\Delta\sigma_L$ according to the appropriate S-N curve ($\Delta\sigma_c = 100 \text{ N/mm}^2$; $\Delta\sigma_L \approx 40 \text{ N/mm}^2$).

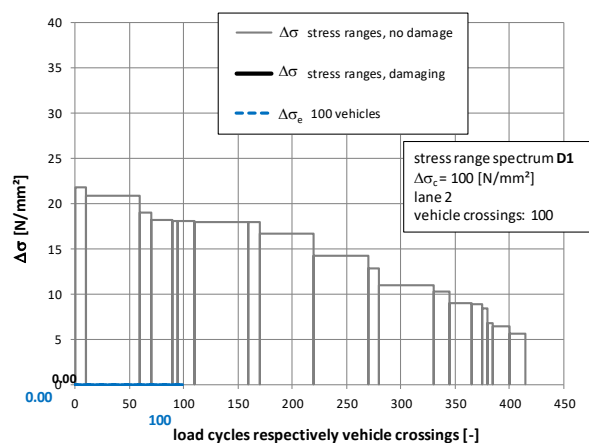


Figure 204: Model B – detail D1b at the web of LR-2: stress range spectrum for a centric track configuration due to FLM 4

b.) Eccentric wheel and vehicle position

A detailed explanation for consideration of heavy traffic driving characteristics with realistic axle geometries can be found in Section 4.7. For every position in cross transverse direction (-40 cm to +40 cm in Figure 205) an influence line in longitudinal bridge direction for single and double wheeled axles was calculated. Figure 206 exemplary illustrates the influence lines in longitudinal bridge direction related to wheel type A for 3 different wheel positions in transverse directions ($x=0\text{cm}$, $x=-20\text{cm}$, $x=+20\text{cm}$). The influence line for $x=0\text{cm}$ is the basis influence line, out of numerical calculations due to a crossing of wheel type A over the bridge deck. The influence lines in longitudinal bridge directions for the lateral positions $x=-20\text{cm}$ and $x=+20\text{cm}$ have been determined by scaling the basis influence line ($x=0\text{cm}$) with the appropriate factor η_A from Figure 205.b ($\eta_{A,-20} = -2.72$ and $\eta_{A,+20} = 2.03$). The sign of the curves in Figure 205.b indicate negative η -values for compressive stress in the detail D1b. Realistic axle geometries were considered by shifting the transverse influence line for double wheeled axles (axle type B) as shown in Figure 205.b. Additional calculations confirmed the most conservative result for detail D1b at Model B via a shifting of the double wheeled axle type B. According to Figure 137 in Section 4.3.4, a lateral shift of wheel type B with $e = 10\text{cm}$ is necessary. Figure 205.a illustrates the appropriate frequency distribution LFT III (see Figure 143.b in Section 4.4) in transverse bridge direction for taking the corresponding number of cycles of each stress range into account.

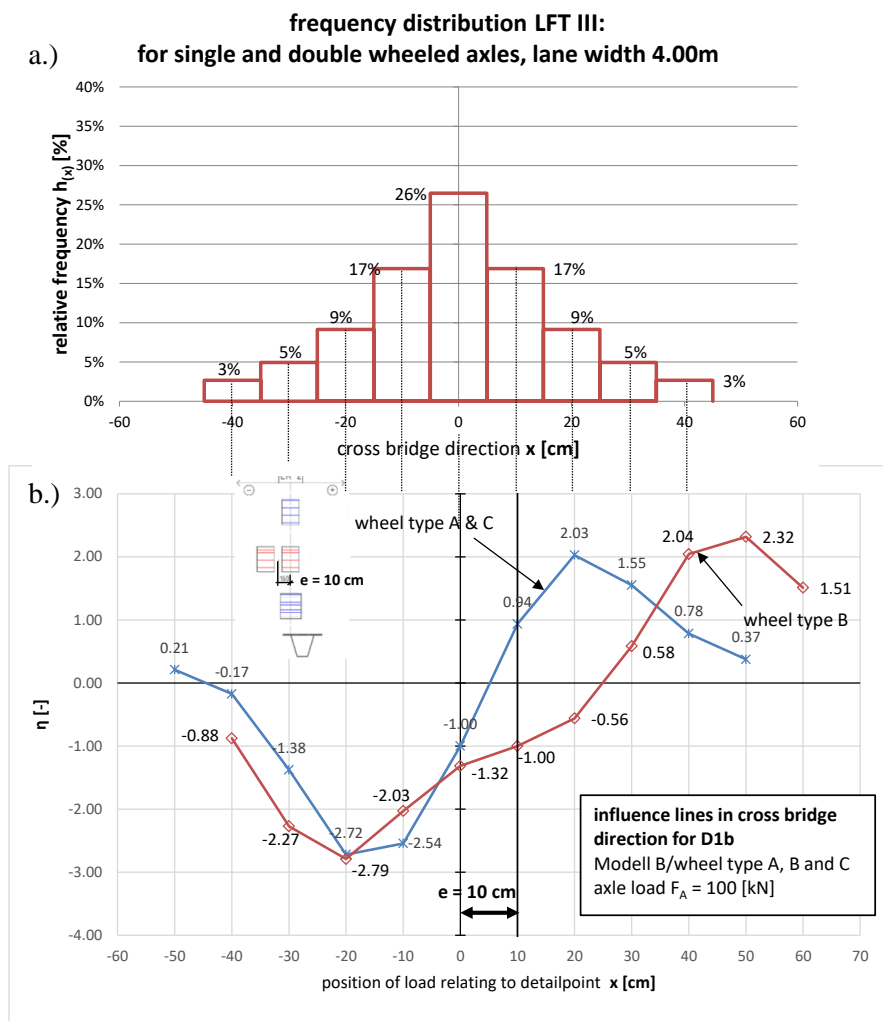


Figure 205: Model B – detail D1b at LR-2: a.) frequency distribution LFT III for a lane width of 4.00m; b.) influence line in transverse bridge direction for single and double wheeled axles (axle type A, B and C);

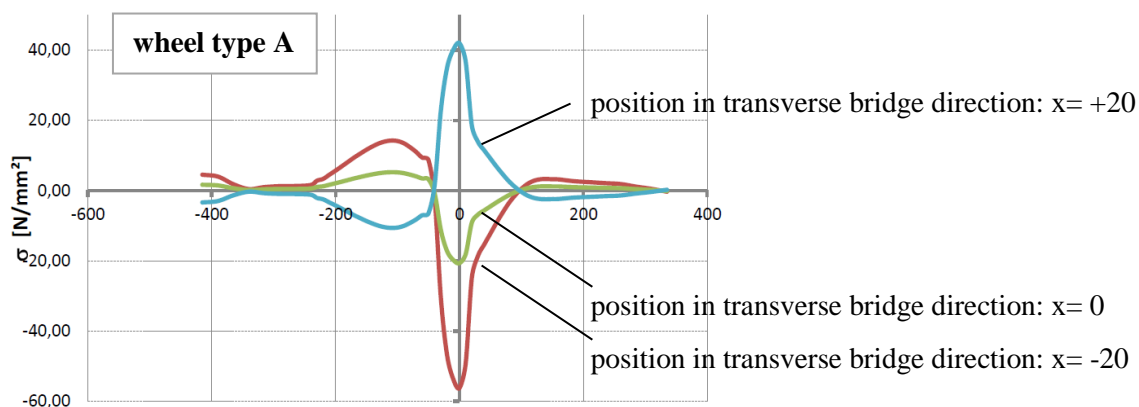


Figure 206: influence lines in longitudinal bridge direction for different positions in transverse bridge direction ($x=0$ cm, $x=+20$ cm, $x=-20$ cm) related to wheel type A – model

The stress history curves due to the lorry crossings (vehicle type T1 to T5) were determined by considering the lorry's axle distances and its axle loads from fatigue load model FLM-4. Figure 207 exemplary shows the stress history curves due to vehicle type T3 for 3 different positions in transverse bridge direction ($x=0\text{cm}$, $x=-20\text{cm}$ and $x=+20\text{cm}$). For every lorry type T1 to T5, a stress history curve for each position in transverse bridge direction referring to the frequency distribution in Figure 205.a has been calculated.

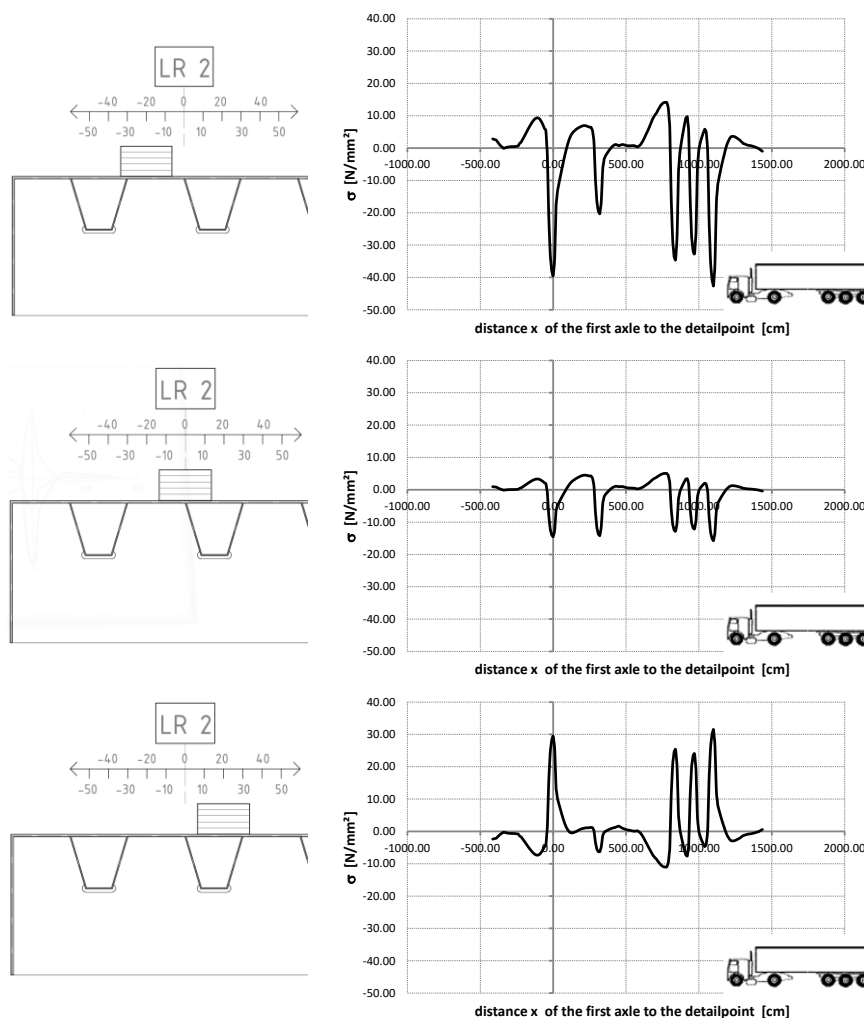


Figure 207: stress history respectively stress-path curves of vehicle type T3 for cross position $x=-20\text{cm}$, $x=0\text{cm}$ and $x=+20\text{cm}$ referring to detail D1b

The in summary 45 stress history curves (9 lane positions for 5 lorry types) were randomly stringed together under consideration of the lorry percentage according to fatigue load model FLM-4 (see Section 2.5.2). These 45 transverse positions of the 5 lorry types with their number of crossings (n_i) relating to frequency distribution LFT III (h_i see Figure 205.a) are already shown in Table 13 in Section 4.7.

The resulting stress range spectrum under consideration of heavy vehicle driving characteristics (eccentric vehicle position) with realistic axle geometries (eccentric wheel position) is presented in Figure 208 for detail D1b at Model B with random sequence 1.

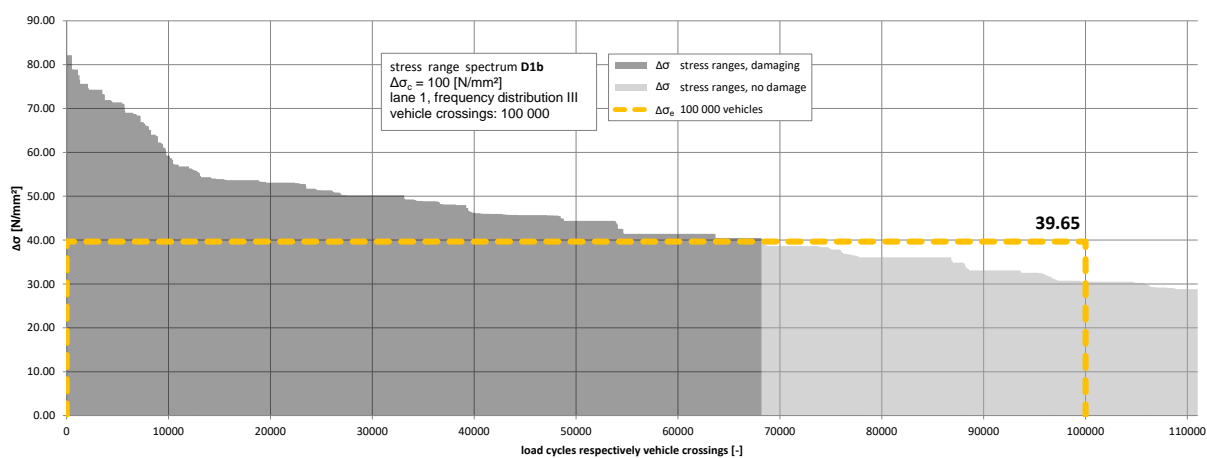


Figure 208: Model B – detail D1b at LR-2: stress range spectrum under consideration of heavy vehicle driving characteristics (LFT III) with realistic axle geometries due to FLM 4-mod (random sequence 1)

A comparison of the damage equivalent stress ranges $\Delta\sigma_e$ is shown in Table 23:

Table 23: Model B – detail D1b at LR-2: comparison of $\Delta\sigma_e$ for $n_e = 100,000$ lorry crossings due to eccentric vehicle and wheel position

	centric wheel position – FLM 4	eccentric vehicle and wheel position – FLM 4-mod
	$\Delta\sigma_{e,I}$	$\Delta\sigma_{e,III}$
$\Delta\sigma_e$ [N/mm ²]	0.0	39.65

As it can be seen in Table 23 the consideration of heavy vehicle driving characteristics with realistic axle geometries causes an essential effect relating to the fatigue assessment at detail D1b. If these considerations would be neglected, the calculations would result in no fatigue damage by using the cut of limit $\Delta\sigma_L$ according to the appropriate S-N curve. Therefore, the damage equivalent stress range $\Delta\sigma_{e,I} = 0$ for centric vehicle and wheel position in transverse bridge direction (see Table 23). On the contrary, under considering eccentric vehicle and wheel position in transverse bridge direction, the calculations result a nameable fatigue damage at detail D1b. The damage equivalent stress range $\Delta\sigma_{e,III} = 39.65$ N/mm² is related to the number of lorries in the analysed lane ($n_e = 100,000$ load cycles in the analyses). By comparing the maximum occurring stress ranges $\Delta\sigma_{max}$ between the stress range spectra in Figure 204 and Figure 208, it can be stated that $\Delta\sigma_{max,III}$ is 3.8 times higher than $\Delta\sigma_{max,I}$ ($\Delta\sigma_{max,III} / \Delta\sigma_{max,I} = 82.1 / 21.8 = 3.8$). Therefore, the consideration of the lateral effects causes a dramatically increase of the occurring stresses in the detail D1b.

Additionally, Figure 209 illustrates the resulting stress range spectrum under consideration of eccentric wheels and vehicles with another random sequence of the lorries (random sequence 2). By comparing the stress range spectra in Figure 208 and Figure 209, no significant difference can be detected. The damage equivalent stress range $\Delta\sigma_e$ is nearly equal ($39.65 / 39.55 = 1.0025$). In summary 4 different random sequences have been analysed which are not presented, but similar results could be determined. Hence, 100,000 vehicles for the simulation of the heavy traffic are enough to include the effects of lateral shifting wheels and vehicles and to get accurate results for the damage in the detail.

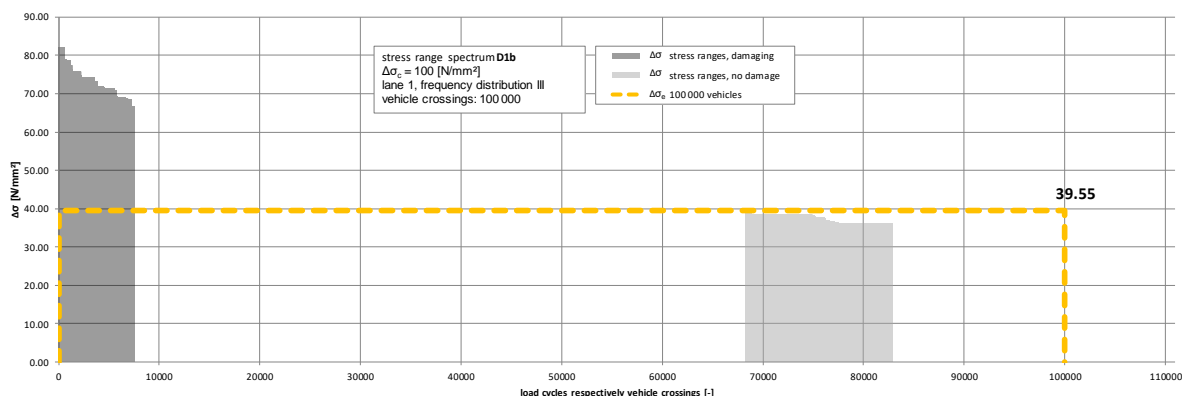


Figure 209: Model B – detail D1b at LR-2: stress range spectrum under consideration of heavy vehicle driving characteristics (LFT III) with realistic axle geometries due to FLM 4-mod (random sequence 2)

4.9.2.3. Detail D2

a.) Reference case: fatigue load model FLM 4 and centric wheel position

A detailed explanation of detail D2 can be found in Section 2.4.4. The reference stress range spectrum, which is presented in Section 3.4.3.3, Figure 103 is again shown in Figure 210 (identical to Figure 182 in Section 4.8.2.3). This reference stress range spectrum is determined due to fatigue load model FLM 4 (see Section 2.5.2, Figure 24) and is related to a centric track configuration of all wheel loads at the web of LR-2 (see Figure 94 in Section 3.4.3).

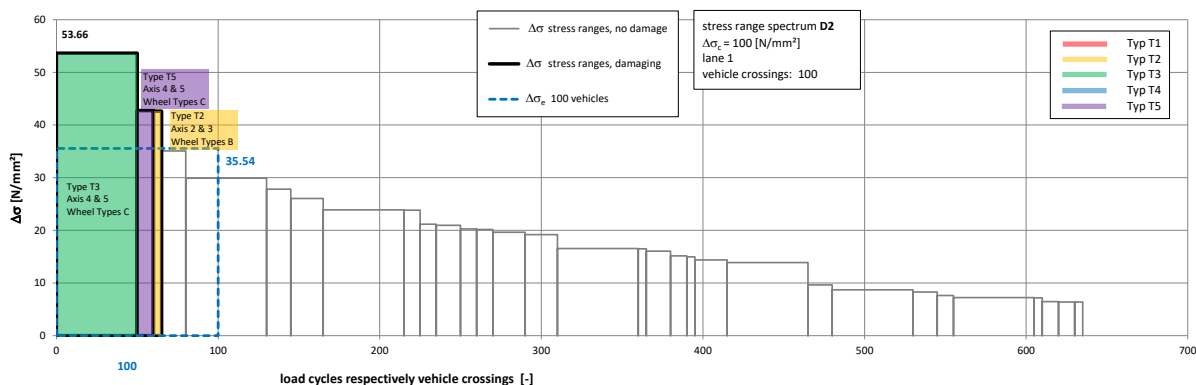


Figure 210: Model B – detail D2 at LR-2: stress range spectrum for a centric track configuration due to FLM 4

b.) eccentric wheel and vehicle position

The procedure for a consideration of heavy traffic driving characteristics with realistic axle geometries is already described in Section 4.9.1.1.b. The same procedure of stress range scaling with η and splitting based on frequency distribution LFT II was performed at detail D2 for model B. The realistic axle geometry was again considered by shifting the transverse influence line for double wheeled axles (axle type B) with $e = 10\text{cm}$ (see Figure 211). The chosen parameters η are shown in Figure 211.b. Negative η -values indicate compressive stress and positive η -values indicate tensile stress. The chosen lateral frequency distribution LFT II is illustrated in Figure 211.a.

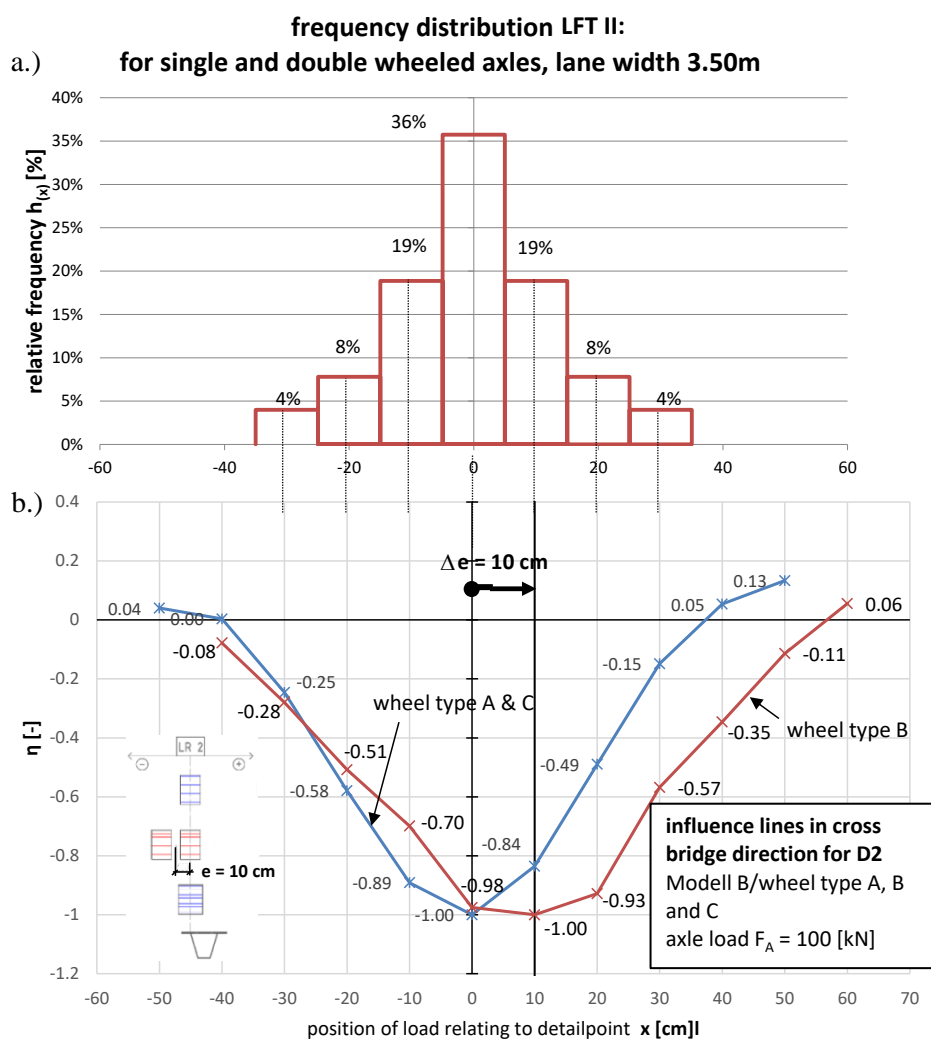


Figure 211: Model B – detail D2 at LR-2: a.) frequency distribution LFT II for a lane width of 3.50m; b.) influence line in transverse bridge direction for single and double wheeled axles (axle type A, B and C);

The resulting stress range spectrum for detail D2 at Model B under consideration of heavy vehicle driving characteristics (eccentric vehicle position) with realistic axle geometries (eccentric wheel position) is presented in Figure 212.

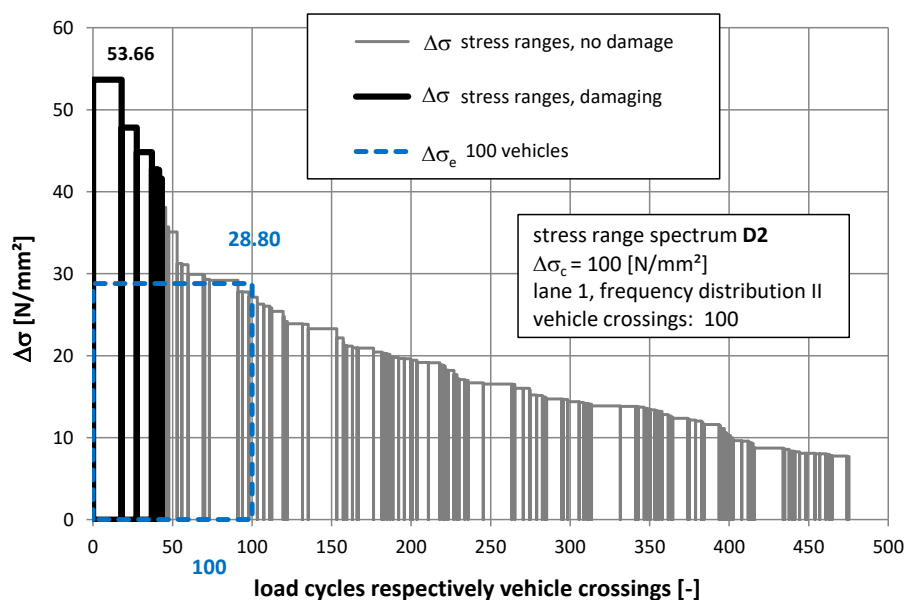


Figure 212: Model B – detail D2 at LR-2: stress range spectrum under consideration of heavy vehicle driving characteristics with realistic axle geometries due to FLM 4-mod

A comparison of the damage equivalent stress ranges $\Delta\sigma_e$ is shown in Table 24:

Table 24: Model B – detail D2 at LR-2: comparison of $\Delta\sigma_e$ for $n_e = 100$ lorry crossings due to eccentric vehicle and wheel position

	centric wheel position – FLM 4 $\Delta\sigma_{e,I}$	eccentric vehicle and wheel position – FLM 4-mod $\Delta\sigma_{e,III}$
$\Delta\sigma_e$ [N/mm ²]	35.54 (1.0)	28.80 (0.81)

As it can be seen in Table 24 the consideration of heavy vehicle driving characteristics with realistic axle geometries causes at detail D2 a reduction of the damage equivalent stress range $\Delta\sigma_e$ of 19% referring to Model B.

Figure 213 illustrates additionally the stress range spectrum considering eccentric wheels and vehicles by using frequency distribution LFT I (see Figure 138 in Section 4.4.1). When comparing the stress range spectrum in Figure 212 with the one in Figure 213 it can be stated, that they are practically

identical. Only the damage equivalent stress range spectrum $\Delta\sigma_{e,D2,LFT-I}$ due to LFT I is higher than $\Delta\sigma_{e,D2,LFT-II}$ due to LFT II ($\Delta\sigma_{e,D2,LFT-I} / \Delta\sigma_{e,D2,LFT-II} = 30.98 / 28.80 = 1.08$). This observation can be declared by the higher percentage of lorries in the critical transverse position (centric position) of LFT I (50%) in relation to LFT II (40%).

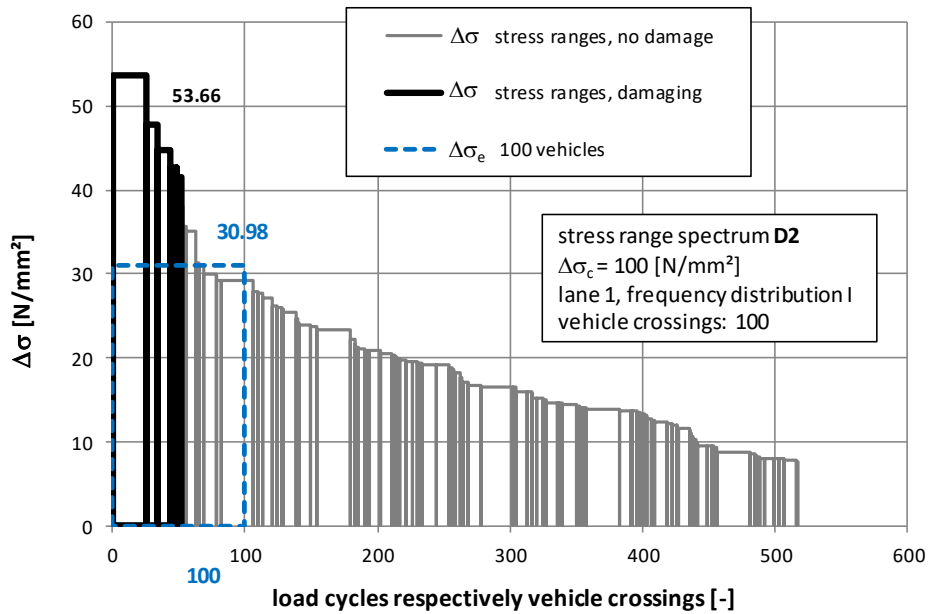


Figure 213: Model B – detail D2 at LR-2: stress range spectrum under consideration of heavy vehicle driving characteristics (LFT I) with realistic axle geometries due to FLM 4-mod

4.9.3. Model C

This Section presents the results of considering heavy traffic driving characteristics with realistic axle geometries at FEM-model C. A detailed description of FEM-model C can be found in Section 3.2.3.

4.9.3.1. Detail D1a

a.) Reference case: fatigue load model FLM 4 and centric wheel position

A detailed explanation of detail D1a can be found in Section 2.4.2. The reference stress range spectrum is presented in Section 3.4.4.1, Figure 107 and again shown in Figure 214 (identical to Figure 185 in Section 4.8.3.1). For this reference stress range spectrum fatigue load model FLM 4 (see Section 2.5.2, Figure 24) is considered which is related to a centric track configuration of all wheel loads at the web of LR-2 (see Figure 104 in Section 3.4.4).

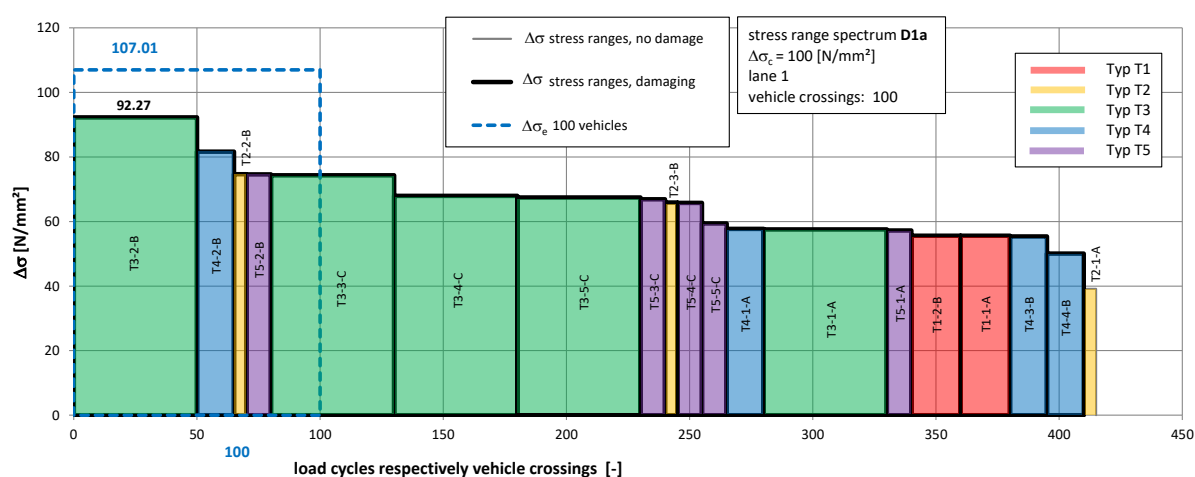


Figure 214: Model C – detail D1a at LR-2: stress range spectrum for a centric track configuration due to FLM 4

b.) Eccentric wheel and vehicle position

Section 4.9.1.1.b already describes the procedure of considering heavy traffic driving characteristics with realistic axle geometries. The same procedure has been performed at detail D1a of model C, where the appropriate stress ranges from Figure 214 were scaled with the corresponding parameter η and have been split based on frequency distribution LFT II (see Figure 215). Realistic axle geometries were considered by shifting the transverse influence line for single wheeled axles (axle type A and C) with $e = 10\text{cm}$ as shown in Figure 215.b.

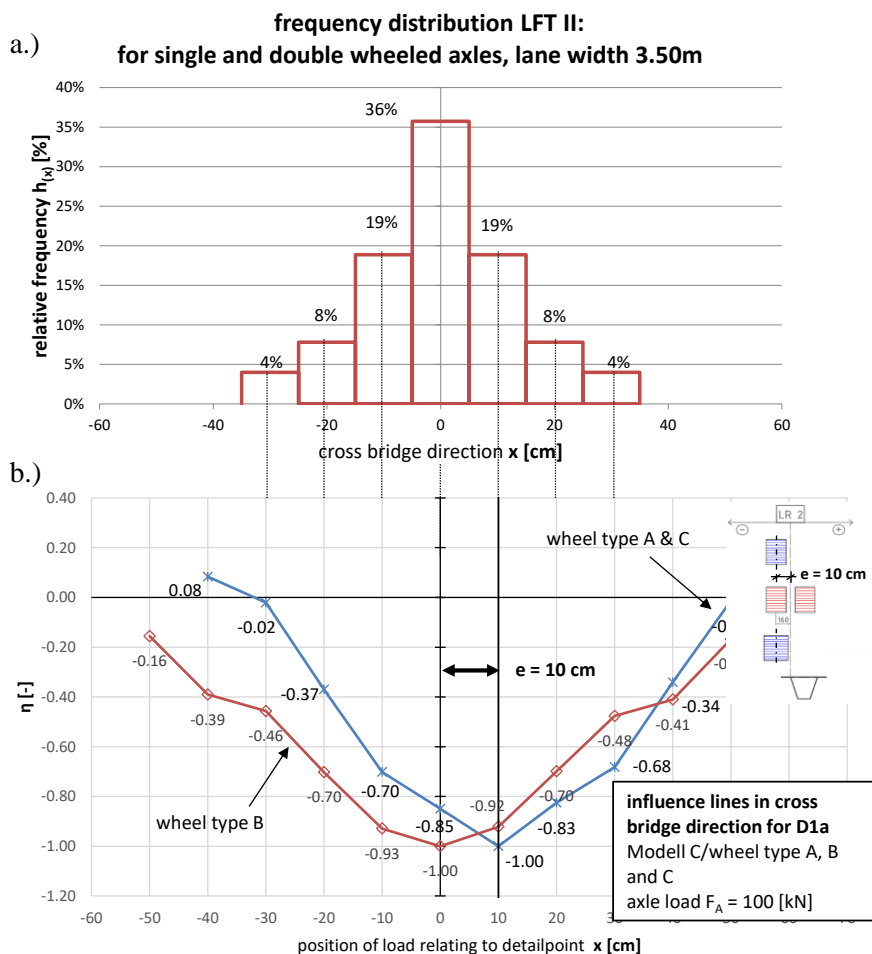


Figure 215: Model C – detail D1a at LR-2: a.) frequency distribution LFT II for a lane width of 3.50m; b.) influence line in transverse bridge direction for single and double wheeled axles (axle type A, B and C);

The resulting stress range spectrum under consideration of heavy vehicle driving characteristics (eccentric vehicle position) with realistic axle geometries (eccentric wheel position) is presented in Figure 216 for detail D1a at Model C.

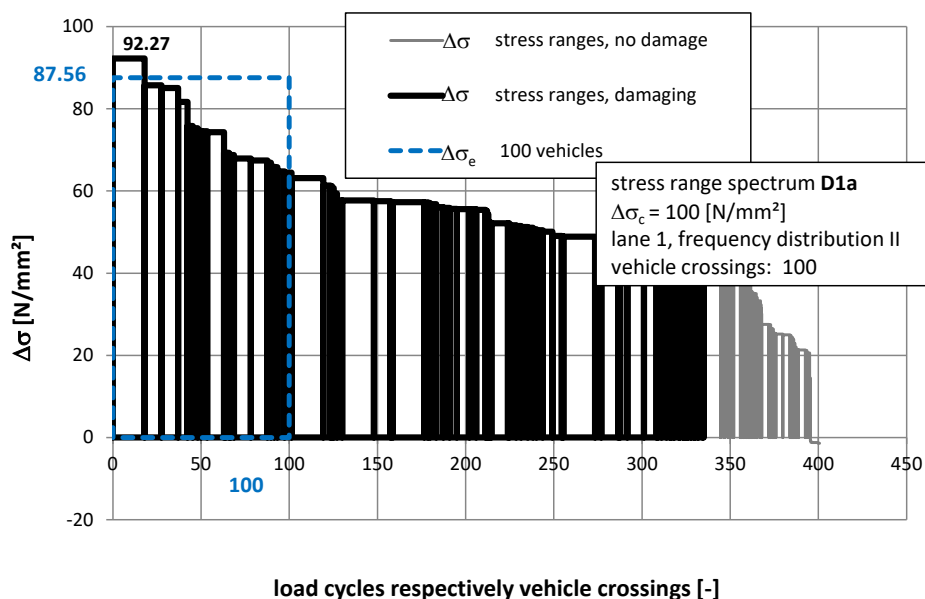


Figure 216: Model C – detail D1a at LR-2: stress range spectrum under consideration of heavy vehicle driving characteristics with realistic axle geometries due to FLM 4-mod

A comparison of the damage equivalent stress ranges $\Delta\sigma_e$ is shown in Table 25:

Table 25: Model B – detail D1a at LR-2: comparison of $\Delta\sigma_e$ for $n_e = 100$ lorry crossings due to eccentric vehicle and wheel position

	centric wheel position – FLM 4 $\Delta\sigma_{e,I}$	eccentric vehicle and wheel position – FLM 4-mod $\Delta\sigma_{e,III}$
$\Delta\sigma_e$ [N/mm ²]	107.01 (1.0)	87.56 (0.82)

As it can be seen in Table 25 the consideration of heavy vehicle driving characteristics with realistic axle geometries causes at detail D1a a reduction of the damage equivalent stress range $\Delta\sigma_e$ of 18% referring to Model C.

In addition, the stress range spectrum due to eccentric wheels and vehicles in transverse direction is shown in Figure 217 under consideration of frequency distribution LFT I (see Figure 138 in Section 4.4.1). The shape of both stress range spectra from Figure 216 (LFT II) and Figure 217 (LFT I) is very similar. The damage equivalent stress range $\Delta\sigma_{e,D1a,LFT-I} = 91.57$ N/mm² due to LFT I is a little bit higher than the one due to LFT II which as a value of $\Delta\sigma_{e,D1a,LFT-II} = 87.56$ N/mm² ($\Delta\sigma_{e,D1a,LFT-I} / \Delta\sigma_{e,D1a,LFT-II} = 1.05$). Therefore, the equivalent stress range $\Delta\sigma_{e,D1a,LFT-I}$ is 5% higher than $\Delta\sigma_{e,D1a,LFT-II}$. The reason therefore is a higher lorry percentage in the critical transverse position ($x = 0$) at LFT I (50%) in comparison to LFT II (40%).

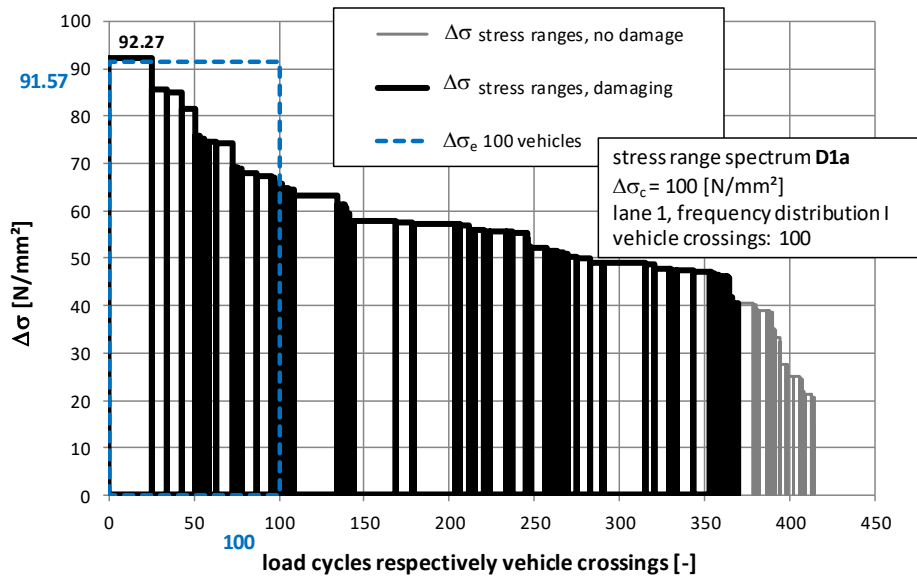


Figure 217: Model C – detail D1a at LR-2: stress range spectrum under consideration of heavy vehicle driving characteristics (LFT I) with realistic axle geometries due to FLM 4-mod

4.9.3.2. Detail D1b

a.) Reference case: fatigue load model FLM 4 and centric wheel position

A detailed explanation of detail D1b can be found in Section 2.4.3. The reference stress range spectrum is presented in Section 3.4.4.2, Figure 110. This reference stress range spectrum has been determined due to fatigue load model FLM 4 (see Section 2.5.2, Figure 24) with a centric track configuration of all wheel loads at the web of LR-2 (see Figure 104 in Section 3.4.4). Figure 218 shows again this reference stress range spectrum (identical to Figure 204 in Section 4.8.3.2). As shown in the picture, no fatigue damage is occurring due to a centric wheel position of all axle/wheel types under consideration of the cut of limit $\Delta\sigma_L$ according to the appropriate S-N curve ($\Delta\sigma_c = 100 \text{ N/mm}^2$; $\Delta\sigma_L \approx 40 \text{ N/mm}^2$).

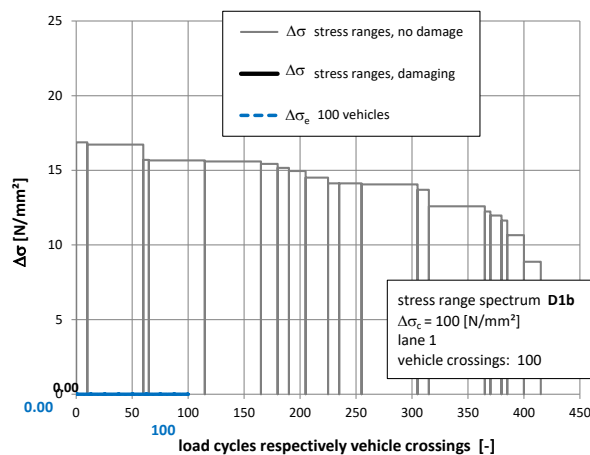


Figure 218: Model C – detail D1b at LR-2: stress range spectrum for a centric track configuration due to FLM 4

b.) Eccentric wheel and vehicle position

Section 4.7 illustrates a detailed explanation for consideration of heavy traffic driving characteristics with realistic axle geometries for detail D1b. An influence line in longitudinal bridge direction for single and double wheeled axles has been calculated for every position in transverse bridge direction (-40 cm to +40 cm in Figure 219).

The influence lines in longitudinal direction due to axle type A, B and C with centric track configuration (see Section 4.2) are the basis influence lines, based on the numerical calculations. The influence lines in longitudinal bridge directions for the lateral positions from $x=-40\text{cm}$ to $x=+40\text{cm}$ have been determined by scaling the basis influence line ($x=0\text{cm}$) with the appropriate factor η_A and η_B from Figure 219.b The algebraic sign of the curves in Figure 219.b indicate negative η -values for compressive stress in the detail D1b. A shifting of the transverse influence line for double wheeled axles (axle type B) as shown in Figure 219.b was necessary for considering realistic axle geometries. Additional calculations confirmed that a lateral shift of the double wheeled axle type B gives the most conservative result for detail D1b at Model C. According to the measured wheel geometries (see Section 4.3) a lateral shift of wheel type B (see Figure 143.b in Section 4.4.2) in transverse bridge direction for taking the corresponding number of cycles of each stress range into account.

The stress history curves due to the lorry crossings (vehicle type T1 to T5) were determined by considering the lorry's axle distances and its axle loads from fatigue load model FLM-4. For every lorry type T1 to T5, a stress history diagram for each position in transverse bridge direction referring to the frequency distribution in Figure 219.a has been calculated. The 45 stress history curves were randomly stringed together under consideration of the lorry percentage according to fatigue load model FLM-4 for long distance routes (see Section 2.5.2) and for altogether 100,000 lorries (see Table 13 in Section 4.7).

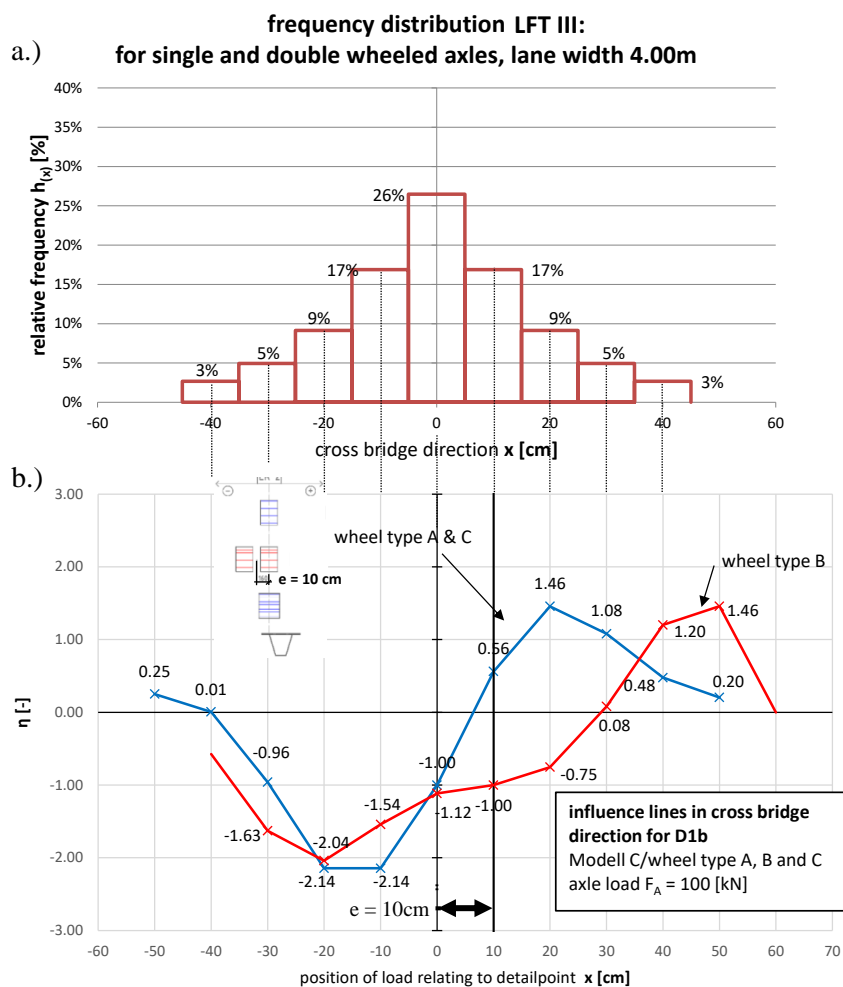


Figure 219: Model C – detail D1b at LR-2: a.) frequency distribution LFT III for a lane width of 4.00m; b.) influence line in transverse bridge direction for single and double wheeled axles (axle type A, B and C);

With Rain flow method as cycle counting concept the stress ranges and its occurring number of cycles have been determined. The resulting stress range spectrum under consideration of heavy vehicle driving characteristics (eccentric vehicle position) with realistic axle geometries (eccentric wheel position) is presented in Figure 220 for detail D1b at Model C.

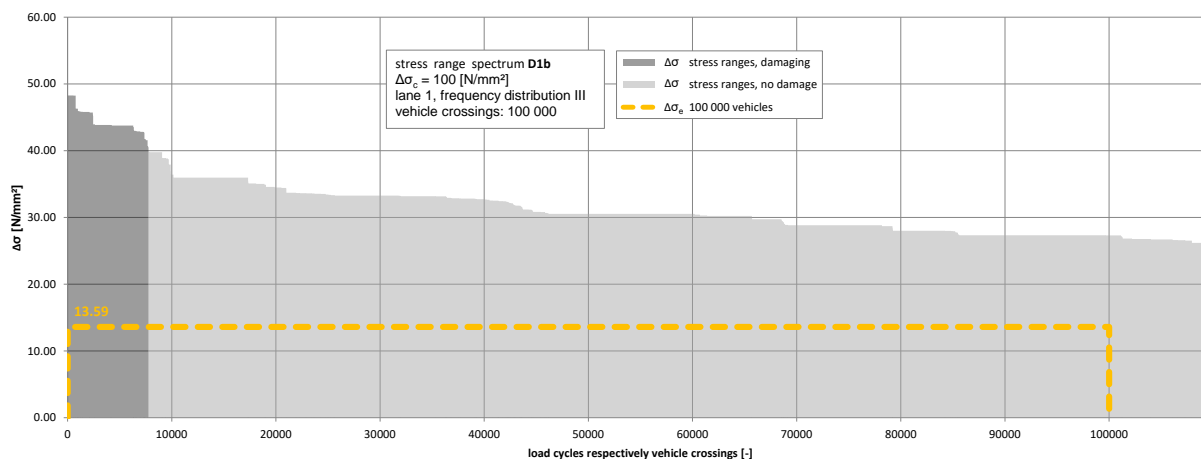


Figure 220: Model C – detail D1b at LR-2: stress range spectrum under consideration of heavy vehicle driving characteristics with realistic axle geometries due to FLM 4-mod

A comparison of the damage equivalent stress ranges $\Delta\sigma_e$ is shown in Table 26:

Table 26: Model C – detail D1b at LR-2: comparison of $\Delta\sigma_e$ for $n_e = 100,000$ lorry crossings due to eccentric vehicle and wheel position

	centric wheel position – FLM 4	eccentric vehicle and wheel position – FLM 4-mod
	$\Delta\sigma_{e,I}$	$\Delta\sigma_{e,III}$
$\Delta\sigma_e$ [N/mm ²]	0.0	13.59

By comparing the results in Table 26 it can be observed that the consideration of heavy vehicle driving characteristics with realistic axle geometries is essential for the fatigue assessment of detail D1b. If these effects of lateral shifting wheels and vehicles would not be taken into account, no fatigue damage would be the result of the calculations. This result is caused by the cut of limit $\Delta\sigma_L$ according to the appropriate S-N curve where stress ranges below this limit can be neglected. Therefore, the damage equivalent stress range $\Delta\sigma_{e,I} = 0$ for centric transverse vehicle and wheel position. On the contrary, under considering eccentric vehicle and wheel position in transverse bridge direction, the calculations show a nameable fatigue damage at detail D1b. The damage equivalent stress range $\Delta\sigma_{e,III} = 13.59$ N/mm² relating to the number of lorries in the analysed lane ($n_e = 100,000$ load cycles in the analyses). The maximum occurring stress range due to centric wheels and vehicles has a value of $\Delta\sigma_{\max,I} = 16.9$ N/mm² (see Figure 218) and due to eccentric wheels and vehicles a value of $\Delta\sigma_{\max,III} = 48.3$ N/mm² (see Figure 220). Hence, the maximum stress range under consideration of lateral shifting wheels and vehicles is 2.9 times higher than due to a centric track configuration ($\Delta\sigma_{\max,III} / \Delta\sigma_{\max,I} = 48.3 / 16.9 = 2.9$). According to the Eurocode [4], the detail would be fatigue endurable also by considering lateral effects, because the maximum occurring stress range $\Delta\sigma_{\max,III} = 48.3$ N/mm² is below the fatigue strength $\Delta\sigma_D = 73.7$ N/mm².

This was neglected in the analyses, because for a fatigue endurable verification fatigue load model FLM 2, that has a higher load level than FLM 4, would be necessary. In addition, Figure 221 shows the stress range spectrum for detail D1b under consideration of eccentric wheels and vehicles in transverse direction for another random sequence of vehicle crossings. By comparing the stress range spectra in Figure 220 and Figure 221, negligible difference can be observed ($13.62 / 13.59 = 1.0022$). In summary 4 different random sequences have been analysed which all lead to very similar results of $\Delta\sigma_e$. Therefore, 100,000 lorries for the traffic simulation are enough to get accurate results regarding to a fatigue assessment of detail D1b.

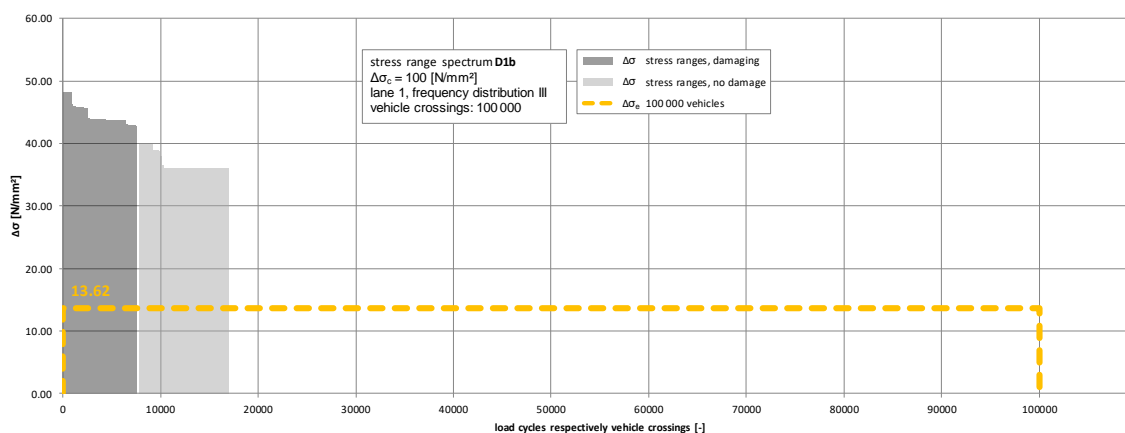


Figure 221: Model C – detail D1b at LR-2: stress range spectrum under consideration of heavy vehicle driving characteristics (LFT III) with realistic axle geometries due to FLM 4-mod (random sequence 2)

4.9.3.3. Detail D2

a.) Reference case: fatigue load model FLM 4 and centric wheel position

A detailed explanation of detail D2 can be found in Section 2.4.4. Figure 113 in Section 3.4.4.3 presents the reference stress range spectrum due to fatigue load model FLM 4 (see Section 2.5.2, Figure 24). This reference stress range spectrum is relating to a centric track configuration of all wheel loads at the web of LR-2 (see Figure 104 in Section 3.4.4). Figure 222 shows again this reference stress range spectrum (identical to Figure 191 in Section 4.8.3.3).

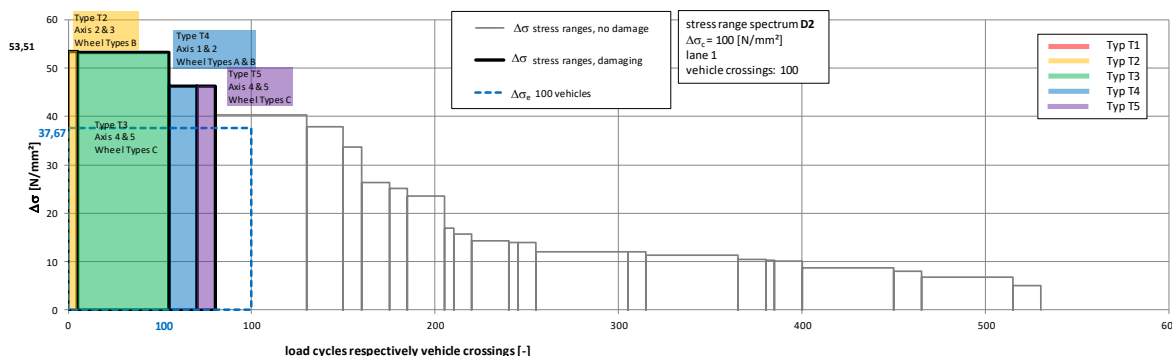


Figure 222: Model C – detail D2 at LR-2: stress range spectrum for a centric track configuration due to FLM 4

b.) Eccentric wheel and vehicle position

A detailed description for a consideration of heavy traffic driving characteristics with realistic axle geometries is already given in Section 4.9.1.1.b. The same procedure of scaling the appropriate stress ranges from Figure 222 with η and splitting it based on frequency distribution LFT II (see Figure 223.a) has been done for detail D2 at model C. A shifting of the transverse influence line for double wheeled axles (axle type B) with $e = 10\text{cm}$ has considered realistic axle geometries. The values for η are illustrated in Figure 223.b. Negative η -values indicate compressive stress and positive η -values indicate tensile stress.

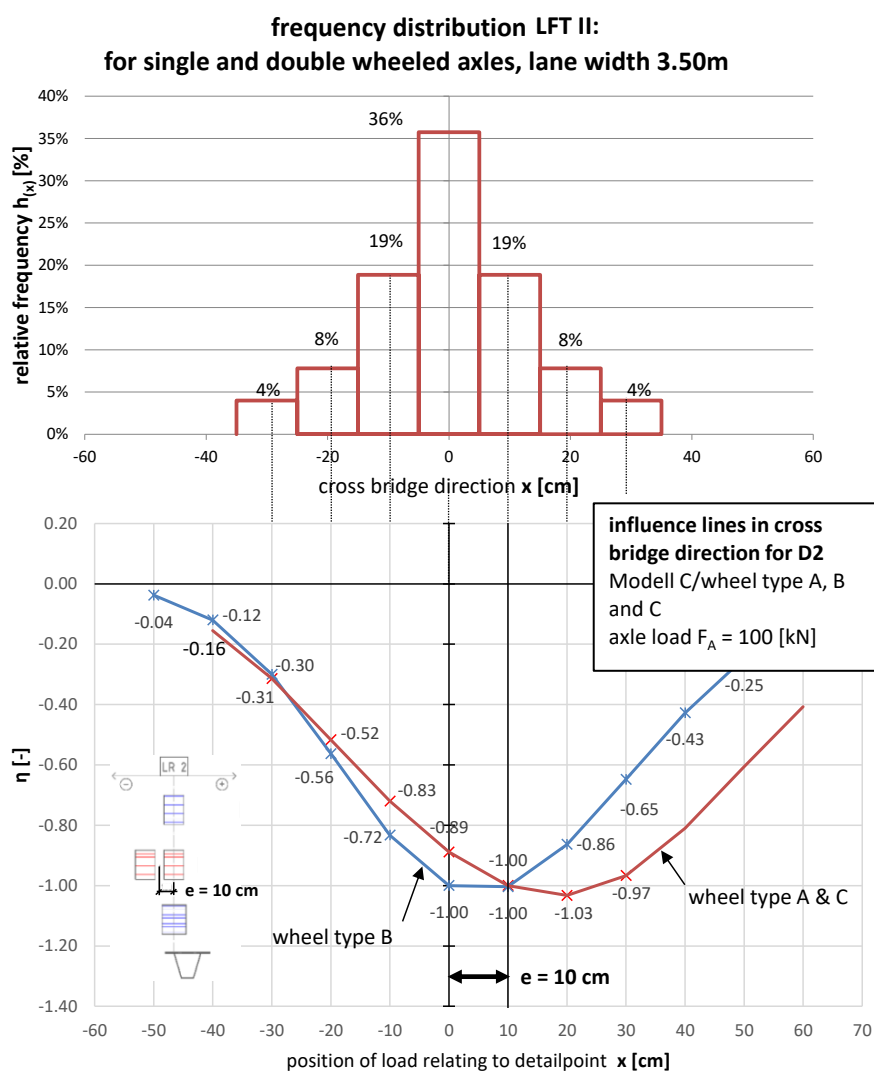


Figure 223: Model C – detail D2 at LR-2: a.) frequency distribution LFT II for a lane width of 3.50m; b.) influence line in transverse bridge direction for single and double wheeled axles (axle type A, B and C);

The resulting stress range spectrum under consideration of heavy vehicle driving characteristics (eccentric vehicle position) with realistic axle geometries (eccentric wheel position) is presented in Figure 224 for detail D2 at Model C.

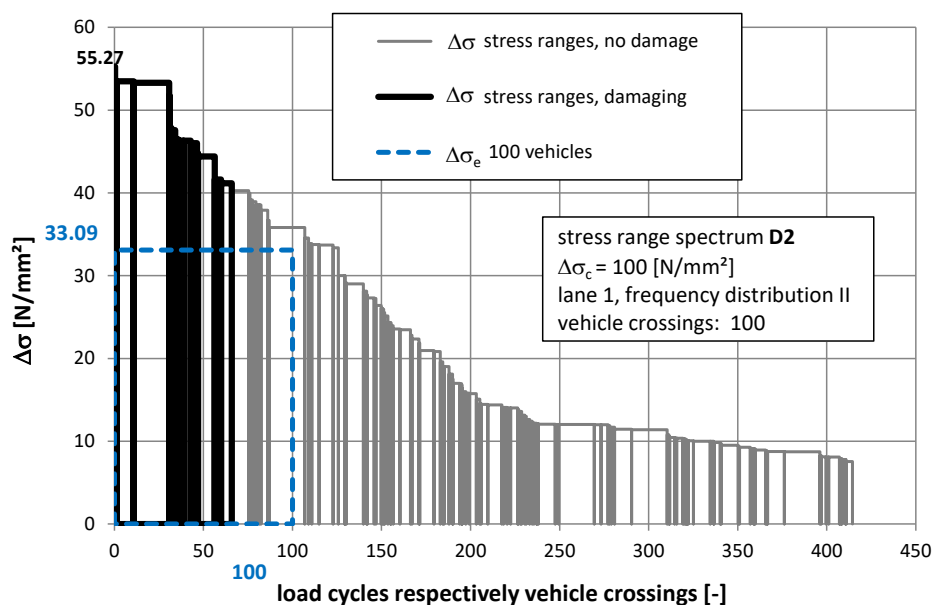


Figure 224: Model C – detail D2 at LR-2: stress range spectrum under consideration of heavy vehicle driving characteristics with realistic axle geometries due to FLM 4-mod

A comparison of the damage equivalent stress ranges $\Delta\sigma_e$ is shown in Table 27:

Table 27: Model B – detail D2 at LR-2: comparison of $\Delta\sigma_e$ for $n_e = 100$ lorry crossings due to eccentric vehicle and wheel position

	centric wheel position – FLM 4 $\Delta\sigma_{e,I}$	eccentric vehicle and wheel position – FLM 4-mod $\Delta\sigma_{e,III}$
$\Delta\sigma_e$ [N/mm ²]	37.67 (1.0)	33.09 (0.88)

As it can be seen in Table 27 the consideration of heavy vehicle driving characteristics with realistic axle geometries causes at detail D2 a reduction of the damage equivalent stress range $\Delta\sigma_e$ of 12% referring to Model C.

Figure 225 illustrates additionally the resulting stress range spectrum due to eccentric wheel and vehicle position in transverse direction by considering frequency distribution LFT I (see Figure 138 in Section 4.4.1). By comparing the stress range spectra from Figure 224 and Figure 225, very less difference can be observed. The damage equivalent stress range due to LFT I is $\Delta\sigma_{e,D2,LFT-I} = 34.23$ N/mm² and the

equivalent stress range due to LFT II is $\Delta\sigma_{e,D2,LFT-II} = 33.09 \text{ N/mm}^2$ ($\Delta\sigma_{e,D2,LFT-I} / \Delta\sigma_{e,D2,LFT-II} = 1.03$).
Hence, the consideration of LFT I and LFT II gives practically the same results.

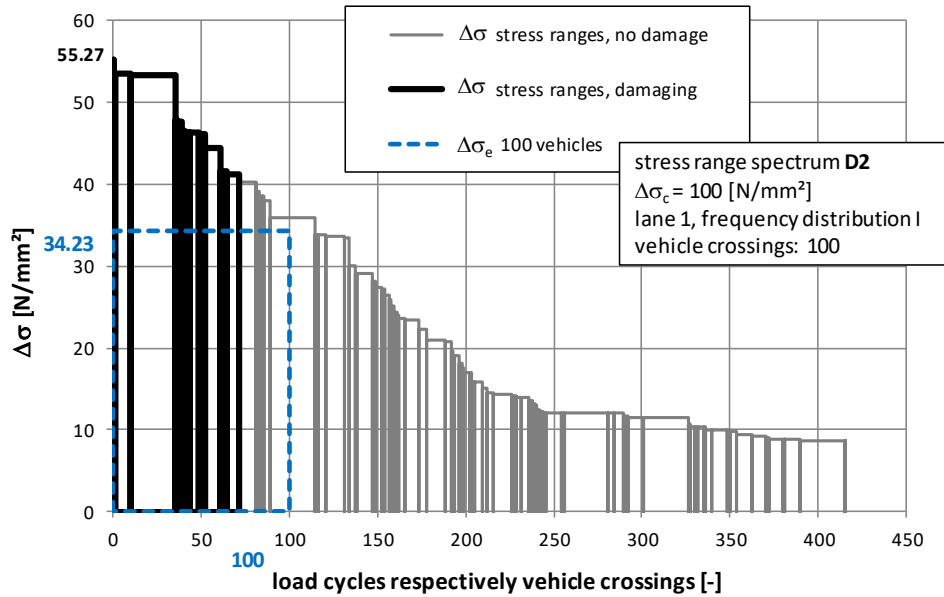


Figure 225: Model C – detail D2 at LR-2: stress range spectrum under consideration of heavy vehicle driving characteristics (LFT I) with realistic axle geometries due to FLM 4-mod

4.10. Comparison of the damage equivalent stress ranges $\Delta\sigma_e$

Table 28 shows a comparison of the results in terms of the damage equivalent stress range $\Delta\sigma_e$ of the numerical simulations according to a consideration of realistic axle geometries (eccentric position of wheels), heavy traffic driving characteristics (eccentric position of vehicles) and both in combination (eccentric position of wheels and vehicles). The values for $\Delta\sigma_e$ are related to a load cycles number equal to the number of crossing lorries in the analysed lane. As reference, the damage equivalent stress ranges $\Delta\sigma_{e,I}$ for a centric track configuration (see Section 4.2, centric position of wheels and vehicles) are also plotted in Table 28. A detailed description of the analysed details D1a, D1b and D2 can be found in Section 2.4 and are additionally illustrated in Figure 226.

Table 28: Comparison of results $\Delta\sigma_e$ for $n_e =$ number of lorries in the lane due to FLM 4 and FLM 4-mod

detail	bridge model	additional characteristics	centric position of wheels and vehicles – FLM 4 $\Delta\sigma_{e,I}$	eccentric position of wheels and centric position of vehicles – FLM 4-mod $\Delta\sigma_{e,II}$	eccentric position of wheels and vehicles – FLM 4-mod $\Delta\sigma_{e,III}$
D1a	Model A	$e_{LR}/t_{DP} = 36$	174.04 (1,0)	167.83 (0.96)	155.78 (0.90)
	Model B	$e_{LR}/t_{DP} = 25$	107.52 (1,0)	101.43 (0.94)	94.22 (0.88)
	Model C	$e_{LR}/t_{DP} = 25$	107.01 (1,0)	96.81 (0.90)	87.56 (0.82)
D1b	Model B	$e_{LR}/t_{DP} = 25$	0	0	39.65
	Model C	$e_{LR}/t_{DP} = 25$	0	0	13.59
D2	Model A	open long. ribs, $e_{CG}=2m$	64.67 (1,0)	74.65 (1.15)	64.65 (1.0)
	Model B	closed long. ribs, $e_{CG}=2m$	35.54 (1,0)	35.51 (1.0)	28.8 (0.81)
	Model C	closed long. ribs, $e_{CG}=4m$	37.67 (1,0)	38.74 (1.03)	33.09 (0.88)

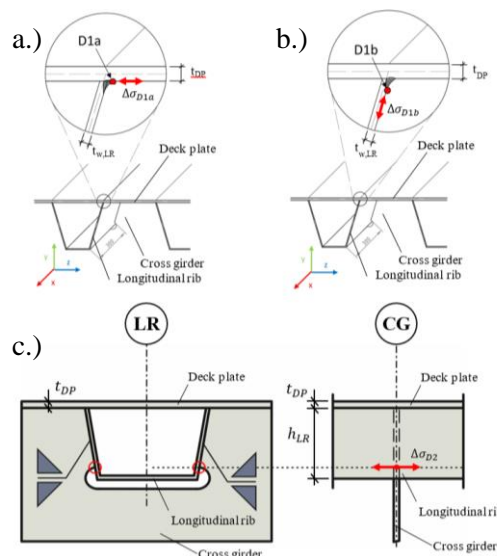


Figure 226: analysed details: a.) detail D1a; b.) detail D1b; c.) detail D2

At detail D1a in Table 28, the damage equivalent stress range $\Delta\sigma_{e,D1a,I}$ decreases due to a lower deck plate slenderness e_{LR} / t_{DP} . Therefore, $\Delta\sigma_{e,D1a,I}$ is for model A 62% higher than for model B and C. For detail D2, the equivalent stress range $\Delta\sigma_{e,D2,I}$ at model A with open longitudinal ribs is 82% higher than at model B with trough longitudinal ribs. The cross girder interval e_{CG} for both models is equal but there is a big difference of the longitudinal rib's bending stiffness (model A: $J_{y,LR} = 2,087\text{cm}^4$; model B: $J_{y,LR} = 4,650\text{cm}^4$) and the stress level $\Delta\sigma$ for each lorry type. Although the cross girder interval of model C is twice times higher than at model B, there is less difference in $\Delta\sigma_{e,D2,I}$. $\Delta\sigma_{e,D2,I}$ for model C is just 6% higher than for model B. This small difference can be explained by the nearly similar relation of the longitudinal rib's bending stiffness to the cross girder interval (model B: $E \cdot J_{y,LR} / e_{CG} = E \cdot 4,650\text{cm}^4 / 200\text{cm} = 23.3 \cdot E$; model C: $E \cdot J_{y,LR} / e_{CG} = E \cdot 10,750\text{cm}^4 / 400\text{cm} = 26.9 \cdot E$) leading to nearly the same stress level $\Delta\sigma$ for each lorry type. This relation is for model C 15% higher than for model B.

By comparing the values in Table 28, a decreasing effect of fatigue damage $\Delta\sigma_{e,D1a,I}$ can be observed for detail D1a due to eccentric wheel position as well as in combination with eccentric vehicle position in transverse direction ($\Delta\sigma_{e,D1a,I} > \Delta\sigma_{e,D1a,II} > \Delta\sigma_{e,D1a,III}$). Although the geometry of model A and B is quite different, the stress reduction at detail D1a due to the analysed lateral load effects is practically equal. Model A has a deck plate slenderness of $e_{LR} / t_{DP} = 36$ and model B has a deck plate slenderness of $e_{LR} / t_{DP} = 25$. Hence, the deck plate slenderness of model A is 44% higher than the one of model B. When taking a closer look to the values for model A and B referring to detail D1a, less difference of stress reduction can be recognised ($\Delta \approx 2\%$). For model C, a more beneficial effect than for model A and B can be detected due to lateral load shifting. For detail D1a, a decrease from 4 to 10 % of $\Delta\sigma_{e,D1a,I}$ can be detected due to a consideration of only realistic axle geometries. A consideration of realistic axle geometries and heavy vehicle driving characteristics always has a decreasing affect to $\Delta\sigma_{e,D1a,I}$ referring to detail D1a at all analysed models, where a reduction of $\Delta\sigma_{e,D1a,I}$ from 10 to 18% can be detected. The highest stress range in detail D1a occurs due to a centric transverse wheel position above the longitudinal rib's web. Therefore, a consideration of lateral shifting wheels and vehicles have to result in a lower equivalent stress range and a lower damage of the analysed detail.

For detail D1b, a dramatically increase of $\Delta\sigma_{e,I}$ can be recognised by taking lateral shifting effects into account ($\Delta\sigma_{e,D1b,I} = \Delta\sigma_{e,D1b,II} = 0 < \Delta\sigma_{e,D1b,III}$). The consideration of eccentric wheel and vehicle position in transverse bridge direction is essential for fatigue assessment of detail D1b. Table 28 shows, that fatigue damage only occurs by taking these effects into account. Because of the random chronology of the vehicle crossings referring to vehicle type and lateral position, the use of a very high number of vehicles in the traffic simulation with at least $n_e = 100,000$ is necessary.

The consideration of only realistic axle geometries (eccentric wheel position and centric located vehicles) causes at detail D2 an increase of $\Delta\sigma_{e,D2,I}$ ($\Delta\sigma_{e,D2,I} < \Delta\sigma_{e,D2,II}$) for model A. Therefore, an increase of 15% can be realised at the model with open longitudinal ribs (Model A). This effect could be observed especially for model A because of the eccentric, one sided connection of the longitudinal rib to the cross girder. Also for a symmetric welded connection this effect appears (with smaller increase) due to the additional bending in the rib about the vertical axis (nearly negligible for centric load position). Under consideration of additional transverse driving characteristics (eccentric position of wheels and vehicles) the damage equivalent stress range $\Delta\sigma_{e,D2,III}$ finally decreases or is equal relating to $\Delta\sigma_{e,D2,I}$ ($\Delta\sigma_{e,D2,I} > \Delta\sigma_{e,D2,III}$ for model B and C with closed longitudinal ribs; $\Delta\sigma_{e,D2,I} = \Delta\sigma_{e,D2,III}$ for model A with open longitudinal ribs). For model B and C a decrease of $\Delta\sigma_{e,D2,I}$ from 12 to 19% referring to detail D2 can be recognised by considering eccentric wheels and vehicles.

4.11. Damage percentage of the individual vehicle types T1 to T5

In this section the damage percentages of the individual lorry types T1 to T5 from fatigue load model FLM 4 (see Section 2.5.2) are again presented referring to the details D1a and D2 at the FEM-Models A, B and C. Now also the effect of the eccentric wheels and eccentric vehicles is taken into account. The results for the centric position of the wheels, shown in Section 3.5, are presented again for comparison. A detailed explanation can be found in Section 2.4.2 for detail D1a and in Section 2.4.4 for detail D2. A description and representation of the analysed FEM-models is in Section 3.2.

The following list gives an overview of the results according to the carried out calculations referring to consideration of heavy traffic driving characteristics with realistic axle geometries and its damage partitioning within the 5 lorry types from fatigue load model FLM 4:

- Detail D1a: welded connection of the longitudinal rib to the deck plate
Damage partition for Model A in Section 4.11.1.1, Model B in Section 4.11.1.2 and Model C in Section 4.11.1.3
- Detail D2: welded connection of the longitudinal rib to the cross girder
Damage partition for Model A in Section 4.11.2.1, Model B in Section 4.11.2.2 and Model C in Section 4.11.2.3

For the following illustrations a colour assignment was chosen – equal as in Section 3.5 – for the 5 lorry types of fatigue load model FLM 4 which is shown in Figure 227.

type	lorry type
T1	
T2	
T3	
T4	
T5	

Figure 227: FLM 4 – colour assignment

4.11.1. Detail D1a

In this section the damage percentage of the individual lorry types T1 to T5 is presented referring to detail D1a, the welded connection of the longitudinal rib to the deck plate.

4.11.1.1. Model A

Figure 228 shows the partition of the damage according to detail D1a at Model A with open longitudinal ribs and a cross girder interval of $e_{CG} = 2.0\text{m}$. In Figure 228.a the results for a centric track configuration (centric wheels and vehicles) are plotted and Figure 228.b displays the results due to a consideration of heavy traffic driving characteristics with realistic axle geometries (eccentric wheels and vehicles).

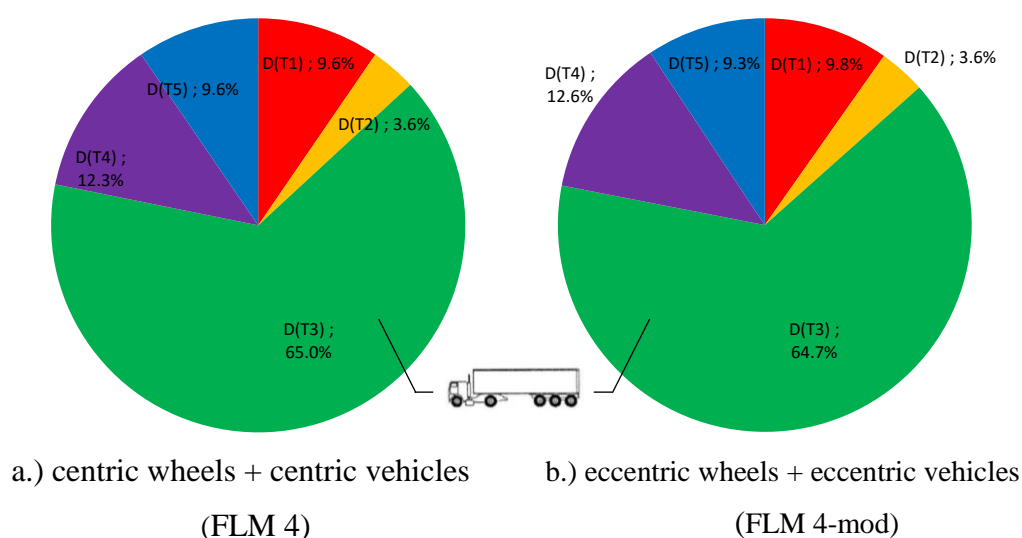


Figure 228: Detail D1a – Model A, percentage of damage of the individual lorry types T1 to T5 according to FLM 4 and FLM 4-mod: a.) centric wheels and vehicles; b.) eccentric wheels and vehicles

As it is illustrated in Figure 228, there is no nameable difference in the damage partitioning between the lorry types referring to centric or eccentric wheels and vehicles. It can be stated, that lorry type T3, the articulated lorry, causes the maximum damage at the analysed detail with 65%.

4.11.1.2. Model B

The damage partition according to detail D1a at Model B with through longitudinal ribs and a cross girder interval of $e_{CG} = 2.0\text{m}$ is shown in Figure 229. In Figure 229.a the results for a centric track configuration (centric wheels and vehicles) are plotted (identical to Figure 121 in Section 3.5.1.2) and Figure 229.b displays the results due to a consideration of heavy traffic driving characteristics with realistic axle geometries (eccentric wheels and vehicles).

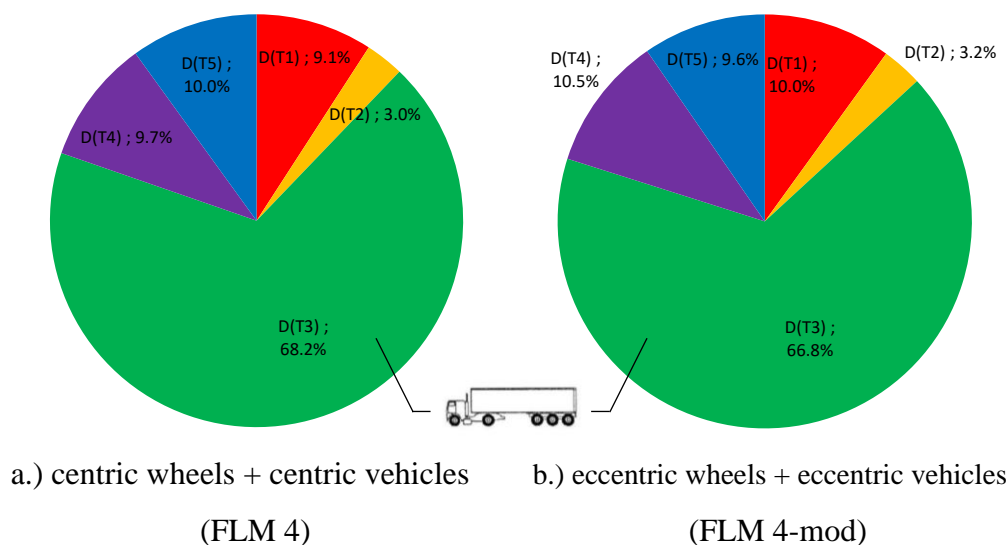


Figure 229: Detail D1a – Model B, percentage of damage of the individual lorry types T1 to T5 according to FLM 4 and FLM 4-mod: a.) centric wheels and vehicles; b.) eccentric wheels and vehicles

By comparing the diagrams in Figure 229, very less difference can be observed in the damage partitioning between the lorry types referring to centric or eccentric wheels and vehicles. It is worth mentioning, that lorry type T3, the articulated lorry, again causes at the analysed detail the maximum damage with a value of 66 to 68%.

4.11.1.3. Model C

Detail D1a’s damage partition at model C with through longitudinal ribs and a cross girder interval of $e_{QR} = 4.0m$ shows Figure 230. Figure 230.a shows the results for a centric track configuration (centric wheels and vehicles, identical to Figure 123) and Figure 230.b displays the results due to a consideration of heavy traffic driving characteristics with realistic axle geometries (eccentric wheels and vehicles).

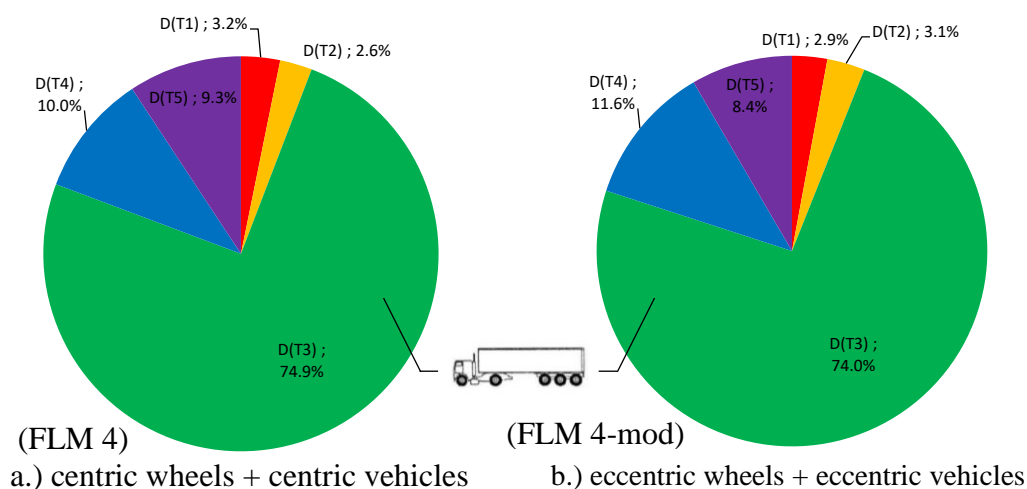


Figure 230: Detail D1a – Model C, percentage of the individual lorry types T1 to T5 according to FLM 4 and FLM 4-mod: a.) centric wheels and vehicles; b.) eccentric wheels and vehicles

Figure 230 shows negligible difference in the damage partitioning between the lorry types referring to centric or eccentric wheels and vehicles. Also at model C, the maximum damage at the analysed detail is caused by lorry type T3, the articulated lorry, with 75%.

4.11.2. Detail D2

In this section the damage percentage of the individual lorry types T1 to T5 is represented referring to detail D2, the welded connection of the longitudinal rib to the cross girder.

4.11.2.1. Model A

Figure 231 shows the partition of the damage according to detail D2 at Model A with open longitudinal ribs and a cross girder interval of $e_{QT} = 2.0\text{m}$. In Figure 231.a the results for a centric track configuration (centric wheels and vehicles) are plotted and Figure 231.b displays the results due to a consideration of heavy traffic driving characteristics with realistic axle geometries (eccentric wheels and vehicles).

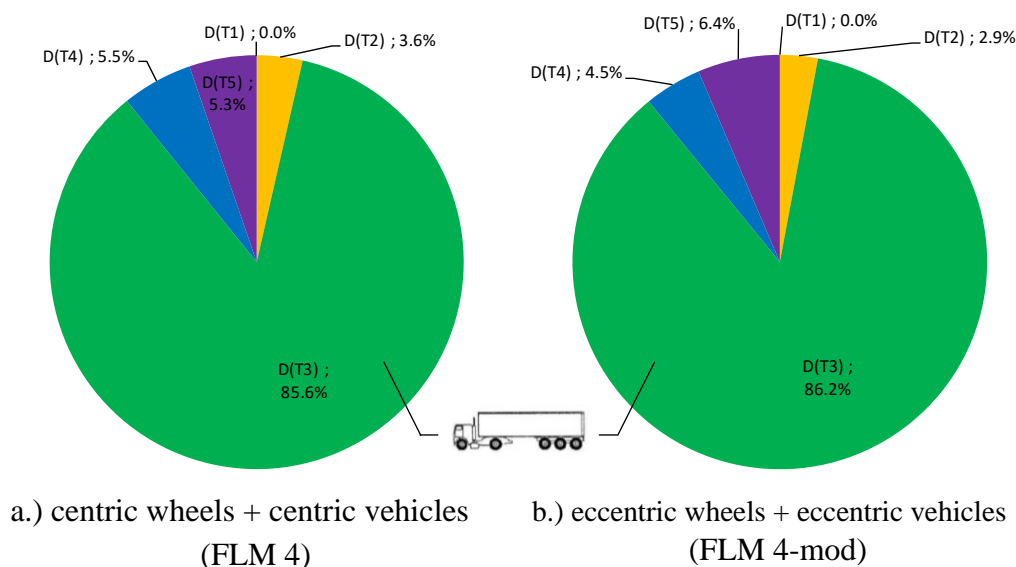


Figure 231: Detail D2 – Model A, percentage of the individual lorry types T1 to T5 according to FLM 4 and FLM 4-mod: a.) centric wheels and vehicles; b.) eccentric wheels and vehicles

Figure 231 illustrates very well that there is less difference in the damage partitioning between the lorry types referring to centric or eccentric wheels and vehicles. A maximum damage at the analysed detail of 86% can be stated due to lorry type T3, the articulated lorry. Additionally, it is worth mentioning that lorry type T1 produces at detail D2 of model A no fatigue damage. The damage in the analysed detail is practically caused only due to lorry type T3 because of its unfavourable axle geometry within the trailer.

4.11.2.2. Model B

The damage partitioning according to detail D2 at Model B with through longitudinal ribs and a cross girder interval of $e_{QT} = 2.0\text{m}$ is shown in Figure 232. The results for a centric track configuration (centric wheels and vehicles) are plotted in Figure 232.a (identical to Figure 127 in Section 3.5.2.2). Figure 232.b displays the results due to a consideration of heavy traffic driving characteristics with realistic axle geometries (eccentric wheels and vehicles).

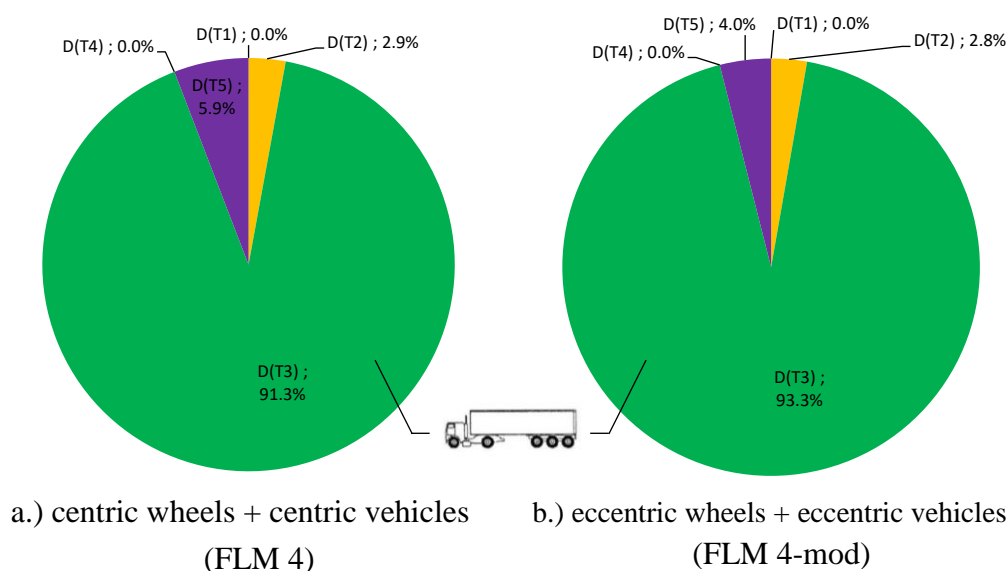


Figure 232: Detail D2 – Model B, percentage of the individual lorry types T1 to T5 according to FLM 4 and FLM 4-mod: a.) centric wheels and vehicles; b.) eccentric wheels and vehicles

When comparing the diagrams in Figure 232, again negligible difference in the damage partitioning between the lorry types referring to centric or eccentric wheels and vehicles can be observed. Lorry type T3, the articulated lorry, produces the maximum damage at the analysed detail with 91 to 93%. Lorry type T1 and T4 doesn't cause any damage in the analysed detail. It can be seen very well that lorry type T3 causes almost the whole damage.

4.11.2.3. Model C

Detail D2's damage partition at model C with through longitudinal ribs and a cross girder interval of $e_{QT} = 4.0\text{m}$ is shown in Figure 233. Figure 233.a visualises the results for a centric track configuration (centric wheels and vehicles, identical to Figure 129 in Section 3.5.2.3). Figure 233.b displays the results due to a consideration of heavy traffic driving characteristics with realistic axle geometries (eccentric wheels and vehicles).

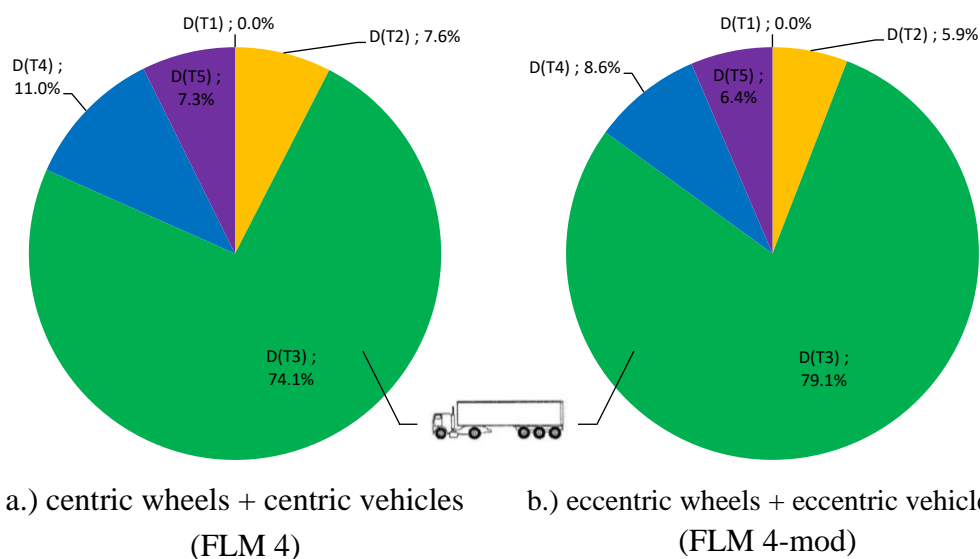


Figure 233: Detail D2 – Model C, percentage of the individual lorry types T1 to T5 according to FLM 4 and FLM 4-mod: a.) centric wheels and vehicles; b.) eccentric wheels and vehicles

The damage partitioning's difference between the lorry types referring to centric or eccentric wheels and vehicles is also negligible small (see Figure 233). It again can be observed, that lorry type T3, the articulated lorry, causes the maximum damage at the analysed detail with 74 to 79%. Lorry type T1 doesn't produce any damage in the analysed detail.

No damage partitioning between the lorry types could be done for the details D1b and D3. At detail D1a and D2, an isolated crossing of each vehicle has been simulated and therefore an assignment of the occurring stress ranges to its individual lorry types is possible. For detail D1b, the crossing of all vehicle types were considered altogether with a random sequence of crossing at different transverse positions. The result was one stress history for all vehicle crossings. Hence, one stress range can be produced due to 2 different lorry types which makes an assignment impossible for this detail.

At detail D3, just the critical lorry type T2 has been taken into account for the analyses (see Section 3.3.4) and therefore a damage partitioning based on the lorry types is also not possible for this detail.

4.12. Concluding Remarks for considering realistic axle geometries and lateral distribution of heavy vehicles

The consideration of heavy traffic driving characteristics in combination with realistic axle geometries has a positive effect to the details D1a and D2. The damage equivalent stress ranges $\Delta\sigma_e$ decrease from 10 to 18% by taking both of these effects at the fatigue assessment into account. A consideration of only realistic axle geometries increases the occurring stresses in detail D2 at model A with open longitudinal ribs up to 15%. At detail D1b, the consideration of eccentric wheel and vehicle position is essential to calculate appropriate results. Without considering these effects, no computational damage occurs at this detail point because a centric track configuration delivers negligible small bending stresses in the through web. A consideration of a wide spreading frequency distribution in transverse bridge direction highly increases the bending stresses in the through web of the longitudinal rib up to 300% and fatigue damage at the detail can be calculated.

The simulations at the three different models showed, that lorry type T3 from fatigue load model FLM 4, the articulated lorry has the highest damage percentage at all analysed details. Depending on the model, the damage percentage of lorry type T3 has a value from 65 to 75% referring to detail D1a. The damage percentage of T3 referring to detail D2 has a significant higher value of 74 to 93% depending on the model. With these results it's convenient to take special care of the lorry type T3. The calculations were carried out by using the lorry percentage for long distance routes, where type T3 has an appearance of 50%. Other lorry distributions with an appearance of type T3 smaller than 50% would deliver another damage partition and less damage percentage of type T3.

Detail D3 was not considered at the analyses referring to lateral shifting wheels and vehicles. But very high fatigue critical stresses do occur at this detail and therefore D3 was again considered for analyses regarding to strengthen the orthotropic steel deck (see Section 5).

5. Strengthening of orthotropic steel decks with a concrete plate

Within this Section the relevant results of a research project are presented, with the challenging aim to increase the service life of such orthotropic bridge decks to at least 50 years after strengthening [33]. In addition, two concepts are shown for the calculation of the remaining fatigue life if a reduced stress level due to the strengthening can be guaranteed. The research activities were based on a very slender orthotropic deck, with a slenderness of $e_{LR}/t_{DP} = 36$ for the deck plate. Two significant details for fatigue of such a representative bridge deck have been analysed. Detail D1a represents the welded connection of the longitudinal rib to the deck plate and Detail D2 is the welded connection of the longitudinal rib to the cross girder. Additionally, Detail D3, the welded connection of the cross girder to the deck plate in the local area of the bolted field splices has also been analysed. Extensive numerical studies were done for the strengthening solution with an UHPC-concrete layer. First the present remaining service life was calculated using a finite element model of the steel deck (see Section 3.4). The beneficial effect of the asphalt layer is considered by an increased wheel contact area [34], [51]. The current fatigue load model FLM 4 from the Eurocode with 5 lorry types and 3 different axle types has been applied and the gross weight of each lorry type was adapted to weigh in motion measurements at an Austrian highway bridge [44] (see Section 2.5.2) to simulate the traffic of the past. For determining the stress reduction factors in the details D1a and D2 after strengthening the finite element model had to be extended with the UHPC layer. The concrete cracking was conservatively considered with an effective Young's Modulus of $E_{c,eff} = E_c/4$ (first assumption; additional studies, shown in Section 5.6.7, showed higher values for $E_{c,eff}$). For both details at least 50 years in service can be guaranteed with an UHPC-pavement that has a thickness of 80mm. Based on these studies full scale tests on an orthotropic deck specimen were done, including overload effects (increased axle loads) and severe temperature effects (simulation of a cold rain event on a very hot summer day) to stimulate concrete cracking. The full scale tests together with the numerical studies showed very good results with regards to the remaining fatigue life. Therefore, in the near future a prototype application on an Austrian highway bridge is intended.

5.1. Modified remaining service life calculation for strengthened structures

5.1.1. Project specific assumptions

The basic concept of the research activities in relation to the strengthening of orthotropic steel decks on road bridges with an UHPFRC pavement (Ultra High Performance Fibre Reinforced Concrete) instead of the asphalt layer is described below. The aim was to guarantee the desired life cycle time of 100 years referring to existing road bridges with this strengthening technique. These analysed existing road bridges were built in the 1960ies and 70ies and the carriageways were not designed under consideration of fatigue phenomena due to the heavy traffic.

The UHPFRC plate increases this load bearing capacity to a very high degree. Also, the increasing axle loads over the decades of usage are covered and no additional verification of the static load carrying behaviour is necessary.

For a warranty of an adequate life cycle time of the orthotropic steel deck a differentiation in relation to the period before and after strengthening has to be done. In the period before strengthening, the orthotropic steel deck was covered with an asphalt layer and the time period was defined from 1970 to 2020. This date, 2020 was chosen as the earliest possible realisation of this strengthening method. Hence, for period I (before strengthening) a time period of 50 years was defined, from 1970 to 2020. For period II (after strengthening) another 50 years have to be guaranteed from 2020 to 2070 to reach the desired life cycle time of 100 years.

The numerical calculations for the steel deck before strengthening and under consideration of an asphalt pavement (period I) are presented in Section 3. The general concept of fatigue assessment at orthotropic steel decks, respectively the heavy traffic simulations over the modelled bridge decks, are shown in Section 3.1. For the calculation of the damage in the notch details due to the heavy traffic in period I, appropriate gross weights and axle loads have to be considered. Also a sufficient number of lorries per year has to be defined for period I. These definitions were done based on weigh in motion measurements on an Austrian road bridge with a high frequency of lorries [44]. The gross weights and axle loads from fatigue load model FLM 4* (see Figure 24 in Section 2.5.2) were taken into account for period I and the number of lorries per year from 1970 to 2020 was defined as shown in Figure 32 in Section 2.6. These values are also based on measurements at the highway A23 near Vienna. From 2000 to 2020 a total amount of lorries at the entire carriageway in one direction of $2 \cdot 10^6$ per year was assumed based on measurements, where 60% of the vehicles are crossing the bridge in the main lane ($2 \cdot 10^6 \cdot 0.6 = 1.2 \cdot 10^6$). From 1970 to 2000 a simplified linear increase of the heavy traffic frequency was chosen as illustrated in Figure 32 which is also based on measurements at highway A10 in Austria. For period II (after strengthening), from 2020 to 2070, a constant heavy traffic frequency as it is visualised in Figure 32 was assumed and the unmodified fatigue load model FLM 4 or FLM 2 (see Figure 24 in Section 2.5.2) has been applied.

In summary, it can be pointed out that a differentiation in 2 periods is necessary for the determination of the stress range spectra and the calculation of the fatigue damage referring to the notch details. The data of the heavy traffic relating to these periods is listed below:

a.) Period I – before strengthening

- Time period between 1970 to 2020, in summary 50 years
- Heavy traffic mix according to FLM 4* (Figure 24 in Section 2.5.2), representative for the actual heavy traffic on mid European highways
- Heavy traffic frequency according to Figure 32 in Section 2.6, in summary $49.2 \cdot 10^6$ heavy vehicles in one lane

b.) Period II – after strengthening

- Time period between 2020 to 2070, in summary 50 years
- Heavy traffic mix according to FLM 4 or FLM 2 (Figure 24 in Section 2.5.2), representative for new bridge projects in the European road network
- Constant heavy traffic frequency according to Figure 32 in Section 2.6 with $1.2 \cdot 10^6$ heavy vehicles per year on the main lane in one direction, in summary $60.0 \cdot 10^6$ heavy vehicles

The requirements to the UHPFRC pavement and its composite interface between steel and concrete are very versatile. Primary, the thickness of the concrete plate, its stiffness as well as the flexibility of the interface layer have to guarantee sufficient resistance through the remaining life cycle time of the bridge. Under consideration of these essential requirements minimum values for the thickness of the UHPFRC pavement will result, depending on the individual deck plate slenderness of the bridge decks and the simulation of fatigue damage in both periods (period I & II). Regarding to the durability of the strengthening method additional analyses referring to the static bearing behaviour and serviceability, especially for the concrete cracking have to be carried out. An increase of the heavy traffic loads in the future has to be considered and therefore the application of fatigue load model FLM 4 or FLM 2 is necessary, based on the fatigue damage of period I (see Section 5.1.2). From today's view FLM 2 includes very high gross weights of the vehicles. For example, the articulated lorry has a gross weight of 630kN (63to). The actual legal maximum loaded vehicle weight in Europe is 440kN (44to) [52] (cf. Figure 24 in Section 2.5.2).

The basic concept of the calculation of the remaining service life regarding to the analysed notch details of the orthotropic steel deck is summed up in the list below:

- a.) Simulation of the heavy traffic crossings at the carriageway before strengthening (see Section 3.4) for period I due to fatigue load model FLM 4* (see Figure 24 in Section 2.5.2) and in summary $49.2 \cdot 10^6$ vehicles (Figure 32 in Section 2.6).
- b.) Determination of the appropriate stress range spectrum via counting and ordering of the occurring stress ranges by its size.

- c.) Calculation of the damage in the analysed notch details according to the modified Miner rule and determination of a damage equivalent constant amplitude stress range $\Delta\sigma_{e,old}$ for period I. The partial damaging stress ranges below the fatigue strength $\Delta\sigma_D$ was considered according to the Eurocode [4] for the damage calculation (also for the stress range spectrum referring to the strengthened steel deck). This procedure is illustrated in Section 2.6. Stress ranges which are lower than the cut off limit of the fatigue strength $\Delta\sigma_L$ were neglected.
- d.) Determination of the remaining service life – calculation of the needed thickness of the UHPFRC plate. 2 concepts have been developed which are presented and described in Section 5.1.2.1 and 5.1.2.2.

5.1.2. Remaining fatigue life for strengthened structures

The relevant load model for a verification of the strengthened deck with an UHPFRC layer in order to extend of the service life of the bridge deck is fatigue load model FLM 4 and FLM 2 (see Section 2.5.2). Under consideration of the standard approach of Concept 1 (see Section 5.1.2.1) fatigue load model FLM 4 is accurate for the heavy traffic simulation. Concept 1 has to be used when a remaining fatigue life exists ($D_{old} < 1.0$) at the bridge deck, after 50 years in service before strengthening. If there is no more calculational service life available after 50 years ($D_{old} \geq 1.0$), Concept 2 (see Section 5.1.2.2) is necessary and therefore fatigue load model FLM 2 has to be applied.

From the heavy traffic simulation at the bridge deck before strengthening, which is presented in Section 3.4, the critical load positions for maximum and minimum stresses (σ_{max} and σ_{min}) are known relating to the analysed details. Therefore, no heavy traffic simulation at the strengthened deck is necessary for Concept 2. Only the critical vehicle with the highest axle loads, which leads to the highest local stresses, has to be applied at its critical positions on the carriageway to calculate the maximum occurring stress range $\Delta\sigma_{max,new}$. In Section 5.4, these critical load positions are presented for Model E-1, E-2 and F referring to the analysed notch details D1a, D2 and D3.

5.1.2.1. Concept 1

In summary, concept 1 is illustrated in Figure 234. At the date of retrofitting and strengthening of the bridge deck in 2020 the actual damage D_{old} is smaller than 1.0 ($D_{old} < 1.0$). This is an essential requirement for the implementation of Concept 1 under consideration of the damage equivalent constant amplitude $\Delta\sigma_{e,old}$ with $n_{old} = 49 \cdot 10^6$ number of cycles, respectively vehicle crossings (Figure 32 in Section 2.6).

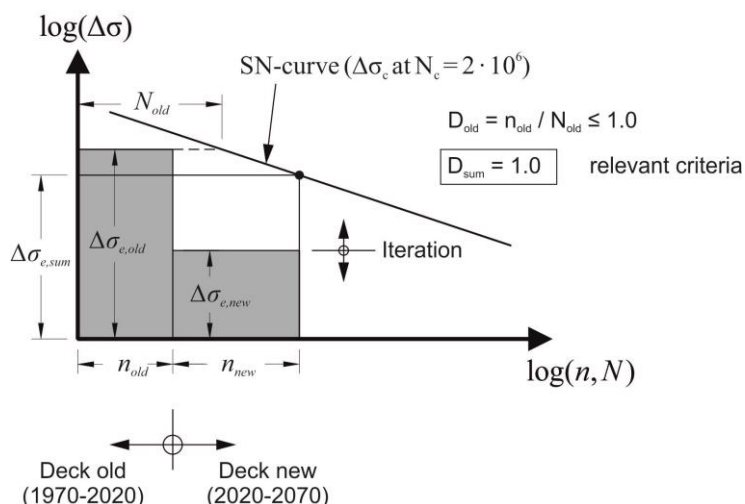


Figure 234: calculation of the remaining service life – concept 1 (simplified illustration without fatigue strength $\Delta\sigma_D$)

Due to the strengthening of the bridge deck with the UHPFRC plate, the stress level in the notch details should be much lower. The heavy traffic simulation with fatigue load model FLM 4 for $60 \cdot 10^6$ vehicles (Figure 32 in Section 2.6), the determination of the stress range spectrum and the damage calculation leads to the damage equivalent constant amplitude stress range $\Delta\sigma_{e,new}$. Under consideration of both constant amplitude stress ranges, $\Delta\sigma_{e,old}$ for the past with n_{old} and $\Delta\sigma_{e,new}$ for the future with n_{new} , an overall constant amplitude stress range $\Delta\sigma_{e,sum}$ results (see Figure 234).

By variation of the concrete plate's thickness t_c , the level of the stress range $\Delta\sigma_{e,new}$ and also $\Delta\sigma_{e,sum}$ is also varying. This iteration has to be done until the overall damage D_{sum} reaches a value of 1.0. With this iteration of the concrete plate's thickness t_c , a minimum required value of $t_{c,min}$ can be indicated. Based on the damage calculations of time period I before strengthening this concept 1 was not applicable, because D_{old} was higher than 1.0.

5.1.2.2. Concept 2

Based on the numerical simulations of the heavy traffic in the past (time period I) the damage D_{old} exceeds 1.0 ($D_{old} > 1.0$) as it can be seen in Figure 235. Conservative assumptions were made for the calculation of the remaining service live before strengthening. Therefore, it can be that there may be no fatigue cracks at the notch details. But an inspection on site and if necessary a renovation of potentially fatigue cracks is required.

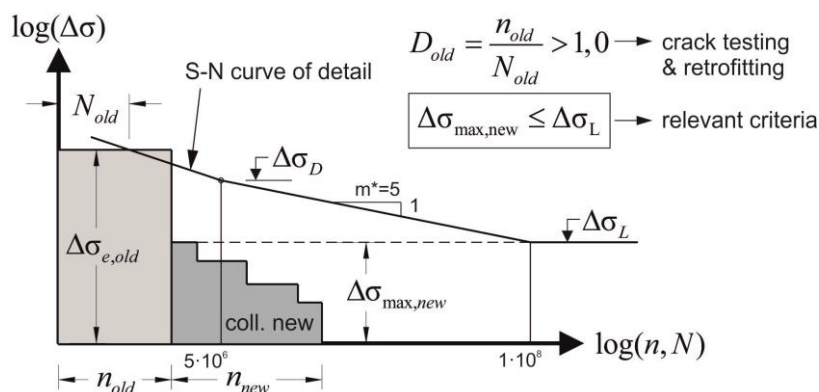


Figure 235: calculation of the remaining service life – concept 2

If there are no cracks at the analysed notch details or detected fatigue cracks have been renovated, a continued service of the bridge is possible under consideration of Concept 2 (see Figure 235). Nevertheless, inspections of the notch details with an appropriate interval are necessary. This interval has to be assigned based on fracture mechanic analyses of the details. No more additional fatigue damage at the analysed notch details is allowed and therefore the maximum occurring stress ranges in the future have to be lower than the cut off limit $\Delta\sigma_L$ (see Figure 235). To cover the future increasing axle loads and frequency [21] of the heavy traffic it is necessary to apply fatigue load model FLM 2 (see Section 2.5.2, Figure 24) which includes much more higher axle loads and gross weights of the individual lorry types (overloading effects were checked in the full scale tests in Section 5.6). The crossing of one lorry type that has the highest axle loads and causes the maximum occurring stress ranges $\Delta\sigma_{\max, \text{new}}$ in the notch details now is sufficient for the fatigue verification. Within this concept, this maximum occurring stress range $\Delta\sigma_{\max, \text{new}}$ has to be lower than the cut off limit of the fatigue strength ($\Delta\sigma_{\max, \text{new}} \leq \Delta\sigma_L$).

By variation of the concrete plate's thickness t_c , the level of the maximum occurring stress range $\Delta\sigma_{\max, \text{new}}$ is also varying. This iteration has to be done until the requirement $\Delta\sigma_{\max, \text{new}} \leq \Delta\sigma_L$ is fulfilled and a minimum thickness of the UHPFRC plate $t_{c, \text{min}}$ can be indicated. Additionally, the concrete thickness t_c is also limited to practical application methods. The analysed notch details are then fatigue endurable and have a computational overall service life of more than 100 years (inspections with an appropriate interval still required).

5.2. Analysed FE-models for the strengthened orthotropic steel deck

For the verification of the additional service life of 50 years, after already 50 years in service before, it was necessary to generate 3 more finite element models referring to the notch details D1a, D2 and D3. A detailed description of the analysed notch details can be found in Section 2.4.

The following list gives an overview of the created finite element models:

- Model E-1 – Section 5.2.1: orthotropic bridge deck with open longitudinal ribs and a cross girder spacing of $e_{CG} = 2.0\text{m}$ (FEM model is based on Model A in Section 3.4.2), including an UHPFRC plate (with a variation of the concrete plate thickness t_c), where a detailed mesh refinement was applied in the steel structure, especially in the local areas of the analysed notch details D1a and D2;
- Model E-2 – Section 5.2.2: orthotropic bridge deck with trough longitudinal ribs and a cross girder spacing of $e_{CG} = 2.0\text{m}$ (FEM model is based on Model A in Section 3.4.2), including an 80mm thick UHPFRC plate, where a detailed mesh refinement in the concrete plate was applied for the calculation of the stresses in the plate and the interface between concrete and steel;
- Model F – Section 5.2.3: orthotropic bridge deck consisting of one cross girder with open longitudinal ribs and bolted field splices (FEM model is based on Model D in Section 3.4.5); including a 80mm thick UHPFRC plate;

5.2.1. Model E-1: Orthotropic bridge deck with open longitudinal ribs – including a concrete pavement (detailed mesh refinement in the steel structure)

The basis for Model E-1 is Model A which is presented and described in Section 3.4.2. Model E-1 consists of the same parts as Model A with the same geometry. Also the boundary conditions as well as the transition conditions referring to the steel structure in the assembly have been taken over from Model A. In Model E-1 an additional concrete pavement as a topping on the steel deck plate was applied which is partitioned in 2 regions as it is shown in Figure 236. Region A has a finer element mesh as Region B. Figure 236 illustrates the modelled regions as well as the chosen element types and its element sizes, whereby at model E-1 solid elements with full integration rule were necessary (Model A is modelled with solid elements and reduced integration rule). The thickness of the concrete pavement has been varied with 60, 70 and 80mm. An overall effective Young's Modulus $E_{c,eff}$ has been set for the UHPFRC plate which should cover the cracking in the concrete plate. At Model E-1, the Young's Modulus of the concrete pavement has a constant value of $E_{c,eff} = 12,500 \text{ N/mm}^2$ (for the properties of the concrete see Section 5.6.2.2).

According to an extended literature research in [33] referring to practically realised interfaces between steel deck plate and concrete pavement, this interconnecting layer is mainly made of an epoxy resin with interspersed Basalt granulate. In addition to the study with limit value observation (with and without composite effect) it was necessary to analyse the accurate flexibility of the interface within the numerical simulations. By using the software ABAQUS, this flexibility was modelled with an interaction condition between the steel deck plate and the concrete plate. As interaction condition between the elements of the concrete and the steel, a cinematic connection of the nodes was implemented which is in ABAQUS called as „cohesive behaviour“, based on the shear stiffness of epoxy resin.

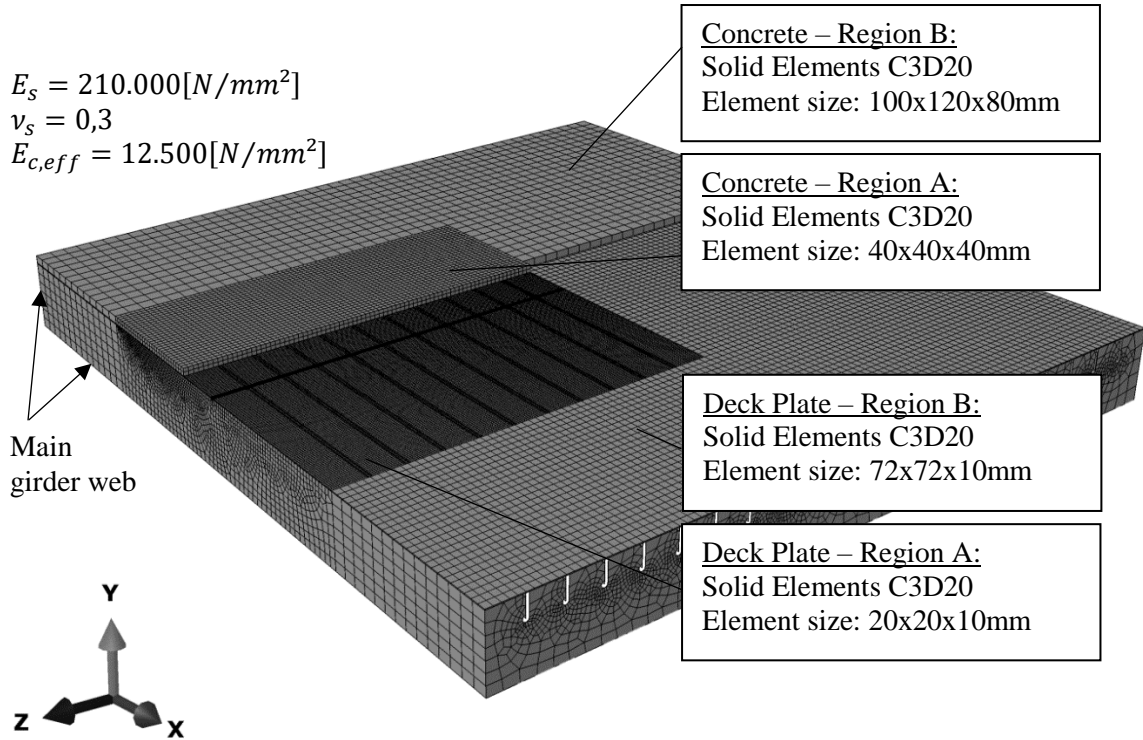


Figure 236: FEM-Modell E-1 – orthotropic steel deck with open longitudinal ribs including a UHPFRC pavement (overview)

Model E-1, the strengthened deck, has the same finite element mesh as Model A, the unstrengthened deck. This equality of the mesh was necessary for the possibility of comparing the results of these two models. Based on this fact it was not possible to match the element nodes of the steel plate and the concrete pavement as it is illustrated in Figure 237.

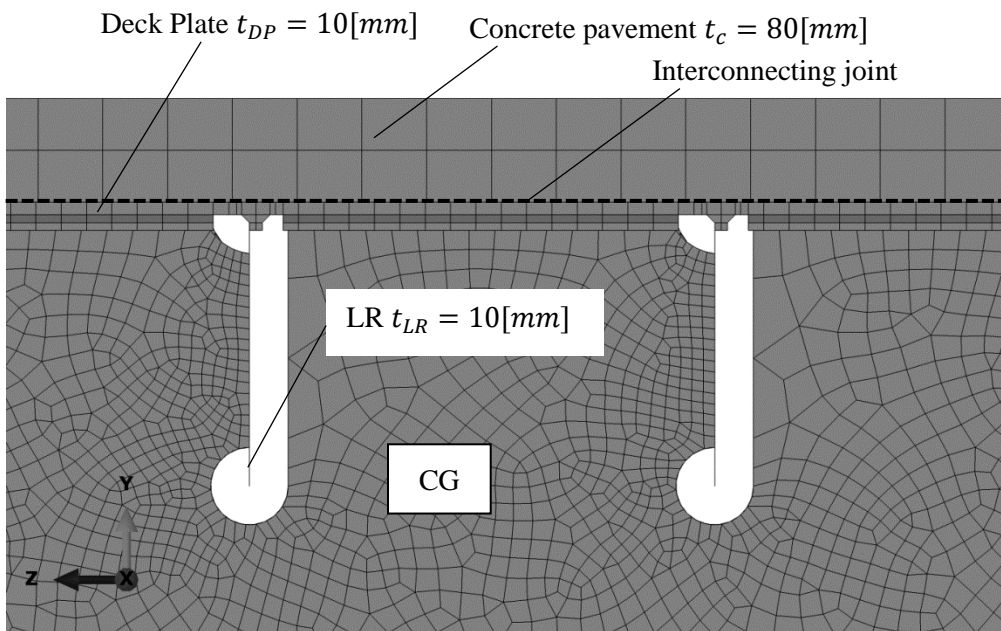


Figure 237: FEM-Modell E-1 – orthotropic steel deck with open longitudinal ribs including a UHPFRC pavement (detailed view of the FEM mesh in the steel structure and the concrete pavement)

If the mesh of the concrete pavement would have been adapted conforming to the mesh of the steel deck plate, an inconvenient mesh geometry of the solid elements and a large amount of degrees of freedom would have been the result. Figure 237 shows the chosen mesh geometries of the solid elements referring to the steel deck plate and the concrete pavement. It can be seen that the nodes of the solid elements at the interconnecting joint doesn't match together. For this reason, the occurring stresses in the solid elements of the concrete and the shear stresses in the interface between steel and concrete elements will have less accuracy. Therefore, an additional finite element model E-2 (see Section 5.2.2) has been created for the calculation of the stresses in the elements of the concrete pavement and in the interface between steel and concrete.

The interaction condition “cohesive behaviour” needs values referring to its flexibility in both in plane directions (K_1 and K_2 , in axes x and z of the model) and in one normal direction (K_3 in axis y of the model) of the interface between steel deck and concrete pavement. For the third direction normal to the plane of the interface, a very high value for the flexibility K_3 was defined to create a nearly rigid connection in normal direction and prevent penetrations. The flexibility of the interconnecting joint in both in plane directions (K_1 and K_2) has been varied to get border line cases and accurate values based on the effective thickness of the epoxy resin. The defined values for the variation of the interface flexibility are plotted in Table 29. These values can be deduced from the shear modulus of an epoxy material whereby the elastic modulus and the Poisson ratio are taken from [53].

Table 29: Variation of the flexibility in the numerical calculations referring to the interface between steel deck plate and concrete pavement

Calculation model	Interconnecting joint – version and description	flexibility K_1 and K_2 [$N/(mm^3)$]
I	No composite	1
II	Epoxy $t_{\text{epoxy}} = 3$ [mm]	400
III	Epoxy $t_{\text{epoxy}} = 1$ [mm]	1200
IV	Rigid composite	10^6

Material properties of epoxy from [53]:

- Young's Modulus: $E_{\text{epoxy}} = 3,200$ N/mm²
- Poisson Ratio: $\nu_{\text{epoxy}} = 0.33$

With these parameters (E_{epoxy} and ν_{epoxy}) the shear modulus can be determined with Equation 10:

$$G_{epoxy} = E_{epoxy} / [2 \cdot (1 + \nu_{epoxy})] \quad \text{Equation 10}$$

Under consideration of an effective epoxy layer thickness t_e , the values for K_1 and K_2 can be determined with Equation 11:

$$K_1 = K_2 = G_{epoxy} / t_{epoxy} \quad \text{Equation 11}$$

5.2.2. Model E-2: Orthotropic bridge deck with open longitudinal ribs – including a concrete pavement (detailed mesh refinement in the UHPFRC plate)

The finite element model E-1, which is described in Section 5.2.1, delivered sufficient results in relation to the occurring stresses in the analysed notch details of the steel structure due to the heavy vehicles. Within Model E-1, the mesh refinement was mainly implemented at the steel structure to get results of high accuracy there and this was necessary for the evaluation of the strengthening technique with an UHPFRC pavement instead of the common asphalt layer. Furthermore, the Young's Modulus of the concrete in Model E-1 was defined with a very low value of $E_{c,eff} = E_c / 4 = 12,500 \text{ N/mm}^2$ to calculate conservative stresses in the notch details (additional studies showed higher values for $E_{c,eff}$, presented in Section 5.6.7).

For the determination of accurate stresses in the concrete layer and adequate shear stresses in the interconnecting joint between steel deck and concrete pavement, an additional finite element model was necessary. This additional FEM model had to have the same geometry, boundary and transition conditions as Model E-1 and Model A. Therefore, Model E-2 was created which has another finite element mesh as Model E-1 and a higher Young's Modulus of the concrete pavement. At Model E-2 the mesh of the steel structure was adapted conforming to the mesh of the concrete plate so that the nodes of all solid elements at the interface fit together. Figure 238 illustrates the geometry of the finite element mesh in the steel structure and the concrete pavement in detail. The nodes from the elements at the upper surface of the deck plate have the same coordinates as the elements at the bottom surface of the concrete plate. By comparing Figure 238 (Model E-2) and Figure 237 (Model E-1) it can be recognized that the solid elements of the welds in Model E-2 have been removed to get a continuous element partitioning in the deck plate. Generally, Model E-2 has a coarse finite element mesh in the steel structure (MG, CG, LR and DP) compared to Model E-1 and Model A, because no stresses in the notch details were

calculated with this model. The same values for the flexibility of the interconnection joint between steel deck and concrete plate were considered as in FE-model E-1 (see Table 29).

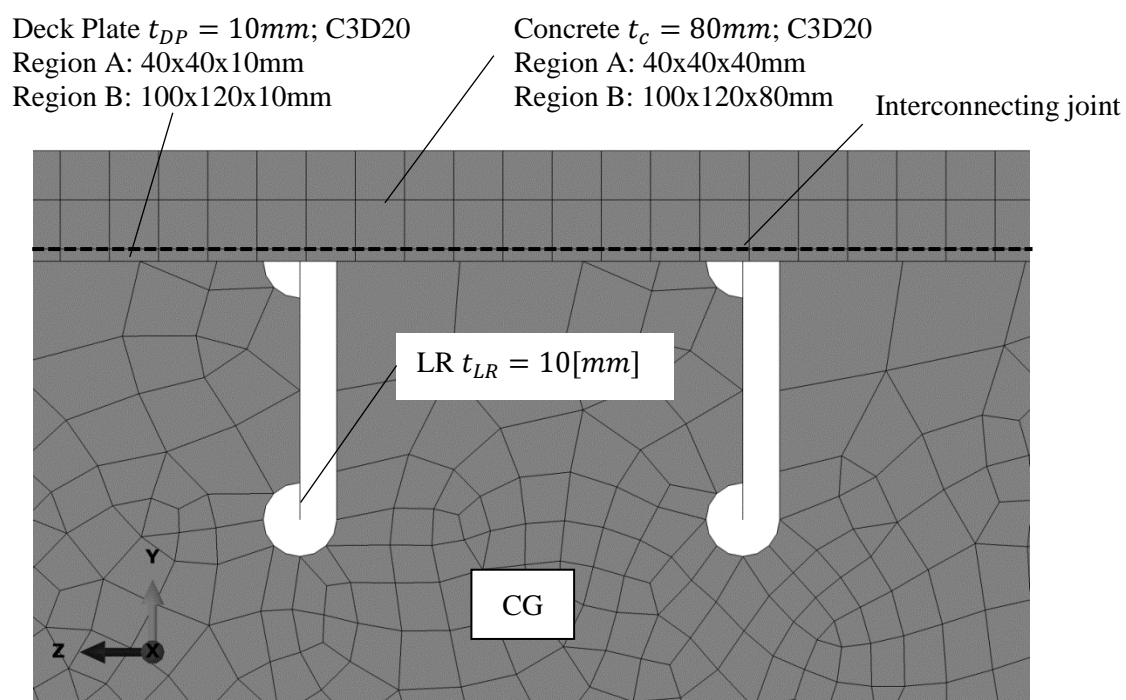


Figure 238: FEM-Modell E-2 – orthotropic steel deck with open longitudinal ribs including a UHPFRC pavement (detailed view of the FEM mesh in the steel structure and the concrete pavement)

5.2.3. Model F: Orthotropic bridge deck with open longitudinal ribs – cross girder with bolted connections – including a concrete pavement

The basis for Model F is Model D which is presented and described in Section 3.4.5. Model F consists of the same parts as Model D with the same geometry (steel deck). The boundary and transition conditions of the steel structure are equal to Model D. An additional concrete pavement as a topping on the steel deck plate was applied in Model F. This concrete plate has been implemented by using composite shell elements under the consideration of a 10mm thick steel plate and an 80mm thick concrete plate. The Young's Modulus of the steel was defined with $E_s = 210,000 \text{ N/mm}^2$ and of the concrete $E_{c,eff} = E_c / 4 = 12,500 \text{ N/mm}^2$. Figure 239 shows an isometric overview of the finite element model relating to Model F and all parts are indicated. For a detailed description of the geometry, boundary and transition conditions take a look at Section 3.2.4.

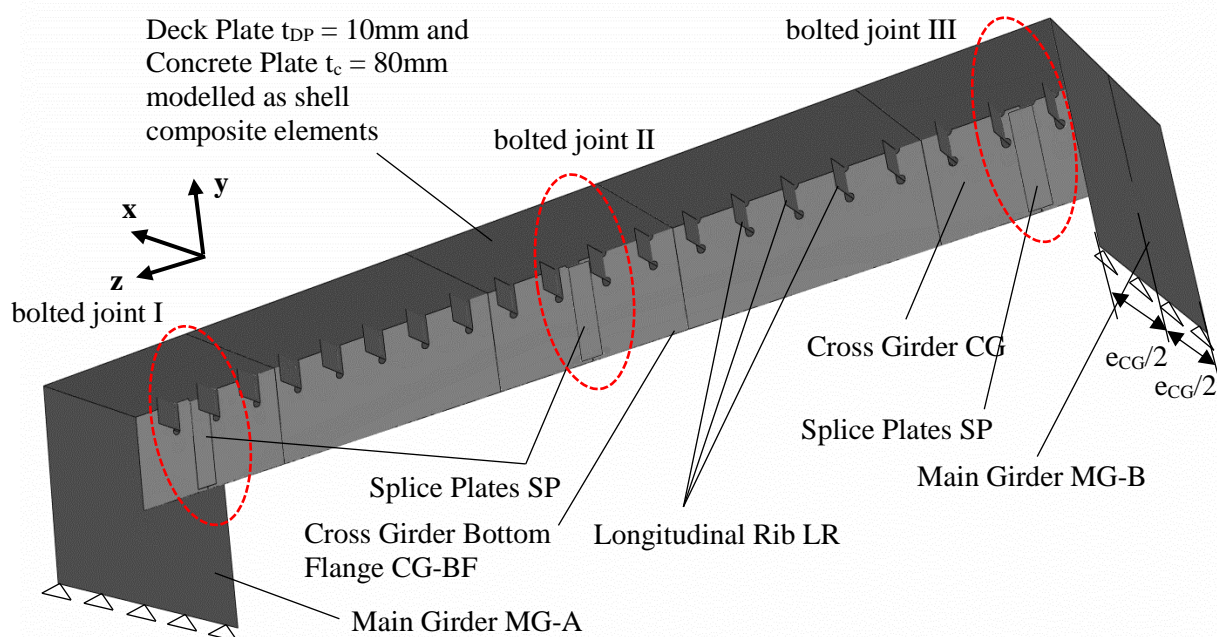


Figure 239: Modell F – orthotropic steel deck with open longitudinal ribs including a 80mm UHPFRC pavement – cross girder with bolted connections (isometric drawing)

5.3. Damage calculation before strengthening in detail D1a, D2, (D3)

5.3.1. General

The simulation of the heavy traffic crossings over the analysed orthotropic steel bridge decks before strengthening are shown in Section 3.4. The illustrated stress range spectra in Section 3.4 relating to the fatigue critical notch details D1a, D2 and D3 (see Section 2.4) are related to a total number of 100 lorries. For an evaluation of the damage before strengthening, a realistic number of load cycles has to be taken into account which is shown in Figure 32 in Section 2.6.

The decisive S-N-curve for notch detail D1a, D2 and D3 has a fatigue strength of $\Delta\sigma_c = 100 \text{ N/mm}^2$ relating to $n_c = 2 \cdot 10^6$ number of load cycles under consideration of the structural stress method (see Section 2.7 and 2.8). The fatigue strength relating to $n_D = 5 \cdot 10^6$ number of load cycles has a value of $\Delta\sigma_D = 73.7 \text{ N/mm}^2$.

5.3.2. Detail D1a – Damage at the steel deck before strengthening

Figure 86 in Section 3.4.2.1 illustrates the stress range spectrum referring to detail D1a at the unstrengthened orthotropic steel deck (Model A) due to the actual fatigue load model FLM 4* for long distance routes (see Section 2.5.2). The corresponding damage equivalent constant amplitude stress range $\Delta\sigma_e$ relating to a crossing of 1 heavy vehicle has a value of $\Delta\sigma_{e,D1a,old} = 140.06 \text{ N/mm}^2$ (see Figure

86). The total number of occurring lorries in the critical main lane and under consideration of time period I (1970 to 2020) has a value of $n_{e,D1a,old} = 49.2 \cdot 10^6$ which is based on measurements [44] (see Figure 32 in Section 2.6).

Under consideration of the appropriate S-N-curve, the maximum allowable number of load cycles regarding to $\Delta\sigma_{e,D1a,old} = 140.06 \text{ N/mm}^2$ can be calculated by a transformation of Equation 5 (see Section 2.6):

$$\begin{aligned} N_{R,D1a,old} &= (\Delta\sigma_D / \Delta\sigma_{e,D1a,old})^3 \cdot 5 \cdot 10^6 = (\Delta\sigma_C / \Delta\sigma_{e,D1a,old})^3 \cdot 2 \cdot 10^6 = (100 / 140.06)^3 \cdot 2 \cdot 10^6 \\ &= 7.3 \cdot 10^5 \end{aligned}$$

Therefore, the damage $D_{D1a,old}$ at notch detail D1a referring to the unstrengthened deck in time period I (1970 to 2020) can be calculated by considering Equation 6 (see Section 2.6):

$$D_{D1a,old} = n_{e,D1a,old} / N_{R,D1a,old} = (49.2 \cdot 10^6) / (7.3 \cdot 10^5) = 67.4 \gg 1.0$$

Hence, the computational service life regarding to fatigue phenomena is already exhausted. In the reference year 2020 the value for the damage $D_{D1a,old}$ exceeds 1.0. Because of the very conservative assumptions in the verification of the remaining service life, there need not necessarily be fatigue cracks at the notch details. But an inspection on site and if necessary, a renovation of potentially fatigue cracks is required.

Because of the exhausted service life after 50 years referring to notch detail D1a, Concept 2 has to be applied, which is described in Section 5.1.2.2. After the strengthening of the deck with an UHPFRC pavement, no more additional damaging stress range is allowed in the future. This means that the maximum future stress range $\Delta\sigma_{\max,D1a,new}$ has to be lower than the cut of limit of fatigue $\Delta\sigma_L$ (see Figure 235).

5.3.3. Detail D2 – Damage at the steel deck before strengthening

The stress range spectrum for detail D2 at the unstrengthened orthotropic steel deck (Model A) is shown in Figure 91 in Section 3.4.2.2 which was determined due to FLM 4* (see Section 2.5.2). The damage equivalent constant amplitude stress range $\Delta\sigma_e$ relating to a crossing of 1 heavy vehicle has a value of $\Delta\sigma_{e,D2,old} = 48.05 \text{ N/mm}^2$ (see Figure 91). For this detail the same traffic condition is given as at detail D1a. This means a total number of occurring lorries in the critical main lane for time period I (1970 to 2020) of $n_{e,D2,old} = 49.2 \cdot 10^6$ (based on measurements [44], see Figure 32 in Section 2.6).

Under consideration of the appropriate S-N-curve and Equation 5, the maximum allowable number of load cycles regarding to $\Delta\sigma_{e,D2,old} = 48.05 \text{ N/mm}^2$ is:

$$\begin{aligned} N_{R,D2,old} &= (\Delta\sigma_D/\Delta\sigma_{e,D2,old})^3 \cdot 5 \cdot 10^6 = (\Delta\sigma_C/\Delta\sigma_{e,D2,old})^3 \cdot 2 \cdot 10^6 = (100/48.05)^3 \cdot 2 \cdot 10^6 \\ &= 18.04 \cdot 10^6 \end{aligned}$$

Therefore, the damage $D_{D2,old}$ at notch detail D2 referring to the unstrengthened deck in time period I (1970 to 2020) can be calculated by considering Equation 6:

$$D_{D2,old} = n_{e,D2,old}/N_{R,D2,old} = (49.2 \cdot 10^6)/(18.04 \cdot 10^6) = 2.7 > 1,0$$

The computational service life regarding to fatigue phenomena at detail D2 is already exhausted after 50 years in service before. In the reference year 2020 the value for the damage $D_{D2,old}$ exceeds 1.0. Also for detail D2 can be stated that very conservative assumptions in the remaining service life verification were considered and therefore not necessarily fatigue cracks are obvious. Therefore, the same recommendations are given as already mentioned at detail D1a.

Because of the exhausted service life after 50 years, Concept 2 has to be applied which is described in Section 5.1.2.2. No additional damage in the detail is allowed and the maximum future occurring stress range $\Delta\sigma_{max,D2,new}$ has to be lower than the cut of limit of fatigue $\Delta\sigma_L = 40.2 \text{ N/mm}^2$ (see Figure 235).

5.3.4. Detail D3 – Simplified damage at the steel deck before strengthening

It is important to mention that for detail D3 the accurate stress spectrum is also influenced by lorry crossings in different lanes. This effect is not considered here. Figure 245.a in Section 5.4.3 illustrates the occurring stresses referring to detail D3 at the unstrengthened orthotropic steel deck (Model D) due to the critical lorry type of FLM 4* at the relevant lane position on the carriageway (see Section 3.3.4). The maximum occurring stress range at the unstrengthened deck has a value of $\Delta\sigma_{max,D3,old} = \Delta\sigma_{T2,D3,old} = 120 \text{ N/mm}^2$ due to lorry type T2 (see Figure 24 in Section 2.5.2). The total number of occurring lorries in the critical main lane has a value of $n_{tot,D3,old} = 49.2 \cdot 10^6$ for time period I (1970 to 2020) which is based on measurements [44] (see Figure 32 in Section 2.6). By considering the lorry percentage for long distance routes (see Figure 24 in Section 2.5.2), vehicle type T2 has an value of 5%. Therefore, the number of occurring lorry types T2 can be calculated to $n_{T2,D3,old} = 49.2 \cdot 10^6 \cdot 0.05 = 2.46 \cdot 10^6$.

Under consideration of the appropriate S-N-curve and Equation 5 (see Section 2.6), the maximum allowable number of load cycles regarding to $\Delta\sigma_{T2,D3,old} = 120 \text{ N/mm}^2$ can be calculated:

$$N_{R,T2,D3,old} = (\Delta\sigma_D/\Delta\sigma_{T2,D3,old})^3 \cdot 5 \cdot 10^6 = (\Delta\sigma_C/\Delta\sigma_{T2,D2,old})^3 \cdot 2 \cdot 10^6 = 1.158 \cdot 10^6$$

Therefore, the damage $D_{T2,D3,old}$ due to lorry type T2 (see Section 2.6) at detail D3 can be calculated with Equation 6 for the unstrengthened deck in time period I (1970 to 2020):

$$D_{T2,D3,old} = n_{T2,D3,old}/N_{R,T2,D3,old} = (2.46 \cdot 10^6)/(1.158 \cdot 10^6) = 2.1 > 1,0$$

Due to a consideration of only the single lorry type T2 the computational service life regarding to fatigue phenomena is already exhausted after 50 years in service before. Hence, additional numerical calculations under consideration of all other lorry types from FLM 4* and also considering the lorry crossing at different lanes are not necessary, because the overall result is the same ($D_{old} > 1.0$). As already mentioned, an inspection on site is required as well as a renovation of potentially fatigue cracks. The calculations regarding detail D3 showed an exhausted service life after 50 years and therefore Concept 2 has to be used (see Section 5.1.2.2). Within this concept no more additional damage in the future is allowed after the strengthening. This requirement can be fulfilled when the maximum future stress range $\Delta\sigma_{max,D3,new}$ is lower than the cut off limit of fatigue $\Delta\sigma_L$ (see Figure 235).

5.4. Stress spectra and stress level after strengthening in detail D1a, D2, (D3)

As presented in Section 5.3, the fatigue damage exceeds the value 1.0 for all analysed details (D1a, D2 and D3) by considering 50 years of service life before strengthening. Therefore, Concept 2 (see Section 5.1.2.2) has to be used for these analysed details regarding to the fatigue life calculation of the strengthened steel deck. In the following the application of this Concept 2 is shown for all details (D1a, D2, D3) and additionally, Concept 1 is presented only for detail D2.

5.4.1. Detail D1a – stress level after strengthening

- Application of Concept 2

As already described in Section 5.1.2.2, the maximum occurring stress range in the future $\Delta\sigma_{max,D1a,new}$ has to be lower than the fatigue's cut off limit $\Delta\sigma_L$. Therefore, this future maximum stress range has to be calculated under consideration of fatigue load model FLM 2 (see Section 2.5.2), which indicates the highest axle loads.

When regarding the stress history curves due to the crossings of the individual lorry types (T1 to T5), exemplary presented in Section 3.4.2.1 - Figure 85, it can be recognised that every axle within a single vehicle causes an isolated stress range $\Delta\sigma_i$. Hence, an isolated analysis of every single axle is sufficient.

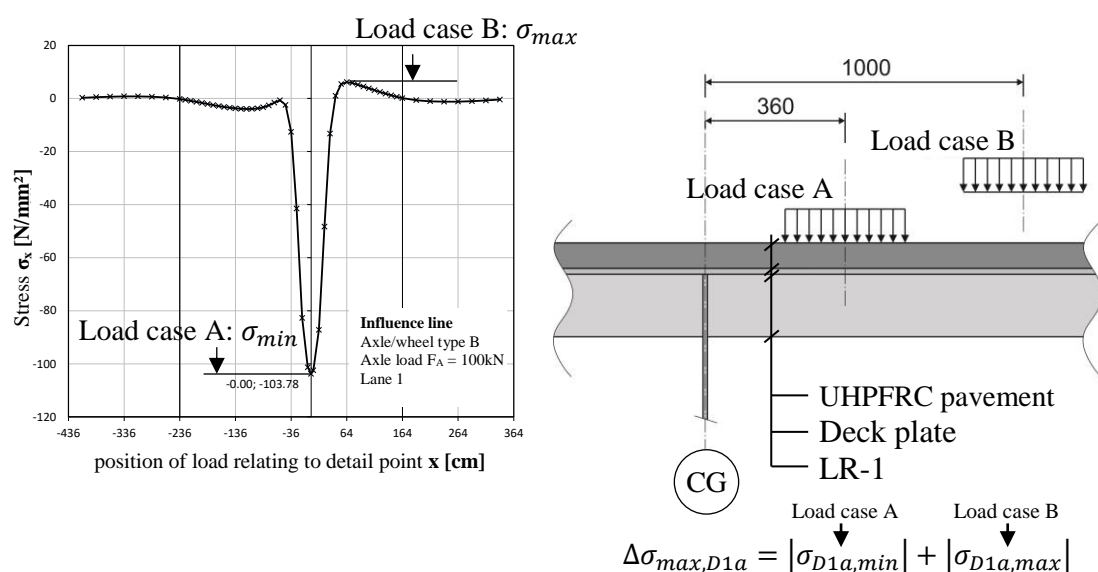


Figure 240: Determination of the maximum stress range $\Delta\sigma_{max}$ for detail D1a at the unstrengthened orthotropic steel deck

The heavy traffic simulations in Section 3.4 showed that the maximum stress range in detail D1a always occur due to the driving axle which consists of axle/wheel type B, the twin tyres. The determination of the maximum occurring stress range $\Delta\sigma_{max,D1a,new}$ at the strengthened deck is therefore restricted by only 2 load cases (A and B) which are shown in Figure 240. This picture illustrates the influence line in longitudinal bridge direction for detail D1a at the unstrengthened deck due to axle/wheel type B with an axle load of $F_A = 100\text{kN}$. The minimum stresses $\sigma_{D1a,min}$ occur when the wheel load is located directly above the detail point (Load case A). The maximum stresses $\sigma_{D1a,max}$ occur when the wheel load is located in a distance of 1000mm away from the mid cross girder CG (Load case B).

A determination of the maximum stress ranges $\Delta\sigma_{max,D1a,new}$ at the strengthened bridge deck was calculated under consideration of the 2 load cases that are illustrated in Figure 240. The thickness of the UHPFRC layer has been varied from 60, 70 to 80mm. An additional variation of the flexibility of the interface between steel deck and concrete pavement has also been done and the different values are plotted in Table 30. The numerical calculations were performed at Model E-1 where the mesh refinement is concentrated in the steel structure. The value for the concrete's Young's Modulus ($E_{c,eff} = E_c/4$) represents a bottom limit value to consider an overall concrete cracking and to calculate conservative stresses for the steel structure.

The results in terms of maximum occurring stress ranges $\Delta\sigma_{max,D1a,new}$ regarding to the strengthening of the orthotropic steel deck with an UHPFRC pavement are visualised in Table 30.

Table 30: Maximum occurring stress ranges $\Delta\sigma_{\max,D1a,new}$ after strengthening – variation of the UHPFRC plate thickness and variation of the flexibility of the interconnecting joint

D1a: stresses [N/mm ²] due to axle/wheel type B with 190 [kN] of FLM 2														
calculation model	interface (steel-concrete)	$E_{c,eff} = 12,500$ [N/mm ²]	concrete thickness											
			60 [mm]			70 [mm]			80 [mm]					
			σ_{min}	σ_{max}	$\Delta\sigma_{\max,D1a,new}$	σ_{min}	σ_{max}	$\Delta\sigma_{\max,D1a,new}$	σ_{min}	σ_{max}	$\Delta\sigma_{\max,D1a,new}$			
I	no composite	100%	-44.3	9.9	22%	54.2	-32.4	8.2	25%	40.7	-27.2	7.0	26%	34.2
II	Epoxy t=3 [mm]		-25.6	10.6	42%	36.2	-17.7	9.4	53%	27.1	-13.7	8.4	61%	22.0
III	Epoxy t=1 [mm]		-25.5	10.6	42%	36.1	-17.9	9.4	52%	27.2	-13.7	8.5	62%	22.2
IV	rigid composite		-25.8	10.6	41%	36.5	-18.4	9.5	52%	27.9	-14.1	8.5	60%	22.5

$\Delta\sigma_{Rd} = 40.2$ [N/mm²] (damage limit $\Delta\sigma_I$)

An evaluation of the results follows in Section 5.5.1 where the appropriate limit value for fatigue damage is also described.

5.4.2. Detail D2 – stress spectra and stress level after strengthening

The following calculations referring to the orthotropic steel deck, that is strengthened via an UHPFRC pavement instead of the common asphalt layer, have been performed under consideration of the listed assumptions below:

- Thickness of the UHPFRC pavement $t_c = 80$ mm
- Conservative value for the flexibility of the interface between steel and concrete under consideration of calculation model II (see Table 29) with an effective thickness of the epoxy layer of $t_{epoxy} = 3$ mm
- Conservative value for the Young's Modulus of the UHPFRC pavement with $E_{c,eff} = E_c/4 = 12,500$ N/mm²

5.4.2.1. Application of Concept 1 – simplified calculation of stress spectra

With regards to the stress history curves due to the crossing of the lorry types T1 to T5 from FLM 4, which are exemplarily illustrated in Section 3.4.2.2 - Figure 90, it can be seen that an isolated consideration of every single axle is not possible. Figure 90 shows very well that the maximum occurring stress range $\Delta\sigma_{\max,D2}$ comprises of a superposition of at least 2 axles. Nevertheless, critical axle load positions and its belonging axle/wheel type can be identified in this stress history of Figure 90. The reduction of the local stresses at the strengthened deck could be determined in a simplified manner under consideration of the stress range spectrum referring to the unstrengthened deck and a scaling of these stress ranges by using an appropriate scaling factor. The stress range spectrum regarding to detail D2 at the steel deck before strengthening is the basis for the scaling procedure which is shown in Figure 91 of Section 3.4.2.2. 2 scaling factors are necessary to include several effects. For a modification regarding to the axle loads (FLM 4* to FLM 4, see Figure 24 in Section 2.5.2), scaling factor $f_{T,i}$ was used. The

consideration of reduced occurring stresses in the details after strengthening has been taken into account by using scaling factor $f_{\sigma,i}$. This scaling factor $f_{\sigma,i}$ differs between single and double wheeled axles. Because of a negligible difference in the geometry of axle type A and C, only one scaling factor was defined for single wheeled axles. The critical load position relating to the maximum occurring compressive stress in notch detail D2 has been defined for the determination of $f_{\sigma,i}$ (see Section 3.3.3).

a.) Scaling factor $f_{T,i}$ regarding to the axle load of the individual lorries

For every lorry type from fatigue load model FLM 4* and FLM 4 (see Figure 24 in Section 2.5.2) a scaling factor based on the vehicle's gross weights has been determined to include future increasing axle loads in Europe. This scaling factor $f_{T,i}$ is identical to the increase of every axle load, because of the load model's equality relating to the distribution of the overall gross weight to the axles within the vehicles.

Figure 241 shows again the appropriate traffic load models regarding to a fatigue verification for the time periods before and after the strengthening of the orthotropic steel deck. On the left side of Figure 241 fatigue load model FLM 4* is plotted with its reduced gross weights and axle loads for time period I (1970 to 2020). On the right side of Figure 241 fatigue load model FLM 4 is visualised for the future time period II (2020 to 2070) with its increased gross weights and axle loads.

type	lorry type	axle spacing [m]	wheel type resp. axleype	lorry percentage \bar{n}_i [%]	FLM-4*		type	lorry type	axle spacing [m]	wheel type resp. axleype	lorry percentage \bar{n}_i [%]	FLM-4	
					A_i	G_{ges}						A_i	G_{ges}
T1		4.50	A	20	49,7	142	T1		4.50	A	20	70	200
			B		92,3	B				130			
T2		4.20	A	5	61,6	273	T2		4.20	A	5	70	310
			B		105,7					B		120	
			B		105,7					B		120	
T3		3.20	A	50	51,4	360	T3		3.20	A	50	70	490
			B		110,2					B		150	
		1.30	C		66,1				C	90			
			C		66,1				C	90			
T4		3.40	A	15	52,1	290	T4		3.40	A	15	70	390
			B		104,1					B		140	
			B		66,9					B		90	
T5		4.80	A	10	49,9	321	T5		4.80	A	10	70	450
			B		92,7					B		130	
		4.40	C		64,2				C	90			
			C		57,1				C	80			
		1.30	C	57,1					1.30	C		80	

traffic load model from 1970 to 2020 → ← traffic load model from 2020 to 2070

Figure 241: Traffic load model for the time periods before (FLM 4*) and after strengthening (FLM 4)

For the determination of the stress range spectrum referring to detail D2 and regarding to time period 2 (2020 to 2070), every stress range of the stress range spectrum for each individual lorry type from the

unstrengthened deck (see Figure 91 in Section 3.4.2.2) was scaled with its appropriate scaling factor $f_{T,i}$ depending on the lorry type T1 to T5.

Note: The scaling factor $f_{T,i}$ of each axle of lorry type i is identical to the scaling factor $f_{T,i}$ of the vehicle's gross weights.

$$f_{T,i} = \frac{\text{gross weight according to FLM 4}}{\text{gross weight according to FLM 4}^*} = \frac{\text{axle load according to FLM 4}}{\text{axle load according to FLM 4}^*}$$

The scaling factors regarding to the increased axle loads are listed below:

- Lorry type T1: $f_{T1} = \frac{200}{142} = 1.41$
- Lorry type T2: $f_{T2} = \frac{310}{273} = 1.14$
- Lorry type T3: $f_{T3} = \frac{490}{360} = 1.36$
- Lorry type T4: $f_{T4} = \frac{390}{290} = 1.34$
- Lorry type T5: $f_{T5} = \frac{450}{321} = 1.40$

b.) Scaling factor $f_{\sigma,i}$ regarding to the stress reduction at the strengthened deck

The stresses at the strengthened orthotropic steel deck, using Model E-2 (see Section 5.2.2), have been determined due to axle/wheel type B and C with an uniform axle load of $F_A = 100\text{kN}$. These stresses, determined at the strengthened deck have been compared to the calculated stresses at the unstrengthened deck for the same load level ($F_A = 100\text{kN}$) where the load position had to be identical. With this ratio relating to the stresses of the strengthened to the unstrengthened deck, the scaling factors $f_{\sigma,i}$ could be verified referring to single and double wheeled axles. The analyses showed that there is much more stress reduction due to the concrete pavement relating to axle type C than to axle type B.

With these determined scaling factors $f_{\sigma,i}$ the stress ranges of the stress range spectrum, which has been calculated at the unstrengthened deck, could be scaled under consideration of its appropriate axle/wheel type.

- $f_{\sigma,B}$ relating to axle/wheel type B (twin tyres)

Figure 242 illustrates the deformations of the analysed orthotropic steel deck due to axle/wheel type B with an axle load of $F_A = 100\text{kN}$. Figure 242.a shows the unstrengthened steel deck without UHPFR pavement and its occurring deformations due to the double wheeled axle type B. Figure 242.b shows the strengthened steel deck with an UHPFR pavement and its occurring deformations also due to the double wheeled axle type B. The load is positioned directly above LR-1 and in a distance of 80cm away from the mid cross girder.

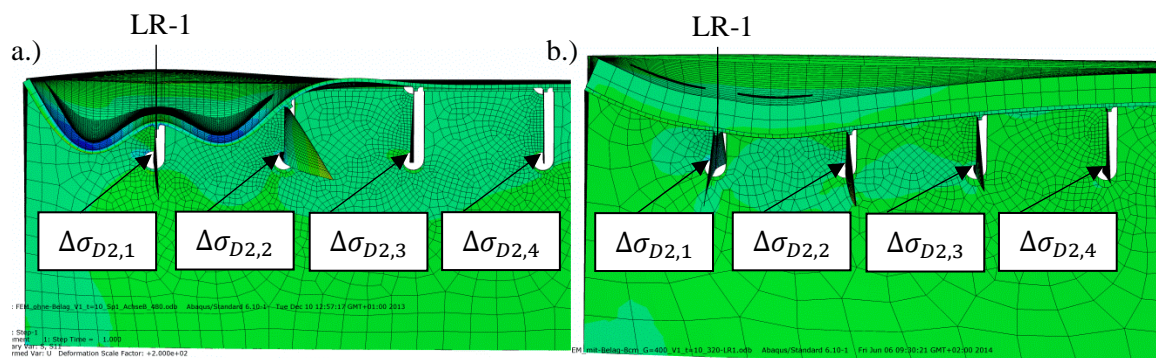


Figure 242: deformations of the orthotropic bridge deck due to axle/wheel type B with an axle load of $F_A = 100\text{kN}$: a.) unstrengthened deck (without UHPFRC pavement); b.) strengthened deck (with UHPFRC pavement)

The occurring stresses in notch detail D2 due to axle/wheel type B with an axle load of $F_A = 100\text{kN}$ at LR-1 are plotted in Table 31 regarding to LR-1 to LR-4 which are additionally marked in Figure 242.

Table 31: stresses in notch detail D2 at LR-1 to LR-4 (see Figure 242) due to axle/wheel type B with an axle load of $F_A = 100\text{kN}$ at LR-1

	Stresses in notch detail D2			
	$\min(\sigma_{D2,1})$ [N/mm ²]	$\min(\sigma_{D2,2})$ [N/mm ²]	$\min(\sigma_{D2,3})$ [N/mm ²]	$\min(\sigma_{D2,4})$ [N/mm ²]
Unstrengthened deck	-27,63	-6,31	1,25	0,84
Strengthened deck	-21,58	-13,72	-3,07	1,00

The scaling factor $f_{\sigma,B}$ relating to the stress reduction of the concrete pavement due to double wheeled axle type B was determined as shown below:

$$f_{\sigma,B} = \frac{|\sigma_{D2,1}| (\text{strengthened deck})}{|\sigma_{D2,1}| (\text{unstrengthened deck})} = \frac{21.58}{27.63} = 0.78$$

As illustrated in Table 31, it can be recognised that due to the concrete pavement the adjacent longitudinal ribs (LR-2 to LR-4) near the loaded LR-1 can be activated for the load transfer.

- $f_{\sigma,C}$ relating to axle/wheel type C (single tyre)

Figure 243 illustrates the deformations of the analysed orthotropic steel deck due to axle/wheel type C with an axle load of $F_A = 100\text{kN}$ at LR-1. Figure 242.a shows the unstrengthened steel deck without UHPFR pavement and its occurring deformations due to the single wheeled axle type C. Figure 242.b shows the strengthened steel deck with UHPFR pavement and its occurring deformations also due to the single wheeled axle C. The load is positioned directly above LR-1 and in a distance of 80cm away from the mid cross girder.

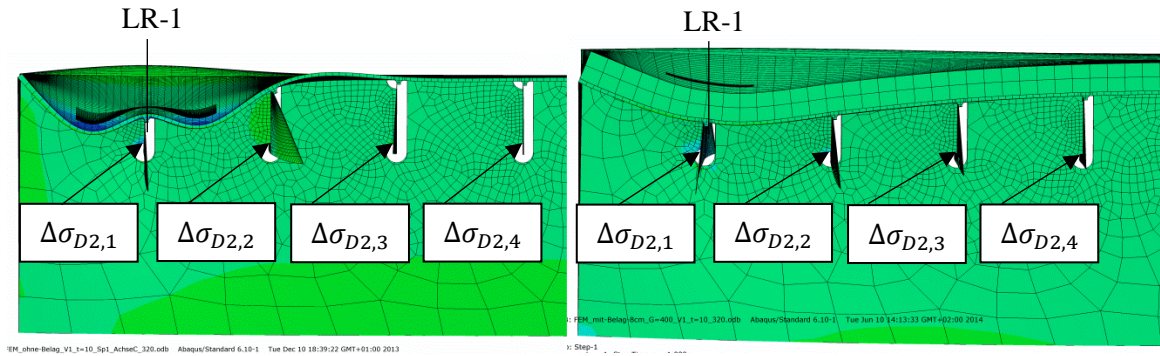


Figure 243: deformations of the orthotropic bridge deck due to axle/wheel type C with an axle load of $F_A = 100\text{kN}$ at LR-1: a.) unstrengthened deck (without UHPFRC pavement); b.) strengthened deck (with UHPFRC pavement)

The occurring stresses in notch detail D2 due axle/wheel type C with an axle load of $F_A = 100\text{kN}$ at LR-1 are plotted in Table 32 regarding to LR-1 to LR-4 which are additionally marked in Figure 243.

Table 32: stresses in notch detail D2 at LR-1 to LR-4 (see Figure 243) due to axle/wheel type C at LR-1 with an axle load of $F_A = 100\text{kN}$

	Stresses in notch detail D2			
	$\min(\sigma_{D2,1})$ [N/mm ²]	$\min(\sigma_{D2,2})$ [N/mm ²]	$\min(\sigma_{D2,3})$ [N/mm ²]	$\min(\sigma_{D2,4})$ [N/mm ²]
Unstrengthened deck	-36,18	-2,02	1,19	0,81
Strengthened deck	-12,92	-6,69	-1,25	0,63

The scaling factor $f_{\sigma,C}$ relating to the stress reduction of the concrete pavement due to single wheeled axle types A and C was determined as shown below:

$$f_{\sigma,C} = \frac{|\sigma_{D2,1}| \text{ (strengthened deck)}}{|\sigma_{D2,1}| \text{ (unstrengthened deck)}} = \frac{12.92}{36.18} = 0.36$$

As illustrated in Table 32, it can be recognised also for single wheeled axles that due to the concrete pavement the adjacent longitudinal ribs (LR-2 to LR-4) near the loaded LR-1 can be activated very well for the load transfer. Especially for single wheeled axles, a very good beneficial load distribution and therefore a high stress reduction can be observed.

c.) Resulting stress spectra – overall Scaling factor $f_{tot,i}$

By multiplication of the 2 scaling factors $f_{T,i}$ and $f_{\sigma,i}$, an overall scaling factor $f_{tot,i}$ could be determined. Under consideration of the appropriate overall scaling factor $f_{tot,i}$, every stress range $\Delta\sigma_i$ of the stress range spectrum (after identification of lorry and axle type), which has been determined at the unstrengthened deck, could be modified. With this procedure the appropriate stress range spectrum at the strengthened deck and the damage of the future heavy traffic in time period II (2020 to 2070) could be determined.

$$f_{tot,i} = f_{T,i} \cdot f_{\sigma,i}$$

The reference stress range spectrum of the heavy traffic simulation at the unstrengthened steel deck can be found in Figure 91, Section 3.4.2.2 and is again shown in Figure 244.a. It can be recognised that only 4 stress ranges have a damaging effect relating to notch detail D2. These 4 stress ranges can definitely be associated to the single axles of the lorry types T2 to T5. Thus only these 4 stress ranges have to be modified with its appropriate scaling factor $f_{tot,i}$ to get the stress spectra of the future heavy traffic. These scaling procedure of the 4 relevant stress ranges $\Delta\sigma_{T_{ij}}$ is shown below (cf. Figure 91, Section 3.4.2.2):

- Type T3 ($n_3=50$), axle C: $f_{tot,T3,C} = f_{T,3} \cdot f_{\sigma,C} = 1.36 \cdot 0.36 = 0.49$
 $\rightarrow \Delta\sigma_{T3,C} = 62.94 \cdot 0.49 = 30.84 \text{ N/mm}^2$
- Type T2 ($n_2=5$), axle B: $f_{tot,T2,B} = f_{T,2} \cdot f_{\sigma,B} = 1.14 \cdot 0.78 = 0.89$
 $\rightarrow \Delta\sigma_{T2,B} = 61.49 \cdot 0.89 = 54.73 \text{ N/mm}^2$
- Type T5 ($n_5=10$), axle C: $f_{tot,T5,C} = f_{T,5} \cdot f_{\sigma,C} = 1.40 \cdot 0.36 = 0.50$
 $\rightarrow \Delta\sigma_{T5,C} = 48.48 \cdot 0.50 = 24.24 \text{ N/mm}^2$
- Type T4 ($n_4=15$), axle B: $f_{tot,T4,B} = f_{T,4} \cdot f_{\sigma,B} = 1.34 \cdot 0.78 = 1.05$
 $\rightarrow \Delta\sigma_{T4,B} = 47.93 \cdot 1.05 = 50.33 \text{ N/mm}^2$

The maximum occurring stress range in detail D2, based on FLM 4, in the future has a value of:

$$\rightarrow \Delta\sigma_{\max,D2,\text{new}} = \Delta\sigma_{T2,B} = 54.73 \text{ N/mm}^2$$

The resulting stress range spectrum due to the presented modifications above is visualised in Figure 244. Figure 244.a shows the stress range spectrum at the analysed steel bridge deck before strengthening (time period I, 1970 to 2020). Figure 244.b shows the stress range spectrum at the analysed bridge deck after the strengthening with an 80mm thick UHPFRC pavement (time period II, 2020 to 2070). Both stress spectra are based on the crossing of 100 lorries.

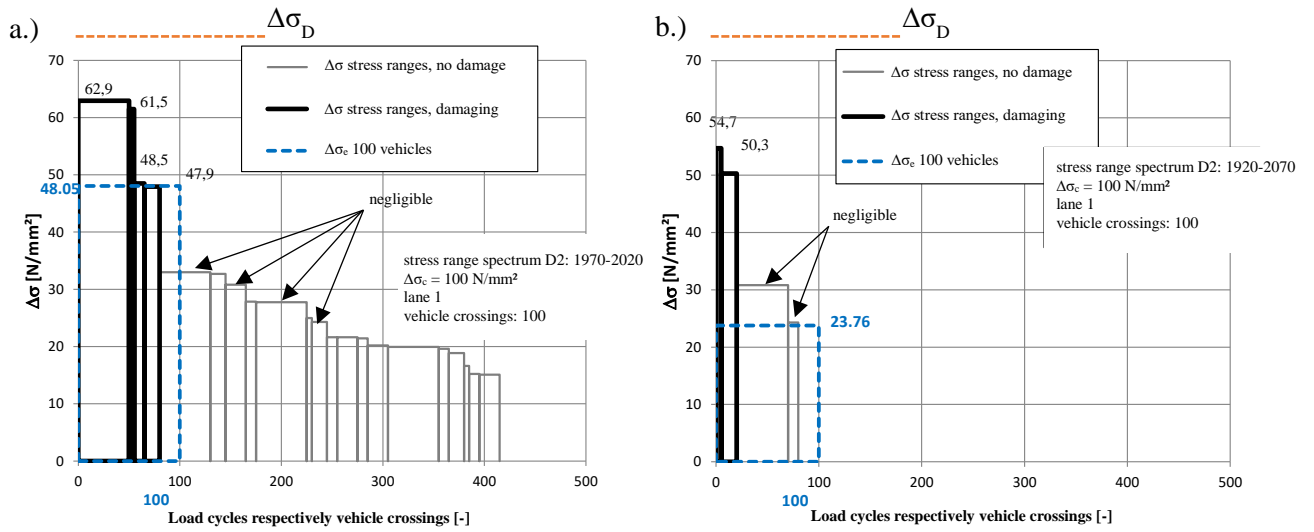


Figure 244: stress range spectrum referring to detail D2 at lane 1 (LR-1) due to 100 vehicles in comparison: a.) before strengthening in time period I (1970 to 2020) due to FLM 4*; b.) after strengthening with an 80mm UHPFRC pavement in time period II (2020 to 2070) due to FLM 4

5.4.2.2. Application of Concept 2

As already shown in Figure 244, the maximum occurring future stress range due to lorry type T2 (axle type B) of FLM 4 in detail D2 has a value of:

$$\rightarrow \Delta\sigma_{\max,D2,\text{new}} = \Delta\sigma_{T2,B} = 54.73 \text{ N/mm}^2 \quad \text{due to FLM 4}$$

For the use of Concept 2, where FLM 2 is necessary, this maximum occurring future stress range plotted above has to be scaled based on the ratio referring to the appropriate axle loads from FLM 4 and FLM 2 (axle loads $F_{A,T2,B,FLM4} = 120$ kN, $F_{A,T2,B,FLM2} = 140$ kN; see Figure 24 in Section 2.5.2):

$$\rightarrow \Delta\sigma_{\max,D2,\text{new}} = 54.73 \cdot 140/120 = 63.85 \text{ N/mm}^2 \quad \text{due to FLM 2}$$

The stress ranges in the notch detail have been determined under consideration of a static numerical analysis and therefore dynamic effects have to be taken into account within Concept 2.

These dynamic effects were considered with an overall dynamic factor of $\varphi = 1.2$:

$$\rightarrow \Delta\sigma_{\max,D2,\text{new}} = 63.85 \cdot 1.2 = 76.62 \text{ N/mm}^2 \quad \text{due to FLM 2, including } \varphi = 1.2$$

5.4.3. Stress reduction level of detail D3

This Section presents the results of the numerical simulations relating to the fatigue critical stresses in the local area of the bolted field splices of the cross girder under consideration of fatigue load model FLM 4* at FE-model F. Fatigue load model FLM 4* was chosen to compare the stresses at the critical details before and after strengthening. Model F represents the strengthened orthotropic steel deck with open longitudinal ribs and the basis for this model is Model D. The deck is strengthened with an 80mm UHPFRC pavement instead of the common asphalt layer (with $E_{c,eff} = E_c/4$). A description of the strengthened deck (Model F) can be found in Section 5.2.3 and an explanation of the unstrengthened deck (Model D) is shown in Section 3.2.4. The appropriate applied fatigue critical load model is presented in Section 2.5.2. The stresses in the critical notch details D3 have been calculated and a detailed description of this point is shown in Section 2.4.5. The determination of the critical vehicle type and its critical lane position referring to detail D3 is shown in Section 3.3.4 (Figure 81).

Figure 245 and Figure 246 illustrate the maximum occurring principal stresses in the local areas of joint I/III and joint II (see Figure 114, in Section 3.4.5) before and after strengthening. The upper edge of the cross girder's web is partitioned into 4 regions (region I to region IV) and the points with the maximum principal stresses in this area are indicated (Point A to Point L). With regard to joint I/III, the results relating to the numerical studies of the unstrengthened deck are shown in Figure 245.a and the results referring to the strengthened deck are shown in Figure 245.b. With regard to joint II, the results relating to the numerical studies of the unstrengthened deck are shown in Figure 246.a and the results referring to the strengthened deck are shown in Figure 246.b.

– Joint I/III

As shown in Figure 245.a, the maximum occurring principal stress in joint I/III at the unstrengthened deck has a value of $\sigma_{max} = \sigma_A = 120 \text{ N/mm}^2$. Under consideration of an 80mm UHPFRC pavement the maximum principal stress decreases in this point down to a value of $\sigma_D = 87 \text{ N/mm}^2$. Therefore, a stress reduction of 27% ($1 - 87 / 120 = 0.73$) can be recognised with this strengthening technique.

– Joint II

As shown in Figure 246.a, the maximum occurring principal stress in joint II at the unstrengthened deck has a value of $\sigma_{max} = \sigma_G = 84 \text{ N/mm}^2$. By considering an 80mm UHPFRC pavement the maximum principal stress decreases in this point down to a value of $\sigma_D = 48 \text{ N/mm}^2$. Therefore, a stress reduction of 43% ($48 / 84 = 0.57$) can be observed.

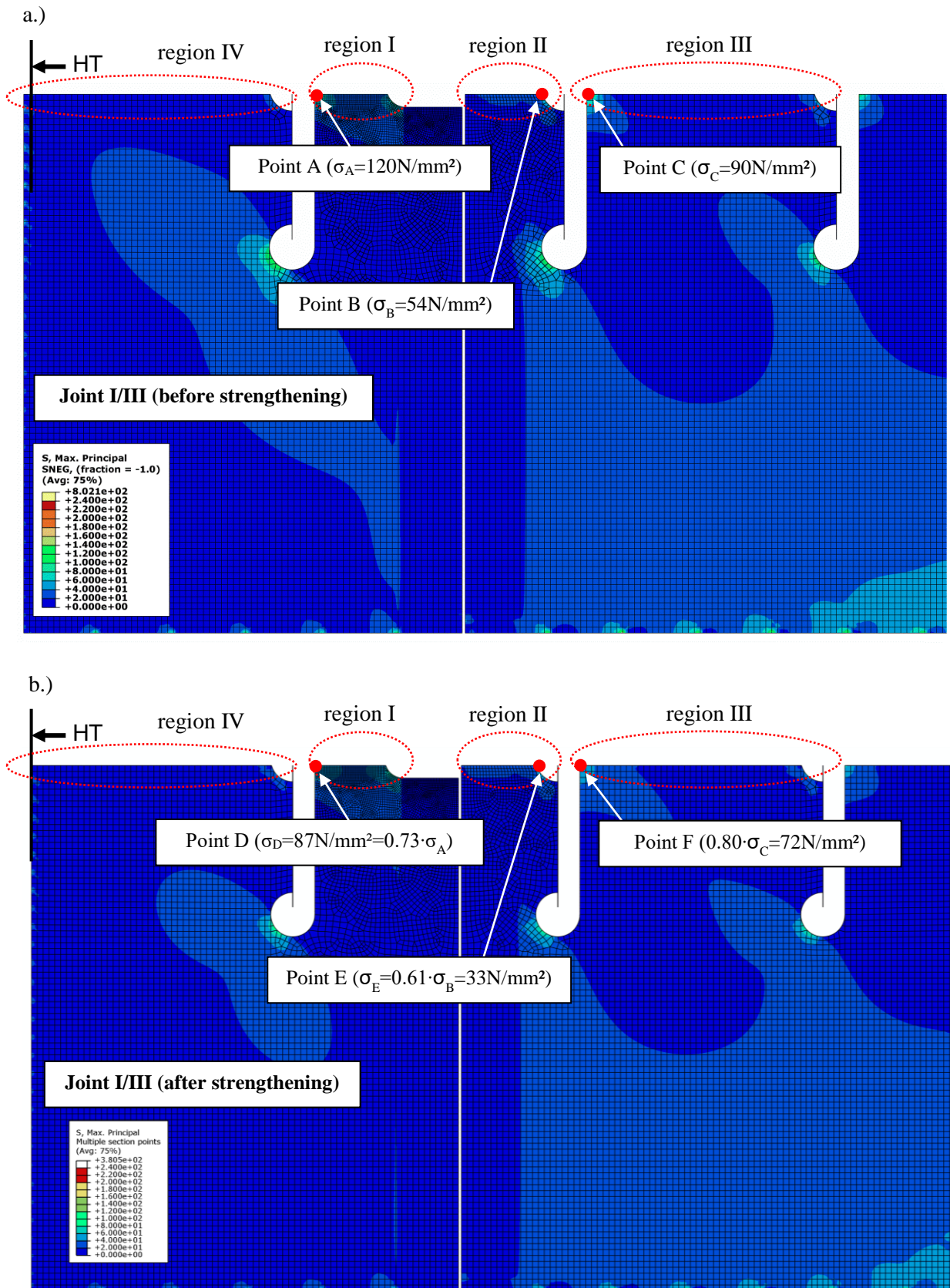


Figure 245: Detail D3 – maximal principal stresses in joint I and III due to lorry type T2 (FLM 4*) and its critical position: a.) Model D, before strengthening; b.) Model F, after strengthening

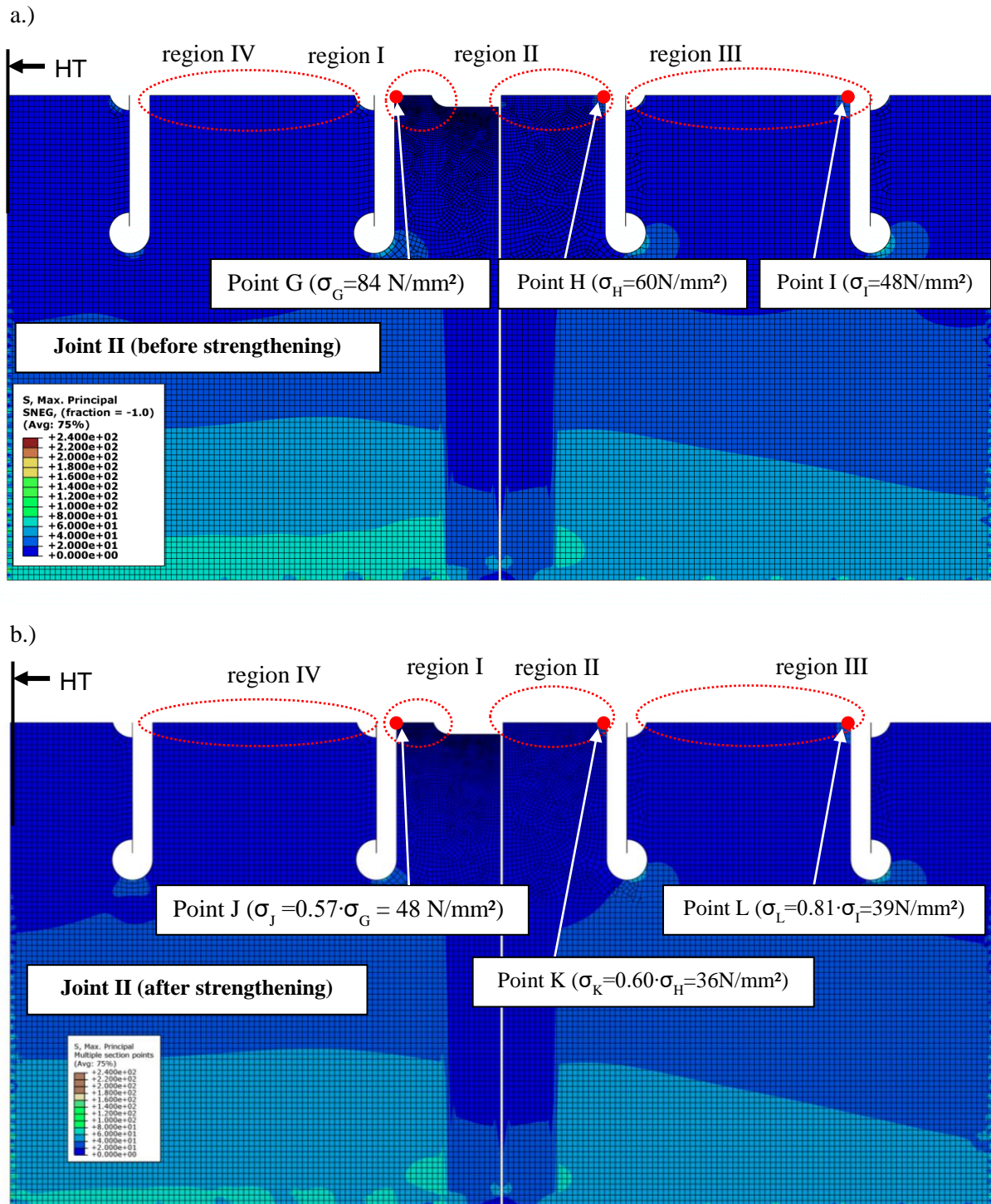


Figure 246: Detail D3 – maximal principal stresses in joint II due to lorry type T2 (FLM 4*) and its critical position: a.) Model D, before strengthening; b.) Model F, after strengthening

The resulting stresses which are illustrated in Figure 245 and Figure 246 due to the critical load position of the critical vehicle type T2 according to FLM 4* (see Figure 81 in Section 3.3.4) can be stated as maximum fatigue critical stresses $\sigma_{\max,D3}$ because of a heavy traffic simulation. The minimum stresses in the detail can be assumed as $\sigma_{\min,D3} = 0$ due to an unloaded condition of the bridge deck. The resulting value of the stress range $\Delta\sigma_{\max,D3,\text{new}}$ has then the same value as $\sigma_{\max,D3,\text{new}}$ ($\Delta\sigma_{\max,D3,\text{new}} = |\sigma_{\min,D3,\text{new}}| + |\sigma_{\max,D3,\text{new}}| = 0 + |\sigma_{\max,D3,\text{new}}| = |\sigma_{\max,D3,\text{new}}|$).

The maximum occurring stress range in detail D3 in the future (after strengthening), based on FLM 4*, has a value of:

$$\rightarrow \Delta\sigma_{\max,D3,\text{new}} = 87.0 \text{ N/mm}^2 \quad \text{Joint I/III}$$

$$\rightarrow \Delta\sigma_{\max,D3,\text{new}} = 48.0 \text{ N/mm}^2 \quad \text{Joint II}$$

Stress reduction factors due to the deck strengthening with an UHPFRC pavement referring to detail D3:

$$\rightarrow f_{\sigma,D3} = \Delta\sigma_{\max,D3,\text{new}} / \Delta\sigma_{\max,D3,\text{old}} = 87.0 / 120.0 = 0.73 \quad \text{Joint I/III}$$

$$\rightarrow f_{\sigma,D3} = \Delta\sigma_{\max,D3,\text{new}} / \Delta\sigma_{\max,D3,\text{old}} = 48.0 / 84.0 = 0.57 \quad \text{Joint II}$$

A simplified evaluation of these results follows in Section 5.5.3 to verify the expected fatigue life.

5.5. Fatigue life predictions including strengthening

5.5.1. Detail D1a

As described in Concept 2, fatigue load model FLM 2 is necessary which has higher axle loads and gross weights than FLM 4. The maximum occurring stress range in the future $\Delta\sigma_{\max,D1a,\text{new}}$ can be expected due to the driving axle of lorry type T2 which has the highest axle load within FLM 2 with a value of $F_A = 190 \text{ kN}$.

The numerically calculated maximum stress ranges $\Delta\sigma_{\max,D1a,\text{new}}$ from the analyses regarding to the strengthening of orthotropic steel decks with an UHPFRC pavement are visualised in Table 30 (see Section 5.4.1). The stress ranges in the notch detail have been determined under consideration of a static numerical analysis and therefore dynamic effects have to be taken into account within Concept 2. These dynamic effects were considered with an overall dynamic factor of $\phi = 1.2$.

As it is shown in Table 30, enough stress reduction can be generated by a thickness $t_c = 70\text{mm}$ of the UHPFRC pavement and under consideration of a very low flexibility of the interconnecting joint. Due

to reasons of the concrete's reliability and for the warranty of sufficient concrete covering, a thickness of at least $t_c = 80\text{mm}$ is necessary.

With a thickness of $t_c = 80\text{mm}$ and a very conservative value of the interface flexibility according to calculation model II (see Table 30), that represents an epoxy layer's thickness of $t_{\text{epoxy}} = 3\text{mm}$, the value of the maximum occurring stress range under consideration of $\varphi = 1.2$ (dynamic effects) is:

$$|\Delta\sigma_{\text{max},D1a,\text{new}+\varphi}| = 22.0[\text{N}/\text{mm}^2] \cdot 1.2 = 26.4 [\text{N}/\text{mm}^2] < |\Delta\sigma_R| = 40.2 [\text{N}/\text{mm}^2]$$

– Note: The fatigue resistance $\Delta\sigma_R$ is equal to $\Delta\sigma_L$ in Figure 235.

A calculated additional service life of at least 50 years is available for notch detail D1a after strengthening the orthotropic steel deck using a UHPFRC pavement. An inspection on site regarding to existing fatigue cracks and if necessary a renovation of these damages before strengthening is required anyway.

- Evaluation including full scale test results

Referring to the fatigue load models FLM 4, FLM 4* and FLM 2, axle type B always indicates higher axle loads than axle type C (see Figure 24 in Section 2.5.2). Therefore, axle type B is taken in the following for more detailed analyses. The numerically calculated stress reduction factor $f_{\sigma,B}$ for detail D1a at LR-1 (near the main girder) due to axle type B can be calculated with the ratio of the maximum occurring stress at model E-1 (strengthened deck) to the one at model A (unstrengthened deck). The strengthened steel deck (model E-1) gives a value of $|\sigma_{D1a,\text{max},E-1}| = 13.7 \text{ N}/\text{mm}^2$ due to axle type B with an axle load of $F_A = 190 \text{ kN}$ and under consideration of a fictive adhesive layer thickness of $t = 3 \text{ mm}$ (see Table 30 in Section 5.4.1). The maximum occurring stress at model A is $|\sigma_{D1a,\text{max},A}| = 103.78 \text{ N}/\text{mm}^2$ due to axle type B with an axle load of $F_A = 100 \text{ kN}$. The following numerical stress reduction factor can therefore be noted, based on an axle load of $F_A = 190\text{kN}$:

$$f_{\sigma,B} = |\sigma_{D1a,\text{max},E-1}| / (1.9 \cdot |\sigma_{D1a,\text{max},A}|) = 13.7 / (1.9 \cdot 103.78) = 0.07$$

This numerically calculated stress reduction factor can simplified be assumed as reduction factor for the stress ranges $\Delta\sigma_{D1a}$ at detail D1a ($f_{\sigma,B} = f_{\Delta\sigma,B}$).

At the full scale tests (see Section 5.6), a reduction factor of $f_{\sigma,B,\text{test}} = f_{\Delta\sigma,B,\text{test}} = 0.11$ (see Table 37) could be measured for axle type B with $F_A = 190 \text{ kN}$, before the extreme thermal constraint. Therefore, the verification shown above has to be scaled as following:

$$\Delta\sigma_{D1a,\text{max},\text{test}+\varphi} = 26.4 \cdot 0.11 / 0.07 = 41.5 \text{ N}/\text{mm}^2 \approx \Delta\sigma_L = 40.2 \text{ N}/\text{mm}^2 \quad (\text{before constraint})$$

After the extreme thermal constraint, a reduction factor of $f_{\sigma,B,\text{test}} = f_{\Delta\sigma,B,\text{test}} = 0.20$ (see Table 40 in Section 5.6.5.1) could be read out. Hence, the verification has to be modified as shown below:

$$\Delta\sigma_{D1a,\text{max},\text{test}+\varphi} = 26.4 \cdot 0.20 / 0.07 = 75.4 \text{ N/mm}^2 > \Delta\sigma_L = 40.2 \text{ N/mm}^2 \quad (\text{after constraint})$$

It must be recognised that the accuracy of this verification is limited. This is because, on the one hand, the reduction factor from the experiment cannot be transferred directly to different load positions ($\sigma_{D1a,\text{max}}$ and $\sigma_{D1a,\text{min}}$ are caused due to different load positions) and, on the other hand, very conservative approaches were used in the verification concept. This also means that a calculated maximum occurring stress range $\Delta\sigma_{D1a,\text{max},\text{new}}$ that exceeds $\Delta\sigma_L$ is not an exclusion criterion of the elaborated strengthening solution. The results only suggest, that additional strain measurements will be required as part of a prototype performance. It is expected that a sufficient residual life will be achieved with the proposed reinforcing solution. In addition, it can be seen that cracking in the concrete plate due to restraining action must be limited by sufficient reinforcement to obtain stress reduction factors in the order of $f \approx 0.10$.

5.5.2. Detail D2

For the use of Concept 2, it is necessary to apply FLM 2 with an additional dynamic factor ($\varphi=1.2$) regarding to a fatigue endurable design of the steel deck including the UHFRC strengthening. As shown in Section 5.4.2.2, the maximum occurring stress range due to the numerical simulations at the strengthened deck is:

$$|\Delta\sigma_{\text{max},D2,FLM2+\varphi}| = 76.62 \text{ [N/mm}^2] > |\Delta\sigma_R| = 40.2 \text{ [N/mm}^2]$$

The maximum occurring future stress range $\Delta\sigma_{\text{max},D2,\text{new}}$ has a higher value than the cut off limit of fatigue resistance and therefore additional fatigue damage has to be expected also after the strengthening. Looking at the determined stress reduction factors $f_{\sigma,B}$ and $f_{\sigma,C}$ presented in Section 5.4.2 it can be noted that the occurring stresses in notch detail D2 are decreasing strongly due to the application of an UHPFRC pavement. Worth particular mention is that the determination of the maximum occurring stress range after strengthening is highly effected by very conservative assumptions. The Young's Modulus of the UHPFRC pavement was conservatively defined with a very low value of $E_{c,\text{eff}} = E_c / 4 = 12.500 \text{ N/mm}^2$. Full scale tests, which have been performed within the research project in [33] and will be presented in Section 5.6 showed a better load carrying behaviour and further investigations relating to a realistic effective overall Young's Modulus for the FE calculations were done based on the

tests. The full scale test as well as the developed effective overall Young's Modulus of the UHPFRC pavement on orthotropic steel decks are presented in Section 5.6.7.

With regards to the illustrated stress range spectrum in Figure 244.a at the steel deck before strengthening, it can be recognised that the maximum occurring stress range has a value of $\Delta\sigma_{\max,D2,old} = 62.9 \text{ N/mm}^2$. This value is lower than the fatigue strength according to the appropriate S-N-curve $\Delta\sigma_D = 73.7 \text{ N/mm}^2$. According to the Eurocode [4], no fatigue damage occurs when the condition $\Delta\sigma_{\max} < \Delta\sigma_D$ can be fulfilled and the notch detail can be seen as fatigue endurable. Because of the occurrence of highly overloaded lorries and for the purpose regarding to the development of a robust strengthening solution, the applied procedure within this thesis is very conservative but seems necessary.

- Evaluation including full scale test results

The numerical analyses at Model A (unstrengthened deck) and E-1 (strengthened deck) showed stress reduction factors of:

- Single wheeled axles (axle type A and C): $f_{\sigma,num,A/C} = 0.36$ (numerical Model E-1 compared to A)
- Double wheeled axles (axle type B): $f_{\sigma,num,B} = 0.78$ (numerical Model E-1 compared to A)

The significantly more beneficial behaviour of the concrete strengthening for detail D2 in the full-scale test (see Section 5.6) also leads to a sufficient residual life according to Concept 2 for this detail, as shown below - in contrast to the previous numerical calculations. On the basis of the numerical simulations, axle type B from lorry type T2 is decisive (stress reduction factor in the test $f_{\sigma,test,B} = 0.24$, see Table 40). Also for axle type C, a more beneficial reduction factor could be verified ($f_{\sigma,test,C} = 0.23$, see Table 44) with the full scale tests and therefore also lorry type T3 was considered for the verification.

- Verification of vehicle type T2, axle type B (for $\Delta\sigma_{D2,max,FLM2+\phi}$ see Section 5.3.3) with stress reduction factor of the full scale test)

$$|\Delta\sigma_{D2,max,new}| = |\Delta\sigma_{D2,max,FLM2+\phi}| \cdot f_{\sigma,test,B} / f_{\sigma,num} = 76.62 \cdot 0.24 / 0.78 = 23.6 \text{ N/mm}^2 < \Delta\sigma_L = 40.2 \text{ N/mm}^2$$

- Verification of vehicle type T3, axle type C (for $\Delta\sigma_{D2,T3,C}$ see Section 5.4.2) with stress reduction factor of the full scale test

$$|\Delta\sigma_{D2,T3,C,FLM2+\phi}| = 30.84 \cdot 120 / 90 \cdot 1.20 = 49.34 \text{ N/mm}^2$$

$$|\Delta\sigma_{D2,T3,new}| = |\Delta\sigma_{D2,T3,C,FLM2+\phi}| \cdot f_{\sigma,test,C} / f_{\sigma,num} = 49.34 \cdot 0.23 / 0.36 = 31.5 \text{ N/mm}^2 < \Delta\sigma_L = 40.2 \text{ N/mm}^2$$

5.5.3. Detail D3

As described in Concept 2, fatigue load model FLM 2 has to be applied which includes higher axle loads and gross weights than FLM 4 regarding to a fatigue endurable design of the UHPFRC pavement.

The maximum occurring stress range in the future $\Delta\sigma_{\max,D3,new}$ can be expected due to the trailer axles of lorry type T2 at its critical load position (see Figure 81 in Section 3.3.4).

As already shown in Figure 245.b and Figure 246.b, the maximum occurring future stress ranges (after strengthening) due to FLM 4* in detail D3 – Joint I/III and Joint II – are having a value of:

$$\begin{aligned} \rightarrow \Delta\sigma_{\max,D3,new} &= 87.0 \text{ N/mm}^2 && \text{due to FLM 4* at Joint I/III} \\ \rightarrow \Delta\sigma_{\max,D3,new} &= 48.0 \text{ N/mm}^2 && \text{due to FLM 4* at Joint II} \end{aligned}$$

For the use of Concept 2, where FLM 2 is necessary, this maximum occurring future stress ranges plotted above have to be scaled based on the ratio referring to the appropriate axle loads from FLM 4* and FLM 2 (axle loads $F_{A,T2,B,FLM4*} = 105.7 \text{ KN}$, $F_{A,T2,B,FLM2} = 140 \text{ KN}$; see Figure 24 in Section 2.5.2):

$$\begin{aligned} \rightarrow \Delta\sigma_{\max,D3,new} &= 87.0 \cdot 140/105.7 = 115.2 \text{ N/mm}^2 && \text{due to FLM 2 at Joint I/III} \\ \rightarrow \Delta\sigma_{\max,D3,new} &= 48.0 \cdot 140/105.7 = 63.6 \text{ N/mm}^2 && \text{due to FLM 2 at Joint II} \end{aligned}$$

The stress ranges in the notch detail have been determined under consideration of a static numerical analysis and therefore dynamic effects have to be taken into account within Concept 2. These dynamic effects were considered with an overall dynamic factor of $\varphi = 1.2$:

$$\begin{aligned} \rightarrow \Delta\sigma_{\max,D3,new} &= 115.2 \cdot 1.2 = 138.2 \text{ N/mm}^2 && \text{due to FLM 2, including } \varphi = 1.2 \text{ at Joint I/III} \\ \rightarrow \Delta\sigma_{\max,D3,new} &= 63.6 \cdot 1.2 = 76.3 \text{ N/mm}^2 && \text{due to FLM 2, including } \varphi = 1.2 \text{ at Joint II} \end{aligned}$$

$$\begin{aligned} - \text{ Fatigue strength } \Delta\sigma_c (n_c = 2 \cdot 10^6) \text{ for D3:} &&& \Delta\sigma_c = 100 \text{ [N/mm}^2\text{]} \\ &&& \Delta\sigma_D = 73.7 \text{ [N/mm}^2\text{]} \\ &&& \Delta\sigma_L = \Delta\sigma_R = 40.2 \text{ [N/mm}^2\text{]} \end{aligned}$$

$$|\Delta\sigma_{\max,D3,new}| = 138.2 \text{ [N/mm}^2\text{]} > |\Delta\sigma_R| = 40.2 \text{ [N/mm}^2\text{]} \quad \text{Joint I/III}$$

$$|\Delta\sigma_{\max,D3,new}| = 76.3 \text{ [N/mm}^2\text{]} > |\Delta\sigma_R| = 40.2 \text{ [N/mm}^2\text{]} \quad \text{Joint II}$$

Note: Higher maximum stress cycles will occur for a parallel crossing of lorries on different lanes.

The maximum occurring future stress range $\Delta\sigma_{\max,D3,\text{new}}$ has at both joints a higher value than the cut off limit of fatigue resistance and therefore additional fatigue damage have to be expected also after the strengthening. Worth particular mention is that the determination of the maximum occurring stress range after strengthening is highly effected by very conservative assumptions.

Local in situ strain measurements in the regions of the bolted field connections are therefore necessary for an accurate fatigue evaluation of this strengthening detail.

5.6. Full scale tests

5.6.1. General

In addition to the extensive numerical studies regarding to the strengthened orthotropic steel deck's fatigue life, full scale tests have been performed to get more accurate stress reduction factors f_σ which are based on strain measurements in the local notch details. In the tests also the effects of overloads and thermal constraints, leading to additional concrete cracks, were studied. For the numerical analyses, also the concrete's effective Young's Modulus was chosen in a very simplified way with a conservative value of $E_{c,\text{eff}} = E_c/4$ to include concrete cracking. This parameter strongly influences the local stresses in the steel structure and for this reason, also the full scale tests were necessary to clarify the lack of knowledge about a realistic effective concrete's Young's Modulus.

The full scale tests with the implemented strain measurements are presented in this Section which have been performed within a research project [33]. In addition to the strain measurements and the resulting analyses regarding to the strengthening of orthotropic steel decks with an UHPFRC pavement and comparison with the old structure, a realistic effective overall UHPFRC Young's Modulus $E_{c,\text{eff,test}}$ has been determined by comparing the measurements with numerical calculations. The numerical analyses showed that a concrete pavement with a thickness of $t_c = 70\text{mm}$ would be sufficient for the stress reduction of detail D1a (see Table 30 in Section 5.5.1). But as already mentioned in Section 5.5.1, a concrete's thickness of at least $t_c = 80\text{mm}$ is necessary because of the concrete's reliability and for the warranty of sufficient concrete covering. Therefore, $t_c = 80\text{mm}$ was selected in the full scale test specimen.

First, the geometrical dimensions and the site conditions as well as the production of the test specimen are described in Section 5.6.2. The structural design, the boundary conditions in the tests, the loading of the test specimen and the position of the in summary 27 strain gauges applied on the steel structure are presented. Additionally, the production of the UHPFRC pavement and the interconnecting joint between steel and concrete are described in this Section.

The measuring instrumentation is illustrated in Section 5.6.3 and an explanation of the performed testing sequence is also included. In summary 7 load levels have been applied, where static as well as dynamic loading was considered.

The numerical results in terms of strains referring to the steel deck with asphalt pavement, which represents the reference case, have been determined with a finite element model that has been developed by using the same modelling techniques as for Model A to Model C (see Section 3.2.1 to 3.2.3). The resulting strains, which have been calculated at the same positions as the strain gauges on the full scale test specimen, are compared and visualised in Section 5.6.4.

The measured strains at the steel structure due to a representative selection of load levels are presented in Section 5.6.5. In addition to the measurements at the steel structure, transducers were applied on the top surface of the concrete pavement and the measured values are shown in Section 5.6.6. A possible slippage in the interface between steel deck and concrete pavement has also been measured. These measurements were negligible small even for the highest load level and are therefore not mentioned in the following. A rigid composite interaction between steel and concrete can be assumed. The evaluation of all the mentioned measurements in the steel structure, the concrete pavement as well as in the interface between these two parts is shown in Section 5.6.5 and Section 5.6.6.

Under consideration of the measurements on the full scale tests and in combination with additional numerical analyses, an overall effective Young's Modulus of the UHPFRC pavement $E_{c,eff,test}$ could be derived. The implemented investigations and the resulting value for this Young's Modulus are presented in Section 5.6.7. Finally concluding remarks can be found in Section 5.6.8.

5.6.2. Geometrical dimensions, production and position of the strain gauges

The geometrical dimensions, the production of the test specimen and the defined measuring positions of the strain gauges on the steel structure are described and visualised in this Section.

Section 5.6.2.1 illustrates the steel structure referring to the orthotropic deck with open longitudinal ribs. Section 5.6.2.2 describes and visualises the UHPFRC pavement as strengthening method of the orthotropic deck. Section 5.6.2.3 includes an explanation of the interconnecting joint's production between steel deck and concrete pavement.

5.6.2.1. Geometry of the steel deck

The geometrical dimensions of the test specimen's orthotropic steel deck are identical to representative Model A which is described and displayed in Section 3.2.1.

The orthotropic steel bridge deck consists of the following parts:

- Cross Girder (CG):
 - Thickness of the web $t_{CG} = 10\text{mm}$
 - Height of the cross girder $h_{CG} = 420\text{mm}$
 - Interval between the cross girders $e_{CG} = 2.0\text{m}$

Note: The cross girder has no bottom flange. The cross girder's web thickness was adapted so that the cross girder's bending curve of the test specimen and Model A is identical.

- Longitudinal Rib (LR):
 - Flat steel plates with a plate thickness of $t_{LR} = 10\text{mm}$
 - Height of the longitudinal ribs $h_{LR} = 210\text{mm}$
 - Interval between the longitudinal ribs $e_{LR} = 360\text{mm}$
- Deck Plate (DP):
 - Thickness of the deck plate $t_{DP} = 10\text{mm}$
 - Deck plate slenderness $e_{LR}/t_{DP} = 360/10 = 36$

Figure 247 shows the geometry and the support of the test specimen as well as the positions of the strain gauges DMS 1 to DMS 27.

- Strain gauges for the evaluation of the strains/stresses in the steel deck plate at the bottom surface (in transverse direction):
 - DMS 1 to DMS 4 in measuring axis MA-1
 - DMS 5 to DMS 8 in measuring axis MA-2
- Strain gauges for the evaluation of the occurring strains/stresses at the longitudinal ribs in longitudinal direction in the local area of the weld connection to the mid cross girder
 - DMS 9 to DMS 17 – longitudinal rib in axis SA (region “Bereich L2”)
 - DMS 18 to DMS 22 – longitudinal rib in axis A4 (region “Bereich L3”)
 - DMS 23 to DMS 27 – longitudinal rib in axis A5 (region “Bereich L1”)

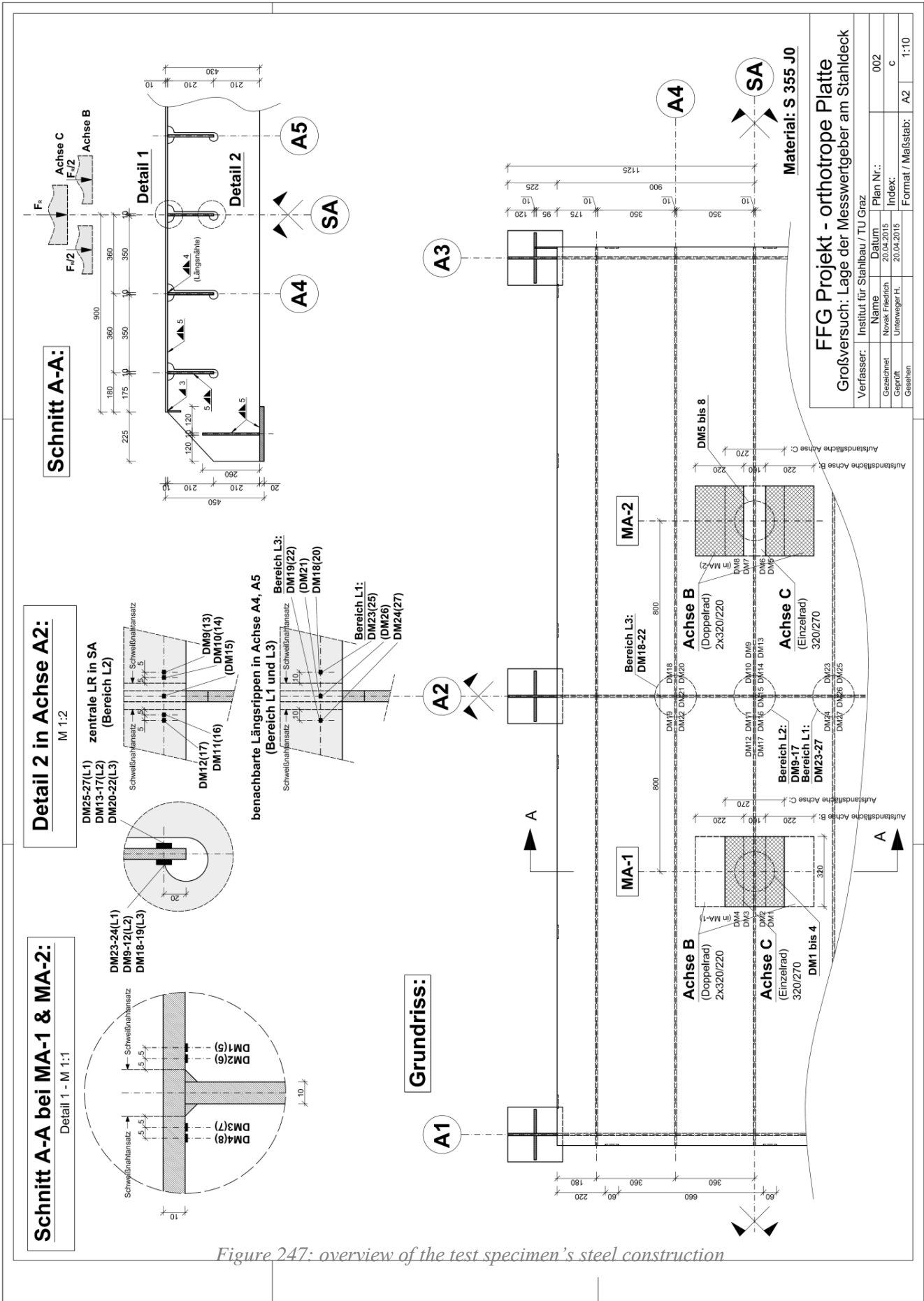


Figure 247: overview of the test specimen's steel construction

5.6.2.2. Concrete pavement and interface between steel and concrete

The UHPFRC pavement has been produced with a thickness of 80mm. An orthogonal conventional reinforcement with a diameter of 8mm, with a distance of 50mm, has been inserted whereby the rebars in longitudinal direction (position number 1, see Figure 248) are lying above the rebars in transverse direction (position number 2, see Figure 248). The concrete covering of the rebars to the finished concrete surface is 30mm and the interconnecting joint has been produced with a Basalt interspersed epoxy resin.

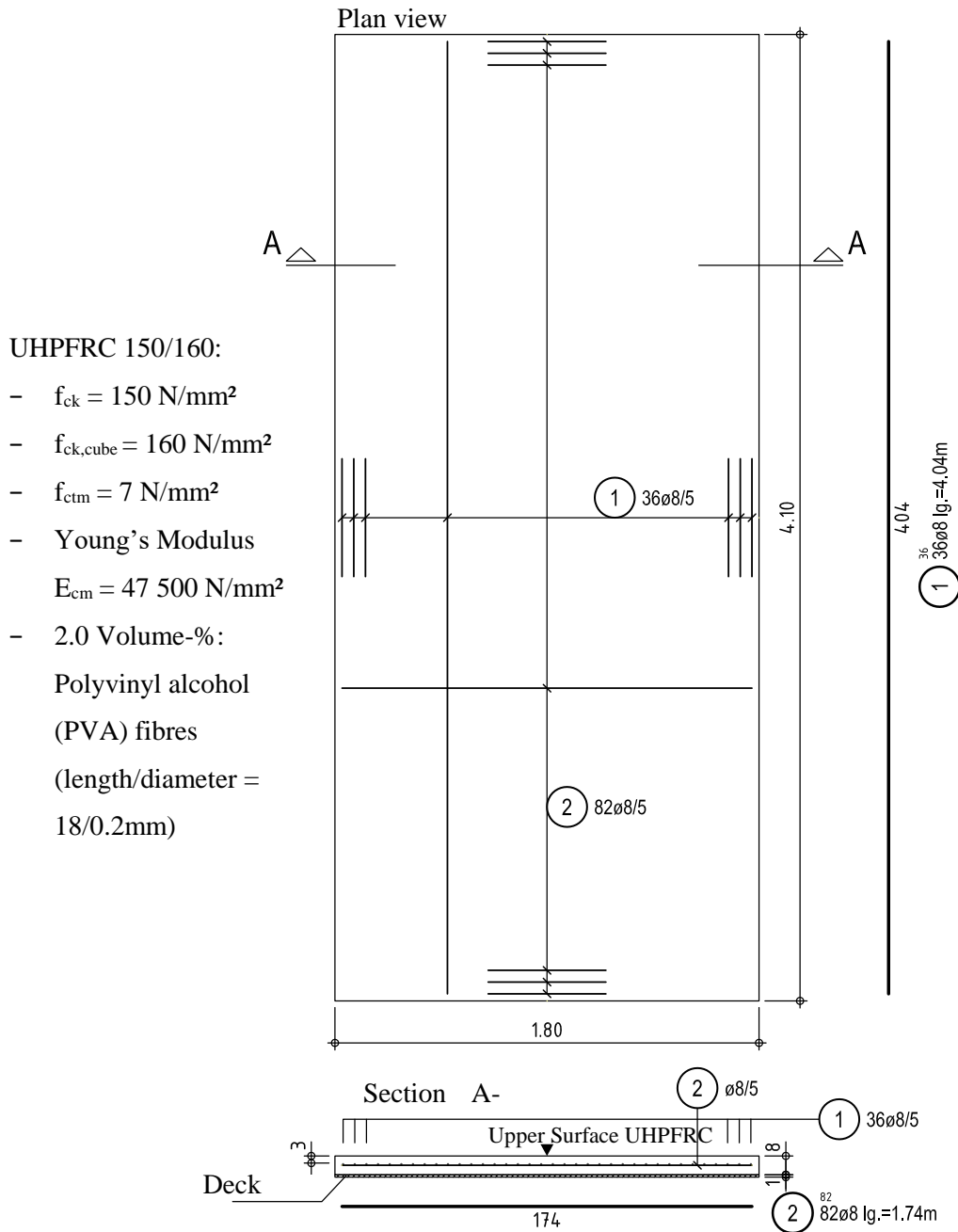


Figure 248: reinforcement plan of the test specimen (values in cm)

5.6.2.3. Production of the concrete strengthening

Table 33 gives an overview of the several operation steps referring to the production of the UHPFRC pavement and the interconnecting joint between steel and concrete at the test specimen.

Table 33: Production sequence of the UHPFRC pavement and the interface between steel and concrete on the test specimen

Operation step	Detailed Information
1 Steel surface Sandblasting (class Sa 2.5)	measured depth of roughness according DIN 4776: 1990-05 $R_a=14\mu\text{m}$, $R_z=76\mu\text{m}$, $R_q=17\mu\text{m}$
2 Application of the epoxy resin	thickness of 3mm; Sikadur 30
3 Intersperse of the Basalt granulate	dried Basalt grit $\text{Ø } 4\text{-}8\text{ mm}$
4 Application of the formwork and reinforcement	steel bars spot-welded
5 Concreting	

In order to achieve a uniform layer thickness of the epoxy resin, the adhesive was field-wise applied by toothed spatula and then the surface has been smoothed by using an aluminium bar (see left picture in Figure 249). Immediately after that the dried basalt granulate was sprinkled by hand and was then pressed into the adhesive layer by using a friction board (see right picture in Figure 249). Excessive grit was loosened in several operation steps by using alternately a coarse brush and an extractor.

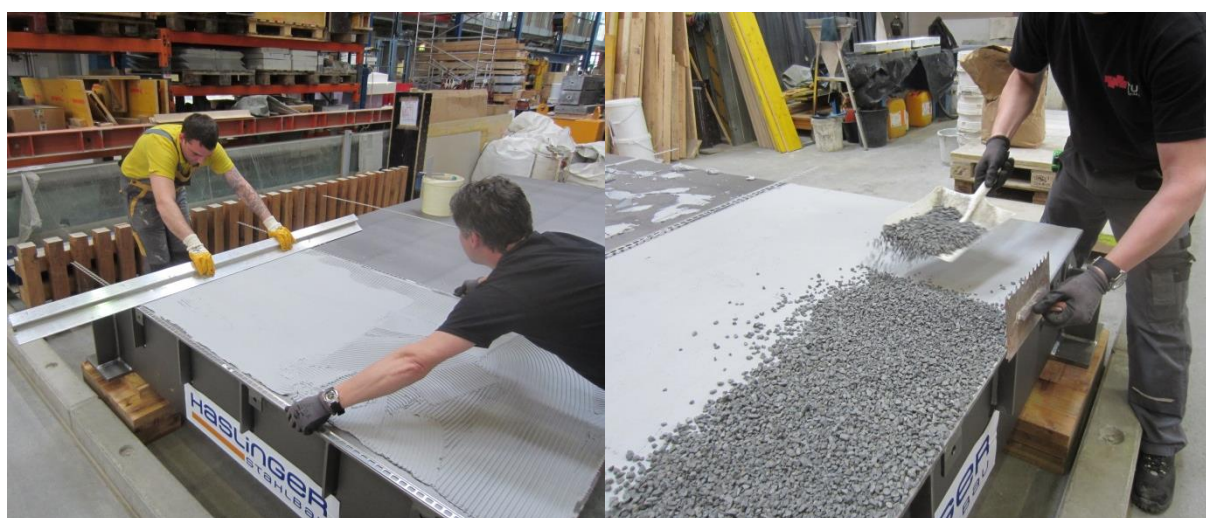


Figure 249: production of the interconnecting joint between steel deck and concrete pavement

The reinforcing bars were welded to an orthogonal grid and placed upon conventional plastic spacers which were placed directly above the split layer.

The application of the concrete was done by using 2 different concrete mixers parallel. In summary 6 mixer fills have been produced which have been merged into a 1000 litre crane bucket (see Figure 250).



Figure 250: manipulation of the fresh concrete

A detailed protocol of the mixing and manipulation process is illustrated in [33]. The process ability of the UHPFRC was checked by spreading test according to ÖNorm EN 12350-5.

The filling of the fresh concrete mixture into the formwork was done directly from the crane bucket, which was led in a serpentine line over the test specimen. The first step of the concrete compaction has been done with a small shaking spatula, the second step was accomplished with a large vibrating screed (over the entire width of the test specimen). By spraying the concrete's surface with water and rubbing it with a friction board, the surface was finalized by hand. The whole process is documented in Figure 251 and Figure 252.



Figure 251: application of the fresh concrete with crane bucket

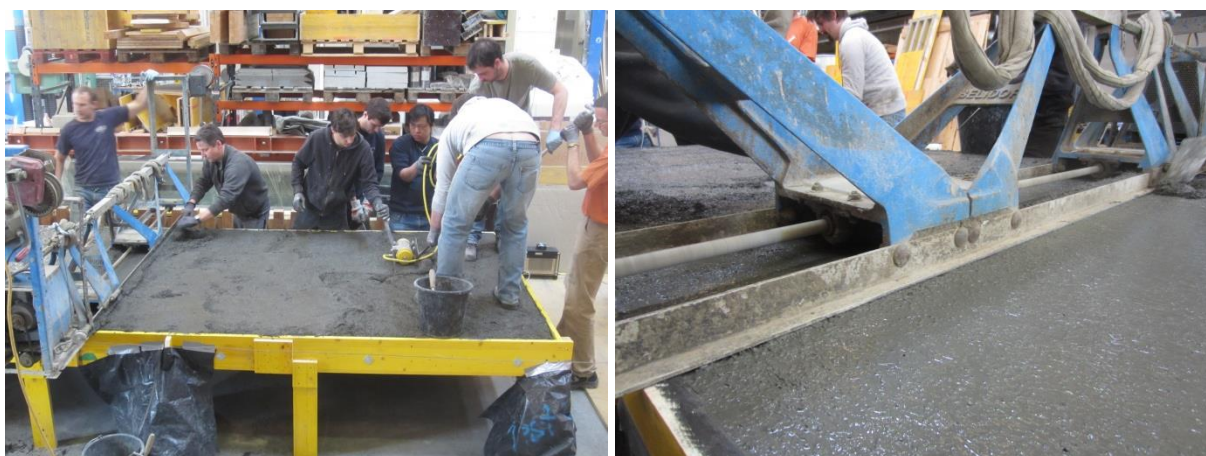


Figure 252: concrete compaction with shaking spatula (left) and vibrating screed (right)

For the material characterization of the UHPFRC-material 28 cubes (100mm) and 12 cylinders (100mm/200mm) were made. Furthermore, large-sized test specimens for tensile (4 pcs.) and bending-tensile tests (3 pcs.) were made and additionally 2 shrinkage channels were filled with UHPFRC (see Figure 253). The results of the material tests of these specimens can be found in [33].



Figure 253: test specimens for accompanying material tests referring to the UHPFRC

5.6.3. Measuring instrumentation and testing load sequence

5.6.3.1. Experimental set-up

The full scale test is a bending test on a plate which is vertically supported at 6 points (see Figure 254). The local stresses in the fatigue critical notch details have to be simulated due to the wheel loads from the heavy traffic at an actual orthotropic steel bridge deck. The bearings are rotatable in all directions and the horizontal degree of freedom should be free at most of the vertical supports to avoid any constraining effect (only 1 fixed support). 2 different surface pressure load arrangements were applied which represent the contact patches of single and double wheeled axles (axle type B and C according to [1], see Figure 25 in Section 2.5.2). Surface load arrangement 1 corresponds to two single wheeled axles (axle type C) positioned centrally on the mid longitudinal rib. The centre of each surface load is positioned in a distance of 800mm away from the mid cross girder. The 2nd arrangement consists of 4 load surfaces, which represent the twin tyres (axle type B). The load surfaces are positioned also centrally above the mid longitudinal rib and the centre of each twin tyre is located in a distance of 800mm away from the mid cross girder. The load concept and the supports are shown in Figure 254.

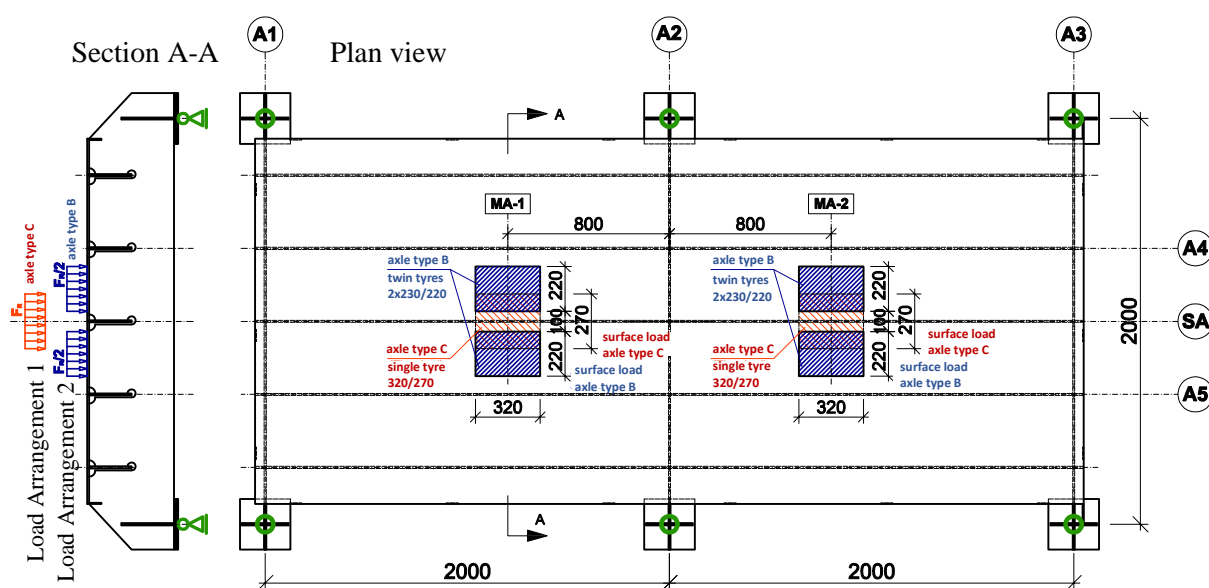


Figure 254: load and support concept of the test specimen

The support on 6 points is statically indefinite and requires the possibility of compensation of the imperfections from the test specimen (deviations from the deck plate level). This requirement was made by using high strength threaded rods ($\varnothing 47$) which create the bearing base. The in the test occurring rotational movements happened in the contact surface between the spherical nut and the attached bearing plate. Additional elastomer plates with a thickness of 3mm have been inserted between the bearing plates

and the test specimen to avoid horizontal constraints. The supporting detail is illustrated in the left picture of Figure 255.

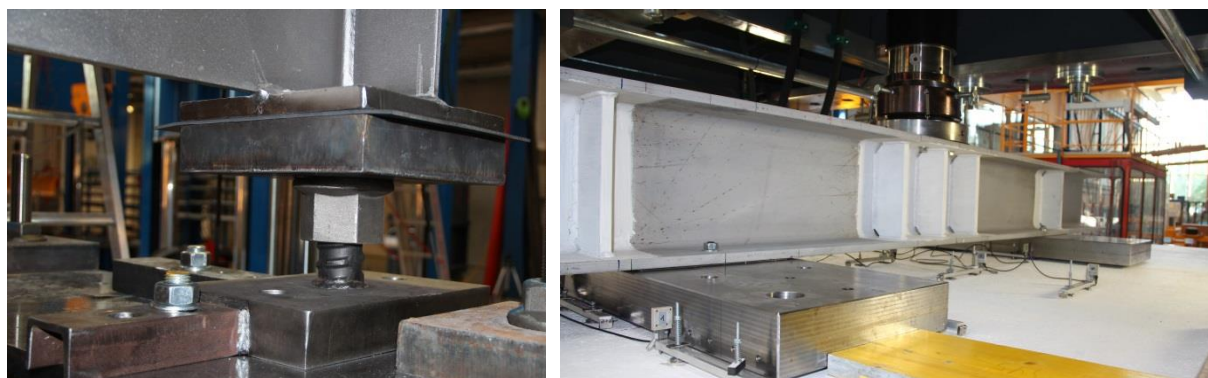


Figure 255: left: storage detail at the ends of the cross girders; right: load introduction through load distributing beam (IPB 300)

The surface pressure loads referring to axle type B and C with its geometrical dimensions as shown in Figure 254 were implemented by using 12.5mm thick elastomer plates. These elastomer plates were laid under load distributing metal foot plates. The load introduction from the test cylinder of the testing facility has been performed by adding a load distribution beam between the metal foot plates and the test cylinder. This load distributing beam was connected with a ball joint to the test cylinder. The right picture in Figure 255 illustrates the load introduction. Figure 256 gives an overview of the entire test specimen and the test facilities. More detailed information of the used experimental equipment can be found in [33].



Figure 256: overview of the entire test specimen and the test facilities

5.6.3.2. Test equipment

Before the concrete pavement was produced, 27 linear strain gauges were applied at the bottom side of the steel deck for the determination of the occurring strains and stresses in the steel structure. The exact positions of the strain gauges are illustrated in Figure 247 and also in Figure 257. Strain gauges of the type LY61/1.5mm/120 Ohm from the manufacturer „Hottinger Baldwin Messtechnik“ (HBM) have been used. Strain gauge DMS 1 to DMS 8 are applied directly to the steel plate in transverse direction. Strain gauges DMS 9 to DMS 27 are applied to the longitudinal ribs in the longitudinal direction.

On the upper surface of the concrete, 12 setting strain transducers from the type DD1 from HBM were installed. These measuring instruments were mounted to evaluate the complete local deformation behaviour of the test specimen and for an early occurring crack recognition in the concrete pavement. The exact positions of the setting strain transducers are illustrated in Figure 257.

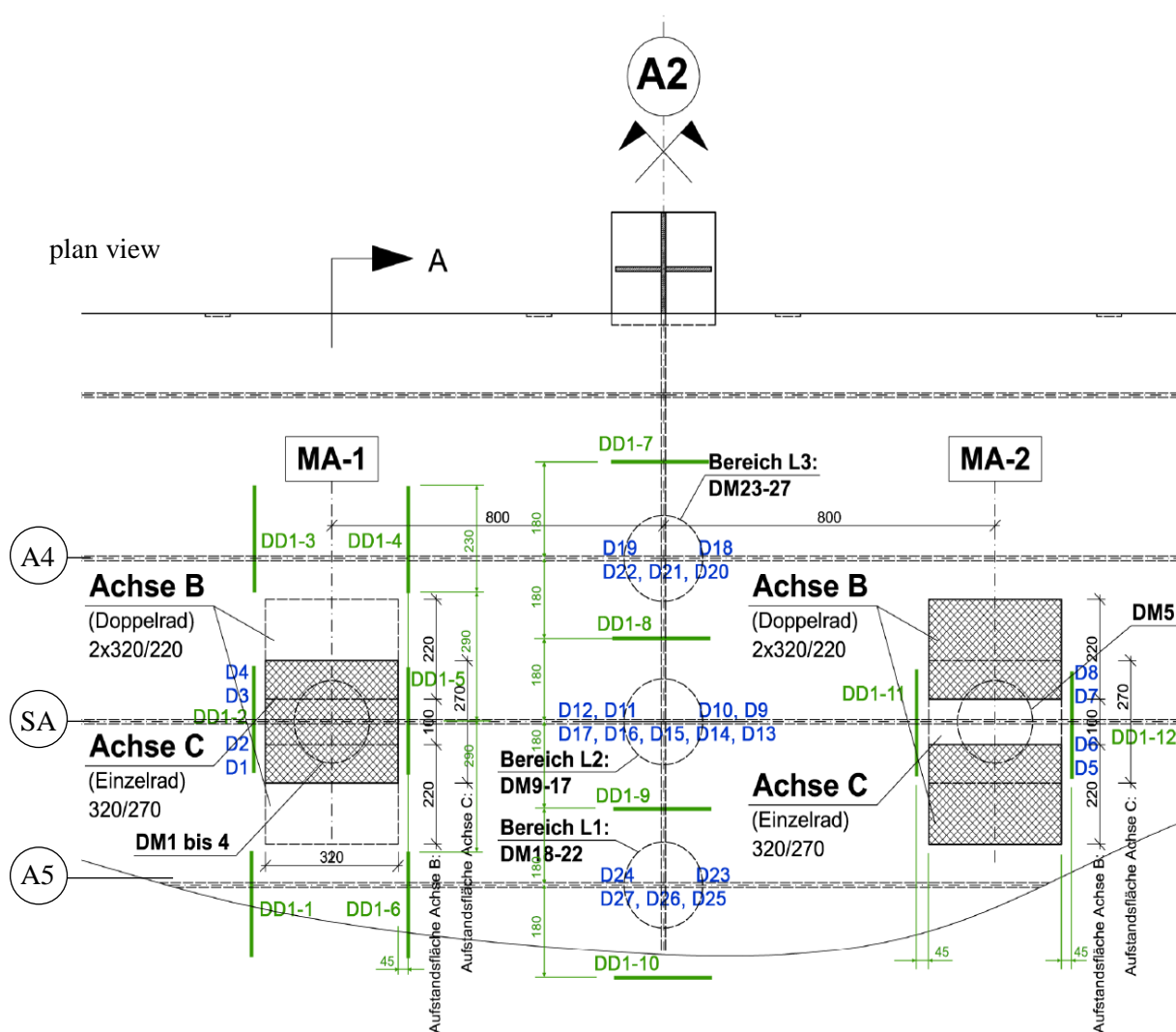


Figure 257: measuring arrangement of the strain gauges D1-D27 and the setting strain transducers (green) on the upper surface of the UHPFRC pavement

5.6.3.3. Testing sequence

The loading of the test specimen was performed with different load arrangements (axle type B and C) as already described in Section 5.6.3.1. For every load arrangement in summary 7 load levels have been taken into account. Additionally, for every load level static and dynamic load application with 1000 load cycles have been performed. The static and dynamic load application have been performed alternating with increasing load levels. The specified load levels are in summary plotted in Table 34. An additional background to the specified load levels in Table 34 is described in the list below:

- Load level 1: estimation of the characteristic service load on road bridges referring to the frequent load combination according to [54]
- Load level 2: reduced fatigue load model FLM 4* based on weigh in motion measurements in [44] (see Figure 24 in Section 2.5.2)
- Load level 3: fatigue load model FLM 4 according to [1], group of idealised heavy vehicles (see Figure 24 in Section 2.5.2)
- Load level 4: fatigue load model FLM 2 according to [1], group of frequent heavy vehicles (see Figure 24 in Section 2.5.2)
- Load level 5 and 6: intermediate steps between FLM 2 and LM 1 for the increase of the load
- Load level 7: load model LM 1 according to [1], maximum axle load for a double axle at the main lane. The static ultimate limit state verifications are made with this load model

Table 34: Specification of the axle and wheel loads in [kN] referring to every load level

load level		1	2	3	4	5	6	7
axle C	total	33(28%)	66(55%)	90(75%)	120(100%)	144(120%)	180(150%)	300(250%)
	per wheel	16,5	33	45	60	72	90	150
axle B	total	55(29%)	110(58%)	150(79%)	190(100%)	228(120%)	285(150%)	
	per wheel	27,5	55	75	95	114	142.5	
background		SLS	ELM4*	ELM4	ELM2	1.2xELM2	1.5xELM2	LM1

In summary 55 tests have been performed at the full scale test specimen and a detailed documentation of the testing sequence is also shown in [33]. After the finalisation of the originally planned experimental program, no visible cracks could be detected in the analysed region of the concrete plate of the test specimen. Therefore, it was decided to perform additional loading tests after a thermal constraining event. The test specimen was stored outdoors in summer on 4 bearing points and the upper surface was covered with a black foil to achieve the greatest possible warming from the sun's rays (see left picture in Figure 258). As a conservative simulation of a heavy rain on a hot summer day, the test specimen had been sprayed with water (see right picture in Figure 258).



Figure 258: storage of the test specimen outdoors and – left: covering the test specimen with a black foil; right: sprinkling the concrete surface with water

To quantify this extreme thermal constraining event, that represents a sudden thunder shower on a very hot summer day, additional temperature measurements were done. The air temperature below the test body, the temperature at the upper concrete surface and the temperature at the bottom surface of the steel deck had been measured. These temperature measurements along the time of the experiment are plotted in Figure 259.

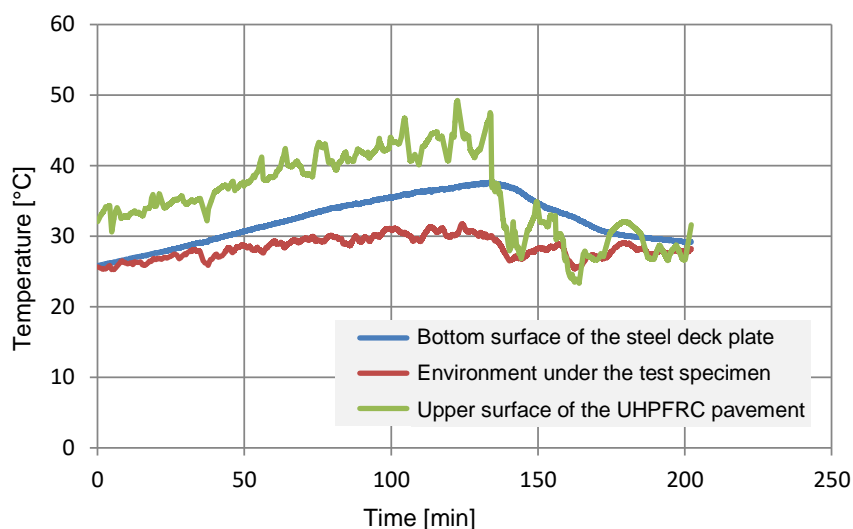


Figure 259: temperature profile during the weathering experiment

After this extreme thermal constraining event cracks in the concrete plate could be detected which are documented in Section 5.6.6.2. The test specimen was again installed into the testing machine after finishing the thermal constraining experiment and then again loaded with predefined load levels (load level 4 with axle type B and load level 7 with axle type C).

5.6.3.4. Tensile bond (pull off) tests at the full scale test specimen

After completion of all full scale tests including the thermal constraining event, the remaining tensile strength between concrete pavement and steel deck was determined at 10 selected points of the test specimen. The location of the measuring points and their designation is shown in Figure 260.

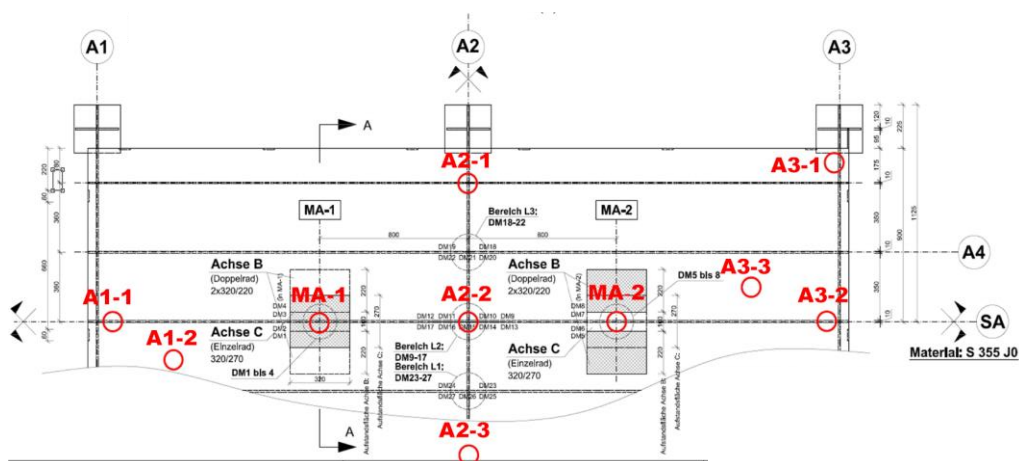


Figure 260: location and designation of the measuring points referring to the tensile bond tests

For this purpose, concrete cylinders with a diameter of approx. 100 mm were first released by using a core drilling machine. A 100 mm high steel stamp was glued to the concrete test cylinder with an epoxy adhesive (see left picture in Figure 261). The steel stamp had a centric threaded hole through which the tension test load was introduced by using a threaded rod. The base of the pull off tester (circular contact patch) had an inside diameter of 185mm and a ring width of 15mm (see right picture in Figure 261). The force was applied with a hydraulic hand pump and has been measured by a strain gauge equipped and force calibrated measuring rod. The results are presented in Section 5.6.6.4.

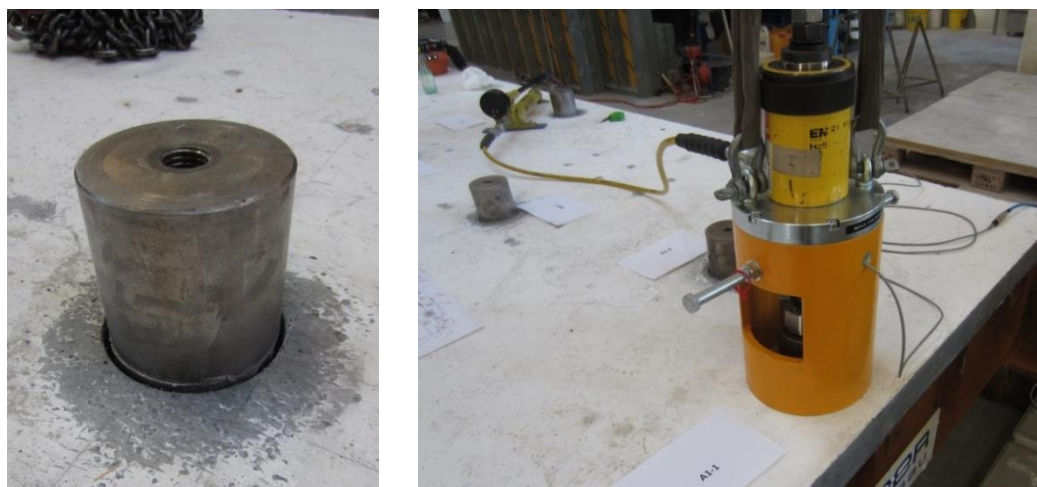


Figure 261: performance of the tensile bond tests; left: glued steel stamp; right: pull off tester

5.6.4. Numerical stresses for steel deck with asphalt pavement – reference values (before strengthening)

For the reference case, before strengthening, the strains in the measuring points of the steel structure have been determined with a finite element model. The locations of the measuring points are illustrated in Figure 247. The numerical model has been developed under consideration of the geometry according to the full scale test specimen. The modelling technique is identically to the finite element model of Model A which is described in Section 3.2.1. Figure 262 shows an overview of the finite element model referring to the full scale tests for the determination of the reference strain values regarding to the unstrengthened steel deck.

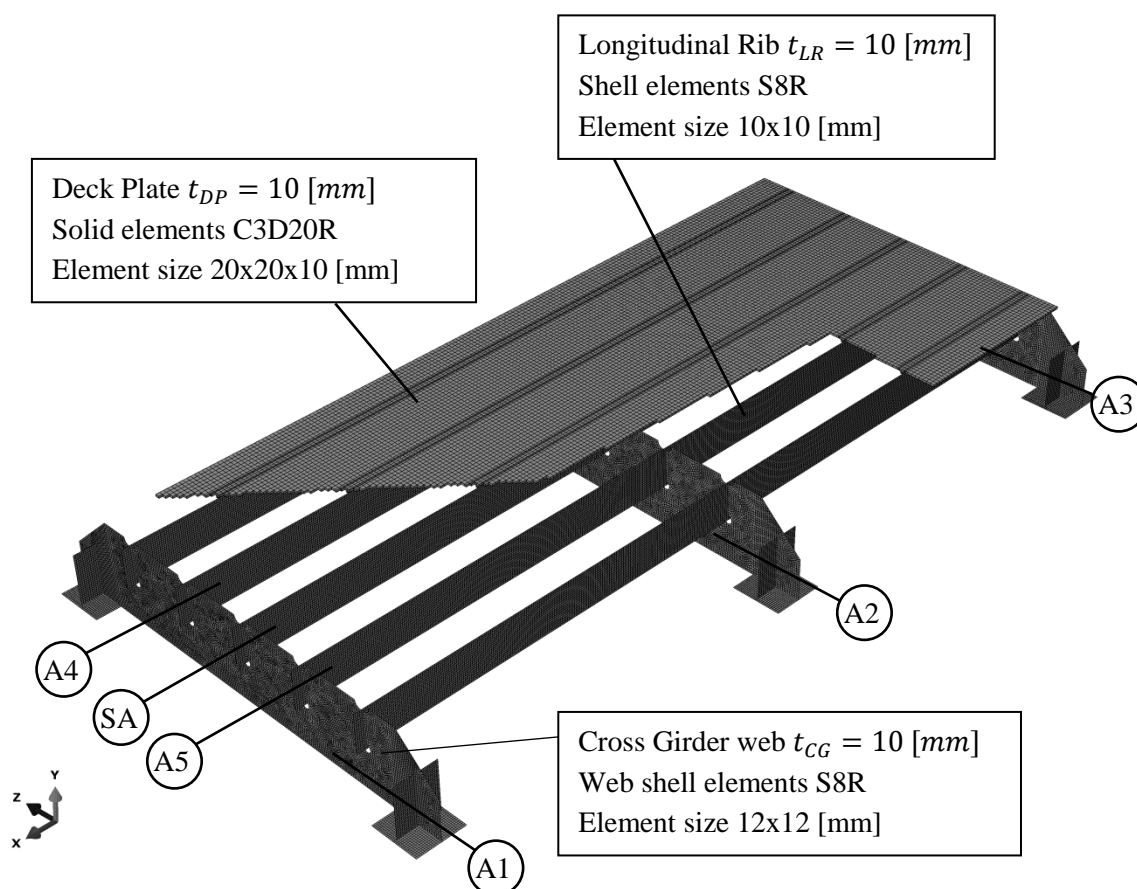


Figure 262: overview of the finite element model referring to the full scale tests – reference case, unstrengthened steel deck

The asphalt pavement was indirectly taken into account by means of an increased wheel contact patch, with a load spreading angle of 45° through the thickness of the asphalt pavement (see Figure 29 in Section 2.5.2). The mesh refinement of the FEM model in detail D1 (connection of longitudinal rib to the deck plate) has been assigned according to the requirements regarding to the structural stress method and can be seen in Figure 35.a (see Section 2.8). The strains in the measuring points DMS 1 to DMS 27 have been calculated due to axle/wheel type B and C and under consideration of the load levels which are presented in Table 34 (see Section 5.6.3.3).

Table 35 shows exemplarily the results of the numerical calculations regarding to the reference case, before strengthening (without UHPFRC pavement), due to load level 4 (FLM 2) for axle /wheel type B and C.

Note: Numerical calculations under consideration of a steel Young's Modulus of $E_S = 210,000 \text{ N/mm}^2$

Table 35: numerical determined strains and stresses in the measuring points due to axle type B and C and load level 4 (FLM 2) – reference values before strengthening

Strain gauge DMS	Axle type B, F=190 [kN]		Axle type C, F=120 [kN]	
	strain [-]	stress [N/mm ²]	strain [-]	stress [N/mm ²]
1	-5.664E-04	-135.7	-3.700E-04	-89.3
2	-6.407E-04	-151.5	-4.316E-04	-102.6
3	-6.455E-04	-152.6	-4.356E-04	-103.5
4	-5.709E-04	-136.7	-3.739E-04	-90.1
5	-5.664E-04	-135.7	-3.700E-04	-89.3
6	-6.407E-04	-151.6	-4.315E-04	-102.6
7	-6.454E-04	-152.6	-4.355E-04	-103.5
8	-5.709E-04	-136.7	-3.738E-04	-90.1
9	-5.267E-04	-112.7	-4.508E-04	-96.5
10	-5.327E-04	-113.4	-4.560E-04	-97.1
11	-5.326E-04	-113.4	-4.559E-04	-97.1
12	-5.264E-04	-112.6	-4.506E-04	-96.4
13	-5.649E-04	-118.1	-4.822E-04	-100.8
14	-5.731E-04	-120.0	-4.890E-04	-102.4
15	-6.289E-04	-133.0	-5.363E-04	-113.4
16	-5.717E-04	-119.7	-4.879E-04	-102.1
17	-5.638E-04	-117.9	-4.812E-04	-100.6
18	-2.759E-04	-59.4	-1.158E-04	-25.0
19	-2.748E-04	-59.1	-1.152E-04	-24.8
20	-1.357E-04	-27.6	-2.119E-05	-3.9
21	-1.315E-04	-26.1	-1.088E-05	-1.2
22	-1.355E-04	-27.6	-2.128E-05	-4.0
23	-1.060E-04	-22.5	-4.958E-06	-1.0
24	-1.064E-04	-22.4	-5.027E-06	-0.9
25	-2.817E-04	-59.7	-1.161E-04	-24.8
26	-3.351E-04	-72.8	-1.437E-04	-31.6
27	-2.817E-04	-59.8	-1.161E-04	-24.8

5.6.5. Steel deck – results and evaluation of the measurements

In the following Sections 5.6.5.1 and 5.6.5.2, the results referring to the strain measurements in the steel structure at the full scale tests are presented for a selection of 2 load levels (load level 4 and 7, see Table 34 in Section 5.6.3.3). The entire strain measurements are plotted in [33].

The following values are pointed out:

- $\varepsilon_{(1)}$ are the strains measured at the test specimen due to the belonging load level (axle type B and C)
- $\varepsilon_{(0)}$ are the numerical determined reference strains referring to the unstrengthened steel deck (see Section 5.6.4) due to the belonging load level (axle type B and C)
- $f = \varepsilon_{(1)} / \varepsilon_{(0)}$... stress reduction factor regarding to the strengthening with UHPFRC pavement

There was always a static loading per load level up to the respective load maximum of the load level. Then a dynamic loading with about 1000 load cycles and the same load maximum from the actual load level has been performed. Finally, there was again a static loading up to the same maximum of the load level. This described procedure was done for every load level and after finishing the entire testing sequence, an extreme thermal constraining event, which is already described in Section 5.6.3.3, took place. After the thermal constraining event, the same loading procedure (static, dynamic, static) was performed again for load level 4 (axle type B) and load level 7 (axle type C) by using the test specimen that had now small cracks in the concrete. Table 36 shows the procedure of load application for each load level.

Table 36: loading mode per load level and additional tests after thermal constraining event

Load level	Load step	Loading type
1 to 7	1	Static loading
	2	Dynamic loading, about 1000 cycles with ~2 Hz
	3	Static loading
<u>thermal constraining event:</u>		
Heating and sudden cool down		
(simulation of a heavy shower on a hot summer day) crack initiation in the concrete pavement		
4 (axle type B) 7 (axle type C)	4	Static loading
	5	Dynamic loading, about 1000 cycles with ~2 Hz
	6	Static loading

In the following, a summary of the most important results from the full scale tests with respect to the stresses on the steel deck at the relevant notch details is given. The detailed results in all measuring points (strain gauge DMS 1 to DMS 27) regarding to the individual examined load levels 1 to 7 and the

two investigated axles (axle type B or C) can be found in [33]. The results of load level 4 and 7 are illustrated in Table 37 to Table 44.

As mentioned before, for each load level, 2 strain measurements were carried out under a static loading, before and after the applied dynamic load cycles. Additionally, after successful completion of all load levels, a realistic extreme thermal constraining event at the unloaded test specimen has been performed (outdoor heating on a hot summer day followed by sprinkling with cold water). A renewed loading due to 2 very high load levels has followed (see Table 36):

- Load level 7 for axle type C
- Load level 4 for axle type B

For a better overview, a comparison of the results for exactly these two load levels has been done with the results before and after the thermal constraining event.

For the evaluation of the results on the steel deck, the measured strains $\varepsilon_{(1)}$ in the individual measuring points alone are not meaningful regarding to the desired remaining service life. The reduction of the stress or strain level compared to the unstrengthened current steel deck with asphalt pavement is essential. Hence, also the results are plotted relating to the steel deck before strengthening in terms of strains $\varepsilon_{(0)}$. These strains $\varepsilon_{(0)}$ were not measured values but numerically calculated ones based on the steel deck with an asphalt pavement. The strain/stress reduction factor $f = \varepsilon_{(1)} / \varepsilon_{(0)}$ due to the strengthening, which is stated for all measuring points and load levels in the result tables, is very important for the assessment of the remaining service life. In the following, this strain reduction factor f will be discussed in detail.

5.6.5.1. Results for load level 4

The measured strains $\varepsilon_{(1)}$ (after strengthening) and the numerically calculated reference strains $\varepsilon_{(0)}$ (before strengthening) are presented in Table 37, relating to the measuring points DMS 1 to DMS 27 (see Figure 247) due to load level 4, load step 1 (see Table 36). The factor $f = \varepsilon_{(1)} / \varepsilon_{(0)}$ indicates the stress reduction due to the UHPFRC pavement.

By comparing the values from the measurements $\varepsilon_{(1)}$ (with concrete pavement) to the numerically calculated ones $\varepsilon_{(0)}$ (without concrete pavement), a change of the algebraic sign can be detected for the strain gauges DMS 1 to DMS 8 (strain gauges for the deck plate bending – detail D1a). Without concrete pavement (values $\varepsilon_{(0)}$), the steel deck plate is mainly acting as a continuous beam in transverse direction which is supported by the longitudinal ribs. Primary bending stresses occur in the deck plate which are compression stresses (negative $\varepsilon_{(0)}$ -values) on the deck plate's bottom side in the area of the longitudinal

rib. On the contrary, the strengthened deck plate is acting primary as a membrane. Due to the composite action of the steel deck plate and the concrete pavement, mainly tensile membrane stresses (positive $\varepsilon_{(1)}$ -values) occur in the deck plate and the concrete's stresses in these area are compression stresses.

Table 37: results of the full scale test at load level 4 and load step 1

Load level 4 – load step 1									
			Static loading, before dynamic loading						
			Axle type C, F = 120[kN]				Axle type B, F = 190[kN]		
			$\varepsilon_{(1)}$	$\varepsilon_{(0)}$	$f=\varepsilon_{(1)}/\varepsilon_{(0)}$	$\varepsilon_{(1)}$	$\varepsilon_{(1)}[\%]$	$\varepsilon_{(0)}$	$f=\varepsilon_{(1)}/\varepsilon_{(0)}$
Strains at the deck plate	MA-1	DMS1	7.52E-05	-3.70E-04	-0.20	5.91E-05	96.2%	-5.66E-04	-0.10
		DMS2	7.38E-05	-4.32E-04	-0.17	5.56E-05	89.9%	-6.41E-04	-0.09
		DMS3	8.12E-05	-4.36E-04	-0.19	6.01E-05	99.0%	-6.45E-04	-0.09
		DMS4	7.47E-05	-3.74E-04	-0.20	6.22E-05	100.0%	-5.71E-04	-0.11
	MA-2	DMS5	6.86E-05	-3.70E-04	-0.19	5.49E-05	89.0%	-5.66E-04	-0.10
		DMS6	6.96E-05	-4.32E-04	-0.16	5.41E-05	88.0%	-6.41E-04	-0.08
		DMS7	6.61E-05	-4.36E-04	-0.15	5.19E-05	83.2%	-6.45E-04	-0.08
		DMS8	6.42E-05	-3.74E-04	-0.17	5.30E-05	85.0%	-5.71E-04	-0.09
Strains at the longitudinal ribs	LR-m	DMS9	-4.68E-05	-4.51E-04	0.10	-9.63E-05	89.5%	-5.27E-04	0.18
		DMS10	-5.70E-05	-4.56E-04	0.12	-1.07E-04	100.0%	-5.33E-04	0.20
		DMS11	-4.68E-05	-4.56E-04	0.10	-9.02E-05	83.4%	-5.33E-04	0.17
		DMS12	-4.95E-05	-4.51E-04	0.11	-9.36E-05	87.0%	-5.26E-04	0.18
		DMS13	-4.24E-05	-4.82E-04	0.09	-8.12E-05	75.8%	-5.65E-04	0.14
		DMS14	-4.03E-05	-4.89E-04	0.08	-7.39E-05	68.7%	-5.73E-04	0.13
		DMS15	-5.64E-05	-5.36E-04	0.11	-1.03E-04	98.2%	-6.29E-04	0.16
		DMS16	-4.62E-05	-4.88E-04	0.09	-8.38E-05	76.6%	-5.72E-04	0.15
	LR-A4	DMS17	-4.28E-05	-4.81E-04	0.09	-8.01E-05	75.3%	-5.64E-04	0.14
		DMS18	-2.08E-05	-1.16E-04	0.18	-6.65E-05	60.6%	-2.76E-04	0.24
		DMS19	-3.16E-05	-1.15E-04	0.27	-8.80E-05	82.3%	-2.75E-04	0.32
		DMS20	-2.06E-05	-2.12E-05	0.97	-6.47E-05	60.3%	-1.36E-04	0.48
		DMS21	-1.12E-05	-1.09E-05	1.03	-5.25E-05	50.6%	-1.31E-04	0.40
	LR-A5	DMS22	-6.43E-06	-2.13E-05	0.30	-3.67E-05	35.6%	-1.36E-04	0.27
		DMS23	-5.51E-06	-4.96E-06	1.11	-3.91E-05	38.1%	-1.06E-04	0.37
		DMS24	-2.54E-06	-5.03E-06	0.51	-3.87E-05	38.3%	-1.06E-04	0.36
		DMS25	-2.11E-05	-1.16E-04	0.18	-6.08E-05	56.1%	-2.82E-04	0.22
DMS26		-1.79E-05	-1.44E-04	0.12	-6.47E-05	60.6%	-3.35E-04	0.19	
DMS27	-2.11E-05	-1.16E-04	0.18	-5.96E-05	57.0%	-2.82E-04	0.21		

Table 38 shows the measured strains $\varepsilon_{(1)}$ (after strengthening) and the numerically calculated reference strains $\varepsilon_{(0)}$ (before strengthening) for DMS 1 to DMS 27 due to load level 4, load step 3 (see Table 36). The stress reduction, caused by the deck strengthening, is indicated with the factor $f = \varepsilon_{(1)} / \varepsilon_{(0)}$.

An additional column shows the strain increase due to the dynamic loading for axle type B in percentage (strain $\epsilon_{(1)}$ of load step 3 relating to strain $\epsilon_{(1)}$ of load step 1).

Table 38: results of the full scale test at load level 4 and load step 3

Load level 4 – load step 3											
			Static loading, after dynamic loading								
			Axle type C, F=120[kN]				Axle type B, F=190[kN]				
			$\epsilon_{(1)}$	$\epsilon_{(0)}$	$f=\epsilon_{(1)}/\epsilon_{(0)}$	$\epsilon_{(1)}$	$\epsilon_{(1)}[\%]$	$\epsilon_{(0)}$	$f=\epsilon_{(1)}/\epsilon_{(0)}$		
Strains at the deck plate	MA-1	DMS1	7.57E-05	-3.70E-04	-0.20	6.02E-05	96%	-5.66E-04	-0.11	1.8%	Increase of the strains due to dynamic loading
		DMS2	7.47E-05	-4.32E-04	-0.17	5.63E-05	90%	-6.41E-04	-0.09	1.2%	
		DMS3	8.13E-05	-4.36E-04	-0.19	6.20E-05	99%	-6.45E-04	-0.10	3.1%	
		DMS4	7.45E-05	-3.74E-04	-0.20	6.26E-05	100%	-5.71E-04	-0.11	0.7%	
	MA-2	DMS5	6.91E-05	-3.70E-04	-0.19	5.57E-05	89%	-5.66E-04	-0.10	1.5%	
		DMS6	7.03E-05	-4.32E-04	-0.16	5.51E-05	88%	-6.41E-04	-0.09	1.8%	
		DMS7	6.64E-05	-4.36E-04	-0.15	5.21E-05	83%	-6.45E-04	-0.08	0.3%	
		DMS8	6.42E-05	-3.74E-04	-0.17	5.32E-05	85%	-5.71E-04	-0.09	0.4%	
Strains at the longitudinal ribs	LR-m	DMS9	-4.70E-05	-4.51E-04	0.10	-9.76E-05	90%	-5.27E-04	0.19	1.4%	
		DMS10	-5.71E-05	-4.56E-04	0.13	-1.09E-04	100%	-5.33E-04	0.20	1.9%	
		DMS11	-4.71E-05	-4.56E-04	0.10	-9.09E-05	83%	-5.33E-04	0.17	0.8%	
		DMS12	-4.98E-05	-4.51E-04	0.11	-9.48E-05	87%	-5.26E-04	0.18	1.3%	
		DMS13	-4.15E-05	-4.82E-04	0.09	-8.26E-05	76%	-5.65E-04	0.15	1.8%	
		DMS14	-3.80E-05	-4.89E-04	0.08	-7.49E-05	69%	-5.73E-04	0.13	1.4%	
		DMS15	-5.57E-05	-5.36E-04	0.10	-1.07E-04	98%	-6.29E-04	0.17	3.6%	
		DMS16	-4.51E-05	-4.88E-04	0.09	-8.35E-05	77%	-5.72E-04	0.15	-0.3%	
	DMS17	-4.20E-05	-4.81E-04	0.09	-8.21E-05	75%	-5.64E-04	0.15	2.5%		
	LR-A4	DMS18	-1.89E-05	-1.16E-04	0.16	-6.61E-05	61%	-2.76E-04	0.24	-0.7%	
		DMS19	-3.16E-05	-1.15E-04	0.27	-8.97E-05	82%	-2.75E-04	0.33	1.9%	
		DMS20	-1.77E-05	-2.12E-05	0.84	-6.57E-05	60%	-1.36E-04	0.48	1.6%	
		DMS21	-1.20E-05	-1.09E-05	1.10	-5.51E-05	51%	-1.31E-04	0.42	5.0%	
		DMS22	-5.78E-06	-2.13E-05	0.27	-3.88E-05	36%	-1.36E-04	0.29	5.8%	
	LR-A5	DMS23	-4.23E-06	-4.96E-06	0.85	-4.15E-05	38%	-1.06E-04	0.39	6.1%	
		DMS24	-9.56E-07	-5.03E-06	0.19	-4.17E-05	38%	-1.06E-04	0.39	7.7%	
		DMS25	-2.10E-05	-1.16E-04	0.18	-6.12E-05	56%	-2.82E-04	0.22	0.6%	
DMS26		-1.96E-05	-1.44E-04	0.14	-6.60E-05	61%	-3.35E-04	0.20	2.0%		
DMS27		-2.03E-05	-1.16E-04	0.17	-6.21E-05	57%	-2.82E-04	0.22	4.2%		

No significant difference can be detected when comparing the measured strain values $\epsilon_{(1)}$ from Table 37 (static load step before dynamic loading) with the ones in Table 38 (static load step after dynamic loading). As it is shown in Table 38, a maximum increase of 3.1% (DMS 3) can be detected for the strain gauges on the deck plate and a maximum increase of 7.7% (DMS 24) can be read out for the strain gauges on the longitudinal ribs.

The strain values $\varepsilon_{(1)}$ (after strengthening) and $\varepsilon_{(0)}$ (before strengthening) are presented in Table 39 due to load level 4, load step 4 (see Table 36). Therefore, these tests have been performed after the thermal constraining event which caused additional cracks in the concrete plate (see Section 5.6.6). Again, the factor $f = \varepsilon_{(1)} / \varepsilon_{(0)}$ indicates the stress reduction due to the UHPFRC pavement. The last column shows the strain increase or decrease in DMS 1 to DMS 27 due to the effect of additional cracks from the thermal constraint in percentage (strain $\varepsilon_{(1)}$ of loading mode 4 relating to strain $\varepsilon_{(1)}$ of load step 1). Axle type C was not considered for load level 4.

Table 39: results of the full scale test at load level 4 and load step 4

Load level 4 – load step 4								
		Static loading after thermal constraining event, before dynamic loading						
		Axle type B, F=190[kN]						
		$\varepsilon_{(1)}$	$\varepsilon_{(1)}$ [%]	$\varepsilon_{(0)}$	$f=\varepsilon_{(1)}/\varepsilon_{(0)}$			
Strains at the deck	MA-1	DMS1	6.41E-05	61.0%	-5.66E-04	-0.11	8.5%	Increase of the strains due to crack initiation in the UHPFRC pavement
		DMS2	6.31E-05	60.1%	-6.41E-04	-0.10	13.5%	
		DMS3	1.00E-04	95.2%	-6.45E-04	-0.16	66.9%	
		DMS4	1.05E-04	100.0%	-5.71E-04	-0.18	69.0%	
	MA-2	DMS5	4.48E-05	42.7%	-5.66E-04	-0.08	-18.4%	
		DMS6	4.38E-05	41.7%	-6.41E-04	-0.07	-19.1%	
		DMS7	6.02E-05	57.3%	-6.45E-04	-0.09	15.9%	
		DMS8	7.15E-05	68.1%	-5.71E-04	-0.13	34.8%	
Strains at the longitudinal ribs	LR-m	DMS9	-1.16E-04	90.6%	-5.27E-04	0.22	20.1%	
		DMS10	-1.28E-04	100.0%	-5.33E-04	0.24	20.3%	
		DMS11	-1.04E-04	81.3%	-5.33E-04	0.20	15.7%	
		DMS12	-1.08E-04	84.4%	-5.26E-04	0.20	15.3%	
		DMS13	-9.56E-05	74.7%	-5.65E-04	0.17	17.7%	
		DMS14	-9.17E-05	71.6%	-5.73E-04	0.16	24.1%	
		DMS15	-1.26E-04	98.4%	-6.29E-04	0.20	22.2%	
		DMS16	-1.02E-04	79.7%	-5.72E-04	0.18	21.9%	
	LR-A4	DMS17	-1.00E-04	78.1%	-5.64E-04	0.18	25.3%	
		DMS18	-7.38E-05	57.7%	-2.76E-04	0.27	11.0%	
		DMS19	-8.70E-05	68.0%	-2.75E-04	0.32	-1.1%	
		DMS20	-6.99E-05	54.6%	-1.36E-04	0.51	8.0%	
		DMS21	-5.28E-05	41.3%	-1.31E-04	0.40	0.5%	
	LR-A5	DMS22	-3.67E-05	28.7%	-1.36E-04	0.27	0.1%	
		DMS23	-2.00E-05	15.6%	-1.06E-04	0.19	-48.7%	
		DMS24	-1.50E-05	11.7%	-1.06E-04	0.14	-61.3%	
		DMS25	-4.53E-05	35.4%	-2.82E-04	0.16	-25.5%	
DMS26		-4.82E-05	37.7%	-3.35E-04	0.14	-25.5%		
DMS27		-4.96E-05	38.8%	-2.82E-04	0.18	-16.7%		

Table 39 shows the in- and decreases of the strains relating to the effect of the thermal constraint where a maximum of 69% can be detected in DMS 4 for the deck plate's strain gauges. For the strain gauges that were applied on the longitudinal rib, a maximum increase of 25.3% can be stated in DMS 17. Also strain decreases could be detected. For example, -19.1% in DMS 6 and -61.3% in DMS 24. Hence, the strain in- and decreases are strongly varying and these observations confirm a rearrangement of the stresses in the steel structure due to the additional cracks in the concrete pavement.

Table 40 shows the results of the measured strains $\varepsilon_{(1)}$ (after strengthening) and the numerically calculated reference strains $\varepsilon_{(0)}$ (before strengthening) due to load level 4, load step 6 (see Table 36). The stress reduction due to the strengthening is shown via the factor $f = \varepsilon_{(1)} / \varepsilon_{(0)}$. Additionally, the last column presents the strain's in- or decrease due to the additional crack initiation from the thermal constraint and the results before and after dynamic loading (strain $\varepsilon_{(1)}$ of load step 6 relating to strain $\varepsilon_{(1)}$ of load step 1).

A maximum increase of 84.1% can be stated in DMS 4 for the strain gauges at the deck plate after an additional dynamic loading (69% before dynamic loading, see Table 39). For the strain gauges at the longitudinal ribs, this additional dynamic loading does not have such a strong effect. A strain increase of 26.6% can be read out from Table 40 for DMS 17 (25.3% before dynamic loading, see Table 39). The maximum strain increase at the longitudinal rib's strain gauges relating to load step 6 can now be found in DMS 16 with a value of 27.7% (21.9% before dynamic loading, see Table 39).

By considering the measurements due to axle type B from Table 37 to Table 40 it can be concluded that the dynamic loading doesn't have a significant effect to the strains of all analysed detail points before the thermal constraining event. The thermal constraining event has a very high influence on the strains in the analysed details of the deck plate which causes a maximum strain increase of 84.1% after an additional dynamic loading. Hence, also the stress reduction factor $f_{\sigma,B}$ for detail D1a increases due to this constraining event from 0.11 up to 0.20 (values for DMS 4). For the strain gauges at the longitudinal ribs, the strain increases due to the constraint effect are not that high as for the ones at the deck plate but are also significant. The stress reduction factor $f_{\sigma,B}$ for detail D2 at the relevant longitudinal rib LR-m increases from 0.20 up to 0.24 (values for DMS 10 at LR-m).

Table 40: results of the full scale test at load level 4 and load step 6

Load level 4 – load step 6								
			Static loading after thermal constraining event, after dynamic loading					
			Axle type B, F=190[kN]					
			$\epsilon_{(1)}$	$\epsilon_{(1)}$ [%]	$\epsilon_{(0)}$	$f=\epsilon_{(1)}/\epsilon_{(0)}$		
Strains at the deck plate	MA-1	DMS1	6.61E-05	58.0%	-5.66E-04	-0.12	11.7%	Increase of the strains due to crack initiation and dynamic loading
		DMS2	6.47E-05	56.8%	-6.41E-04	-0.10	16.3%	
		DMS3	1.09E-04	95.6%	-6.45E-04	-0.17	81.4%	
		DMS4	1.14E-04	100.0%	-5.71E-04	-0.20	84.1%	
	MA-2	DMS5	4.51E-05	39.6%	-5.66E-04	-0.08	-17.7%	
		DMS6	4.41E-05	38.7%	-6.41E-04	-0.07	-18.4%	
		DMS7	6.04E-05	53.0%	-6.45E-04	-0.09	16.4%	
		DMS8	7.27E-05	63.8%	-5.71E-04	-0.13	37.1%	
Strains at the longitudinal ribs	LR-m	DMS9	-1.15E-04	89.8%	-5.27E-04	0.22	19.7%	
		DMS10	-1.28E-04	100.0%	-5.33E-04	0.24	20.4%	
		DMS11	-1.05E-04	82.0%	-5.33E-04	0.20	16.3%	
		DMS12	-1.08E-04	84.4%	-5.26E-04	0.21	15.7%	
		DMS13	-9.70E-05	75.8%	-5.65E-04	0.17	19.5%	
		DMS14	-8.88E-05	69.4%	-5.73E-04	0.15	20.1%	
		DMS15	-1.28E-04	100.0%	-6.29E-04	0.20	23.9%	
		DMS16	-1.07E-04	83.6%	-5.72E-04	0.19	27.7%	
	LR-A4	DMS17	-1.01E-04	78.9%	-5.64E-04	0.18	26.6%	
		DMS18	-6.84E-05	53.4%	-2.76E-04	0.25	2.8%	
		DMS19	-8.34E-05	65.2%	-2.75E-04	0.30	-5.2%	
		DMS20	-6.27E-05	49.0%	-1.36E-04	0.46	-3.1%	
		DMS21	-4.73E-05	37.0%	-1.31E-04	0.36	-9.9%	
		DMS22	-3.12E-05	24.4%	-1.36E-04	0.23	-15.0%	
	LR-A5	DMS23	-1.70E-05	13.3%	-1.06E-04	0.16	-56.6%	
		DMS24	-1.08E-05	8.4%	-1.06E-04	0.10	-72.0%	
		DMS25	-4.23E-05	33.0%	-2.82E-04	0.15	-30.5%	
DMS26		-4.28E-05	33.4%	-3.35E-04	0.13	-33.9%		
DMS27		-4.84E-05	37.8%	-2.82E-04	0.17	-18.7%		

5.6.5.2. Results for load level 7

The measured strains $\epsilon_{(1)}$ (after strengthening) and the numerically calculated reference strains $\epsilon_{(0)}$ (before strengthening) are presented in Table 41, relating to the measuring points DMS 1 to DMS 27 (see Figure 247) at the steel structure of the full scale test specimen and due to load level 7, load step 1 (see Table 36). The strain reduction due to UHPFRC pavement is indicated by the factor $f = \epsilon_{(1)} / \epsilon_{(0)}$. At load level 7 only the results for axle type C are presented.

Table 41: results of the full scale test at load level 7 and load step 1

Load level 7 – load step 1						
			Static loading, before dynamic loading			
			Axle type C, F=300[kN]			
			$\epsilon_{(1)}$	$\epsilon_{(1)}$ [%]	$\epsilon_{(0)}$	$f = \epsilon_{(1)} / \epsilon_{(0)}$
Strains at the deck plate	MA-1	DMS1	1.79E-04	98.5%	-9.25E-04	-0.19
		DMS2	1.75E-04	96.2%	-1.08E-03	-0.16
		DMS3	1.82E-04	100.0%	-1.09E-03	-0.17
		DMS4	1.82E-04	100.0%	-9.35E-04	-0.19
	MA-2	DMS5	1.69E-04	92.8%	-9.25E-04	-0.18
		DMS6	1.70E-04	93.4%	-1.08E-03	-0.16
		DMS7	1.65E-04	90.7%	-1.09E-03	-0.15
		DMS8	1.64E-04	90.2%	-9.35E-04	-0.18
Strains at the longitudinal ribs	LR-m	DMS9	-2.14E-04	90.4%	-1.13E-03	0.19
		DMS10	-2.37E-04	100.0%	-1.14E-03	0.21
		DMS11	-1.98E-04	83.7%	-1.14E-03	0.17
		DMS12	-2.06E-04	87.0%	-1.13E-03	0.18
		DMS13	-1.75E-04	73.8%	-1.21E-03	0.14
		DMS14	-1.67E-04	70.7%	-1.22E-03	0.14
		DMS15	-2.30E-04	97.2%	-1.34E-03	0.17
		DMS16	-1.88E-04	79.5%	-1.22E-03	0.15
	LR-A4	DMS17	-1.79E-04	75.8%	-1.20E-03	0.15
		DMS18	-1.45E-04	61.4%	-2.90E-04	0.50
		DMS19	-1.72E-04	72.8%	-2.88E-04	0.60
		DMS20	-1.38E-04	58.3%	-5.30E-05	2.61
		DMS21	-1.05E-04	44.5%	-2.72E-05	3.87
	LR-A5	DMS22	-8.59E-05	36.3%	-5.32E-05	1.62
		DMS23	-7.71E-05	32.6%	-1.24E-05	6.22
		DMS24	-6.88E-05	29.1%	-1.26E-05	5.47
		DMS25	-1.11E-04	46.8%	-2.90E-04	0.38
DMS26		-1.22E-04	51.4%	-3.59E-04	0.34	
		DMS27	-1.13E-04	47.7%	-2.90E-04	0.39

When comparing the strain reduction factors $f_{\sigma,C}$ due to axle type C from Table 37 (load level 4, load step 1) to the ones from Table 41 (load level 7, load step 1), very less difference can be observed for DMS 1 to DMS 8 although the axle load of load level 7 is 2.5 times higher than at load level 4 ($300\text{kN}/120\text{kN} = 2.5$). Both strain reduction factors were determined based on the measurements before the thermal constraint. It is worth mentioning that the measured strains on the strengthened deck in some strain gauges increase extremely, compared to the deck with asphalt pavement. For example, DMS 23 shows in Table 41 a factor $f_{\sigma,C}$ with a value of 6.22. This effect is caused by the very good load

distribution due to the concrete pavement where the nearby longitudinal ribs next to the directly loaded rib are stressed much more than without concrete layer. Nevertheless, the measured strains $\varepsilon_{(1)}$ in DMS 23 are much lower than the ones in the strain gauges of the directly loaded longitudinal rib ($\varepsilon_{(1,DMS23)} / \varepsilon_{(1,DMS10)} = -7.71E-05 / -2.37E-04 = 0.33$).

The strain values $\varepsilon_{(0)}$ and $\varepsilon_{(1)}$ due to load level 7, load step 3 (see Table 36) are illustrated in Table 42. The factor $f = \varepsilon_{(1)} / \varepsilon_{(0)}$ again indicates the stress reduction. The strain in- or decrease due to the dynamic loading is additionally shown (strain $\varepsilon_{(1)}$ of load step 3 relating to strain $\varepsilon_{(1)}$ of load step 1).

Table 42: results of the full scale test at load level 7 and load step 3

Load level 7 – load step 3								
			Static loading, after dynamic loading					
			Axle type C, F=300[kN]					
			$\varepsilon_{(1)}$	$\varepsilon_{(1)} [\%]$	$\varepsilon_{(0)}$	$f = \varepsilon_{(1)} / \varepsilon_{(0)}$		
Strains at the deck plate	MA-1	DMS1	1.80E-04	98.5%	-9.25E-04	-0.19	0.8%	Increase of the strains due to dynamic loading
		DMS2	1.77E-04	96.5%	-1.08E-03	-0.16	1.0%	
		DMS3	1.83E-04	100.0%	-1.09E-03	-0.17	0.8%	
		DMS4	1.83E-04	99.8%	-9.35E-04	-0.20	0.6%	
	MA-2	DMS5	1.71E-04	93.3%	-9.25E-04	-0.18	1.3%	
		DMS6	1.72E-04	94.0%	-1.08E-03	-0.16	1.3%	
		DMS7	1.66E-04	90.9%	-1.09E-03	-0.15	1.0%	
		DMS8	1.65E-04	90.3%	-9.35E-04	-0.18	0.9%	
Strains at the longitudinal ribs	LR-m	DMS9	-2.17E-04	90.5%	-1.13E-03	0.19	1.3%	
		DMS10	-2.40E-04	100.0%	-1.14E-03	0.21	1.3%	
		DMS11	-2.01E-04	83.8%	-1.14E-03	0.18	1.4%	
		DMS12	-2.09E-04	87.3%	-1.13E-03	0.19	1.6%	
		DMS13	-1.76E-04	73.6%	-1.21E-03	0.15	1.0%	
		DMS14	-1.69E-04	70.5%	-1.22E-03	0.14	1.0%	
		DMS15	-2.33E-04	97.2%	-1.34E-03	0.17	1.3%	
		DMS16	-1.88E-04	78.4%	-1.22E-03	0.15	-0.1%	
	LR-A4	DMS17	-1.81E-04	75.7%	-1.20E-03	0.15	1.1%	
		DMS18	-1.44E-04	59.9%	-2.90E-04	0.50	-1.3%	
		DMS19	-1.73E-04	72.0%	-2.88E-04	0.60	0.2%	
		DMS20	-1.38E-04	57.4%	-5.30E-05	2.60	-0.4%	
		DMS21	-1.05E-04	43.8%	-2.72E-05	3.86	-0.3%	
	LR-A5	DMS22	-8.48E-05	35.4%	-5.32E-05	1.60	-1.3%	
		DMS23	-7.70E-05	32.1%	-1.24E-05	6.22	-0.1%	
		DMS24	-6.97E-05	29.1%	-1.26E-05	5.54	1.3%	
		DMS25	-1.12E-04	46.6%	-2.90E-04	0.38	0.8%	
DMS26		-1.24E-04	51.9%	-3.59E-04	0.35	2.2%		
		DMS27	-1.17E-04	48.6%	-2.90E-04	0.40	3.3%	

There is no significant difference in the measured strains $\epsilon_{(1)}$ of Table 41 and Table 42 and for detail D1a, a maximum increase due to the dynamic loading of 1.3% can be detected in DMS 5. For detail D2, a maximum increase of 1.6% can be read out at the directly loaded longitudinal rib LR-m.

The strain values $\epsilon_{(1)}$ and $\epsilon_{(0)}$ due to load level 7, load step 4 (see Table 36) are presented in Table 43. The strain reduction is indicated via $f = \epsilon_{(1)} / \epsilon_{(0)}$. The last column of the table shows the strain's increase respectively decrease due to the thermal constraining event (strain $\epsilon_{(1)}$ of load step 4 relating to strain $\epsilon_{(1)}$ of load step 1).

Table 43: results of the full scale test at load level 7 and load step 4

Load level 7 – load step 4								
			Static loading after crack initiation, before dynamic loading					
			Axle type C, F=300[kN]					
			$\epsilon_{(1)}$		$\epsilon_{(0)}$		$f = \epsilon_{(1)} / \epsilon_{(0)}$	
Strains at the deck plate	MA-1	DMS1	1.85E-04	71.6%	-9.25E-04	-0.20	3.7%	Increase of the strains due to crack initiation
		DMS2	1.86E-04	71.8%	-1.08E-03	-0.17	6.4%	
		DMS3	2.58E-04	99.6%	-1.09E-03	-0.24	42.2%	
		DMS4	2.59E-04	100.0%	-9.35E-04	-0.28	42.7%	
	MA-2	DMS5	1.52E-04	58.7%	-9.25E-04	-0.16	-9.8%	
		DMS6	1.53E-04	58.9%	-1.08E-03	-0.14	-10.1%	
		DMS7	1.85E-04	71.5%	-1.09E-03	-0.17	12.4%	
		DMS8	2.01E-04	77.8%	-9.35E-04	-0.22	23.0%	
Strains at the longitudinal ribs	LR-m	DMS9	-2.27E-04	89.9%	-1.13E-03	0.20	6.0%	
		DMS10	-2.52E-04	100.0%	-1.14E-03	0.22	6.6%	
		DMS11	-2.10E-04	83.1%	-1.14E-03	0.18	5.8%	
		DMS12	-2.17E-04	86.0%	-1.13E-03	0.19	5.4%	
		DMS13	-1.87E-04	74.3%	-1.21E-03	0.16	7.3%	
		DMS14	-1.74E-04	68.9%	-1.22E-03	0.14	4.0%	
		DMS15	-2.47E-04	98.0%	-1.34E-03	0.18	7.5%	
		DMS16	-2.02E-04	80.1%	-1.22E-03	0.17	7.5%	
	LR-A4	DMS17	-1.97E-04	77.9%	-1.20E-03	0.16	9.5%	
		DMS18	-1.17E-04	46.2%	-2.90E-04	0.40	-19.7%	
		DMS19	-1.44E-04	57.0%	-2.88E-04	0.50	-16.4%	
		DMS20	-1.07E-04	42.4%	-5.30E-05	2.02	-22.6%	
		DMS21	-7.88E-05	31.2%	-2.72E-05	2.90	-25.1%	
		DMS22	-5.56E-05	22.0%	-5.32E-05	1.05	-35.3%	
	LR-A5	DMS23	-3.35E-05	13.3%	-1.24E-05	2.70	-56.6%	
		DMS24	-2.62E-05	10.4%	-1.26E-05	2.08	-62.0%	
		DMS25	-8.05E-05	31.9%	-2.90E-04	0.28	-27.4%	
DMS26		-8.17E-05	32.4%	-3.59E-04	0.23	-32.9%		
DMS27		-8.55E-05	33.9%	-2.90E-04	0.29	-24.3%		

A significant strain increase can be recognised for the strain gauges at the deck plate due to the thermal constraint. DMS 4 shows in Table 43 a maximum strain increase of 42.7% for detail D1a. On the contrary, there is very less strain increase at the longitudinal rib's strain gauges. The directly loaded rib shows in DMS 17 a maximum increase of only 9.5%. The strain gauges on the nearby longitudinal ribs (LR-A4 and LR-A5) all show a strain decrease from -16.4% to -62%.

Table 44 shows the strains $\epsilon_{(1)}$ and $\epsilon_{(0)}$ due to load level 7, load step 6. The strain reduction is shown via $f = \epsilon_{(1)} / \epsilon_{(0)}$ and the strain in- or decrease ($\epsilon_{(1)}$ of load step 6 relating to $\epsilon_{(1)}$ of load step 1).

Table 44: results of the full scale test at load level 7 and load step 6

Load level 7 – load step 6								
			Static loading after crack initiation, after dynamic loading					
			Axle type C, F=300[kN]					
			$\epsilon_{(1)}$		$\epsilon_{(0)}$	$f = \epsilon_{(1)} / \epsilon_{(0)}$		
Strains at the deck plate	MA-1	DMS1	1.89E-04	69.9%	-9.25E-04	-0.20	5.9%	Increase of the strains due to crack initiation and dynamic loading
		DMS2	1.89E-04	69.8%	-1.08E-03	-0.18	8.3%	
		DMS3	2.71E-04	99.8%	-1.09E-03	-0.25	49.0%	
		DMS4	2.71E-04	100.0%	-9.35E-04	-0.29	49.4%	
	MA-2	DMS5	1.53E-04	56.4%	-9.25E-04	-0.17	-9.3%	
		DMS6	1.53E-04	56.5%	-1.08E-03	-0.14	-9.6%	
		DMS7	1.86E-04	68.6%	-1.09E-03	-0.17	12.9%	
		DMS8	2.05E-04	75.6%	-9.35E-04	-0.22	25.2%	
Strains at the longitudinal ribs	LR-m	DMS9	-2.33E-04	89.9%	-1.13E-03	0.21	8.7%	
		DMS10	-2.59E-04	100.0%	-1.14E-03	0.23	9.3%	
		DMS11	-2.15E-04	83.1%	-1.14E-03	0.19	8.6%	
		DMS12	-2.22E-04	85.9%	-1.13E-03	0.20	8.0%	
		DMS13	-1.91E-04	73.8%	-1.21E-03	0.16	9.3%	
		DMS14	-1.77E-04	68.4%	-1.22E-03	0.14	5.8%	
		DMS15	-2.55E-04	98.5%	-1.34E-03	0.19	10.8%	
		DMS16	-2.08E-04	80.5%	-1.22E-03	0.17	10.7%	
	LR-A4	DMS17	-2.01E-04	77.8%	-1.20E-03	0.17	12.2%	
		DMS18	-1.16E-04	45.0%	-2.90E-04	0.40	-19.9%	
		DMS19	-1.44E-04	55.8%	-2.88E-04	0.50	-16.2%	
		DMS20	-1.04E-04	40.2%	-5.30E-05	1.97	-24.6%	
		DMS21	-7.75E-05	29.9%	-2.72E-05	2.85	-26.4%	
	LR-A5	DMS22	-5.32E-05	20.6%	-5.32E-05	1.00	-38.1%	
		DMS23	-2.86E-05	11.1%	-1.24E-05	2.31	-62.9%	
		DMS24	-2.75E-05	10.6%	-1.26E-05	2.19	-60.0%	
		DMS25	-7.91E-05	30.5%	-2.90E-04	0.27	-28.6%	
DMS26		-7.92E-05	30.6%	-3.59E-04	0.22	-34.9%		
DMS27		-8.45E-05	32.6%	-2.90E-04	0.29	-25.2%		

There is no significant difference between the values of Table 43 and Table 44 recognisable. Hence, the additional dynamic loading after the thermal constraining event doesn't have a notable effect to the measured strains due to load level 7 with axle type C. The strains at the deck plate's strain gauges slightly increase. For example, the measured strain in DMS 4 increases from $2.59 \cdot 10^{-4}$ to $2.71 \cdot 10^{-4}$ which means an increase of 5%. The same observation can be done for the strain gauges on the longitudinal ribs. The measured strain in DMS 10 increases from $2.52 \cdot 10^{-4}$ to $2.59 \cdot 10^{-4}$ which causes an increase of only 3%.

Under consideration of the measurements due to axle type C from Table 41 to Table 44, in summary it can be stated that the dynamic loading never has a significant effect to the measured strains in the analysed details D1a and D2. The thermal constraining event, leading to additional cracks in the concrete, strongly affects the measured strains in both analysed details. For detail D1a, a maximum strain increase of 49.4% could be observed in DMS 4 (see Table 44) and also the stress reduction factor $f_{\sigma,C}$ for axle type C increases due to this constraining event from 0.19 up to 0.29 (values for DMS 4). For detail D2, a maximum strain increase of 12.2% could be detected at the directly loaded longitudinal rib LR-m in DMS 17 (see Table 44). The stress reduction factor $f_{\sigma,C}$ for detail D2 at the maximum stressed strain gauge (DMS 10) increases from 0.21 to 0.23. It is additionally worth mentioning that the strains in the nearby longitudinal ribs (LR-A4 and LR-A5) are decreasing in every strain gauge (DMS 18 to DMS 27) due to the effect of the thermal constraint.

5.6.5.3. Evaluation of the results in detail

a.) Detail D1a – Deck Plate bending

The strains, respectively the stresses in notch detail D1a (see Section 2.4.2) were at the full scale tests reproduced by the strain gauges DMS 1 to DMS 8. The results of all these transmitters are very similar, therefore the most heavily stressed detail point (DMS 4) is taken as representative (Utilization ratio 100% in Table 37 to Table 44).

It is remarkable that in the full scale test tensile strains $\varepsilon_{(1)}$, respectively tensile stresses, occurred on the bottom side of the deck plate close to the longitudinal rib (see DMS 1 to DMS 8 in Table 37). This is also in contradiction to the numerical analyses that have been carried out on the strengthened steel deck (based on Model A) Model E-1 (see Table 30 in Section 5.4.1). This difference is because of the fact that another location for detail D1a was investigated there. At the numerical analyses in Section 3.4, detail D1a is located very close to the cross girder with an offset of $e_{LR} = 360$ mm. At the full scale tests, this offset from detail D1a to the cross girder is significantly larger with $e = 800$ mm. Additionally, in the numerical calculations of the bridge deck in Section 3.4, the first longitudinal rib LR-1 close to the

main girder was considered whereas at the full scale tests, the analysed longitudinal rib is more like in a central position between the main girders. Figure 263 shows the deformations and the occurring strains in detail D1a due to axle type B with an axle load of $F_A = 100$ kN regarding to the numerical simulations at the finite element models Model A and Model E-1 with and without UHPFRC pavement.

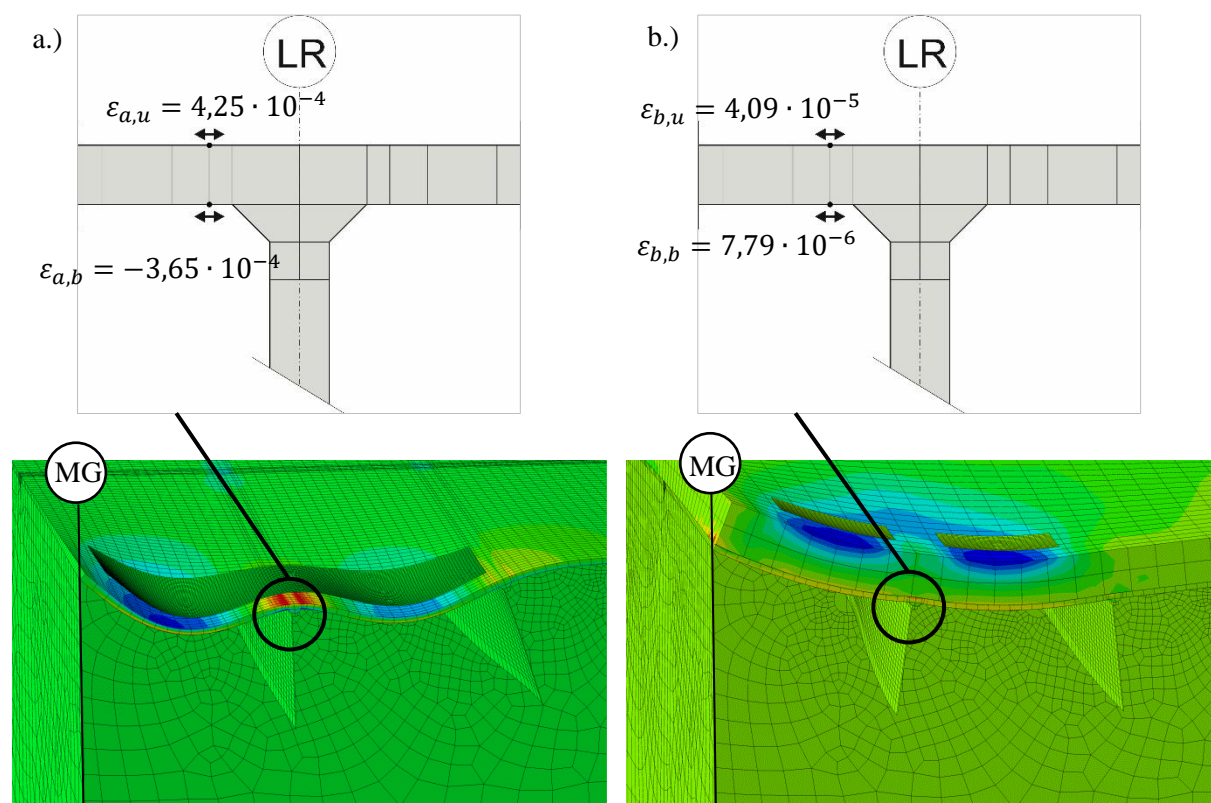


Figure 263: deformations and strains due to axle type B with an axle load of $F_A = 100$ kN at LR-1 of Model A; a.) unstrengthened steel deck; b.) strengthened steel deck

Tensile strains, respectively tensile stresses predominate on the bottom side of the strengthened steel deck (see Figure 263.b), whereby local bending stresses dominate on the unstrengthened steel deck (see Figure 263.a), which are resulting in compressive strains at the deck plate's bottom side (negative sign for $\varepsilon_{(0)}$ in the result tables).

There must be a differentiation between the results with single wheeled (axle type C) and double wheeled axles (axle type B). Before the thermal constraint, the stress reduction due to the strengthening has for single wheeled axles (axle type C) a value of $f = 0.19 - 0.20$ (see Table 41 and Table 42). After the constraint, this stress reduction factor increases up to $f = 0.28 - 0.29$ (see Table 43 Table 44). A higher stress reduction factor can be recognised for double wheeled axles (axle type B). Before the thermal constraint, the stress reduction due to the strengthening has for double wheeled axles a value of $f = 0.11$ (see Table 37 and Table 38) and after the thermal constraint, this value increases up to $f = 0.18 - 0.20$ (see Table 39 and Table 40).

As a result of the extreme thermal constraint, which caused cracks in the concrete, the stress level due to axle C increases by about 50% (see Table 44) and due to axle B by about 80% (see Table 40). Therefore, the following stress reduction factors due to the strengthening via UHPFRC pavement can be indicated for single and double wheeled axle types, including overloads and high constraining effects:

- Single wheeled axles (axle type A and C, see Table 44): $f_{\sigma,A/C} = 0.29$
- Double wheeled axles (axle type B, see Table 40): $f_{\sigma,B} = 0.20$

b.) Detail D2 – Longitudinal rib to cross girder connection

When taking a closer look at Table 37 and Table 38 (DMS 9 to DMS 17), it can be recognised that there is generally more stress reduction for axle type C than for axle type B due to load level 4 and before the constraining event. Additionally, it can be stated that the dynamic loading did not change the stress reduction factors significantly. For axle type C (load level 4) and before the thermal constraint, a stress reduction factor of $f = 0.12 - 0.13$ can be read out from Table 37 and Table 38 (DMS 10). For axle type B and also before the thermal constraint, a stress reduction factor of $f = 0.20$ is shown Table 37 and Table 38 (DMS 10). Hence, also for detail D2, a differentiation between single and double wheeled axles has to be done. By considering axle type B due to load level 4, a strain increase of about 20% can be seen in Table 39 and Table 40 due to additional concrete cracking after the thermal constraint. After the constraint, the stress reduction factor for axle type B increases up to $f = 0.24$ (see Table 39 and Table 40).

Under consideration of load level 7 (load step 1 and 3, before thermal constraint), a stress reduction factor of $f = 0.21$ can be read out for axle type C from Table 41 and Table 42 (DMS 10). This value is higher than the one due to load level 4, which is shown above ($f = 0.12 - 0.13$). After the thermal constraint, a strain increase of about 7 – 9 % can be detected for axle type C in Table 43 and Table 44 (DMS 10). The stress reduction factor for axle type C increases up to $f = 0.22 - 0.23$ (see DMS 10 in Table 43 and Table 44). Hence, there is not that very high stress decrease for axle type C at detail D2 due to the additional concrete cracks after the thermal constraining event.

In summary, the stress level due to the constraint effect before increases for axle type C by about 10% (see Table 44) and due to axle B by about 20% (see Table 40). Therefore, the following stress reduction factors referring to detail D2 can be indicated for single and double wheeled axle types due to the analysed strengthening method, including overloads and high constraining effects:

- Single wheeled axles (axle type A and C, see Table 44): $f_{\sigma,A/C} = 0.23$
- Double wheeled axles (axle type B, see Table 40): $f_{\sigma,B} = 0.24$

The stresses of the highest stressed detail D2 on the test specimen are reproduced by the strain gauges DMS 9 to DMS 17 (central longitudinal rib, see Figure 257). The outer longitudinal ribs (axis A4 - strain gauges DMS 18 to 22, axis A5 - strain gauges DMS 23 to 27) receive significantly lower stresses. Due to the only one-sided connection of the flat steel longitudinal rib to the cross girder, additional transverse bending stresses occur in the longitudinal ribs. Their size can be additionally evaluated by applying the strain gauges on both web sides of the longitudinal rib (for example: DMS 9 and 13, DMS 12 and 17, DMS 10 and 14, DMS 11 and 16). This evaluation is shown below in Table 45 (before thermal constraint) and Table 46 (after thermal constraint). $\varepsilon_{(l)}$ are the measured strains at the full scale experiments. $\varepsilon_{(m)}$ are the membrane strains. $\varepsilon_{(M)}$ indicates the transverse bending part and Figure 264 shows the determination of $\varepsilon_{(M)}$ graphically.

Table 45: Transverse bending parts in D2 at the longitudinal ribs in the connection area to the cross girder, before thermal constraint (load level 6 – load step 1 and load level 7 – load step 1)

Load level 6 – load step 1					
Axle type B, F=285[kN]					
		$\epsilon_{(l)}$	$\epsilon_{(m)}$	$\epsilon_{(m)}$ in [%]	$\epsilon_{(M)}/\epsilon_{(m)}$
LR-m	DMS9	-1.68E-04	-1.53E-04	96.1%	10.2%
	DMS13	-1.37E-04			
	DMS12	-1.62E-04	-1.53E-04	96.2%	5.9%
	DMS17	-1.44E-04			
	DMS10	-1.86E-04	-1.59E-04	100.0%	17.1%
	DMS14	-1.32E-04			
	DMS11	-1.56E-04	-1.53E-04	95.8%	2.4%
	DMS16	-1.49E-04			
LR-A4	DMS18	-1.35E-04	-1.33E-04	83.4%	1.8%
	DMS20	-1.30E-04			
	DMS19	-1.57E-04	-1.20E-04	75.2%	31.2%
	DMS22	-8.23E-05			
LR-A5	DMS23	-7.79E-05	-9.09E-05	57.1%	14.4%
	DMS25	-1.04E-04			
	DMS24	-7.19E-05	-8.81E-05	55.4%	18.4%
	DMS27	-1.04E-04			
Load level 7 – load step 1					
Axle type C, F=300[kN]					
		$\epsilon_{(l)}$	$\epsilon_{(m)}$	$\epsilon_{(m)}$ in [%]	$\epsilon_{(M)}/\epsilon_{(m)}$
LR-m	DMS9	-2.14E-04	-1.94E-04	96.2%	10.1%
	DMS13	-1.75E-04			
	DMS12	-2.06E-04	-1.93E-04	95.4%	6.9%
	DMS17	-1.79E-04			
	DMS10	-2.37E-04	-2.02E-04	100.0%	17.2%
	DMS14	-1.67E-04			
	DMS11	-1.98E-04	-1.93E-04	95.6%	2.6%
	DMS16	-1.88E-04			
LR-A4	DMS18	-1.45E-04	-1.42E-04	70.2%	2.6%
	DMS20	-1.38E-04			
	DMS19	-1.72E-04	-1.29E-04	63.9%	33.4%
	DMS22	-8.59E-05			
LR-A5	DMS23	-7.71E-05	-9.39E-05	46.5%	17.9%
	DMS25	-1.11E-04			
	DMS24	-6.88E-05	-9.08E-05	44.9%	24.3%
	DMS27	-1.13E-04			

Table 46: Transverse bending parts in D2 at the longitudinal ribs in the connection area to the cross girder, after thermal constraint (load level 4 – load step 6 and load level 7 – load step 6)

Load level 4 – load step 6					
Axle type B, F=190[kN]					
		$\epsilon_{(1)}$	$\epsilon_{(m)}$	$\epsilon_{(m)}$ in [%]	$\epsilon_{(M)}/\epsilon_{(m)}$
LR-m	DMS9	-1.16E-04	-1.06E-04	95.9%	9.5%
	DMS13	-9.56E-05			
	DMS12	-1.08E-04	-1.04E-04	94.6%	3.6%
	DMS17	-1.00E-04			
	DMS10	-1.28E-04	-1.10E-04	100.0%	16.7%
	DMS14	-9.17E-05			
	DMS11	-1.04E-04	-1.03E-04	93.8%	1.0%
	DMS16	-1.02E-04			
LR-A4	DMS18	-7.38E-05	-7.19E-05	65.3%	2.8%
	DMS20	-6.99E-05			
	DMS19	-8.70E-05	-6.19E-05	56.2%	40.7%
	DMS22	-3.67E-05			
LR-A5	DMS23	-2.00E-05	-3.27E-05	29.7%	38.7%
	DMS25	-4.53E-05			
	DMS24	-1.50E-05	-3.23E-05	29.3%	53.7%
	DMS27	-4.96E-05			
Load level 7 – load step 6					
Axle type C, F=300[kN]					
		$\epsilon_{(1)}$	$\epsilon_{(m)}$	$\epsilon_{(m)}$ in [%]	$\epsilon_{(M)}/\epsilon_{(m)}$
LR-m	DMS9	-2.27E-04	-2.07E-04	97.2%	9.5%
	DMS13	-1.87E-04			
	DMS12	-2.17E-04	-2.07E-04	97.0%	4.9%
	DMS17	-1.97E-04			
	DMS10	-2.52E-04	-2.13E-04	100.0%	18.4%
	DMS14	-1.74E-04			
	DMS11	-2.10E-04	-2.06E-04	96.6%	1.8%
	DMS16	-2.02E-04			
LR-A4	DMS18	-1.17E-04	-1.12E-04	52.4%	4.4%
	DMS20	-1.07E-04			
	DMS19	-1.44E-04	-9.98E-05	46.8%	44.3%
	DMS22	-5.56E-05			
LR-A5	DMS23	-3.35E-05	-5.70E-05	26.7%	41.2%
	DMS25	-8.05E-05			
	DMS24	-2.62E-05	-5.58E-05	26.2%	53.1%
	DMS27	-8.55E-05			

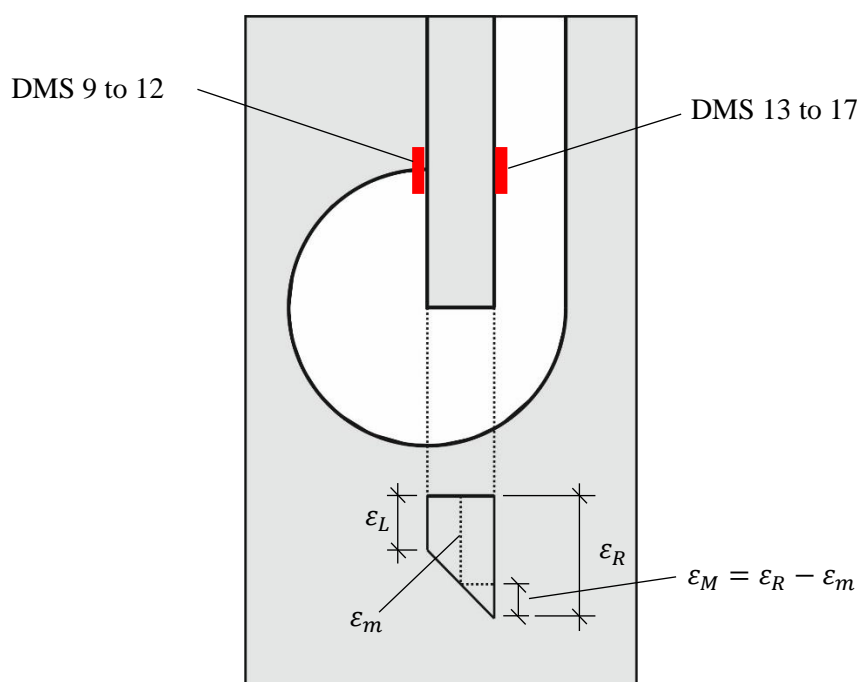


Figure 264: detail D2 – stress distribution through the thickness of the longitudinal rib

With regards to the column where the percentages for the membrane strain $\varepsilon_{(m)}$ are listed in Table 45 and Table 46, it can be seen that the strain/stress level in the outer longitudinal ribs at axis A4 and A5 is significantly lower (percentage comparison of the membrane stress $\varepsilon_{(m)}$).

It can be seen from the results in Table 45 and Table 46 that the highest transverse bending strain/stress occurs at the unloaded longitudinal rib in Axis A4 (comparison of the last column of results – $\varepsilon_{(M)} / \varepsilon_{(m)}$). Because of the one sided welded joint between the longitudinal rib and the cross girder at the test specimen there is no axis of symmetry at the inner longitudinal rib and the results in axis A4 and A5 are different. In the decisive central longitudinal rib, the transverse bending component amounts to a maximum of about 17% ($\varepsilon_{(M)} / \varepsilon_{(m)}$) and this value is nearly the same for axle type B and C.

Worth mentioning is that the strains in the adjacent longitudinal ribs are changing due to the effect of the thermal constraint. Below the stress reduction at the highest stressed measuring point at each longitudinal rib is shown:

- Before the thermal constraint (stress percentage relating to the directly loaded mid longitudinal rib)
 - Longitudinal rib in axis A4:
 - Axle type C – 72% (Table 42, DMS 19)
 - Axle type B – 82% (Table 38, DMS 19)

- Longitudinal rib in axis A5:
 - Axle type C – 52% (Table 42, DMS 26)
 - Axle type B – 61% (Table 38, DMS 26)

- After the thermal constraint (stress percentage relating to the directly loaded mid longitudinal rib)
 - Longitudinal rib in axis A4:
 - Axle type C – 56% (Table 44, DMS 19)
 - Axle type B – 65% (Table 40, DMS 19)
 - Longitudinal rib in axis A5:
 - Axle type C – 33% (Table 44, DMS 27)
 - Axle type B – 38% (Table 40, DMS 27)

The results confirm the increase of the stresses at the directly loaded longitudinal rib after the thermal constraint, which leads to the illustrated relief of the nearby longitudinal ribs.

It should also be noted that, despite the strengthening, the strains in the measuring points DMS 20 to DMS 24, which are located at the unloaded longitudinal ribs in axis A4 and A5, have increased (compared to the unstrengthened solution) under an axle load. The highest increase of the strains took place in measuring point DMS 23 (for example at load level 7, axle C, $f = 6.22$, see Table 41 in Section 5.6.5.2). This very high strain increase due to the strengthening is caused by the very good load distribution of the concrete pavement. The longitudinal ribs next to the directly loaded rib become more activated for the load transfer due to the UHPFRC plate and are therefore more stressed than without concrete layer. It should be recognised that the strains in DMS 23 only amount approx. 33% of the value relating to the most heavily stressed measuring point DMS 10 at the directly loaded central longitudinal rib. Therefore, these measuring points like DMS 23 are not decisive.

5.6.6. Concrete plate – results and evaluation of the measurements

5.6.6.1. Strains at the surface of the concrete

Figure 265 shows the measured strains in the setting strain transducers at axis MA-1 (DD1-1 to DD1-6, see Figure 257) which were applied at the upper surface of the UHPFRC pavement.

Figure 266 shows the measured strains in the setting strain transducers at axis A2 (DD1-7 to DD1-10, see Figure 257) which were also applied at the upper surface of the UHPFRC pavement.

The locations of the setting strain transducers DD1-i are shown in Figure 257 (see Section 5.6.3.2). Every strain value belongs to a load level and therefore the horizontal axis of this diagram indicates the sequential number of the respective partial test. Accordingly, it is actually not a curve but there are individual points. The individual points were linear connected in order to get a better readability of the diagram. For each setting strain transducer, 2 values were read out per test. One value corresponding to the load F according to the applied load level and one value measured at the beginning of the appropriate partial experiment at $F = 0$.

It should be noted that the strain values are an average of the strains over a length of 230 mm. As shown in Figure 265, the transmitters DD1-1 to DD1-6 just measured negative strains which means compressive stresses in these areas. The transmitters DD1-7 to DD1-10 shown in Figure 265 recorded mainly positive strains and therefore tensile stresses have to be assumed in this region.

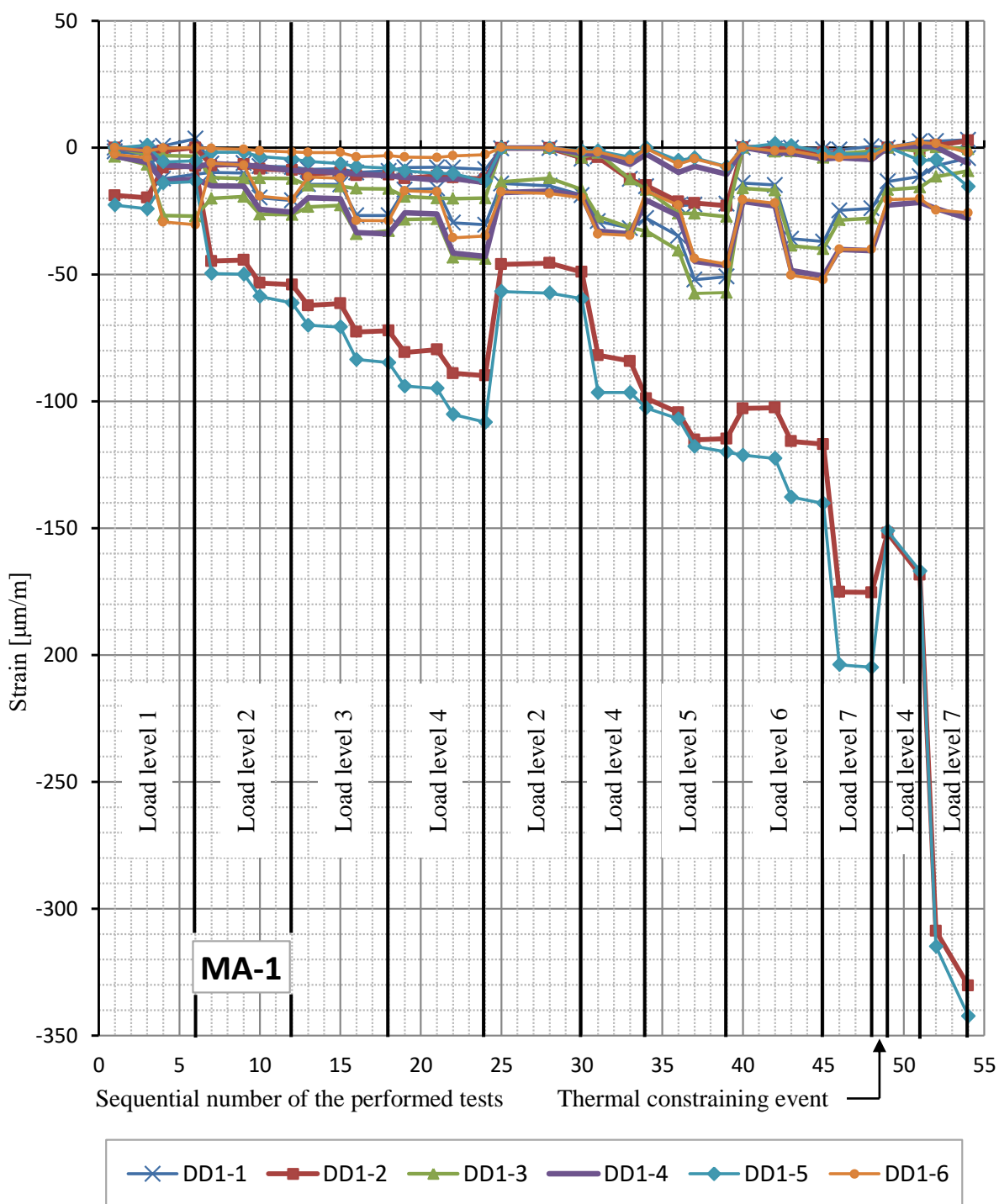


Figure 265: measured strains at the upper surface of the UHPFRC pavement (setting strain transducers at axis MA-1)

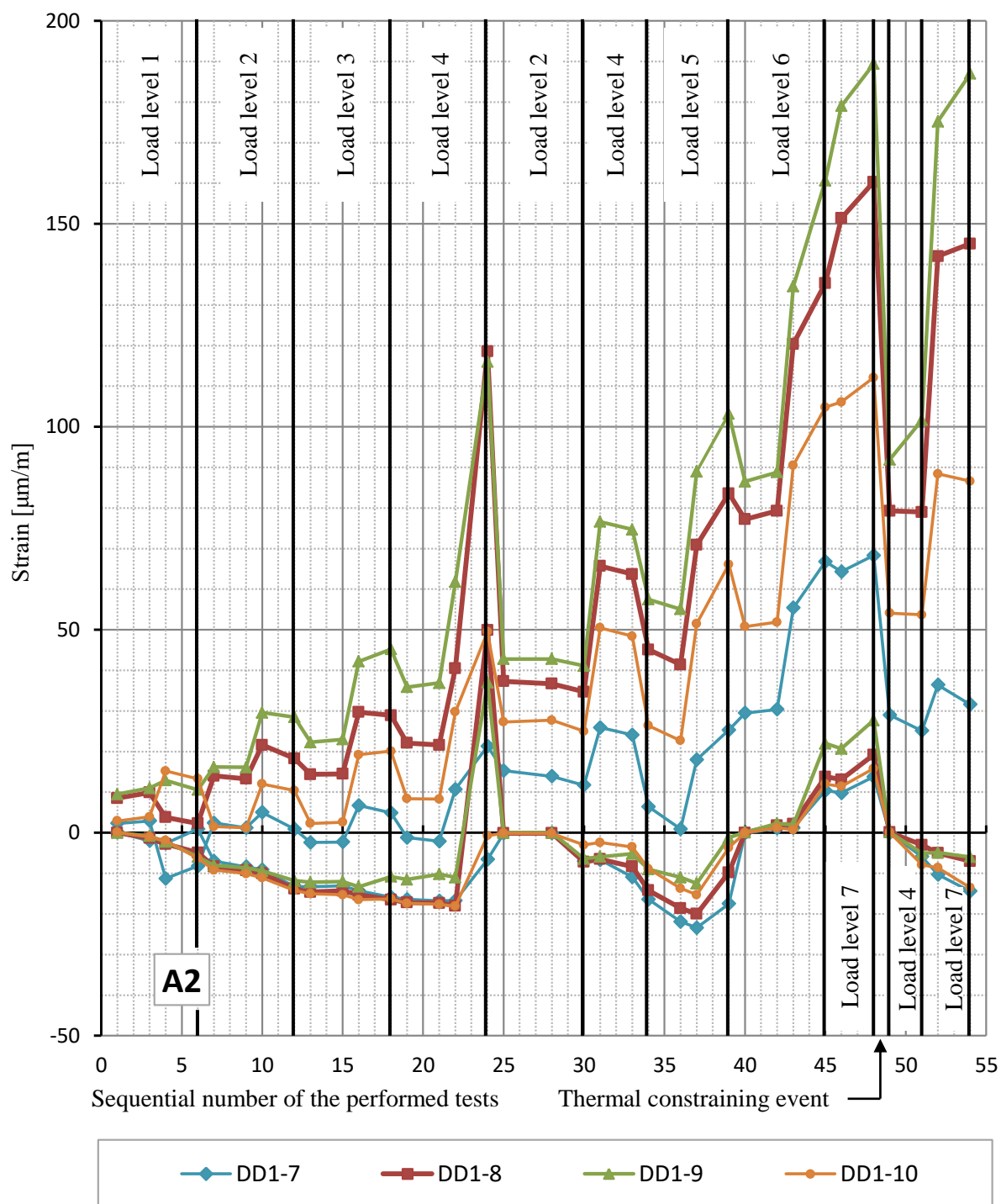


Figure 266: measured strains at the upper surface of the UHPFRC pavement (setting strain transducers at axis A2)

5.6.6.2. Concrete cracking

Before the beginning of all loading tests, it was possible to detect approximately 10 cm long cracks in the four corners of the concrete plate and in the southern edge of axis A2 (not visible in Figure 267). The concrete surface was painted with a white emulsion and was inspected relating to possible new

cracks before each new load level. Figure 267 gives an overview of the final crack pattern after completion of all experiments.

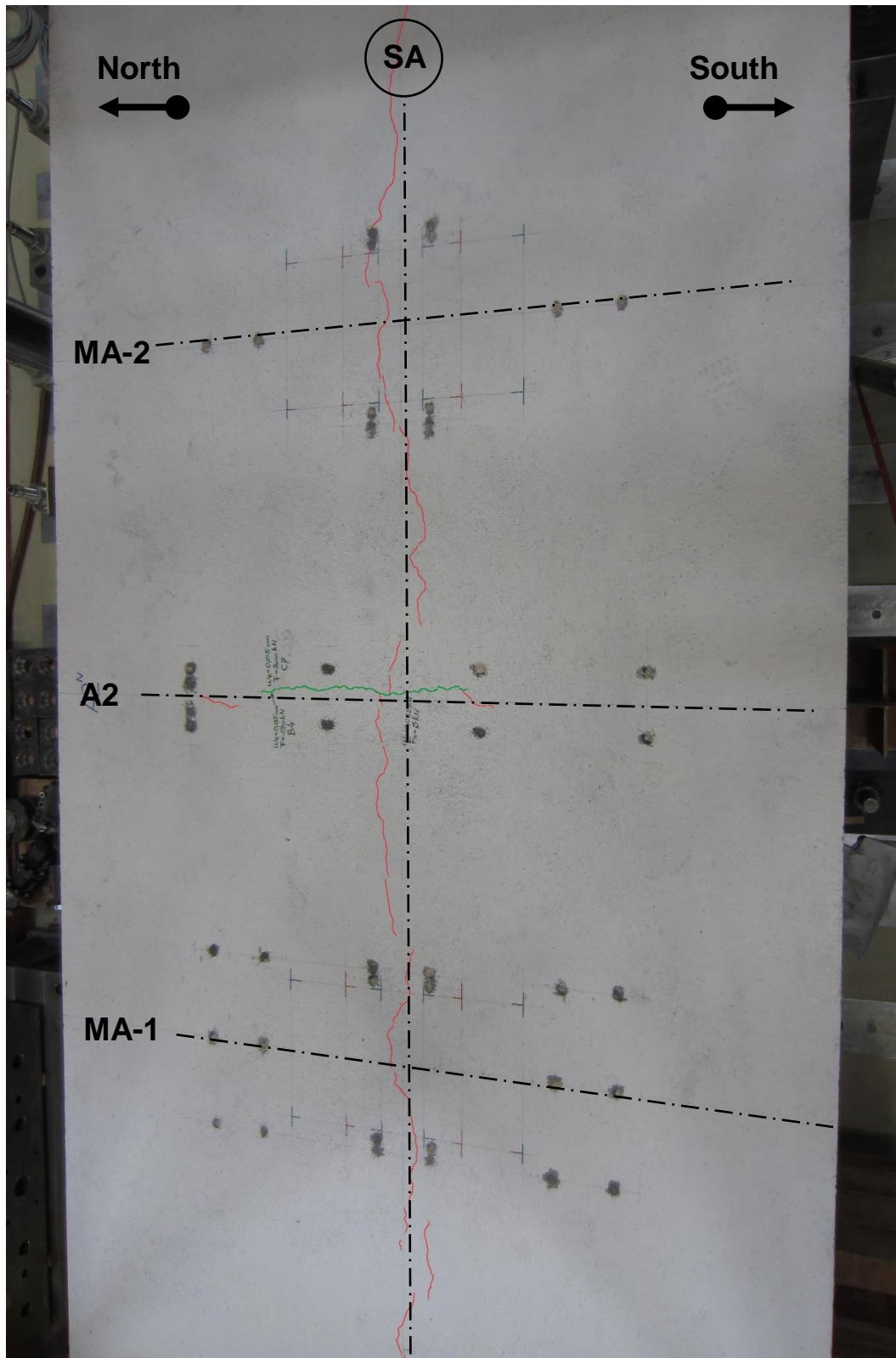


Figure 267: overview of the crack pattern in the UHPFRC pavement after finishing of all tests

The green markings in Figure 267 indicate the cracks before the thermal constraining event and the red markings highlight the cracks after the constraint.

The maximum crack width, measured in the unloaded state immediately before the thermal constraint (after sequential number 48, see Figure 266), at axis A2 was 0.025mm. During the weathering test, the crack spread in both directions (about 15cm to the "north", about 5cm to the "south"). In addition, another crack occurred along the symmetry axis SA. This crack (red lines in Figure 267) had a crack width of about 0.05 mm. Due to the additional loadings after weathering (see Table 36), no further crack propagation could be detected.

5.6.6.3. Evaluation of the results based on the measurements on the concrete

The measurements on the full scale tests confirm the results of the numerical investigations and show that the thermal constraint is predominating for the cracks in the concrete pavement. The occurring stresses in the UHPFRC pavement are very low due to the heavy traffic loads.

– Before thermal constraint

The maximum measured strains before the thermal constraint occur in

- Transmitter DD1-9 due to load level 7, axle type C: $\varepsilon \approx 0.19\text{‰}$ (see Figure 266, sequential number 48, immediately before the constraint) and
- Transmitter DD1-8 due to load level 7, axle type C: $\varepsilon \approx 0.16\text{‰}$ (see Figure 266, sequential number 48, immediately before the constraint).

Hence, these measured values are below the the maximum available cracking strain of the used concrete that has a maximum tensile strain resistance of $0.184 \pm 0.042\text{‰}$ [33]. But within the crack inspections before and after all partial tests before the constraint no cracks could be detected in the region of the transmitters mentioned above. Additionally, no significant discontinuities could be observed regarding to the curves from the strain measurements which confirms the visual inspections.

– After thermal constraint

The maximum measured strains after the thermal constraint occur in

- Transmitter DD1-9 due to load level 7, axle type C: $\varepsilon \approx 0.188\text{‰}$ (see Figure 266, sequential number 54, last test at all) and
- Transmitter DD1-8 due to load level 7, axle type C: $\varepsilon \approx 0.145\text{‰}$ (see Figure 266, sequential number 54, last test at all).

The measured strain values showed similar results due to axle type C at load level 7 in the transmitters DD1-8 and DD1-9 before and after the thermal constraining event. The occurred crack in the axis A2, where DD1-8 and DD1-9 were applied, had a measured crack width of about 0.025mm.

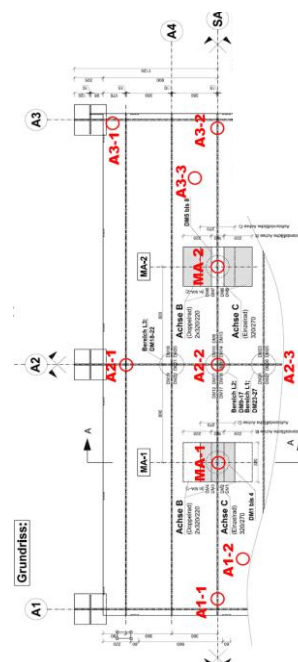
The highest crack width was measured in axis SA with 0.05mm which occurred due to the extreme thermal constraining event. In summary, it can be noted that all measured values are lower than the desired crack width of 0.10mm. Under the assumption of a one-dimensional stress condition for the bending in axis A2, the maximum tensile stresses on the upper concrete's surface due to the traffic loads can be determined based on the measurements in the transmitter DD1-9 ($\varepsilon_{\max} \approx 0.19\%$ due to load level 7, axle type C, see Figure 266). The concrete's Young's Modulus has a value of $E_{\text{cm}} = 47\,500 \text{ N/mm}^2$. The maximum concrete's tensile stress in axis A2 due to the heavy traffic has a value of $\sigma_{\text{t,max}} = E_{\text{cm}} \cdot \varepsilon_{\max} = 47\,500 \cdot 1.9 \cdot 10^{-4} = 9 \text{ N/mm}^2$. This value is higher than the concrete's tensile strength ($f_{\text{ctm}} = 7 \text{ N/mm}^2$) but as already mentioned, all appeared crack widths were under 0.10 mm (desired value). Additionally, it has to be kept in mind that load level 7 includes a very high axle load of $F_{\text{A}} = 300\text{kN}$. Also the maximum compression stresses due to the heavy traffic loads can be determined under the same assumptions for transmitter DD1-5 in axis MA-1 ($\varepsilon_{\min} \approx -0.342\%$ due to load level 7, axle type C, see Figure 265): $\sigma_{\text{c,max}} = E_{\text{cm}} \cdot \varepsilon_{\min} = 47\,500 \cdot 3.42 \cdot 10^{-4} = 16.2 \text{ N/mm}^2$. In summary, it can be stated that the occurring compression stresses are relatively low in relation to the very high strength of the UHPFRC ($f_{\text{ck}} = 150 \text{ N/mm}^2$). But the very high concrete's Young's Modulus is essential for an adequate load distribution of the local wheel loads to reduce significantly the local stresses in the analysed details. Additionally, also the very high density of the UHPFRC is necessary for the durability of the pavement against the aggressive atmosphere on road surfaces (e.g. de-icing salt).

5.6.6.4. Results of the measurements at the interface between steel and concrete

The results of the pull off tests are illustrated in Table 47, in terms of tensile adhesion strength f_t . The location of these tests can be found in Figure 260 (see Section 5.6.3.4) and is additionally again shown in Table 47. The measured tensile adhesion strength is varying from 1.6 to 5.0 N/mm^2 and therefore an average of 3.5 N/mm^2 can be determined.

Table 47: results of the pull off tests

Nr.	sample identifier	$F_{\text{B}}[\text{kN}]$	$\phi[\text{mm}]$	$A_{\text{c}}[\text{mm}^2]$	$f_t[\text{N/mm}^2]$
1	A1-1	32,8	99,5	7776	4,2
2	A1-2	25,2	99,4	7760	3,2
3	MA-1	38,9	99,4	7760	5,0
4	A2-1	25,8	99,4	7760	3,3
5	A2-2	16,1	99,4	7760	2,1
6	A2-3	12,3	99,4	7760	1,6
7	MA-2	36,6	99,3	7744	4,7
8	A3-1	22,4	99,4	7760	2,9
9	A3-2	37,8	99,5	7776	4,9
10	A3-3	25,9	99,5	7776	3,3



The maximum tensile adhesion strengths could be measured in the regions of the load introduction at axis MA-1 ($f_t = 5.0 \text{ N/mm}^2$) and MA-2 ($f_t = 4.7 \text{ N/mm}^2$) where compression stresses occur in the concrete plate. The strain transmitters in these regions measured only compression strain on the concrete's bottom surface (see Figure 265). The minimum tensile adhesion strengths were measured above the mid cross girder in axis A2. The values vary a lot from 1.6 to 3.3 N/mm^2 (average 2.3 N/mm^2). In these regions, tensile stresses are expected in the wheel load tests in the concrete which also could be confirmed by the measurements of the transmitters at axis A2 (see Figure 266). The tensile adhesion strengths in the regions of axis A1 and A3 vary from 2.9 to 4.9 N/mm^2 and an average of 3.7 N/mm^2 can be determined. Based on these results it can be recognised that the tensile adhesion strength in the local over pressured regions, directly underneath the wheel loads, is increased. The tensile adhesion strength is decreased in the regions where tensile stresses occur in the concrete plate.

5.6.7. Effective Young's Modulus of the concrete $E_{c,eff}$ based on steel deck measurements at the full scale tests

For the numerical simulations regarding to the strengthened orthotropic steel deck Model E-1, presented in Section 5.2.1, based on Model A, an overall effective Young's Modulus of the UHPFRC pavement was assumed. With regards to a conservative determination of the stresses in the steel structure, this assumed concrete's effective Young's Modulus was chosen with a very low value of $E_{c,eff} \approx E_c / 4 = 12,500 \text{ N/mm}^2$.

Under consideration of the strain measurements in the steel deck which were carried out on the full scale tests, a determination of a more realistic effective concrete's Young's Modulus by modification of this value within the finite element simulations was done. Figure 268 visualises an overview of the finite element model referring to the investigations in the full scale tests including an UHPFRC pavement. The steel part of the finite element model in Figure 268 is identical to the model that is presented in Section 5.6.4, which has been developed for the calculation of the reference strains referring to the unstrengthened deck. The concrete pavement was modelled by using quadratic solid elements with reduced integration, called C3D20R, with 3 elements through its thickness.

The element size of the concrete was adapted according to the finite element mesh of the deck plate and has the geometrical dimensions 20x20x26.7mm. By considering a pavement thickness of 80mm, 3 elements through the whole plate thickness were modelled. The interface between the elements of the concrete pavement and the elements of the steel deck have been performed with a complete rigid transition condition. The measurements regarding to a slip in the interconnecting joint between steel and concrete at the full scale tests confirmed a rigid connection of these 2 parts.

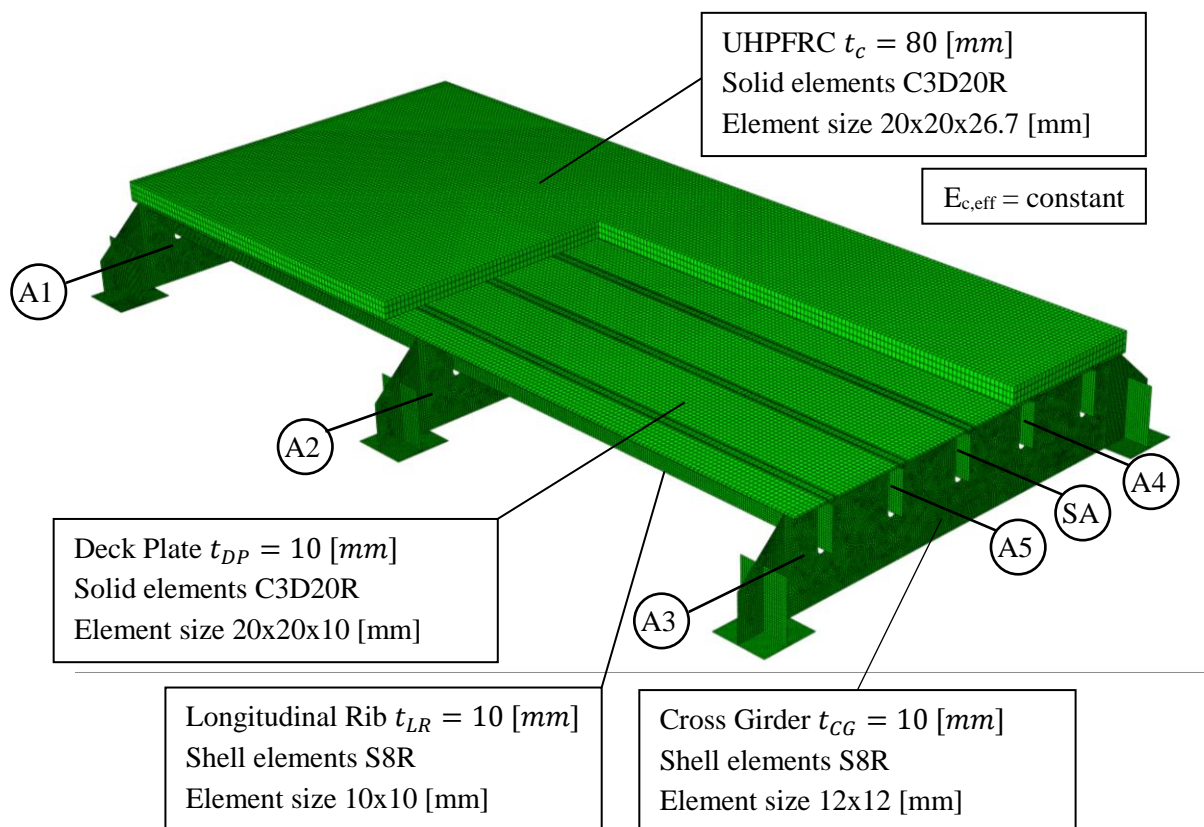


Figure 268: overview of the finite element model referring to the full scale tests including a UHPFRC pavement

Within the numerical analyses referring to the full scale tests including an UHPFRC pavement the Young's Modulus $E_{c,eff}$ of the concrete pavement has been varied and the resulting strains have been selected from the measuring points DMS 1 to DMS 27 for the significant load levels before and after the thermal constraining event which are shown in Figure 247.

The strains due to load level 4, axle type B are listed in Table 48 for the measurements at the full scale tests (before and after thermal constraint – load step 1 and 6) and the numerical calculations. Figure 269 shows a schematic illustration of the analysed load application at the experimental specimen with load level 4, axle type B and an axle load of $F_A = 190\text{kN}$ (application as distributed load, same as in the test). The accompanying experiments at the small scale concrete test specimens according to the cube compressive strength delivered an averaged concrete Young's Modulus of $E_{c,a} = 52\,145\text{ N/mm}^2$ after 28 days of curing time. The concrete Young's Modulus based on the cylindric small scale test specimens gave a mean value of $E_{c,m} = 47\,500\text{ N/mm}^2$. But for the following comparisons regarding to the full scale test measurements with numerical values, the highest concrete's Young's Modulus based on the cube test specimens $E_{c,a} = 52\,145\text{ N/mm}^2$ was chosen. Based on this value $E_{c,a}$, a variation of the concrete's elastic material properties has been done with: i) $E_{c,eff,1} = E_{c,a}$; ii) $E_{c,eff,2} = 0.6 \cdot E_{c,a}$; iii) $E_{c,eff,3} = 0.4 \cdot E_{c,a}$. Additionally, the ratio of the numerically calculated strains relating to the measurements due to load step 6, after the thermal constraint (maximum crack width of 0.05mm) is plotted in Table 48.

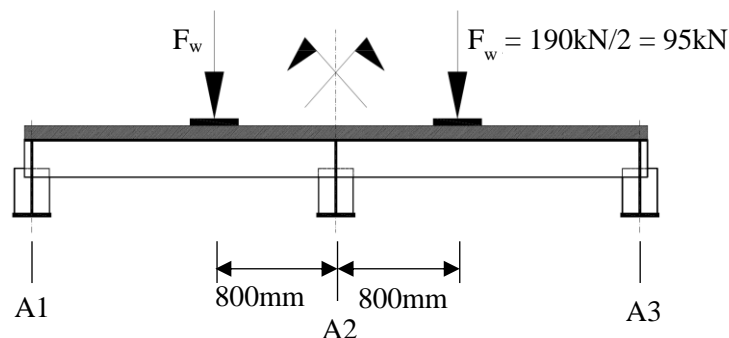


Figure 269: longitudinal section of the test specimen and load application

Table 48: Full scale test – strain measurements and numerically calculated strains in comparison due to load level 4, axle type B

		Measured values at the full scale test – load level 4		$E_{c,eff,1} = E_{c,a} = 52145$		$E_{c,eff,2} = 0.6 \cdot E_{c,a}$		$E_{c,eff,3} = 0.4 \cdot E_{c,a}$	
		Load step 1 – ε_1	Load step 6 – ε_2	ε_3 [-]	$\varepsilon_3 / \varepsilon_2$	ε_4 [-]	$\varepsilon_4 / \varepsilon_2$	ε_5 [-]	$\varepsilon_5 / \varepsilon_2$
deck plate	DMS 1	5.91E-05	6.61E-05	4.99E-05	0.75	5.22E-05	0.79	5.12E-05	0.78
	DMS 2	5.56E-05	6.47E-05	4.71E-05	0.73	4.38E-05	0.68	3.65E-05	0.56
	DMS 3	6.01E-05	1.09E-04	4.65E-05	0.43	4.30E-05	0.39	3.54E-05	0.32
	DMS 4	6.22E-05	1.14E-04	4.97E-05	0.44	5.19E-05	0.46	5.08E-05	0.45
deck plate	DMS 5	5.49E-05	4.51E-05	4.99E-05	1.11	5.22E-05	1.16	5.12E-05	1.14
	DMS 6	5.41E-05	4.41E-05	4.71E-05	1.07	4.38E-05	0.99	3.65E-05	0.83
	DMS 7	5.19E-05	6.04E-05	4.65E-05	0.77	4.30E-05	0.71	3.54E-05	0.59
	DMS 8	5.30E-05	7.27E-05	4.97E-05	0.68	5.19E-05	0.71	5.08E-05	0.70
LR axis SA	DMS 9	-9.63E-05	-1.15E-04	-1.01E-04	0.88	-1.29E-04	1.12	-1.56E-04	1.36
	DMS 10	-1.07E-04	-1.28E-04	-1.02E-04	0.80	-1.30E-04	1.02	-1.57E-04	1.23
	DMS 11	-9.02E-05	-1.05E-04	-1.02E-04	0.97	-1.15E-04	1.09	-1.57E-04	1.50
	DMS 12	-9.36E-05	-1.08E-04	-1.01E-04	0.93	-1.15E-04	1.06	-1.56E-04	1.44
	DMS 13	-8.12E-05	-9.70E-05	-1.11E-04	1.15	-1.40E-04	1.44	-1.68E-04	1.73
	DMS 14	-7.39E-05	-8.88E-05	-1.12E-04	1.27	-1.42E-04	1.59	-1.70E-04	1.91
	DMS 15	-1.03E-04	-1.28E-04	-1.20E-04	0.94	-1.52E-04	1.19	-1.83E-04	1.43
	DMS 16	-8.38E-05	-1.07E-04	-1.12E-04	1.05	-1.29E-04	1.21	-1.70E-04	1.59
	DMS 17	-8.01E-05	-1.01E-04	-1.11E-04	1.10	-1.27E-04	1.26	-1.68E-04	1.66
LR axis A4	DMS 18	-6.65E-05	-6.84E-05	-9.95E-05	1.45	-1.20E-04	1.76	-1.39E-04	2.03
	DMS 19	-8.80E-05	-8.34E-05	-9.91E-05	1.19	-1.20E-04	1.44	-1.39E-04	1.66
	DMS 20	-6.47E-05	-6.27E-05	-8.66E-05	1.38	-1.03E-04	1.64	-1.18E-04	1.88
	DMS 21	-5.25E-05	-4.73E-05	-9.61E-05	2.03	-1.14E-04	2.41	-1.30E-04	2.74
	DMS 22	-3.67E-05	-3.12E-05	-8.62E-05	2.77	-1.03E-04	3.29	-1.17E-04	3.77
LR axis A5	DMS 23	-3.91E-05	-1.70E-05	-5.70E-05	3.36	-6.13E-05	3.61	-8.25E-05	4.87
	DMS 24	-3.87E-05	-1.08E-05	-5.71E-05	5.27	-7.04E-05	6.50	-8.27E-05	7.63
	DMS 25	-6.08E-05	-4.23E-05	-8.60E-05	2.03	-1.05E-04	2.48	-1.22E-04	2.90
	DMS 26	-6.47E-05	-4.28E-05	-9.03E-05	2.11	-1.11E-04	2.60	-1.13E-04	2.64
	DMS 27	-5.96E-05	-4.84E-05	-1.11E-04	2.30	-1.05E-04	2.16	-1.22E-04	2.52

Worth mentioning is that the strains of DMS 2, DMS 3, DMS 6 and DMS 7 are decreasing when the effective concrete's Young's Modulus also decreases. For an explanation of this effect, a more detailed analyse of the numerically calculated strain values is necessary. Table 49 shows therefore again the strains for the above mentioned strain gauges on the bottom side of the deck plate $\varepsilon_{3,\text{bottom}}$, $\varepsilon_{4,\text{bottom}}$, $\varepsilon_{5,\text{bottom}}$ ($\varepsilon_{i,\text{bottom}} = \varepsilon_i$ in Table 48, for $i = 3$ to 5) as well as the numerically calculated strains on the deck plate's top side $\varepsilon_{3,\text{top}}$, $\varepsilon_{4,\text{top}}$, $\varepsilon_{5,\text{top}}$. Additionally, the membrane strains in the deck plate's mid position $\varepsilon_{3,\text{mid}}$, $\varepsilon_{4,\text{mid}}$, $\varepsilon_{5,\text{mid}}$ are plotted and the strain's bending parts $\Delta\varepsilon_3$, $\Delta\varepsilon_4$, $\Delta\varepsilon_5$ are visualised in its size and percentage ($\Delta\varepsilon_i / \varepsilon_{i,\text{mid}}$, for $i = 3$ to 5) relating to the membrane strains. The diagrams on the right side of Table 49 illustrate the membrane- and bending strain distributions through the deck plate's thickness for DMS 2 which was exemplarily chosen.

Table 49: Full scale test – numerically calculated strains due to load level 4, axle type B for the deck plate's bottom, mid and top surface and additional bending parts

$E_{c,\text{eff},1} = E_{c,a}$					
	$\varepsilon_{3,\text{bottom}}$	$\varepsilon_{3,\text{mid}}$	$\varepsilon_{3,\text{top}}$	$\Delta\varepsilon_3 = \varepsilon_{3,\text{mid}} - \varepsilon_{3,\text{top}} $	$\Delta\varepsilon_3 / \varepsilon_{3,\text{mid}} (\%)$
DMS 1	4.99E-05	3.99E-05	2.99E-05	1.00E-05	25%
DMS 2	4.71E-05	3.77E-05	2.83E-05	9.40E-06	25%
DMS 3	4.65E-05	3.76E-05	2.87E-05	8.90E-06	24%
DMS 4	4.97E-05	3.98E-05	2.98E-05	9.95E-06	25%

$E_{c,\text{eff},2} = 0.6 \cdot E_{c,a}$					
	$\varepsilon_{4,\text{bottom}}$	$\varepsilon_{4,\text{mid}}$	$\varepsilon_{4,\text{top}}$	$\Delta\varepsilon_4 = \varepsilon_{4,\text{mid}} - \varepsilon_{4,\text{top}} $	$\Delta\varepsilon_4 / \varepsilon_{4,\text{mid}} (\%)$
DMS 1	5.22E-05	4.10E-05	2.98E-05	1.12E-05	27%
DMS 2	4.38E-05	3.92E-05	3.45E-05	4.65E-06	12%
DMS 3	4.30E-05	3.91E-05	3.51E-05	3.95E-06	10%
DMS 4	5.19E-05	4.09E-05	2.98E-05	1.11E-05	27%

$E_{c,\text{eff},3} = 0.4 \cdot E_{c,a}$					
	$\varepsilon_{5,\text{bottom}}$	$\varepsilon_{5,\text{mid}}$	$\varepsilon_{5,\text{top}}$	$\Delta\varepsilon_5 = \varepsilon_{5,\text{mid}} - \varepsilon_{5,\text{top}} $	$\Delta\varepsilon_5 / \varepsilon_{5,\text{mid}} (\%)$
DMS 1	5.12E-05	4.07E-05	3.01E-05	1.06E-05	26%
DMS 2	3.65E-05	3.94E-05	4.22E-05	2.85E-06	7%
DMS 3	3.54E-05	3.93E-05	4.31E-05	3.85E-06	10%
DMS 4	5.08E-05	4.05E-05	3.02E-05	1.03E-05	25%

It can be seen that the membrane strains slightly increases when $E_{c,\text{eff}}$ decreases from $E_{c,a}$ to $0.6 \cdot E_{c,a}$ ($0.15 / 3.77 = 0.04 \cong 4\%$). It is interesting that the bending strain distributions show tensile strains on the bottom side of the deck plate. Generally, compression bending strains might be expected because of a simplified static model where the steel deck plate acts like a continuous beam which is supported by the longitudinal ribs. The bending strains in the diagrams of Table 49 are decreasing when $E_{c,\text{eff}}$ also decreases. From $E_{c,a}$ to $0.6 \cdot E_{c,a}$ a decrease of 50% ($-0.47 / +0.94 = -0.5$) and from $0.6 \cdot E_{c,a}$ to $0.4 \cdot E_{c,a}$ a decrease of 36% ($-0.17 / 0.47 = -0.36$) can be recognised. Hence, the more the effective concrete's

Young's Modulus decreases, the more changes the deck plate's bending moment from a positive direction (tension on the bottom) to a negative direction (compression on the bottom). Because of this effect, the positive strain values in Table 48 for the positions DMS 2, DMS 3, DMS 6 and DMS 7 decrease due to a decrease of $E_{c,eff}$. Hence, the strains ε_4 ($E_{c,eff,2} = 0.6 \cdot E_{c,a}$) and ε_5 ($E_{c,eff,3} = 0.4 \cdot E_{c,a}$) are lower tensile strains (respectively stresses) than ε_3 ($E_{c,eff,1} = E_{c,a}$).

When taking a closer look to the values for the strain gauges DMS 1, DMS 4, DMS 5 and DMS 8 in Table 48, it can be recognised that the numerically calculated strains ε_3 , ε_4 and ε_5 don't have a big variance (less than 5%). Under consideration of the values for DMS 1 and DMS 4 in Table 49, it can be noted that the bending strains first increase due to a decrease of $E_{c,eff}$ from $E_{c,a}$ to $0.6 \cdot E_{c,a}$ ($1.12 / 1.00 \cong 1.11 / 0.995 \cong 1.12$). The membrane strains in the same points also increase slightly due to a decrease of $E_{c,eff}$ from $E_{c,a}$ to $0.6 \cdot E_{c,a}$ ($4.10 / 3.99 \cong 4.09 / 3.98 \cong 1.03$). But due to an additional decrease of $E_{c,eff}$ from $0.6 \cdot E_{c,a}$ to $0.4 \cdot E_{c,a}$, the bending strains in these points decreases ($1.06 / 1.12 \cong 1.03 / 1.11 \cong 0.94$) as well as the membrane strains ($4.07 / 4.10 \cong 4.05 / 4.09 \cong 0.99$). In summary, the values in Table 49 and the subsequent analyses confirm the very small difference of the strain values for DMS 1, DMS 4, DMS 5 and DMS 8 in Table 48. An additional significant decrease of $E_{c,eff}$ would result in the same effect as shown above for DMS 2, DMS 3, DMS 6 and DMS 7.

The plotted values of Table 48 are visualised in Figure 270. The results, relating to the strains at the bottom side of the deck plate that should represent the local bending behaviour of the deck at the longitudinal ribs, are plotted in Figure 270.a. The strains referring to the directly loaded mid longitudinal rib are illustrated in Figure 270.b which reproduce the bending behaviour of the longitudinal rib at the cross girder. The measured and calculated strain values regarding to the unloaded nearby longitudinal ribs in axis A4 and A5 are shown in Figure 270.c.

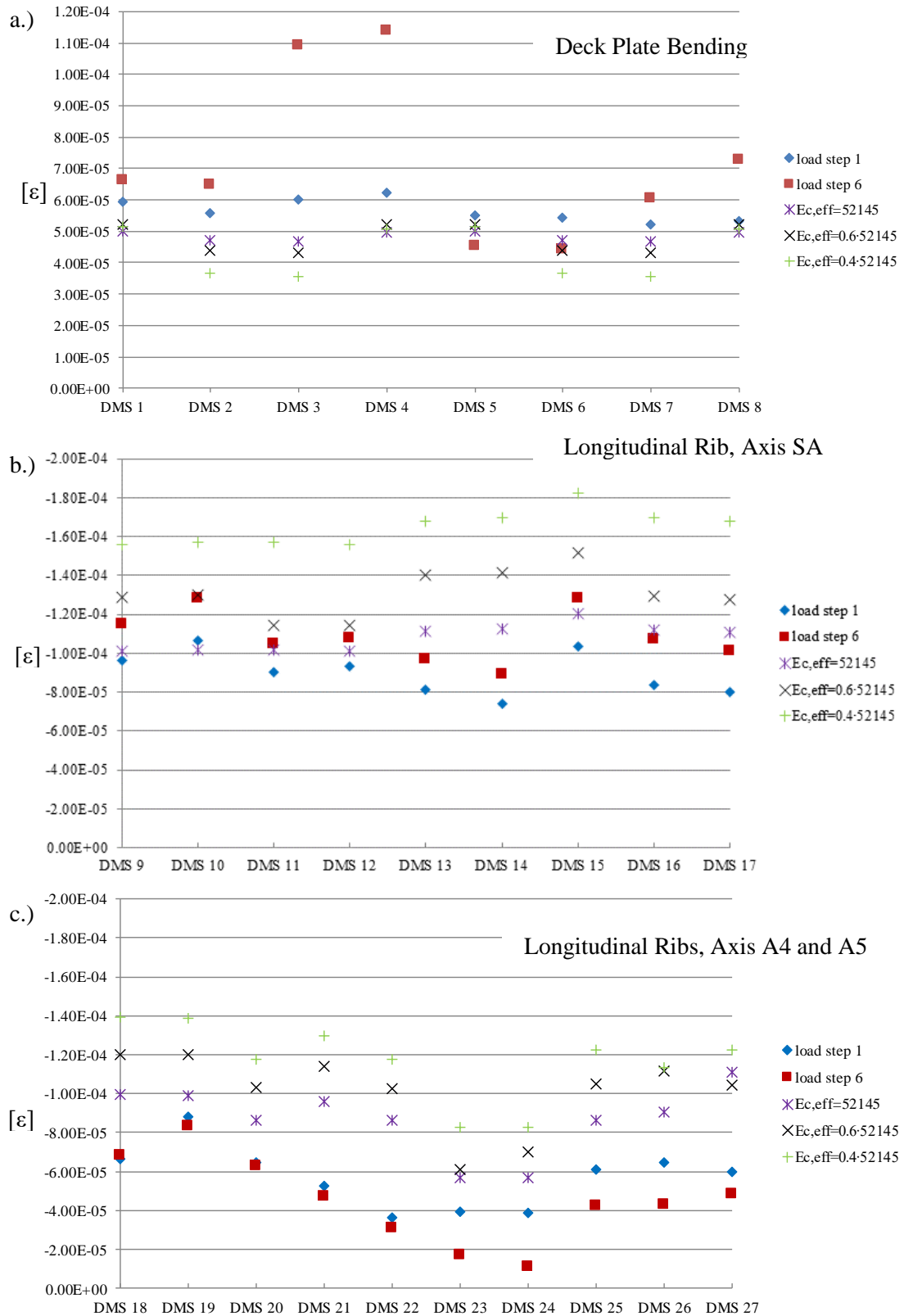


Figure 270: Full scale test – strain measurements and numerically calculated strains in comparison due to load level 4, axle type B; a.) deck plate bending DMS 1 to DMS 8; b.) longitudinal rib in axis SA, DMS 9 to DMS 17; c.) longitudinal rib in axis A4 and A5, DMS 18 to DMS 27

– Deck plate bending - Figure 270.a:

By comparing the measured strains to the numerically calculated ones it can be recognised that even with the highest effective overall Young's Modulus $E_{c,eff} = E_{c,a}$, the numerical strains and therefore the resulting stresses are smaller than the measured values. By taking a look at Table 48 and under consideration of $E_{c,eff} = E_{c,a}$, a deviation from 7 to 32% can be recognised (except DMS 3 and DMS 4). Strain gauges DMS 3 and 4 were excepted from the comparison by reason of undefined force redistributions because of concrete cracks due to the thermal constraint.

– Longitudinal Rib, Axis SA - Figure 270.b:

Also by comparing the measured strains at the directly loaded mid longitudinal rib to the numerically calculated ones, the assumption of the highest effective overall Young's Modulus $E_{c,eff} = E_{c,a}$ delivers the best accordance. For DMS 9 to DMS 12 (at the connected side to the cross girder), a deviation from 3 to 20% can be detected under consideration of $E_{c,eff} = E_{c,a}$. For DMS 13 to DMS 17 (at the cope hole side of the cross girder), a deviation from 6 to 27% can be detected under consideration of $E_{c,eff} = E_{c,a}$.

– Longitudinal Ribs, Axis A4 and A5 - Figure 270.c:

It can be observed, that even under consideration of a concrete's Young's Modulus of $E_{c,eff} = E_{c,a}$, the strains due to the numerical calculations are conservatively higher than the measured values.

Figure 271 shows additionally the numerically calculated strains (for $E_{c,eff,1}$, $E_{c,eff,2}$, $E_{c,eff,3}$) in comparison to the measurements due to load level 7 (load step 1 and load step 6) with axle type C and an axle load of $F_A = 300\text{kN}$ in the same way as Figure 270.

By comparing the diagrams in Figure 270 and Figure 271, it can be recognised that the numerical model gives sufficient results. The assumption of an overall effective Young's Modulus of $E_c/4$, as usually considered is not appropriate in this case. Causes of the deviations are numerical inaccuracies of the simplified model (modelling of the concrete pavement with an overall Young's Modulus) and also measuring inaccuracies at the tests. It can be concluded, that these comparisons in Figure 271 give similar results as before at load level 4 with axle type B. The assumption of the highest effective Young's Modulus $E_{c,eff} = E_{c,a}$ also shows the best accordance for load level 7 with axle type C.

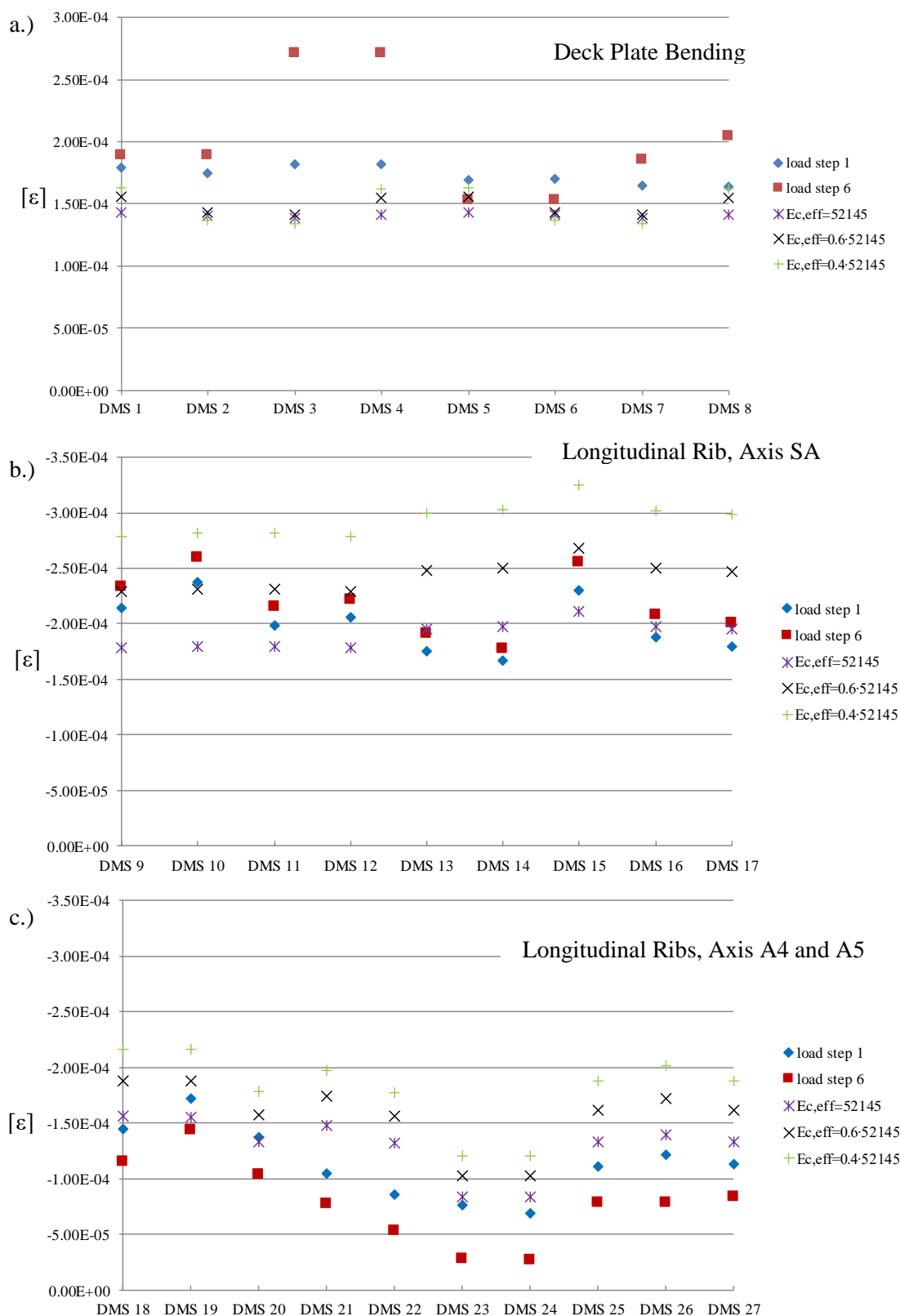


Figure 271: Full scale test – strain measurements and numerically calculated strains in comparison due to load level 7, axle type C; a.) deck plate bending DMS 1 to DMS 8; b.) longitudinal rib in axis SA, DMS 9 to DMS 17; c.) longitudinal rib in axis A4 and A5, DMS 18 to DMS 27

5.6.8. Concluding Remarks regarding to the full scale tests

The stresses in the critical details of the steel deck after strengthening can be reduced significantly. The measured stress reduction factors f_{σ} at the full scale tests are much more beneficial, than the stress reduction factors determined in the numerical studies (FEM-models, with and without concrete pavement). Also for detail D2, the welded connection of the longitudinal rib to the cross girder, a beneficial behaviour of the concrete layer could be verified. Based on the measurements at the full scale tests, the desired additional 50 years of service life can be guaranteed with this proposed strengthening method of an 80 mm thick concrete pavement, after already 50 years in service before. For a practical implementation of this strengthening solution a prototype application seems useful with additional measurements, to evaluate the effects of the concrete plate to the global load carrying behaviour.

Under consideration of the full scale tests, including the strengthening with an 80mm UHPFR pavement, the best accuracy of stresses and strains in the steel deck in the numerical investigations (variation of an overall effective concrete's Young's Modulus $E_{c,eff}$) are detected with the full averaged concrete's Young's Modulus $E_{c,a} = E_{c,eff}$. Therefore, this unexpected high value should also be used for remaining service life calculations of the strengthened deck.

6. Conclusions and Outlook

Altogether it can be stated that a simplified load model, as it is presented in the actual Eurocode with five lorry types (FLM 4; possibly with national modifications, e.g. FLM 4* for Austria), is sufficient for a fatigue assessment on existing highway bridges with orthotropic steel decks when actual measured traffic and stress spectrum data is taken into consideration. Based on that, the numerical model for the calculation of the stress spectra should be verified and adapted if necessary. The occurring stresses due to the heavy traffic depends on many parameters which do vary more or less, because the notch details within the orthotropic deck are very local. Additionally, there are uncertainties regarding to the dynamic effects due to the heavy vehicle crossings over the bridge. Therefore, in situ measurements are strictly necessary for an accurate determination of the remaining life cycle time of orthotropic decks on existing bridges. For detail locations where there is no access for applying strain gauges, appropriate fracture mechanic models are necessary which are calibrated on tests. A calibration of the fatigue load model FLM 4 is possible, based on the measured strain- respectively stress range spectra and the number of individual lorry types within the measured period. Hence, a more complex load model does not seem to be more efficient for practical applications, because this calibration is necessary anyway.

In summary the following conclusions can be stated regarding to existing orthotropic steel decks on highway bridges under fatigue aspects:

- Based on the data studies of existing bridges in Germany and Austria in Section 2.3, three significant details were analysed in this thesis. Detail D1 is the longitudinal rib to deck plate connection. For trapezoidal, closed longitudinal ribs detail D1 has to be split in detail D1a and D1b. For detail D1a, the transversal stresses on the deck plate's bottom side at the weld toe are relevant, as also for open longitudinal ribs. For detail D1b, the bending stresses at the weld toe in the web of the longitudinal rib are relevant. Detail D2 is the longitudinal rib to cross girder connection and detail D3 is the bolted connection within the cross girders. These details are frequent on orthotropic steel decks and are quite independent of the global load carrying behaviour (deck plate acts as the upper flange of the main girders).
- With regards to the numerical service life analyses of three representative steel bridge decks in Section 3 and the evaluations in Section 5.3, it is worth mentioning that the fatigue life of all three details (detail D1 with deck plate slenderness $e_{LR} / t_{DP} > 25$) within the analysed decks is exhausted after 50 years due to FLM 4* ($D_i > 1.0$, under assumption of a heavy traffic volume and load level which was measured on an highly frequented Austrian highway bridge).
- The axle geometries of the actual fatigue load models according to the Eurocode [1] show deviations to realistic heavy vehicles. Within this thesis, the effects of these deviations to the damage equivalent

stress range $\Delta\sigma_e$ of the analysed details D1 and D2 could be determined. Additionally, the effect of realistic heavy traffic driving characteristics (lateral distribution of heavy vehicles in the transverse direction) to the detail's equivalent stress range for D1 and D2 could be quantified.

It can be recognised, that the damage equivalent stress ranges $\Delta\sigma_e$ for detail D1a and D2 decrease from 10 to 18% by taking both of these effects into account. Hence, these effects are positive for detail D1a and D2, extending the calculated fatigue life. The consideration of only realistic axle geometries at model A (open longitudinal ribs) leads to an increase of $\Delta\sigma_e$ of +15% for detail D2 because of the specific one-sided connection of the longitudinal rib to the cross girder.

For detail D1b, the consideration of a lateral distribution of the heavy vehicles is essential for an adequate determination of the fatigue critical stresses (only necessary for closed longitudinal ribs). Without taking these effects into account nearly no fatigue damage occurs due to the numerical calculations. A consideration of a wide-spreading frequency distribution for the wheel position in transverse direction highly increases the bending stresses in the web of the trough rib, up to 300%.

- The numerical simulations on the three different FE-models showed that lorry type T3 (fatigue load model FLM 4), the articulated lorry, causes the maximum damage in the details D1 and D2. For detail D1a, the damage percentage of lorry type T3 has a value of 65 to 75%. The same lorry type causes at detail D2 74 to 93% of the whole damage. It therefore makes sense to take special care of the geometries and axle loads of lorry type T3. Additionally, these results confirm the sufficiency of a practically simplified fatigue load model, because one lorry type strongly dominates the fatigue damage in the analysed details.

The analyses regarding to the strengthening of existing orthotropic steel decks with an UHPFRC pavement instead of the asphalt, which is based on a solution that was developed in the Netherlands, showed very good results for the notch details D1 and D2. Especially the full scale tests, where also overloads and thermal constraints were simulated, confirmed the beneficial effect of the concrete pavement to the local load bearing behaviour. For detail D1a, a stress reduction factor of $f_{\sigma,B} = 0.20$ for double wheeled axles (axle type B) and $f_{\sigma,A/C} = 0.29$ for single wheeled axles (axle type A and C) could be determined. For detail D2, the resulting stress reduction factor is $f_{\sigma,B} = 0.24$ for double wheeled axles (axle type B) and $f_{\sigma,A/C} = 0.23$ for single wheeled axles (axle type A and C).

With the knowledge of all these results, a prototype application with accompanying measurements on the steel structure, the concrete and the interface layer would be the next useful step to quantify the effects of the global load carrying behaviour. This procedure seems necessary, especially for the detection of additional shear stresses in the interface, due to the global load transfer (the very high Young's Modulus of the concrete leads to significant normal stresses σ_c in the concrete). Based on that,

possibly additional shear studs are necessary. Also a possible lift off of the concrete pavement due to a local tensile bond failure of the epoxy layer should be verified with a prototype. This effect can be expected to be dangerous for example in the field region of a girder bridge where the concrete pavement gets compression membrane stresses due to the heavy traffic. Nevertheless, this strengthening method is highly promising for the renovation of existing bridges, to extend its service life and further investigations would complete the knowledge about the load carrying behaviour.

REFERENCES

- [1] EN 1991-2, Eurocode 3: Actions on structures, Part 2: Traffic loads on bridges, Issue 2012-03-01.
- [2] H. Unterweger and A. Taras, Remaining fatigue life for a specific bridge deck detail - joint between longitudinal rib and cross girder, Institut für Stahlbau - TU Graz, 2015.
- [3] H. Unterweger, F. Novak and A. Kamplleitner, Montagestöße der Querrippen - Rissaufnahme und Tragsicherheitsberechnung, Institut für Stahlbau - TU Graz, 2017.
- [4] EN 1993-1-9, Eurocode 3: Design of steel structures, Part 1-9: Fatigue, Issue: 2013.
- [5] G. Sedlacek and J. Jacquemoud, Herleitung eines Lastmodells für den Betriebsfestigkeitsnachweis von Straßenbrücken, Forschung Straßenbau und Straßenverkehrstechnik, Heft 430, Bundesministerium für Verkehr, Abteilung Straßenbau, Bonn-Bad Godesberg, 1984.
- [6] J. Jacquemoud, Analyse du Comportement a la fatigue des Ponts-Routes, Ecole Polytechnique Federal de Lausanne, Lausanne, 1981.
- [7] British Standards Institution, Steel, Concrete and Composite Bridges, Part 10, Code of Practice for Fatigue, BSI, London, BS 5400, Part 10, 1980.
- [8] R. Blab, Die Fahrspurverteilung als Einflussgröße bei der Bemessung des Straßenoberbaus, Wien: Institut für Straßenbau und Straßenerhaltung, TU Wien, 1995.
- [9] F. Nather and K. Schütz, Statische und dynamische Beanspruchung der Adenauerbrücke in Forchheim infolge Verkehrsbelastung, Versuchsbericht 152., Lehrstuhl für Stahlbau, TU München, 1990.
- [10] K. G. Schütz, Verkehrslasten und deren Wirkung auf Straßenbrücken, Mitteilungen aus dem Lehrstuhl für Stahlbau Technische Universität München, Heft 26, München, 1991.
- [11] G. König and H.-C. Gerhardt, Verkehrslastmodell für Straßenbrücken, Bauingenieur 60, 1985.
- [12] M. Puche and H.-C. Gerhardt, Absicherung eines Verkehrslastmodells durch Messungen von Spannstahldehnungen, Bauingenieur 61, 1986.
- [13] F. Nather, Prüfvorschrift für die Haseltalbrücke an der BAB A3 Würzburg-Frankfurt, München, 1986.
- [14] G. Klassen, Vorschlag zur Durchführung des Betriebsfestigkeitsnachweises der Donaubrücke Donaustauf, Lehrstuhl Stahlbau, TU München, 1985.
- [15] F. Tschemmerneegg, Zur Bemessung von Fahrbahnübergängen, Bauingenieur 63, 1988.
- [16] P. Tschemmerneegg, H. Passer and O. Neuner, Verbreiterung und Sanierung von Stahlbrücken, Stahlbau 58, 1989.

- [17] Schweizer Ing.- und Architekten-Verein: SIA 160, Einwirkungen auf Tragwerke. Verständigung; Sicherheit und Gebrauchstauglichkeit; Berechnung, Bemessung und Nachweise; Einwirkungen; Entwurf 3.88.
- [18] Normenausschuss Bauwesen DIN 1072, Straßen- und Wegbrücken. Lastannahmen, Berlin: Beuth Verlag, 1985.
- [19] H. P. Lehrke, H. Steinhilber and O. Buxbaum, Entwicklung eines ersten Moduls für ein Verkehrslastsimulationsprogramm, Darmstadt: Fraunhofer-Institut für Betriebsfestigkeit, 1988.
- [20] V. Ladda and H. Steinhilber, Messung und statistische Beschreibung der Verkehrslasten einer Autobahn - Schlussbericht, Darmstadt: Fraunhofer-Institut für Betriebsfestigkeit, 1985.
- [21] L. Sanpaolesi and P. Croce, Design of Bridges, Guide to basis of bridge design related to Eurocodes supplemented by practical examples, Leonardo da Vinci Pilot Project CZ/02/B/F/PP-134007, 2005.
- [22] E. Haibach, Betriebsfestigkeit - Verfahren und Daten zur Bauteilberechnung, Springer Verlag, 2006.
- [23] D. Radaj and M. Vormwald, Ermüdungsfestigkeit, Springer Verlag, 2009.
- [24] T. Anderson, Fracture Mechanics - Fundamentals and Applications 3rd Edition, CRC Press, Taylor and Francis Group, 2005.
- [25] M. Kuna, Numerische Beanspruchungsanalyse von Rissen - Finite Elemente in der Bruchmechanik, Vieweg + Teubner, 2008.
- [26] J. Maljaars, D. Gration, E. Vonk and F. van Dooren, International Association for Bridge and Structural Engineering(IABSE) Conference Proceedings, Rotterdam, 2013.
- [27] J. Maljaars, F. van Dooren and H. Kolstein, Fatigue assessment for deck plates in orthotropic bridge decks, Steel Construction 5, No. 2, Ernst & Sohn, 2012.
- [28] F. de Jong, Renovation techniques for fatigue cracked orthotropic steel bridge decks, TU Delft, 2007.
- [29] E. Luangkhot, L. Dieng, S. Brisard, C. Le Quere and J. Raoul, Eurosteel, Proceedings of the Conference - Volume B, Budapest, 2011.
- [30] J. Murakoshi and H. Ishii, Research on Fibre Reinforced Concrete Pavement for Orthotropic Steel Deck as a Countermeasure for Fatigue, 2008.
- [31] M. D. Denkinger and P. Buitelaar, Ertüchtigung orthotroper Fahrbahnplatten von Stahlbrücken, Stahlbau 75, Heft 7, 2006.
- [32] F. v. Dooren, D. Gration, S. den Blanken, G. Nagtegaal, D. Ashurst and P. Kunst, Orthotropic Deck Fatigue: Renovation of 8 Bridges in the Netherlands, Structural Faults & Repair, 2010.

- [33] H. Unterweger, F. Novak, T. Nguyen, T. Hofer, P. Hadl and B. Freytag, Verstärkung orthotroper Stahlfahrbahnplatten mit Hochleistungsbeton zur Erzielung einer deutlich erhöhten Restlebensdauer, General Report for FFG-Research Project 840487, October 2015.
- [34] H. Unterweger, F. Novak and A. Taras, Fatigue verification of orthotropic bridge decks - improvement of load models for old highway bridges in practice, Proceedings of the Eurosteel Conference, Naples, 2014.
- [35] D. Radaj, C. M. Sonsino, W. Fricke, Fatigue assessment of welded joints by local approaches, Second edition, ISBN: 978-1-85573-948-2, 2006.
- [36] US Department of Transportation - Federal Highway Administration, Manual for design, construction and maintenance of orthotropic steel deck bridges, 2012.
- [37] F. R. Weitz, Entwurfsgrundlagen und Entscheidungskriterien für Konstruktionssysteme, Darmstadt: Dissertation, Technische Hochschule Darmstadt, 1975.
- [38] A. Ogris, Betriebsfaktoren zur Ermüdungsbeanspruchung, Masterthesis, Graz, 2016.
- [39] E. Fiedler, Die Entwicklung der orthotropen Fahrbahnplatte in Deutschland, Stahlbau 78, Heft 8, Ernst & Sohn, 2009.
- [40] G. Sedlacek, H. Eisel, W. Hensen, B. Kühn and M. Paschen, Leitfaden zum DIN Fachbericht 103: Stahlbrücken, Berlin: Ernst & Sohn Verlag, 2003.
- [41] EN 1993-2, Eurocode 3: Design of steel structures, Part 2: Steel bridges, Issue: 2007-04-01.
- [42] EN 1993-1-5, Eurocode 3 - Design of steel structures, Part 1-5: Plated structural elements, Issue: 2012.
- [43] J. S. Leendertz, Fatigue Behaviour of Closed Stiffener to Crossbeam Connections in Orthotropic Steel Bridge Decks, TU Delft, 2008.
- [44] H. Unterweger, A. Taras, A23-Praterbrücke/Stromtragwerk, Lebensdauerberechnung für das Fahrbahndeck infolge der lokalen Schwerverkehrsbelastung, Institut für Stahlbau, TU-Graz, Graz, März 2012.
- [45] M. H. Kolstein, Fatigue Classification of Welded Joints, Delft, Netherland: Delft University of Technology, 2007.
- [46] Kraftfahrzeuggesetz 1967, BGBl. Nr. 267/1967 zuletzt geändert durch BGBl. I Nr. 57/2007.
- [47] Richtlinie 96/53/EG des Rates vom 25. Juli 1996 zur Festlegung der höchstzulässigen Abmessungen für bestimmte Straßenfahrzeuge im innerstaatlichen und grenzüberschreitenden Verkehr in der Gemeinschaft sowie zur Festlegung der höchstzulässigen Gewichte im grenzüberschreitenden Verkehr, September 1996.

- [48] International Institute of Welding (IIW), Recommendations for Fatigue Design of welded Joints, 2008.
- [49] *Software ABAQUS, v. 6.14-3; Dassault Systemes Simulia Corp, Providence, RI, USA*, 2014.
- [50] RAS-Q 96: Richtlinien für die Anlage von Straßen, Teil: Querschnitte, Ausgabe 1996.
- [51] F. Novak, Lastmodelle für den Ermüdungsnachweis von orthotropen Fahrbahnplatten bei Straßenbrücken, Masterthesis, Graz, 2013.
- [52] Richtlinie 92/106/EWG des Rates vom 7. Dezember 1992: Festlegung gemeinsamer Regeln für bestimmte Beförderungen im kombinierten Güterverkehr zwischen Mitgliedstaaten, Dezember 1992.
- [53] H. Czichos, M. Hennecke, Akademischer Verein, Hütte, Das Ingenieurwissen 34. Auflage, ISBN 978-3-642-22850-6, Springer Verlag, 2012.
- [54] EN 1990, Eurocode 0: Basis of structural design, Issue: 2013-03-15.

ANNEX A – SIMULATION OF HEAVY TRAFFIC CROSSINGS

In this Section the relevant results of the heavy traffic simulations at model A, B, C and D are presented referring to the analysed notch details D1a, D1b, D2 and D3. Fatigue load model FLM 4 and FLM 4* were considered with its 5 lorry types and 3 axle types. For detail D1a to D2 (at model A to C), influence lines in longitudinal bridge direction regarding to axle type A, B and C are shown first relating to an axle load of $F_A = 100\text{kN}$. Stress history curves relating to the 5 lorry types are subsequently shown under consideration of the axle loads and distances of the chosen fatigue load model. Finally, stress range spectra are shown regarding to the details D1a to D2 and a damage equivalent constant amplitude stress range $\Delta\sigma_e$ is additionally plotted in the diagrams. For detail D3 (at model D), the maximum and minimum principal stresses are shown in the local regions of the bolted cross girder connections. A representative selection of the diagrams shown in this Section is already illustrated in Section 3.4.

A-1. MODEL A: ORTHOTROPIC BRIDGE DECK WITH OPEN LONGITUDINAL RIBS

This Section presents a complete summary of the results regarding to the numerical calculations at model A which is described in Section 3.2.1. The simulation of the lorry crossings has been performed at LR-1 (lane 1) and LR-3 (lane 2) which are shown in Section 3.4.2.

A-1.1. Detail D1a

The influence lines in longitudinal bridge direction and the stress history curves referring to detail D1a are shown in this Section. The stress range spectra due to FLM 4 and FML 4* at LR-1 (lane 1) and LR-3 (lane 2) are already displayed in Figure 86, Figure 87 and Figure 88 in Section 3.4.2 and therefore they are not shown any more.

A.1.1.1. Influence lines in longitudinal direction for wheel types A, B and C

The longitudinal influence lines for axle type B and C at LR-1 and LR-3 are already shown in Figure 84. Figure A. 1 shows the longitudinal influence lines due to axle type A at LR-1 and LR-3.

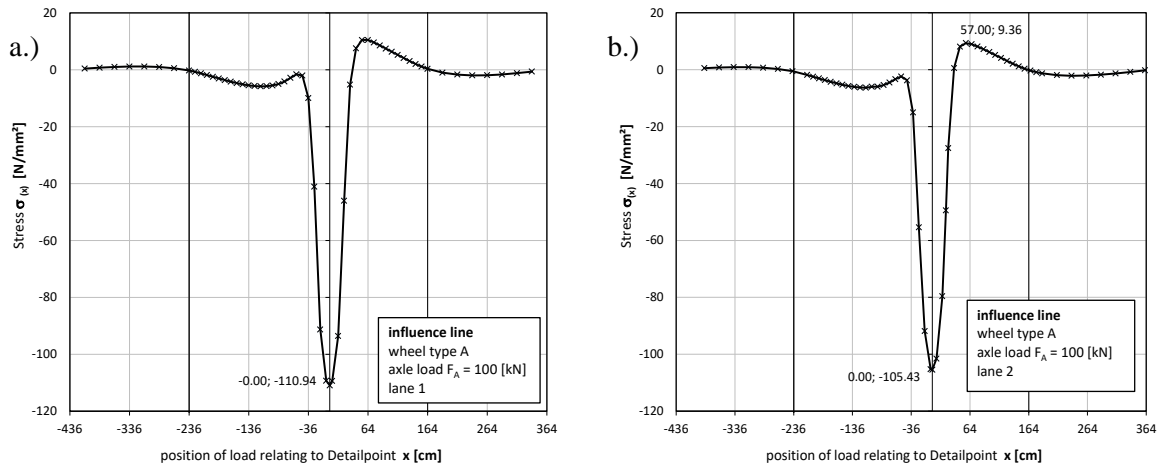


Figure A. 1: Model A – Detail D1a – influence lines in longitudinal bridge direction due to axle type A and an axle load of $F_A = 100\text{kN}$: a.) axle type A at LR-1 (lane 1); b.) axle type A at LR-3 (lane 2);

A.1.1.2. Lorry crossings at LR-1 (Lane 1) according to FLM 4*

Figure A. 2 to Figure A. 6 illustrate the stress history curves for the lorry crossings of T1 to T5 at LR-1 (lane 1). Additionally, the occurring stress ranges are indicated in the diagrams.

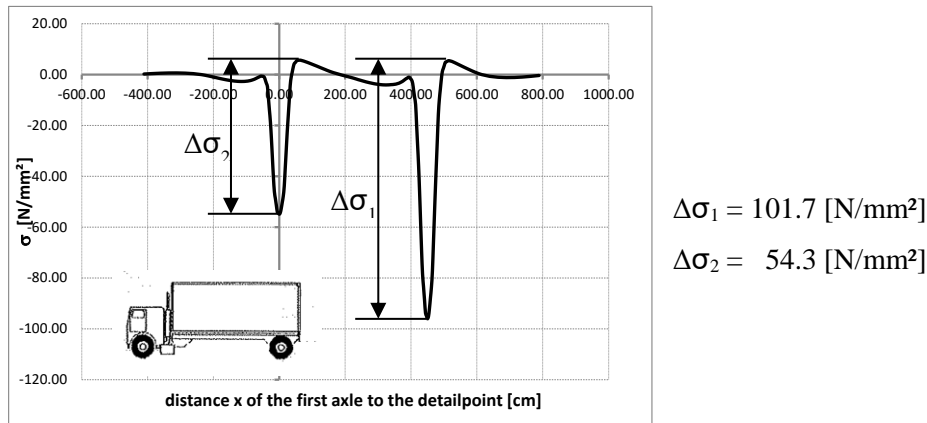


Figure A. 2: Model A – Detail D1a at LR-1 – stress history relating to a crossing of lorry type T1 according to FLM 4* at lane 1

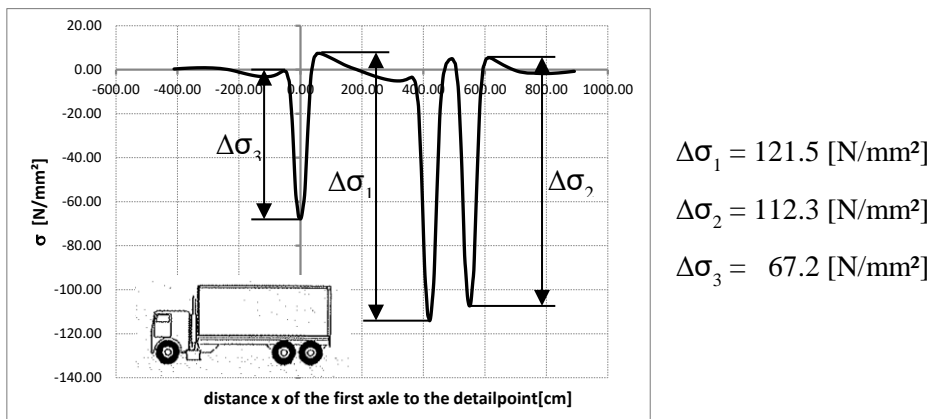


Figure A. 3: Model A – Detail D1a at LR-1 – stress history relating to a crossing of lorry type T2 according to FLM 4* at lane 1

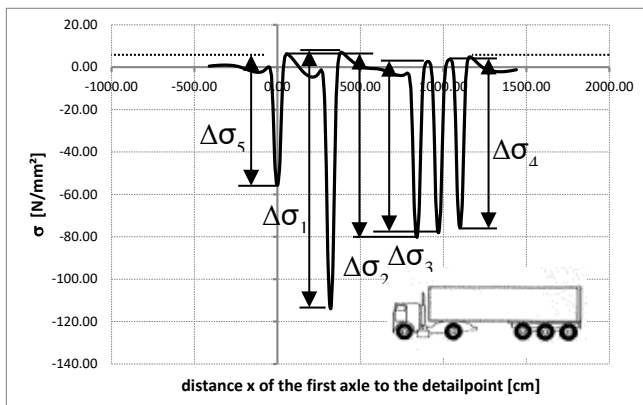


Figure A. 4: Model A – Detail D1a at LR-1 – stress history relating to a crossing of lorry type T3 according to FLM 4* at lane 1

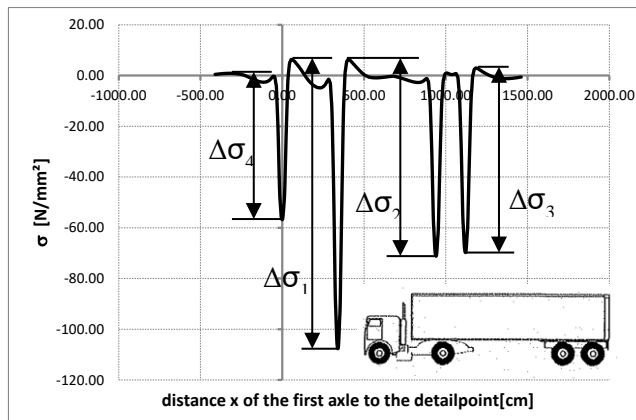


Figure A. 5: Model A – Detail D1a at LR-1 – stress history relating to a crossing of lorry type T4 according to FLM 4* at lane 1

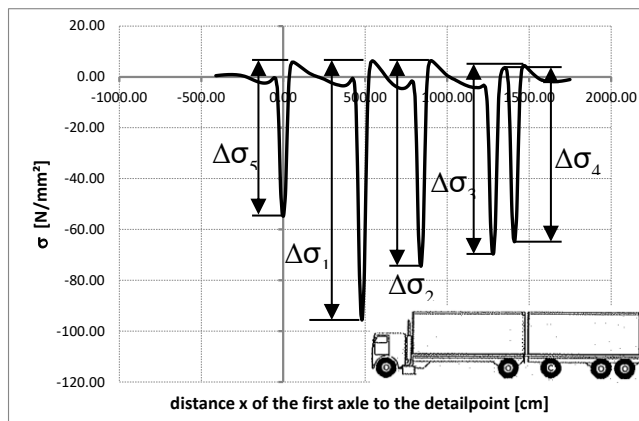


Figure A. 6: Model A – Detail D1a at LR-1 – stress history relating to a crossing of lorry type T5 according to FLM 4* at lane 1

A.1.1.3. Lorry crossings at LR-3 (Lane 2) according to FLM 4

Figure A. 7 to Figure A. 10 illustrate the stress history curves for the lorry crossings of T1 to T5 at LR-3 (lane 2). The stress history curve for lorry type T3 is already shown in Figure 85. Additionally, the occurring stress ranges are indicated in the diagrams.

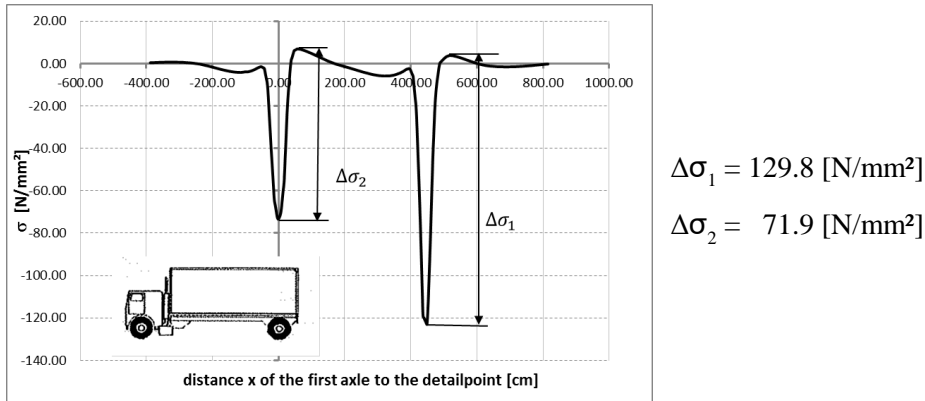


Figure A. 7: Model A – Detail D1a at LR-3 – stress history relating to a crossing of lorry type T1 according to FLM 4* at lane 2

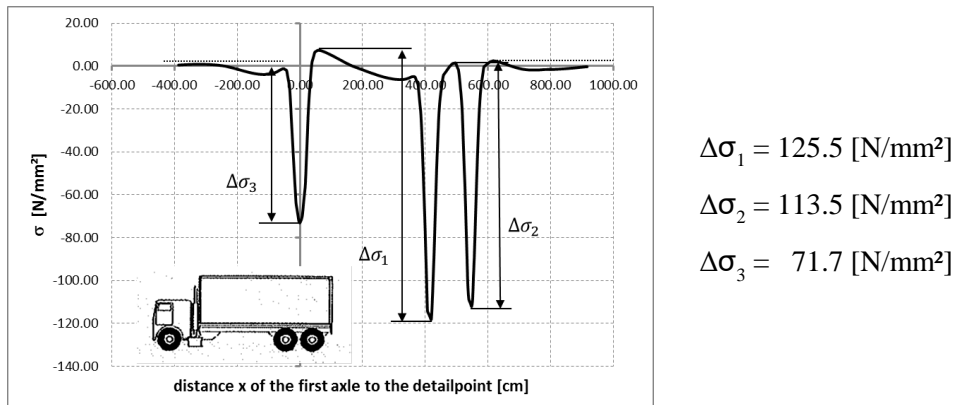


Figure A. 8: Model A – Detail D1a at LR-3 – stress history relating to a crossing of lorry type T2 according to FLM 4* at lane 2

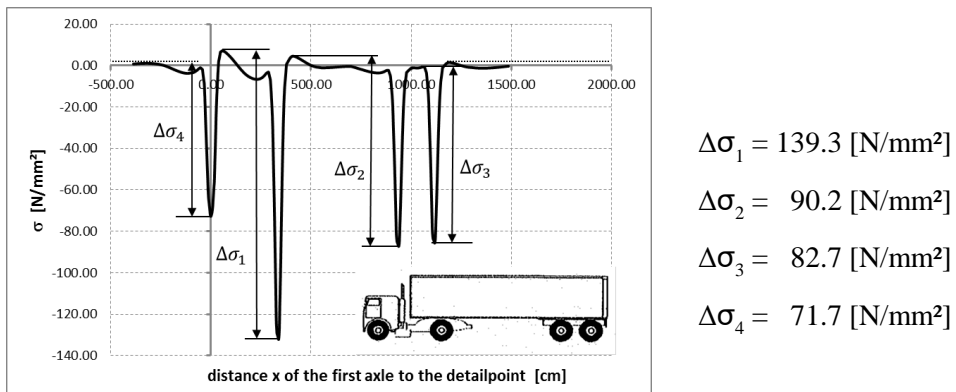


Figure A. 9: Model A – Detail D1a at LR-3 – stress history relating to a crossing of lorry type T4 according to FLM 4* at lane 2

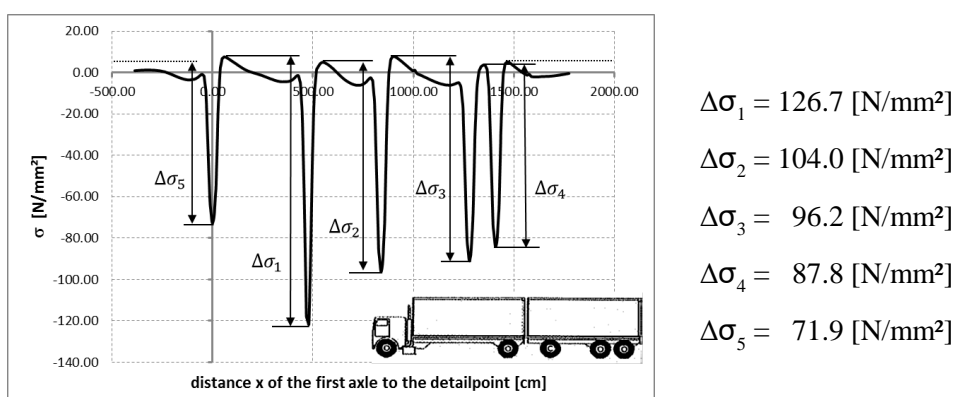


Figure A. 10: Model A – Detail D1a at LR-3 – stress history relating to a crossing of lorry type T5 according to FLM 4* at lane 2

A-1.2. Detail D2

The influence lines in longitudinal bridge direction and the stress history curves referring to detail D2 are shown in this Section. The stress range spectra due to FLM 4 and FML 4* at LR-1 (lane 1) and LR-3 (lane 2) are already displayed in Figure 91, Figure 92 and Figure 93 in Section 3.4.2 and therefore they are not shown any more.

A.1.2.1. Influence lines in longitudinal direction for wheel types A, B and C

The longitudinal influence lines for axle type B and C at LR-1 and LR-3 are already shown in Figure 89. Figure A. 11 shows the longitudinal influence lines due to axle type A at LR-1 and LR-3.

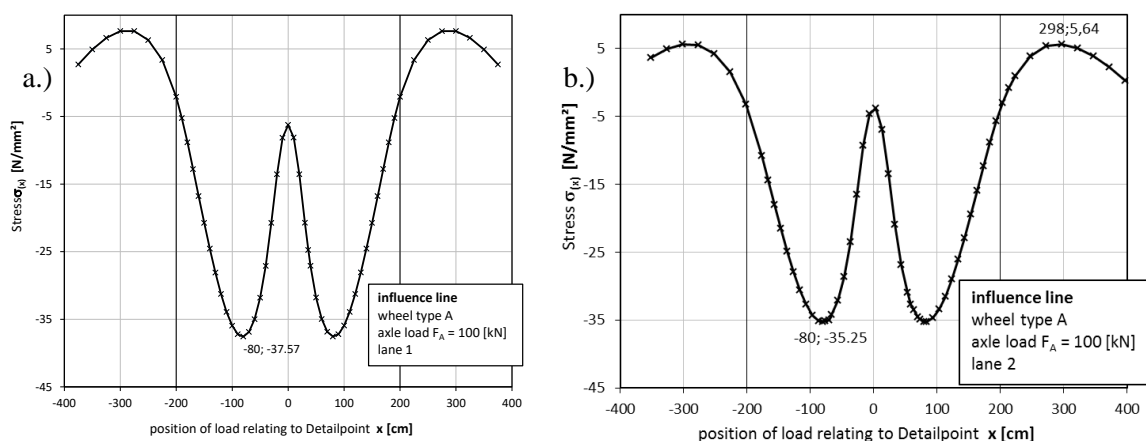
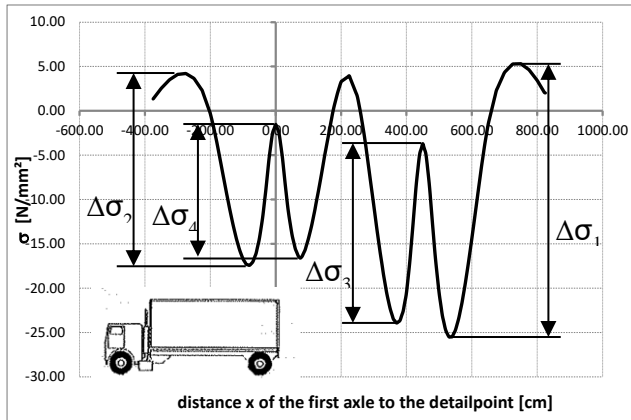


Figure A. 11: Model A – Detail D2 – influence lines in longitudinal bridge direction due to axle type A and an axle load of $F_A = 100\text{kN}$: a.) axle type A at LR-1 (lane 1); b.) axle type A at LR-3 (lane 2);

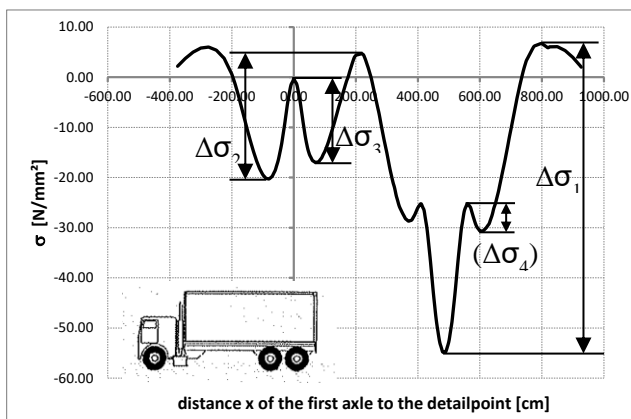
A.1.2.2. Lorry crossings at LR-1 (Lane 1) according to FLM 4*

Figure A. 12 to Figure A. 16 illustrate the stress history curves for the lorry crossings of T1 to T5 at LR-1 (lane 1). Additionally, the occurring stress ranges are indicated in the diagrams.



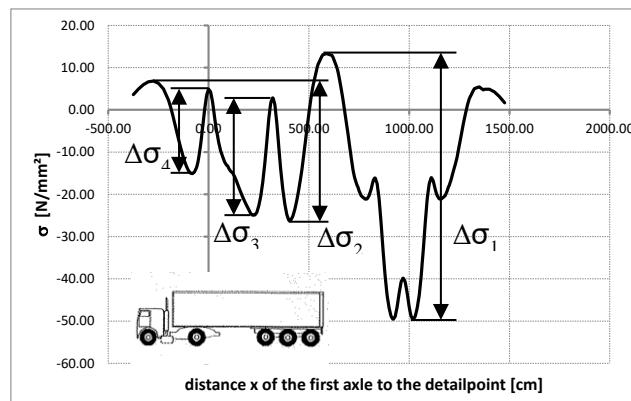
$$\begin{aligned}\Delta\sigma_1 &= 30.8 \text{ [N/mm}^2\text{]} \\ \Delta\sigma_2 &= 21.6 \text{ [N/mm}^2\text{]} \\ \Delta\sigma_3 &= 20.2 \text{ [N/mm}^2\text{]} \\ \Delta\sigma_4 &= 15.5 \text{ [N/mm}^2\text{]}\end{aligned}$$

Figure A. 12: Model A – Detail D2 at LR-1 – stress history relating to a crossing of lorry type T1 according to FLM 4* at lane 1



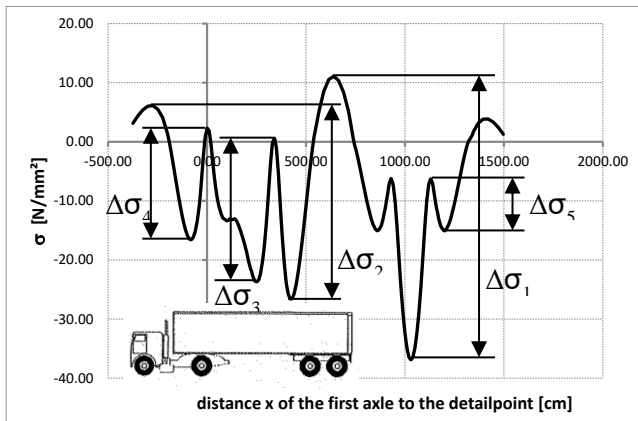
$$\begin{aligned}\Delta\sigma_1 &= 61.5 \text{ [N/mm}^2\text{]} \\ \Delta\sigma_2 &= 25.0 \text{ [N/mm}^2\text{]} \\ \Delta\sigma_3 &= 16.6 \text{ [N/mm}^2\text{]}\end{aligned}$$

Figure A. 13: Model A – Detail D2 at LR-1 – stress history relating to a crossing of lorry type T2 according to FLM 4* at lane 1



$$\begin{aligned}\Delta\sigma_1 &= 62.9 \text{ [N/mm}^2\text{]} \\ \Delta\sigma_2 &= 33.0 \text{ [N/mm}^2\text{]} \\ \Delta\sigma_3 &= 27.7 \text{ [N/mm}^2\text{]} \\ \Delta\sigma_4 &= 20.2 \text{ [N/mm}^2\text{]}\end{aligned}$$

Figure A. 14: Model A – Detail D2 at LR-1 – stress history relating to a crossing of lorry type T3 according to FLM 4* at lane 1



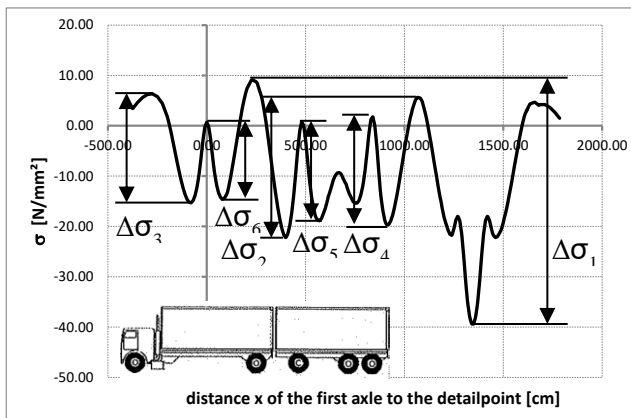
$$\Delta\sigma_1 = 47.9 \text{ [N/mm}^2\text{]}$$

$$\Delta\sigma_2 = 32.7 \text{ [N/mm}^2\text{]}$$

$$\Delta\sigma_3 = 24.3 \text{ [N/mm}^2\text{]}$$

$$\Delta\sigma_4 = 18.9 \text{ [N/mm}^2\text{]}$$

Figure A. 15: Model A – Detail D2 at LR-1 – stress history relating to a crossing of lorry type T4 according to FLM 4* at lane 1



$$\Delta\sigma_1 = 48.5 \text{ [N/mm}^2\text{]}$$

$$\Delta\sigma_2 = 27.8 \text{ [N/mm}^2\text{]}$$

$$\Delta\sigma_3 = 21.6 \text{ [N/mm}^2\text{]}$$

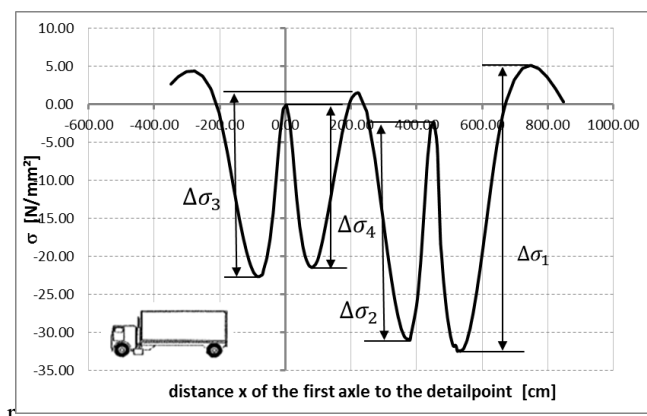
$$\Delta\sigma_4 = 21.4 \text{ [N/mm}^2\text{]}$$

$$\Delta\sigma_5 = 19.6 \text{ [N/mm}^2\text{]}$$

Figure A. 16: Model A – Detail D2 at LR-1 – stress history relating to a crossing of lorry type T5 according to FLM 4* at lane 1

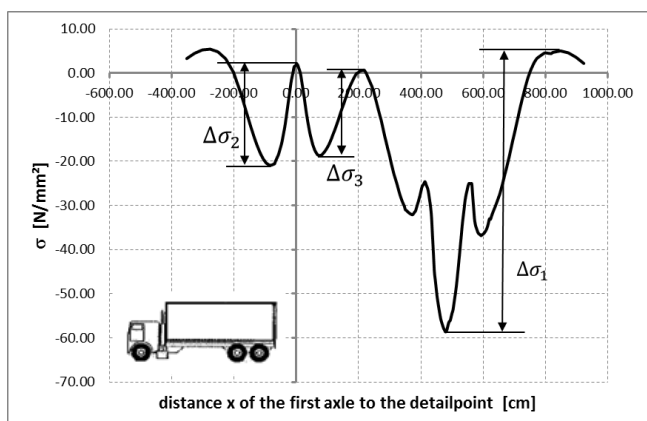
A.1.2.3. Lorry crossings at LR-3 (Lane 2) according to FLM 4

Figure A. 17 to Figure A. 20 illustrate the stress history curves for the lorry crossings of T1 to T5 at LR-3 (lane 2). The stress history curve for lorry type T3 is already shown in Figure 90. Additionally, the occurring stress ranges are indicated in the diagrams.



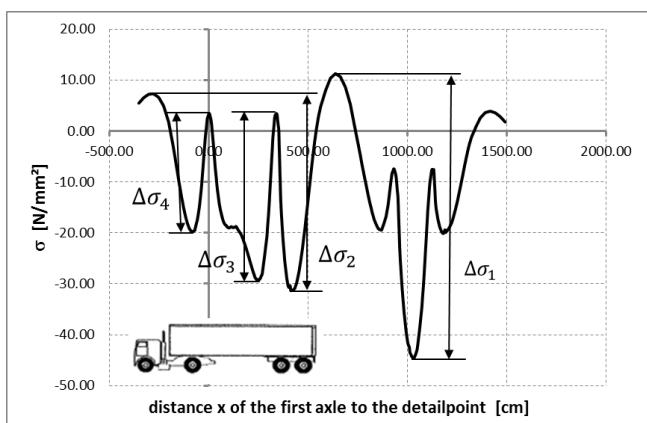
$\Delta\sigma_1 = 37.5 \text{ [N/mm}^2\text{]}$
 $\Delta\sigma_2 = 28.7 \text{ [N/mm}^2\text{]}$
 $\Delta\sigma_3 = 25.0 \text{ [N/mm}^2\text{]}$
 $\Delta\sigma_4 = 21.4 \text{ [N/mm}^2\text{]}$

Figure A. 17: Model A – Detail D2 at LR-3 – stress history relating to a crossing of lorry type T1 according to FLM 4 at lane 2



$\Delta\sigma_1 = 63.7 \text{ [N/mm}^2\text{]}$
 $\Delta\sigma_2 = 22.9 \text{ [N/mm}^2\text{]}$
 $\Delta\sigma_3 = 18.0 \text{ [N/mm}^2\text{]}$

Figure A. 18: Model A – Detail D2 at LR-3 – stress history relating to a crossing of lorry type T2 according to FLM 4 at lane 2



$\Delta\sigma_1 = 55.8 \text{ [N/mm}^2\text{]}$
 $\Delta\sigma_2 = 38.6 \text{ [N/mm}^2\text{]}$
 $\Delta\sigma_3 = 32.7 \text{ [N/mm}^2\text{]}$
 $\Delta\sigma_4 = 23.2 \text{ [N/mm}^2\text{]}$

Figure A. 19: Model A – Detail D2 at LR-3 – stress history relating to a crossing of lorry type T4 according to FLM 4 at lane 2

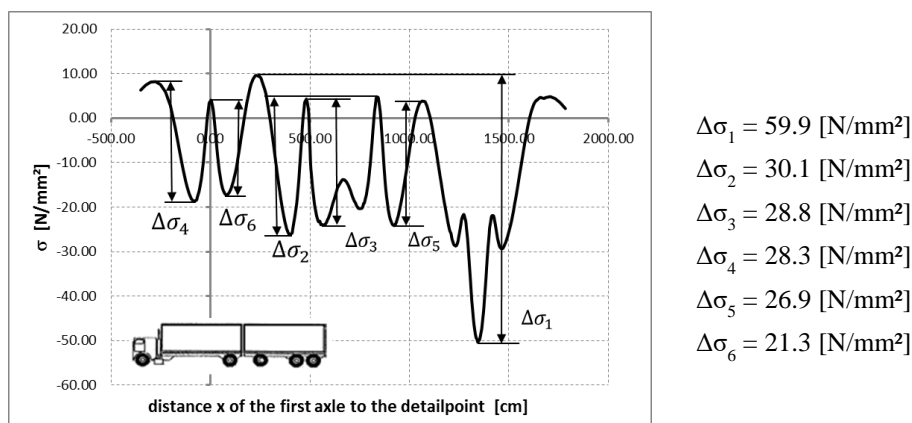


Figure A. 20: Model A – Detail D2 at LR-3 – stress history relating to a crossing of lorry type T5 according to FLM 4 at lane 2

A-2. MODEL B: ORTHOTROPIC BRIDGE DECK WITH TROUGH LONGITUDINAL RIBS AND CROSS GIRDER SPACING OF 2M

This Section presents a complete summary of the results regarding to the numerical calculations at model B which is described in Section 3.2.2. The simulation of the lorry crossings has been performed at the left web of LR-2 (lane 1) which is shown in Section 3.4.3.

A-2.1. Detail D1a

The influence lines in longitudinal bridge direction and the stress history curves referring to detail D1a are shown in this Section. The stress range spectrum due to FLM 4 at the left web of LR-2 (lane 1) is already displayed in Figure 97 in Section 3.4.3 and therefore this is not shown any more.

A.2.1.1. Influence lines in longitudinal direction for wheel types A, B and C

The longitudinal influence lines for axle type B and C at the left web of LR-2 are already shown in Figure 95. Figure A. 21 shows the longitudinal influence lines due to axle type A at the left web of LR-2.

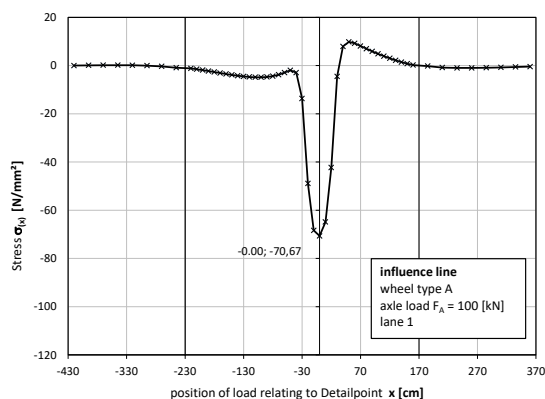


Figure A. 21: Model B – Detail D1a – influence line in longitudinal bridge direction due to axle type A and an axle load of $F_A = 100\text{kN}$ at the left web of LR-2 (lane 1);

A.2.1.2. Lorry crossings at the left web of LR-2 (Lane 1) according to FLM 4

Figure A. 22 to Figure A. 25 illustrate the stress history curves for the lorry crossings of T1 to T5 at the left web of LR-2 (lane 1). The stress history curve for lorry type T3 is already shown in Figure 96. Additionally, the occurring stress ranges are indicated in the diagrams.

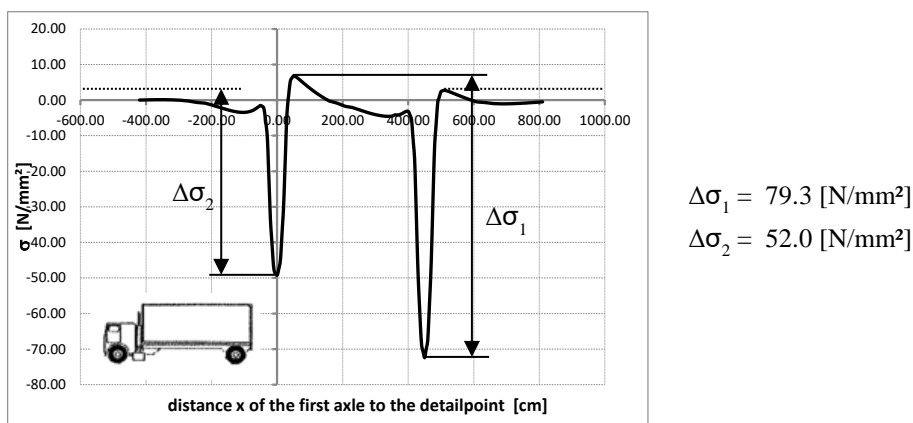


Figure A. 22: Model B – Detail D1a at the left web of LR-2 – stress history relating to a crossing of lorry type T1 according to FLM 4 at lane 1

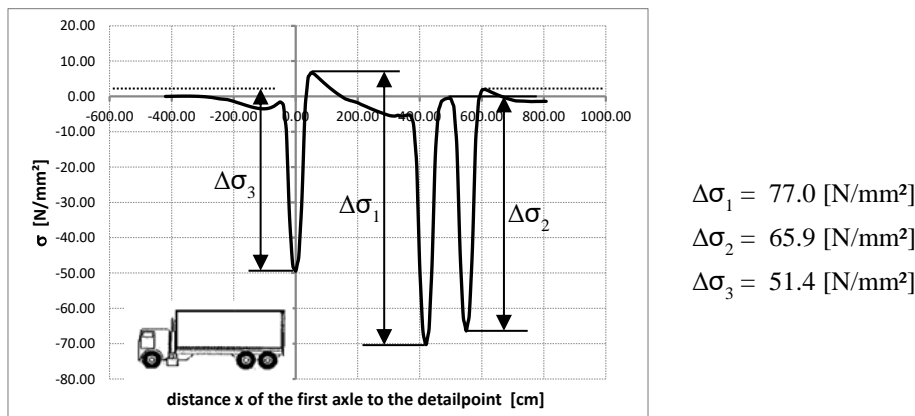


Figure A. 23: Model B – Detail D1a at the left web of LR-2 – stress history relating to a crossing of lorry type T2 according to FLM 4 at lane 1

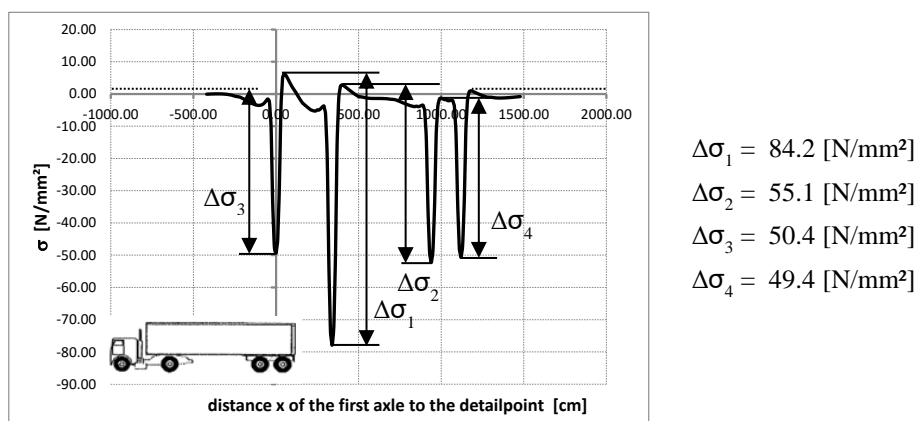


Figure A. 24: Model B – Detail D1a at the left web of LR-2 – stress history relating to a crossing of lorry type T4 according to FLM 4 at lane 1

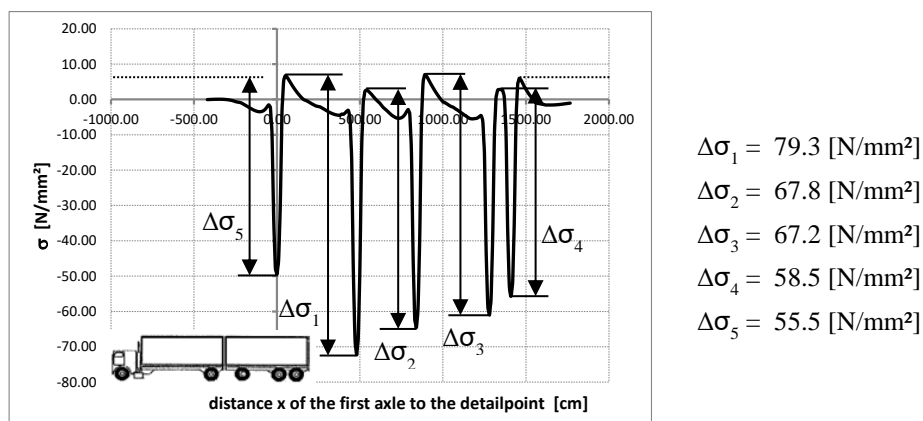


Figure A. 25: Model B – Detail D1a at the left web of LR-2 – stress history relating to a crossing of lorry type T5 according to FLM 4 at lane 1

A-2.2. Detail D1b

The influence lines in longitudinal bridge direction and the stress history curves referring to detail D1b are shown in this Section. The stress range spectrum due to FLM 4 at the left web of LR-2 (lane 1) is already displayed in Figure 100 in Section 3.4.3 and therefore this is not shown any more.

A.2.2.1. Influence lines in longitudinal direction for wheel types A, B and C

The longitudinal influence lines for axle type B and C at the left web of LR-2 are already shown in Figure 98. Figure A. 26 shows the longitudinal influence lines due to axle type A at the left web of LR-2.

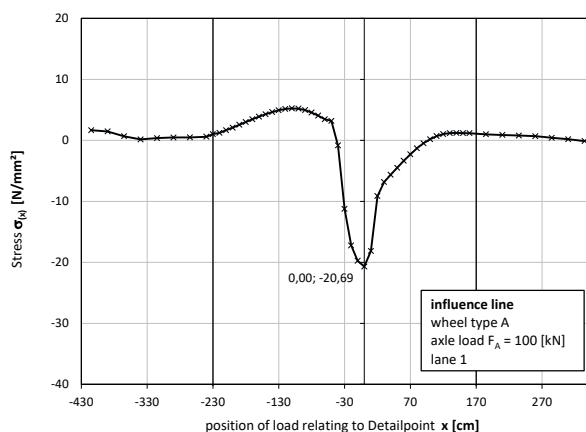


Figure A. 26: Model B – Detail D1b – influence line in longitudinal bridge direction due to axle type A and an axle load of $F_A = 100\text{kN}$ at the left web of LR-2 (lane 1);

A.2.2.2. Lorry crossings at left web of LR-2 (Lane 1) according to FLM 4

Figure A. 27 to Figure A. 30 illustrate the stress history curves for the lorry crossings of T1 to T5 at the left web of LR-2 (lane 1). The stress history curve for lorry type T3 is already shown in Figure 99. Additionally, the occurring stress ranges are indicated in the diagrams.

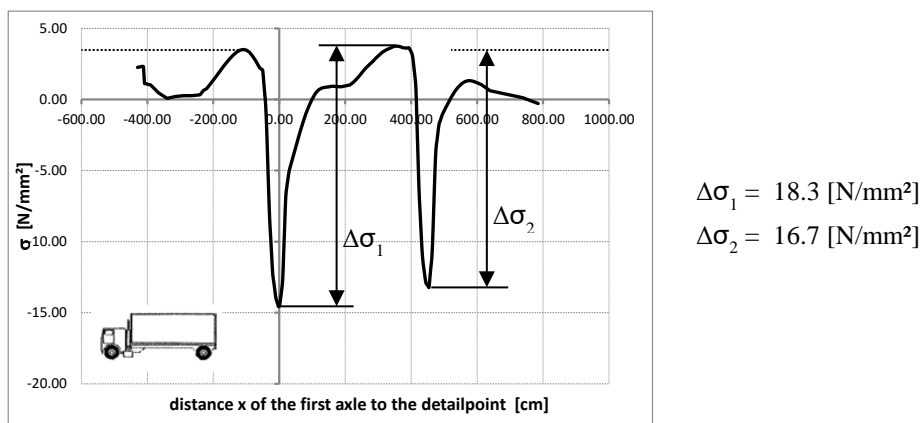


Figure A. 27: Model B – Detail D1b at the left web of LR-2 – stress history relating to a crossing of lorry type T1 according to FLM 4 at lane 1

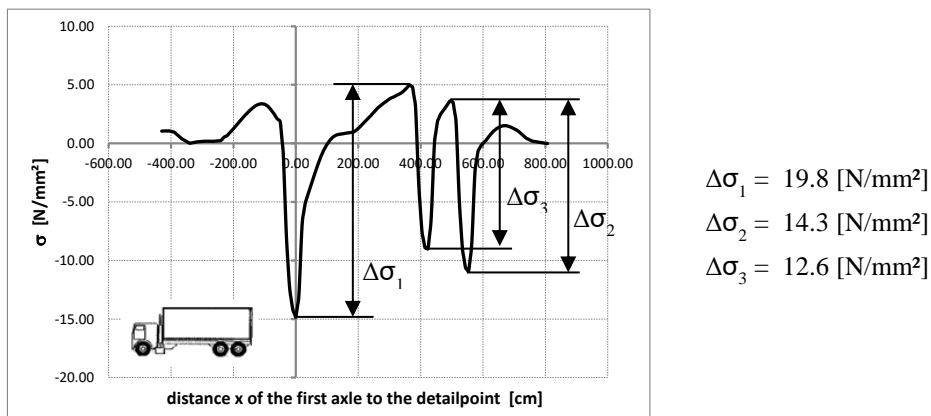


Figure A. 28: Model B – Detail D1b at the left web of LR-2 – stress history relating to a crossing of lorry type T2 according to FLM 4 at lane 1

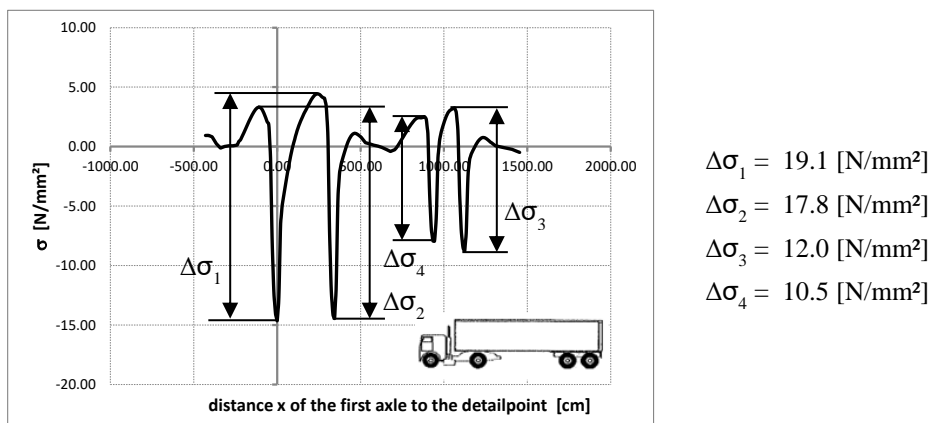


Figure A. 29: Model B – Detail D1b at the left web of LR-2 – stress history relating to a crossing of lorry type T4 according to FLM 4 at lane 1

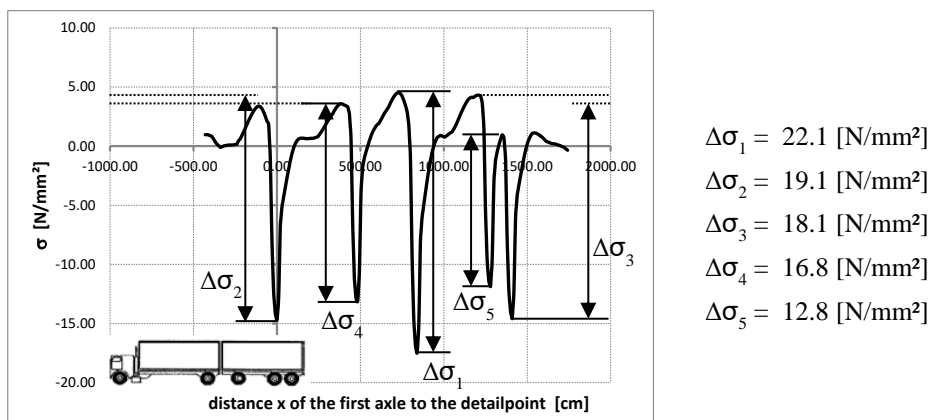


Figure A. 30: Model B – Detail D1b at the left web of LR-2 – stress history relating to a crossing of lorry type T5 according to FLM 4 at lane 1

A-2.3. Detail D2

The influence lines in longitudinal bridge direction and the stress history curves referring to detail D2 are shown in this Section. The stress range spectrum due to FLM 4 at the left web of LR-2 (lane 1) is already displayed in Figure 103 in Section 3.4.3 and therefore this is not shown any more.

A.2.3.1. Influence lines in longitudinal direction for wheel types A, B and C

The longitudinal influence lines for axle type B and C at the left web of LR-2 are already shown in Figure 101. Figure A. 31 shows the longitudinal influence lines due to axle type A at the left web of LR-2.

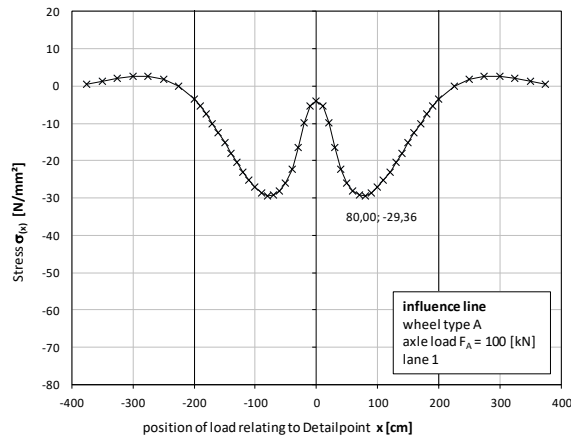


Figure A. 31: Model B – Detail D2 – influence line in longitudinal bridge direction due to axle type A and an axle load of $F_A = 100\text{kN}$ at the left web of LR-2 (lane 1);

A.2.3.2. Lorry crossings at the left web of LR-2 (Lane 1) according to FLM 4

Figure A. 32 to Figure A. 35 illustrate the stress history curves for the lorry crossings of T1 to T5 at the left web of LR-2 (lane 1). The stress history curve for lorry type T3 is already shown in Figure 102. Additionally, the occurring stress ranges are indicated in the diagrams.

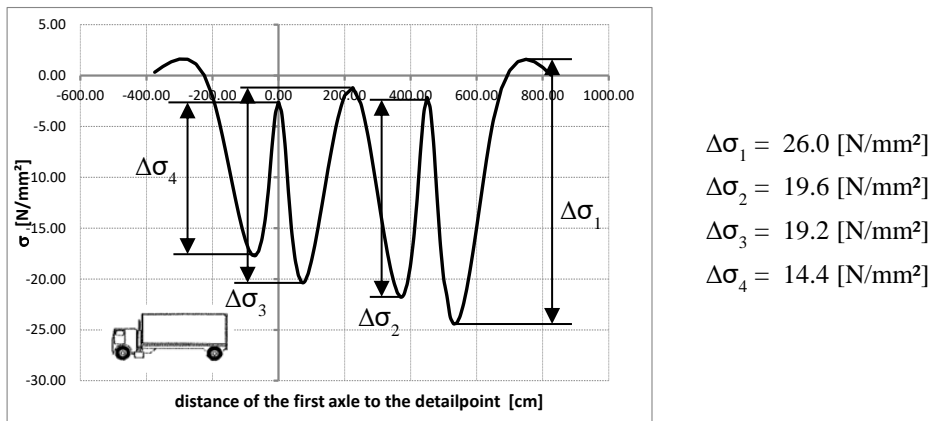


Figure A. 32: Model B – Detail D2 at the left web of LR-2 – stress history relating to a crossing of lorry type T1 according to FLM 4 at lane 1

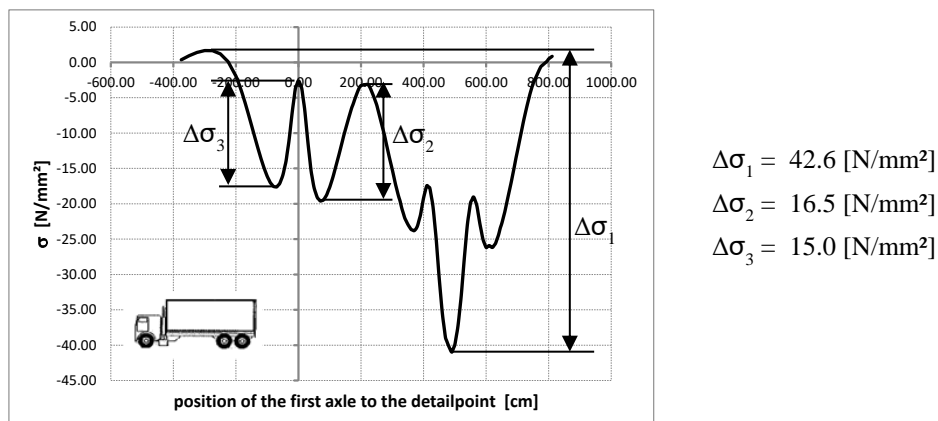


Figure A. 33: Model B – Detail D2 at the left web of LR-2 – stress history relating to a crossing of lorry type T2 according to FLM 4 at lane 1

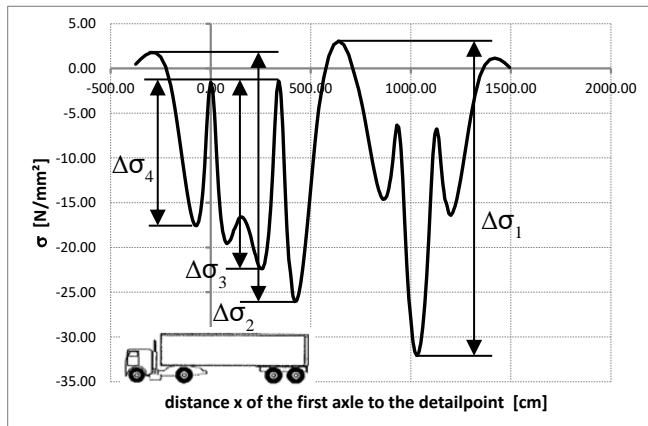


Figure A. 34: Model B – Detail D2 at the left web of LR-2 – stress history relating to a crossing of lorry type T4 according to FLM 4 at lane 1

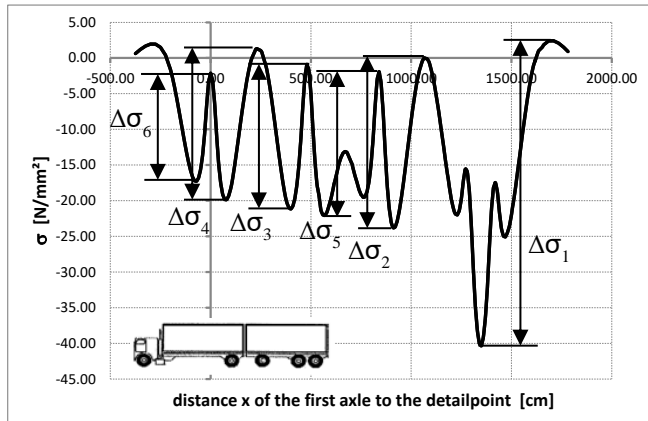


Figure A. 35: Model B – Detail D2 at the left web of LR-2 – stress history relating to a crossing of lorry type T5 according to FLM 4 at lane 1

A-3. MODEL C: ORTHOTROPIC BRIDGE DECK WITH TROUGH LONGITUDINAL RIBS AND CROSS GIRDER SPACING OF 4M

This Section presents a complete summary of the results regarding to the numerical calculations at model C which is described in Section 3.2.3. The simulation of the lorry crossings has been performed at the left web of LR-2 (lane 1) which is shown in Section 3.4.4.

A-3.1. Detail D1a

The influence lines in longitudinal bridge direction and the stress history curves referring to detail D1a are shown in this Section. The stress range spectrum due to FLM 4 at the left web of LR-2 (lane 1) is already displayed in Figure 107 in Section 3.4.4 and therefore this is not shown any more.

A.3.1.1. Influence lines in longitudinal direction for wheel types A, B and C

The longitudinal influence lines for axle type B and C at the left web of LR-2 are already shown in Figure 105. Figure A. 36 shows the longitudinal influence lines due to axle type A at the left web of LR-2.

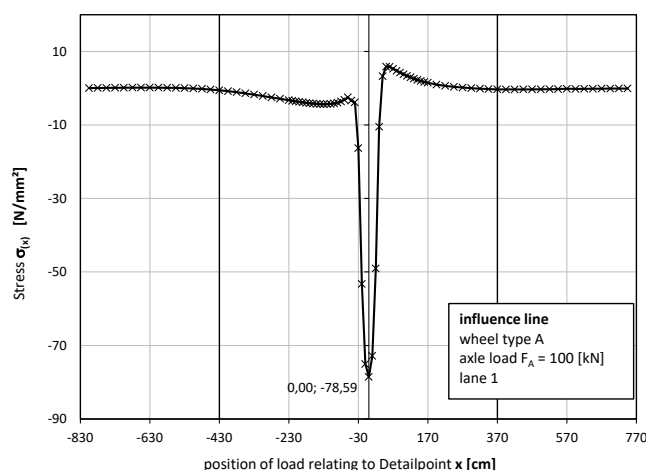
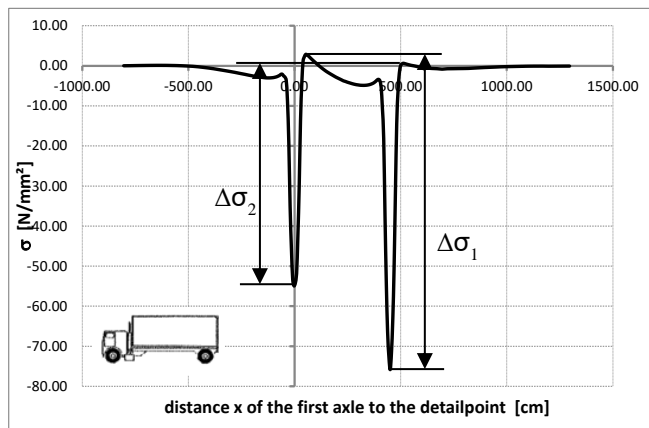


Figure A. 36: Model C – Detail D1a – influence line in longitudinal bridge direction due to axle type A and an axle load of $F_A = 100\text{kN}$ at the left web of LR-2 (lane 1);

A.3.1.2. Lorry crossings at the left web of LR-2 (Lane 1) according to FLM 4

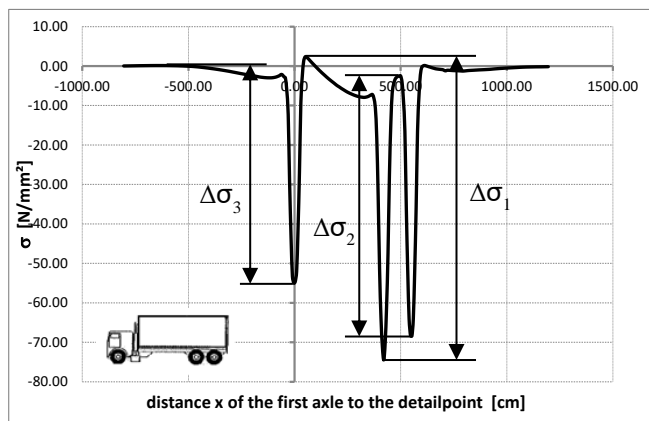
Figure A. 37 to Figure A. 40 illustrate the stress history curves for the lorry crossings of T1 to T5 at the left web of LR-2 (lane 1). The stress history curve for lorry type T3 is already shown in Figure 106. Additionally, the occurring stress ranges are indicated in the diagrams.



$$\Delta\sigma_1 = 78.7 \text{ [N/mm}^2\text{]}$$

$$\Delta\sigma_2 = 55.6 \text{ [N/mm}^2\text{]}$$

Figure A. 37: Model C – Detail D1a at the left web of LR-2 – stress history relating to a crossing of lorry type T1 according to FLM 4 at lane 1

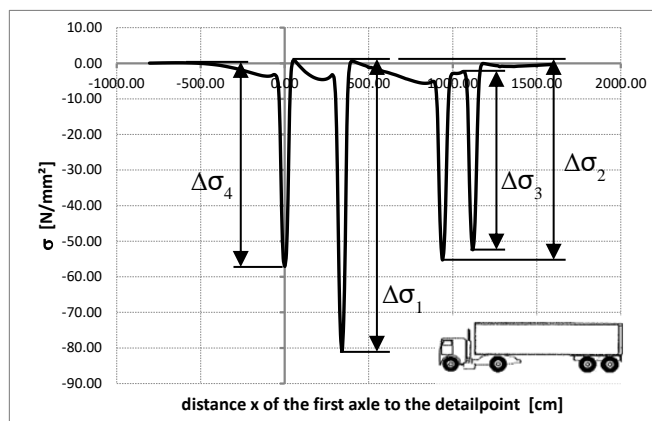


$$\Delta\sigma_1 = 74.7 \text{ [N/mm}^2\text{]}$$

$$\Delta\sigma_2 = 65.9 \text{ [N/mm}^2\text{]}$$

$$\Delta\sigma_3 = 39.2 \text{ [N/mm}^2\text{]}$$

Figure A. 38: Model C – Detail D1a at the left web of LR-2 – stress history relating to a crossing of lorry type T2 according to FLM 4 at lane 1



$$\Delta\sigma_1 = 81.7 \text{ [N/mm}^2\text{]}$$

$$\Delta\sigma_2 = 57.7 \text{ [N/mm}^2\text{]}$$

$$\Delta\sigma_3 = 55.4 \text{ [N/mm}^2\text{]}$$

$$\Delta\sigma_4 = 50.1 \text{ [N/mm}^2\text{]}$$

Figure A. 39: Model C – Detail D1a at the left web of LR-2 – stress history relating to a crossing of lorry type T4 according to FLM 4 at lane 1

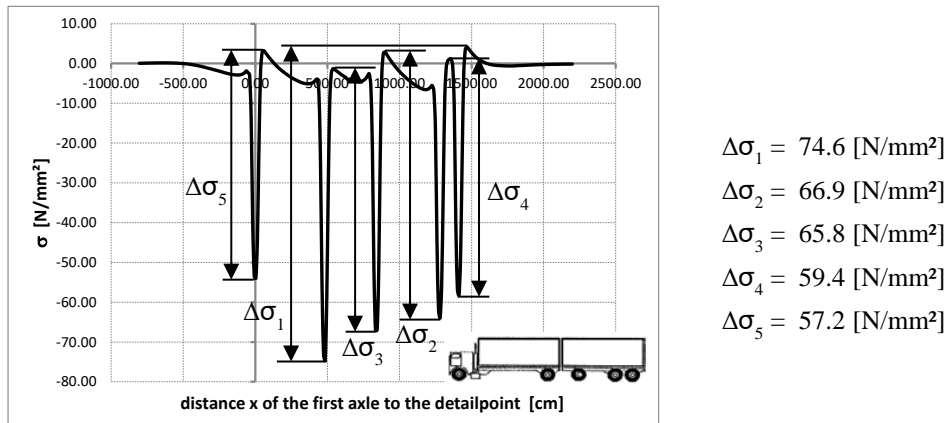


Figure A. 40: Model C – Detail D1a at the left web of LR-2 – stress history relating to a crossing of lorry type T5 according to FLM 4 at lane 1

A-3.2. Detail D1b

The influence lines in longitudinal bridge direction and the stress history curves referring to detail D1b are shown in this Section. The stress range spectrum due to FLM 4 at the left web of LR-2 (lane 1) is already displayed in Figure 110 in Section 3.4.4 and therefore this is not shown any more.

A.3.2.1. Influence lines in longitudinal direction for wheel types A, B and C

The longitudinal influence lines for axle type B and C at the left web of LR-2 are already shown in Figure 108. Figure A. 41 shows the longitudinal influence lines due to axle type A at the left web of LR-2.

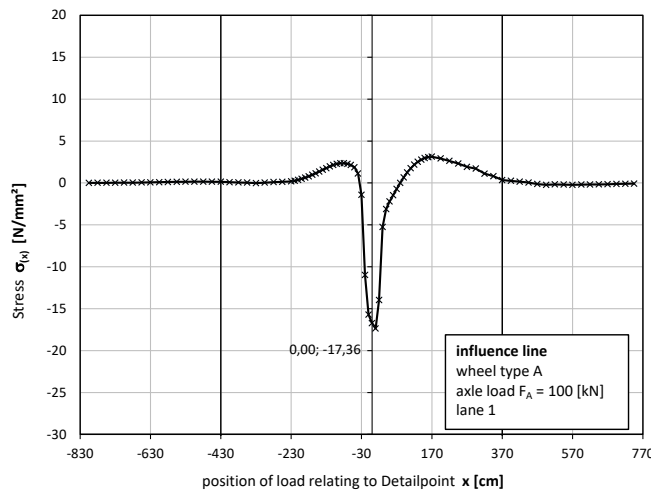


Figure A. 41: Model C – Detail D1b – influence line in longitudinal bridge direction due to axle type A and an axle load of $F_A = 100\text{ kN}$ at the left web of LR-2 (lane 1);

A.3.2.2. Lorry crossings at the left web of LR-2 (Lane 1) according to FLM 4

Figure A. 42 to Figure A. 45 illustrate the stress history curves for the lorry crossings of T1 to T5 at the left web of LR-2 (lane 1). The stress history curve for lorry type T3 is already shown in Figure 109. Additionally, the occurring stress ranges are indicated in the diagrams.

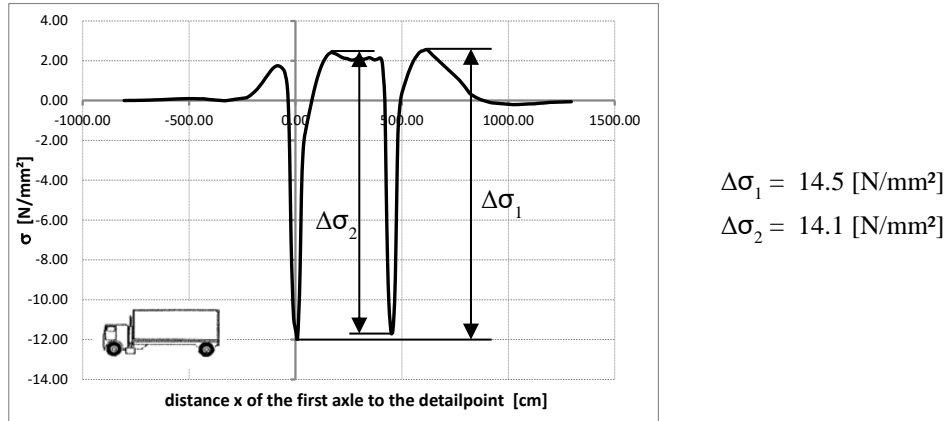


Figure A. 42: Model C – Detail D1b at the left web of LR-2 – stress history relating to a crossing of lorry type T1 according to FLM 4 at lane 1

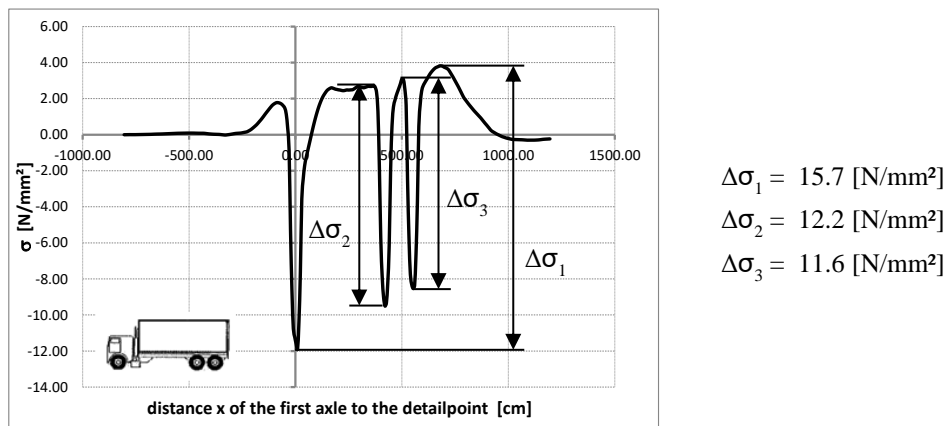


Figure A. 43: Model C – Detail D1b at the left web of LR-2 – stress history relating to a crossing of lorry type T2 according to FLM 4 at lane 1

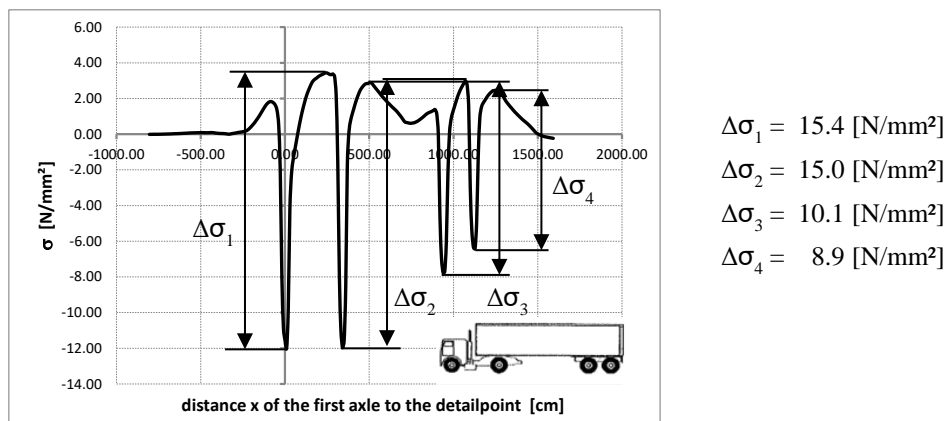


Figure A. 44: Model C – Detail D1b at the left web of LR-2 – stress history relating to a crossing of lorry type T4 according to FLM 4 at lane 1

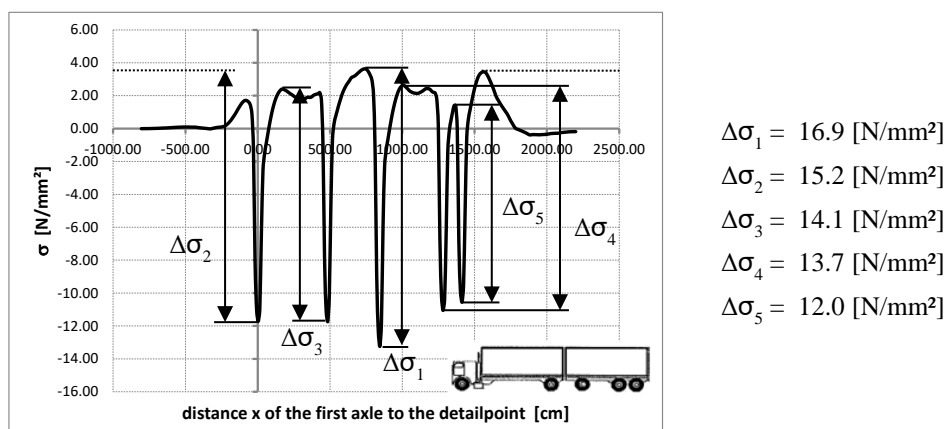


Figure A. 45: Model C – Detail D1b at the left web of LR-2 – stress history relating to a crossing of lorry type T5 according to FLM 4 at lane 1

A-3.3. Detail D2

The influence lines in longitudinal bridge direction and the stress history curves referring to detail D2 are shown in this Section. The stress range spectrum due to FLM 4 at the left web of LR-2 (lane 1) is already displayed in Figure 113 in Section 3.4.4 and therefore this is not shown any more.

A.3.3.1. Influence lines in longitudinal direction for wheel types A, B and C

The longitudinal influence lines for axle type B and C at the left web of LR-2 are already shown in Figure 111. Figure A. 46 shows the longitudinal influence lines due to axle type A at the left web of LR-2.

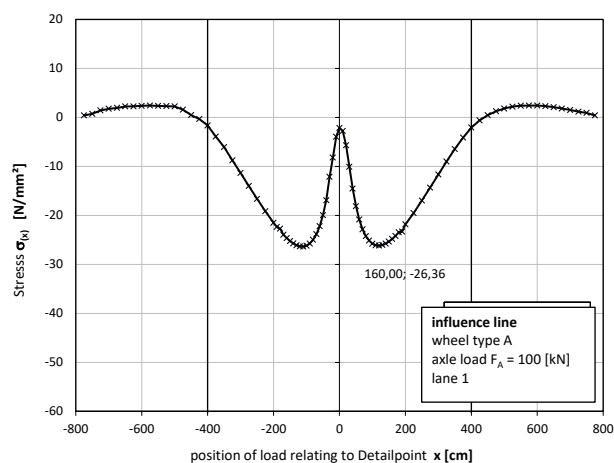


Figure A. 46: Model C – Detail D2 – influence line in longitudinal bridge direction due to axle type A and an axle load of $F_A = 100\text{kN}$ at the left web of LR-2 (lane 1);

A.3.3.2. Lorry crossings at the left web of LR-2 (Lane 1) according to FLM 4

Figure A. 47 to Figure A. 50 illustrate the stress history curves for the lorry crossings of T1 to T5 at the left web of LR-2 (lane 1). The stress history curve for lorry type T3 is already shown in Figure 112. Additionally, the occurring stress ranges are indicated in the diagrams.

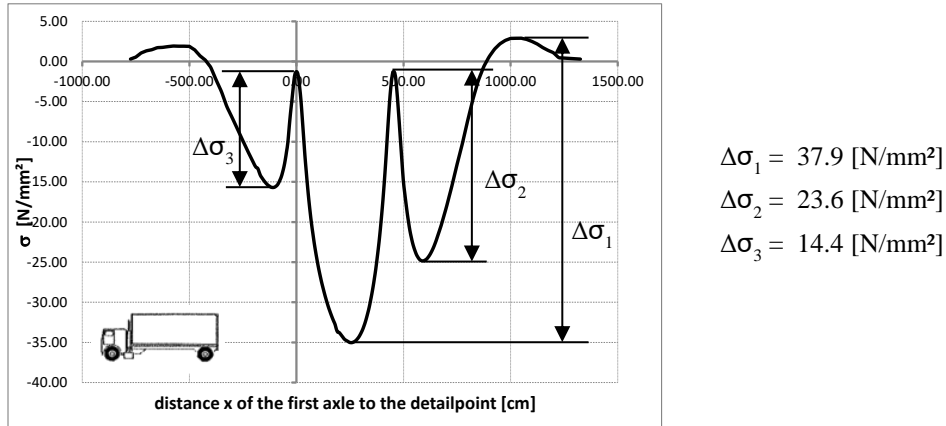


Figure A. 47: Model C – Detail D2 at the left web of LR-2 – stress history relating to a crossing of lorry type T1 according to FLM 4 at lane 1

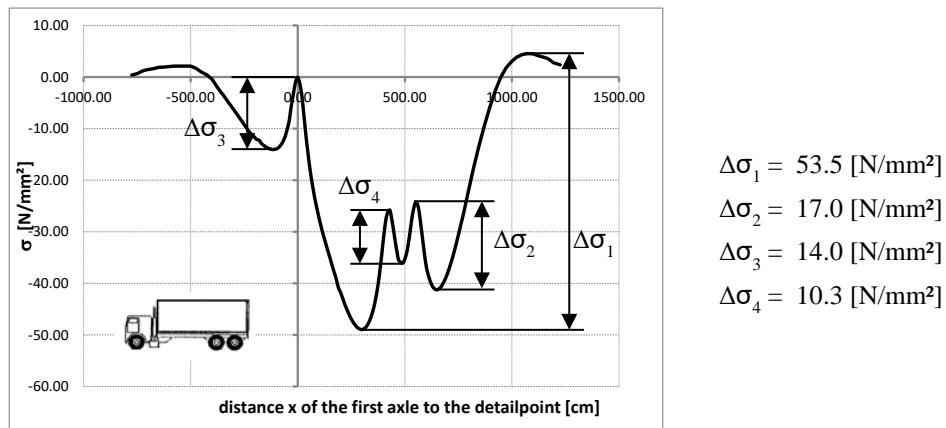


Figure A. 48: Model C – Detail D2 at the left web of LR-2 – stress history relating to a crossing of lorry type T2 according to FLM 4 at lane 1

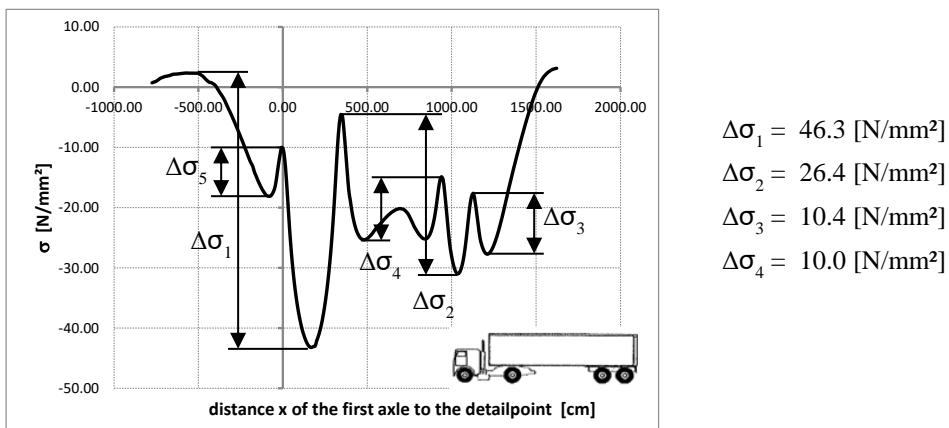


Figure A. 49: Model C – Detail D2 at the left web of LR-2 – stress history relating to a crossing of lorry type T4 according to FLM 4 at lane 1

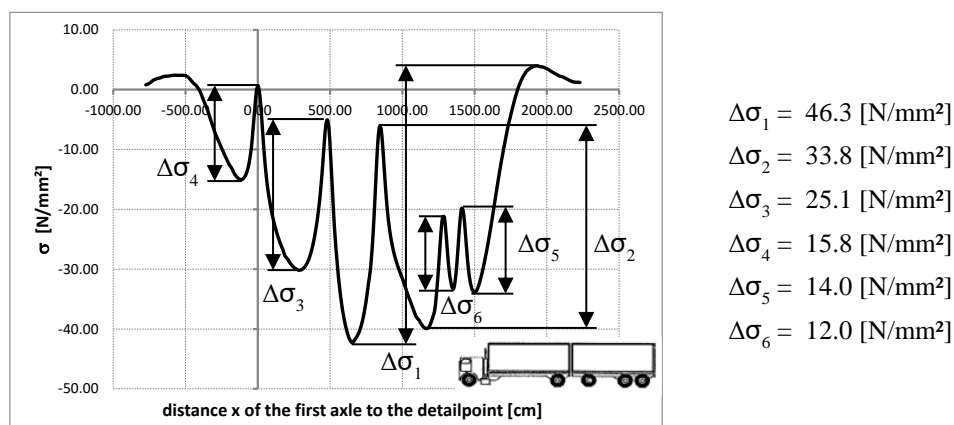


Figure A. 50: Model C – Detail D2 at the left web of LR-2 – stress history relating to a crossing of lorry type T5 according to FLM 4 at lane 1

A-4. MODEL D: ORTHOTROPIC BRIDGE DECK WITH OPEN LONGITUDINAL RIBS – CROSS GIRDER WITH FIELD SPLICES

This Section shows a complete summary of the results of the numerical calculations for detail D3 (see Section 2.4.5) at model D under consideration of the appropriate lad case (lorry type T2), which is presented in Figure 81 in Section 3.3.4. The finite element model is illustrated and described in Section 3.2.4. The relevant results of these simulations are already shown in Figure 115 (joint I/III) and Figure 116 (joint II) in Section 3.4.5. These pictures also illustrate an overview of the analysed regions (region I to region IV) in the local areas of the bolted connections. In the following, the determined maximum and minimum principal stresses are shown in detail referring to the analysed regions mentioned above.

A-4.1. Joint I

The following Figures A.51 to A.60 show the calculated max. and min. principal stresses in region I to IV.

A.4.1.1. Region I of joint I/III

Figure A. 51 illustrates the maximum and Figure A. 52 the minimum principal stresses in region I of joint I/III.

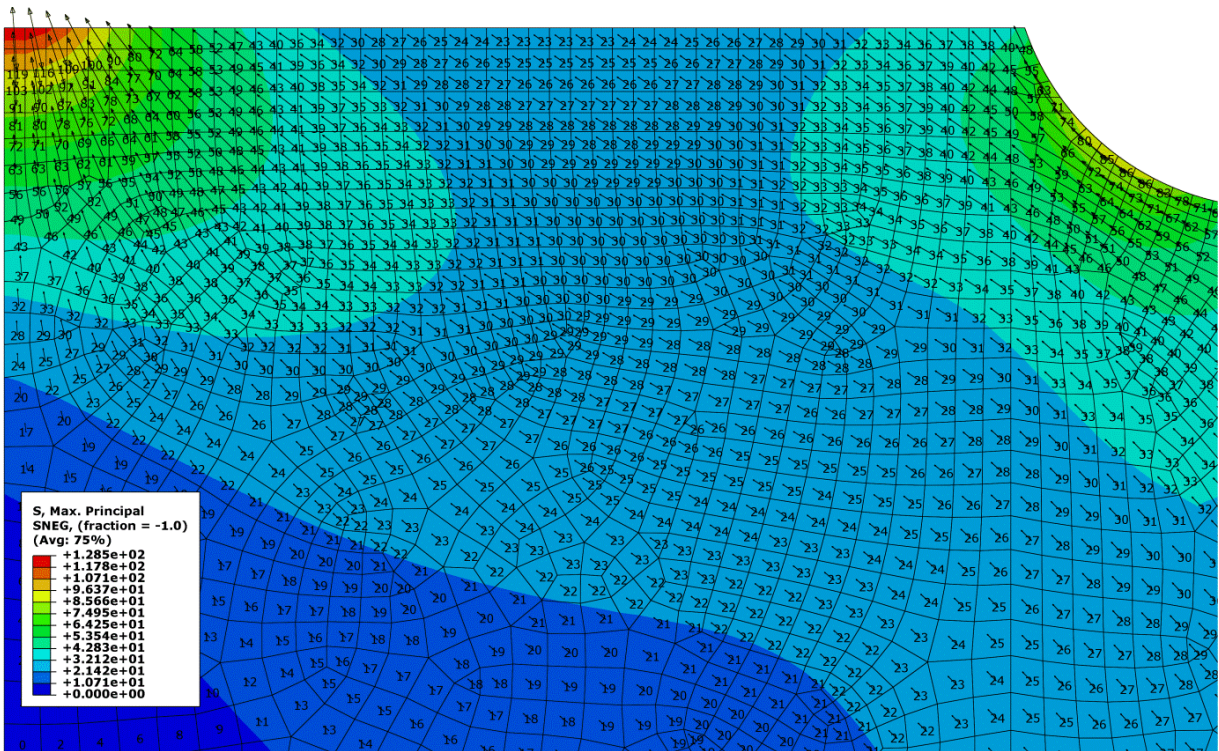


Figure A. 51: Model D – Detail D3 at joint I/III, region I – maximum principal stresses due to lorry type T2 according to FLM 4* at lane 2

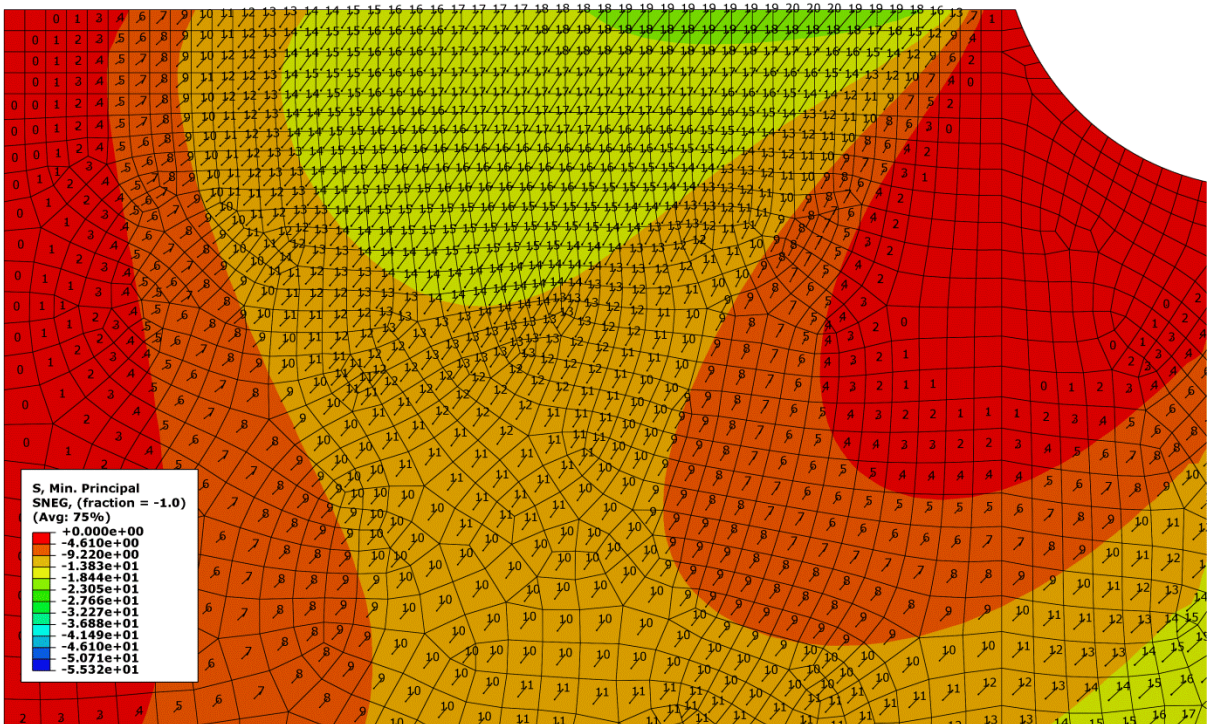


Figure A. 52: Model D – Detail D3 at joint I/III, region I – minimum principal stresses due to lorry type T2 according to FLM 4* at lane 2

A.4.1.2. Region II of joint I/III

Figure A. 53 illustrates the maximum and Figure A. 54 the minimum principal stresses in region II of joint I/III.

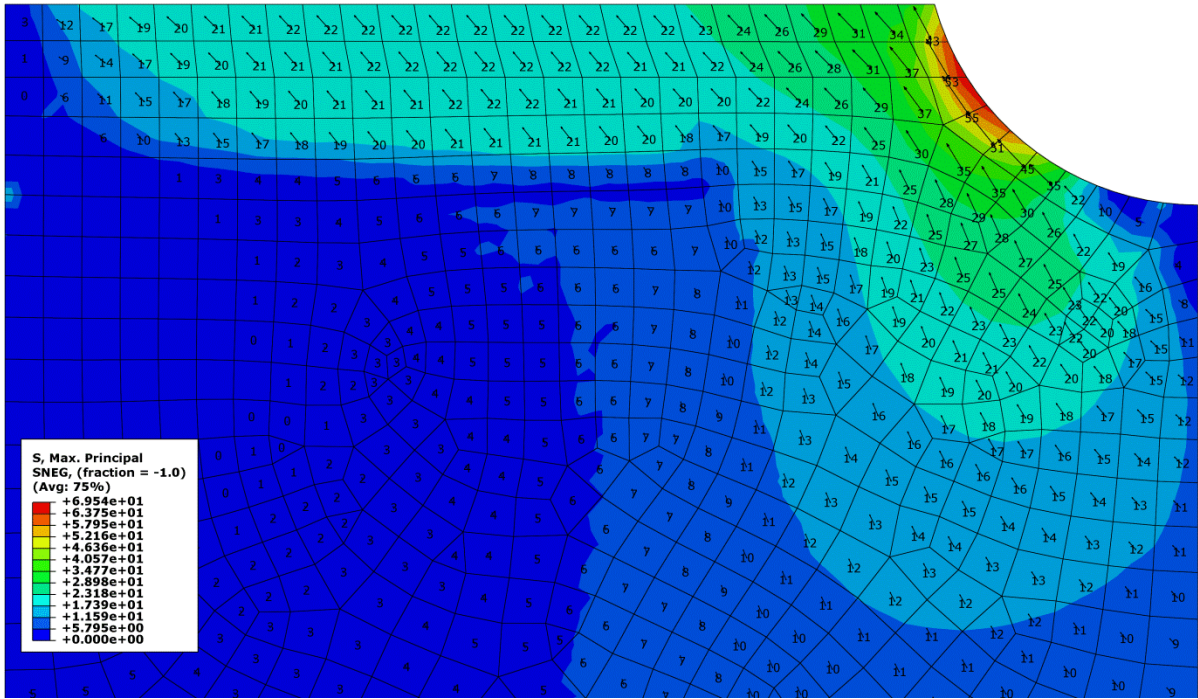


Figure A. 53: Model D – Detail D3 at joint I/III, region II – maximum principal stresses due to lorry type T2 according to FLM 4* at lane 2

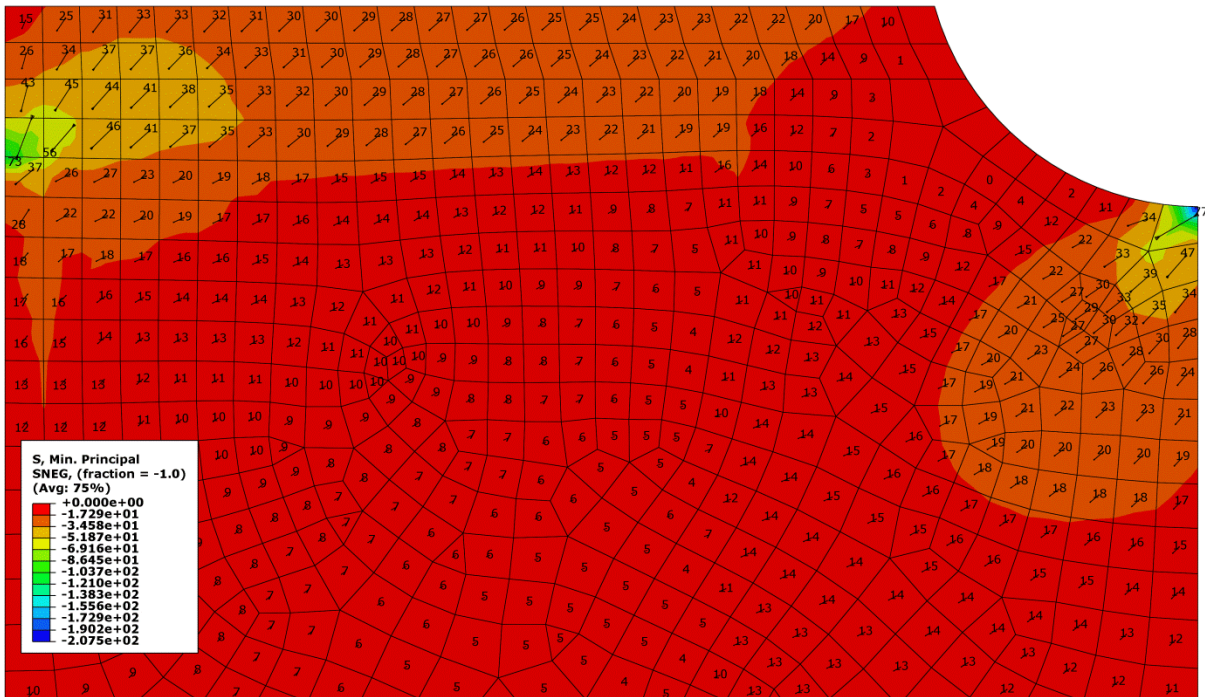


Figure A. 54: Model D – Detail D3 at joint I/III, region II – minimum principal stresses due to lorry type T2 according to FLM 4* at lane 2

A.4.1.3. Region III of joint I/III

Figure A. 55 illustrates the maximum and Figure A. 56 the minimum principal stresses in region III of joint I/III.

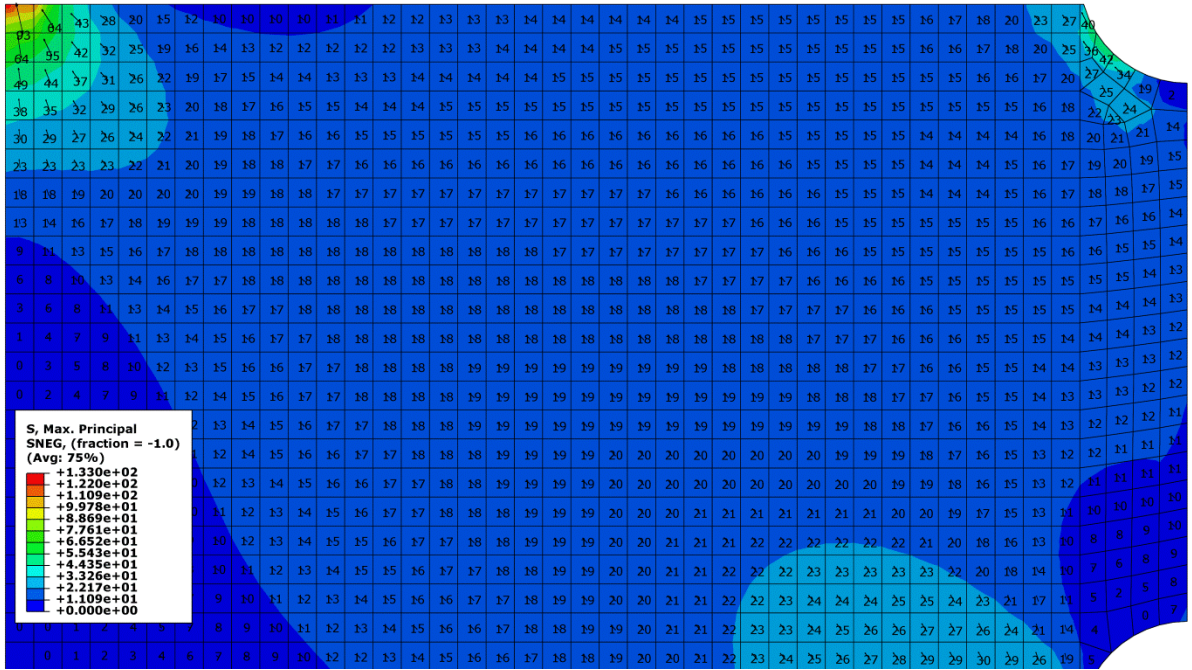


Figure A. 55: Model D – Detail D3 at joint I/III, region III – maximum principal stresses due to lorry type T2 according to FLM 4* at lane 2

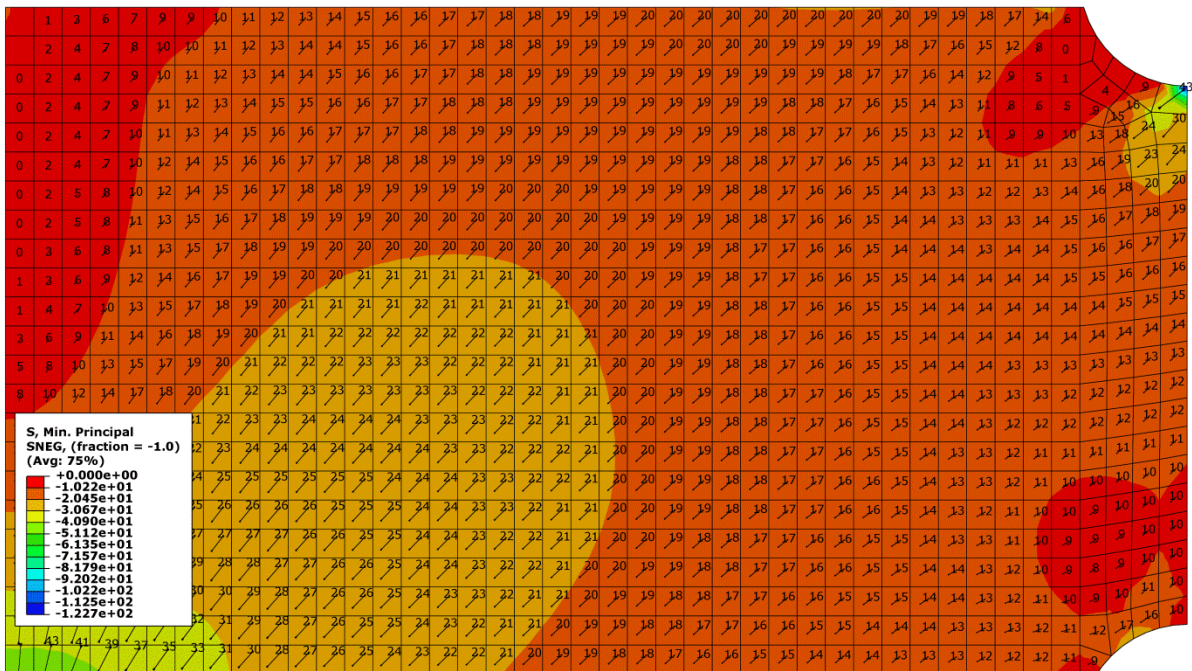


Figure A. 56: Model D – Detail D3 at joint I/III, region III – minimum principal stresses due to lorry type T2 according to FLM 4* at lane 2

A.4.1.4. Region IV of joint I/III

Figure A. 57 illustrates the maximum and Figure A. 58 the minimum principal stresses in region IV of joint I/III.

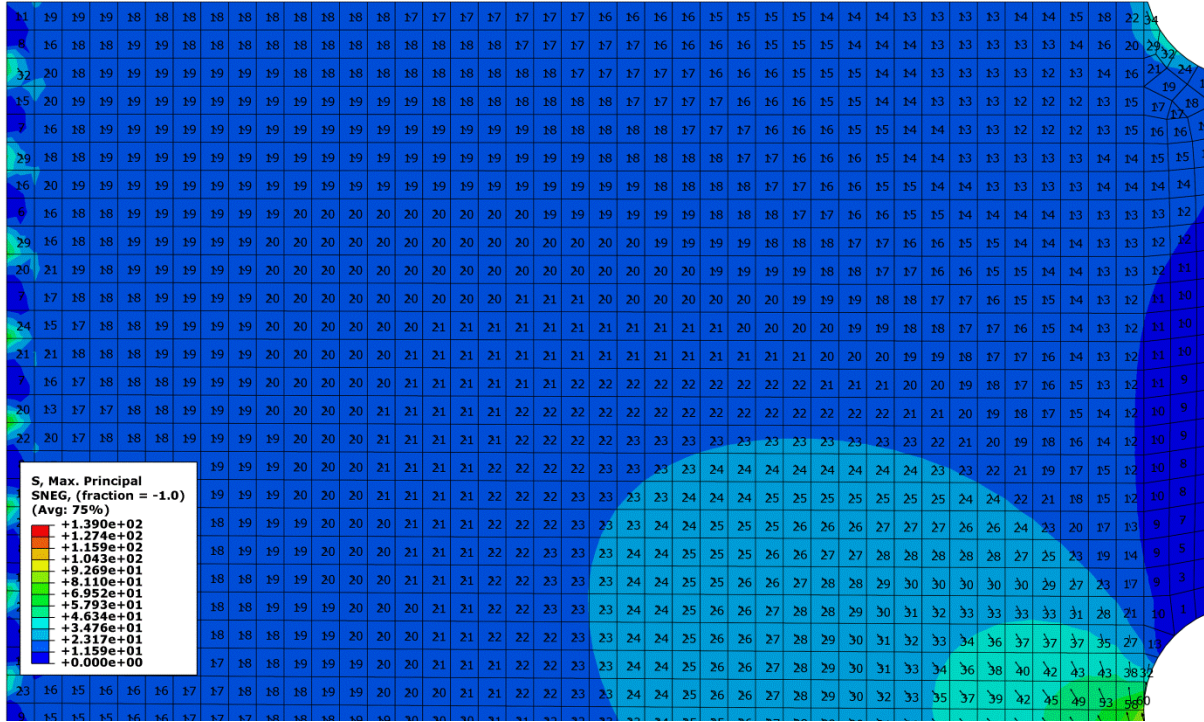


Figure A. 57: Model D – Detail D3 at joint I/III, region IV – maximum principal stresses due to lorry type T2 according to FLM 4* at lane 2



Figure A. 58: Model D – Detail D3 at joint I/III, region IV – minimum principal stresses due to lorry type T2 according to FLM 4* at lane 2

A-4.2. Joint II

The following Figures A.59 to A.66 show the calculated max. and min. principal stresses in region I to IV.

A.4.2.1. Region I of joint II

Figure A. 59 illustrates the maximum and Figure A. 60 the minimum principal stresses in region I of joint II.

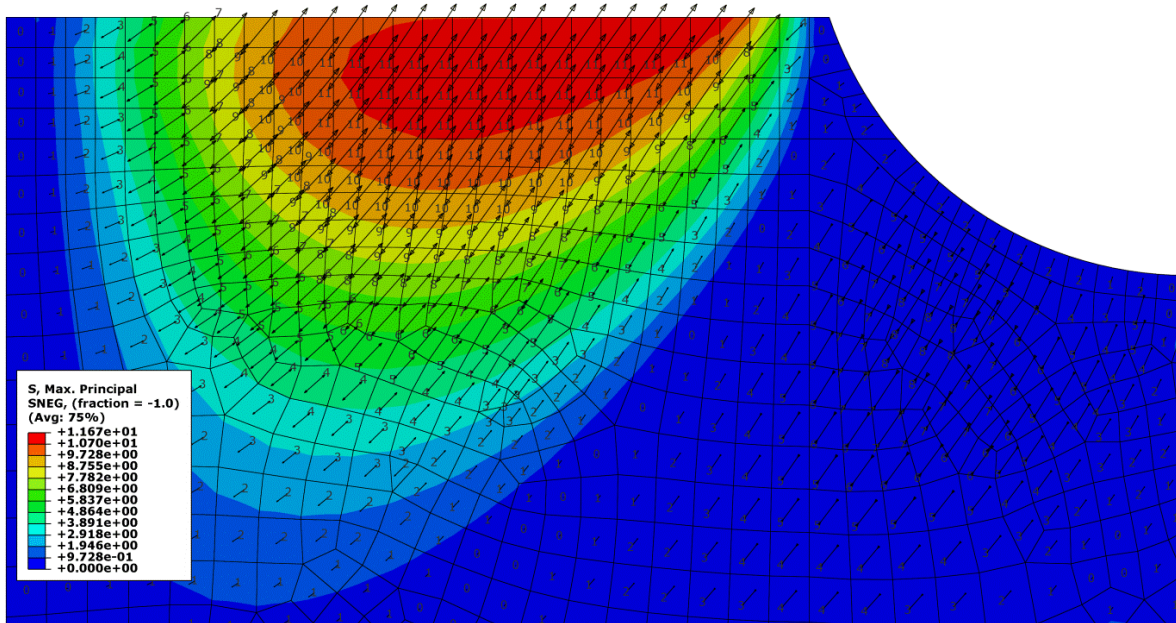


Figure A. 59: Model D – Detail D3 at joint II, region I – maximum principal stresses due to lorry type T2 according to FLM 4* at lane 2

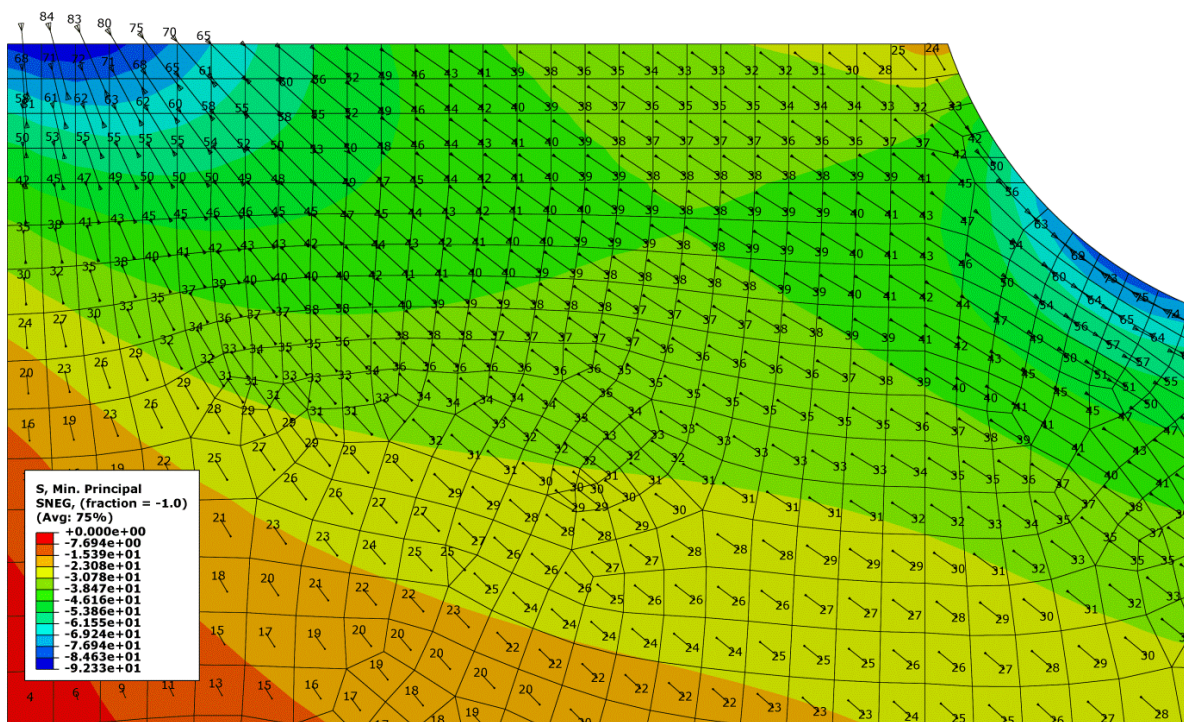


Figure A. 60: Model D – Detail D3 at joint II, region I – minimum principal stresses due to lorry type T2 according to FLM 4* at lane 2

A.4.2.2. Region II of joint II

Figure A. 61 illustrates the maximum and Figure A. 62 the minimum principal stresses in region II of joint II.

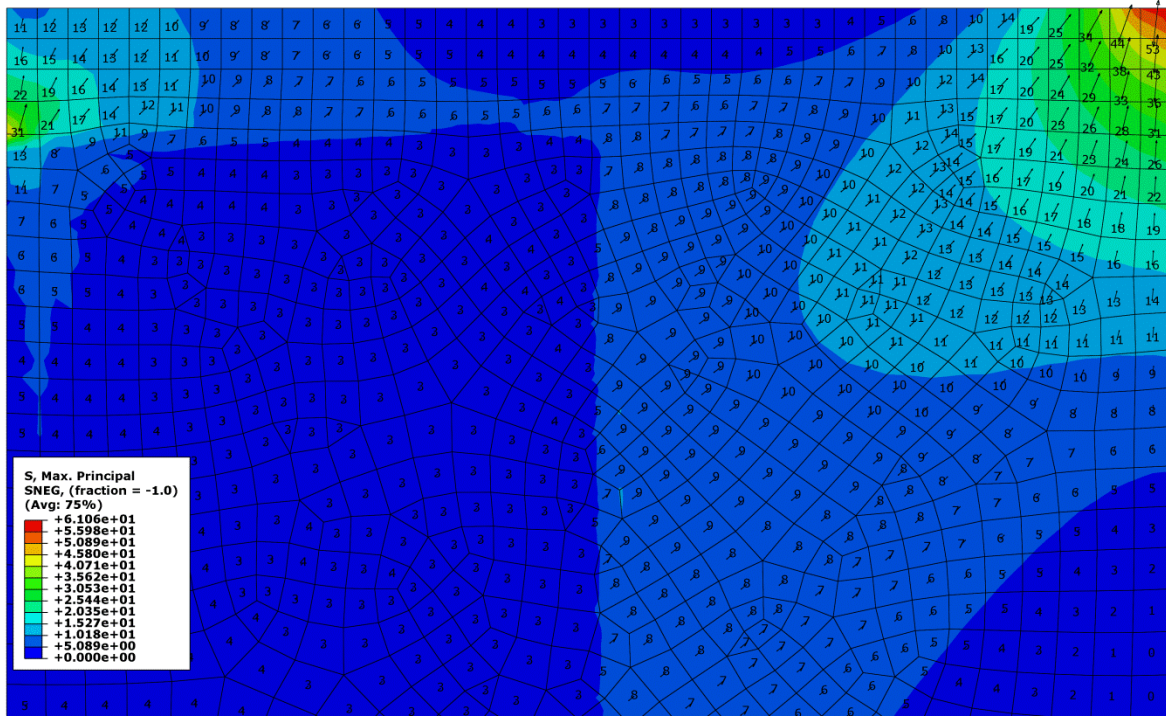


Figure A. 61: Model D – Detail D3 at joint II, region II – maximum principal stresses due to lorry type T2 according to FLM 4* at lane 2

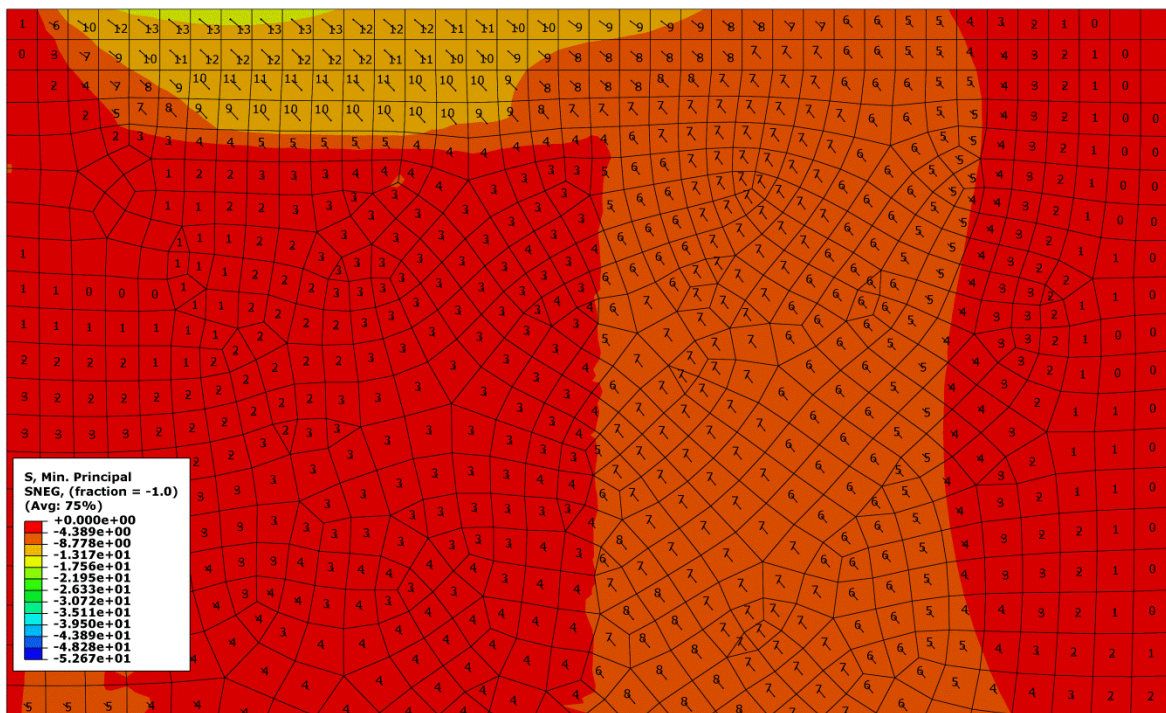


Figure A. 62: Model D – Detail D3 at joint II, region II – minimum principal stresses due to lorry type T2 according to FLM 4* at lane 2

A.4.2.3. Region III of joint II

Figure A. 63 illustrates the maximum and Figure A. 64 the minimum principal stresses in region III of joint II.

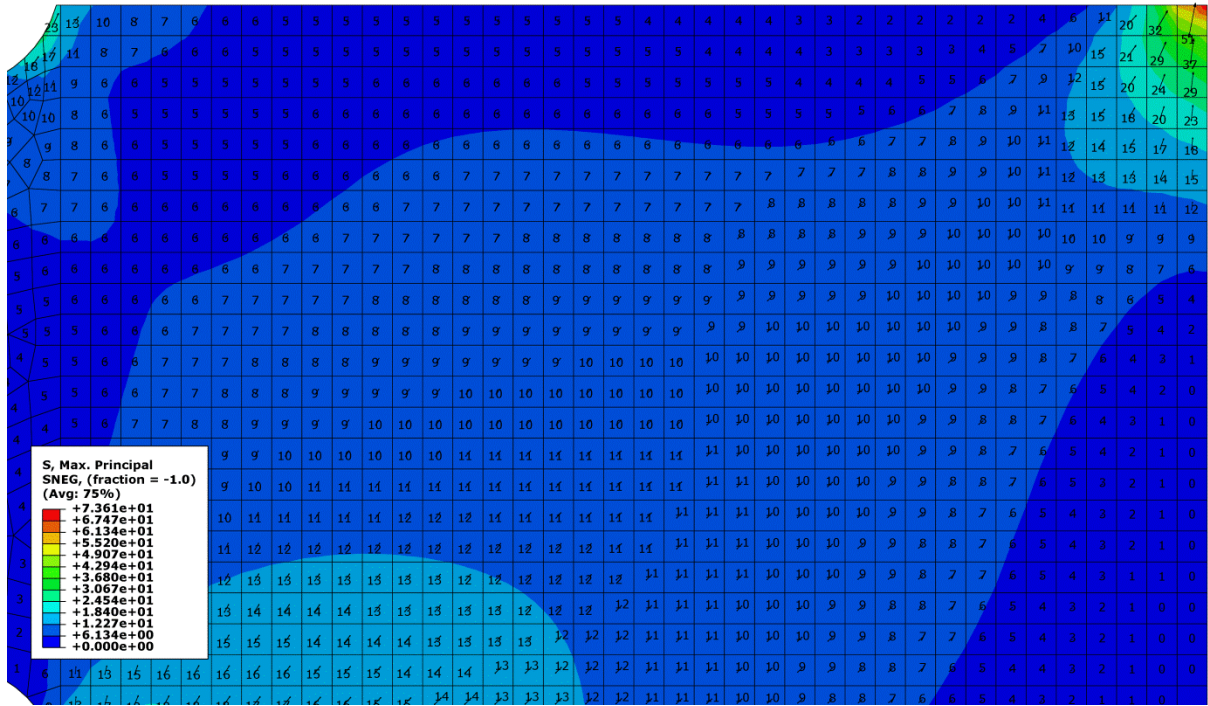


Figure A. 63: Model D – Detail D3 at joint II, region III – maximum principal stresses due to lorry type T2 according to FLM 4* at lane 2

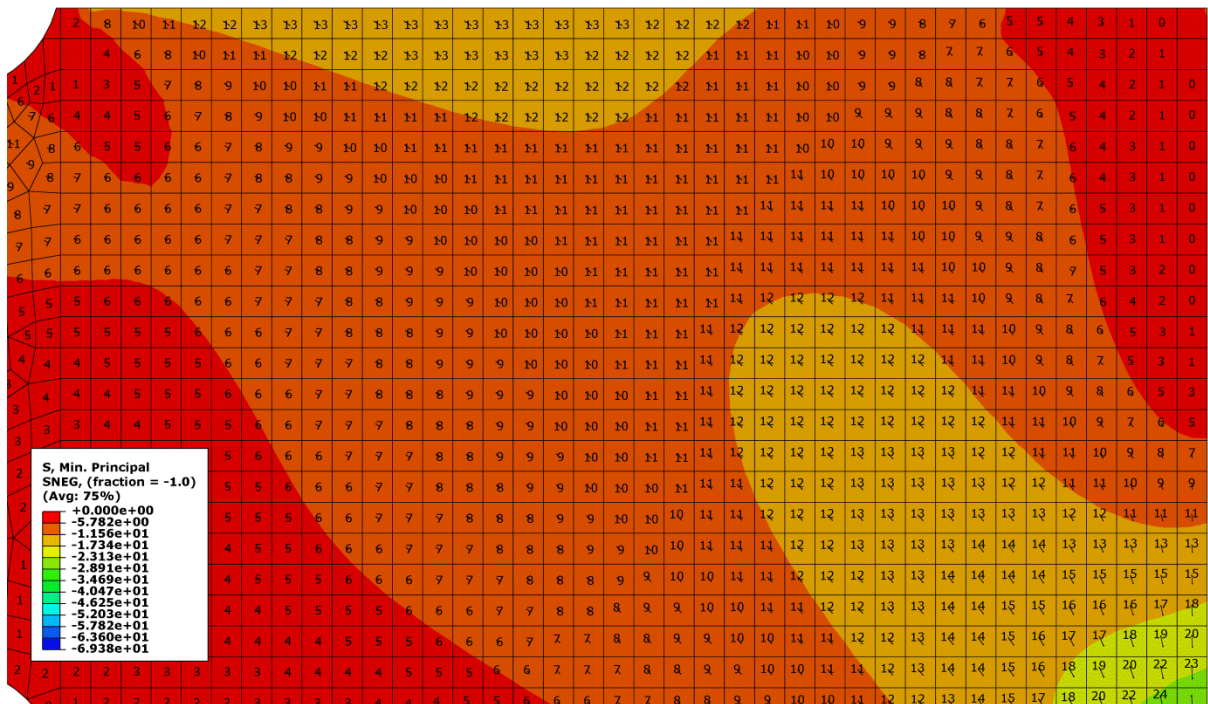


Figure A. 64: Model D – Detail D3 at joint II, region III – minimum principal stresses due to lorry type T2 according to FLM 4* at lane 2

A.4.2.4. Region IV of joint II

Figure A. 65 illustrates the maximum and Figure A. 66 the minimum principal stresses in region IV of joint II.

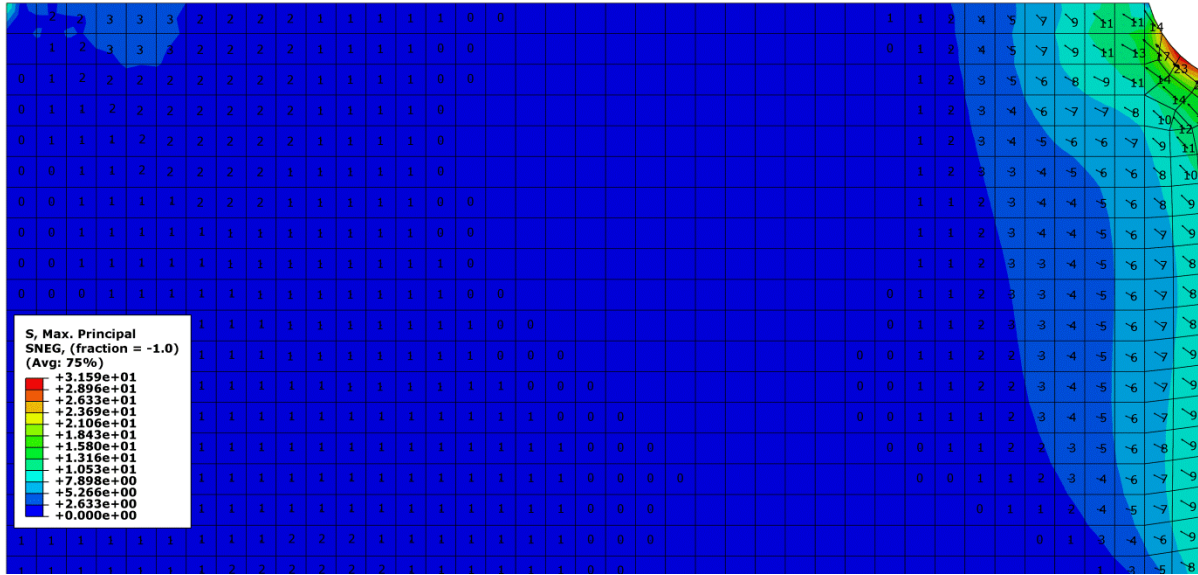


Figure A. 65: Model D – Detail D3 at joint II, region IV – maximum principal stresses due to lorry type T2 according to FLM 4* at lane 2



Figure A. 66: Model D – Detail D3 at joint II, region IV – minimum principal stresses due to lorry type T2 according to FLM 4* at lane 2